

**Pre-Conceptual Design Report (pCDR)  
for  
The Science and Experimental Equipment  
for  
The 12 GeV Upgrade of CEBAF**

Draft 14.2

Jefferson Lab

May 16, 2004

Jefferson Lab is managed and operated by  
the Southeastern Universities Research Association (SURA) for  
the Office of Science of the U.S. Department of Energy.

Thomas Jefferson National Accelerator Facility  
12000 Jefferson Avenue  
Newport News, VA 23606  
[www.jlab.org](http://www.jlab.org)  
(757)-269-7100



## Abstract

This Pre-Conceptual Design Report (pCDR) presents the compelling scientific case for upgrading the Continuous Electron Beam Accelerator Facility (CEBAF) at Jefferson Lab to 12 GeV. Such a facility will make profound contributions to the study of nuclear matter. In particular, it will allow breakthrough programs to be launched in four main areas:

- *The experimental study of gluonic excitations in order to understand the fundamentally new dynamics that underpins all of nuclear physics: the confinement of quarks.* Theoretical conjectures, now strengthened by lattice QCD simulations, indicate that the most spectacular new prediction of QCD – quark confinement – occurs through the formation of a string-like “flux tube” between quarks. This conclusion (and proposed mechanisms of flux tube formation) can be tested by determining the spectrum of the gluonic excitations of mesons.
- *The determination of the quark and gluon wavefunctions of the nuclear building blocks.* A vast improvement in our knowledge of the fundamental structure of the proton and neutron can be achieved. Not only can existing “deep inelastic scattering” cross sections be extended for the first time to cover the critical region where their basic three-quark structure dominates, but also measurements of new “deep exclusive scattering” cross sections will open the door to a comprehensive characterization of these wavefunctions using the framework of the Generalized Parton Distributions; these data will provide access to information on the correlations among the quarks. These studies will be complemented by detailed measurements of elastic and transition form factors, determining the dynamics underlying the quark-gluon wavefunctions through measurements of their high-momentum-transfer behavior and providing essential constraints on the wavefunctions.
- *Exploring the limits of our understanding of atomic nuclei.* A broad and diversified program of measurements that (taken together with the hadron studies outlined above) aims to provide a firm intellectual underpinning for all of nuclear physics by answering the question “How does the phenomenological description of nuclei as nucleons interacting via an effective interaction parameterized using meson exchange arise from the underlying dynamics of quarks and gluons?” It has two main components:

*The short-range behavior of the Nucleon–Nucleon ( $N - N$ ) interaction and its QCD basis.* Experiments aimed at identifying the physics of strong QCD that gives rise to the  $N - N$  force and exploring the short range behavior of the  $N - N$  force through a novel program of deep inelastic scattering.

*Identifying and exploring the transition from the nucleon/meson description of nuclei to the underlying quark and gluon description.* This program will explore and determine the limits of applicability of the nucleon/meson description of nuclei, identifying the distance and energy scales at which it fails and the physics of nuclei is better described directly via strong QCD.

- *Tests of the Standard Model of electro-weak interactions and the determination of fundamental parameters of this model.* Precision, parity-violating electron scattering experiments made feasible by the 12 GeV Upgrade have the sensitivity to search for deviations from the Standard Model that could signal the presence of new physics. Planned studies of the three neutral pseudoscalar mesons, the  $\pi^0$ ,  $\eta$  and  $\eta'$ , will provide fundamental information about low energy QCD, characterizing the strengths of the chiral anomalies.

This science program has expanded significantly in the two years since the project was first presented to the Nuclear Sciences Advisory Committee (NSAC) in the form of a White Paper [WP01] produced as part of the 2001-2002 NSAC Long Range Planning Process. While focusing on science, this pCDR also provides a detailed description of the required detector and accelerator upgrades so that it can serve as an overview of the entire plan for the 12 GeV project.





## PREFACE

When the scientific case was made for the facility that became CEBAF, there was unanimous agreement on the importance of a continuous-beam electron accelerator but a great deal of discussion about the optimum beam energy. A subcommittee of NSAC (the Nuclear Science Advisory Committee of the U.S. Department of Energy and the National Science Foundation) chaired by Peter Barnes concluded [Ba82] that the accelerator’s design energy should be 4 GeV, rather than the 2 GeV favored by some, because the higher energy would permit its experimental program “to study the largely unexplored transition between the nucleon-meson and the quark-gluon descriptions of nuclear systems”. In anticipation of the future need to extend this experimental program to even higher momentum and energy transfers, the CEBAF accelerator was designed in the mid-1980s so that future extensions to energies of order 25 GeV would be straightforward.

As CEBAF’s scientific program has progressed, the wisdom of these design choices has become increasingly clear. This White Paper outlines the scientific case for the upgrade of CEBAF to 12 GeV, and documents the accelerator and experimental equipment improvements necessary to carry out the scientific program. It is the result of lengthy discussions within the Jefferson Lab community that began as the 4 GeV program was just underway in the mid-1990s. In this preface we remind the reader of the main activities leading to this plan for the 12 GeV Upgrade.

As CEBAF neared completion and its experimental program was about to begin, the CEBAF User Group began an examination of the physics accessible with an upgraded CEBAF energy. This decision led to the organization of a workshop held at Jefferson Lab from 14 to 16 April 1994. It was organized into four working groups centered around four main physics topics, by an organizing committee consisting of T. Barnes, R. Ent, B. Frois, R. Holt, R. Milner, P. Mulders, J. Napolitano, M. Petratos, and P. Stoler. Each working group was represented by one or two plenary speakers who were asked to summarize the outstanding physics issues that could be addressed by an upgrade, and by many shorter parallel contributions dealing with specific issues. Members of the organizing committee then summarized their presentations and their personal views on the physics case for an upgrade of CEBAF to higher energies. The result was the “yellow book” report, *CEBAF at Higher Energies*, edited by Paul Stoler for the CEBAF User Group and Nathan Isgur for Jefferson Lab, which marked the first step toward the goal of defining the physics program that would form the basis of an upgrade of CEBAF.

The compelling science which emerged from this workshop led to a study of the upgrade options by a laboratory strategic planning group, and to two “village meetings”. These studies indicated that a cost-effective upgrade of CEBAF is possible. These conclusions were presented to NSAC, which responded in the recommendations of its 1996 Long Range Plan that “the community looks forward to future increases in CEBAF’s energy and to the scientific opportunities that would bring”.

With this encouragement, the users held a second workshop from 15 to 18 June 1998. This

workshop, organized by Steve Dytman, Howard Fenker, and Phil Roos, was structured to review the physics motivation for the Upgrade, but to focus on the specification of the equipment and instrumentation necessary for measurements at 12 GeV. It began with plenary sessions on physics, on the issues faced by Halls A, B, and C at 12 GeV, on the preliminary designs of a new Hall D for photoproduction, and on state-of-the-art detector and polarized-source developments. Next came parallel sessions organized by physics topic on photoproduction, high- $Q^2$  reactions, hadrons in the nuclear medium, and inclusive and semi-inclusive reactions. These were followed by parallel sessions organized by hall. More than 180 scientists participated in the workshop; their work is recorded in *Physics and Instrumentation with 6–12 GeV Beams*, edited by the three organizers. A remarkable feature of this workshop was the quick consensus reached on the set of detectors needed to exploit the vast new physics potential of the 12 GeV Upgrade.

In anticipation of the 2001 NSAC Long Range Plan, the User Group organized a special workshop in January 2000 that was devoted to delineating the 12 GeV program for the existing experimental halls. It commissioned five follow-on working groups to develop crisp scientific cases and identify key experiments or key experimental programs in five target areas focused on these halls. Following the January workshop, at their March 2000 meeting the User Group Board of Directors appointed a White Paper Steering Committee: Lawrence Cardman, Rolf Ent, Nathan Isgur, Jean-Marc Laget, Christoph Leemann, Curtis Meyer, and Zein-Eddine Meziani.

Prior to and in parallel with this effort, the new Hall D Collaboration produced a design for a new meson photoproduction facility designed to discover and investigate the properties of gluonic excitations. Their design underwent a rigorous review in December 1999 by a distinguished external committee; the collaboration emerged from the review having received high praise for both their physics goals and their experimental design.

In 2000 the users reviewed an early draft version of this White Paper at their annual June meeting, which was once again devoted to the Upgrade. At that meeting, key experiments were selected from the many ideas that emerged from the planning for the Upgrade. These experiments were developed in greater detail, for inclusion as part of the scientific case for the Upgrade, and presented to the Jefferson Lab Program Advisory Committee at a special meeting of that committee. The PAC commented on each proposal in a manner similar to their review of research proposals for the present accelerator. In summarizing their review, the PAC noted:

*The laboratory and the user community have developed an impressive scientific case that demands this new capability. The Jefferson Lab Program Advisory Committee was charged by the laboratory to review this science, and to review the plans for the associated experimental equipment.*

*The committee concludes that an outstanding scientific case has been identified which requires the unique capabilities of the JLab 12 GeV upgrade. The results of these experiments are likely to significantly change the way we think about nuclear physics and the*

*strong (nonperturbative) limit of QCD. Two major new thrusts can produce definitive results: the experimental verification of the origin of quark confinement by QCD flux tubes as predicted by lattice gauge calculations, and the determination of the quark and gluon wave functions of the nuclear building blocks. The full technical capabilities of the upgrade are required for this progress. New research domains are also opened up that show great promise in leading existing research efforts to new levels of understanding.*

*The proposed experimental equipment is well suited to addressing these new physics opportunities. The choices capitalize on the powerful existing equipment at the laboratory without compromising the physics goals.*

*The Program Advisory Committee was excited by the research potential that the 12 GeV upgrade makes possible. The scope of the upgrade is very well matched to the problems we see driving the field for the next decade. The time has come to bring these opportunities to nuclear physics.*

The White Paper was improved, based on the PAC discussions, on discussion at the NSAC Long Range Plan Town Meeting held at Jefferson Lab in December 2000, and on additional community input, and a final version was published in February 2001 as a formal submission to the larger nuclear physics community as part of the Long Range Planning process. That White paper served to document both the science and the technical aspects of the proposed Upgrade, and provided essential information for the discussions of the Upgrade that were held as part of the formal “resolution” meeting of the NSAC LRP held in SantaFe, NM during the week of March 25, 2001.

The formal report of the NSAC Long Range Plan included the Upgrade as one of its four major recommendations:

**We strongly recommend the upgrade of CEBAF at Jefferson Laboratory to 12 GeV as soon as possible.** *The 12 GeV upgrade of the unique CEBAF facility is critical for our continued leadership in the experimental study of hadronic matter. This upgrade will provide new insights into the structure of the nucleon, the transition between the hadronic and quark/gluon description of matter, and the nature of quark confinement.*

The Long Range Plan further indicated that it considered the project “*ready to initiate construction*”, and included it in the basic funding scenario developed for the field: “*The Jefferson Lab Upgrade is included as a construction project starting in fiscal year 2005, leading into a modest increase for Jefferson Lab operations later in the decade.*”

Encouraged by the NSAC recommendation, the Jefferson Lab community began a two-year effort to further refine the science case and the design of the experimental equipment in preparation for the writing of a Conceptual Design Report for the Upgrade. Each of the groups working in

the present experimental halls, and the GLUEX collaboration began work in earnest to prepare pre-Conceptual Design Reports (pCDR's) with the goal of outlining the physics that motivated their equipment designs, documenting the technical aspects of the equipment designs at a level that it could be reviewed thoughtfully against the planned science program, and developing detailed examples of experiments addressing the science issues that could be carried out using their equipment. There were a series of workshops and collaboration meetings held during the first half of 2002 devoted to this effort.

The July 2002 User's Group Meeting was devoted to a series of workshops on both the scientific motivations for the Upgrade and on the equipment designs. At that meeting the User's Group Board of Directors appointed an editorial board that was given responsibility for writing this document, a pre-Conceptual Design Report for the experimental equipment that summarized all aspects of the proposed Upgrade except for the technical details of the accelerator and civil construction portion of the project. The Board was also given responsibility for preparing presentations on the science case to a special session of the Program Advisory Committee that was to be held in conjunction with the Winter 2002-3 Meeting and provide independent review of the proposed programs and equipment.

Goal of this pCDR is to present the science case for the upgrade "across the halls", consolidating the physics by topic (not surprisingly, in many of the areas of interest there are key experiments that are best done using different equipment). It also aims to present a condensed version of the hall equipment to provide technical details for anyone interested in evaluating specifics. The Editorial Board was divided into groups and each group was given responsibility for text on a science or equipment topic. Specifically:

1. Gluonic Excitations and the Origin of Quark Confinement  
Curtis Meyer, Alex Dzierba, Ted Barnes, Carlos Salgado (and David Richards re lattice)
2. Developing a Unified Description of Hadron Structure
  - (a) Valence Quark Structure and Parton Distributions  
Zein-Eddine Meziani, Sebastian Kuhn, Oscar Rondon, Wally Melnitchouk
  - (b) The Generalized Parton Distributions as Accessed via Deep(ly) Exclusive Reactions  
Volker Burkert, Charles Hyde-Wright, Xiangdong Ji
  - (c) Form Factors and Polarizabilities - Constraints on the Generalized Parton Distributions  
Paul Stoler, Mark Jones, Bogdan Wojtsekhowski, Anatoly Radyushkin
  - (d) Other Topics in Hadron Structure  
(duality, single-spin asymmetries,  $Q^2$  evolution of the GDH sum rule, etc.) Gordon Cates, Latifa Elouadrhiri, Thia Keppel, Sabine Jeschonnek

### 3. The Physics of Nuclei

#### (a) Probing the Limits of the Nucleon-Based Description of Nuclei

Haiyan Gao, Roy Holt, Carl Carlson Rocco Schiavilla, Larry Weinstein, and Paul Ulmer

#### (b) The High-Density Frontier in Cold Nuclei

John Arrington, Doug Higinbotham, Jean-Marc Laget, and Will Brooks

#### (c) Symmetry Tests in Nuclear Physics

##### i. Standard Model Tests

Paul Reimer, Mike Ramsey-Musolf, Paul Souder, and Dave Mack

##### ii. Spontaneous Symmetry Breaking

Aron Bernstein, Ashot Gasparian, Jose Goity

### 4. The Experimental Equipment

#### (a) Hall A: J.-P. Chen, Kees de Jager

#### (b) Hall B: Volker Burkert

#### (c) Hall C: Howard Fenker

#### (d) Hall D: Curtis Meyer and Alex Dzierba

#### (e) Experiment-Specific Equipment: Group by Group

Work by this group, and by each of the major hall collaborations, continued over the second half of 2002, and culminated with a series of presentations to a special session of PAC23 devoted to the Upgrade plans. During this period the pCDR's for each hall were written and distributed to the larger community and the PAC. These documents contained extensive details on the experimental equipment, and a presentation of the science motivating the equipment choices, including the development of many "example" experiments that used the equipment. The PAC Upgrade meeting included two sessions: a public presentation of the science programs that took place at the laboratory on January 17-18, 2003; and an executive session that reviewed the technical plans for the hall equipment and then discussed the science and equipment, which was held in Duck, NC on January 19-22, 2003. The presentations of the science were made by members of the pCDR Editorial Board

The PAC was charged to: comment on the intellectual framework presented for the 12 GeV pCDR; review the new research programs that are under consideration for being highlighted in the executive summary of the pCDR; ask if we omitted any key science initiatives that could be supported by a 12 GeV electron beam; and see if the experimental equipment proposed (is) well matched to the key physics experiments motivating the Upgrade. Their report concluded:

*Overall it is the judgment of the PAC that the envisioned JLab Upgrade offers an outstanding opportunity for exploring new and fundamental physics issues of wide spread*

*interest to the community of nuclear and particle physicists. In many respects the new experimental facilities will be unique in the world. They will also impact issues raised at other facilities. Therefore the PAC enthusiastically endorses the JLab 12 GeV Upgrade in view of the timeliness and high impact it can have on physics issues of concern to a broad spectrum of the nuclear and particle physics community.*

Based on the PAC review, the Editorial Board began work in earnest on the pCDR. On December 18, 2002 (as the JLab community was preparing for the PAC23 review) Dr. Raymond Orbach, Director of the Office of Science of the Department of Energy, as part of the effort to develop a long-range plan for major facility development in the fields supported by his office, charged NSAC to “consider what new or upgraded facilities in your discipline will be necessary to position the Office of Nuclear Physics at the forefront of scientific discovery, and he requested that NSAC discuss each proposed facility in terms of two criteria: 1) the importance of the science that the facility would support; and 2) the readiness of the facility for construction.

The Ad-hoc Facilities Subcommittee of the Nuclear Science Advisory Committee met on February 15, 2003 to hear presentations from the proponents of each project in the field. Both the written submissions to the committee and the presentations made to the committee on behalf of the Upgrade were based on the work documented in this pCDR, and the executive summary of this document (in a slightly earlier form) was the key element of that submission.

In discussing the scientific merits of the Upgrade, the NSAC report placed it in “Category 1” (absolutely central) and noted:

*The 2002 NSAC Long Range Plan “strongly recommend[s] the upgrade of CEBAF at Jefferson Laboratory to 12 GeV as soon as possible. [It] is critical for our continued leadership in the experimental study of hadronic matter” This was one of the four major recommendations of the LRP. The Upgrade has the support of a large and active user community ( 1100 scientists from 29 countries); it has been enthusiastically reviewed by numerous outside peer groups and will be unique worldwide. The realization of the Upgrade will create synergies with other fields of research, most notably with large-scale computing, high-energy physics, and astrophysics.*

*The 12 GeV Upgrade will provide answers to questions of fundamental importance, probing issues that are absolutely central to nuclear science.....*

and went on to detail the research programs outlined in this pCDR. In discussing the technical readiness of the Upgrade, the NSAC Report placed it in “Readiness Category 1” (Ready to initiate construction), and noted:

*The Upgrade project is a proposal to double the maximum energy of the CEBAF accelerator at Jefferson Lab, to build a fourth experimental facility dedicated to the study of*



*gluonic excitations, and to upgrade the existing experimental facilities. The accelerator portion of the upgrade is straightforward; CEBAF was designed with such an upgrade in mind. The key issues were increasing the performance of the superconducting RF cavities and cost-effectively increasing the bending power of the recirculation arcs; both have been addressed successfully. The major equipment in the new end station is a refurbished large superconducting solenoid previously used at LAMPF and SLAC. All aspects of the project, as well as a detailed budget, have been described in reports. The scientific goals and proposed design of the Upgrade have been positively evaluated by internal and peer review committees, including the 2001 Institutional Plan Review and the 2002 DOE S&T Review of JLab, which noted that “It appeared that the 12 GeV upgrade project is technically ready to proceed.” The 2002 LRP considered the project “ready to initiate construction”. All remaining R&D is focused on cost reduction and/or improved technical contingency; no R&D is needed to demonstrate feasibility. The project is fully ready to initiate construction. A CD-0 package has been generated and is awaiting approval.*

The Upgrade has been included in DOE’s long range plans for facility development, which was announced on November 10, 2003 by Secretary of Energy Spencer Abraham. Included in the Office of Science’s so-called “20-year plan” (more formally, *Facilities for the Future of Science: A 20 Year Plan*, is the recommendation that:

*The upgrade to the Continuous Electron Beam Accelerator Facility (CEBAF) at Thomas Jefferson Laboratory is a cost-effective way to double the energy of the existing beam, and thus provide the capability to study the structure of protons and neutrons in the atom with much greater precision than is currently possible.*

The plan identifies as the basic motivation for the facility:

*Quarks are the particles that unite to form protons and neutrons, which, with electrons, combine to form the atoms that make up all the matter that we are familiar with. As yet, scientists are unable to explain the properties of these entities why, for example, we do not seem to be able to see individual quarks in isolation (they change their natures when separated from each other) or understand the full range of possibilities of how quarks can combine together to make up matter.*

On April 12, 2004 Deputy Secretary of Energy Kyle McSlarrow formally announced the Department of Energy’s approval of “Critical Decision Zero” (the statement of mission need) for the Upgrade project, which authorizes the laboratory and its user community to begin work on the formal Conceptual Design Report for the Upgrade and to start work on essential R&D in support of the project. It is anticipated that this pCDR will be the very solid basis for the experimental

equipment portion of the Conceptual Design Report. Following the signing of “CD-0” the Editorial Board undertook a final set of “tweeks” to the pCDR to incorporate comments received from the community as a result of the posting of the draft document in June 2003 for comments from the entire JLab User community. This final version of the pCDR incorporates as many of those suggestions as was practical. We have not attempted to update the document to reflect developments in either the science or the equipment since that date (this will be undertaken as part of the effort to write the full CDR).

The pCDR presented here is based on this long-term effort of the entire JLab community. It reflects intense discussion at many workshops, the published proceedings of those workshops, unpublished presentations to those workshops and the PAC, and the published and unpublished work of many individuals on the physics opportunities that would open up with CEBAF at 12 GeV.

The author list at the end of this document includes the names of all contributors to the effort known to us. Many of them commented extensively on the earlier drafts, resulting in a much-improved document. This White Paper would have been impossible without their intelligence, enthusiasm, time, and just plain hard work. We apologize to anyone whose contributions we have inadvertently failed to acknowledge.

#### **The 12 GeV Upgrade pCDR Editorial Board:**

John Arrington, Argonne National Lab (johna@anl.gov)  
 Ted Barnes, Oak Ridge National Lab (barnesfe@ornl.gov)  
 Aron Bernstein, Massachusetts Institute of Technology (bernstein@mitlns.mit.edu)  
 Will Brooks, Jefferson Lab (brooksw@jlab.org)  
 Volker Burkert, Jefferson Lab (burkert@jlab.org)  
 Lawrence Cardman, Jefferson Lab (cardman@jlab.org)  
 Carl Carlson, College of William & Mary (carlson@physics.wm.edu)  
 Gordon Cates, University of Virginia (cates@Virginia.EDU)  
 J.-P. Chen, Jefferson Lab (jpchen@jlab.org)  
 Alex Dzierba, Indiana University (dzierba@indiana.edu)  
 Latifa Elouadrhiri, Jefferson Lab (latifa@jlab.org)  
 Howard Fenker, Jefferson Lab (hcf@jlab.org)  
 Haiyan Gao, Duke University/MIT (gao@tunl.duke.edu)  
 Ashot Gasparian, North Carolina A & T/Jefferson Lab (gasparan@jlab.org)  
 Jose Goity, Hampton University/Jefferson Lab (goity@jlb.org)  
 Doug Higinbotham, Jefferson Lab (doug@jlab.org)  
 Roy Holt, Argonne National Lab (holt@anl.gov)  
 Charles Hyde-Wright, Old Dominion University (chyde@odu.edu)  
 Kees de Jager, Jefferson Lab (kees@jlab.org)  
 Sabine Jeschonnek, Ohio State University (jeschonnek.L@osu.edu)



Xiangdong Ji, University of Maryland (xji@physics.umd.edu)  
 Mark Jones, Jefferson Lab (jones@jlab.org)  
 Thia Keppel, Hampton University/Jefferson Lab (keppel@jlab.org)  
 Sebastian Kuhn, Old Dominion University (skuhn@odu.edu)  
 Jean-Marc Laget, Centre d'Etudes Nucleaire, Saclay (laget@hep.saclay.cea.fr)  
 Dave Mack, Jefferson Lab (mack@jlab.org)  
 Curtis Meyer, Carnegie Mellon University (cmeyer@ernest.phys.cmu.edu)  
 Wally Melnitchouk, Jefferson Lab (wmelnitc@jlab.org)  
 Zein-Eddine Meziani, Temple University (Meziani@vm.temple.edu)  
 Anatoly Radyushkin, Old Dominion University/Jefferson Lab (radyush@jlab.org)  
 Mike Ramsey-Musolf, California Institute of Technology (mjrm@krl.caltech.edu)  
 Paul Reimer, Argonne National Lab (reimer@anl.gov)  
 David Richards, Jefferson Lab (dgr@jlab.org)  
 Oscar Rondon, University of Virginia (rondon@Virginia.edu)  
 Carlos Salgado, Norfolk State University/Jefferson Lab (salgado@jlab.org)  
 Rocco Schiavilla, Old Dominion University/Jefferson Lab (schiavil@jlab.org)  
 Paul Souder, Syracuse University (souder@suhep.phy.syr.edu)  
 Paul Stoler, Rensselaer Polytech Institute (stoler@rpi.edu)  
 Paul Ulmer, Old Dominion University (pulmer@odu.edu)  
 Larry Weinstein, Old Dominion University (lweinste@odu.edu)  
 Bogdan Wojtsekhowski, Jefferson Lab (bogdanw@jlab.org)



# Contents

<b>1 EXECUTIVE SUMMARY</b>	<b>1</b>
1.A Physics Overview . . . . .	2
1.A.1 Gluonic Excitations and the Origin of Quark Confinement . . . . .	3
1.A.2 The Fundamental Structure of the Nuclear Building Blocks . . . . .	8
Form Factors - Constraints on the Generalized Parton Distributions . . . . .	11
Valence Quark Structure and Parton Distributions . . . . .	13
The Generalized Parton Distributions as Accessed via Deeply Exclusive Reactions . . . . .	15
Other Topics in Hadron Structure . . . . .	19
Transverse parton distributions . . . . .	19
The extended GDH integral and sum rule . . . . .	19
Duality: the transition from a hadronic to a quark-gluon description of Deep Inelastic Scattering . . . . .	21
1.A.3 The Physics of Nuclei . . . . .	21
The Short-Range Behavior of the $N - N$ Interaction and Its QCD Basis . . .	23
Color transparency. . . . .	23
Learning about the $NN$ force by the measurement of the threshold $\psi N$ cross section and by searching for $\psi$ -nucleus bound states. . . . .	23
Quark propagation through cold QCD matter: nuclear hadronization and transverse momentum broadening. . . . .	24
Short-range correlations in nuclei: the nature of QCD at high density and the structure of cold, dense nuclear matter. . . . .	24
Identifying and Exploring the Transition from the Meson/Nucleon Description of Nuclei to the Underlying Quark and Gluon Description. . . . .	25
The onset of scaling behavior in nuclear cross sections . . . . .	26

Helicity conservation in nuclear reactions . . . . .	26
The charged pion form factor . . . . .	28
Pion photoproduction from the nucleon and in the nuclear medium . .	28
1.A.4 Symmetry Tests in Nuclear Physics . . . . .	30
Standard Model Tests . . . . .	30
Properties of Light Pseudoscalar Mesons via the Primakoff Effect . . . . .	31
1.B Upgrade Project Summary . . . . .	33
1.B.1 The Accelerator . . . . .	34
1.B.2 The Experimental Equipment . . . . .	36
Hall A and the Medium Acceptance Device (MAD) . . . . .	36
Hall B Upgrade and CLAS <sup>++</sup> . . . . .	38
Hall C and the Super High Momentum Spectrometer (SHMS) . . . . .	42
Hall D and the GlueX Experiment . . . . .	45
<b>2 THE SCIENCE DRIVING THE 12 GeV UPGRADE OF CEBAF</b>	<b>49</b>
2.A Gluonic Excitations and the Origin of Quark Confinement . . . . .	49
2.A.1 Introduction . . . . .	49
2.A.2 Conventional light mesons . . . . .	52
2.A.3 Gluonic excitations and confinement . . . . .	55
2.A.4 Observation of gluonic excitations . . . . .	57
Glueballs . . . . .	57
Exotic hybrid mesons . . . . .	58
2.A.5 Photoproduction of exotic hybrids . . . . .	61
Why photoproduction? . . . . .	61
Current photoproduction data . . . . .	62

2.A.6	Complementarity with other searches . . . . .	64
2.A.7	Production and analysis of hybrid mesons . . . . .	65
	Kinematics . . . . .	65
	PWA requirements . . . . .	66
	Linear polarization of the beam . . . . .	67
	Linear and circular polarization . . . . .	67
	Linear polarization and statistics . . . . .	67
	Linear polarization and production mechanism . . . . .	68
	Linear polarization as an exotics filter . . . . .	68
2.B	The Fundamental Structure of the Nuclear Building Blocks . . . . .	69
2.B.1	Form Factors – Constraints on the Generalized Parton Distributions . . . . .	73
	Form Factors at Large Momentum Transfer . . . . .	76
	Form Factors and Generalized Parton Distributions . . . . .	76
	The Charged Pion Form Factor . . . . .	79
	Baryon Form Factors and GPDs . . . . .	80
	pQCD - Constituent Scaling, Helicity Conservation . . . . .	89
	Summary . . . . .	91
2.B.2	Valence Quark Structure and Parton Distributions . . . . .	92
	Theoretical predictions for large- $x$ distributions . . . . .	95
	The structure of the free neutron . . . . .	97
	“Tagged” neutron structure function . . . . .	97
	Deep inelastic scattering from $A = 3$ nuclei . . . . .	97
	Longitudinal–transverse separation . . . . .	99
	Moments of structure functions . . . . .	99

The spin structure of the nucleon . . . . .	102
Neutron spin structure functions . . . . .	102
Higher-twist effects . . . . .	105
Semi-inclusive scattering . . . . .	108
2.B.3 The Generalized Parton Distributions as Accessed via Deeply Exclusive Scat- tering . . . . .	112
The Physics of the Generalized Parton Distributions . . . . .	112
Spin Structure of the Nucleon . . . . .	115
Gravitational Form Factors . . . . .	115
“Tomographic” Images of the Nucleon . . . . .	116
Modeling GPDs . . . . .	117
Probing GPDs Through 12 GeV Upgrade . . . . .	117
DVCS at JLab with 12 GeV Electrons . . . . .	120
Deeply Virtual Meson Production at JLab with 12 GeV Electrons . .	129
From Observables to GPDs . . . . .	136
2.B.4 Other Topics in Hadron Structure . . . . .	138
Transverse parton distributions . . . . .	138
The extended GDH integral and sum rule . . . . .	143
Quark-Hadron Duality . . . . .	145
2.C The Physics of Nuclei . . . . .	149
2.C.1 Hadron Structure in the Nuclear Medium . . . . .	151
Nuclear Matter at High Densities . . . . .	153
Modification to Hadron Structure in Nuclei . . . . .	154
High-Density Configurations in Nuclei . . . . .	155
Color Transparency . . . . .	158

	Color Transparency in $A(e,e'p)$ . . . . .	159
	Color Transparency in Few-Body Systems . . . . .	160
	Color Transparency in Meson Production . . . . .	160
	$J/\psi$ Photoproduction Near Threshold . . . . .	163
	Space-Time Characteristics of Hadronization . . . . .	166
	Transverse Momentum Broadening . . . . .	169
2.C.2	Short-Range Correlations in Nuclei . . . . .	171
	Electrodisintegration of the Deuteron . . . . .	171
	$A(e, e'pN)$ Processes . . . . .	174
	Inclusive $A(e, e')X$ Processes . . . . .	176
2.C.3	The Parton-Hadron Transition in Nuclei . . . . .	178
	Elastic Form Factor of Charged Pion . . . . .	179
	Few-Body Form Factors . . . . .	180
	Deuteron Photodisintegration . . . . .	183
	Nucleon Photopion Production . . . . .	185
	Pion Photoproduction in the Nuclear Medium . . . . .	187
2.D	Symmetry Tests in Nuclear Physics . . . . .	189
2.D.1	Standard Model Tests . . . . .	189
2.D.2	Properties of Light Pseudoscalar Mesons via the Primakoff Effect . . . . .	199
<b>3</b>	<b>EXPERIMENTAL EQUIPMENT FOR THE 12 GeV UPGRADE</b>	<b>213</b>
3.A	Hall A and the Medium Acceptance Device (MAD) . . . . .	213
3.A.1	Design Characteristics of the MAD Spectrometer . . . . .	215
3.A.2	Optical Characteristics of the MAD Spectrometer . . . . .	224
3.A.3	Simulations of the MAD Spectrometer . . . . .	227

3.A.4	MAD Spectrometer Detector Systems . . . . .	230
	Scintillators . . . . .	231
	Drift Chambers . . . . .	233
	Gas Čerenkov Counter . . . . .	234
	Aerogel Čerenkov Counters . . . . .	235
	Electromagnetic Calorimeter . . . . .	237
	Focal Plane Proton Polarimeter . . . . .	238
	Trigger Electronics . . . . .	239
	Data Acquisition . . . . .	240
3.A.5	High Performance Calorimeter . . . . .	241
3.A.6	The Hall A Beam Line . . . . .	242
3.B	Hall B Upgrade and the CLAS <sup>++</sup> Detector . . . . .	245
3.B.1	Overview . . . . .	245
3.B.2	CLAS Torus Magnet . . . . .	247
3.B.3	Central Detector . . . . .	247
	Superconducting Solenoid Magnet . . . . .	249
	Magnet Design . . . . .	249
	Central Electromagnetic Calorimeter . . . . .	251
	Overview . . . . .	251
	Requirements . . . . .	251
	Scintillating Fiber/Tungsten Powder Calorimeter Design . . . . .	251
	Expected Performance . . . . .	252
	Prototyping and Simulations . . . . .	254
	Central Time-of-Flight System . . . . .	254



Expected Rates . . . . .	255
Options . . . . .	255
Central Tracker . . . . .	257
Silicon Strip Detector . . . . .	258
Instrumentation . . . . .	260
Prototyping . . . . .	260
Forward Detector . . . . .	260
Overview . . . . .	260
High Threshold Čerenkov Counter (HTCC) . . . . .	262
Forward Tracking Chambers . . . . .	263
Low Threshold Čerenkov Counter . . . . .	266
Outer TOF System . . . . .	266
Inner Calorimeter . . . . .	269
Forward Angle Calorimeter . . . . .	270
Pre-shower calorimeter . . . . .	270
3.B.4 Polarized Target Operation in CLAS <sup>++</sup> . . . . .	273
Longitudinally polarized Target in Solenoid Magnet . . . . .	273
Transversely Polarized Target. . . . .	274
3.B.5 Beam Line . . . . .	274
Faraday Cup . . . . .	274
Møller Polarimeter . . . . .	275
Magnetic Chicane . . . . .	275
Beam raster magnets . . . . .	275
3.B.6 Data Acquisition System and Trigger . . . . .	275

Design criteria for the system . . . . .	275
System upgrade . . . . .	276
3.B.7 Event Reconstruction and Offline Computing . . . . .	276
Data Reduction and Online Event Reconstruction . . . . .	276
3.C Hall C and the Super High Momentum Spectrometer (SHMS) . . . . .	278
3.C.1 Overview . . . . .	278
3.C.2 The High-Momentum Spectrometer . . . . .	278
3.C.3 The Super-High-Momentum Spectrometer . . . . .	281
Overview . . . . .	281
The SHMS Magnets and Structural Design . . . . .	282
General . . . . .	282
Q1 at 8.6 T/m . . . . .	283
QD30 Superconducting Magnet for the SHMS . . . . .	284
Magnet DC Power and Energy Dump System . . . . .	286
Magnet Control System . . . . .	289
Support Structure . . . . .	290
Spectrometer Motion System . . . . .	290
Shield House . . . . .	292
SHMS Cryogenic System . . . . .	292
SHMS Vacuum Systems . . . . .	294
SHMS Optics and Monte Carlo . . . . .	294
SHMS Optics Design . . . . .	294
COSY magnet model . . . . .	296
LSA tune . . . . .	298

SHMS model in the ‘physics’ Monte Carlo . . . . .	299
SHMS Performance (Resolution/Acceptance) . . . . .	301
SHMS Detector Systems . . . . .	302
Wire Chambers . . . . .	308
Quartz Čerenkov Hodoscope . . . . .	308
Particle Identification . . . . .	313
Focal Plane Polarimeter . . . . .	324
Trigger, Data Acquisition, and On-line Computing . . . . .	324
Stand-Alone (Third-Arm) Calorimeter . . . . .	327
3.D Hall D and the GlueX Experiment . . . . .	327
3.D.1 Introduction . . . . .	327
3.D.2 The Photon Beam and Polarization . . . . .	328
The Photon Tagger and Beam Collimation . . . . .	328
Polarization via Coherent Bremsstrahlung . . . . .	330
3.D.3 The GLUEX Detector . . . . .	332
The Super-conducting Solenoid . . . . .	332
Particle Tracking and Particle Identification . . . . .	333
The Vertex Detector . . . . .	333
The Cylindrical Drift Chamber . . . . .	334
The Forward Drift Chambers . . . . .	335
Electromagnetic Calorimetry . . . . .	336
The Forward Calorimeter . . . . .	336
The Barrel Calorimeter . . . . .	337
The Upstream Photon Veto . . . . .	339

Charged Particle Identification . . . . .	340
The Time-of-Flight System . . . . .	341
The Čerenkov Detector . . . . .	342
Sub-system Installation and Integration . . . . .	343
3.D.4 Rates, Electronics, Trigger and Data Acquisition . . . . .	343
3.D.5 Computing and Partial Wave Analysis . . . . .	347
3.D.6 Summary . . . . .	352
3.E Experiment-Specific Equipment . . . . .	352
3.E.1 Properties of Light Pseudoscalar Mesons via the Primakoff Effect . . . . .	352
<b>REFERENCES</b>	<b>361</b>
<b>FIGURES</b>	<b>390</b>
<b>TABLES</b>	<b>402</b>
<b>CONTRIBUTORS TO THE pCDR</b>	<b>404</b>

# 1 EXECUTIVE SUMMARY

There has been a remarkably fruitful evolution of our picture of the behavior of strongly interacting matter during the almost two decades that have passed since the parameters of the Continuous Electron Beam Accelerator Facility (CEBAF) at Jefferson Lab were defined. These advances have revealed important experimental questions best addressed by a CEBAF-class machine at higher energy. Fortunately, favorable technical developments coupled with foresight in the design of the facility make it feasible to triple CEBAF's beam energy from the original design value of 4 GeV to 12 GeV (corresponding to doubling the achieved energy of 6 GeV) in a cost-effective manner: the Upgrade can be realized for a modest fraction of the cost of the initial facility. This Upgrade would provide the worldwide community using CEBAF with greatly expanded physics horizons.

Raising the energy of the accelerator to 12 GeV provides three general advantages:

1. It allows crossing the threshold above which the origins of quark confinement can be investigated. Specifically, 12 GeV will enable the production of certain “exotic” mesons, whose discovery and spectrum will establish the origin of quark confinement as due to the formation of QCD flux tubes and whose spectrum encodes information on the mechanism within QCD responsible for their formation. If these exotic mesons are not found their absence will present a serious challenge to our present understanding of “strong” QCD, and the meson spectra that will be accumulated with unprecedented statistics (including spectra of mesons containing strange quarks and antiquarks) will provide essential information for revising that theory. With 12 GeV one also crosses the threshold for charmed meson production.
2. It allows direct exploration of the quark-gluon structure of hadrons and nuclei. It is known that inclusive electron scattering at the high momentum and energy transfers available at 12 GeV is governed by elementary interactions with quarks and gluons. The design energy of the original CEBAF accelerator has proven to be not fully adequate for study of this critical regime. This is not unexpected; at the time the energy was chosen, among other things, to “just” get into the deep inelastic scattering regime. With continuous 12 GeV beams one can cleanly access hadron structure throughout the entire “valence quark region” and exploit the newly discovered Generalized Parton Distributions to access experimentally both the correlations in the quark wavefunctions of the hadrons and their transverse momentum distributions. 12 GeV beams will allow us to identify precisely the limits of the long-standing nucleon and meson based description of nuclei, and to fully access and characterize the transition from this description to the underlying quark-gluon description.
3. In addition to these qualitative changes in the physics reach of CEBAF, the 12 GeV Upgrade also allows important new thrusts in CEBAF's present research program, generally involving the extension of measurements to substantially higher momentum transfers (probing correspondingly smaller distance scales). We also note that most experiments that want to run

at a presently accessible momentum transfer can do so more efficiently (*e.g.*, consuming less total beam time) at higher electron beam energy.

In the examples highlighted in this executive summary and in the more complete discussions of Chapter 2, these benefits of the energy upgrade will always be significant.

## 1.A Physics Overview

Chapter 2 provides a detailed discussion of the science motivation driving the 12 GeV Upgrade; it is summarized here. The research program of the new facility is focused on four major research themes that coincide with broad directions of the field of nuclear physics as identified in two key documents: the 2002 Long Range Plan [NS02] of the Nuclear Science Advisory Committee of the U.S. Department of Energy and the National Science Foundation and the recent decadal survey [NA99] of the field by the National Research Council of the National Academy of Sciences. We identify these themes here to place our research program in this broader context. Each addresses outstanding questions in nuclear physics that the laboratory’s users address with a concerted program of experimental and theoretical work.

### **Gluonic Excitations and the Origin of Quark Confinement**

Experiments and theory aimed at examining the fundamentally new dynamics that underpins all of nuclear physics: the confinement of quarks.

### **How are the Nuclear Building Blocks Made from Quarks and Gluons?**

A program of measurements addressing the first question that must be answered in the quest to understand nuclear physics in terms of the fundamental theory of strongly interacting matter: quantum chromodynamics (QCD).

### **On the Structure of Nuclei**

Three broad programs that take advantage of the precision, spatial resolution, and interpretability of electromagnetic interactions to address long-standing issues in nuclear physics. They aim to understand the QCD basis of nuclear physics through investigations of the origins of the Nucleon–Nucleon ( $N - N$ ) force and its short range behavior, and by identifying and exploring the transition from the meson/nucleon description of nuclei to the underlying quark and gluon description.

### **In Search of the New Standard Model**

Experiments aimed at identifying physics beyond the Standard Model of electro-weak interactions through precision tests of its predictions, and by measuring low energy parameters of the theory to deepen our understanding of chiral symmetry breaking.

Each of these programs is a major motivation for the energy upgrade. The first, a program of *gluonic spectroscopy*, will provide data needed: i) to test experimentally our current understanding that quark confinement arises from the formation of QCD flux tubes; and ii) to explore the mechanism behind the formation of these flux tubes. If our present understanding is incorrect, the experiment

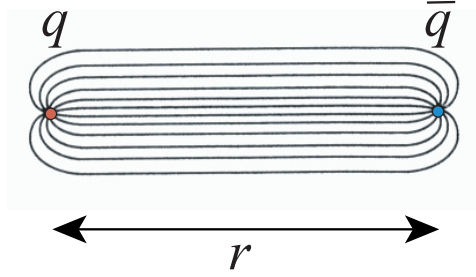


Figure 1: In QCD a confining flux tube forms between distant static charges. The Hall D program is designed to verify this fundamental new feature of chromodynamics.

has the sensitivity necessary to decisively test first-principles lattice QCD calculations of the mesons – the simplest of the strongly-interacting systems. The second program will explore the *complete wavefunctions* of the nucleons through measurements: i) of quark momentum distributions in the critical, but previously unreachable, valence quark region; and ii) of exclusive reactions that build on the framework of the newly discovered Generalized Parton Distributions. The third will address outstanding issues in nuclear physics, completing a very fruitful area presently under investigation with CEBAF at 6 GeV and extending this program in important new directions. Finally, the last program will use precision measurements at modest energies to explore the validity of the Standard Model of electro-weak interactions and measure key parameters of that theory. In Sections 1.A.1 through 1.A.4 we summarize these four key science drivers of the 12 GeV Upgrade. Section 1.B then completes the picture by summarizing the accelerator and experimental equipment upgrades required to accomplish these physics goals.

### 1.A.1 Gluonic Excitations and the Origin of Quark Confinement

In the early 1970s, evidence that the masses of strongly interacting particles increased without limit as their internal angular momentum increased led the theorist Yoichiro Nambu [Na70] to propose that the quarks inside these particles are “tied together” by strings. Numerical simulations of QCD (“lattice QCD”) have demonstrated [Ba00] that Nambu’s conjecture was essentially correct: in chromodynamics, a stringlike chromoelectric flux tube forms between distant static quarks, leading to their confinement with an energy proportional to the distance between them (see Figs. 1 and 2). The phenomenon of confinement is the most novel and spectacular prediction of QCD – unlike anything seen before. It is also the basic feature of QCD that underpins nuclear physics, from the mass of the proton and other nuclear building blocks to the  $NN$  interaction.

The ideal experimental test of this new feature of QCD would be to study the flux tube directly by anchoring a quark and antiquark several fermis apart and examining the flux tube that forms between them. In such ideal circumstances one of the fingerprints of the gluonic flux tube would be its model-independent spectrum [Lu81] (see Fig. 3): its required two degenerate first excited states

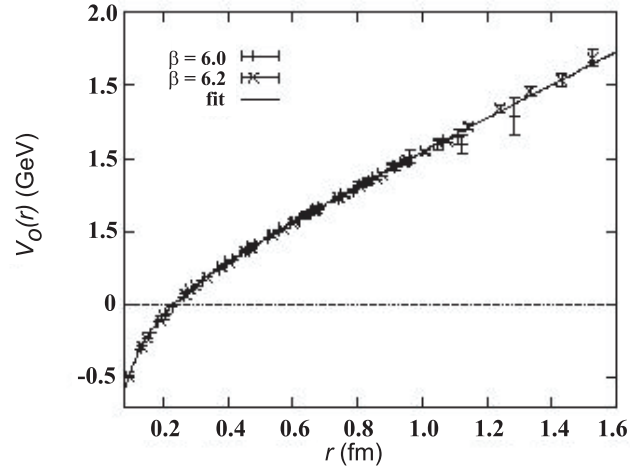
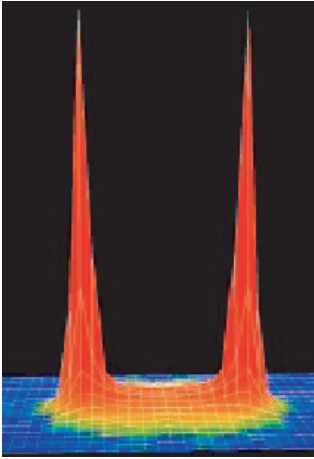


Figure 2: Lattice QCD has confirmed the existence of flux tubes between distant static charges for heavy quarks. In addition to the intense color fields in the immediate vicinity of each quark, one can see the formation [Ba00] along the line connecting the two quarks of a flux tube of constant thickness, leading to the linearly rising potential seen on the right [Ba97].

are the two longest-wavelength vibrational modes of this system, while their excitation energy is required to be  $\pi/r$  since both the mass and the tension of this “relativistic string” arise from the energy stored in its color force fields. Such a direct examination of the flux tube is of course not possible experimentally, but such a picture is indicated by lattice calculations, at least at large separations [Ju02]. In real life we have to be content with systems in which the quarks move. Fortunately, we know both from general principles [Is85] and from lattice QCD calculations [Ju99] that an approximation to the dynamics of the full system that ignores the impact of these two forms of motion on each other works quite well – at least down to quark masses of the order of 1 GeV.

To extend this firm understanding to yet lighter quarks, models are required [Is85], but the most important properties of this system are determined by the model-independent features described above. In particular, in a region around 2 GeV, a new form of hadronic matter must exist in which the gluonic degree-of-freedom of a quark-antiquark system is excited. The smoking gun characteristic of these new states is that the vibrational quantum numbers of the gluonic “string”, when added to those of the quarks, can under certain circumstances produce a total angular momentum  $J$ , a total parity  $P$ , and a total charge conjugation symmetry  $C$  not allowed for ordinary  $q\bar{q}$  states. These unusual  $J^{PC}$  combinations (such as  $0^{+-}$ ,  $1^{-+}$ , and  $2^{+-}$ ) are called exotic, and the states are referred to as exotic hybrid mesons [Ba77]. Not only general considerations and flux tube models, but also first-principles lattice QCD calculations, require that these states have masses around 2 GeV; furthermore, they demonstrate that the levels and their orderings will provide experimental information on the mechanism that produces the flux tube.

On the experimental front, tantalizing evidence has appeared in recent years both for exotic



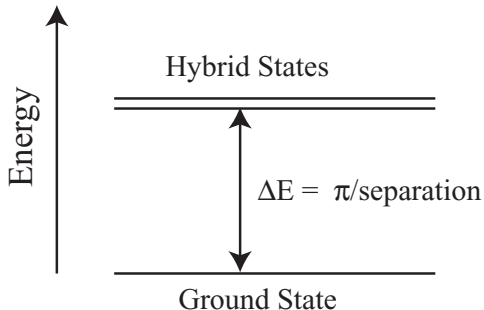


Figure 3: Model-independent spectrum of the glue (flux tube) of Fig. 1.

hybrids and for glueballs (gluonic excitations with no quarks). For the last two years a group of 90 physicists from 26 institutions in seven countries has been working on the design of the definitive experiment to map out the spectrum of these new states required by the confinement mechanism of QCD. Photon beams are expected to be particularly favorable for the production of the exotic hybrids [Is85]. The reason is that the photon can easily fluctuate into a “virtual vector meson” with total quark spin  $S = 1$ .

When the flux tube in this  $S = 1$  system is excited, both ordinary and exotic  $J^{PC}$  are possible. In contrast, when the spins are antiparallel ( $S = 0$ ), as in pion or kaon probes, the exotic combinations are not generated. (In the approximation that flux tube and quark dynamics separate, hybrid production would occur by pure flux tube excitation, and these selection rules would be strictly true. In practice, these two degrees-of-freedom interact with one another to produce corrections to the rules.) To date, most meson spectroscopy has been done with incident pion, kaon, or proton probes, so it may not be surprising that the experimental evidence to date for flux tube excitation is tentative.

In contrast to hadron beams, high-flux photon beams of sufficient quality and energy to perform meson spectroscopy studies have not been available, so there are virtually no data on the photoproduction of mesons with masses in the 1.5 to 3 GeV region. Thus, experimenters have not been able to search for exotic hybrids precisely where they are expected to be found. The planned experiment will have a dramatic impact on this situation. Even if initial running is at only 10% of the planned photon fluxes of  $10^8/\text{s}$ , the experiment will accumulate statistics during the first year of operation that will exceed the world’s supply of published meson data obtained by pion production by at least a factor of 10, and the existing photon production data set by at least a factor of 1000. With the planned detector (described below), high statistics, and linearly polarized photons, it will be possible to map out the full spectrum of the decay modes of these gluonic excitations.

The Glue Excitations Experiment (GlueX) is complementary to the recently approved CLEO-c program at Cornell, which will include the collection of nearly one billion  $J/\psi$  decays. The radiative  $J/\psi$  decays are expected to be glue-rich, the system recoiling against the radiated photon having the quantum numbers of a two-gluon system. Thus the glueball search of CLEO-c is complementary

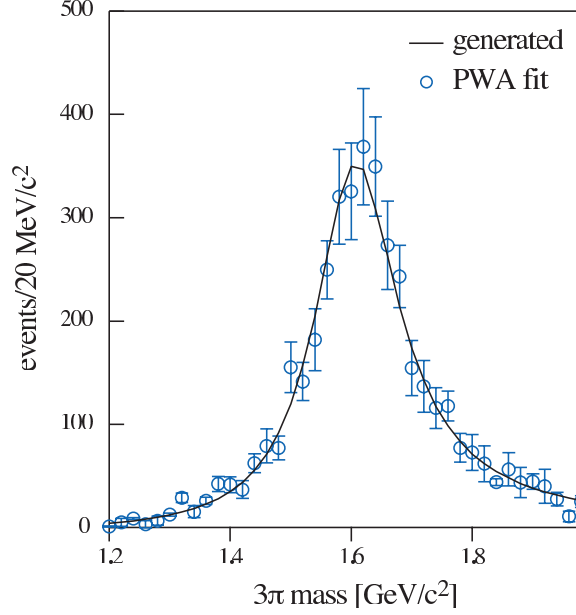


Figure 4: The results of a double-blind Monte Carlo exercise showing the  $J^{PC} = 1^{-+}$  exotic wave after fitting (open circles) and the exotic wave input (curve) into the mix of  $\gamma p \rightarrow \pi^+ \pi^+ \pi^- n$  events that were generated in this study.

to the hybrid search of GlueX and while GlueX is not ideal for glueball searches, CLEO-c is not ideal for exotic hybrid searches. In addition, GlueX and CLEO-c physicists are working together to develop the software and analysis tools needed to perform the spin analysis of the large datasets expected in both experiments. The complete mapping of the spectrum of gluonic excitation in these programs will be the definitive data needed to understand confinement.

The performance of the GlueX detector and the flux and linear polarization of the photon beam determine the level of sensitivity for mapping the hybrid spectrum. A double-blind exercise was carried out in which an exotic signal, a  $J^{PC} = 1^{-+}$  state with a mass of 1.6 GeV/c<sup>2</sup> decaying into  $\rho\pi$ , was generated along with a mix of three well-established non-exotic states with masses of 1.2, 1.3 and 1.7 GeV/c<sup>2</sup>. In this exercise the exotic signal was generated at the level of 2.5% of the total sample. The momenta of the decay products of these particles were smeared according to the expected resolution of the detector. The acceptance of the detector was also applied. The resulting data set was passed through a partial wave analysis (PWA) fitting procedure to determine the relative contributions of each wave. The plot in Fig. 4 shows the input exotic wave as a solid curve and the result of the PWA fit as points with error bars. The input wave is reproduced extremely well, and this demonstrates the capabilities of the detector and sensitivity of the experiment. The experiment is described in Section 3.D; a much more complete discussion of the physics driving the experiment is given in Section 2.A.

*When the spectrum and decay modes of these gluonic excitations have been mapped out experimentally, we will have made a giant step forward in understanding one of the most important*

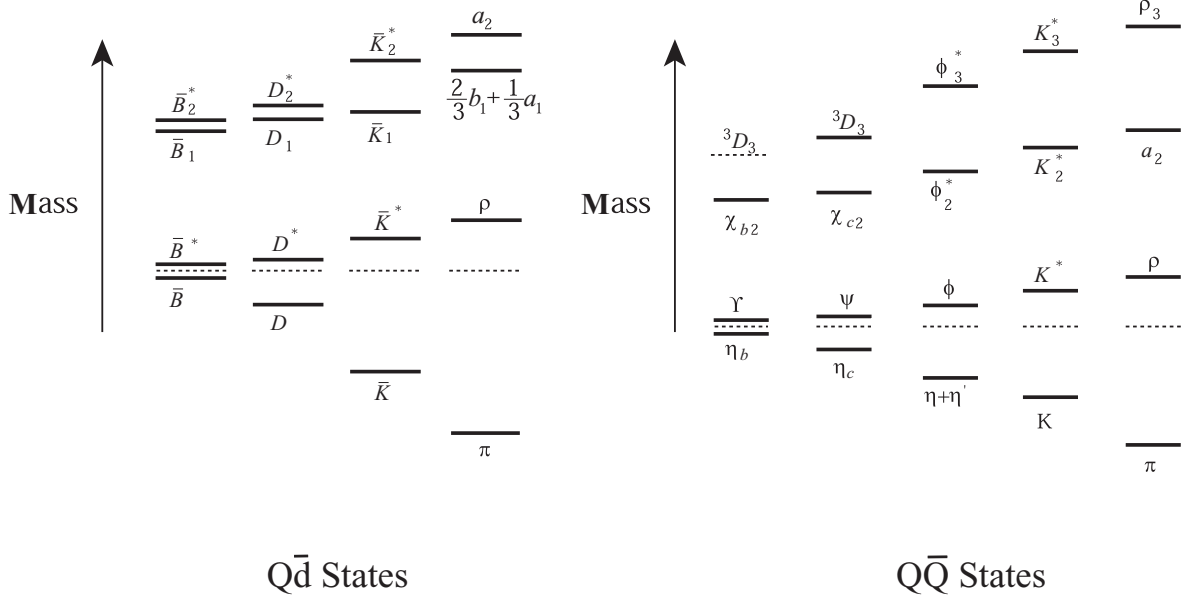


Figure 5: (Left) The relative splittings of the  $Q\bar{d}$  states are shown to scale from the heaviest to the lightest with the center-of-gravity of the ground state multiplets aligned:  $b\bar{d}$ ,  $c\bar{d}$ ,  $s\bar{d}$ , and  $u\bar{d}$ .  $\bar{B}^*$  and  $\bar{B}$  are the  $J^P = 1^-$  and  $0^-$  “ground state” multiplet with light-degrees-of-freedom spin-parity  $s_\ell^{\pi_\ell} = \frac{1}{2}^+$ , while  $\bar{B}_2^*$  and  $\bar{B}_1$  with  $J^P = 2^+$  and  $1^+$  are an excited heavy-quark spin multiplet with  $s_\ell^{\pi_\ell} = \frac{3}{2}^+$  [Is91]. (Right) The  $Q\bar{Q}$  states are shown from the heaviest to the lightest:  $b\bar{b}$ ,  $c\bar{c}$ ,  $s\bar{s}$ ,  $s\bar{d}$ , and  $u\bar{d}$ . Shown are the states in each sector with  $J^{PC} = 0^-, 1^-, 2^+, \text{ and } 3^-$ ; relative splittings are shown to scale with the center-of-gravity of the “ground states”  $0^-$  and  $1^-$  aligned.

*phenomena discovered in the twentieth century: quark confinement.*

The data that will be accumulated as part of the search for gluonic excitation will also provide new information on the spectroscopy of  $s\bar{s}$  mesons that is essential for completing our understanding of QCD. The left half of Fig. 5 shows some of what we know about the spectra of  $Q\bar{q}$  mesons for  $\bar{q}$  a light ( $\bar{d}$ ) quark and  $Q = b, c, s$ , and  $u$ . The rigorous results of Heavy Quark Effective Theory (HQET) should only be applicable for  $Q = b, c$ , but these data suggest that there is a remarkable similarity between the dynamics of “true” heavy-light systems and those where  $Q = s$  or even  $Q = u$  or  $d$ . It appears that the creation of the constituent quark mass through spontaneous chiral symmetry breaking is enough to boost any quark into the heavy-quark world, at least qualitatively. The right half of Fig. 5 shows heavy quarkonia ( $Q\bar{Q}$  systems) starting from the heaviest  $b\bar{b}$  system to the lightest. Once again, even though there is no known rigorous explanation, there seems to be a great similarity between the spectra of the heavy quarkonia (which have a well-understood quark-model-like connection to QCD) and light-quark systems.

These interesting data showing possible relationships between heavy- and light-quark systems exist because nature has presented us with an interesting selection of quark masses. Historically the quarks have been divided into two groups based on their masses: the light-quark ( $u, d$ ) world (or, by extension, the  $u, d, s$  world of SU(3)) and the heavy-quark world. It is ironic that in many critical

areas we know much more (both experimentally and theoretically) about the heavy-quark world than we know about our own world. In this respect, these figures strongly suggest that it would be desirable to know much more about  $s\bar{s}$  spectroscopy. Given that the photon often fluctuates into an  $s\bar{s}$  pair, a great deal of data will automatically be available from this sector as part of the planned exotic meson program, creating the opportunity to correct this situation. Mapping out the  $s\bar{s}$  spectrum presents some challenges. Given that the intrinsic  $s\bar{s}$  content of the proton is expected to be small, photon-initiated  $s\bar{s}$  spectroscopy will strongly favor the production of diffractive-type  $C = -1$  states. The exception will be channels where OZI-violating  $t$ -channel exchanges (like those of the  $\eta - \eta'$  system) can occur. These effects will result in an uneven population of the spectrum. The very high data rates anticipated should nevertheless lead to a data set of sufficient quality that the weakly excited states will still be identifiable.

### 1.A.2 The Fundamental Structure of the Nuclear Building Blocks

The nucleons are the basic building blocks of atomic nuclei. Their internal structure, which arises from their quark and gluon constituents, determines their mass, spin, and interactions. These, in turn, determine the fundamental properties of the nuclei. To make further progress in our understanding of nuclei, it is crucial that we understand in detail how the nucleon's basic properties are derived from the theory of strong interactions: quantum chromodynamics (QCD).

Over the past half century much progress has been made toward unraveling the structure of the nucleon. However, our understanding is fragmented and incomplete, and many puzzles remain. For example, we only partially understand how the nucleon's spin is "assembled" from the quark spins and the quark and gluon angular momenta, and we don't know the details of the spatial and momentum distributions of the quarks and gluons within the nucleon. Our understanding of nucleon structure is, quite simply, very far from the level of our understanding of atomic structure.

The JLab 12 GeV Upgrade will support a great leap forward in our knowledge of hadron structure through major programs in three areas: nucleon form factors at large  $Q^2$ , valence quark structure, and deep exclusive scattering. It will also support important initiatives in a number of other areas of hadron structure. These data can be understood and interpreted coherently, using the theoretical framework of the recently-discovered Generalized Parton Distributions (GPDs), to provide truly remarkable and revealing images of the proton's structure that will enable us to understand these fundamental "building blocks" of nuclear physics.

**Nucleon Form Factors at Large  $Q^2$ .** Historically, the internal structure of the nucleons was first studied by using elastic electron-proton scattering in which a proton at rest is struck by a virtual photon of mass  $Q^2$ , and the probability that the proton remains intact is measured. This elastic form factor can be directly related to the nucleon's spatial electric charge and current distributions. The first measurements of the proton's electric form factor taught us that the nucleon

has a finite size of about one femtometer ( $10^{-15}\text{m}$ ); Robert Hofstadter was awarded the Nobel prize for this discovery. Form factors at large  $Q^2$  are difficult to measure because they require a dedicated accelerator with high luminosity. For many years after Hofstadter’s initial measurements there were no further fundamental breakthroughs in our understanding of the nucleon because no appropriate facility was available.

The theoretical understanding of the form factors has expanded significantly. It was realized that they can be interpreted as the Fourier transformations of charge and current (or quark) density distributions in the transverse plane. This is similar to the Feynman parton distribution, which can be interpreted in a frame of reference in which the nucleon travels with the speed of light.

**Parton Distributions at Large  $x$ .** A second window on nucleon structure came with the development of deep inelastic lepton-nucleon scattering (DIS) in the 1970s at SLAC. In these experiments the hadronic reaction products are not detected. DIS data led to the experimental confirmation of the existence of quarks and helped to establish QCD as the fundamental theory governing all strongly interacting (*i.e.*, nuclear) matter. Friedman, Kendall, and Taylor won the Nobel prize for pioneering this research.

What one infers from DIS data are the quark distributions in momentum space. In frames of reference in which the nucleon travels with speed approaching the velocity of light, the DIS cross sections determine the probability of the struck quark having a fraction,  $x$ , of the nucleon’s longitudinal momentum. In such situations the elastic form factors and the deep-inelastic structure functions provide complementary information. The former gives the coordinate space distribution in the transverse direction, and the latter yields the momentum space distribution in the longitudinal direction. Together, they provide parts of a 3-dimensional picture of nucleon structure.

Even though DIS experiments have been pursued vigorously for nearly 30 years, it is remarkable that there has never been an experimental facility that could measure the DIS cross sections throughout the kinematic regime where the three basic (“valence”) quarks of the proton and neutron dominate the wavefunction. The contribution of the valence quarks peaks at  $x \simeq 0.2$ . However, if one is in the conventionally defined deep inelastic regime, the probability of finding a quark in the high- $x$  “valence quark region” is small, and becomes smaller and smaller as  $x \rightarrow 1$ . Moreover, with “pollution” from gluons and quark-antiquark pairs, it is only for  $x > 0.5$  that the valence quarks dominate the wavefunction. The 12 GeV Upgrade will allow us to map out the quark distribution functions in this “clean” valence quark region with high precision. Such measurements will have a profound impact on our understanding of the structure of the proton and neutron.

**Deep Exclusive Scattering and the Generalized Parton Distributions** While the elastic form factors and parton distributions provide the distributions of quarks in the transverse coordinate and longitudinal momentum spaces, respectively, they do not yield a complete picture. To

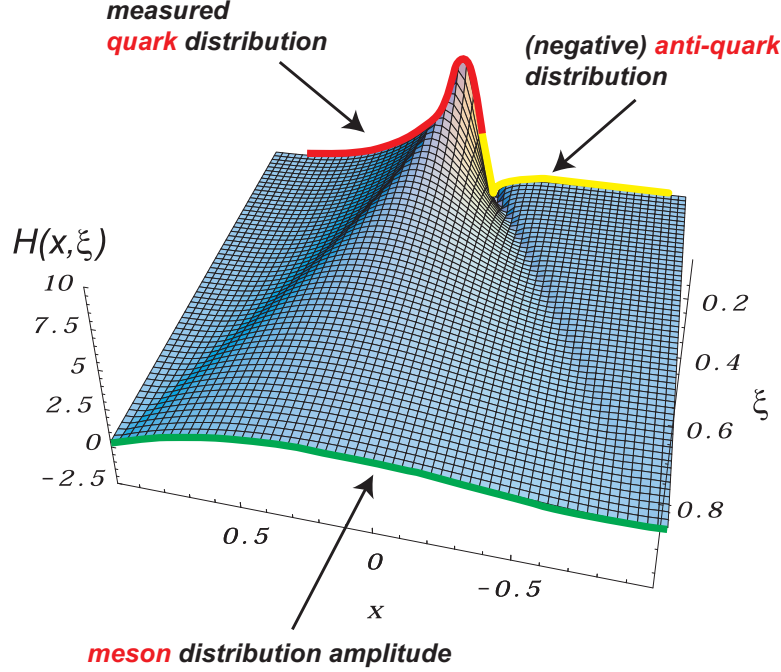


Figure 6: Model representation of the Generalized Parton Distribution (GPD)  $H(x, \xi, t = 0)$  in two dimensions. The known parton momentum densities constrain the distribution at  $\xi = 0$ . The new physics is contained in the  $\xi$ - and  $t$ -dependence of this surface, which can currently only be modeled. The dramatic change in the shape of the surface reflects changes in the underlying physics. As  $\xi$  increases, the correlations between the quarks and anti-quarks increase leading to meson-like distributions at large  $\xi$ .

have this, one would need a joint distribution representing the density of quarks having a fixed longitudinal momentum and *simultaneously* a fixed transverse position. Such a distribution has been discovered recently: the Generalized Parton Distribution (GPD) [Mu94, Ji97, Ra96].

A GPD depends on three kinematic variables:  $x$ , which specifies the fraction of the nucleon momentum carried by partons (as in the Feynman distribution);  $t$ , which characterizes the momentum transfer to the nucleon (as in the elastic form factors); and  $\xi$ , which measures the difference in momentum fraction between the initial and final parton. When  $t = \xi = 0$ , a GPD reduces to a regular Feynman parton distribution; when integrated over  $x$  the GPD gives an ordinary electromagnetic form factor. There are four leading-order GPDs for each quark flavor. For example,  $H(x, \xi, t)$  and  $E(x, \xi, t)$  are quark helicity-independent distributions, and  $\tilde{H}(x, \xi, t)$  and  $\tilde{E}(x, \xi, t)$  are helicity-dependent distributions. A model of the  $H$  distribution with factorized  $t$ -dependence is shown in Fig. 6. At  $\xi = 0$ , the physical interpretation of  $H(x, 0, t)$  is very simple [Be02], as illustrated in Fig. 7. Its Fourier transformation in  $t$  gives the joint probability distribution for a quark with longitudinal momentum  $x$  and transverse position  $b_\perp$ .

These remarkable functions capture the full richness of the nucleon's structure. In addition to providing a consistent theoretical framework for interpreting a broad variety of available data

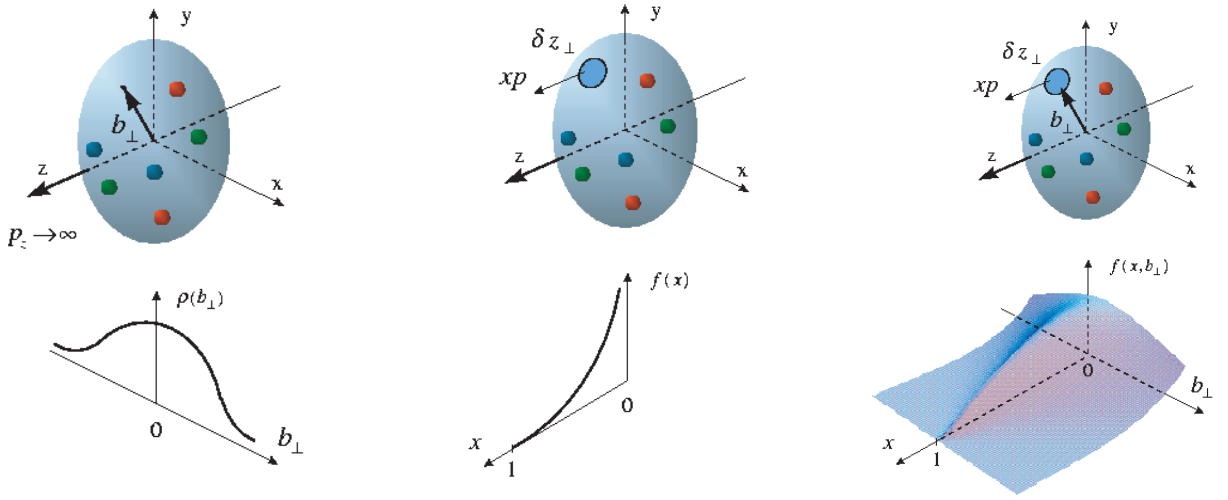


Figure 7: Representations of the proton properties probed in elastic scattering (left), deeply inelastic scattering (center), and deeply exclusive scattering (right). Elastic scattering measures the charge density  $\rho(b_\perp)$  as a function of the transverse coordinate  $b_\perp$ . DIS measures the longitudinal parton momentum fraction density  $f(x)$ . GPDs measure the full correlation function  $H(x, b_\perp)$ .

probing nucleon structure, they provide critically needed access to essential, but almost unknown aspects of nucleon structure such as the correlations among the quarks and the quarks' contribution to the nucleon's spin. In the remainder of this section we discuss the advances anticipated in each of the important areas of nucleon structure studies that will be supported by the 12 GeV Upgrade.

**Form Factors - Constraints on the Generalized Parton Distributions** The hadronic form factors are moments of the GPDs; they provide precise information on the distribution of charge and magnetization in protons, neutrons and nuclei, and are essential tests of our understanding of nucleon structure. Using the formalism of the GPDs outlined above (and discussed below), elastic and transition form factors can be connected directly to the parton structure of the hadrons. They are complementary to deeply virtual exclusive (DVE) reactions (discussed below), which probe the GPDs more directly; the form factors uniquely access the GPD moments. Another important consideration is that while DVE reactions access GPDs only at relatively low  $|t|$ , the form factors connect at high  $|t|$  ( $=Q^2$  for elastic scattering). High- $Q^2$  data are required to obtain the small  $b_\perp$  structure of the hadron.

For nucleon elastic scattering there are four form factors – two for the proton ( $G_E^p$  and  $G_M^p$ ), and two for the neutron ( $G_E^n$  and  $G_M^n$ ); taken together they determine the charge and current distributions of the nucleon. They are the first moments of the GPDs. It is important to extend the measurement of the four nucleon form factors to the highest possible  $Q^2$  and to express all four in terms of common GPDs. Only the magnetic form factor of the proton,  $G_M^p$ , has been measured



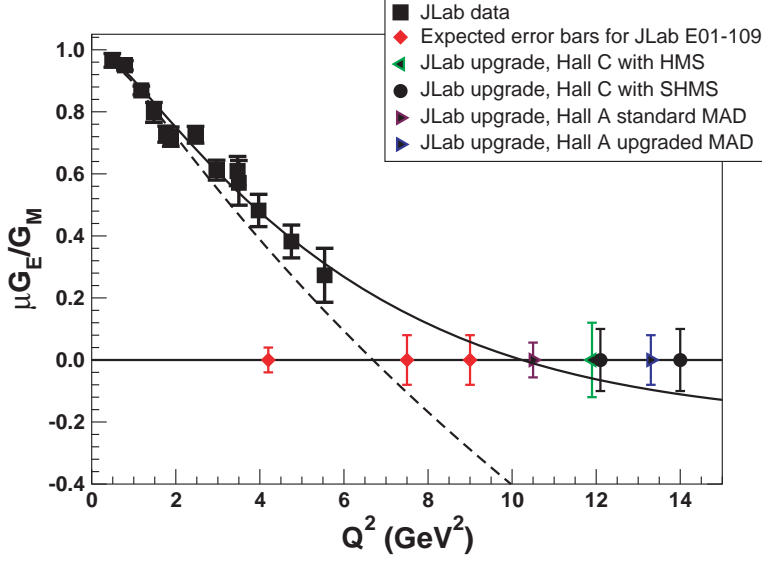


Figure 8: The result of the JLab measurement of  $G_E^p/G_M^p$  (black squares), and the range of the projected measurements. The dashed curve corresponds to the purely soft GPD of Burkardt [Bu02], and the solid curve results when an additional short range component is added. The difference between these two curves demonstrates how high  $Q^2$  form factor data will constrain our knowledge of the short range behavior of the nucleon wave function.

to high  $Q^2$  ( $\sim 30$  (GeV/c) $^2$ ) with relatively good accuracy. With the 12 GeV upgrade,  $G_E^p/G_M^p$  can be measured up to 14 (GeV/c) $^2$ . Knowledge of neutron form factors at high  $Q^2$  is equally important. For the neutron,  $G_M^n$  would be extended up to about 14 (GeV/c) $^2$ , and for  $G_E^n$  to 5 (GeV/c) $^2$ .

Recent JLab results (Fig. 8) show the potential for discovery with increasing  $Q^2$ ; before this experiment it was thought that  $G_E^p$  was roughly equal to  $G_M^p/\mu$ . These data demonstrate that charge and magnetization distributions in the proton are quite different. It provides a challenge for theory to explain these results. By extending the  $Q^2$  range of this data by over a factor of two, JLab at 12 GeV will probe the proton's structure to distances as small as 0.1 fm.

Real Compton Scattering (RCS) at high  $|t|$  and wide angles involves the measurement of cross sections and longitudinal and transverse polarizations. In the GPD picture the observables involve the  $\langle 1/x \rangle$  moments. The recent JLab data have been interpreted in this framework. The high  $|t|$  behavior of the GPDs and therefore the transverse distribution of quarks at small impact parameters in the nucleon will be significantly constrained by extended RCS measurements. With the 12 GeV upgrade it will be possible to extend  $|t|$  and  $s$  up to 20 (GeV/c) $^2$ . The RCS form factors  $R_V$ ,  $R_T$ , and  $R_A$  are expected to scale with  $s$  and  $|t|$  according to pQCD. The higher  $|t|$  data could provide important information on this transition to pQCD, and an essential complement to Virtual Compton Scattering data.

Resonance transition form factors access additional GPD components that are not directly



probed by elastic scattering or Real Compton Scattering. The form factors for the transition to the first excited state of the nucleon (the  $N \rightarrow \Delta$  transition) are connected to the isovector components of the GPDs. With the 12 GeV upgrade the dominant  $N \rightarrow \Delta$  form factor would be extended to almost 18 (GeV/c)<sup>2</sup>. Similarly, the multipole ratio  $E_{1+}/M_{1+}$ , which at small  $|t|$  is related to the deformation of the nucleon and the  $\Delta$ , would be extended up to about 12 (GeV/c)<sup>2</sup>. One might see the ratio depart from its current near zero value to approach the pQCD prediction that  $E_{1+}/M_{1+} = 1$  in this  $Q^2$  range. The transition to  $S_{11}(1535)$  will also be studied. The  $S_{11}$  amplitude is expected to scale with  $Q^3$ . Current data to  $Q^2 = 4$  (GeV/c)<sup>2</sup> do not yet show the expected scaling behavior. The upgraded facility would allow extensions of the data up to about 20 (GeV/c)<sup>2</sup>.

**Valence Quark Structure and Parton Distributions** The 12 GeV Upgrade will allow us to map out the quark distribution functions with high precision in the “clean” high- $x$  region where the three basic (“valence”) quarks dominate the proton and neutron wavefunction. Such measurements will have a profound impact on our understanding of the structure of the proton and neutron. They will also provide essential inputs for calculating hard cross sections at high energy hadron colliders such as the LHC or the Tevatron, in searches for the Higgs boson or for physics beyond the Standard Model.

Figure 9 shows an example of a measurement that can be done with the proposed Upgrade. The neutron polarization asymmetry  $A_1^n$  is determined by the spin wavefunction of the quarks, and most dynamical models predict that in the limit where a single valence up or down quark carries all of the nucleon’s momentum ( $x \rightarrow 1$ ), it will also carry all of the spin polarization (so, *e.g.* for the neutron,  $A_1^n \rightarrow 1$  as  $x \rightarrow 1$ ). Existing data on  $A_1^n$  end before reaching the region of valence quark dominance, and show no sign of making the predicted dramatic transition  $A_1^n \rightarrow 1$  (the recent data from the Hall A experiment E99-117 show the first hint of a possible upturn at the largest  $x$  value). There are similar paucities of data on all other DIS observables in this region.

Figures 10 and 11 show two more examples of the power of the 12 GeV upgrade for the study of valence quark structure (in both cases focused on  $d$ -quark structure). For the down quarks in the proton even the sign of the polarization at large  $x$  is not known (see Fig. 10). The polarization of individual quark flavors can be determined by detecting final state hadrons (such as pions or kaons) in coincidence with the scattered electron. These “semi-inclusive” deep inelastic scattering experiments will, in addition, allow us to study the “sea” quarks belonging to the quark-antiquark pairs at lower  $x$ , independently of the valence quarks. They will also provide access to new, hitherto unmeasured distributions such as the “transversity”, which describes the distribution of transversely polarized quarks in a transversely polarized nucleon.

Even in unpolarized DIS, where the available data are best, there are unresolved issues. To extract the ratio of such a simple and basic a property as the relative probability of finding a  $d$  quark vs. a  $u$  quark at high  $x$  requires measurements on both the proton and neutron. However, high- $x$  neutron information is difficult to disentangle from nuclear binding corrections due to the deuterium

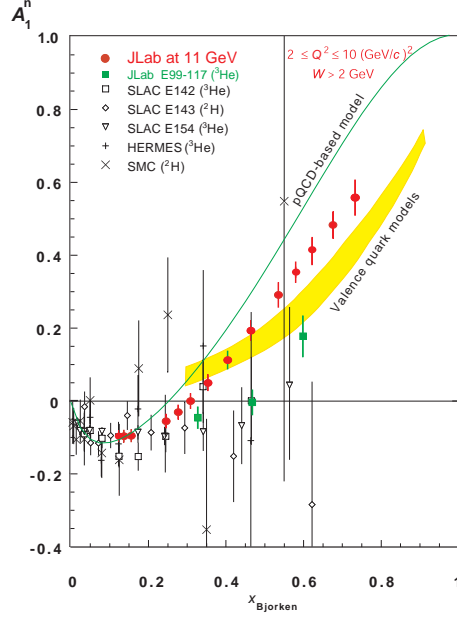


Figure 9: A projected measurement of the neutron polarization asymmetry  $A_1^n$ , determined by the spin structure of the valence quarks, made possible by the proposed 12 GeV Upgrade. The shaded band represents the range of predictions of valence quark models; the solid line is the prediction of a perturbative QCD (pQCD)-based quark model.

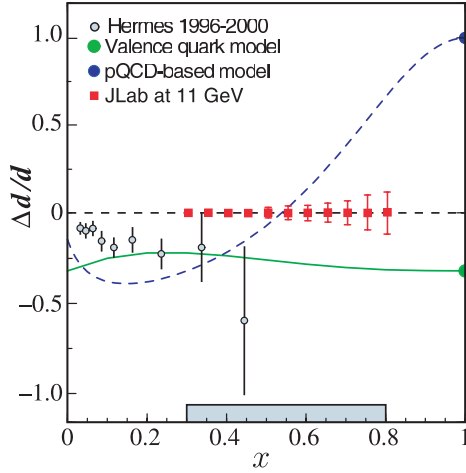


Figure 10: The ratio of polarized to unpolarized valence down quark distribution functions measured in semi-inclusive deep inelastic scattering. The solid squares represent the predicted accuracy with a 12 GeV Upgrade, with the systematic error indicated by the blue band. The solid (green) curve uses wavefunctions from a valence quark model, while the dashed (blue) uses pQCD-constrained fits to the world data set.

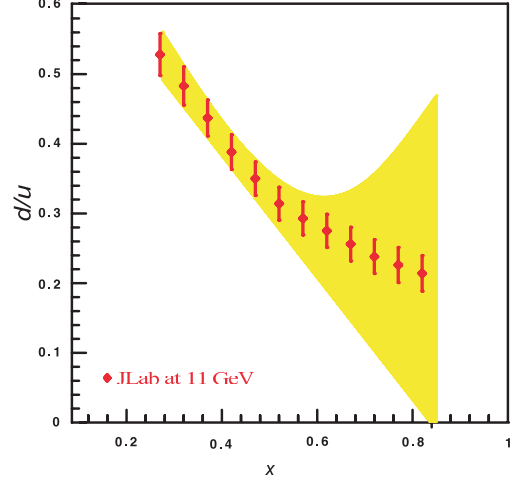


Figure 11: A projected measurement of the ratio of momentum distributions of valence  $d$  quarks to  $u$  quarks made possible by the proposed 12 GeV Upgrade. The shaded band represents the uncertainty in existing experiments due to nuclear Fermi motion effects.

target. Figure 11 shows the precision with which this fundamental ratio (which is intimately related to the fact that the proton and neutron, and not the  $\Delta$ , are the stable building blocks of nuclei) can be measured with the proposed Upgrade. The proposed experiment will utilize a novel technique, currently being pioneered at JLab; a recoil proton detector “tags” scattering events on a nearly on-shell neutron in a deuteron target. The mirror symmetry of  $A = 3$  nuclei could be exploited through simultaneous measurements of the inclusive structure functions for  ${}^3\text{He}$  and  ${}^3\text{H}$  to provide an independent measurement of this ratio. Both methods are designed to largely eliminate the nuclear corrections, thereby permitting the neutron-to-proton ratio (and thus the  $d/u$  ratio) to be extracted with unprecedented precision.

The measurement of structure functions over the large kinematic range made available with the 12 GeV Upgrade will also allow moments, or  $x$ -weighted integrals, of both spin-polarized and unpolarized structure functions to be determined accurately. Certain moments of polarized structure functions, for example, are related to the color-electric and magnetic polarizabilities of the nucleon, which characterize the response of the gluon fields to the nucleon’s polarization. These moments are also directly calculable from first principles using lattice QCD simulations, and will thus provide critical tests of QCD itself.

### **The Generalized Parton Distributions as Accessed via Deeply Exclusive Reactions**

The Generalized Parton Distributions tell us a great deal more about the physics of partons than do the individual Feynman distributions and the form factors. For example, one can determine the quark angular momentum distribution from the GPDs. The total quark contribution to the spin of the nucleon can be determined by the following sum rule [Ji97]:

$$J^q = \frac{1}{2}\Delta\Sigma - L^q = \frac{1}{2} \int_{-1}^1 x dx [H^q(x, \xi, 0) + E^q(x, \xi, 0)] \quad (1)$$

The quark spin part contribution,  $\Delta\Sigma$ , has been measured for the last decade through polarized deep-inelastic scattering. Therefore, an experimental determination of  $J^q$  allows a measurement of the quark orbital angular momentum, a quantity hard to determine otherwise.

One of the striking findings that has emerged from the theoretical study of the GPDs is that they can be measured through a new class of “hard” exclusive processes: Deeply Virtual Compton Scattering (DVCS) and Deeply Virtual Meson Production (DVMP). Both of these reactions are a subset of deep inelastic scattering in which specific exclusive final states are measured. As shown schematically in Fig. 12, in DVCS the electron knocks a quark out of the proton by exchanging a deeply virtual (massive) photon. The quark then emits a high energy photon and is put back into the proton. In DVMP a  $q\bar{q}$  pair is created, and a quark is returned into the proton while the  $\bar{q}$  picks up a quark from the vacuum to form a meson. At sufficiently high energy and virtuality of the exchanged photon (Bjorken regime) these hard processes can be described by perturbative QCD, and the cross sections can be used to extract the “soft” information of the nucleon described by the GPDs.

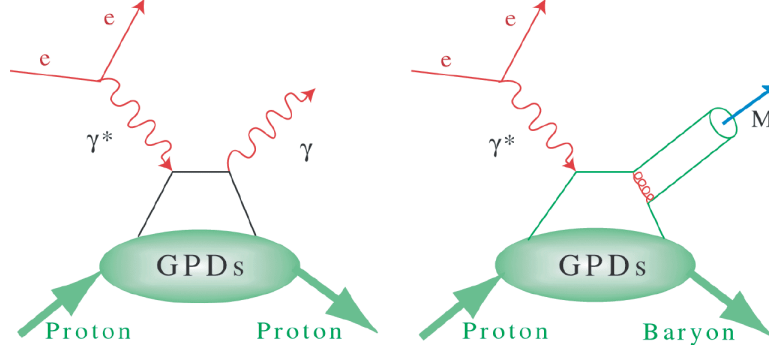


Figure 12: The “handbag” diagrams for deeply virtual Compton scattering (left), and for deeply virtual meson production (right). Four GPDs describe the “soft” proton structure part. They depend on the longitudinal quark momentum fraction  $x$ , and two more variables: the longitudinal momentum imbalance of the quark before and after the interaction,  $\xi$ , and the momentum transferred to the proton,  $t$ .

At energies and momentum transfers currently available at JLab, photons are produced not only via DVCS but also (even more copiously) via the electromagnetic Bethe-Heitler (BH) process. The two processes interfere, and the BH term, which is completely determined by the well known elastic form factors, “boosts” the much smaller and unknown DVCS term, which is determined by the GPDs, to comfortably measurable levels. During the past two years DVCS has become an established tool of GPD studies with experimental results from CLAS [St01] at JLab and from the HERA experiments H1 [Ad01], ZEUS [Sa01], and HERMES [Ai01]. These data are well described in a consistent GPD analysis in leading order (LO) and next to leading order (NLO) QCD [Fr01], supporting the applicability of the GPD formalism to exclusive photon production even at relatively low  $Q^2$ . An example of the broad kinematic coverage in  $Q^2$ ,  $x_B$ , and  $t$  for the DVCS program, achievable with the equipment proposed for the 12 GeV upgrade, is shown in Fig.13. Similar coverage can be achieved for the GPD program in meson production.

Polarized beam asymmetry measurements allow the extraction of GPDs or linear combinations of GPDs at fixed kinematics  $x = \xi$ , while cross section measurements determine integrals of GPDs at fixed values of  $\xi$  and  $t$ . Different combinations of GPDs can be measured using polarized targets. DVCS off unpolarized protons cannot separate contributions from different quark flavors or separate the spin-dependent from the spin-independent GPDs. DVMP is another tool to study GPDs; it can make these separations. Vector meson production, (*e.g.*  $\rho$  and  $\omega$ ) permit the isolation of the spin-independent GPDs and separate  $u$  and  $d$  quark contributions, while pseudoscalar meson production (*e.g.*  $\pi^0$ ,  $\eta$ ) accesses the spin-dependent GPDs.

A full program to extract GPDs from measurements requires coverage of a large kinematic range in  $\xi$ ,  $t$ , and  $Q^2$ , and measurement of several final states together with the use of polarized beam and polarized targets with longitudinal and transverse polarization. The 12 GeV upgrade of the electron accelerator and of the equipment required for the GPD program will provide the kinematic coverage needed for a broad program of DVCS and DVMP. Doubling the energy of the

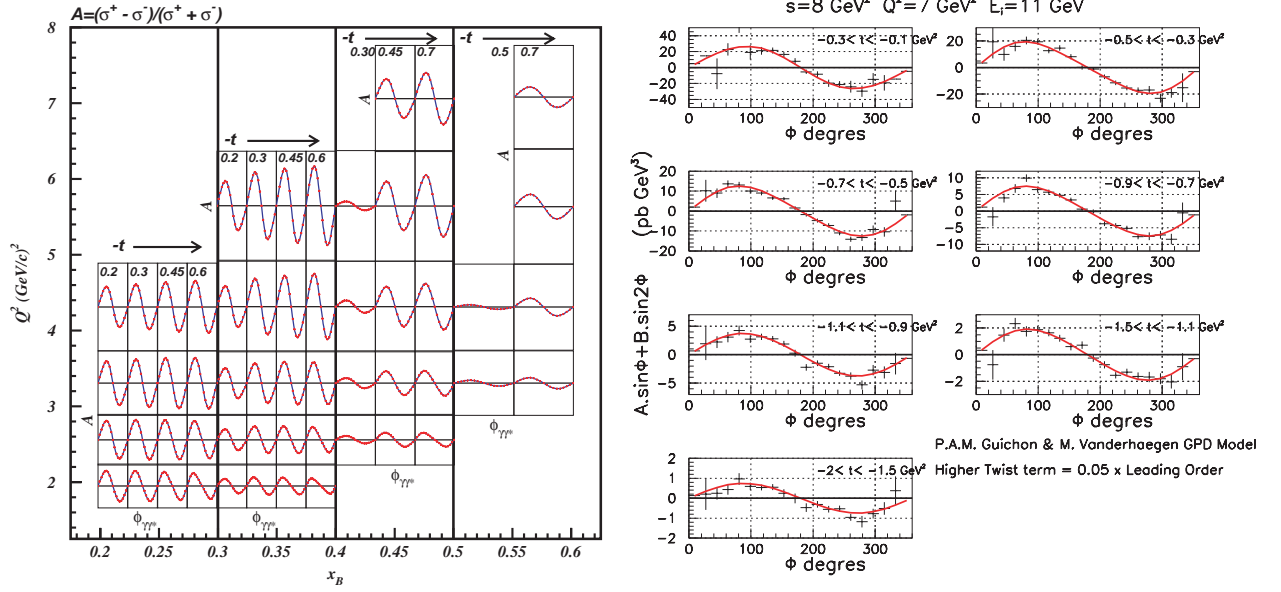


Figure 13: Beam spin asymmetry for  $\vec{e}p \rightarrow ep\gamma$ . Projected data and error bars for kinematic coverage of DVCS/BH asymmetry measurements. The left panel shows the lower  $t$  portion of azimuthal asymmetries that can be accessed simultaneously. The curves represent a specific model for the GPDs. The right panel shows projected data at the highest  $Q^2$  for cross section differences. In kinematics, where the DVCS cross section is large, absolute cross section measurements will be possible giving access to moments of different combinations of GPDs.

current accelerator in conjunction with the very high luminosity will allow access to the highest  $Q^2$  and  $\xi$  values of any facility worldwide. These unprecedented capabilities will allow a comprehensive program of DVCS and DVMP to be carried out.

The results of this program, together with results at smaller  $\xi$  from other laboratories, will form the basis for the ultimate extraction of the GPDs. Recently, it has been realized that the GPDs provide the quantum phase-space (Wigner) distributions of the quarks and gluons [Ji03c, Be03a]. A phase-space function represents a correlated momentum and coordinate distribution and is much more powerful than the momentum or coordinate space distribution alone. While quantum phase-space distributions have been widely used in many different areas, they have not been studied systematically for subatomic systems. Using a GPD parametrization fitted to measured form factors and parton distributions, Belitsky *et al.* [Be03a] obtained the phase-space charge distributions shown in Fig. 14. These quark images are 3D pictures of the quark charge distribution for selected Feynman momentum  $x$ , corresponding to the full distribution seen through Feynman momentum (“color”) filters. At very small  $x$ , the quarks spread out in the direction of the momentum, going as far as  $1/x$ . At large  $x$ , the quantum nature of the distribution becomes very clear and the image looks like a diffraction pattern. At intermediate  $x$  where the valence quarks dominate, the image is like what we normally think of the proton.

An alternate visualization of nucleon structure, showing the quark-flavor distribution and the

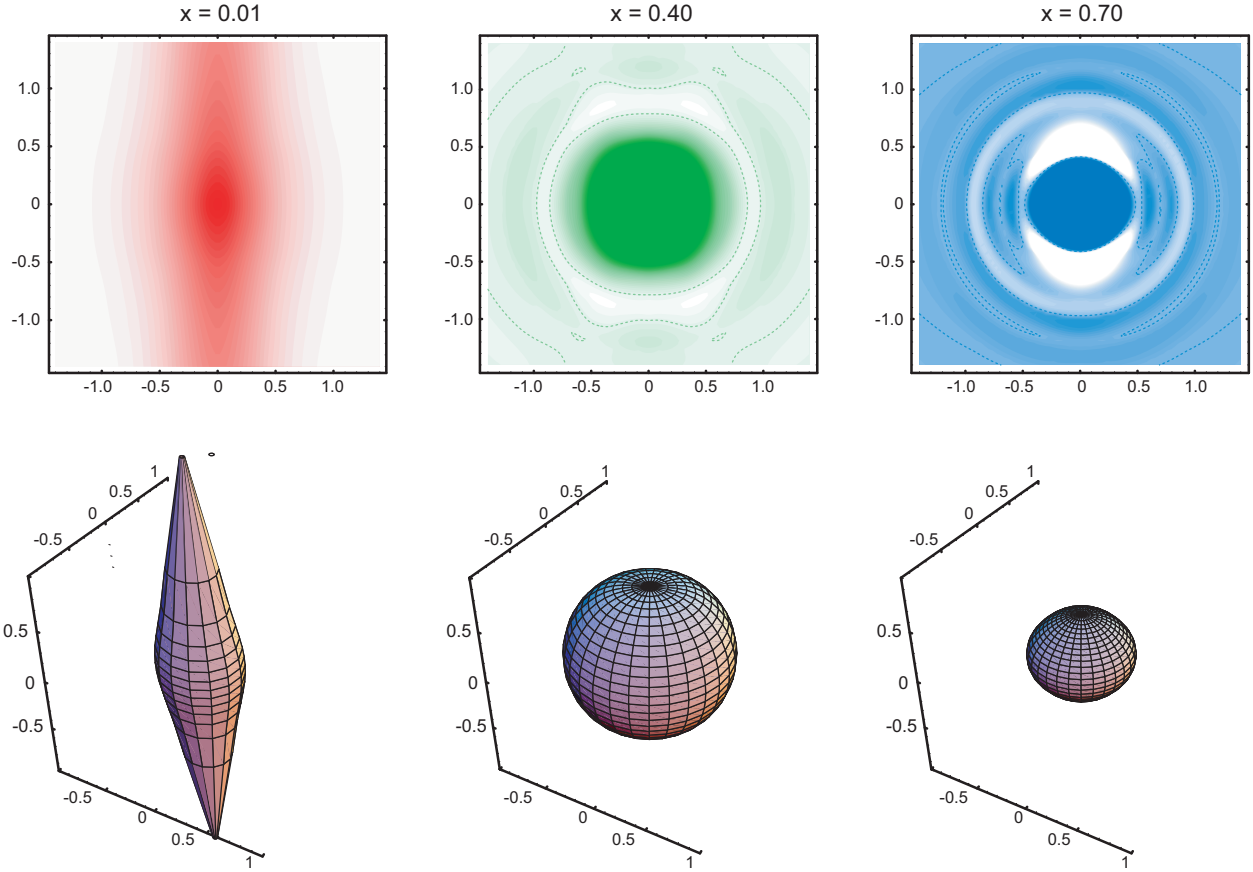


Figure 14: A model  $u$ -quark phase space charge distribution in 3D coordinate space for three Feynman momentum fractions:  $x= 0.01, 0.40$ , and  $0.70$ . In the upper pictures the vertical axis corresponds to the longitudinal direction selected by the virtual photon that defined  $x$ . The pictures are rotationally symmetric in the transverse direction, which is shown here as the horizontal axis. The lower set of figures show the shape of a constant density contour for the corresponding distribution above.

spin-flavor polarization for the  $u$  and  $d$  quarks in unpolarized and transversely polarized protons, is shown in Figure 15. These distributions were constructed by Burkardt [Bu02] from models for the GPDs  $H(x, \xi = 0, b_\perp)$  and  $E(x, \xi = 0, b_\perp)$ . Even five years ago it was unimaginable that we would ever be able to obtain such detailed and revealing images of proton structure.

**Other Topics in Hadron Structure** In addition to the broadly focused programs described above, the 12 GeV Upgrade will support important research directions into other aspects of hadron structure. Three examples presented here are the use of semi-inclusive scattering to access quark transverse momentum effects, measurements of the evolution of the spin structure of the nucleon with distance scale, and the study of duality – the emergence of the nucleon as an object in its own right from its quark-gluon substructure.

**Transverse parton distributions** The transverse momentum dependent (TMD) parton distributions [Ra88, Mu96] are a class of functions that represent information on the transverse hadron structure; they are complementary to the GPDs and encode information on the orbital motion of quarks. Experimentally, TMDs can be accessed in measurements of azimuthal distributions of final state photons or hadrons in semi-inclusive deep inelastic scattering. From this quark transverse momentum distributions can be obtained. A theoretical understanding of this new information is now emerging. It has been shown [Co93, Br02] that initial and final state interactions at the parton level are probed. TMDs also provide a new avenue for probing the chiral nature of the partonic structure of hadrons [Co02]. Single spin asymmetries are sensitive to this information even at lower energies [Ba02, Be01]. The first experimental data show significant asymmetries using polarized targets (HERMES at DESY), (SMC at CERN), and polarized beams (CLAS at JLab). Already at the 4-6 GeV energies at JLab, the data are consistent with a partonic interpretation. At the 12 GeV Upgrade the single spin asymmetries with polarized beams and polarized targets could become another pillar in the study of the quark spatial and spin distribution in the transverse momentum plane, with the ultimate goal of unraveling the new parton physics encoded in the GPDs and TMDs, especially in the effort to understand the orbital motion of quarks.

**The extended GDH integral and sum rule** The extended GDH integral [Ji01, Dr00],  $I(Q^2)$ , can be measured from arbitrarily small  $Q^2$ , where behavior is dominated by hadronic degrees of freedom, to arbitrarily large  $Q^2$ , where behavior is dominated by quark degrees of freedom [Am02]. A weighted integral over the difference of the spin-dependent total cross sections for virtual photoabsorption,  $I(Q^2)$  is firmly tied theoretically by the GDH sum rule at  $Q^2 = 0$  [Ge66, Dr66], and by both experimental and theoretical constraints as  $Q^2 \rightarrow \infty$ . As such, it is an excellent proving ground for quantitative tests of our understanding of the transition from perturbative to non-perturbative regimes. Accurate determinations of  $I(Q^2)$ , however, require measurements over a wide range of  $Q^2$  at energies corresponding to both the resonance region as well as deep inelastic scattering. At 6 GeV, measurements are confined largely to the resonance region. With the 12 GeV



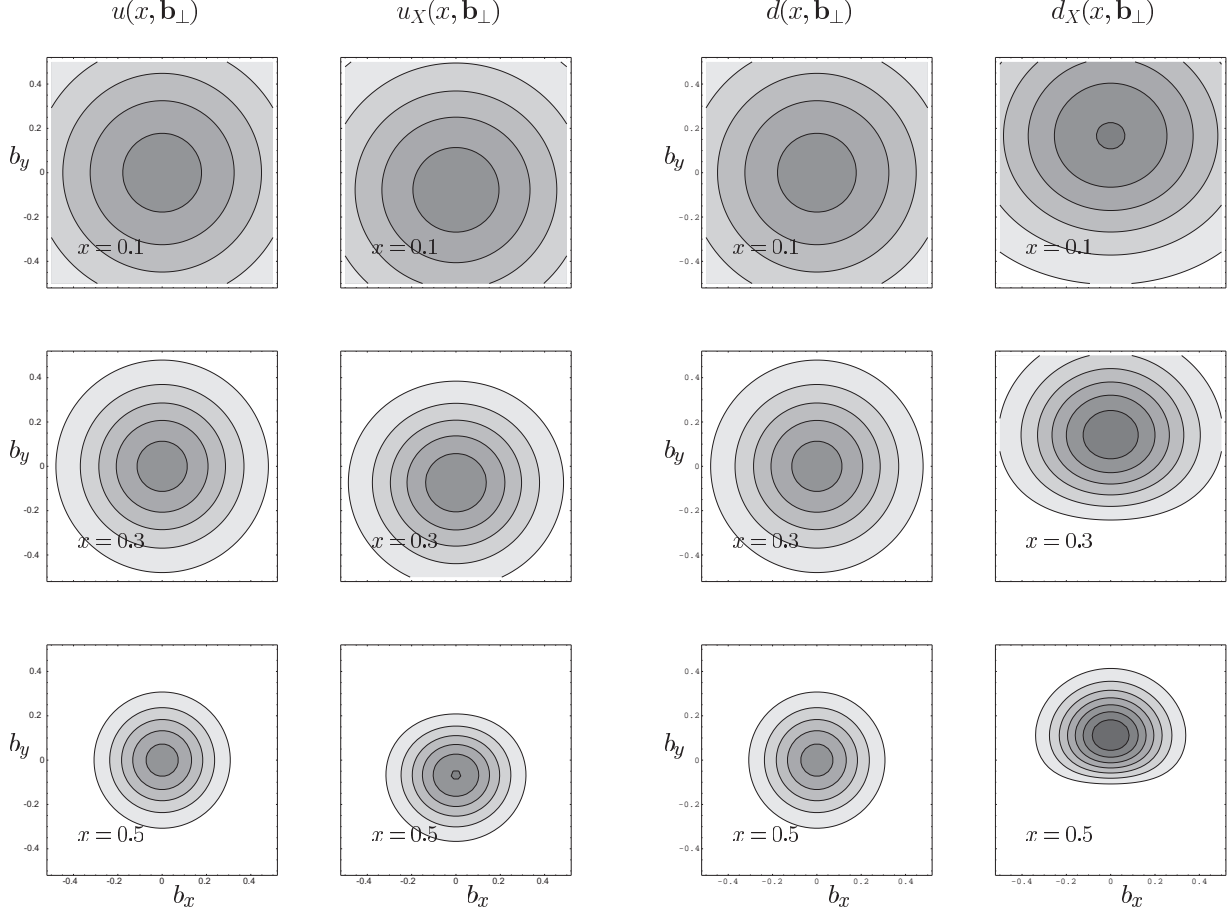


Figure 15: The quark spatial and spin distributions in the transverse plane from model calculations. The left panels show the  $u$  quark longitudinal momentum and helicity distributions in transverse impact parameter space. The panels on the right show the corresponding images for the  $d$  quarks in the proton. A strong correlation between the transverse size and the longitudinal momentum is evident. For small quark momentum fractions  $x$ , the proton has a large transverse size, and it becomes very dense at large  $x$ . The right columns in each panel show the quark spin distributions in a transversely polarized proton.  $u$  and  $d$  quarks exhibit a strong and opposite spatial asymmetry. Quarks in a transversely polarized protons have a strong spin-flavor polarization, especially at high  $x$ . The general features of these plots are model independent.



upgrade, studies of the extended GDH sum rule will have the kinematic coverage necessary to probe the high-energy piece of the extended GDH integral. The program will compliment real-photon studies planned at SLAC, and bring GDH studies to a new level of quantitative precision.

**Duality: the transition from a hadronic to a quark-gluon description of Deep Inelastic Scattering** For many years, particle and nuclear physicists have noticed a striking similarity between data measured at extremely high energies, where electrons scatter from quarks in relative isolation, and data at lower energies, where electrons scatter from a proton that responds coherently. This observed similarity is known as quark-hadron duality. This quark-hadron duality at low energy naturally examines the transition between strongly interacting matter and the quark-gluon descriptions of perturbative QCD. Recently, there has been significant progress in quantifying and understanding duality. To further understand the phenomena underlying duality, however, studies with different flavor and spin filters (including L/T separations) are needed with the much wider range of kinematics accessible with 11 GeV electrons. For structure functions where duality is demonstrably valid, parton distribution functions can be extracted at higher  $x$  than possible if traditional limits defining the quark-gluon regime are imposed. Duality studies are also crucial in establishing kinematics where fragmentation can be applied in the interpretation of semi-inclusive scattering experiments.

### 1.A.3 The Physics of Nuclei

A great deal of nuclear properties and reactions over a wide energy range – from the few keV regime of astrophysical relevance to the MeV regime of nuclear spectra to the tens to hundreds of MeV regime measured in nuclear response experiments – can be understood quantitatively by describing nuclei as assemblies of individual nucleons bound by effective interactions.

The dominant two-body interaction has a component at large internucleon distances ( $\geq 2$  fm) due to pion exchange, which is theoretically well understood. The main feature of this one-pion-exchange component is its tensor character, which leads to a strong coupling between the nucleons' spatial and spin degrees of freedom. These spin-space correlations make nuclei markedly different from other systems where the dominant interaction is independent of the particles' internal degrees of freedom (spin and isospin), such as the Coulomb interaction in atoms and molecules and the van der Waals interaction in liquid Helium.

At short internucleon distances, the two-body interaction is thought to be influenced by heavy-meson and quark-exchange mechanisms, and by the excitation of nucleon resonances. It is poorly understood, although it is well constrained phenomenologically (at least below the pion production threshold) by the large body of  $pp$  and  $np$  elastic scattering data. It is predominantly characterized by a strong repulsion.

The interplay between these two aspects of the nucleon-nucleon interaction—its short-range repulsion and long-range tensor character—have profound consequences for the spatial and spin structure of nuclei [Fo96]. For example, the deuteron, the simplest nucleus consisting of a proton and neutron bound together, has a toroidal shape when the proton’s and neutron’s spins are opposite, and a dumbbell shape when their spins are aligned. This picture of the deuteron has been confirmed experimentally, in its broad outlines, by the recent measurement of the tensor polarization of the deuteron in elastic  $eD$  scattering at Jefferson Lab.

These short-range and tensor correlations are reflected in many nuclear properties. For example, the density distributions in nuclei of two-nucleon states with deuteron-like quantum numbers are very small at small internucleon separations and exhibit strong anisotropies depending on the relative orientation of the two nucleons’s spins; in the region  $r \leq 2$  fm, they are found to differ from those in the deuteron only by an overall scale factor depending on the mass number of the nucleus [Fo96]. Another example of the impact of correlations is the increase in the relative probability of finding, within the nucleus, a nucleon with a very high momentum.

The  $N - N$  interaction at large distances is well-represented by pion exchange; at short and intermediate distances, meson-exchange mechanisms (with phenomenologically determined couplings and short-range cutoffs) provide a good representation that leads naturally to effective many-body currents. There is a great deal of experimental evidence for the presence of these meson-exchange currents in nuclei from measurements of the charge and magnetic form factors of the hydrogen and helium isotopes, deuteron electrodisintegration at threshold, and low-energy radiative capture reactions involving few-nucleon systems.

While the description of nuclei outlined above provides a coherent and deceptively simple framework for the understanding of their properties over the range of energy and momentum transfers measured so far, it leaves unanswered several crucial questions:

- How do these effective interactions involving nucleons and mesons arise from the underlying dynamics of quarks and gluons ?
- Down to what distance scale does the short-range structure of nuclei implied by these interactions remain valid ?
- How does the transition from the nucleon-meson- to the quark-gluon-based description of nuclei occur and what are its signatures ?

Answers to these questions, taken together with an understanding of the QCD basis for the structure of the hadrons (the focus of the second major research thrust of the Upgrade, as outlined in Section 1.A.2 above) will provide an intellectually firm foundation for our understanding of nuclear physics that is analogous to our understanding of the physics of atoms, molecules and condensed matter based on the underlying theory of quantum electrodynamics.

**The Short-Range Behavior of the  $N - N$  Interaction and Its QCD Basis** The 12 GeV Upgrade will provide unique opportunities for an understanding of how the  $N - N$  interaction emerges from the underlying quark-gluon structure of the individual nucleons, identifying of the responsible mechanisms through, for example, studies of the phenomenon of color transparency in exclusive processes, color van der Waals-type interactions in  $\psi$ -meson photoproduction, and quark propagation and hadronization in the nuclear medium. The details of the short range behavior of the  $N - N$  force will also be explored by a novel program of deep inelastic scattering aimed toward identifying the heretofore elusive (to experiment) short range correlations among the nucleons. Relevant experimental programs are outlined below, and described in detail in Chapter 2. Much of the information gained from these experiments will also be useful in the second major program in the physics of the nucleus, completing our understanding of the transition from the meson-nucleon description of nuclei to the underlying quark and gluon description, which is outlined below.

**Color transparency.** The nature of hadronic interactions can be investigated via tests of the prediction of “color transparency”. Color transparency is one of the few direct manifestations of the underlying color degrees-of-freedom in nuclear physics. Under the right conditions, three quarks, each of which (alone) would have interacted very strongly with nuclear matter, could form an object that passes undisturbed through the nuclear medium. A similar phenomenon occurs in QED, where an  $e^+e^-$  pair of small size has a small cross section determined by its electric dipole moment. In QCD, a  $q\bar{q}$  or  $qqq$  system with a small color dipole moment is predicted to have similarly reduced interactions due to cancelation of the color fields of the quarks. While the  $q\bar{q}$  case is completely analogous to the QED example, color transparency in the  $qqq$  case would be one of the rare demonstrations of the  $SU(3)$  nature of the underlying color degrees of freedom. While the nucleonic example is more exotic, meson production may provide a more practical setting for observing this phenomenon. Intuitively, one expects an earlier onset of color transparency for meson production, as it is much more probable to produce a small sized configuration in a  $q\bar{q}$  system than in the  $qqq$  system. Color transparency can be observed experimentally by measuring a reduced attenuation of particles as they exit a nucleus, or by measuring a decrease in production of particles produced via two-step rescattering mechanisms, which allows the use of few-body nuclei. A series of attenuation and rescattering measurements for both protons and mesons will allow us to separate the necessary ingredients: formation of the small sized configuration, the reduced color interaction of these configurations, and the evolution of these exotic configurations back into ordinary hadrons. The observation of color transparency and characterization of the non-perturbative evolution of a mini-hadron to its physical size will lead to a better understanding of the dynamics of confinement.

**Learning about the  $NN$  force by the measurement of the threshold  $\psi N$  cross section and by searching for  $\psi$ -nucleus bound states.** Threshold  $\psi$  photoproduction is a unique process since the small  $c\bar{c}$  state is produced by the interaction of its calculable small color dipole moment with a nucleon (in which it is presumed to *induce* a large, but uncalculable,

color dipole moment). This simple color van der Waals-type force is a prototype for a potentially important component of the  $NN$  force. It is quite possible that this interaction is sufficiently strong that  $\psi N$  or  $\psi$ -nucleus bound states exist. Such relatively long-lived objects might be detected in subthreshold  $\psi$  production off nuclei. Based on the same picture, one could also look for  $\phi N$  states. Each exchanged gluon may also couple to a colored cluster and reveal the hidden color part of the nuclear wave function, as well as multiquark correlations, a domain of short range nuclear physics at high density where nucleons lose their identity. Finally the formation time of the  $\psi$  is quite short, and takes place over a distance that is much shorter than the size of the nucleus; this permits a more reliable determination of the  $\psi - N$  scattering cross section, an important input in the search for signatures of the quark-gluon plasma. Only the high intensity and duty factor of the beams available from an upgraded CEBAF make it possible to exploit the potential of discovery of such an almost virgin field.

**Quark propagation through cold QCD matter: nuclear hadronization and transverse momentum broadening.** The properties of isolated quarks are generally experimentally inaccessible due to quark confinement in hadrons. In hard interactions, such as in deep inelastic scattering, the struck quark in a nucleon must separate from the rest of the residual system. When this separation distance is comparable to nuclear radii, it is possible to study the properties of the propagating quark by varying the radii of the nuclear targets and observing modifications of the final hadronic states. The distances over which the struck quark transforms into a new hadron can be characterized as a function of multiple variables. This provides completely new information on how the color field of the hadron is restored in real time through the fundamental process of gluon emission. The analogous process has been studied and understood in QED. The propagating quark is expected to experience some interaction with the nuclear medium. One prediction is that it undergoes multiple soft scatterings mediated by gluon emission. In this picture, the quark experiences a medium-induced energy loss that may be experimentally accessible and which may exhibit exotic coherence phenomena. This process measurably broadens the transverse momentum distribution of the hadron emerging from larger nuclei. It is anticipated that a quark-gluon correlation function, and the quark energy loss, can be extracted from the measured broadening. The topics of color field restoration by gluon emission, quark-gluon correlations, and quark energy loss, offer fundamental and interesting insights into the nature of QCD and confinement. In addition, they are of very high interest in the study of relativistic A-A and p-A collisions, where they are basic and essential ingredients that must be understood.

**Short-range correlations in nuclei: the nature of QCD at high density and the structure of cold, dense nuclear matter.** The upgrade will allow substantial extensions to JLab's studies of high-momentum components of nuclear wavefunctions and short-range nucleon-nucleon correlations. With a variety of measurements made in the three existing halls, the upgrade will answer several questions about nuclear many-body theory and map out the strength and nature

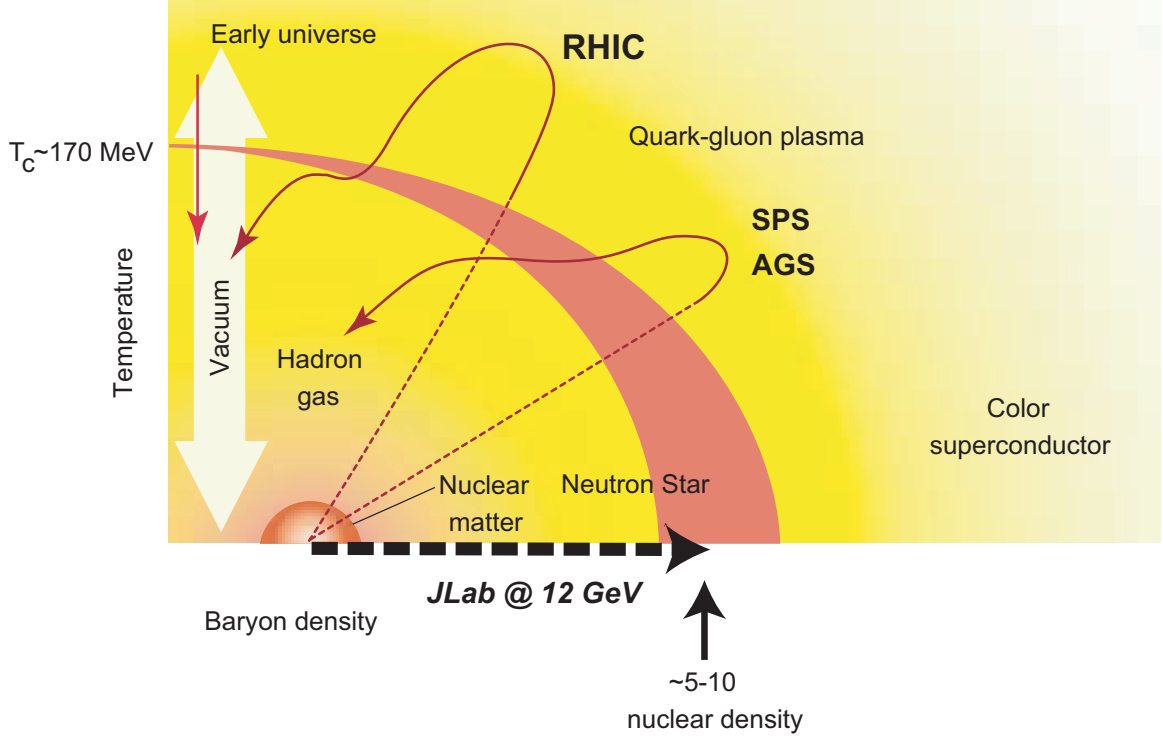


Figure 16: Phase diagram for nuclear matter. With the energy upgrade, JLab will be able to probe cold nuclear matter at extremely high density. The red band indicates the phase transition from hadronic to quark matter.

of two-nucleon and multi-nucleon correlations in nuclei. These short-range correlations represent high density droplets of nuclear matter with instantaneous densities comparable to those at which the zero temperature quark-gluon phase transition is expected to occur (Fig. 16). The structure of nucleons and the distribution of high-momentum quarks may be substantially altered in this region, where significant overlap of nucleons should allow direct interaction between quarks in different nucleons. These measurements will allow us to determine if such modification of nucleon structure is responsible for the EMC effect, and will help us understand the quark-gluon phase transition at high density. This complements RHIC studies of this same transition at high temperature, while at the same time providing us information on the structure of matter at extremely high densities. Probing these high density components in nuclei is the only way to directly study high density nuclear matter, and what we learn here will be important in understanding neutron stars and other compact astronomical objects.

**Identifying and Exploring the Transition from the Meson/Nucleon Description of Nuclei to the Underlying Quark and Gluon Description.** The hadron to parton transition region is another interesting and important open question in nuclear physics. Low energy nuclear physics has been described successfully using effective interactions among nucleons, *i.e.* in terms

of hadronic degrees of freedom. On the other hand, at sufficiently high energy, perturbative QCD (pQCD) describes hadronic reactions in terms of quark and gluon degrees of freedom. Very little is known about the transition between these two regimes, in particular there are no clear indications from theory as to the energy range in which it should occur; it must be mapped out by experiment.

An important search for this elusive transition region can be carried out with the 12-GeV upgrade envisioned for Jefferson Lab. The strategy outlined below is to search for it in the simplest systems, *i.e.* in the pion and nucleon, since these are the hadronic building blocks of nuclei at low energy, and in the deuteron and Helium isotopes, since these nuclei are particularly amenable to theoretical interpretation. Some proposed signals for the transition region are observation of scaling and hadron helicity conservation (in addition to other possible signals, such as color transparency, which is described above). The proposed high-current 12-GeV electron beam coupled with relatively large acceptance detectors will be essential tools in searching for these exotic effects. Relevant experimental programs are outlined below, and described in detail in Chapter 2. Much of the information gained from these experiments will also be useful in developing an understanding of the short range behavior of the  $N - N$  interaction and of how it emerges from the underlying quark-gluon structure of the individual nucleons.

**The onset of scaling behavior in nuclear cross sections**      Scaling in the differential cross section  $d\sigma/dt$ , and hadron helicity conservation have been pursued experimentally for many years as providing signatures of the transition from the meson/nucleon description of nuclei to the underlying quark and gluon description. The deuteron photodisintegration reaction,  $\gamma d \rightarrow pn$ , is one of the simplest reactions for studying explicit quark effects in nuclei. In recent years, extensive studies of deuteron photo-disintegration have been carried out at SLAC and JLab [Na88, Sc01]. Figure 17 shows the scaled differential cross-section ( $s^{11}d\sigma/dt$ ) for deuteron photodisintegration as a function of photon energy. The available data [Sc01] seem to show scaling at  $70^\circ$  and  $90^\circ$ , and suggest the onset of scaling at higher photon energies at  $52^\circ$  and  $36^\circ$ . The threshold for this scaling behavior corresponds to a transverse momentum slightly over 1 GeV. Theoretical efforts [Fr01, Ko93, Gr01, Rapc] to describe this behavior agree qualitatively with the data, but do not reproduce them precisely. While none of the theories agree with all of the data as well as one would like, they do indicate that quark models can approximately reproduce the cross section data, and therefore re-establish the importance of the deuteron photodisintegration process in the study of the transition region. The Upgrade will permit the extension of these data to photon energies near 8 GeV, as shown in the figure, permitting a confirmation of the apparent constant transverse momentum onset of scaling behavior.

**Helicity conservation in nuclear reactions**      While global scaling behavior has been observed in many exclusive processes [An76], no experimental evidence supports hadron helicity conservation, which was predicted in the same approach, in the similar energy and momentum transfer region. The hadron helicity conservation arises from the vector coupling nature of the

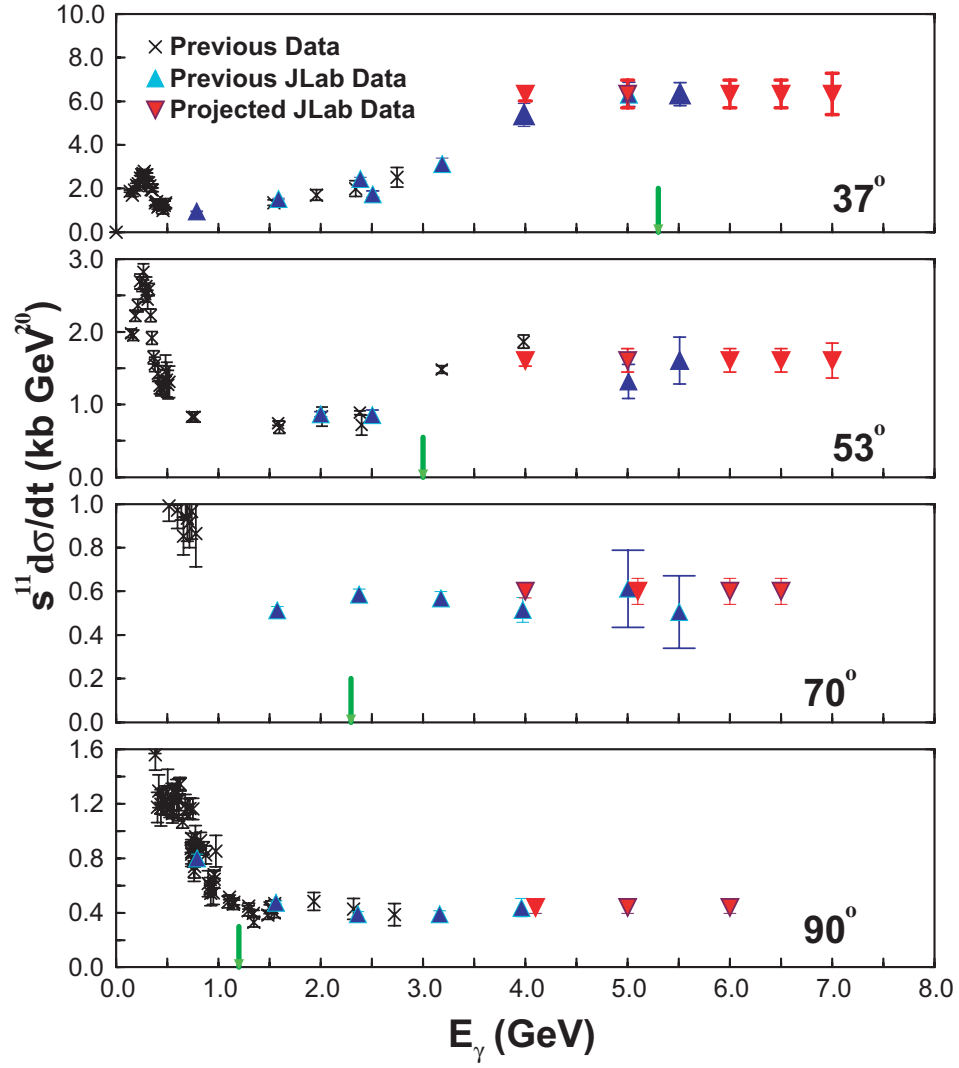


Figure 17: Available data projected results for a differential cross-section measurement of deuteron photodisintegration.

quark-gluon interaction, the quark helicity conservation at high energies, and the neglect of the non-zero quark orbital angular momentum state in the nucleon. The parton orbital angular momentum was considered for the first time by Chernyak and Zhitnitsky [Ch77a] for form factors. Recently, Ji, Ma, and Yuan [Ji03] derived a generalized counting rule for exclusive processes at fixed angles involving parton orbital angular momentum and hadron helicity flip. This generalized counting rule opens a new window for probing the quark orbital angular momentum state inside the nucleon by employing exclusive processes. A natural connection between the study of the parton-hadron transition through exclusive processes and generalized parton distributions typically probed through deeply virtual processes is therefore established.

Polarization measurements can play a crucial role in understanding reaction mechanisms of exclusive processes at large momentum transfers. Therefore, they are important measurements in the transition region that will provide insights into the underlying mechanism governing the onset of the scaling behavior and test the hadron helicity conservation rule. Furthermore, the combination of precise differential cross-section and polarization measurements allows unique access to the parton orbital angular momentum inside the nucleon based on the newly-derived generalized counting rule [Ji03]. The upgrade would permit the extension of polarization data from deuteron photo-disintegration [Kr01] to  $\sim 4$  GeV, and from  $\vec{\gamma}p \rightarrow \vec{p}\pi^0$  reaction to approximately 8 GeV.

**The charged pion form factor** To complete our understanding of ‘strong’ QCD one essential piece of information is an understanding of how the dynamics of the strong interaction makes a transition from being dominated by the strong QCD [Cl95a] of confinement to perturbative QCD. This transition should occur first in the simplest systems. In particular, because of its simple  $q\bar{q}$  valence structure, the pion and its electromagnetic form factor is unique in that the transition is estimated to take place in the region where data may be taken; there are many calculations, including some based on NLO pQCD, for this transition. Figure 18 shows available data on the pion form factor, and how well the proposed 12 GeV Upgrade can explore this transition.

**Pion photoproduction from the nucleon and in the nuclear medium** Due to its simplicity, the pion form factor provides our best hope for direct comparison with rigorous QCD calculations. As can be seen from Fig. 18, it is still dominated by non-perturbative effects at a few (GeV/c)<sup>2</sup>. An earlier onset to the scaling associated with pQCD may be seen by forming ratios of differential cross sections from exclusive processes. The simplest of such ratios is the charged pion photoproduction differential cross-section ratio,  $\frac{d\sigma}{dt}(\gamma n \rightarrow \pi^- p) / \frac{d\sigma}{dt}(\gamma p \rightarrow \pi^+ n)$ .

In such a ratio, non-perturbative effects may cancel and one may expect the  $\pi^-/\pi^+$  ratio to give the first indication of the onset of pQCD. Calculations of this ratio have been performed in the framework of handbag mechanism [Hu00, Hu03], in which the amplitude is factorized into a parton-level subprocess  $\gamma q_a \rightarrow P q_b$  and generalized parton distributions (GPD). The GPD part of the contribution describing the soft hadron-parton transitions indeed cancels in this ratio provided the



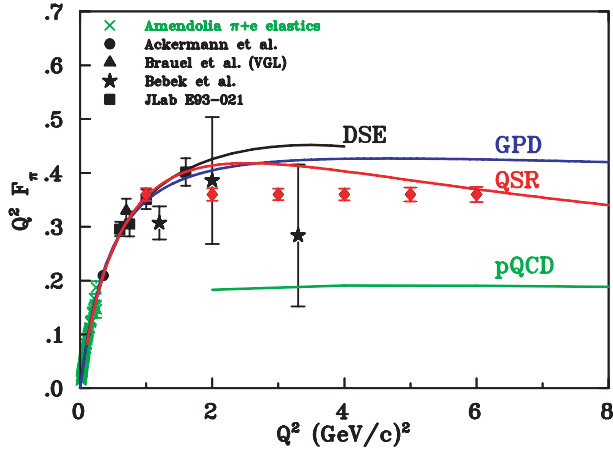


Figure 18: The projected measurements of the pion elastic form factor through the expected transition region from confinement-dominated dynamics to perturbative-dominated dynamics made possible by the proposed 12 GeV Upgrade. Also shown are a few of the dozens of model predictions, all characterized by being confinement-dominated below about  $2 \text{ (GeV/c)}^2$  and making a transition to being perturbative-dominated with a value of  $Q^2 F_\pi \simeq 0.1 \text{ (GeV/c)}^2$  in the region of  $10 \text{ (GeV/c)}^2$ .

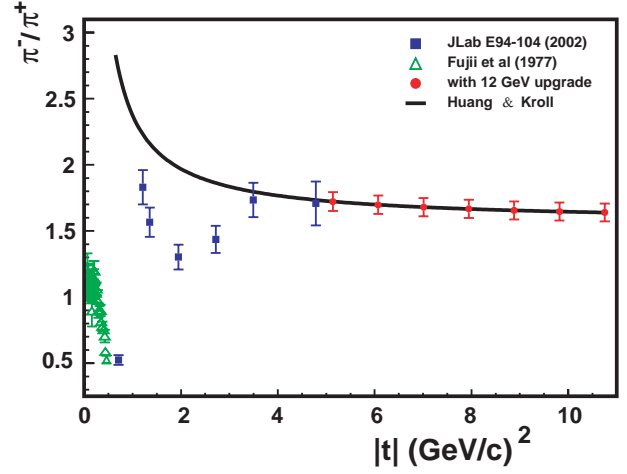


Figure 19: The charged pion photoproduction differential cross-section ratio at a C.M. angle of  $90^\circ$ , as a function of  $|t| \text{ (GeV/c)}^2$  (blue) along with the projected measurements for JLab at 11 GeV (red). The solid curve is a prediction by Huang and Kroll [Hu00].

assumption of negligible quark helicity flip contributions and the dominance of a helicity conserving amplitude of the parton-level subprocess  $\gamma q_a \rightarrow P q_b$  for pseudoscalar meson production [Hu03]. The most recent charged pion ratio data [Zh03a] from experiment E94-104 for momentum transfers up to  $5.0 \text{ (GeV/c)}^2$  indicate that indeed one of the helicity conserving amplitudes dominates. This ratio measurement can be extended to a  $|t|$  value of about  $10 \text{ (GeV/c)}^2$  with an 11 GeV beam. Figure 19 shows both the available data and projected results for this ratio at 11 GeV, together with a prediction of Huang and Kroll [Hu00].

Nucleon photopion production processes are also essential probes of the hadron/parton transition region. Because they decrease relatively slowly with energy compared to other photon-induced processes (quark counting rules predict a  $s^{-7}$ -dependence for the differential cross-section), the cross sections of these processes are advantageous for the investigation of an observed oscillatory QCD scaling behavior. This behavior is thought to arise from the interference of the hard pQCD (short-distance) amplitude and the long-distance (Landshoff) amplitude; it is analogous to the QED effect of Coulomb-nuclear interference observed in low energy charged particle scattering. The relatively higher rates for these processes will allow investigations of the  $t$  and  $p_T$  dependence of scaling behavior and the study of the  $s$  dependence. Recent results from deuteron photo-disintegration [Sc01] show for the first time an angular dependent onset for the scaling behavior in photoreactions and  $p_T$  seems to be the physical observable governing the onset of the scaling behavior. Therefore, it is essential to carry out similar studies in other photon induced exclusive processes. Photopion production from nuclei also allows the search for novel pQCD effects such as nuclear filtering and color transparency.

#### 1.A.4 Symmetry Tests in Nuclear Physics

Precision parity-violating electron scattering experiments made feasible by the 12 GeV Upgrade have the sensitivity to search for deviations from the Standard Model that could signal the presence of new gauge bosons  $Z'$ s, the existence of leptoquarks, or particles predicted by supersymmetric theories, *i.e.* physics beyond the Standard Model. Planned studies of the three neutral pseudoscalar mesons, the  $\pi^0$ ,  $\eta$  and  $\eta'$ , will provide fundamental information about low energy QCD, including certain critical low energy parameters, the effects of SU(3) and isospin breaking by the  $u$ ,  $d$ , and  $s$  quark masses, and the strengths of the two types of chiral anomalies. These two programs are described briefly below, and in detail in Chapter 2.

**Standard Model Tests** Precision electro-weak measurements are potentially sensitive to physics beyond the Standard Model even below the energies needed to produce new particles directly. At the same time, they can provide new insights into novel aspects of hadron structure. For these reasons, the ongoing JLab program of Standard Model tests using parity violating electron scattering, exemplified by the approved weak proton charge experiment, will be extended to 12 GeV with exciting new opportunities.

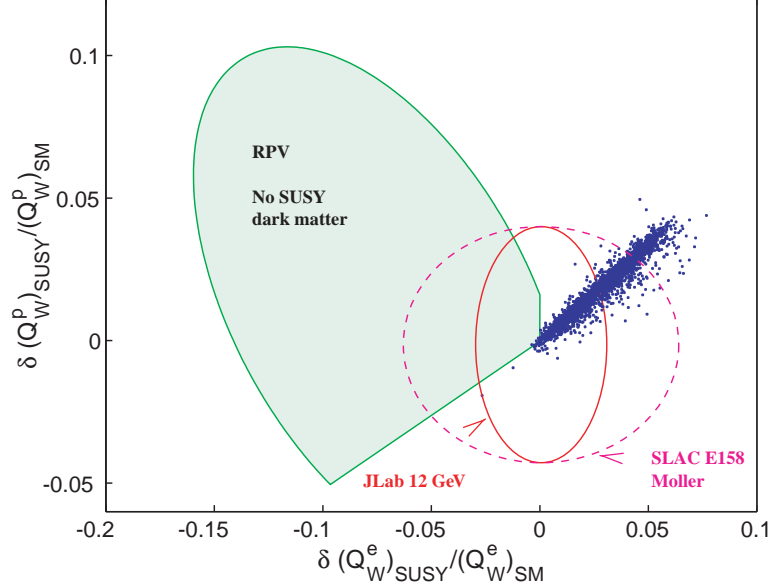


Figure 20: Relative shifts in  $Q_{\text{weak}}^e$  and  $Q_{\text{weak}}^{\text{proton}}$  from SUSY effects. The blue dots indicate MSSM loop corrections for approximately 3000 SUSY-breaking parameter choices. The interior of the green truncated ellipse shows possible shifts due to R-parity violation. In this region, SUSY dark matter is excluded [Ku02]. The dashed magenta ellipse illustrates the expected uncertainty from SLAC E-158 Møller and JLab Q-Weak, while the red ellipse represents what could be achieved with a 12 GeV Møller experiment at Jefferson Laboratory.

Of clear importance will be an improved measurement of the weak charge of the electron. In principle, an uncertainty which is half that of the anticipated SLAC E158 error can be achieved. A measurement with this precision would be a powerful tool in the search for “new physics”, and even a result in agreement with the Standard Model would have significant consequences. For example, such a result would severely constrain the viability of SUSY models that lack a candidate particle for dark matter, the non-luminous and unexplained source of 90% of the mass of the universe (see Fig. 20). However, a precision measurement of such a small asymmetry (40 ppb) will require extraordinary control of systematic errors and 200 days of running time.

In contrast, parity violation in deep inelastic scattering (DIS) is characterized by much larger asymmetries implying shorter running times. The measurement of this reaction by Prescott *et al.* established the Standard Model as the theory of the neutral weak interaction. A recent study of neutrino-nucleus DIS by the NuTeV collaboration suggests that the Standard Model is incomplete. An 11 GeV measurement of parity violating DIS could help determine whether the NuTeV “anomaly” is an artifact of poorly understood hadronic physics or a true indication of new physics. It could also provide a new window on higher-twist structure functions.

**Properties of Light Pseudoscalar Mesons via the Primakoff Effect** Two basic phenomena in QCD, namely the spontaneous breaking of chiral symmetry and the chiral anomalies, are mani-

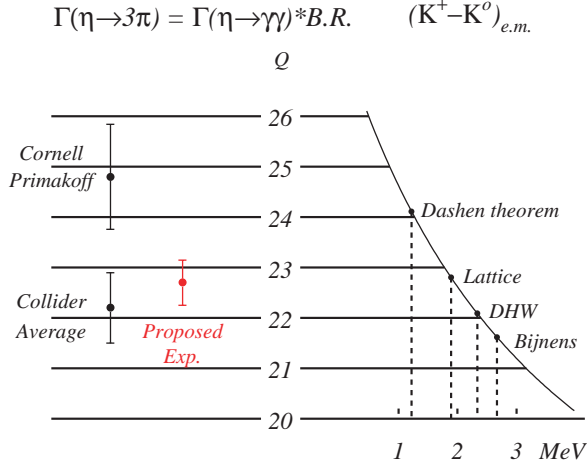


Figure 21: The importance of  $\Gamma_{\eta \rightarrow \gamma\gamma}$  in the measurement of the quark mass ratio  $Q$ , where  $Q^2 = \frac{m_s^2 - \hat{m}^2}{m_d^2 - m_u^2}$  and  $\hat{m} = (m_u + m_d)/2$ . The *l.h.s.* indicates the values of  $Q$  corresponding to the Primakoff and collider experimental results for  $\Gamma_{\eta \rightarrow \gamma\gamma}$ , and the projected result for Jefferson Laboratory with 12 GeV. The *r.h.s.* shows the results for  $Q$  obtained with four different theoretical estimates of the electromagnetic self energies of the kaons. The figure is adapted from Leutwyler.

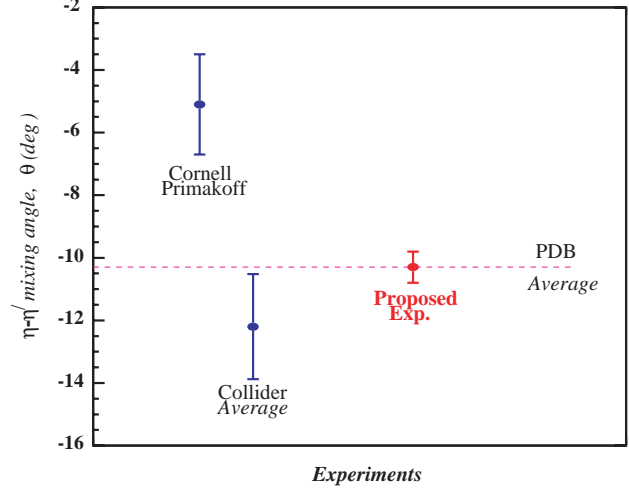


Figure 22: The  $\eta-\eta'$  mixing angle as determined by a previous Primakoff measurement,  $\gamma-\gamma$  collisions, and the projected result with the Jefferson Laboratory 12 GeV Upgrade

fested in their most unambiguous form in the sector of light pseudoscalar mesons. The anomalies particularly drive the two-photon decays of the  $\pi^0$ ,  $\eta$ , and  $\eta'$  and also provide a large fraction of the  $\eta'$  mass. The effects of explicit chiral symmetry breaking by the non-vanishing  $u$ ,  $d$ , and  $s$  quark masses also show through in the masses of these neutral pseudoscalars as well as in some of their decays. Indeed, important information about quark masses can be obtained from these mesons.

The advent of a 12 GeV electron beam at Jefferson Laboratory will make it possible to extend the current development of a high precision measurement of the  $\pi^0 \rightarrow \gamma\gamma$  decay width via the Primakoff effect to include the  $\eta$  and  $\eta'$  mesons. It will also enable a measurement of the transition form factors of these mesons. These measurements would have a significant impact on our knowledge of the ratios of quark masses, and particularly on ratios involving the differences in the masses of the  $u$  and  $d$  quarks. As indicated in Fig. 21, an important limitation on our knowledge of a ratio of the light quark masses is the experimental discrepancy between the  $\eta$  width determined by the  $\gamma\gamma \rightarrow \eta$  reaction in  $e^+e^-$  collisions and that determined by a previous Primakoff experiment. An improved measurement of the Primakoff cross sections would significantly improve this situation.

More precise measurements of both the  $\eta$  and  $\eta'$  widths would provide stringent tests of both

QCD and QCD based models, particularly for the magnitude of  $\eta - \eta'$  mixing as shown in Fig. 22. At a more general level, these measurements impact the issue of whether the  $\eta'$  meson can be considered to be an approximate Goldstone Boson in the combined chiral and large  $N_c$  expansions. The proposed measurements of the  $\pi^0$ ,  $\eta$  and  $\eta'$  transition form factors at very low  $Q^2$  ( $\sim 0.001$ – $0.5 \text{ GeV}^2$ ) would provide a first measurement of these important quantities. The  $\eta'$  form factor slope specifically tests the U(3) flavor symmetry implied by the large  $N_c$  limit. In this limit, the same low energy constant in chiral perturbation theory determines all three transition form factor slopes.

The proposed instrumentation for this program involves an upgraded version of the photon detection system used in the  $\pi^0$  lifetime experiment. This instrumentation will be of general utility for both this program and future experiments, and will provide a new and powerful experimental window on QCD at Jefferson Laboratory in an arena where the basic theory is well established. In addition, more precise knowledge of the transition form factors of the pseudoscalar mesons is required for a better determination of the so called light-by-light scattering contributions to the anomalous magnetic moment of the muon, which is one of the most sensitive quantities to new physics beyond the Standard Model.

## 1.B Upgrade Project Summary

While this Pre-Conceptual Design Report is focused on a description of the science driving the 12 GeV Upgrade, in order to provide a complete overview, this section gives a brief summary of the laboratory's plans for the accelerator, based on a 25 May 1999 internal JLab report, *Interim Point Design for the CEBAF 12 GeV Upgrade* and additional work that has been carried out to refine the design since that report was issued. It also outlines our plans for the new detector and detector upgrade projects necessary to carry out the program.

The key features of CEBAF that make the Upgrade so cost-effective are easily defined. By the summer of 1994, CEBAF had installed what was the world's largest superconducting radio-frequency (SRF) accelerator: an interconnected pair of antiparallel linacs, each comprising 20 cryomodules, with each cryomodule in turn containing eight SRF accelerating cavities. On average, these cavities exceed their design specifications by 50% in the two critical performance measures: accelerating gradient and  $Q$ . It is the success of this technology that has opened up the possibility of a relatively simple and inexpensive upgrade of CEBAF's top energy. This technological success would not be so readily multiplied if considerable foresight had not also been exercised in laying out the CEBAF tunnel "footprint", which was designed so that the magnetic arcs could accommodate an electron beam of up to 24 GeV. The latent accelerating power of the installed SRF cavities has already brought CEBAF to close to 6 GeV, 50% above its design energy, and recent successes in SRF development have led to the production of two cryomodules that are more than a factor of 2 more powerful than the original design. A staged development program is underway that is aimed at

a cryomodule that exceeds the original specification by a factor of 5 using higher-performing seven-cell cavities but fits into the same space as the original cryomodules based on five-cell cavities). The cryomodule developed as the first step in this program shows initial performance that is a factor of 4 better than the original specifications, consistent with the design goals. Using the space already available in the linac tunnels to install ten of the final-design cryomodules 12 GeV can be attained at a modest cost.

The equipment planned for the Upgrade project takes full advantage of apparatus developed for the present program. In each of the existing halls, new spectrometers are added and/or present equipment upgraded to meet the demands of the 12 GeV program. Then a new hall, Hall D, will be added to support the meson spectroscopy program.

In Hall A, the Upgrade will add a large angular- and momentum-acceptance, moderate-resolution magnetic spectrometer (to be called the Medium-Acceptance Device, or MAD) and a high-resolution electromagnetic calorimeter. The spectrometer will provide a tool for high-luminosity, high- $x$  studies of the properties of nucleons with an 11 GeV beam, and will also be used for selected investigations of the GPD's, where high luminosity and good resolution are needed. Details are provided in Section 3.A of this document. In Hall B, the CEBAF Large Acceptance Spectrometer (CLAS), which was designed to study multi-particle, exclusive reactions with its combination of large acceptance and moderate momentum resolution, will be upgraded to CLAS<sup>++</sup> and optimized for studying exclusive reactions (emphasizing the investigation of the GPD's) at high energy. It will also be used for selected valence quark structure studies involving neutron “tagging” or polarized targets capable of supporting only very low beam current. Most importantly, the maximum luminosity will be upgraded from  $10^{34}$  to  $10^{35}$  cm<sup>-2</sup> s<sup>-1</sup>. The present toroidal magnet, time-of-flight counters, Čerenkov detectors, and shower counter will be retained, but the tracking system and other details of the central region of the detector will be changed to match the new physics goals. Details are provided in Section 3.B. In Hall C a new, high-momentum spectrometer (the SHMS, Super-High-Momentum Spectrometer) will be constructed to support high-luminosity experiments detecting reaction products with momenta up to the full 11 GeV beam energy. This feature is essential for studies such as the pion form factor, color transparency, duality, and high- $Q^2$   $N^*$  form factors. The spectrometer will be usable at very small scattering angles. See Section 3.C for details. Finally, in Hall D, a tagged coherent bremsstrahlung beam and solenoidal detector will be constructed in support of a program of gluonic spectroscopy aimed at testing experimentally our current understanding that quark confinement arises from the formation of QCD flux tubes. This apparatus is described in detail in Section 3.D.

### 1.B.1 The Accelerator

The accelerator portion of the Upgrade is straightforward. The basic elements can be seen in Fig. 23, and the key parameters of the upgraded accelerator are listed in Table 1. The Upgrade utilizes the existing tunnel and does not change the basic layout of the accelerator. There are four

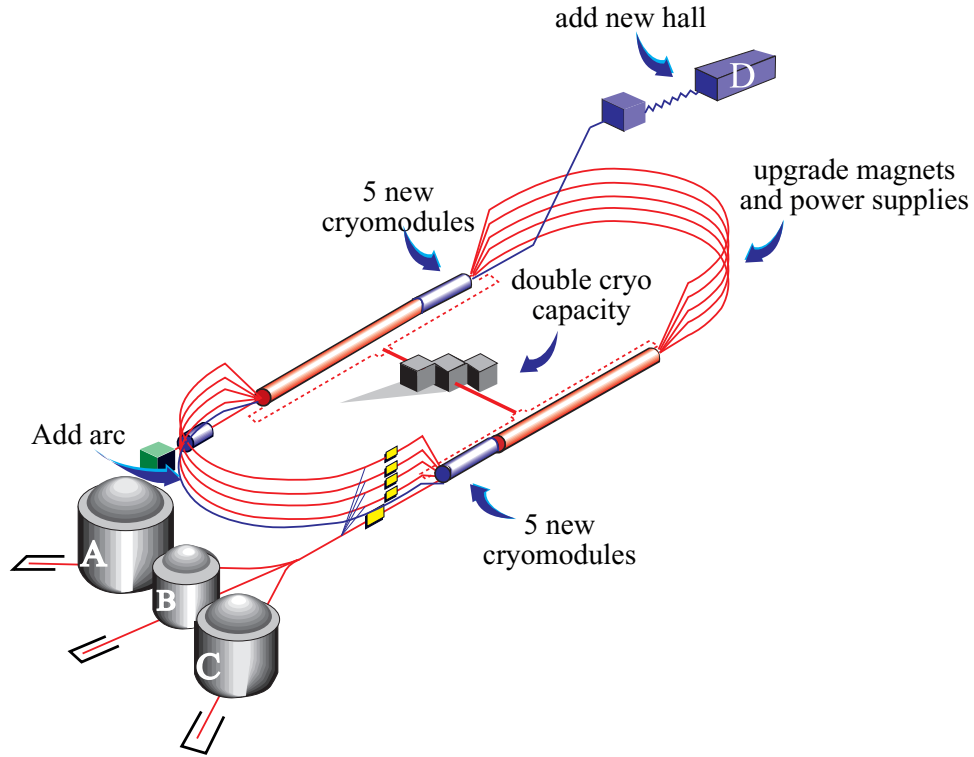


Figure 23: The configuration of the proposed 12 GeV CEBAF Upgrade.

Table 1: Selected key parameters of the CEBAF 12 GeV Upgrade

Parameter	Specification
Number of passes for Hall D	5.5 (add a tenth arc)
Max. energy to Hall D	12.1 GeV (for 9 GeV photons)
Number of passes for Halls A, B, C	5
Max. energy to Halls A, B, C	11.0 GeV
Max. energy gain per pass	2.2 GeV
Range of energy gain per pass	3:1
Duty factor	cw
Max. summed current to Halls A, C* (at full, 5-pass energy)	85 $\mu$ A
Max. summed current to Halls B, D	5 $\mu$ A
New cryomodules	10 (5 per linac)
Central Helium Liquifier upgrade	10.1 kW (from present 4.8 kW)

\*Max. *total* beam power is 1 MW.

main changes: additional acceleration in the linacs, stronger magnets for the recirculation, an upgraded cryoplant, and the addition of a tenth recirculation arc. The extra arc permits an additional “half pass” through the accelerator to reach the required 12 GeV beam energy, followed by beam transport to Hall D that will be added to support the meson spectroscopy initiative.

Motivated by the science, the 12 GeV Upgrade derives its name from the fact that it will deliver a 12 GeV electron beam to the new end station, Hall D, where it will be used to produce 9 GeV polarized photons for the new gluonic and  $s\bar{s}$  spectroscopies. The accelerator will, in addition, be able to simultaneously send electrons of 2.2, 4.4, 6.6, 8.8, or 11.0 GeV to the existing Halls A, B, and C. The increased physics power of the present halls comes from the qualitative jump in energy and momentum transfer that the Upgrade brings, and from the enhanced instrumentation capabilities planned for the detector complements in each of them. In describing the physics in Halls A, B, and C we will often refer to an 11 GeV electron beam (to be precise about the maximum beam energy available in these halls) but we will use the phrase “12 GeV” to describe the overall Upgrade.

## 1.B.2 The Experimental Equipment

**Hall A and the Medium Acceptance Device (MAD)** With the Jefferson Lab 12 GeV upgrade a large kinematics domain becomes accessible in deep inelastic scattering. The high luminosity and high polarization of beam and targets allow a unique contribution to the understanding of nucleon and nuclear structure, and the strong interaction in the high  $x$  region (which is dominated by the valence quarks). To fully utilize the high luminosity available at CEBAF (up to  $10^{39}$  e · nucleons/cm<sup>2</sup>/s), a well-matched spectrometer, given the name Medium-Acceptance Device (MAD), which can take this full luminosity while providing large angular and momentum acceptance, moderate momentum resolution, and good angular resolution, has been designed as the instrumental upgrade for Hall A. This spectrometer, which is shown in Fig. 24, will be used in conjunction with the existing HRS Spectrometers in Hall A.

The main elements of MAD are two warm-bore, combined-function (dipole and quadrupole) superconducting magnets. MAD has an angular acceptance of 28 msr for scattering angles  $> 35^\circ$ . Forward of  $35^\circ$  the distance between the target and the first quadrupole is increased, linearly decreasing the acceptance down to 6 msr at  $12^\circ$ . This acceptance remains available to scattering angles as forward as  $6^\circ$  through the use of a septum magnet. One of the existing HRS spectrometers will complement MAD, with an angular acceptance of up to 12 msr, an angular range between  $6^\circ$  -  $150^\circ$ , and a maximum momentum of 4.3 GeV/c. MAD can be oriented flexibly in order to accommodate the septum magnet while retaining a pointing accuracy  $\leq 0.5$  mrad as is required for accurate L/T separations. The design characteristics are summarized in Table 2.

A detector package has been designed for the detection of electrons and hadrons. The electron detection system will consist of four planes of scintillators for triggering, two drift chambers and one multi-wire proportional chamber for tracking and a gas Čerenkov counter and an electromagnetic



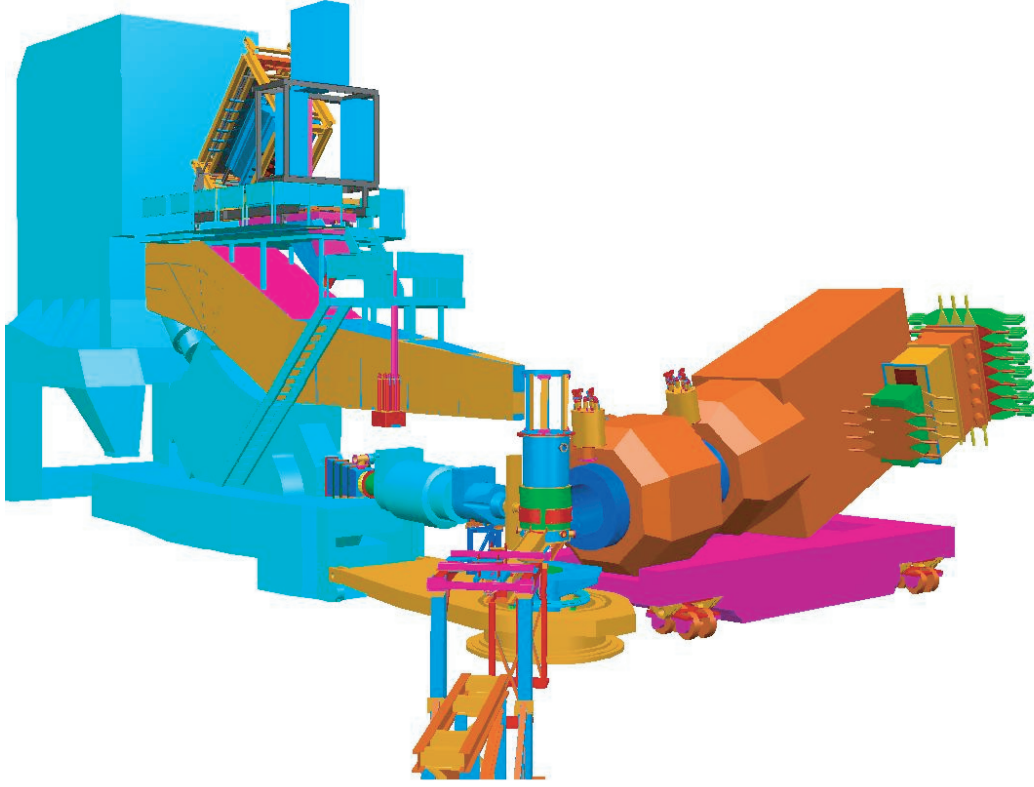


Figure 24: Three-dimensional CAD drawing of the MAD spectrometer

Table 2: The design characteristics of the MAD spectrometer shown along with HRS performance.

Parameter	MAD design	HRS performance
Central momentum range	0.4 - 6.0 GeV/c	0.2 - 4.3 GeV/c
Scattering angle range	6° - 130°	6° - 150°
Momentum acceptance	±15%	±5%
Momentum resolution	0.1%	0.02%
Angular acceptance	28 msr ( $\geq 35^\circ$ ) 6 msr (6° - 12°)	6 msr (standard) 12 msr (forward)
Angular resolution (hor)	1 mrad	0.5 mrad
Angular resolution (ver)	1 mrad	1 mrad
Target length acceptance (90°)	50 cm	10 cm
Vertex resolution	0.5 cm	0.1 cm
Maximum DAQ rate	20 kHz	5 kHz
e/h Discrimination	$0.5 \times 10^5$ at 98%	$2 \times 10^5$ at 99%
$\pi$ /K Discrimination	100 at 95%	100 at 95%

calorimeter for particle-identification purposes. For hadron detection two aerogel Čerenkov counters and a focal plane polarimeter will be additionally available. Both packages provide excellent ( $e^\pm, \pi^\pm, K^\pm$  and  $p$ ) identification over the full momentum range. Pion rejection as good as a few times  $10^{-5}$  will be provided. The data acquisition system is designed with a new generation of pipeline digitizing front-end electronics to be able to handle event rates up to 20 kHz.

In combination with the MAD spectrometer, a 100 msr lead-glass calorimeter is available for studies of nucleon form factors and of Real Compton Scattering. A large acceptance, high granularity calorimeter with 1296 element array of  $\text{PbF}_2$  crystals is proposed to optimally study Generalized Parton Distributions through Deep Virtual Compton Scattering. It will also benefit other experiments, such as photo-production of neutral mesons at large transverse momenta.

In combination with the existing HRS in Hall A MAD will open up a window to a rich program of semi-inclusive experiments. The 12 GeV upgrade crosses the charm production threshold. Threshold charm production will benefit from MAD and the high luminosity. Precision experiments on nuclei at DIS conditions will become possible, and measurements of fundamental quantities (such as nucleon form factors) and novel QCD phenomena (such as color transparency) can be extended to higher  $Q^2$ . Because the cross sections drop rapidly with increasing  $Q^2$ , a high luminosity and a large acceptance spectrometer are crucial for precision measurements. Photoproduction at high energy provides a powerful tool to investigate the transition from the non-perturbative QCD region to the pQCD region. Again the rapidly falling cross section with increasing photon energy demands high luminosity and a large acceptance spectrometer. Precision data in this region will also have a significant impact on a search of new physics beyond the standard model at very high energies.

**Hall B Upgrade and CLAS<sup>++</sup>.** The CLAS<sup>++</sup> detector is shown in Fig. 25. It is designed to meet the basic requirements for the study of the Generalized Parton Distributions (GPDs) in deeply exclusive and semi-exclusive processes. CLAS<sup>++</sup> also accommodates the requirements for measurements of polarized and unpolarized structure functions in inclusive processes. The main features of CLAS<sup>++</sup> are:

- High operating luminosity of  $10^{35} \text{cm}^{-2} \text{s}^{-1}$  for hydrogen targets, a ten-fold increase over current CLAS operating conditions.
- Improved detection capabilities for forward-going high momentum particles. Charged particles that bend outwards in the torus field can be reconstructed for angles as low as 5 degrees. Photon detection will be possible for angles as low as 3 degrees. Acceptance for electrons ranges from about 8 degrees to 40 degrees.
- Larger momentum range for the separation of electrons, pions, kaons, and protons obtained through better resolution time-of-flight counters, and a new threshold gas Čerenkov detector.
- Capability to detect the recoiling baryons at large laboratory angles.

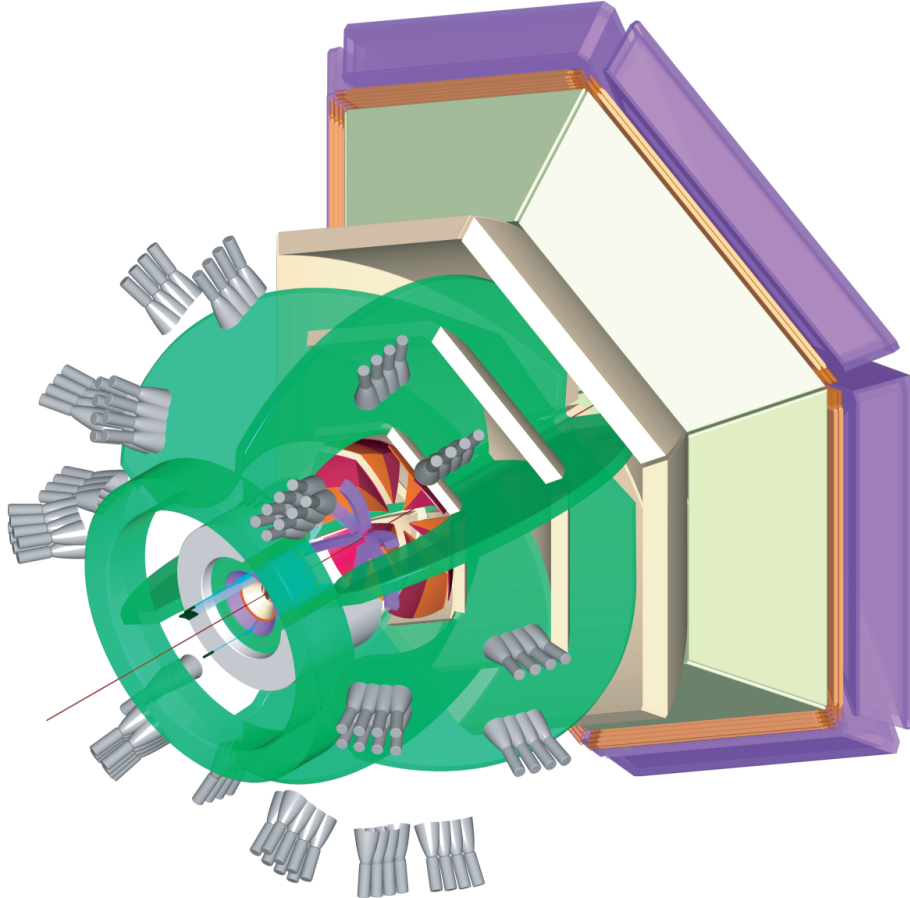


Figure 25: Three dimensional CAD drawing of the CLAS<sup>++</sup> detector.

- Improved hermeticity for the detection of charged particles and photons in regions where CLAS currently has no detection capabilities, achieved by instrumenting the regions in front of the coils, and by extending the polar angle range for photon detection to 135 degrees.
- Capability to operate polarized solid state targets.

CLAS<sup>++</sup> makes use of many of the components of the current CLAS detector, such as the Torus magnet, the forward electromagnetic calorimeters, Čerenkov detectors, and time-of-flight counters. Also, much of the drift chamber electronics will be reused. A new and essential component of CLAS<sup>++</sup> is the Central Detector. Its main component is a superconducting solenoid magnet, which has a dual function: It replaces the existing mini-torus for shielding of the Møller electrons, and it provides the magnetic field for the momentum analysis of charged particles at large angles. Time-of-flight scintillators are used to provide particle identification at lab angles greater than 40 degrees. Due to the limited space available excellent timing resolution is essential. Tracking at large angles is provided by a combination of drift chambers with cathode strip readout and a microstrip detector near the vertex. Since most charged tracks will have momenta of 1.5 GeV/c or less, sufficient momentum resolution can be achieved even in the limited space available for tracking. A compact electromagnetic calorimeter based on tungsten powder and scintillating fiber technology provides photon detection capability for the angle range from 40-135 degrees.

Some modifications and additional detectors are needed in the Forward Detector as well. The main new component is a threshold gas Čerenkov counter for triggering on electrons. It will allow electron and pion separation up to nearly 5 GeV/c. Beyond 5 GeV/c, electrons are identified in the forward electromagnetic calorimeter. There is also additional electromagnetic calorimetry placed in front of the torus coils for improved hermeticity. Lead-tungstate crystals have emerged as a good choice for this detector.

A pre-shower detector will be inserted in front of the existing CLAS electromagnetic calorimeters. This detector will allow separation of single photons from  $\pi^0 \rightarrow \gamma\gamma$  events; this is especially needed for deeply virtual Compton scattering. All drift chambers in CLAS will be replaced by new ones that will cover a smaller angle range with a factor of two smaller cell sizes to reduce the accidental hit occupancy due to photon interactions allowing for a corresponding gain in luminosity.

The existing forward detection system will be modified to extend particle identification and reconstruction to higher momenta. This will be accomplished by several means: The timing resolution of the scintillation counters will be improved by using smaller scintillator slabs, by adding an additional layer of scintillators, and by replacing the PMTs by new ones with better timing characteristics. This is expected to improve the timing resolution to about 60 psec. The existing gas Čerenkov counter will be modified slightly for improved pion detection capabilities for momenta greater than 2.7 GeV/c.

Tables 3 and 4 summarize the expected performance of CLAS<sup>++</sup>. With these modifications and

Table 3: CLAS<sup>++</sup>: acceptance and resolution

	Forward detector	Central Detector
Angular coverage		
Tracks (inbending)	8° – 37°	40° – 135°
Tracks (outbending)	5° – 37°	40° – 135°
Photons	3° – 37°	40° – 135°
Track resolution		
$\delta p/p$	0.003 + 0.001 $p$	$\delta p_T/p_T = 0.02$
$\delta\theta(mr)$	1	8
$\delta\phi(mr)$	2-5	2
Photon detection		
Energy range (MeV)	> 150	> 60
$\delta\theta$ (mr)	4 (1 GeV)	15 (1 GeV)
Neutron detection		
$\eta_{eff}$	0.5 ( $p > 1.5$ GeV/c)	NA
Particle id		
Electron/pion	> 1000 ( $p < 4.8$ GeV/c) > 100 ( $p > 4.8$ GeV/c)	NA NA
$\pi^+/\pi^-$	full range	<0.65 GeV/c
$K/\pi$	full range	<0.65 GeV/c
$K^+/p, K^-/\bar{p}$	<4.5 GeV/c	<0.90 GeV/c
$\pi^0 \rightarrow \gamma\gamma$	full range	full range
$\eta \rightarrow \gamma\gamma$	full range	full range

Table 4: CLAS<sup>++</sup>: operating luminosity

Target	Luminosity ( $10^{34} cm^{-2} s^{-1}$ )
$H_2$	10
$^3He$	15
$^2H, ^4He, ^{12}C, ^{16}O, \dots, Pb$	20
$NH_3, ND_3$ (long. polarization)	20
$NH_3, ND_3$ (trans. polarization)	2

additions to the existing CLAS components, CLAS<sup>++</sup> will be able to carry out the core program for the study of the internal nucleon dynamics and hadronization processes as listed here:

- Quark-gluon dynamics and nucleon tomography through measurement of deeply virtual Compton scattering and deeply virtual meson production, both with unpolarized and polarized hydrogen and deuterium targets.
- Polarized and unpolarized valence quark distributions at high  $x_B$ , using polarized hydrogen and deuterium targets, and by employing a novel technique of neutron tagging. Values of  $x_B$  up to 0.85 can be accessed in deep inelastic processes. A broad program of semi-inclusive measurements will allow quark-flavor tagging and give access to transverse quark structure functions.
- The magnetic structure of the neutron will be probed through magnetic form factor measurements up to  $14 \text{ GeV}^2$ , and the C2/M1 ratio for  $N - \Delta(1232)$  up to  $Q^2 = 12 \text{ GeV}^2$ . Higher mass resonance transitions can be studied in multiple meson decays at high  $Q^2$  as well.
- Space-time characteristics of quark hadronization and color transparency can be studied in nuclei in highly sensitive processes.
- Meson spectroscopy on  $^4\text{He}$ ,  $^3\text{He}$  with a small angle quasi-real photon tagger, allows to eliminate baryonic background. Heavy baryon spectroscopy (e.g.  $\Xi^*$ ) can be studied on hydrogen targets.

**Hall C and the Super High Momentum Spectrometer (SHMS)** At a 12-GeV Jefferson Lab, Hall C will provide a new magnetic spectrometer, the Super High Momentum Spectrometer (SHMS), powerful enough to analyze charged particles with momenta approaching that of the highest energy beam. Together with its companion, the existing High Momentum Spectrometer (HMS), this will make Hall C the only facility in the world capable of studying (deep) exclusive reactions up to the highest momentum transfers,  $Q^2 \simeq 18 (\text{GeV}/c)^2$ , with appropriate high luminosity. By extension, only Hall C will be able to fully exploit semi-exclusive reactions in the critical region where the electro-produced hadron carries almost all of the transferred energy .

Charged particles with such high momenta are boosted by relativistic kinematics into the forward detection hemisphere. Therefore, the SHMS is designed to achieve angles down to  $5.5^\circ$ , and up to  $25^\circ$ . The SHMS will cover a solid angle up to 4 msr, and boasts a large momentum and target acceptance. The existing HMS complements SHMS well, with a solid angle of up to 10 msr, an angular range between  $10.5^\circ$  and  $90^\circ$ , and a maximum momentum of  $7.3 \text{ GeV}/c$ .

Hall C's magnetic spectrometer pair will be rigidly connected to a central pivot that permits rapid, remote angle changes and reproducible rotation characteristics, which simplify accurate measurements such as Rosenbluth-type separations. From its inception, the SHMS momentum

and target acceptances were designed to be large and nearly uniform, allowing for both fast and accurate data collection. The SHMS could operate at a luminosity of  $10^{39} \text{ cm}^{-2}\text{s}^{-1}$ , with a 40% momentum acceptance.

The large momentum acceptance, in combination with the large luminosity, will enable the measurement of the smallest cross sections, and allow for a complete map of the nucleon's response all the way from elastic scattering through deep inelastic scattering. The latter will greatly facilitate studies in the transition region from hadronic to quark-gluon degrees-of-freedom, including a novel determination of the spin and flavor dependence of low-energy quark-hadron duality and hadronization. The final product of these experiments will be a precise determination of the lowest moments of both spin- and flavor-dependent quark distributions for  $Q^2 \leq 10 \text{ (GeV/c)}^2$ , providing a direct connection with Lattice QCD calculations.

Hall C will also retain its general infrastructure to offer collaborations an opportunity to do one-of-a-kind experiments, with dedicated experimental setups. Already at 6 GeV, the experimental program in Hall C will provide for 2 kW cryogenic target running, the use of an  $\approx 100 \text{ msr}$  electromagnetic calorimeter, and a focal-plane polarimeter suited for both HMS and SHMS operation at 12 GeV.

Figure 26 shows the new SMS spectrometer installed in the hall along with the existing HMS and SOS spectrometers. The overall specifications for the Hall C spectrometer setup for 12-GeV running are summarized in Table 5.

With the new equipment, Hall C will be able to deliver, amongst others:

- Nucleon elastic and transition form factors up to  $Q^2 \simeq 18 \text{ (GeV/c)}^2$ ,
- Real Compton Scattering up to  $s \simeq 20 \text{ GeV}^2$ ,
- Deep exclusive pion and kaon electroproduction up to  $Q^2 \simeq 10 \text{ (GeV/c)}^2$ , including precise longitudinal-transverse separations and spin-dependent measurements.
- A charged pion form factor measurement up to  $Q^2 = 6 \text{ (GeV/c)}^2$ .
- Complete separation of the  $F_L, F_T, g_1$ , and  $g_2$  inclusive structure functions of the proton (in the valence quark region) up to  $Q^2 \simeq 10 \text{ (GeV/c)}^2$ .
- Precision measurements of the  $Q^2$ -dependence of nuclear effects in both inclusive structure functions and (deep) exclusive scattering, crossing the charm threshold.
- A parity-violating deep inelastic scattering experiment with unprecedented precision, to search for extensions of the Standard Model.



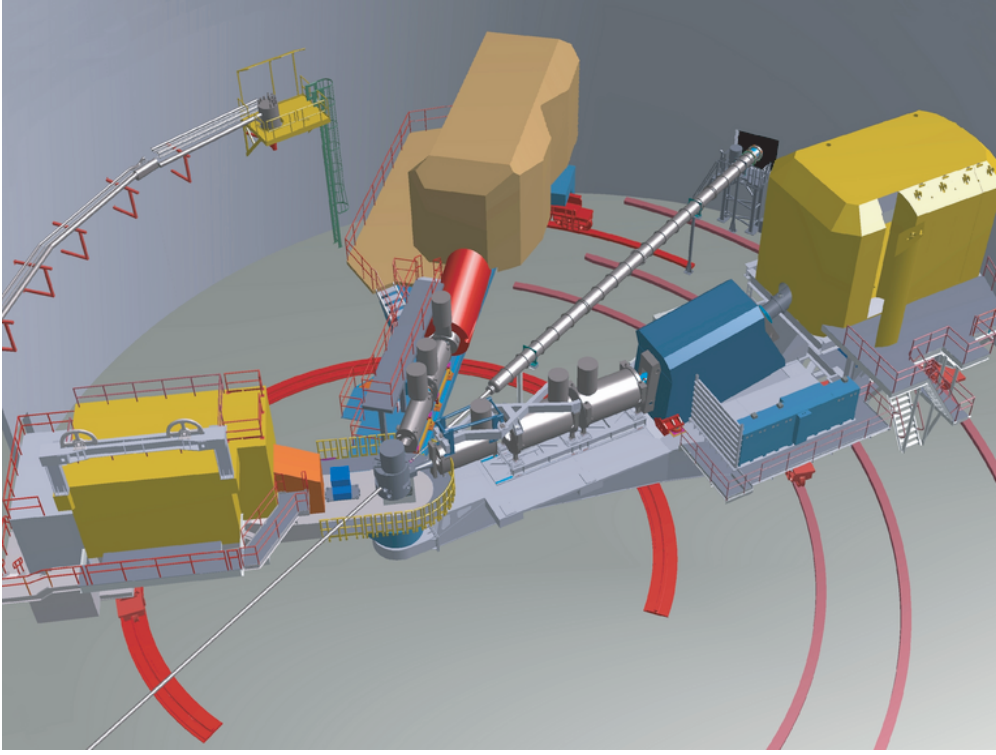


Figure 26: A CAD drawing of the new SHMS spectrometer installed in Hall C together with the existing HMS and SOS spectrometers.

Table 5: Summary of the HMS performance and the design specifications for the SHMS.

<i>Parameter</i>	<i>HMS Performance</i>	<i>SHMS Specification</i>
Range of Central Momentum	0.4 to 7.3 GeV/c	2.5 to 11 GeV/c
Momentum Acceptance	$\pm 10\%$	-15% to +25%
Momentum Resolution	0.1% – 0.15%	$< 0.2\%$
Scattering Angle Range	10.5 to 90 degrees	5.5 to 25 degrees
Target Length Accepted <sup>†</sup> at 90°	10 cm	50 cm
Horizontal Angle Acceptance	$\pm 32$ mrad	$\pm 18$ mrad
Vertical Angle Acceptance	$\pm 85$ mrad	$\pm 50$ mrad
Solid Angle Acceptance	8.1 msr	4 msr (LSA tune) 2 msr (SSA tune)
Horizontal Angle Resolution (yptar)	0.8 mrad	2-4 mrad
Vertical Angle Resolution (xptar)	1.0 mrad	1-2 mrad
Vertex Reconstruction Resolution (ytar)	0.3 cm	0.2 - 0.6 cm
Maximum DAQ Event Rate	2,000 events/second	10,000 events/second
Maximum Flux within Acceptance	$\sim 5$ MHz	$\sim 5$ MHz
e/h Discrimination	$>1000:1$ at 98% efficiency	1000:1 at 98% efficiency
$\pi/K$ Discrimination	100:1 at 95% efficiency	100:1 at 95% efficiency

<sup>†</sup> This length corresponds to what the spectrometer can “see” perpendicular to its optic axis.

The acceptable target length at any accesible scattering angle is, to first order, the projection of this length.



**Hall D and the GlueX Experiment** The GlueX experiment will be housed in a new above-ground experimental hall (Hall D) located at the east end of the CEBAF north linac. A collimated beam of linearly polarized photons (with 40% polarization) of energy 8 to 9 GeV will be produced via coherent bremsstrahlung with 12 GeV electrons. This requires thin diamond crystal radiators (no more than  $20\ \mu$  thick). The scattered electron from the bremsstrahlung will be tagged with sufficient precision to know the photon energy to within 0.1%.

The GlueX detector (see Fig. 27) uses an existing 2.25 T superconducting solenoid that is now being refurbished. An existing 3000-element lead-glass electromagnetic calorimeter will be reconfigured to match the downstream aperture of the solenoid. A threshold Čerenkov counter followed by a scintillator time-of-flight (TOF) wall will be placed between the solenoid and lead glass detector. Inside the full length of the solenoid a lead and scintillating fiber electromagnetic calorimeter will provide position and energy measurement for photons and TOF information for charged particles. A scintillating fiber vertex detector will surround the 30-cm long liquid hydrogen target. A cylindrical drift chambers will fill the region between the vertex detector and cylindrical calorimeter. Planar drift chambers will also be placed inside the solenoid downstream of the target.

This detector configuration has  $4\pi$  hermeticity and momentum/energy and position information for charged particles and photons optimized for partial wave analysis. Extensive Monte Carlo studies for a wide variety of final states were carried out to certify the design parameters and the suitability of the detector for carrying out the final analysis.

An active program of R&D has been underway now for at least three years on each of the subsystems. Rocking curve measurements of diamond wafers have been carried out in the UK, and the coherent bremsstrahlung technique has been successfully demonstrated in Hall B. Prototypes of tracking elements and the cylindrical calorimeter have been built and more are planned. Beam tests in Russia on TOF prototypes have resulted in a finalized design. Prototype flash ADCs have been built and tested as have TDCs based on F1 chips. Work on optimizing electronics continues. More beam tests are planned. The magnet refurbishment project at the Indiana University Cyclotron Facility includes a plan to place detector elements inside the magnet and test them with an energized magnet.

The primary characteristics of the detector are given in Table 6. The hermetic design for the detector makes it an ideal tool to

- determine the masses and quantum numbers of mesons in the mass range of 1.5 to 2.5 GeV
- study properties of hybrid mesons produced at rates as low as a percent of normal mesons
- map out the poorly known spectra of  $s\bar{s}$  mesons

The collaboration has carried out a partial wave analysis using simulated GlueX data. They are continuing to develop the collaboration, software and analysis tools needed to carry out partial

Table 6: Summary of the GlueX detector’s characteristics.

<i>Capability</i>	<i>Quantity</i>	<i>Range</i>
Charged particles	Coverage	$1 \leq \theta \leq 170^\circ$
	Momentum resolution ( $5 \leq \theta \leq 140^\circ$ )	$\sigma_p/p \approx 1\text{-}2\%$
	Position resolution	$\sigma \approx 150\text{-}200\mu\text{m}$
	dE/dx measurements	$20 \leq \theta \leq 140^\circ$
	Vertex detector	$\sigma \approx 500\mu\text{m}$
	Time-of-flight scintillators	$\sigma_t \approx 50\text{ ps}$
	Čerenkov for $\pi/K$ separation	$\theta \leq 14^\circ$
	Barrel time resolution	$\sigma_t \approx 250\text{ ps}$
Photon detection	Energy measurements	$1 \leq \theta \leq 120^\circ$
	Veto capability	$\theta \geq 120^\circ$
	Lead glass energy resolution ( $E_\gamma \geq 150\text{ MeV}$ )	$\sigma_E/E \approx 2 + 5\%/\sqrt{E}$
	Barrel energy resolution ( $E_\gamma \geq 20\text{ MeV}$ )	$\sigma_E/E \approx 4.4\%/\sqrt{E}$
	Barrel position resolution	$\sigma_z \approx 1\text{ cm}$
DAQ / trigger	Level 1	200 KHz
	Event Rate	15 KHz to tape
	Data Rate	100 MB/s
Electronics	fully pipeline	Flash ADCs, TDCs
Photon Flux	Tagged rate	$10^8\gamma/\text{s}$

wave analysis on petabyte-size data sets starting with several tens of terabyte data sets (from other experiments) in hand. The collaboration is also developing experience in operating computer clusters at several different sites and plans to implement GRID tools and technologies which are deemed necessary to for the experiment.

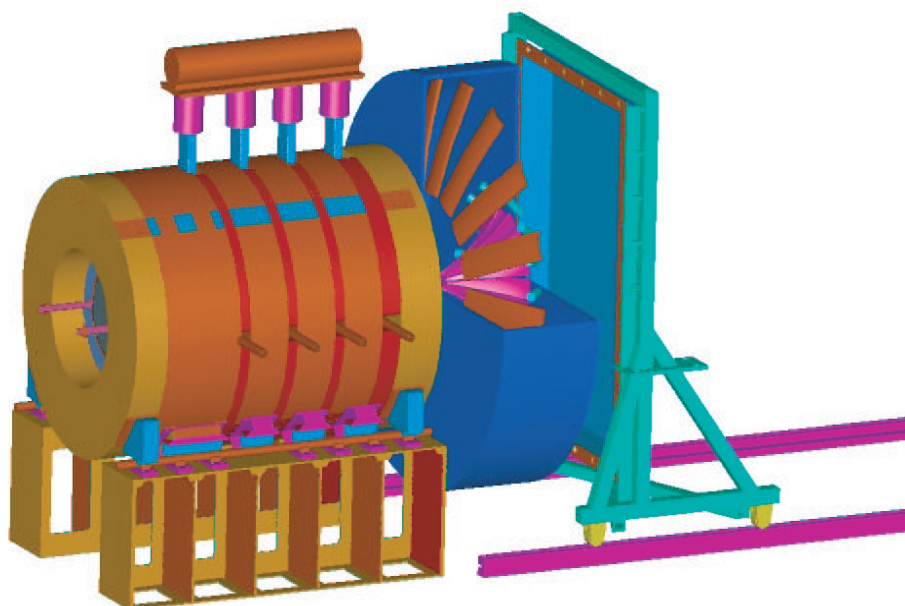
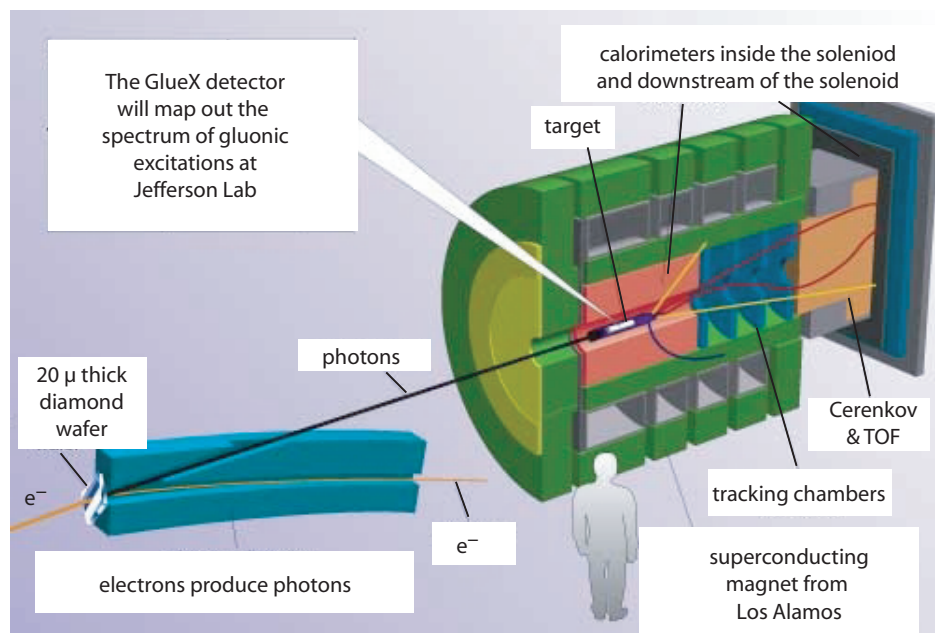


Figure 27: The proposed detector for the study of the photoproduction of mesons in the mass region around 2 GeV.



## 2 THE SCIENCE DRIVING THE 12 GeV UPGRADE OF CEBAF

### 2.A Gluonic Excitations and the Origin of Quark Confinement

#### 2.A.1 Introduction

The primary goal of the GLUEX project is the definitive and detailed mapping of the spectrum of a new family of particles called *hybrid mesons*. Linearly polarized photons produced by electrons from an energy-upgraded CEBAF will be the probe used to uncover this spectrum. This experimental information is absolutely critical in finding the answer to an outstanding and fundamental questions in physics – a quantitative understanding of the confinement mechanism in quantum chromodynamics.

The spectrum of mesons and baryons uncovered during the 1960's led to the quark model within which mesons are bound states of a quark and antiquark,  $q\bar{q}$ , and baryons are bound states of three quarks,  $qqq$ . Further experimental work indicated that quarks are dynamical objects as well and this led to the development of quantum chromodynamics (QCD), the theory of quarks and gluons and their interactions modeled after the very successful theory of quantum electrodynamics (QED). Just as charged particles interact by the exchange of photons, quarks, with their color charge, interact by exchanging gluons. There are however important and fundamental differences between the two theories. There are three types of color charge as opposed to one kind of electrical charge. And the gluons of QCD also carry color charge and can interact with quarks and each other. In contrast, the photons of QED do not carry charge. Bound states involving quarks and gluons or quarks alone are thus possible and indeed should exist. QCD also incorporates the experimental fact that the quarks and gluons do not exist as free particles by requiring that only color singlet combinations exist as free particles in nature. In addition to the color singlet combinations  $q\bar{q}$  and  $qqq$  others are possible, such as  $q\bar{q}g$  (*hybrid mesons*) and  $gg$  or  $ggg$  (*glueballs*). These new states, collectively known as *gluonic excitations*, are fascinating since this is the only case of a theory in which the gauge particle is also a constituent. The analogous states in QED, like atoms of light, cannot exist. Although there is tantalizing evidence for these gluonic excitations, their spectra have not been mapped out.

The confinement of quarks and gluons within the particles of which they are the constituents is a unique feature of QCD. But a quantitative understanding of the confinement mechanism still eludes us. Theoretical progress is being made and lattice QCD, based on first-principle calculations, will ultimately be able to predict a detailed spectrum, including masses and decays, of hybrid mesons and glueballs. The experimental information about the spectrum of this new form of matter as predicted by QCD is an essential ingredient for the ultimate understanding of the confinement mechanism.

The low-lying glueball states will be searched for in the glue-rich  $J/\psi$  radiative decays as part

of the planned CLEO-c project at Cornell's CESR. However the low-lying glueballs possess  $J^{PC}$  quantum numbers that are the same as  $q\bar{q}$  states and therefore mixing with conventional  $q\bar{q}$  mesons is possible and that can complicate glueball identification. In contrast, hybrid mesons can possess  $J^{PC}$  quantum numbers not possible for  $q\bar{q}$ . These *exotic hybrid mesons* thus have a *smoking gun signature*. Just as nonets of  $q\bar{q}$  mesons made of the three light quarks ( $u$ ,  $d$  and  $s$ ) exist, nature should also reveal nonets of hybrids with the same flavor quantum numbers but with now with the possibility of exotic  $J^{PC}$ . Hybrid mesons should also have widths comparable to conventional mesons. This is supported by theoretical considerations and by the possible sighting of an exotic hybrid in  $\pi^-$ -induced interactions.

Hybrid mesons can be thought of as  $q\bar{q}g$  bound states in which the gluon is a constituent. An attractive alternative picture is one in which a gluonic flux tube forms between the  $q$  and  $\bar{q}$  in a meson. This flux tube forms because of the self-interaction of the gluons and qualitatively accounts for confinement. It leads to a linear potential, or a force that is constant as the distance between the quark and anti-quark varies. Infinite energy is required to separate the quarks to infinity, thus qualitatively accounting for confinement. This notion of a relativistic string or flux tube between the quarks was introduced in the 1970's to account for the observed linear dependence of particle mass-squared ( $m^2$ ) on spin ( $J$ ). The flux tube concept is supported by lattice QCD studies. Within this picture conventional mesons result when the flux tube is in its ground state. Hybrid mesons arise when the flux tube is excited. The lack of information on this spectroscopy is due in part to the complicated decay modes favored by these states and also due to the apparent suppression of exotic hybrid mesons in production mechanisms with  $\pi$  or  $K$  probes. On the other hand production of exotic hybrid mesons is expected to be favored using beams of photons and essentially no data exist on the photoproduction of light mesons. The GLUEX project will remedy this situation.

In addition to providing for a linearly polarized photon beam of sufficient energy, the GLUEX project includes construction of a hermetic detector to allow for particle identification and momentum and energy determination sufficient to allow for complete kinematic reconstruction of events with a wide variety of final states. This is essential for the spin analysis – partial wave analysis (PWA) – needed to determine the  $J^{PC}$  quantum numbers, to map out the flavor quantum numbers of the hybrid nonets and to test assumptions about the details of confinement that would lead to predicting specific decay modes.

In this chapter we expand on the following:

1. *Spectroscopy of Light Mesons*. This will include a brief review of the conventional quark model and the status of the light quark meson spectrum.
2. *Gluonic excitations and the role in QCD*. This will include a discussion of how the gluons form flux tubes, and how their excitations lead to QCD mesons, in particular exotic hybrids. This general picture is not restricted to a particular model but follows from the first-principles QCD calculations.

3. *The current evidence for gluonic excitations.* The evidence comes from overpopulation of conventional nonets and from possible glueball and exotic hybrid sightings in  $\bar{p}p$  annihilations and  $\pi$ -induced interactions.
4. *Photons are expected to be particularly effective in producing exotic hybrids.* Its spin structure makes the photon a qualitatively different probe from  $\pi$  and  $K$  beams. The first excited transverse modes of the flux tube can lead to exotic hybrids only when the quark spins are aligned. This argument is consistent with expectations from models based on phenomenological analyses of existing data that predict cross sections for photoproduction of exotic hybrids comparable to those of normal mesons. And there are essentially no data on photoproduction of light mesons so this is *terra incognita*. The existing photoproduction data will be discussed.
5. *The complementarity of this study with other planned projects that will study gluonic excitations.* We will compare this to searches in the charm quark or beauty quark sectors or  $e^+e^-$  annihilations, in particular the GSI Project and the CLEO-c Project at Cornell.
6. *The importance of the PWA technique in uncovering exotic mesons.* The PWA is a powerful analysis tool that has been successfully employed in experiments to uncover states which are not evident from a simple examination of mass spectra (bump-hunting). PWA is absolutely essential for this project as is the development of the formalism for incident photon beams and an understanding of the phenomenology. The importance of a hermetic detector with excellent resolution and rate capability and sensitivity to a wide variety of decay modes will be discussed.
7. *Linear polarization of the photon beam is essential for this study.* Linear polarization is important in the determination of the  $J^{PC}$  quantum numbers and it is essential in determining the production mechanism. Linear polarization can be used as a filter for exotics once the production mechanism is isolated.
8. *The ideal photon energy range.* In order to reach the desired mass range we need to be far enough above threshold so that the decay products of produced mesons can be detected and measured with sufficient precision. High enough energies are also important to avoid line-shape distortions of higher-mass mesons. We also want to be high enough in energy to kinematically separate production of baryon resonances from production of meson resonances. This need for higher energies, however is balanced by the need to limit the maximum energy to allow for a solenoid-only-based detector to accurately determine the momenta of the highest energy charged particles. These considerations lead to an ideal photon energy in the range from 8 to 9 GeV.
9. *The desired electron energy.* Having established the desired photon beam energy of 9 GeV the electron energy must be sufficiently high compared to the desired photon beam energy to achieve a sufficient degree of linear polarization. With 12 GeV electrons, the degree of linear polarization is 40%. If the electron energy drops to 10 GeV the degree of polarization drops

to 5%. The ratio of tagged hadronic rate to total hadronic rate in the detector drops as the electron energy approaches the desired photon energy. The conclusion is that an electron energy of 12 GeV suffices but lower energies will severely compromise the physics goals.

### 2.A.2 Conventional light mesons

The early version of the quark model described the observed mesons as bound states of a quark and antiquark, where the quarks were assumed to be the  $u$ ,  $d$  and  $s$  quarks. Thus mesons were grouped in families with nine members – a nonet – characterized by a given  $J^{PC}$  determined by the relative spin of the two quarks and their relative orbital angular momentum. Within the nonet three are members of an isotriplet with zero strangeness. Two are members of an isodoublet with positive strangeness and another two with negative strangeness. And the remaining two members have zero strangeness and isospin. This flavor pattern holds for all the nonets. Radial excitations are also allowed.

The rules for allowed values of  $J^{PC}$  follow from the requirements of a fermion–antifermion system: the quark spins can be parallel ( $S = 1$ ) or antiparallel ( $S = 0$ ) with relative orbital angular momentum ( $L$ ),  $\vec{J} = \vec{L} + \vec{S}$ ,  $P = (-1)^{L+1}$  and  $C = (-1)^{L+S}$ . Thus the low-lying nonet with  $\vec{L} = 0$  and  $\vec{S} = 0$  leads to  $J^{PC} = 0^{-+}$ , the pseudoscalar nonet, including the  $\pi$ ,  $K$ ,  $\eta$  and  $\eta'$  mesons. The nonet with  $\vec{L} = 0$  and  $\vec{S} = 1$  leads to  $J^{PC} = 1^{--}$ , the vector mesons, including the  $\rho$ ,  $K^*$ ,  $\omega$  and  $\phi$  mesons. The combination  $\vec{L} = 1$  and  $\vec{S} = 1$  leads to three nonets: scalar ( $J^{PC} = 0^{++}$ ), axial vector ( $J^{PC} = 1^{++}$ ) and tensor ( $J^{PC} = 2^{++}$ ).

Using the rules for determining  $J^{PC}$  for a fermion-antifermion system, certain  $J^{PC}$  combinations are not allowed for  $q\bar{q}$  systems and these include  $J^{PC} = 0^{--}, 0^{+-}, 1^{-+}, 2^{+-}, \dots$ . Such combinations are referred to as *exotic* quantum numbers. Indeed, that such combinations were not initially observed gave credence to the quark model.

Figure 28 shows our current knowledge of conventional  $q\bar{q}$  states. The exact association of an observed meson with a particular  $q\bar{q}$  state within a nonet depends on a good understanding of the various decay modes of the meson as well as its mass, width and production characteristics. Figure 28 also shows the expected range of masses for glueballs, hybrid mesons and meson-meson molecular states. These will be described in more detail below.

The range of masses of the known conventional meson nonets and their radial excitations extend from the  $\pi$  mass up to about  $2.5 \text{ GeV}/c^2$ . Figure 29 shows the spectrum of  $q\bar{q}$  states in more detail including radial excitations. There is also now clear evidence that the observed meson spectrum includes states which cannot be accommodated within the naive quark model. For example, there are at least five scalar states reported with masses below  $2 \text{ GeV}/c^2$ . These, along with indications of exotic  $J^{PC}$  sightings will be discussed below.



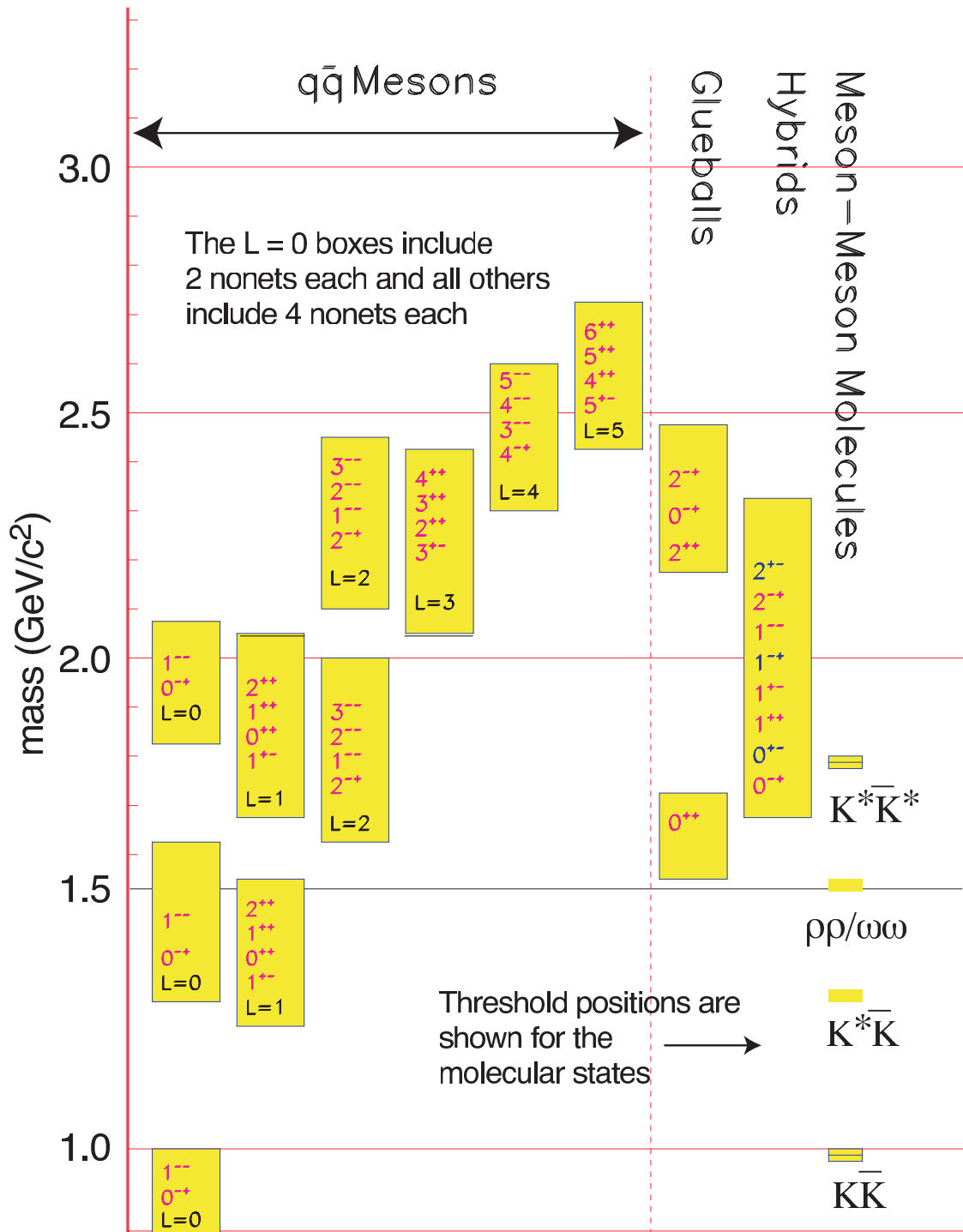


Figure 28: A level diagram showing conventional nonets and expected masses of glueballs, hybrids and molecular thresholds. The vertical axis is in units of  $\text{GeV}/c^2$ . For the  $q\bar{q}$  boxes the L refers to the angular momentum between the quarks and each  $J^{PC}$  refers to a nonet of mesons. Note also that exotic  $J^{PC}$ ,  $-0^{+-}$ ,  $1^{-+}$ ,  $2^{+-}$  – occur only among the hybrids for the range of masses shown.

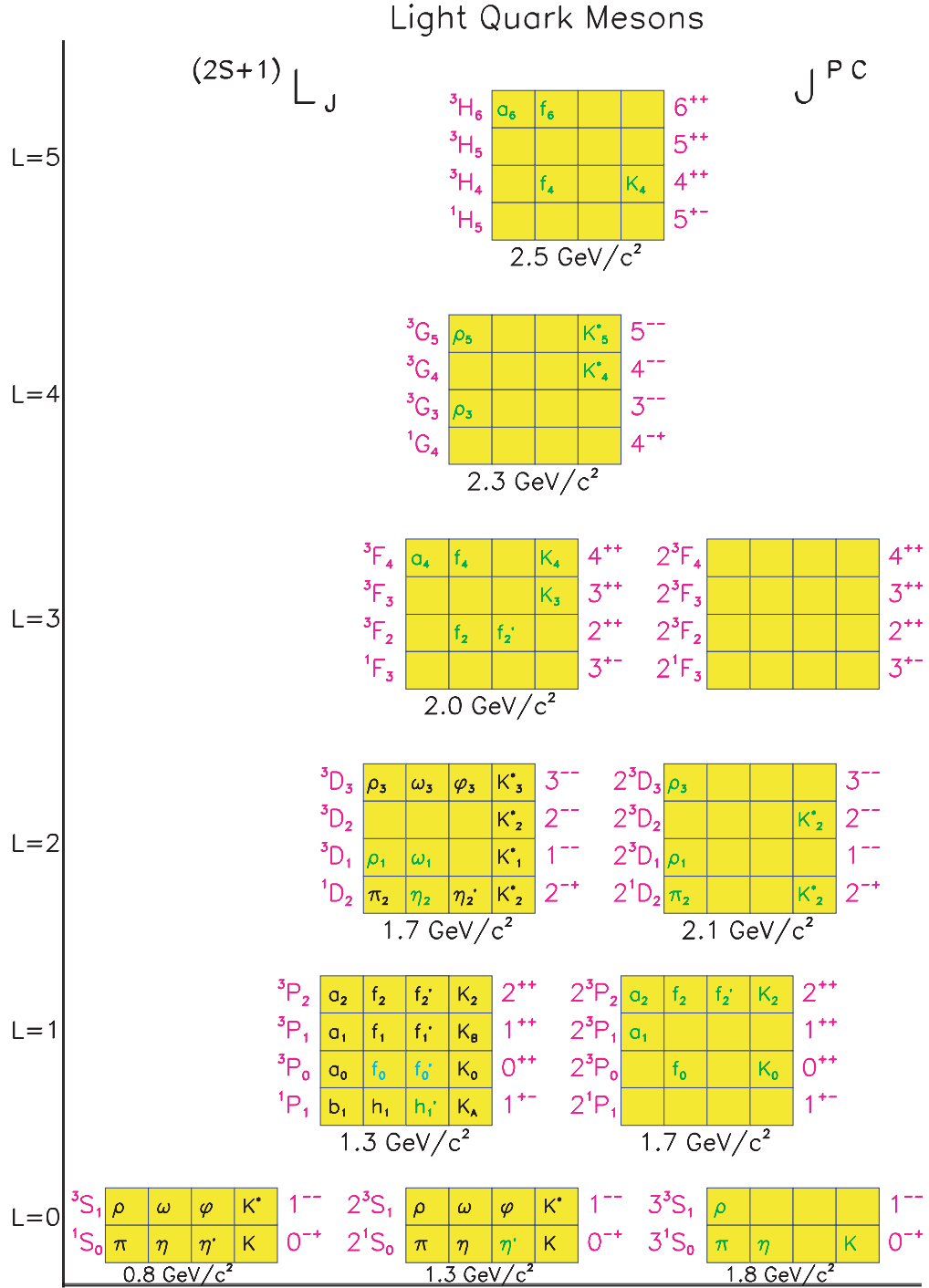


Figure 29: The  $q\bar{q}$  spectrum of states. The assignments of the light colored states are speculative, while the empty boxes are missing states. The orbital angular momentum of the nonet is plotted on the vertical axis, while the towers of radial excitations are shown along the horizontal axis.

### 2.A.3 Gluonic excitations and confinement

The Standard Model of elementary particles includes the electroweak theory and QCD, the latter describing the strong interactions among the quarks and gluons. At short distances – the regime of asymptotic freedom – perturbative techniques are applicable and QCD describes high energy experimental phenomena both qualitatively and quantitatively. At large distance scales – the confinement regime – the situation is far different. Here the successful calculational techniques of the perturbative regime cannot be used. We must rely on first-principles lattice QCD calculations or QCD-inspired models. There has been significant theoretical effort in this area recently and more progress can be expected in the near future, especially as multi-teraflop lattice QCD centers come into operation.

Understanding confinement in QCD requires a detailed understanding of the role of gluons. QCD is distinct from QED in that the force carriers of the former (gluons) carry color charge whereas for the latter the photons are electrically neutral. As illustrated in Fig. 30, the force between two electrically charged particles falls off like the inverse square of the distance between the charges. The number of field lines intersecting a unit area midway between the charges and perpendicular to the line connecting them would decrease as the inverse square of the distance between the charges. In contrast, the color field lines between a quark and an anti-quark do not fill all of space as in the case with electrical charges. Rather the field lines form flux tubes. A unit area placed midway between the quarks and perpendicular to the line connecting them intercepts a constant number of field lines, independent of the distance between the quarks. This leads to a constant force between the quarks – and a large force at that, equal to about 16 metric tons. The potential associated with this constant force is linear and grows with increasing distance. It takes infinite energy to separate the quarks to infinity and thus, qualitatively at least, this accounts for confinement.

Lattice QCD calculations support this notion of the formation of a flux tube between the quark and anti-quark. Figure 31 shows the energy density in the color field between a quark and an anti-quark in a meson with a separation of 1.2 fm. The density peaks at the positions of the quarks and is confined to a tube between the quarks. This calculation is for heavy quarks in the quenched approximation. Figure 31 also shows the corresponding potential between the quarks. The ground state potential has a  $1/r$  dependence at small distances and is linear for large distances.

This notion of the formation of flux tubes was first introduced in the 1970's by Yoichiro Nambu [Na70] to explain the observed linear Regge trajectories – the linear dependence of mass squared,  $m^2$ , of hadrons on their spin,  $J$ . This linear dependence results if one assumes that massless quarks are tied to the ends of a relativistic string with constant mass (energy) per length with the system rotating about its center. The linear  $m^2$  versus  $J$  dependence only arises when the mass density per length is constant, which is equivalent to a linear potential.

Within this picture, conventional mesons arise when the flux tube is in its ground state.

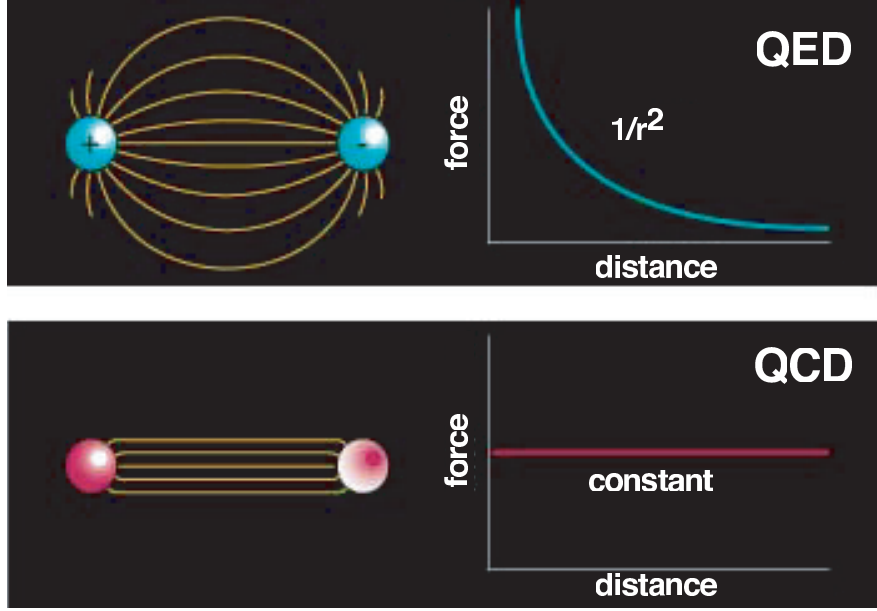


Figure 30: Field lines associated with the electrical force between two electrically charged particles (top) and the corresponding dependence of force on the distance between the charges and the field lines associated with the color force (bottom) between two quarks and the corresponding dependence of force on distance.

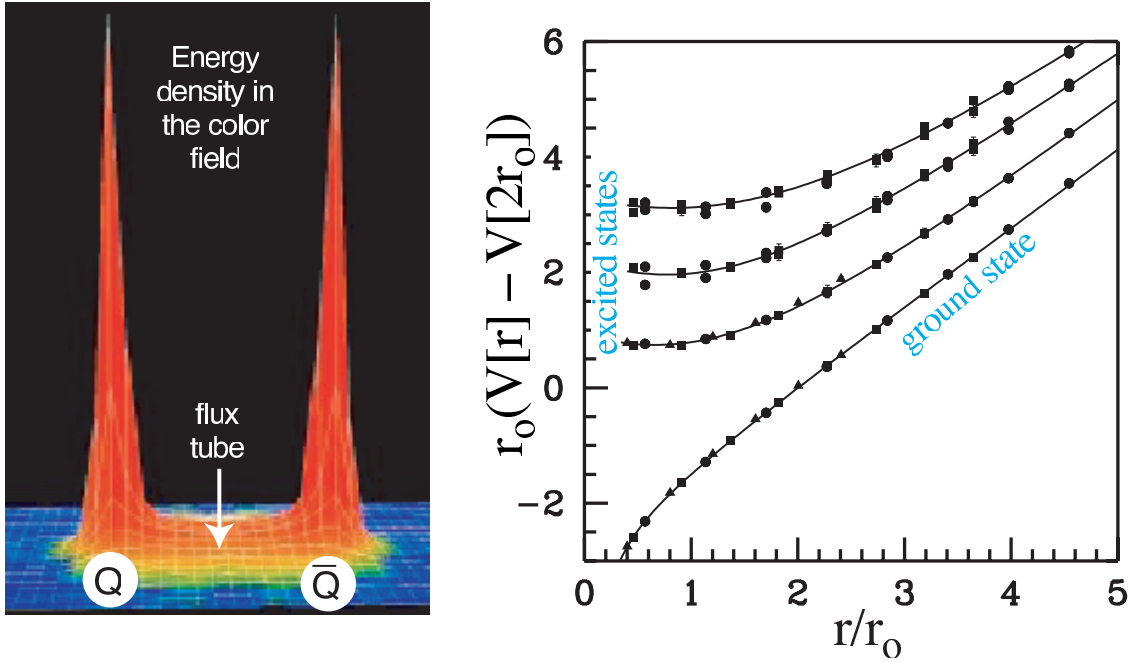


Figure 31: A lattice QCD calculation (left) of the energy density in the color field between a quark and an anti-quark. The density peaks at the positions of the quarks and is confined to a tube between the quarks. This calculation is for heavy quarks in the quenched approximation. The corresponding potential between the quarks (right). The ground state potential has a  $1/r$  dependence at small distances and is linear for large distances.

Excitations of the flux tube lead to hybrid mesons that exhibit both the quark and gluonic degrees of freedom. The first excited state of the flux tube is a transverse excitation. The flux tube, or string, spins clockwise or counter-clockwise around the  $q\bar{q}$  line leading to two degenerate states – degenerate since the energy should not depend on which way the flux tube is spinning. Lattice QCD and flux tube models both indicate that the lowest excited flux tube has  $J = 1$  [Be97, Is85a, La97]. The linear combinations of the clockwise or counter-clockwise rotations are eigenstates of parity and charge conjugation leading to two possibilities for the excited flux tube:  $J^{PC} = 1^{-+}$  or  $J^{PC} = 1^{+-}$ . Suppose we start with the  $q\bar{q}$  in the  $S = 0$  and  $L = 0$  (or  $J^{PC} = 0^{-+}$  – the  $\pi$  or  $K$ ) configuration. Combining this with  $J^{PC} = 1^{-+}$  or  $J^{PC} = 1^{+-}$  of the excited flux tube results in hybrid mesons with  $J^{PC} = 1^{++}$  or  $J^{PC} = 1^{--}$ . These are non-exotic quantum numbers. If, however, we start with  $q\bar{q}$  in the  $S = 1$  and  $L = 0$  (or  $J^{PC} = 1^{--}$  – the vector photon) configuration, the resulting hybrid meson can have  $J^{PC} = [0, 1, 2]^{+-}$  for the flux tube with  $J^{PC} = 1^{-+}$  and  $J^{PC} = [0, 1, 2]^{-+}$  for the flux tube with  $J^{PC} = 1^{+-}$ . We note that of these six possible  $J^{PC}$  combinations, three are exotic:  $J^{PC} = 0^{+-}$ ,  $J^{PC} = 1^{-+}$  and  $J^{PC} = 2^{+-}$ . These states will not mix with  $q\bar{q}$  and thus have unique signatures.

Meson production proceeds with an incoming probe interacting with the target particle and one result of the scattering can be the excitation of the flux tube. If the probe is a  $q\bar{q}$  in  $L = 0$  and  $S = 0$  ( $\pi$  or  $K$ ), production of exotic hybrids will not be favored. But if the  $q\bar{q}$  probe has  $L = 0$  and  $S = 1$ , for example a photon, one expects exotic hybrids to be produced readily.

Finally we consider the expected masses for hybrid mesons. We would expect the mass difference between the ground state (conventional) mesons and hybrid mesons to be given by the level spacing between the ground state of the flux tube and the first excited transverse mode and that is simply given by  $\pi/r$  where  $r$  is the quark separation. When translated to appropriate units this corresponds to about 1 GeV/c<sup>2</sup>.

In this discussion the motion of the quarks was ignored, but we know from general principles [Is85] that an approximation that ignores the impact of the flux tube excitation and quark motion on each other seems to work quite well.

#### 2.A.4 Observation of gluonic excitations

**Glueballs** Lattice QCD calculations indicate that lightest glueball is a scalar with a mass in the range from 1.5 to 1.7 GeV/c<sup>2</sup> [Mo97, Ba93, Se95, Ba98]. Indeed there is evidence from the Crystal Barrel experiment, which studied  $p\bar{p}$  annihilations at CERN, that the  $f_0(1500)$  is a leading candidate for a glueball [Am95, Am96]. There are, however, indications that this state is not a pure glueball but has some mixing with conventional  $q\bar{q}$  [CI01]. There are also strong indications that the scalar meson sector contains one or more glueballs since there are several more observed states than can be accommodated in the simple  $q\bar{q}$  model. However, the unique identification of a glueball is exacerbated by the possibility of mixing with  $q\bar{q}$ . Lattice QCD indicates a rich spectrum

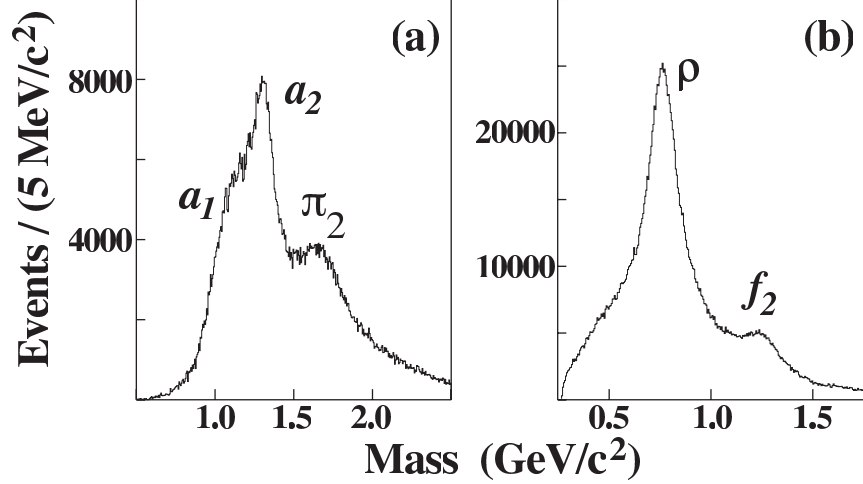


Figure 32: Acceptance corrected effective mass distributions for the (a)  $\pi^+\pi^-\pi^-$  combination and (b)  $\pi^+\pi^-$  combination (two entries per event) from E852 [Ad98].

of glueballs, all with non-exotic quantum numbers, from 1.5 to 2.5  $\text{GeV}/c^2$ . The lightest glueball with exotic quantum numbers is predicted to have  $J^{PC} = 2^{+-}$  and to have a mass of 4  $\text{GeV}/c^2$  [Mo97].

**Exotic hybrid mesons** After about two decades of experimental searches there have been reports of experimental observations of states with exotic  $J^{PC} = 1^{-+}$  by the Brookhaven E852 collaboration in  $\pi^-p$  interactions at 18  $\text{GeV}/c$ . One of these has a mass of  $(1593 \pm 8_{-47}^{+29}) \text{ MeV}/c^2$  and width of  $(168 \pm 20_{-12}^{+150}) \text{ MeV}/c^2$  and decays into  $\rho^0\pi^-$  [Ad98]. This state was observed in the reaction  $\pi^-p \rightarrow \pi^+\pi^-\pi^-p$  at a beam momentum of 18  $\text{GeV}/c$ . In Fig. 32, the acceptance-corrected (average acceptance was 25%) distributions of the  $\pi^+\pi^-\pi^-$  and  $\pi^+\pi^-$  effective masses are shown. The positions of well-established meson states are shown, including the  $a_1(1260)$ , which does not show up as a prominent peak in the overall mass distribution. The partial wave analysis (PWA) performed on these data assumes an *isobar model* – a parent decaying into a  $\pi\pi$  state and an unpaired  $\pi$  followed by the decay of the  $\pi\pi$  state. The resulting decomposition into various waves is shown in Fig. 33. The decomposition clearly shows the  $\pi(1800)$  in the  $0^{-+}$  wave, the  $a_1(1260)$  in the  $1^{++}$  wave, the  $\pi_2(1670)$  in the  $2^{-+}$  wave, and the  $a_2(1320)$  in the  $2^{++}$  wave. Evidence for the exotic  $1^{-+}$   $\rho\pi$  is shown in Fig. 34. If an isovector  $\rho\pi$  resonates in an  $L = 1$  wave, it has  $J^{PC} = 1^{-+}$ . Also shown in this figure is the effect of leakage of non-exotic waves. Finally in Fig. 35 a coupled fit to the wave intensities and phase difference between the  $1^{-+}$  and  $2^{-+}$  waves is shown.

Another state reported by E852 has a similar mass,  $(1597 \pm 10_{-10}^{+45}) \text{ MeV}/c^2$ , but with a significantly larger width,  $(340 \pm 40_{-50}^{+50}) \text{ MeV}/c^2$ , and decays into  $\eta'\pi^-$  [Iv01]. It has not been determined whether these represent two decay modes of the same state or whether they are due to two different mechanisms.

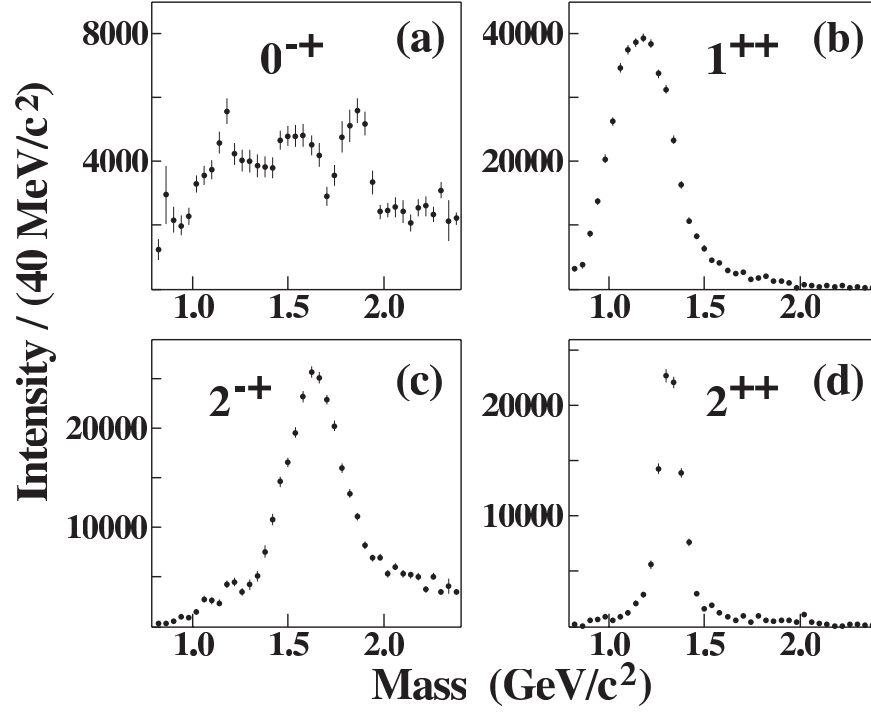


Figure 33: Combined intensities for all (a)  $0^{-+}$  waves; (b)  $1^{++}$  waves; (c)  $2^{-+}$  waves; and (d)  $2^{++}$  waves (from E852 [Ad98]).

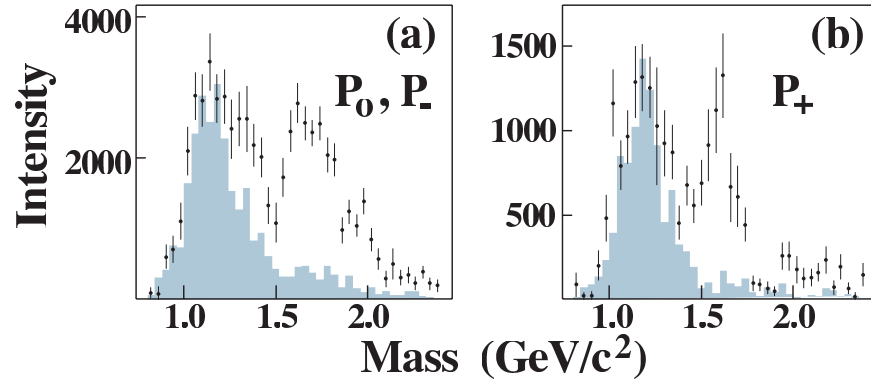


Figure 34: The intensities for the waves corresponding to  $1^{-+}$  into  $\rho\pi$ . The shaded distributions are an estimate of leakage due to non-exotic waves (from E852 [Ad98]).

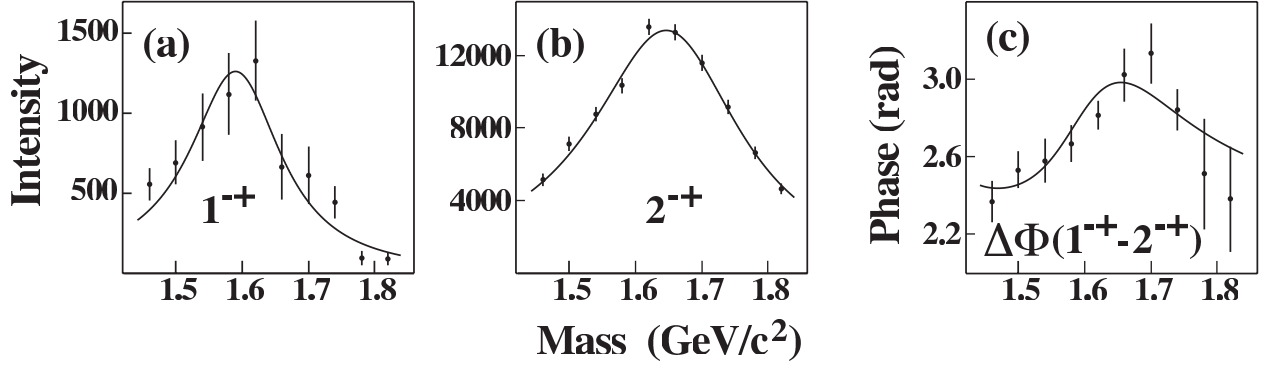


Figure 35: Results of a coupled mass-dependent Breit-Wigner fit of the  $1^{-+}$  and  $2^{-+}$  waves showing the phase difference as well (from E852 [Ad98]).

The E852 collaboration also reported observation of another  $J^{PC} = 1^{-+}$  state with mass  $(1370 \pm 16^{+50}_{-30})$  MeV/ $c^2$  and a width of  $(385 \pm 40^{+65}_{-105})$  MeV/ $c^2$  decaying into  $\eta\pi^-$  [Th97]. If an  $\eta\pi$  system is in a  $P$  wave, the resulting  $J^{PC}$  quantum number combination is exotic ( $1^{-+}$ ). In these studies the dominant state observed in the  $\eta\pi$  channel is the  $J^{PC} = 2^{++}$   $a_2(1320)$  seen in the  $D$ -wave. Critical to the identification of this state is not only showing the presence of a  $P$ -wave, but also that the resulting line shape is consistent with a Breit-Wigner and that the phase motion of the  $P$ , as determined by its interference with the dominant  $D$ -wave, cannot be due solely to the  $a_2^-(1320)$  resonance. Soon after the E852 report, the Crystal Barrel Collaboration reported an exotic  $J^{PC} = 1^{-+}$  state produced in  $\bar{p}n \rightarrow \pi^-\pi^0\eta$  obtained by stopping antiprotons in liquid deuterium [Ab98]. They reported a mass of  $(1400 \pm 20^{+20}_{-20})$  MeV/ $c^2$  and a width of  $(310 \pm 50^{+50}_{-30})$  MeV/ $c^2$ .

The first claim of an exotic meson decaying into  $\eta\pi^0$  with a mass of 1400 MeV/ $c^2$  was made by the GAMS collaboration in the reaction  $\pi^-p \rightarrow \eta\pi^0n$  [Al88] but a later analysis by the group [Yu95] led to ambiguous results. The VES collaboration also presented evidence for a  $P$ -wave contribution in  $\eta\pi$  [Be93] and at KEK a claim was made for an exotic  $\eta\pi$  state [Ao93] as well, but with a mass and width close to that of the  $a_2(1320)$ ; leakage from the dominant  $D$  wave could not be excluded.

In all the observations in  $\pi$ -induced reactions, the  $\eta\pi$   $P$ -wave enhancements have cross sections that are substantially smaller than the dominant  $a_2(1320)$  so leakage, usually due to an imperfect understanding of experimental acceptance, is a source of concern. In contrast, the observed yield of the  $\pi_1(1400)$  yield in  $\bar{p}p$  annihilations is of the same magnitude as the  $a_2(1320)$ . Apart from these experimental issues, the interpretation of the nature of low-mass  $\eta\pi$   $P$ -wave amplitude and phase motion should be guided by the principle of parsimony – less exotic interpretations must also be considered. In a recent analysis of the  $\eta\pi^0$  system in the reaction  $\pi^-p \rightarrow \eta\pi^0n$  from data using the E852 apparatus, a  $P$ -wave is observed but it is not consistent with a Breit-Wigner resonance. The observed  $P$ -wave phase motion is consistent with  $\eta\pi^0$  final state interactions. This could explain the relatively wide width of the observed  $\eta\pi^-$  state and could also explain the broad  $\eta'\pi^-$  enhancement. The  $\pi^-p \rightarrow \eta\pi^0n$  and  $\pi^-p \rightarrow \eta\pi^-p$  have some notable differences. For the former charge conjugation ( $C$ ) is a good quantum number but not for the latter and for the former both



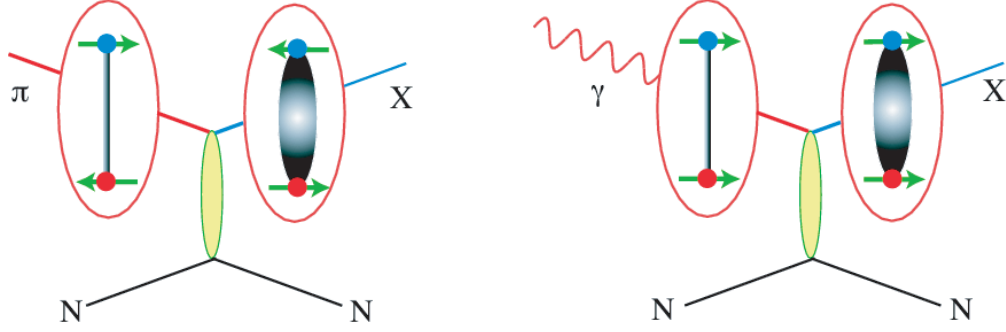


Figure 36: With a  $\pi$  probe (left) the incoming quarks have  $L = 0$  and  $S = 0$ . The excited flux tube from the scattering results in hybrid mesons with non-exotic quantum numbers. With a photon probe (right) the incoming quarks have  $L = 0$  and  $S = 1$ . When the flux tube is excited, hybrid mesons with exotic quantum numbers are possible.

the  $a_0(980)$  and  $a_2(1320)$  are prominently present but for the latter only the  $a_2(1320)$  is strongly produced. This is an important factor in selecting the physical solutions among mathematically ambiguous solutions.

The conclusion from these studies is that there indeed are tantalizing hints of gluonic excitations in both the glueball and hybrid sectors but the results are not conclusive. The large statistics samples of high quality data to be collected with the GLUEX detector will provide the definite resolution of the murky situation. Furthermore there is good reason to believe that whereas exotic hybrids may be suppressed in  $\pi$  production, they are enhanced in photoproduction where essentially no data exist. In the glueball sector, the large samples of glue-rich radiative  $J/\psi$  decays should shed light on the spectrum of these gluonic excitations.

### 2.A.5 Photoproduction of exotic hybrids

**Why photoproduction?** Based on the arguments presented above, the photon is expected to be particularly effective in producing the *smoking gun* signature for gluonic excitations: hybrids with exotic  $J^{PC}$ . In this regard, we will compare the effectiveness of the  $\pi$  or  $K$  as a probe with that of the photon. In the former case, the meson is a  $q\bar{q}$  with spins anti-aligned ( $S = 0$ ) and in the latter, the photon is a virtual  $q\bar{q}$  with spins aligned ( $S = 1$ ). In both cases, the relative orbital angular momentum is zero ( $L = 0$ ) and the flux tube connecting the quarks is in its ground state. Figure 36 illustrates the differences between a  $\pi$  probe and a  $\gamma$  probe. If the scattering results in excitation of the flux tube, one expects exotic hybrid mesons to be suppressed in  $\pi$ -induced interactions and enhanced in photoproduction.

Current phenomenology also supports the notion that photons should be more effective at producing exotic hybrids [Af98, Sz01]. Figure 37 shows an estimate of the photoproduction cross sections at 8 GeV for the  $a_2(1320)$  and the exotic  $\pi_1(1600)$  [Sz01]. The model uses as input the

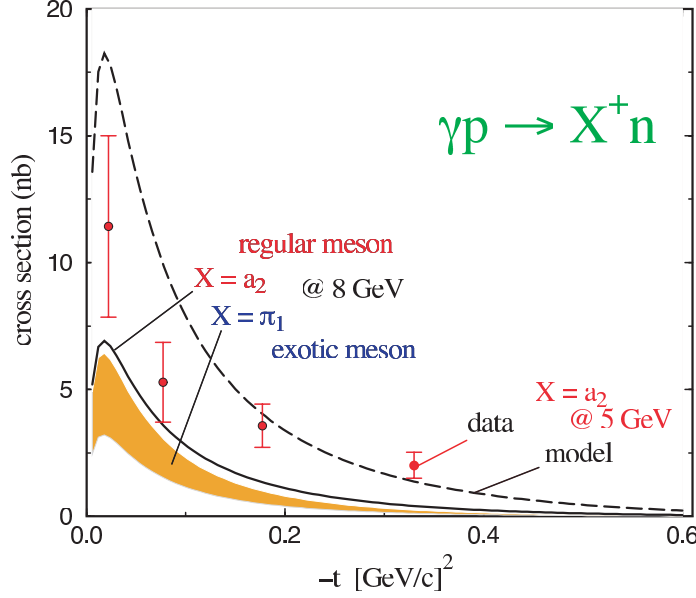


Figure 37: Estimates of the photoproduction cross sections for  $a_2(1320)$  and the exotic  $\pi_1(1600)$  at 8 GeV based on a phenomenological analysis described in [Sz01]. The model uses as input the ratio of  $\pi_1(1600)$  to  $a_2(1320)$  as observed in E852. The model is compared with photoproduction of the  $a_2(1320)$  at 5 GeV.

ratio of  $\pi_1(1600)$  to  $a_2(1320)$  as observed in E852. The model is compared with photoproduction of the  $a_2(1320)$  at 5 GeV. Whereas in E852, with a  $\pi$  beam, the  $\pi_1(1600)$  is produced at about 5% of the rate for  $a_2(1320)$ , in photoproduction the rates for  $\pi_1(1600)$  are expected to be comparable for that of the  $a_2(1320)$ . In the case of the incident  $\pi$ , the  $\pi_1(1600)$  is produced by  $\rho$  exchange and the suppression at very low- $|t|$  due to angular momentum – spin 0 in and spin 1 out – decreases the cross section. This is to be compared to photoproduction of the  $\pi_1(1600)$  with  $\pi$  exchange where there is no suppression at very low- $|t|$  since now we have spin 1 in and spin 1 out. Furthermore the  $N\rho N$  coupling at the baryon vertex in the incident  $\pi$  case is lower by a factor of 4 compared to the  $N\pi N$  in the photoproduction case.

To underscore the differences between existing photoproduction and  $\pi$  production, the corresponding largest data sets on  $3\pi$  production are compared in the plots of Fig. 38. The  $3\pi$  mass spectrum from the reaction  $\pi^- p \rightarrow \pi^+ \pi^- \pi^- p$  at 18 GeV/c from E852 at Brookhaven is shown. Also shown is the  $3\pi$  mass spectrum from the reaction  $\gamma p \rightarrow \pi^+ \pi^+ \pi^- n$  at 19 GeV from SLAC. We note the large difference in statistics between the two and we also note the differences in the structure of the spectra.

**Current photoproduction data** Table 7 is a partial compilation of known photoproduction cross sections and the numbers of events from the existing experiments. The typical cross sections range from of order  $0.1 \mu\text{b}$  up to of order  $10 \mu\text{b}$ , with most measurements involving rather small numbers of events, typically on the order of a few thousand. The extant data from photoproduction

Table 7: A sample of measured photoproduction cross sections from several references. Note the small numbers of events in any given channel.

<i>Reaction</i>	$E_\gamma$ GeV	$\sigma$ ( $\mu b$ )	<i>Events</i>	<i>Ref.</i>
$\gamma p \rightarrow p\pi^+\pi^-$	9.3		3500	[Ba73]
$\gamma p \rightarrow p\pi^+\pi^-$	19.3		20908	[Ab84]
$\gamma p \rightarrow p\pi^+\pi^-\pi^0$	2.8		2159	[Ba73]
$\gamma p \rightarrow p\pi^+\pi^-\pi^0$	4.7		1606	[Ba73]
$\gamma p \rightarrow p\pi^+\pi^-\pi^0$	9.3		1195	[Ba73]
$\gamma p \rightarrow p\pi^+\pi^-\pi^0$	4.7–5.8	$13.5 \pm 1.5 \mu b$	3001	[Ei72]
$\gamma p \rightarrow p\pi^+\pi^-\pi^0$	6.8–8.2	$11.8 \pm 1.2 \mu b$	7297	[Ei72]
$\gamma p \rightarrow n\pi^+\pi^+\pi^-$	4.7–5.8	$4.6 \pm 1.4 \mu b$	1723	[Ei72]
$\gamma p \rightarrow n\pi^+\pi^+\pi^-$	6.8–8.2	$4.0 \pm 1.2 \mu b$	4401	[Ei72]
$\gamma p \rightarrow n\pi^+\pi^+\pi^-$	16.5–20		3781	[Co93a]
$\gamma p \rightarrow p\pi^+\pi^-\pi^0$	20–70		14236	[At84]
$\gamma p \rightarrow p\pi^+\pi^-\pi^+\pi^-$	4–6	$4.0 \pm 0.5 \mu b$	$\sim 330$	[Da73]
$\gamma p \rightarrow p\pi^+\pi^-\pi^+\pi^-$	6–8	$4.8 \pm 0.5 \mu b$	$\sim 470$	[Da73]
$\gamma p \rightarrow p\pi^+\pi^-\pi^+\pi^-$	8–12	$4.5 \pm 0.6 \mu b$	$\sim 470$	[Da73]
$\gamma p \rightarrow p\pi^+\pi^-\pi^+\pi^-$	12–18	$4.4 \pm 0.6 \mu b$	$\sim 380$	[Da73]
$\gamma p \rightarrow p\pi^+\pi^-\pi^+\pi^-$	15–20		6468	[Ab85]
$\gamma p \rightarrow p\pi^+\pi^-\pi^0\pi^0$	20–70		8100	[At84a]
$\gamma p \rightarrow p\pi^+\pi^+\pi^-\pi^-\pi^0$	19.5		2553	[Bl97]
$\gamma p \rightarrow \Delta^{++}\pi^-\pi^+\pi^-$	4–6	$1.65 \pm 0.2 \mu b$	$\sim 200$	[Da73]
$\gamma p \rightarrow \Delta^{++}\pi^-\pi^+\pi^-$	6–8	$1.8 \pm 0.2 \mu b$	$\sim 200$	[Da73]
$\gamma p \rightarrow \Delta^{++}\pi^-\pi^+\pi^-$	8–12	$1.1 \pm 0.2 \mu b$	$\sim 200$	[Da73]
$\gamma p \rightarrow \Delta^{++}\pi^-\pi^+\pi^-$	12–18	$1.15 \pm 0.2 \mu b$	$\sim 200$	[Da73]
$\gamma p \rightarrow p\omega$	4.7–5.8	$2.3 \pm 0.4 \mu b$	$< 1600$	[Ei72]
$\gamma p \rightarrow p\omega$	6.8–8.2	$2.0 \pm 0.3 \mu b$	$< 1200$	[Ei72]
$\gamma p \rightarrow p\omega$	4.7	$3.0 \pm 0.3 \mu b$	1354	[Ba73]
$\gamma p \rightarrow p\omega$	9.3	$1.9 \pm 0.3 \mu b$	1377	[Ba73]
$\gamma p \rightarrow p\phi$	4.7	$0.41 \pm 0.09 \mu b$	136	[Ba73]
$\gamma p \rightarrow p\phi$	9.3	$0.55 \pm 0.07 \mu b$	224	[Ba73]
$\gamma p \rightarrow na_2^+$	4.7–5.8	$1.7 \pm 0.9 \mu b$		[Ei72]
$\gamma p \rightarrow na_2^+$	6.8–8.2	$0.9 \pm 0.9 \mu b$		[Ei72]
$\gamma p \rightarrow na_2^+$	19.5	$0.29 \pm 0.06 \mu b$	$\sim 100$	[Co93a]

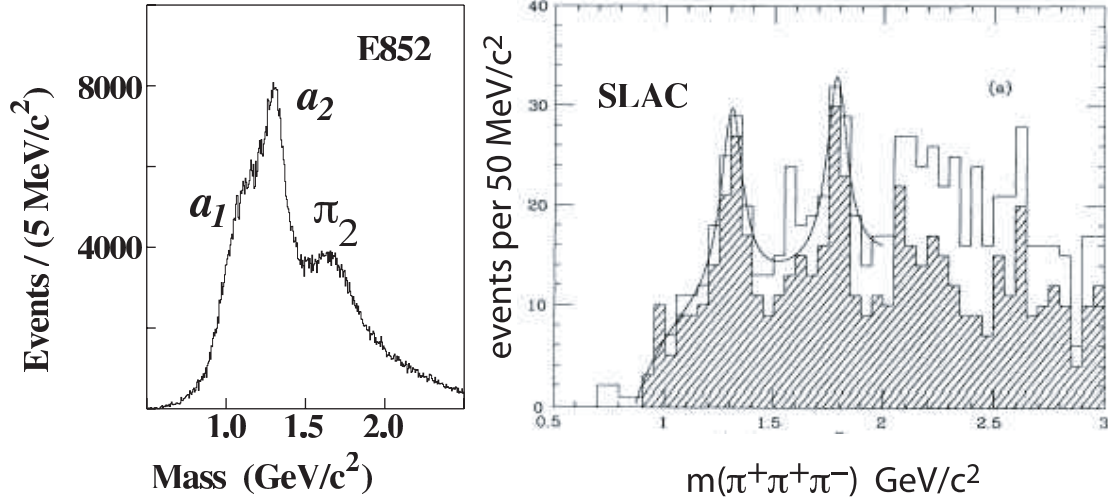


Figure 38: (left) The  $3\pi$  mass spectrum from the reaction  $\pi^- p \rightarrow \pi^+ \pi^- \pi^- p$  at 18 GeV/c from E852 at Brookhaven. (right) The  $3\pi$  mass spectrum from the reaction  $\gamma p \rightarrow \pi^+ \pi^+ \pi^- n$  at 19 GeV from SLAC. The shaded area identifies the portion of the  $3\pi$  spectrum that included a  $\rho$  meson.

are far too meager to perform the analysis necessary to unambiguously identify gluonic excitations. For example, after one year of low intensity running at  $10^7$  photons/sec, the yield of  $a_2(1320)$  in GLUEX will be five orders of magnitude greater than the same collected in the SLAC photoproduction experiment. The yield of the exotic  $\pi_1(1600)$  in the published E852 results will be increased by four orders of magnitude by GLUEX after one year of running.

There are reasonable sized data sets in  $2\pi$  and  $2\pi$  photoproduction from the CLAS detector at JLab that are currently under analysis. However, these arise from unpolarized photon beams and are produced from an incoherent bremsstrahlung spectrum that peaks at around 5 GeV.

#### 2.A.6 Complementarity with other searches

Gluonic excitations include both exotic and non-exotic hybrid mesons and glueballs. Hybrid mesons exist in both the light quark ( $u$ ,  $d$  and  $s$ ) and heavy quark ( $c$  and  $b$ ) sectors. Clearly, existing data collected with incident  $\pi$  beams, central collisions,  $p\bar{p}$  annihilations and  $e^+e^-$  collisions have not uncovered a wealth of information about these states. As discussed earlier, the focus of the GLUEX project is in the light-quark hybrid sector. The initial benchmark states will be the exotic hybrids, which cannot mix with  $q\bar{q}$  and therefore have a *smoking gun* signature. There are good reasons to expect that photoproduction will be particularly effective at uncovering the exotic hybrid mesons. And the existing photoproduction data are meager indeed.

The glueball and heavy hybrid sectors are not accessible to GLUEX. Glueballs are not preferentially produced in photoproduction because they do not couple to photons. Moreover, according to lattice QCD, the lightest exotic glueball has a mass of 4 GeV/c². One fruitful area of investigation

are  $J/\psi$  radiative decays since the system recoiling from the photon should be rich in two-gluon states. The planned CLEO-c project at CESR will collect a billion  $J/\psi$  radiative decays.

The direct production of exotic hybrids in  $e^+e^-$  collisions is complicated by the fact that the angular momentum barrier (the excited flux-tube carries  $J = 1$ ) suppresses this production mode.

Lattice QCD predictions about heavy-quark exotic hybrids are at least as reliable as for the light-quark hybrids but the experimental situation is far more problematic. The photoproduction cross-sections are a few orders of magnitude lower. At the higher energies needed to produce these more massive states many other uninteresting processes can contribute to background. Finally, to unambiguously tag a charm or beauty hybrid one must identify detached vertices, further complicating the experimental challenge.

### 2.A.7 Production and analysis of hybrid mesons

**Kinematics** Consider a specific exclusive photoproduction reaction:

$$\gamma p \rightarrow X p \quad (2)$$

The center-of-mass energy squared,  $s$ , and the momentum-transfer-squared,  $t$ , between the incoming beam and outgoing  $X$  are defined in terms of the four-vectors of the particles:

$$s = (p_\gamma + p_p)^2 \quad (3)$$

$$t = (p_\gamma - p_X)^2 \quad (4)$$

The dependence of the cross section on  $s$  and  $t$  depend on the production mechanism, which is usually described in terms of the particle or particles which can be exchanged as shown in Fig. 39. For example, if the exchange particle is the pomeron (diffractive process) the cross section is nearly constant in  $s$ . For meson-exchange processes, cross sections typically fall off with increasing  $s$ . The dependence on  $t$  is typically exponential:

$$\frac{dN}{dt} \propto e^{-\alpha|t|} \quad (5)$$

For the process ( 2) at high enough photon beam energy,  $E_\gamma$ , we can make the approximation  $s \approx 2 \cdot E_\gamma$  where  $E_\gamma$  is in GeV and  $s$  is in  $GeV^2$ . For fixed  $s$  and mass of  $X$ ,  $m_X$ , there is a minimum value of  $|t|$ , or  $|t|_{min}$ , needed to produce  $X$ . This  $|t|_{min}$  increases with increasing  $m_X$  for fixed  $E_\gamma$  and decreases with increasing  $E_\gamma$  for fixed  $m_X$ . Coupled with the steep dependence implied in equation ( 5), the dependence of  $|t|_{min}$  on  $m_X$  will affect event yields. In addition, the line shape of a resonance can be distorted if there is too rapid a variation of  $|t|_{min}$  across the width of a resonance.

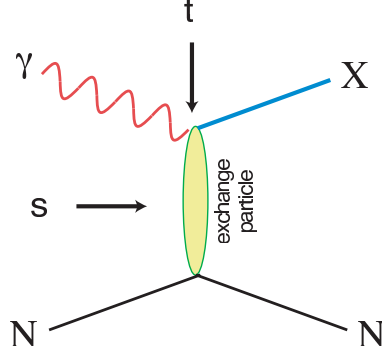


Figure 39: Diagram for the photoproduction of particle  $X$ . The variables  $s$  and  $t$  are the center-of-mass energy squared and the momentum-transfer-squared from incoming photon to outgoing particle  $X$ . The process shown here proceeds through the exchange of a particle in the  $t$ -channel.

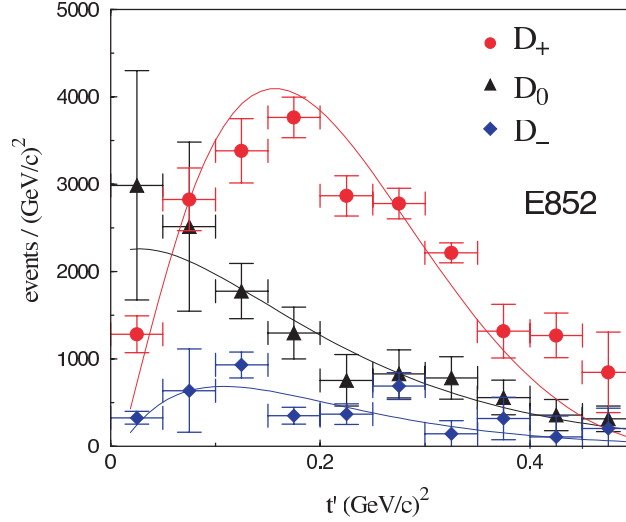


Figure 40: The distribution in  $|t'|$  where  $t' = t - t_{min}$  for the  $D$ -waves after a PWA of the  $\eta\pi^0$  system from the reaction  $\pi^-p \rightarrow \eta\pi^0n$  at 18 GeV/c. The curves are fits to expected Regge exchanges for the various  $D$ -waves.

Figure 40 shows an example of how the dependence in  $t$  is correlated with particle exchange. The distribution is in  $|t'|$  where  $t' = t - t_{min}$  for the  $D$ -waves after a PWA of the  $\eta\pi^0$  system from the reaction  $\pi^-p \rightarrow \eta\pi^0n$  at 18 GeV/c. The curves are fits to expected Regge exchanges for the various  $D$ -waves.

**PWA requirements** The PWA technique is described in a later chapter. It is important to stress here that the detector design focuses on hermeticity and resolution to insure nearly uniform coverage with well-understood acceptance functions for various decay angles for particle  $X$ . Kinematic fitting will also be used to identify exclusive processes. The design focuses on the requirements of the PWA. The existence of well established resonances will be used as benchmarks for the PWA. They also provide benchmarks for the phase variation of candidate exotic states. Furthermore, candidate

exotics can appear with multiple decay modes which must give consistent results. As an example, a meson which decays into  $\eta\pi$  should be observed in channels where  $\eta \rightarrow \pi^+\pi^-\pi^0$ ,  $\eta \rightarrow 3\pi^0$ , and  $\eta \rightarrow 2\gamma$ . Each of these modes leads to different acceptances and systematics. This provides a powerful check on PWA results.

## Linear polarization of the beam

**Linear and circular polarization** We start with a review of the relationship between linear and circular polarization. A right-handed-circularly ( $|R\rangle$ ) polarized photon has  $m = 1$  while for a  $|L\rangle$  photon  $m = -1$ . These are related to the linear polarization states,  $|x\rangle$  (in production plane) and  $|y\rangle$  (perpendicular to production plane) by:

$$|x\rangle = \frac{1}{\sqrt{2}} (|L\rangle - |R\rangle) \quad (6)$$

$$|y\rangle = \frac{i}{\sqrt{2}} (|L\rangle + |R\rangle) \quad (7)$$

States of linear polarization are eigenstates of parity. We will use these relations in several straightforward cases to show how linear polarization:

1. can provide information on decays in lieu of statistics,
2. is essential in isolating production mechanisms, and
3. can be used as an exotics filter if the production mechanism is known.

**Linear polarization and statistics** To illustrate how linear polarization provides useful information in the PWA, consider the case of the photoproduction of a vector meson which subsequently decays into two pseudoscalar mesons. Possible examples are  $\rho \rightarrow \pi\pi$  or  $\phi \rightarrow K\bar{K}$ . Suppose the production mechanism produces the vector with the same helicity as the incident photon (or *s-channel helicity conservation*). In the rest frame of the vector the two-pseudoscalar wave function is described by

$$Y_1^m(\theta, \phi) \propto \sin\theta \cdot e^{im\phi} \quad (8)$$

For circularly polarized photons (either  $m = 1$  or  $m = -1$ ) the square of this amplitude carries no  $\phi$  information while for in-plane photons there is a  $\cos^2\phi$  dependence and out-of-plane a  $\sin^2\phi$  dependence in the decay angular distribution, since in these cases we have the sum or difference of  $Y_1^{+1}$  and  $Y_1^{-1}$  according to equations ( 6) and ( 7). Although not essential in determining spin, a gain of statistics is needed to recover a drop in the degree of linear polarization. For example, our Monte Carlo simulation studies indicate that when the degree of linear polarization decreases from 0.40 to 0.2 a factor of two increase in statistics is needed to achieve the same relative error in determination of spin amplitudes.

**Linear polarization and production mechanism** This is best illustrated by considering a specific example. Suppose we produce a vector particle ( $J^P = 1^-$ ) by the exchange of a scalar particle ( $J^P = 0^+$  – natural parity exchange) or a pseudoscalar particle ( $J^P = 0^-$  – unnatural parity exchange). We wish to determine whether the vector is produced by natural (amplitude  $A_N$ ) or unnatural (amplitude  $A_U$ ) parity exchange. In the center-of-mass of the vector particle, the momentum vectors of the beam photon and exchange particle are collinear. For circularly polarized photons, the  $m$  of the vector is the same as that of the photon. From parity conservation, the orbital angular momentum between the photon and exchange particle is  $L = 0$  or  $L = 2$  for natural parity exchange and  $L = 1$  for unnatural parity exchange. So for circularly polarized photons, with  $m = +1$ , the total amplitude is  $A_N + A_U$  whereas for  $m = -1$ , the total amplitude is  $A_N - A_U$ . This follows simply from the addition of angular momenta. Circularly polarized photons allow us to measure only the sum or difference of the two exchange amplitudes. If however, we have linearly polarized photons along the  $x$ -direction, we extract  $A_N$  using equation ( 6) and for polarization along the  $y$ -direction, we extract  $A_U$  using equation ( 7).

**Linear polarization as an exotics filter** Using arguments similar to those above, it has been shown [Af00c] that linear polarization can be used as a tool to filter exotics. For example, a  $\rho\pi$  system with  $I = 1$  has  $C = +$ . Suppose that one can determine the naturality of the exchange particle by selecting data within a range of  $|t|$ . For a produced  $C = +$  particle with spin one we can have natural parity ( $J^{PC} = 1^{-+}$  – exotic) or unnatural parity ( $J^{PC} = 1^{++}$  – non-exotic). In the case of natural parity exchange the in-plane polarization selects the  $J^{PC} = 1^{-+}$  wave while out-of-plane polarization selects  $J^{PC} = 1^{++}$ . For unnatural parity exchange the reverse is true. Note that in this case, we are specifying the naturality of the exchange and using linear polarization to select the naturality of the produced particle. In the previous section, we specified the naturality of the produced particle and used linear polarization to select the naturality of the exchanged particle.



## 2.B The Fundamental Structure of the Nuclear Building Blocks

The nucleons are the basic building blocks of atomic nuclei. Their internal structure, which arises from their quark and gluon constituents, determines their mass, spin, and interactions. These, in turn, determine the fundamental properties of the nuclei. To make further progress in our understanding of nuclei, it is crucial that we understand in detail how the nucleon’s basic properties are derived from the theory of strong interactions: quantum chromodynamics (QCD). Over the past half century much progress has been made toward unraveling the structure of the nucleon. However, our understanding is fragmented and incomplete, and many puzzles remain. For example, we only partially understand how the nucleon’s spin is “assembled” from the quark spins and the quark and gluon angular momenta, and we don’t know the details of the spatial and momentum distributions of the quarks and gluons within the nucleon. Our understanding of nucleon structure is, quite simply, very far from the level of our understanding of atomic structure.

The JLab 12 GeV Upgrade will support a great leap forward in our knowledge of hadron structure through major programs in three areas: nucleon form factors at large  $Q^2$ , valence quark structure, and deep exclusive scattering. It will also support important initiatives in a number of other areas of hadron structure. These research programs are described in detail below. The data on hadron structure that will be obtained using the Upgrade can be understood and interpreted coherently, using the theoretical framework of the recently-discovered Generalized Parton Distributions (GPDs), to provide truly remarkable and revealing images of the proton’s structure that will enable us to understand these fundamental “building blocks” of nuclear physics.

Protons and neutrons (nucleons) make up most of the visible matter in the Universe. Their masses contribute to the gravitational pull that controls the evolution of galactic structure and keeps our feet firmly on the ground. Their strong interactions fuel the Sun and shape the structure of the atomic nuclei. The nuclei, in turn, (together with the well-understood electromagnetic interactions and the associated electrons) determine the chemical elements and their properties. The spin of both the nucleons and more complex nuclei provides an essential tool, Magnetic Resonance Imaging (MRI), that is broadly used to examine our bodies without harming them.

Why does strongly-interacting matter have so many fascinating features? The answer lies in the complex inner structure of the nucleons. According to the fundamental theory of strong interactions, quantum chromodynamics (QCD), protons and neutrons are ultimately made of simple particles called quarks and gluons. But QCD is so complex that we are still unable to make reliable calculations of nucleon structure to the desired accuracy. The nucleon structure problem is one of the most important missing links in our developing understanding of the evolution of the universe from the quarks to the cosmos. Its place in that evolution is analogous to the role that the structure of DNA plays as the key link between molecular structure and life. While biological behaviors may be traced to the structure of DNA, it is not yet possible to determine how that structure was formed by the molecules in the first place. Therefore, it is indispensable to sequence DNA in order

to understand the functions of the biological building blocks.

Similarly, to understand the properties of the nucleon, we must map out the complete distributions of quarks and gluons through experiments. This effort began in the mid 1950's, with the first measurements of the elastic scattering of high energy electrons from protons, continued through 1970's, and thrives today. Nearly half a century of study has brought many exciting discoveries and surprises. The first electron scattering experiments of Hofstadter, *et al.* determined the finite size of the proton. Two decades later quarks were discovered inside the nucleon through deep-inelastic scattering of higher energy electrons. More recently, we have learned from the scattering of still higher energy electrons that the density of quarks carrying a small fraction of the nucleon momentum saturates, and from the spin dependence of electron scattering from aligned nucleons that the quark spin actually carries very little of the spin of the nucleon. Despite these fruitful results, we are far from a complete mapping of the quark and gluon distributions inside the nucleon. The information we have gathered so far provides only a sketchy outline of the full picture.

Our understanding of nucleon structure has evolved dramatically each time a new experimental tool has become available. The simplest probe of the nucleon's structure is elastic electron scattering, in which one measures the probability that the nucleon remains whole after absorbing a photon. Measurement of elastic scattering form factors (the ratio of the observed scattering to that predicted for a structureless, point particle) as a function of the photon's wavelength determines (in the low-momentum transfer regime) the Fourier transforms of the nucleon's charge and current distributions. This measurement is analogous to the study of the internal structure of the human body using traditional, 2-dimensional x-ray techniques. While much of what we know about the structure of the nucleon has been learned this way, elastic scattering does not tell us how fast the quarks are moving or how much momentum and energy they carry.

At higher momentum transfers, the elastic scattering form factors are excellent observables for exploring the perturbative QCD reaction mechanism (how the nucleon recoils as a whole after receiving a large momentum kick) and for testing the leading light-cone wave functions. Unfortunately, the form factors and the reaction cross sections become very small as the momentum transfer increases. To make progress, we need an electron accelerator with both high energy *and* high luminosity. JLab with the 12 GeV upgrade will be the first accelerator capable of careful exploration of the elastic form factors in the large momentum regime.

A second approach to mapping the quark and gluon structure of the nucleon is to study deep-inelastic scattering (DIS), in which the electron is scattered from individual quarks within the nucleon, knocking them out and, in the process, destroying the nucleon. A similar technique has been used in condensed matter physics to study the momentum distribution of atoms in liquid helium, in atomic physics to measure the momentum distributions of electrons in each atomic shell, and in nuclear physics to study the momentum distributions of individual nucleons within nuclei. A DIS experiment measures the distributions of the momentum component of the quarks in the nucleon that is along the direction of the probing photon, providing information that is

complementary to the elastic scattering form factors.

Over the last three decades, we have obtained much information about the quark and gluon (the parton) distributions through DIS and related processes. The results of these experiments have been summarized in several standard sets of phenomenological fits to the data that parameterize the distributions of quarks, anti-quarks and gluons as a function of the Feynman variable,  $x$ , which is the fraction of the nucleon’s momentum carried by the parton. One clear deficiency of our knowledge is the “high- $x$ ” behavior of the partons: the part of the distribution that corresponds to instances when the struck parton was carrying nearly all of the momentum of the nucleon. The fundamental reason is exactly the same as that for the paucity of form factors at large  $Q^2$ : one must have dedicated facility with high luminosity to measure the small cross sections. Once again, JLab with the 12 GeV Upgrade will allow, for the first time, a systematic study of high- $x$  parton distributions.

These traditional experimental observables do not, however, tell us the position and momentum (or phase space) correlations of the quarks and gluons that contain essential information about the partons in the nucleon. We know that in classical physics the state of a particle is specified by knowing both its position  $\vec{r}$  and momentum  $\vec{p}$ . In a classical gas of identical particles, the single-particle properties are described by a phase-space distribution  $f(\vec{r}, \vec{p})$  representing the density of particles at the phase-space coordinates  $(\vec{r}, \vec{p})$ . In quantum mechanics, the notion of a phase-space distribution seems to contradict fundamental principles: the momentum and position of a particle cannot be determined simultaneously. Nevertheless, physicists have devised various quantum phase-space distributions that reduce to  $f(\vec{r}, \vec{p})$  in the classical limit. These distributions have proven extremely useful in a broad variety of studies, including heavy-ion collisions, quantum molecular dynamics, signal analysis, quantum information, non-linear dynamics, optics, image processing, and many more.

One of the most frequently used phase-space distributions is the Wigner distribution,  $W(\vec{r}, \vec{p})$ , introduced by Wigner in 1932. Integrating this distribution over the particle coordinate  $\vec{r}$  yields the momentum density  $|\psi(\vec{p})|^2$ ; integrating it over the particle momenta  $\vec{p}$  yields the coordinate space density  $|\psi(\vec{r})|^2$ . For arbitrary  $\vec{p}$  and  $\vec{r}$  the Wigner distribution is a quantum distribution in phase-space. It is not positive definite because of quantum interference, and therefore does not have, strictly speaking, a probabilistic interpretation. However, it can be used just like a classical phase-space distribution to calculate the average of any quantum mechanical observable. In the classical limit, it reduces to the positive-definite probabilistic distribution.

Wigner-type phase-space distributions can be devised naturally to describe the coordinate and momentum space correlations of quarks and gluons in the nucleon [Ji03]. By integrating over some unobserved variables in these distributions, we can obtain the quark charge and current distributions,  $\rho(\vec{r}, x)$  and  $j(\vec{r}, x)$ , in the reduced phase-space  $(\vec{r}, x)$ , where  $\vec{r}$  is the position vector and  $x$  is the Feynman momentum fraction (discussed above in the context of the parton distributions). These phase space distributions can also be used to learn about other nucleon properties. An

example is the orbital motion of quarks in the proton: the total quark contribution to the spin of the proton is connected to the phase space distribution via a sum rule.

Fourier transforms of the phase-space distributions yield observables, referred to as the generalized parton distributions (GPDs) [Mu94, Ji97, Ra96], that are hybrids of the elastic form factors and the parton distributions. The GPDs are a new class of nucleon matrix elements that generalize the diagonal matrix elements in the Feynman parton distributions to include the off-diagonal terms. They depend on the Feynman  $x$  (as do the parton distributions), the  $t$ -channel momentum transfer (as do the form factors), and a new parameter, the skewness parameter,  $\xi$ , that characterizes the momentum fraction difference between the correlated partons. GPDs have been studied extensively theoretically over the last few years, and experiments demonstrating the feasibility of measuring them have been carried out, but research in this fascinating new area has really only just begun.

The GPDs can be measured via a new class of hard exclusive processes that can be understood rigorously using perturbative QCD tools. The simplest example is deeply-virtual Compton scattering (DVCS), in which a lepton scatters inelastically from a nucleon producing a high-energy real photon plus the recoiling nucleon. DVCS can be viewed as a Compton scattering on a single quark in the nucleon. The cross section can be expressed as a convolution of perturbatively-calculable coefficient functions (characterizing the hard interaction between the lepton and the quark) and GPDs. Another example of a hard exclusive processes is deeply-virtual meson production, which provides powerful way to access different spin and flavor combinations of the GPDs. Recent experimental data from the CLAS Collaboration at JLab and from the HERMES experiment at DESY demonstrate the feasibility of DVCS experiments and the dominance of the single-quark scattering mechanism in this reaction at moderately-large  $Q^2$ . However, detailed measurements of the GPDs will require a comprehensive, systematic experimental program at a facility with high luminosity and energy. The JLab with 12 GeV Upgrade will offer a first such opportunity, and will be unmatched by any other facility in the world.

If GPDs are determined directly from experimental data and constrained by measured elastic form factors and parton distributions, the quantum phase-space distributions of the quark charge  $\rho(\vec{r}, x)$  and current  $\vec{j}(\vec{r}, x)$  can be obtained. These Wigner-type distributions yield full 3D-images of the quarks in the proton for each fixed Feynman momentum fraction,  $x$ , that correspond to an image of the nucleon as seen through a momentum (or Feynman  $x$ -) filter. Since each picture represents a slice in the phase space, measurements of the GPDs correspond to phase-space tomography. The skewness parameter,  $\xi$ , has a natural interpretation: it is a measure of the proton deformation along the direction selected by the virtual photon probe. When the set of quark images for all values of  $x$  is assembled we recover a round nucleon. On the other hand, if we integrate over the longitudinal coordinate along the direction of the virtual photon, we obtain [Bu02] a 2-D projection of the 3D-picture in the transverse space, which is related to GPDs at  $\xi = 0$ . One virtue of these 2D pictures is that they are simply particle densities that avoid the conceptual constraints that arise from the quantum mechanical uncertainty principle and from relativistic recoil.

The JLab 12 GeV Upgrade will support a great leap forward in our knowledge of hadron structure through major programs in at least three areas: nucleon form factors at large  $Q^2$ , high- $x$  (valence) quark structure, and deep exclusive scattering. It will also support important initiatives in a number of other areas of hadron structure. These research programs are described in detail below. The data they will provide can be understood and interpreted coherently using the theoretical framework of the GPDs and quantum phase-space distributions to provide truly remarkable and revealing images of the proton’s structure that will enable us to visualize these fundamental “building blocks” of nuclear matter.

### 2.B.1 Form Factors – Constraints on the Generalized Parton Distributions

One of the primary goals of nuclear physics is to understand the structure of hadrons in terms of quarks and gluons, the fundamental fields of quantum chromodynamics (QCD). This task is complicated, since confinement, one of the most important features of QCD, is a non-perturbative phenomenon. One strategy has been to incorporate another feature of QCD, asymptotic freedom. This approach was very successful in applications to hard inclusive processes, and made possible the extraction of much information about hadronic structure in terms of quark and gluon longitudinal momentum distributions.

It was anticipated that a similar approach would be applicable to form factors and other exclusive processes at momentum transfers significantly larger than  $\Lambda_{QCD}$ , so that it would be possible to use perturbative QCD (pQCD) together with QCD sum rules to map valence distribution amplitudes of the hadrons. However, several recent experimental results from Jefferson Lab (JLab) involving exclusive form factors [Fr98a, Vo01, Jo00, Ga02, Na02] have unequivocally demonstrated that pQCD is not applicable at few  $(\text{GeV}/c)^2$  momentum transfers.

A recent important breakthrough has been the introduction of the formalism of generalized parton distributions (GPD), which offers a unified framework for accessing the complex structure of hadrons through a variety of exclusive reactions, and promises to yield the first three dimensional description of hadrons. Thus, one of the unique opportunities of JLab at 12 GeV will be to study the structure of hadrons by means of a comprehensive program of exclusive reactions. As described in the following, the measurement of exclusive form factors at high momentum transfer will be an essential part of this program, especially in constraining the GPD based description of the nucleon’s short distance structure.

Exclusive form factors are the fundamental measurable quantities in electron scattering, and have direct connection to the charge and current structure of hadronic states. Form factor measurements have provided a wealth of information about the structure of nuclei, and, when extended to the highest accessible  $Q^2$ , have revealed the short distance features of the nucleon’s structure.

Similarly, the connection of form factors to the structure of hadrons in terms of their quark-

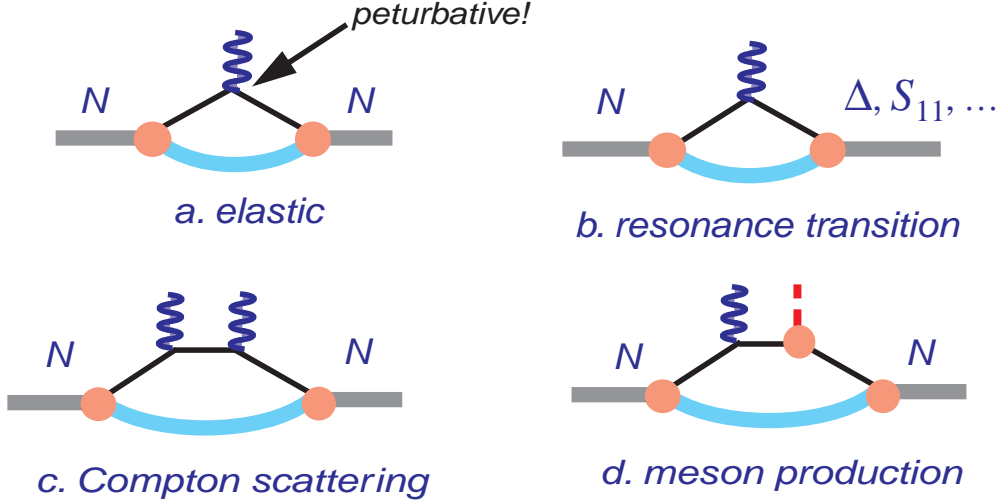


Figure 41: Schematic diagrams of the form factor reactions discussed in the text that can be expressed in terms of the GPD formalism: a) elastic, b) transition, c) Compton scattering, and d) high- $t$  meson production.

gluon distributions has been the subject of a great deal of theoretical study. The introduction during recent years of the concept of generalized parton distributions within the context of soft-hard factorization is an important breakthrough in connecting exclusive reactions at high momentum transfer with the full complexity of non-perturbative hadronic structure. This is illustrated in Fig. 41, where the non-perturbative structure is represented by the lower part of the “handbag”, which can be parametrized in terms of four functions, the GPDs.<sup>1</sup> The GPDs are functions of three variables: the longitudinal momentum fraction,  $x$ , of the struck quark; the momentum transfer to the nucleon,  $-t$ ; and a *skewedness* parameter  $\xi$ . There are GPDs corresponding to different current structures,  $H$  and  $E$  for the quark spin-averaged, and  $\tilde{H}$  and  $\tilde{E}$  for the quark-spin dependent combinations.

The hadronic form factors provide moments of the GPDs, offering important constraints on our description of the nucleon’s structure. Form factors are complementary to deeply virtual exclusive reactions. In contrast to deeply virtual exclusive reactions (DVE), form factors uniquely access the GPD moments independently of  $\xi$ . This offers an additional simplicity compared to the integrals involved in deeply virtual processes. The Fourier transforms of GPDs over  $t$ , constrained by form factors, are directly interpretable as the transverse impact parameter dependence  $b_\perp$  of the hadron’s quark charge and magnetic moment distributions [Bu00]. Thus GPDs provide 3-dimensional pictures of hadronic structure not obtainable by DIS, as illustrated further below.

Another important consideration which makes form factor measurements a necessary complement to DVE is that while deep exclusive reactions access GPDs only at relatively low  $-t$ , the GPD formalism for form factors is applicable at high  $-t$  ( $=Q^2$  for form factors), which is specifi-

<sup>1</sup>The formalism is illustrated for the case of the nucleon, but can also be applied to the pion, see section 2.B.1.

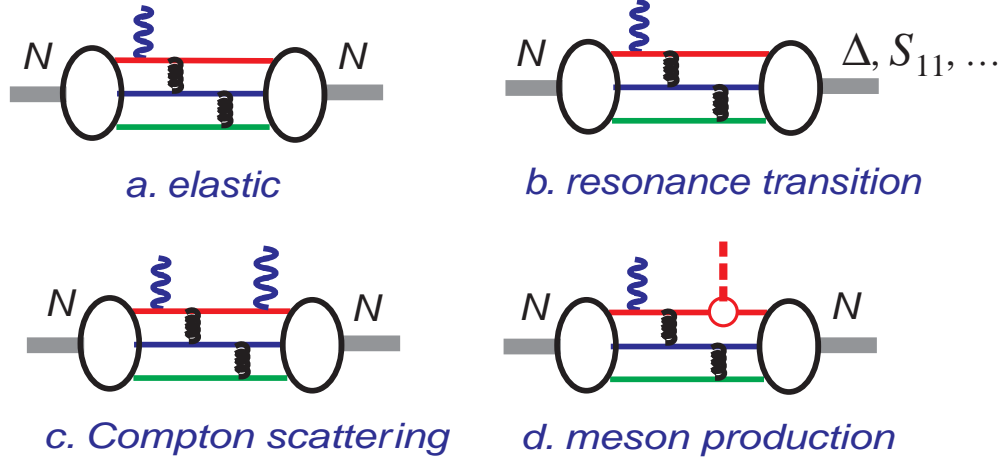


Figure 42: Form factor reactions discussed in the text that can be expressed in terms of the valence pQCD formalism: a) elastic, b) transition, c) Compton scattering, and d) high  $t$  meson production.

cally necessary to obtain the small  $b_{\perp}$  structure of the hadron. Passing to the limits of very high  $Q^2$  or  $-t$  the form factors are expected to uniquely access the very simplest short distance valence quark structure of the hadron through the mechanism of pQCD.

There exists an immense theoretical literature focused on connection of this short distance meson and nucleon form factors in terms of the quark-gluon structure of the hadron, through the formalism of *valence-pQCD* (pQCD). Analogously to Fig. 41, schematic representations of form factor reactions in the pQCD framework are shown in Fig. 42. Some seminal papers have literally thousands of citations<sup>2</sup>. This leads to the famous constituent  $Q^2$  or  $s$  scaling laws, and important relationships between helicity leading and non-leading amplitudes. The great theoretical productivity was matched by considerable experimental effort. Despite the effort, the region of  $-t$  or  $Q^2$  where the transition from the soft handbag description to hard pQCD description occurs has not yet been experimentally determined.

In summary, the hadron form factor program at JLab at 12 GeV aims to access the three dimensional structure of the hadron by studying a variety of *form factor like* reactions. The GPDs will serve as the common framework for these studies. At the highest momentum transfers we will try to observe the transition to the simplest small size configurations connected through the valence pQCD formalism. Indeed, some of these measurements have already been started at more moderate momentum transfers and already have a profound affect on how we view the structure of hadrons. In the following sections we briefly describe our experimental program, illustrating where the measurements are today, and pointing out the dramatic increase in momentum transfer made possible with the 12 GeV upgrade.

<sup>2</sup>For example, three papers by Shifman, Zakharov, and Vainshtein [Sh79] on QCD sum rules have been cited almost 5,000 times, two articles by Lepage and Brodsky [Br79a, Br80] on the pQCD formalism, more than 2,000 times, and an article by Chernyak and Zhitnitsky [Ch77] applying the former two to obtain pion and proton elastic form factors more than 600 times, and still counting!



**Form Factors at Large Momentum Transfer** Our goal is to observe the evolution with momentum transfer of the non-perturbative hadronic structure from its fully developed complexity at low momentum transfer, through to its simplest small configurations at the highest possible momentum transfers. In the following we describe the reactions that we intend to study, and their kinematic ranges in  $-t$  that we be able to cover.

We will begin by discussing the charged pion form factor  $F_{\pi^+}$ , since this is the benchmark reaction due to its relatively simple structure. We then move to the nucleon case and discuss the various form factors that are accessible, and their specific connection to the GPDs. For example, the elastic nucleon form factors  $F_1$  and  $F_2$  are the zero'th moments  $\langle x \rangle^0$  of  $H(x, t)$  and  $E(x, t)$ . For the protons and neutrons these are connected and constrained by isospin invariance. The  $N \rightarrow \Delta$  form factor  $G_M^*$  is connected to the isovector part of  $E(x, t)$ , and the  $N \rightarrow S_{11}$  to the negative parity member of the nucleon's parity doublet. The real Compton scattering form factors  $R_V, R_A$  and  $R_T$  provide the  $\langle x \rangle^{-1}$  moments of  $H(x, t)$ ,  $\tilde{H}(x, t)$ , and  $E(x, t)$ , as well as important polarization observables  $K_{LL}$ ,  $K_{LT}$  and  $P_N$  which constrain the GPDs. High  $-t$  exclusive meson production involving different mesons access moments of new nucleon form factors which are sensitive to different contributions depending on the meson produced. For example,  $\pi^0$  and  $\eta$  production involves  $\tilde{H}(x, t)$ . Finally, we will discuss the evolution to the highest momentum transfer and the approach of the aforementioned form factors to pQCD. This involves the questions of pQCD constituent scaling and helicity conservation, which are contained in these form factors.

**Form Factors and Generalized Parton Distributions** Much has been said and written about GPDs during the past several years, and it is not our aim to go into details about the formalism. Rather, after a brief review of the most salient features, and their physical interpretation in terms of the three-dimensional structure of hadrons, we intend to show how a program of form factor measurements at high  $Q^2$  or  $-t$  uniquely provides a connection with the various substructures of GPD models which are complementary to deep virtual exclusive reactions. In the GPD picture, the incident real or virtual photon interacts with one of the quarks within the hadron, and is followed by either of two processes: the quark is re-absorbed into the hadron leaving it either intact or in a higher resonant state. The GPD formalism, for the first time, provides us with a unified description of the complex hadronic structure accessed by different exclusive reactions. Because of the correlations of the initial and final parton wave functions in their definition, the GPDs are sensitive to the actual hadron wave functions in a way that traditional inclusive process of deep inelastic scattering (DIS) is not. In particular, while structure functions entering inclusive scattering give information about distribution functions of longitudinal momentum fractions  $x$ , GPDs entering exclusive reactions contain information about the longitudinal and transverse momentum distributions,  $x$  and  $k_\perp$ , and through their correlations give a three dimensional snapshot of the hadronic structure.

The relation between wave functions, form factors and GPDs can be demonstrated through the well known Drell-Yan expression



$$F(t) = \int \Psi^*(x, k_\perp + \bar{x}\Delta_\perp) \Psi(x, k_\perp) \frac{d^2 k_\perp}{16\pi^3} \quad (9)$$

where  $\Delta_\perp^2 = -t$ . As a simple illustration we choose an effective wave function [Ra98a] with a Gaussian  $k_\perp$  dependence

$$\Psi(x, k_\perp) = \Phi(x) e^{-k_\perp^2/2x\bar{x}\lambda^2}, \quad (10)$$

where  $\bar{x} \equiv 1 - x$  and  $\lambda$  is a transverse size parameter. This expression for the form factor yields the following GPD

$$H(x, 0; \Delta_\perp) = \frac{x\bar{x}\lambda^2}{16\pi^2} \Phi^2(x) e^{-\Delta_\perp^2 \bar{x}/4x\lambda^2} \equiv f(x) e^{-\Delta_\perp^2 \bar{x}/4x\lambda^2}. \quad (11)$$

Note that we took  $\xi = 0$  here, although generally it need not be so. GPDs at  $\xi = 0$  are sometimes called “nonforward parton densities” [Ra98a]. The correlation of the longitudinal and transverse momentum distributions is manifestly seen in Eq. 10. As emphasized in Ref. [Bu00], the double Fourier transform with respect to the momentum transfer  $\Delta_\perp$

$$H(x, b_\perp) = \int_0^\infty H(x, 0, \Delta_\perp^2) e^{i\Delta_\perp \cdot b_\perp} d\Delta_\perp. \quad (12)$$

has the meaning of the parton density distribution in the impact parameter space. The result is shown in Fig. 43. Note, the limits of the integral in Eq. 12 require the knowledge of the  $-t$  dependence to as high a value of  $-t$  as possible.

Factorization of the reaction into a hard kernel and soft GPD is a necessary condition for the application of the formalism. For deep virtual reactions this requires *off-forward* kinematics, with simultaneously high  $Q^2$  and low  $-t$ . A measurement at a particular  $t$ ,  $x_B$  and  $Q^2$  involves an integral over the relevant variables  $x$  and knowledge of the skewedness parameter  $\xi$ . The great power of this approach is discussed in the physics section on deep virtual reactions. For the present purposes we point out that in the off-forward kinematics the low  $-t$  constrains access to rather low  $k_\perp$ , or equivalently, large transverse impact parameter  $b_\perp$ . Conversely, form factor experiments for which the GPD formalism is applied involve high  $-t$ , and therefore access large  $k_\perp$ , or small transverse impact parameter  $b_\perp$ . The price is that a specific measurement always involves an integral (moment) over the full range of  $x$ . However, the integrals have a simplicity in that they are independent of skewedness parameter, so that they constrain GPDs at any  $\xi$ . Since different form factors access different moments of GPDs, and different structural components of the GPDs, a complete set of measurements will provide the greatest constraints on wave function models.

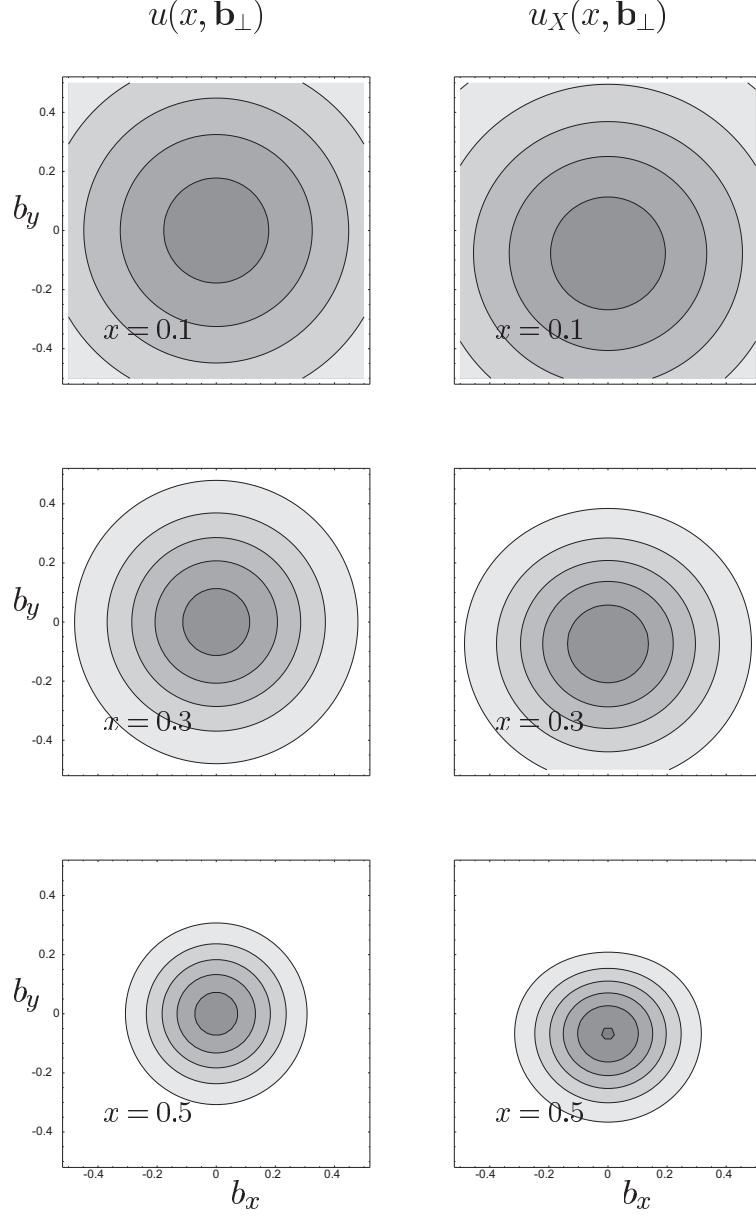


Figure 43: The GPD  $H(x, b_\perp) = u(x, b_\perp)$  obtained by ref. [Bu00] from the GPD  $H(x, 0; \Delta_\perp)$  in eq. 11. Shown are contour plots of transverse density for various slices of longitudinal momentum fraction  $x$ .  $u_X(x, b_\perp)$  is the probability distribution for the proton polarized in the  $x$  direction.

One of our abiding interests is to obtain a three dimensional mapping of the nucleon structure by modeling the GPDs as a function of  $x$  and  $t$ , constrained by various form factor measurements as a function of  $t$ , and structure functions measurements as a function of  $x$ . For illustrative purposes, in the examples which follow, we assume that the handbag can be expressed as an effectively two-body process, as in Eq. 11.

**The Charged Pion Form Factor** The form factor of the charged pion  $F_{\pi^+}$  is of key interest in the study of the quark-gluon structure of hadrons. One of the reasons is that the valence structure of the pion, being  $\langle q\bar{q} \rangle$ , is relatively simple. Thanks to this relatively simple structure, direct (model) calculations of the pion wave function are possible, from which a direct connection to GPD and (p)QCD formalisms can be made. For the same reason it is expected that the value of the four-momentum transfer squared  $Q^2$ , down to which a pQCD approach to the pion structure can be applied, is lower than for the nucleon. Finally, the asymptotic normalization of the pion wave function, in contrast to that of the nucleon, is known from the pion decay. Therefore, all models used to calculate the structure of hadrons use the pion form factor as a benchmark. The interest is especially in the transition from the soft regime, governed by all kinds of quark-gluon correlations, at low  $Q^2$ , to the perturbative regime at high  $Q^2$ .

There have been a large number of calculations of  $F_{\pi^+}$ . These include perturbative ones, including next-to-leading order and transverse corrections, QCD sum-rule calculations, and calculations in a Bethe-Salpeter approach, see ref. [St00, Ra91, Ma00] for some representative examples. The recent calculations suggest that pQCD contributions start to dominate the pion form factor at  $Q^2 \geq 5 \text{ (GeV/c)}^2$ .

The pion form factor is related to the pion GPD as [Ra98a, Mu02]

$$F_{\pi}(t) = \int_{-1}^1 \sum_q H_{\pi}^q(x, t) dx .$$

One can model the nonforward parton density  $H_{\pi}^q(x, t)$  by an expression similar to Eq.(11) with an exponential  $t$ -dependent factor or use an ansatz with a power-law behavior [Mu02]. The result of a GPD calculation [Mu02] using a simple power-law dependence of  $H_{\pi}^q(x, t)$  is shown together with the existing experimental data and the results of various direct calculations of  $F_{\pi^+}$  in Fig. 44. We note that for elastic scattering  $-t = Q^2$ , and they are denoted interchangeably. To date, the most accurate measurement of  $F_{\pi^+}$  has been carried out in Hall C using the  $^1\text{H}(e, e'\pi^+)\text{n}$  reaction [Vo01]. These data extend to a value of  $Q^2$  of  $1.6 \text{ (GeV/c)}^2$ . Recently those measurements were extended to  $Q^2 = 2.5 \text{ (GeV/c)}^2$  [E01004], the largest value that can be reached with a 6 GeV beam. The measurement of this form factor to  $Q^2 = 6 \text{ (GeV/c)}^2$  and possibly higher, depending on the magnitude of  $F_{\pi^+}$ , is one of the high priority components of the Hall C 12 GeV upgrade program. The goal is to observe the transition to the pQCD dominated regime, thereby putting

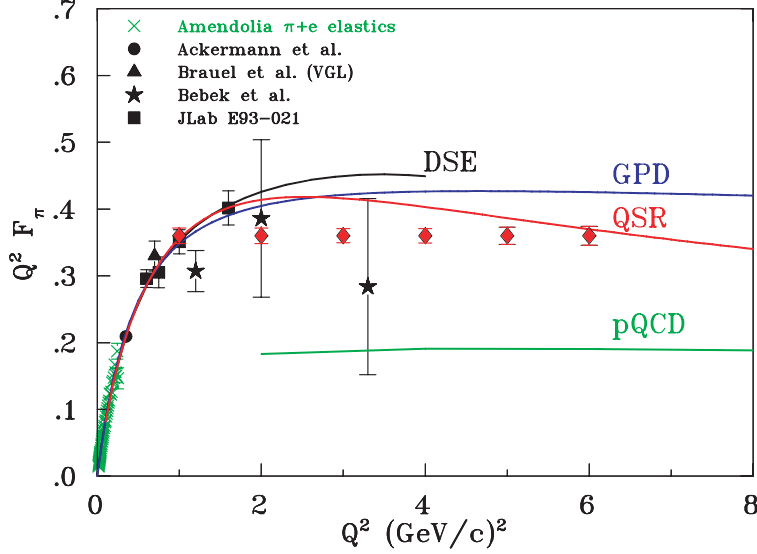


Figure 44: The  $\pi^+$  form factor. Recent Hall C data are denoted by black squares. The red diamonds denote the projected data points with their anticipated error bars in Hall C at 12 GeV. Other available data are shown as well. The curves are the results of various theoretical calculations: the GPD based calculation [Mu02] using a power law dependent GPD is shown by a blue; a recent pQCD calculation (including transverse corrections etc.) [St00] in green; the QCD sum-rule prediction of ref. [Ra91] in red; and the Dyson-Schwinger result of ref. [Ma00] in black.

severe constraints on valence non-perturbative models and their higher twist corrections, as well as other model approaches.  $F_{\pi^+}$  is extracted from the data by effectively extrapolating the longitudinal cross section to the (non-physical) pion pole. The larger values of the invariant mass  $W$  that can be accessed with an 11 GeV beam will allow one to take data closer to this pole, and to check the pole dominance. The combination of the HMS and proposed SMS spectrometers is ideally suited for such measurements.

**Baryon Form Factors and GPDs** The description of baryons in terms of GPDs is more complex. In case of the nucleon we have four functions  $H$ ,  $E$ ,  $\tilde{H}$  and  $\tilde{E}$ . Examples of form factor type reactions involving baryons which will be measured are the proton electric to magnetic form factor ratio  $G_{Ep}/G_{Mp}$ , the  $N \rightarrow \Delta$  resonance transition form factors, the  $N \rightarrow S_{11}$  transition amplitude  $A_{1/2}$ , and high  $-t$  Compton scattering from the nucleon. In each case, there is a direct relationship between the form factor and a GPD.

*Elastic Scattering from the Proton* For nucleon elastic scattering, the Dirac (helicity non-flip) and Pauli (helicity flip) form factors are the zero'th moments of the GPDs  $H$  and  $E$  respectively.

$$F_1(t) = \sum_q F_1^q(t) = \int_{-1}^1 \sum_q H^q(x, \xi; t) dx \quad F_2(t) = \sum_q F_2^q(t) = \int_{-1}^1 \sum_q E^q(x, \xi; t) dx, \quad (13)$$

where  $q$  signifies both quark and anti-quark flavors. We take the reference frame in which the momentum transfer is transverse so that  $\xi=0$ , and denote  $H^q(x, t) \equiv H^q(x, 0; t)$ ,  $E^q(x, t) \equiv E^q(x, 0; t)$ , etc. There exist also other very important and useful sum rule constraints on the GPDs in eqs. 13. GPDs. They are that in the  $-t = 0$  limit,  $H^q(x, 0) = f_q(x)$ , and  $E^q(x, 0) = g_q(x)$ , that is, the GPDs coincide with the unpolarized and polarized structure functions which are measured in deep inelastic scattering. Also, for the proton  $F_{1,u}^p(0) = 4/3$  and  $F_{1,d}^p(0) = -1/3$ , the charges carried by the proton's  $u$  and  $d$  valence quarks, such that  $F_{1,u}^p(0) + F_{1,d}^p(0) = F_1^p(0) = 1$ . Also, for  $F_2^p$  we have  $F_{2,u}^p(0) = \kappa_{p,u}$ , and  $F_{2,d}^p(0) = \kappa_{p,d}$ , the anomalous magnetic moments carried by the quarks such that  $\kappa_{p,u} + \kappa_{p,d} = k_p \sim 1.79$ . Similar constraints hold for neutrons as well.

Experimentally, it has been more convenient to present the Sachs form factors, which are linear combinations of the Fermi and Pauli form factors, defined by the relationships

$$G_M(Q^2) = F_1(Q^2) + \kappa F_2(Q^2) \quad G_E(Q^2) = F_1(Q^2) - \tau \kappa F_2(Q^2) . \quad (14)$$

Here,  $\tau = Q^2/4M^2$ ,  $M$  is the mass of the nucleon (either proton or neutron) and  $\kappa$  is the nucleon's anomalous magnetic moment. The measurement of either set is equivalent to the measurement of the other.

Of the four nucleon form factors, the magnetic form factor of the proton  $G_{Mp}(Q^2)$  has been the most accessible in the multi GeV range, and had been extracted from  $ep$  elastic cross section measurements with rather good accuracy out to high  $Q^2$ . This is shown in Fig. 45.

The proton electric form factor  $G_E^p(Q^2)$  is difficult to obtain via a Rosenbluth separation, which is especially subject to systematic errors, and it had previously been obtained with rather poor systematic and statistical accuracy out to about 8 (GeV/c)<sup>2</sup>. Recently, new measurements were performed in Hall A using a recoil polarization technique, which is not as subject to the same systematic errors as the Rosenbluth technique. This result, and its possible interpretations have been the most highly cited and most highly publicized JLab experiment to date, even reaching the popular press. The ratio  $G_E^p/G_M^p$ , shown in Fig. 46, actually falls quite dramatically as a function of  $Q^2$ , which contradicts previously held assumptions about the proportionality of  $G_E^p$  and  $G_M^p$  with  $Q^2$ , and suggests the intuitively baffling idea that the electric charge distribution is spatially softer (larger size) than the magnetic moment distribution. One is naturally led to the question of whether  $G_E^p/G_M^p$  will continue to fall with increasing  $Q^2$  (even becoming negative!) It is projected that with the 12 GeV upgrade,  $G_E^p/G_M^p$  could be measured up to  $Q^2 = 14$  (GeV/c)<sup>2</sup>, in either Halls C or Hall A. Projections are shown in Fig 46. This result has also forced us to go back and re-evaluate existing  $G_M^p$  data, yielding small modifications in the accepted values.

An initial application of GPDs to nucleon form factors [Ra98a] was for the proton  $F_{1p}$  based on nonforward parton density of Eq. 10, with the constraint  $H^q(x, 0) = f^q(x)$ . With a single parameter  $\lambda$  having the reasonable value around 300 MeV for the average transverse momentum

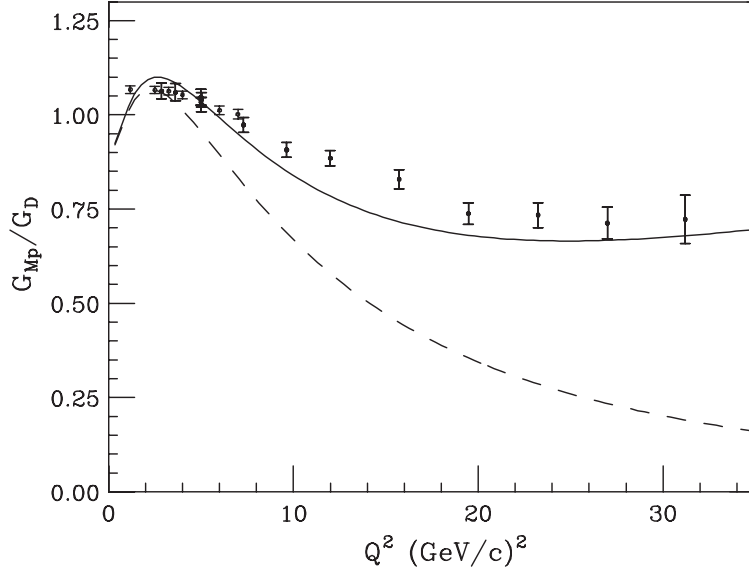


Figure 45: The proton magnetic form factor. The data [Si93] , from SLAC, has been adjusted to account for the recent JLab measurements of  $G_E^p/G_M^p$ . The dashed curve is obtained [St02] by applying the phenomenological soft wave function of Ref. [Ra98a] of Eq. 10, and the solid curve results from the addition of a power law in  $k_\perp$  component to account for the quark high momentum tail.

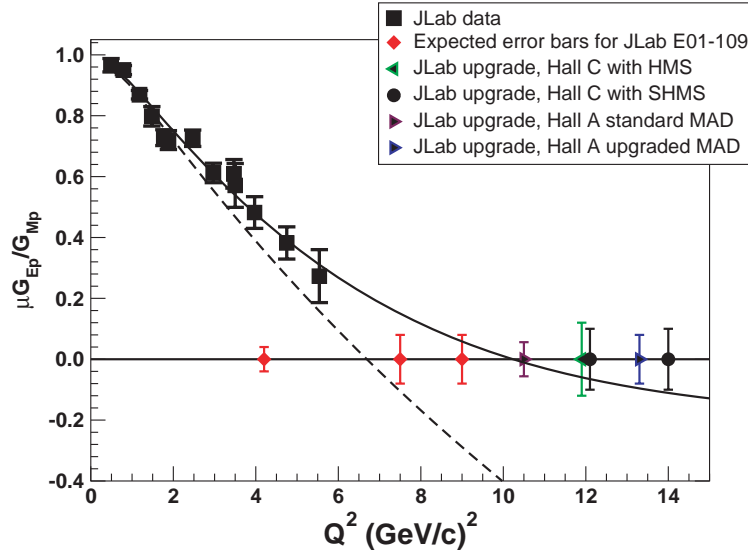


Figure 46: The status of the JLab measurement of  $G_E^p/G_M^p$  and the range of the projected measurements with either Hall A or Hall C equipment. The dashed and solid curves are the result of the calculation using a soft GPD [Af99, St02] as in eq. 11, and one with additional high momentum components in  $k_\perp$  modeled by a power law dependence [St02], respectively.

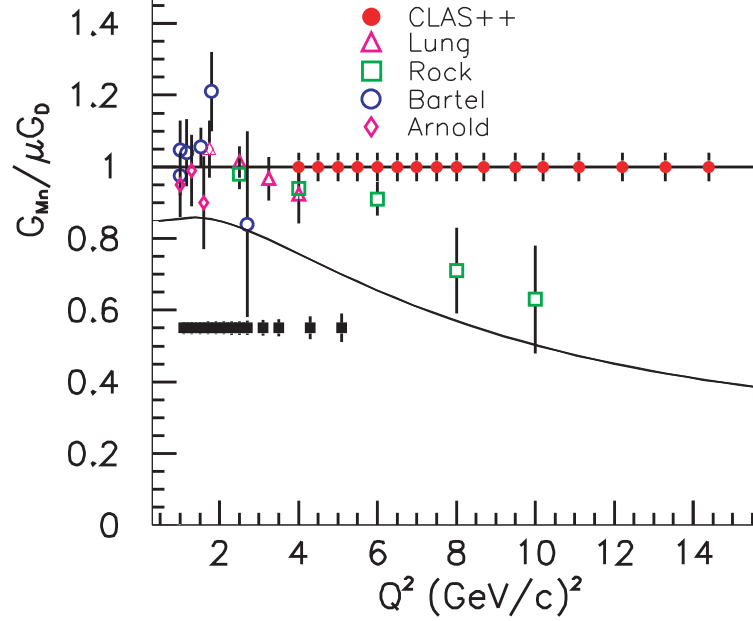


Figure 47: The current status of the data [Lu93, Ro82, Ba73, Ar88] for  $G_M^n$ , and the projections, denoted by red circles, for the Hall B program with the 12 GeV upgrade. The open points are existing data and the solid squares are the error projections for data already taken in Hall B. Also shown are the predictions based on the GPD calculations [St03] for the proton form factors as in eqs. Figs. 47 and 46 invoking isospin invariance. The meaning of the solid curve is as in Fig. 45.

of quarks, a rather good fit was obtained for  $F_{1p}$  up to  $Q^2 \sim 8 \text{ (GeV/c)}^2$ . With the addition to  $\Psi(x, k_\perp)$  of a “hard” component in  $k_\perp$  in the form of a power law [St02] a good fit to  $F_{1p}$  was obtained over the entire range of  $Q^2$  up to about  $32 \text{ (GeV/c)}^2$ . A similar application for  $F_{2p}$  was made in Ref. [Af99] with the interesting result that, taken together with other data from DIS, it was found that about 50% of the proton spin is carried by the quarks, and half of that (50%) is due to orbital angular momentum. The result of a consistent fit of parameters for  $F_{1p}$  and  $F_{2p}$ , including high momentum tails [St02] yields the curves for  $G_M^p$ , and  $G_E^p/G_M^p$  as shown in Figs. 45 and 46.

*Elastic Scattering from Neutrons.* The measurement of form factors of the neutron is vitally important because to first order the neutron’s quark wave functions are related to those of the proton by simple isospin invariance. Thus, a consistent modeling of all four elastic form factors,  $G_E^p$ ,  $G_M^p$ ,  $G_{En}$  and  $G_{Mn}$ , is a necessary constraint for any quark based nucleon wave function model. Unfortunately, because the stable neutron only exists within a more complex nucleus, the neutron form factors are much more difficult to measure than those for the proton, and the existing data, even for  $G_{Mn}$  are not in very good shape, plagued by the systematic uncertainty introduced by various assumptions about the relative  $Q^2$  dependences of  $G_{En}$  and  $G_{Mn}$ . Thus, there is a major experimental program planning to measure  $G_{Mn}$  in Hall B. Fig. 47 shows the current experimental status of  $G_{Mn}$ , and the projections of the Hall B program for the 12 GeV upgrade.

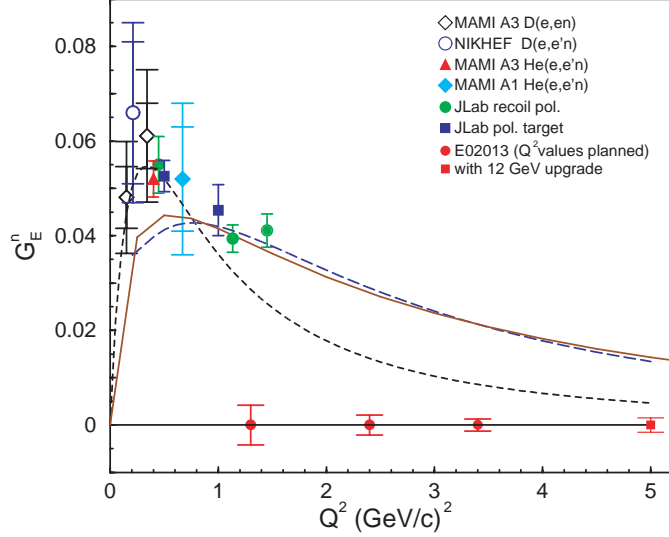


Figure 48: The neutron electric form factor  $G_E^n$ . Current data is plotted as open black circle [Pa99], open black diamond [Os99], filled red triangle [Zh01] and filled cyan diamond [Ro99]. The filled green circles [Ma93] are the Hall C JLab results employing recoil polarization, and the filled blue squares [Da93] are the Hall C results obtained using a polarized target. The filled red circles on the baseline are the projected  $Q^2$  and errors for the approved experiment in Hall A [Ca02]. The filled red square at  $Q^2 = 5$  (GeV/c) $^2$  is the projection for Hall A with the 12 GeV upgrade. The curve denoted by black dashes is the Galster [Ga71] parameterization. The red solid curve is the result of a calculation due to Miller [Mi02]. The blue dashed curve is a result based on the GPD fit by Stoler [St03] to the proton form factors invoking isospin symmetry as in the previous figures.

The neutron electric form factor  $G_{En}$  at increasing  $Q^2$  cannot practically be extracted from unpolarized cross sections, and all measurements are obtained from polarization measurements. Two JLab measurements in Hall C with different techniques have been able to extract high quality results up to  $Q^2 = 1.5$  (GeV/c) $^2$ . The results are shown in Fig. 48. There are preparations to extend  $G_{En}$  measurements in Hall A to  $Q^2 \sim 3.5$  (GeV/c) $^2$ . Future plans for Hall A with the 12 GeV upgrade call for eventual measurements of  $G_{En}$  up to  $Q^2 \sim 5$  (GeV/c) $^2$ . Although it may never be possible to obtain  $G_{En}$  at momentum transfers approaching those of the other three elastic form factors, having  $G_{En}$  in the proposed range would be extremely valuable as a constraint on the GPDs, and there is no guarantee it will remain very small in comparison to the other form factors at higher  $Q^2$ . The situation is summarized in Fig. 48.

In Figs. 47, and 48 are shown the predictions for  $G_{Mn}$  and  $G_{En}$  obtained with the wave functions used to calculate the proton  $G_M^p$  and  $G_E^p$  curves in Figs. 45 and 46, employing isospin symmetry. The predictions of these wavefunctions underestimate the  $G_M^p$  data by about 20%, but the data may be somewhat high due to systematics in the way  $G_M^p$  was extracted from the cross section data. One must not over-interpret these curves because they are phenomenological at best, and not based upon rigorous theoretical principles. However, they do illustrate the power of the GPD technique and the need for quality high- $Q^2$  data.



### High $-t$ Compton Scattering and Meson Electroproduction.

**High  $-t$  Compton Scattering.** For Compton scattering the appropriate *form factor-like* quantities are the  $\langle x \rangle^{-1}$  moments of the GPDs

$$R_V(t) = \int_{-1}^1 \sum_q \frac{1}{x} H^q(x, t) dx, \quad (15)$$

$$R_T(t) = \int_{-1}^1 \sum_q \frac{1}{x} E^q(x, t) dx, \quad (16)$$

$$R_A(t) = \int_{-1}^1 \sum_q \frac{1}{x} \tilde{H}^q(x, t) dx. \quad (17)$$

The unpolarized cross section  $d\sigma/dt$  at a particular  $s$  contains all three form factors, but is sensitive primarily to a combination of  $R_V(t)$  and  $R_A(t)$ . It turns out that the longitudinal and transverse polarization transfer observables  $K_{LL}$  and  $K_{LT}$  are sensitive to the ratios  $R_A(t)/R_V(t)$  and  $R_T(t)/R_V(t)$ , so that a measurement of  $d\sigma/dt$ ,  $K_{LL}$  and  $K_{LT}$  is sufficient to determine all three form factors. A polarization transfer measurement [Na02] for the reaction  $p(\gamma, \gamma p)$  at  $E_\gamma = 3.2$  GeV and  $\theta_{p,cm} = 120^\circ$  has been performed, and the quantity  $K_{LL}$  was extracted. The result of this experiment is shown in Fig. 49. The data was compared to a number of different theoretical approaches. An important result is that the data is in excellent agreement with a GPD based theoretical calculation [Di99] using wave functions similar to that in Eq. 10. This again appears to show the soundness of the GPD approach. Many unpolarized cross section points were also obtained, and a new proposal aims to complete the Hall A experiment by mapping  $K_{LL}$  and  $K_{LT}$  over a range of  $\theta_{p,cm}$  shown in Fig. 50. This will enable one to obtain  $R_A/R_V$  and  $R_T/R_V$  over a range of  $1 \leq -t \leq 5$  (GeV/c)<sup>2</sup>. Plans now exist with the 12 GeV to make a complete set of Compton scattering measurements up to  $s = 20$  (GeV/c)<sup>2</sup> and  $-t = 20$  (GeV/c)<sup>2</sup> making full use of the capabilities of the new detection facilities in Halls A and C. In addition to cross sections, the recoil polarization observables will be obtained over a large range of the available kinematics. The kinematic coverage is illustrated graphically in Fig. 49.

**High  $-t$  Low  $Q^2$  Meson Electroproduction.** The cross section for exclusive single meson production can be expressed in terms of form factors analogous to those accessed in Compton scattering. Assuming factorization, the longitudinal cross section corresponding to Fig. 41d. can be written as [Di99, Hu00]

$$\frac{d\sigma_{-L}^{\pi^0}}{dt} \sim \left[ R_A^{\pi^0}(t) \int_0^1 d\tau \phi_M(\tau) f_0^q(\tau, s, Q^2, t) \right]^2 \quad (18)$$

$$R_A^{\pi^0}(t) = \int_{-1}^1 \sum_q \frac{1}{x} \tilde{H}^q(x, t) dx \quad (19)$$

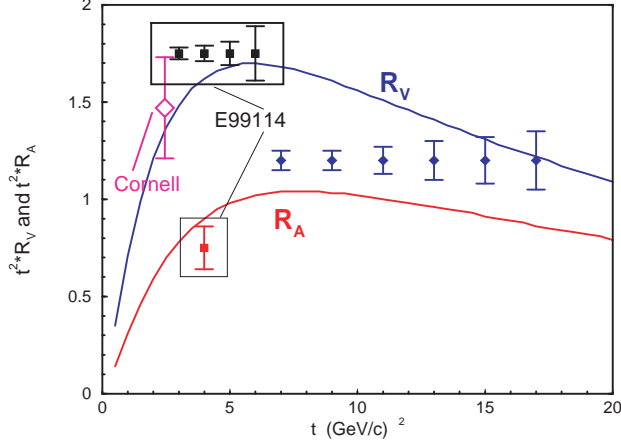


Figure 49: Proposed kinematic coverage of the planned RCS experiments in Halls A and C with the 12 GeV upgrade. Also shown are the results from the earlier Cornell experiment [Sh79a] and the projected uncertainties for E99114, an experiment to be carried out at 5.5 GeV.

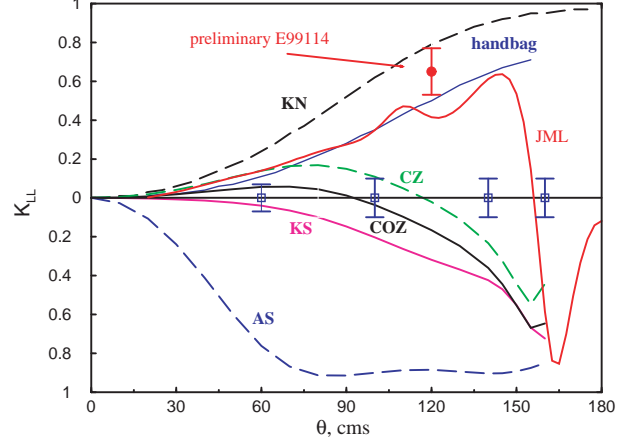


Figure 50: The recoil polarization observable  $K_{LL}$  measured in the recent Hall A real Compton scattering experiment, as well as the projected data for the proposed experiment at  $E_\gamma = 3.2$  GeV. The solid blue curve is the result of a GPD based calculation [Di99], and the curves at negative  $K_{LL}$  are the result of various pQCD based calculation.

Technically, only  $\sigma_{-L}$  results in the factorized form in Eq. 18, where the integral represents a convolution over the meson's valence quark momentum fraction  $\tau$  of the quark distribution function with the pion hard scattering amplitude. At moderate momentum transfer, Ref. [Hu00] finds that  $\sigma_{-L}$  is already dominant, but this needs to be experimentally verified. An important part of the Hall B GPD program is extensive measurements of exclusive  $\pi^0$  and  $\eta$  at high  $-t$ . As in the case of the other form factor measurements, this will enable us to obtain information about the short distance (small  $b_\perp$ ) structure of the GPDs, which is not available from low  $-t$  measurements. Figure 51 is an example of the kind of statistical precision on  $R_A^{\pi^0}(t)$  anticipated in the Hall B measurement.

*Resonance Transition Form Factors* Resonance transition form factors access components of the GPDs which are not accessed in elastic scattering or wide angle Compton scattering. The envisaged upgrade program includes high  $Q^2$  measurements of the  $N \rightarrow \Delta(1232)$ , and  $N \rightarrow S_{11}(1535)$ . The  $\Delta(1232)$ , and  $S_{11}(1535)$  are to lowest approximation the chiral and parity doublet partners of the nucleon. The  $N \rightarrow \Delta$  form factors are related to isovector components of the GPDs.

$$G_M^* = \int_0^1 \sum_q H_M^q(x, t) dx \quad (20)$$

$$G_E^* = \int_{-1}^1 \sum_q H_E^q(x, t) dx \quad (21)$$

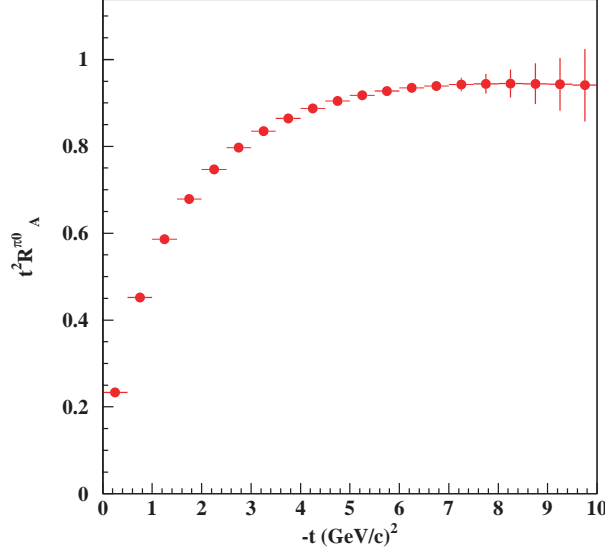


Figure 51: The statistical accuracy of  $R_A^{\pi^0}(t)$  anticipated in the Hall B measurement of the exclusive  $\pi^0$  electroproduction.

$$G_C^* = \int_{-1}^1 \sum_q H_C^q(x, t) dx \quad (22)$$

where  $G_M^*$ ,  $G_E^*$  and  $G_C^*$  are magnetic, electric and Coulomb transition form factors, which are equivalent to the  $M_{1+}$ ,  $E_{1+}$ , and  $C_{1+}$  in CGLN multipole notation.  $H_M^q$ ,  $H_E^q$ , and  $H_C^q$  are *isovector* GPDs, which can be related to elastic GPDs in the large  $N_C$  limit through isospin rotations [Fr99a, Go01]. The  $N \rightarrow S_{11}$  transition form factor is also important, as it probes fundamental aspects of dynamical chiral symmetry breaking in QCD. If chiral symmetry were not broken, the  $S_{11}$  would be the nucleon's parity partner and the  $N$  and  $S_{11}$  masses would be degenerate.

A major component of the Hall C and B program will be to measure all of these resonance form factors to the highest  $Q^2$  attainable. Figs. 52 and 54 shows the existing  $G_M^*$ , and  $G_E^*/G_M^*$  and  $G_C^*/G_M^*$  data, as well as the 12 GeV upgrade projections.

There is a remarkable falloff of  $G_M^*$  relative to the elastic  $G_M^p$ ; this falloff can be related (via the GPD formalism) to the falloff of  $G_E^p/G_M^p$  (Fig. 46). The black curve [St02] in Fig. 52 is obtained (using isospin rotation) from the same wave functions used to calculate the nucleon form factors. Figure 53 shows the ratio  $E_{1+}/M_{1+}$  (or  $-G_E^*/G_M^*$ ). The  $G_E$  amplitude is a chiral non-leading process, and cannot be calculated by simply a naive isospin rotating the nucleon form factor, but requires a more sophisticated approach, which is currently being pursued. The  $p \rightarrow \Delta$  form factor  $G_M^*$  and the  $p \rightarrow S_{11}$  form factors will be measured in Halls B and C, extending the currently maximum  $Q^2$  of 4 (GeV/c) $^2$  to almost 18 (GeV/c) $^2$ , and the ratio  $E_{1+}/M_{1+}$  will be extended to about 12 (GeV/c) $^2$  (assuming that ratio stays small; if it grows then even higher  $Q^2$  is possible).

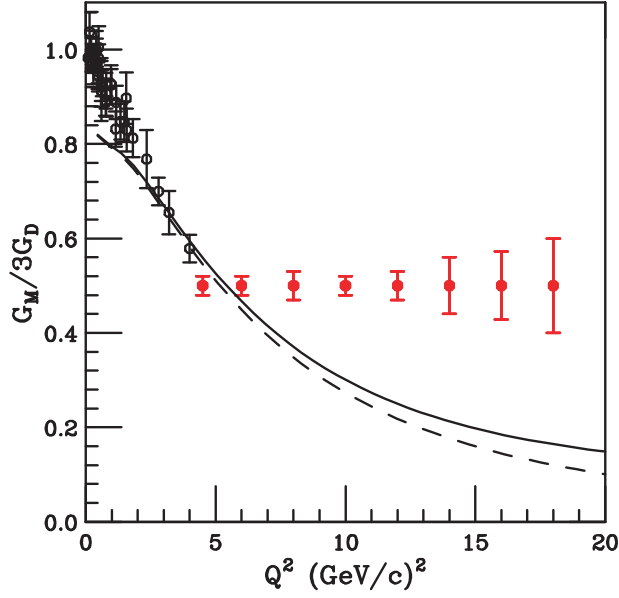


Figure 52: The Delta resonance transition form factor  $G_M^*$ , as compared to the dipole  $G_D$ . Existing exclusive Hall B and C and other data are in black, with projected 12 GeV upgrade Hall C results are in red. The curves are the result of applying the isovector GPD obtained from the isospin rotated elastic scattering GPD's as discussed in the previous figures and the text.

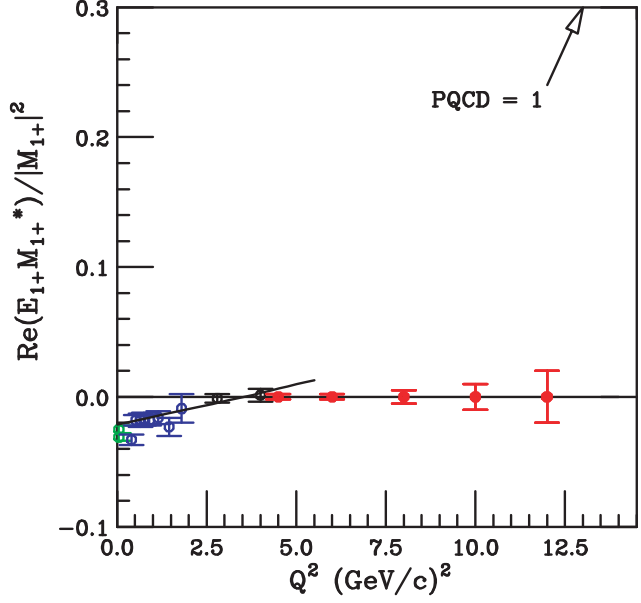


Figure 53: The  $E_{1+}/M_{1+}$  (or -  $G_E^*/G_M^*$ ) ratio for Delta excitation, including JLab data from Halls B (blue) and C (black) [Jo02, Fr98a], and projected Hall C 12 GeV upgrade data. The curve below 4 (GeV/c)<sup>2</sup> is the MAID dynamical model fit [Dr99]. In the pQCD limit  $G_M^*/G_D \rightarrow \text{const}$  and  $E_{1+}/M_{1+} \rightarrow 1$ . The dashed curve is due to the soft Gaussian dependent part.

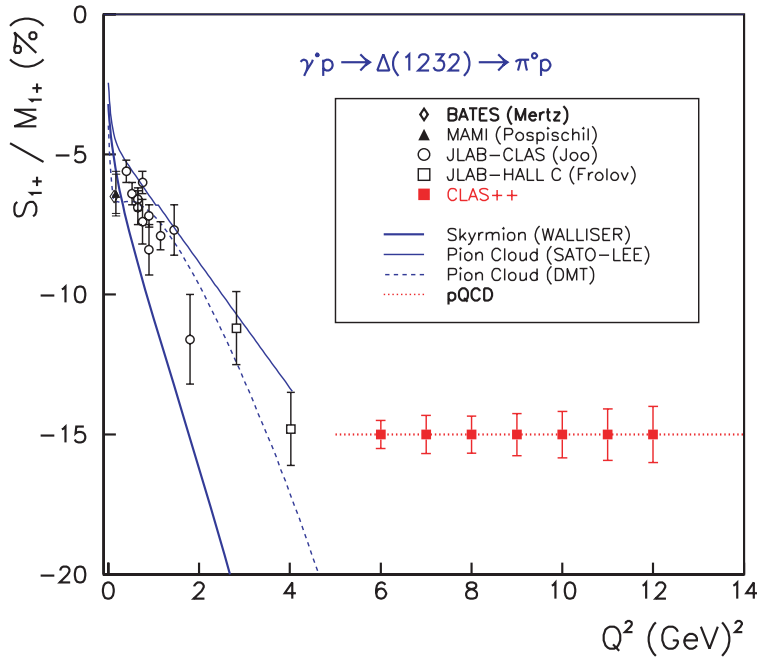


Figure 54: Existing JLab data for  $S_{1+}/M_{1+}$  and JLab Hall B 12 GeV projections.

**pQCD - Constituent Scaling, Helicity Conservation** At very high momentum transfer ( $Q^2$  or  $-t$ ), exclusive reactions are expected to access the small but non-perturbative leading Fock state configurations consisting only of the valence quarks, which perturbatively exchange the minimum number of gluons necessary to keep the entire hadron intact. Examples of reactions which have been theoretically studied by means of the pQCD framework are those discussed in regard to GPDs. In analogy with Fig. 41, the same reactions are shown diagrammatically in Fig. 42 a propos of pQCD.

A well known prediction of pQCD is *constituent scaling*: asymptotically the amplitudes have power-law behavior  $\sim (1/Q^2)^N$ , with the power  $N$  determined by the number of valence constituents. Another prediction of pQCD is *hadron helicity conservation*: the amplitudes involving helicity flip are suppressed by powers of  $1/Q^2$  compared to non-flip or spin-averaged amplitudes. The crucial question is how large the relevant  $Q^2$  should be to guarantee the dominance of the asymptotic hard scattering mechanism. A power-law behavior with powers close to those given by pQCD was experimentally observed for many form factors and hard exclusive reactions, and that was often considered as evidence that the pQCD mechanism dominates starting from few  $(\text{GeV}/c)^2$  region. The reaction for which pQCD is expected to be applicable at the lowest  $Q^2$  is the neutral pion form factor  $F_{\gamma^*\gamma\pi^0}$ , which has been measured at CLEO [Gr97] and does indeed exhibit the requisite behavior starting with  $Q^2 \sim 2 (\text{GeV}/c)^2$ . The theoretical explanation of the early onset of pQCD scaling in this process is the absence of the competing soft mechanism. On the other hand, the charged pion form factor gets contributions both from hard pQCD and soft (or Feynman) mechanisms. In many models, the latter easily fits existing experimental data and, furthermore, imitates the constituent scaling  $1/Q^2$  behavior in a wide range of  $Q^2$ . This provides an example that observation of the “correct” power-law behavior may be not sufficient for establishing the reaction mechanism.

The pion form factor  $F_{\pi^+}(Q^2)$  is a rare case where the normalization of the pQCD term can be estimated with a rather high precision using the  $F_{\gamma^*\gamma\pi^0}$  data, the main source of ambiguity being the size of the strong coupling constant  $\alpha_s$ . With the (usually accepted) value  $\alpha_s \sim 0.4$ , the pQCD term is well below the estimates for the soft term for  $Q^2 < 2 (\text{GeV}/c)^2$ . The study of  $F_{\pi^+}(Q^2)$  offers the best chance of observing the transition to pQCD at the smallest  $Q^2$ , since the pion has the smallest number of valence quarks. The most recent theoretical studies of  $F_{\pi^+}$  seem to indicate that hard mechanisms may become larger than the soft ones by  $Q^2 \approx 5 (\text{GeV}/c)^2$ . As mentioned in section 2.B.1, the most accurate measurements of  $F_{\pi^+}$  have been carried out in Hall C to a maximum  $Q^2$  of around  $2.5 (\text{GeV}/c)^2$ . One of the highest priorities for the Hall C program is to measure  $F_{\pi^+}$  as accurately as possible to the highest  $Q^2$  possible, which will exceed  $6 (\text{GeV}/c)^2$ . The experimental projections and results of various theoretical calculations have been shown in Fig. 44.

For the case of baryons the pQCD mechanism involves two hard gluon exchanges and its dominance for this reason is expected at higher  $Q^2$  than for  $F_{\pi^+}(Q^2)$ . Experimentally, the proton

magnetic form factor  $G_M^p(Q^2)$  and Dirac form factor  $F_{1p}(Q^2)$  appear to begin to scale at momentum transfers as low as a few  $(\text{GeV}/c)^2$ . The dominance of the pQCD mechanism, however, also implies helicity conservation. It should be experimentally tested before any strong conclusions are made.

Results of four published JLab form factor experiments discussed above suggest that at current energies the pQCD regime for nucleons is still elusive. These experiments include: 1) the elastic scattering ratio  $F_{2p}/F_{1p}$  in Hall A; 2) the transition form factors  $N \rightarrow \Delta(1232)$ ; 3) the  $N \rightarrow S_{11}(1535)$  in Halls B and C; and 4) Compton scattering  $p(\gamma, \gamma)p$  in Hall A. With the 12 GeV upgrade, these experiments are expected to greatly increase obtainable momentum transfers, and to involve all three halls; A, B and C.

*The proton elastic electric form factor.* pQCD predicts that for elastic scattering the ratio of the helicity non-conserving to helicity conserving form factors are expected to scale as  $F_{2p}/F_{1p} \propto \Lambda^2/Q^2$ . Within the pQCD scenario, helicity conservation is violated by effects due to quark masses and primordial transverse momentum (Fermi motion) of quarks, hence  $\Lambda^2 \sim \langle k_\perp^2 \rangle$ . The measurements [Jo00, Ga02] in Hall A up to a  $Q^2 \sim 5.6 (\text{GeV}/c)^2$  shows that the ratio  $Q^2 F_{2p}(Q^2)/F_{1p}(Q^2)$  is still rising with  $Q^2$ , reaching the value about  $1.5 (\text{GeV}/c)^2$ , which is a huge number compared to  $\langle k_\perp^2 \rangle \sim 0.1 (\text{GeV}/c)^2$ . The data indicate a  $1/Q$  dependence of  $F_{2p}/F_{1p}$  (see Fig. 46) which contradicts the pQCD prediction and earlier SLAC data which had indicated a  $1/Q^2$  behavior. However, recently [?], a pQCD calculation has been carried out for  $F_2(Q^2)$  in the asymptotically large  $Q^2$  limit, which includes the helicity non-conservation provided by quarks with one unit of orbital angular momentum. It was found that the leading contribution to  $F_2(Q^2)$  has indeed a  $1/Q^6$  power behavior, consistent with the well-known result in the literature, but also that to logarithmic accuracy the asymptotic scaling obeys  $F_2(Q^2)/F_1(Q^2) \sim (\log^2 Q^2/\Lambda^2)/Q^2$ , which appears to describes recent Jefferson Lab data well. One is naturally led to the question of whether pQCD becomes important for the nucleon already at experimentally attainable energies. It is projected that with the 12 GeV upgrade,  $G_E^p/G_M^p$  could be measured up to  $Q^2 = 14 (\text{GeV}/c)^2$ , in either Hall C or Hall A. Projections are shown in Fig 46.

*Resonance transition form factors* The leading baryon transition amplitudes are also expected to scale with  $Q^2$ . The  $S_{11}(1535)$  is uniquely accessed by its strong  $\eta$  channel (via the  $p(e, e'p)\eta$  reaction, with the  $\eta$  reconstructed by missing mass). For the  $N \rightarrow S_{11}$  transition, the amplitude, which is purely helicity conserving, is expected to scale as  $Q^3 A_{1/2} \rightarrow \text{constant}$ . As Fig. 55 shows, this has not yet occurred, but the cross section is shows signs that it may be approaching scaling.

In the  $N \rightarrow \Delta(1232)$  transition, as in the case of the nucleon, the magnetic transition form factor is predicted by pQCD to scale as  $G_{Mp}^* \rightarrow 1/Q^4$ . As seen in Fig. 52, experimental results from Halls C and B do not show the onset of constituent scaling up to  $Q^2 \sim 4 (\text{GeV}/c)^2$ . In fact, as already noted,  $Q^4 G_{Mp}^*$  appears to be decreasing with  $Q^2$ , just as in the case of the elastic  $G_E^p$ , which are indicative of related soft processes. Furthermore, helicity conservation, which is a strict criterion for pQCD, requires the ratio of electric to magnetic multipole amplitudes  $E_{1+}/M_{1+}$  to approach 1. However, it is quite apparent in Fig. 53 from the JLab results in Halls C and B that

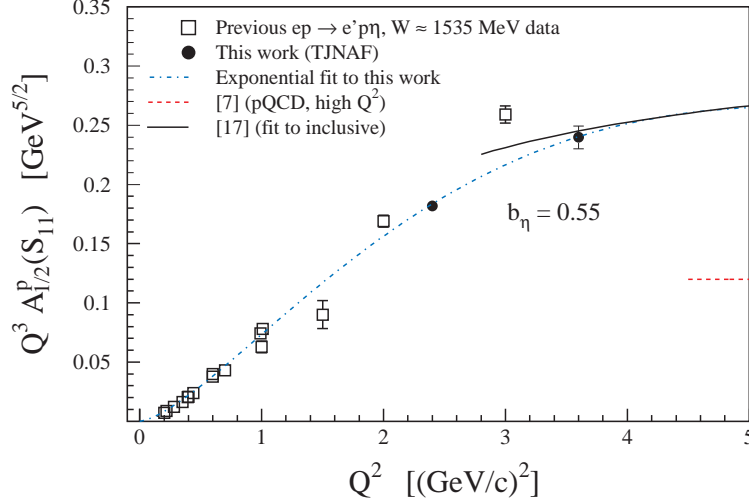


Figure 55: The JLab data for the  $p \rightarrow S_{11}$  helicity amplitude  $Q^3 A_{1/2}$ . The lower  $Q^2$  data are from Hall B [Th01], and the higher  $Q^2$  (filled circles) are from Hall C [Ar99]. With the 12 GeV upgrade these measurements can be extended in Hall C to  $Q^2 = 18$  (GeV/c) $^2$ .

they remain nearly zero up to  $Q^2 = 4$  (GeV/c) $^2$ . Clearly, we would like to see where  $G_{Mp}^*$  begins to scale, and  $E_{1+}/M_{1+}$  begin to turn over and ultimately increase in the direction required in pQCD. The plans in Halls B and C to extend the  $Q^2$  these quantities by a factor of three to four should help to answer that question.

*Compton scattering asymmetries.* Real Compton scattering involves form factors resulting from the *high-t* transverse kick given to the target proton, which remains intact after the reaction. In the pQCD framework it is schematically represented in Fig. 42 by diagram *d*. The results of recent cross section measurements in Hall A over the range  $1.5 \leq -t \leq 6.5$  (GeV/c) $^2$ , and  $5 \leq s \leq 11$  (GeV/c) $^2$  are yet to appear. However, the longitudinal recoil asymmetry  $K_{LL}$  shown in Fig. 49 strongly disagrees with pQCD. According to pQCD, the Compton form factors  $R_V$ ,  $R_T$  and  $R_A$  are also expected to scale with respect to  $s$  and  $-t$ . The planned high  $s$  and  $-t$  measurements of  $R_V$ ,  $R_T$ ,  $R_A$ ,  $K_{LL}$  and  $K_{LL}$  in Halls A and C at dramatically increased ranges in  $s$  and  $-t$  with the 12 GeV upgrade should give us information about the transition to pQCD.

**Summary** The measurement of exclusive form factors at high momentum transfer will open a new era in which a three dimensional picture of the non-perturbative structure of hadrons can be obtained. Simple models have already demonstrated the value of these experiments, and high momentum transfer experiments made possible by the 12 GeV upgrade, together with the development of a more sophisticated theoretical approach, will teach us much about this complex structure. In the extreme high momentum transfer limit, the non-perturbative structure is simplified to three valence quarks, which may be studied with pQCD techniques. The 12 GeV upgrade and associated experimental equipment will give us an excellent opportunity to observe whether the holy grail of the evolution toward pQCD is indeed a practically achievable goal.



### 2.B.2 Valence Quark Structure and Parton Distributions

One of the most fundamental properties of the nucleon is the structure of its valence quark distributions. Valence quarks are the irreducible kernel of each hadron, responsible for its charge, baryon number and other macroscopic properties. Sea quarks, which at very high  $Q^2$  are largely generated through gluon bremsstrahlung and subsequent splitting into quark-antiquark pairs, represent one source of the nonperturbative “dressing” of the valence quarks at low  $Q^2$ . At higher  $x$  values these  $q\bar{q}$  contributions drop away, and the physics of the valence quarks is cleanly exposed [Is99].

Experimentally, most of the recent studies of nucleon structure have emphasized the small- $x$  region populated mainly by sea quarks, while the valence quark structure has for some time now been thought to be understood. Starting with the Nobel Prize-winning work of Friedman, Kendall, and Taylor [Bl69] in the 1970s, three decades of deep inelastic and other high-energy scattering experiments have provided a detailed map of the nucleon’s quark distributions over a large range of kinematics with one major exception – the deep valence region, at very large  $x$  ( $x \gtrsim 0.5$ ). The valence structure of the nucleon can be probed most directly at very large  $x$  since sea quark distributions, which must be subtracted from the measured cross sections to reveal the valence structure, are negligibly small beyond  $x \sim 0.2 - 0.3$ . It is both surprising and unfortunate that the large- $x$  region has been so poorly explored experimentally.

The valence  $u$  and  $d$  quark distributions are usually obtained from measurements of the proton and neutron  $F_2$  (or  $F_1$ ) structure functions. At high energy, these functions are defined in leading order perturbative QCD as the charge-squared weighted sums of the quark and antiquark distributions of various flavors ( $q = u, d, s, \dots$ ):

$$F_2(x) = 2xF_1(x) = x \sum_q e_q^2 (q(x) + \bar{q}(x)) . \quad (23)$$

While the  $u$  quark distribution is relatively well constrained by the proton  $F_2^p$  data for  $x < 0.8$ , the absence of free neutron targets has left large uncertainties in the  $d$  quark distribution beyond  $x \sim 0.5$  arising from incomplete understanding of the nuclear medium modifications in the deuteron, from which the neutron  $F_2^n$  is extracted. For instance, depending on how one corrects for Fermi motion and binding (off-shell) effects in the deuteron, the extracted ratio  $R^{np} \equiv F_2^n/F_2^p$  of neutron to proton structure functions can differ by  $\sim 50\%$  already at  $x \sim 0.75$  [Wh92, Me96] (see Fig. 56).

These large uncertainties have prevented answers to such basic questions as why the  $d$  quark distribution at large  $x$  appears to be smaller (or “softer”) than that of the  $u$ , softer even than what would be expected from flavor symmetry. Furthermore, since the precise  $x \rightarrow 1$  behavior of the  $d/u$  ratio is a critical test of the mechanism of spin-flavor symmetry breaking, the large errors on the current data preclude any definitive conclusions about the fundamental nature of quark-gluon dynamics in the valence quark region. Knowledge of quark distributions at large  $x$  is also essential



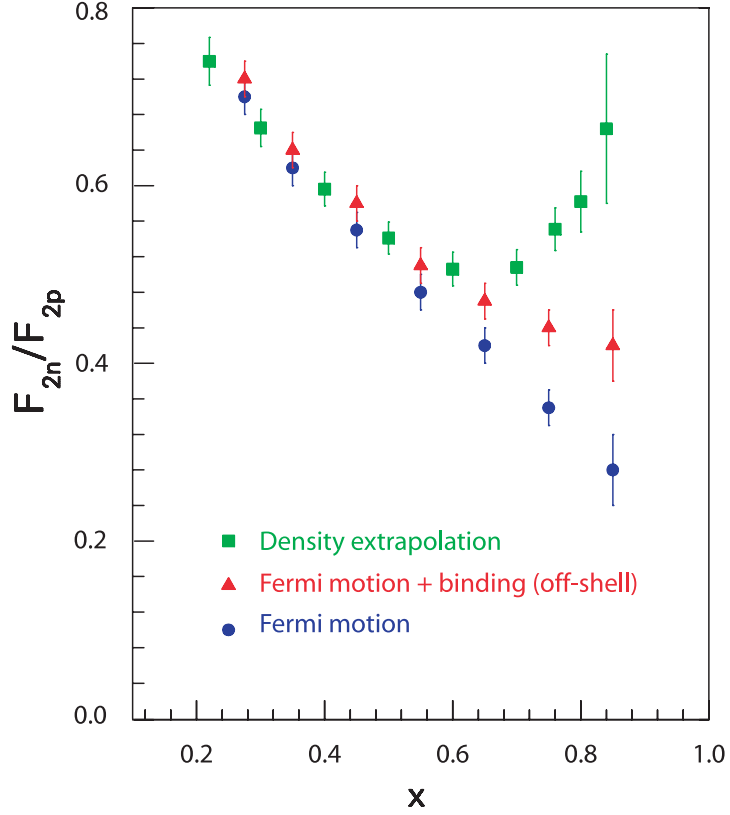


Figure 56: Ratio  $R^{np}$  of neutron to proton structure functions as a function of  $x$ , extracted from the SLAC data on the deep inelastic proton and deuteron structure functions. The three sets of data points represents  $R^{np}$  extracted from the *same* data according to different prescriptions for treating nuclear effects in the deuteron: Fermi smearing only [Bo81, Wh92] (blue circles), Fermi motion and nuclear binding (off-shell) corrections [Me96] (red triangles), and assuming the nuclear EMC effect in the deuteron scales with nuclear density [Fr88] (green squares).

for determining high-energy cross sections at collider energies, such as in searches for the Higgs boson or for new physics beyond the Standard Model [Ca00b, Ku00], where structure information at  $x \sim 0.6 - 0.8$  feeds down to lower  $x$  at higher values of  $Q^2$  through perturbative  $Q^2$  evolution.

The need for reliable large- $x$  data is even more pressing for the spin-dependent quark distributions. Spin degrees of freedom allow access to information about the structure of hadrons not available through unpolarized processes. Spin-dependent quark distributions are usually extracted from measurements of the spin-polarization asymmetry,  $A_1$ , which is approximately given by the ratio of spin-dependent to spin-averaged structure functions:

$$A_1(x) \approx \frac{g_1(x)}{F_1(x)} , \quad (24)$$

where, to leading order,

$$g_1(x) = \frac{1}{2} \sum_q e_q^2 (\Delta q(x) + \Delta \bar{q}(x)) , \quad (25)$$

with  $\Delta q$  defined as the difference between quark distributions with spin aligned and anti-aligned with the spin of the nucleon,  $\Delta q = q^\uparrow - q^\downarrow$ . The first spin structure function experiments at CERN [As88] on the moment, or integral, of  $g_1$  suggested that the total spin carried by quarks was very small, or even zero, prompting the so-called “proton spin-crisis”. A decade of subsequent measurements of spin structure functions using proton, deuteron, and  $^3\text{He}$  targets have determined the total quark spin much more accurately, with the current world average value being  $\sim 20\text{--}30\%$  [La00], which is still considerably less than the value expected from the most naïve quark model in which valence quarks carry all of the proton spin.

While the spin fractions carried by quarks and gluons (or generically, partons) are obtained by integrating the spin-dependent parton momentum distributions, the distributions themselves, as a function of the momentum fraction  $x$ , contain considerably more information about the quark-gluon dynamics than their integrals do. Furthermore, the spin-dependent distributions are generally even more sensitive than the spin-averaged ones to the quark-gluon dynamics responsible for spin-flavor symmetry breaking. Considerable progress has been made in measuring spin-dependent structure functions over the last decade, especially in the small- $x$  region. However, relatively little attention has been paid to the polarized structure functions in the pure valence region at large  $x$ . The lack of data in the valence region is particularly glaring in the case of the neutron, where there is no data with useful accuracy on the polarization asymmetry  $A_1^n$  for  $x \geq 0.4$ . (The only exception is the recent preliminary Hall A  $A_1^n$  data which extend to  $x \approx 0.6$ ; recent Hall B data on  $A_1^p$  and  $A_1^d$  have also been extended to a maximum of  $x \approx 0.6$ .)

**Theoretical predictions for large- $x$  distributions** The simplest model of the proton, polarized in the  $+z$  direction, has three quarks described by a wavefunction that is symmetric in spin and flavor [Cl73]:

$$\begin{aligned} |p^\uparrow\rangle &= \frac{1}{\sqrt{2}} |u^\uparrow(ud)_{S=0}\rangle + \frac{1}{\sqrt{18}} |u^\uparrow(ud)_{S=1}\rangle - \frac{1}{3} |u^\downarrow(ud)_{S=1}\rangle \\ &\quad - \frac{1}{3} |d^\uparrow(ud)_{S=1}\rangle - \frac{\sqrt{2}}{3} |d^\downarrow(ud)_{S=1}\rangle, \end{aligned} \quad (26)$$

where  $q^{\uparrow\downarrow}$  represents the active quark that undergoes the deep inelastic collision, and  $(qq)_S$  denotes the two-quark configuration with spin  $S$  that is a spectator to the scattering. (The neutron wavefunction can be obtained by simply interchanging the  $u$  and  $d$  quarks in this expression.) On the basis of exact spin-flavor symmetry, which is described by the group  $SU(6)$ , the  $S = 0$  and  $S = 1$  “di-quark” states contribute equally, giving rise to simple relations among the quark distributions, such as  $u = 2d$  and  $\Delta u = -4\Delta d$ , which in terms of the structure functions correspond to:

$$R^{np} = \frac{2}{3}; \quad A_1^p = \frac{5}{9}; \quad \text{and} \quad A_1^n = 0. \quad (27)$$

In nature the spin-flavor  $SU(6)$  symmetry is, of course, broken. It has been known for some time that the  $d$  quark distribution is softer than the  $u$  quark distribution, reflecting the fact that the ratio  $R^{np}$  (shown in Fig. 56) deviates strongly from the  $SU(6)$  expectation beyond  $x \sim 0.4$ . On the other hand, the data for the polarization asymmetries  $A_1^p$  and  $A_1^n$  (shown in Fig. 57) are so poor in the valence region that it is presently not possible to discern whether the  $SU(6)$  predictions are borne out for the spin-dependent distributions.

A number of models have been developed for quark distributions that incorporate mechanisms for the breaking of the  $SU(6)$  symmetry; some of these models can be linked directly to phenomena such as the hyperfine splitting of the baryon and meson mass spectra. Feynman and others [Fe72, Cl73, Ca75a] observed that there was a correlation between the nucleon and  $\Delta$  mass difference and the suppression of  $R^{np}$  at large  $x$ . A quark hyperfine interaction, such as that due to one-gluon exchange, instantons or pion exchange (which can induce a higher energy for the  $S = 1$  spectator “di-quark” in Eq. (26)) will necessarily give rise to a larger mass for the  $\Delta$  since the quark wavefunction for the  $\Delta$  has all “di-quark” configurations with  $S = 1$ . If the  $S = 0$  states are dominant at large  $x$ , Eq.(26) implies that the  $d$  quark distribution will be suppressed relative to that of the  $u$ . This expectation has, in fact, been built into most phenomenological fits to the parton distribution data [Ei84, Di88, Ma94a, La95]. Available data from HERA, Fermilab, SLAC, and JLab show disagreement with the predictions of these fits that need to be resolved. This mechanism also leads to specific predictions for the polarization asymmetries as  $x$  becomes large and close to unity. The ratio  $R^{np}$  is expected to decrease to a value of  $1/4$ , while  $A_1$  will increase to a positive limiting value of unity for both the proton and neutron.

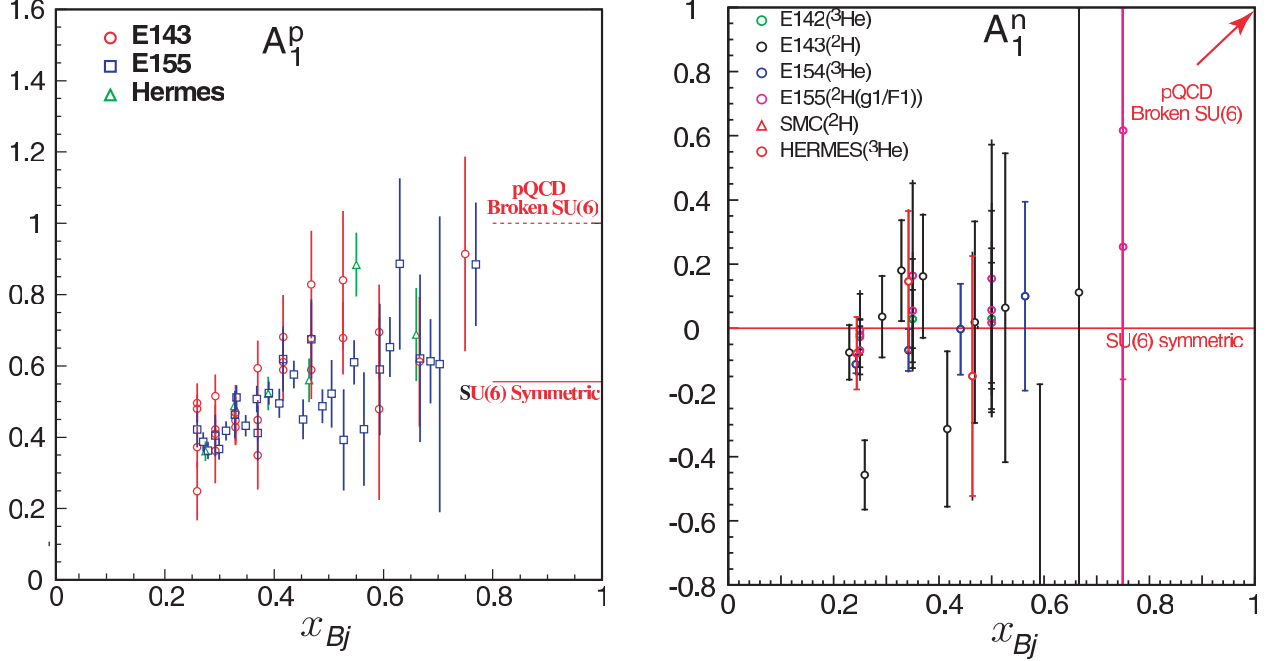


Figure 57: Sample of large- $x$  data for  $A_1^p$  (left) and  $A_1^n$  (right). The predictions of SU(6) and models based on broken SU(6) for  $x \rightarrow 1$  are indicated.

More radical nonperturbative models of SU(6) breaking, such as those which include instantons as important degrees of freedom, predict dramatically different behavior for  $A_1$  as  $x$  approaches 1; *i.e.*, that it goes to a limiting of  $-1$  for the proton and a value close to zero for the neutron[Ko97].

Arguments based on hadron helicity conservation (HHC) within perturbative QCD, on the other hand, predict that the dominant components of the proton valence wavefunction at large  $x$  are those associated with states in which the total “di-quark” helicity, or spin projection,  $S_z$ , is zero [Fa75]. Consequently, scattering from a quark polarized in the opposite direction to the proton polarization is suppressed relative to the helicity-aligned configuration. This leads to a stronger  $x$  dependence in the ratio  $R^{np}$ , with a limiting value of  $3/7$  as  $x \rightarrow 1$ , and a faster approach to unity for the asymmetries  $A_1^p$  and  $A_1^n$ .

The novelty of the hadron helicity conservation predictions, especially for  $A_1^p$  and  $A_1^n$ , is that they can be related to the large  $Q^2$  behavior of elastic form factors, whose detailed  $Q^2$  dependence can provide information about the role of orbital angular momentum of quarks in the nucleon [Ra03, Ji03a]. Furthermore, because  $A_1$  depends weakly on  $Q^2$  we expect these predictions to still be valid in the  $Q^2$  range accessible experimentally. However, it is not clear *a priori* at which  $x$  the transition from the nonperturbative dynamics, embodied in the above predictions, to perturbative QCD takes place, so experimental guidance on this issue is essential.

While the trend of the existing  $R^{np}$  data is consistent with models with broken SU(6) symmetry, they cannot discriminate between the competing mechanisms of SU(6) breaking (see Fig. 56)

because of uncertainties in the extraction procedure associated with nuclear corrections. For the asymmetries  $A_1^n$  and  $A_1^p$ , while we do not expect the SU(6) predictions to be accurate, the existing measurements at high  $x$  lack the precision to even distinguish any of the predictions from the naïve SU(6) result.

**The structure of the free neutron** If the nuclear EMC effect (the modification of the free nucleon structure function in the nuclear environment) in deuterium were known, one could apply nuclear smearing corrections directly to the deuterium data to obtain the free neutron  $F_2^n$ . However, the EMC effect in the deuteron requires knowledge of the free neutron structure function itself, so the argument becomes cyclic. As seen in Fig. 56, the current experimental impasse has prevented a full understanding of the structure of valence quarks in the nucleon. The 12 GeV Upgrade will finally provide a solution to this 30-year old problem.

**“Tagged” neutron structure function** The cleanest way to obtain the free neutron structure function is with a novel method currently being pioneered at Jefferson Lab in Hall B, in which a recoil detector is used to tag scattering events on a nearly on-shell neutron in a deuteron target. By detecting slow protons emitted in the backward hemisphere in coincidence with the scattered electron, the initial four-momentum of the struck neutron can be inferred from the observed spectator proton.

A newly designed time-projection-chamber-like recoil detector, in combination with sufficiently thin targets, will allow protons to be detected down to momenta around 70 MeV/c, where the bound neutron is only around 7 MeV away from its mass-shell. The choice of backward kinematics for the spectator proton serves to suppress effects from final state interactions (rescattering of the spectator proton by the deep inelastic remnants of the scattered neutron) [Me97, Ci02], as well as independent target fragmentation [Ci93, Bo94], while the restriction to small proton momenta mostly eliminates uncertainties associated with the deuteron wave function and on-shell extrapolation [Me94].

This new technique will allow the structure of the free neutron to be accessed with unprecedented accuracy over the range  $0.2 \leq x \leq 0.82$ , and with a minimum of uncertainty associated with nuclear corrections. It opens up a completely new program of measurements on the neutron, in analogy with those which have been carried out in the past on the proton. Figure 58 illustrates the expected errors on the ratio  $R^{np}$  extracted from such a measurement. Note that this method can be used to study not only the deep inelastic structure functions of the neutron, but also the structure of neutron resonances, and neutron elastic form factors, essentially free of nuclear effects.

**Deep inelastic scattering from  $A = 3$  nuclei** An alternative, independent method to reliably determine  $R^{np}$ , free of the large uncertainties associated with nuclear corrections at large  $x$ , is through simultaneous measurements of the inclusive  $^3\text{He}$  and  $^3\text{H}$  structure functions, maximally

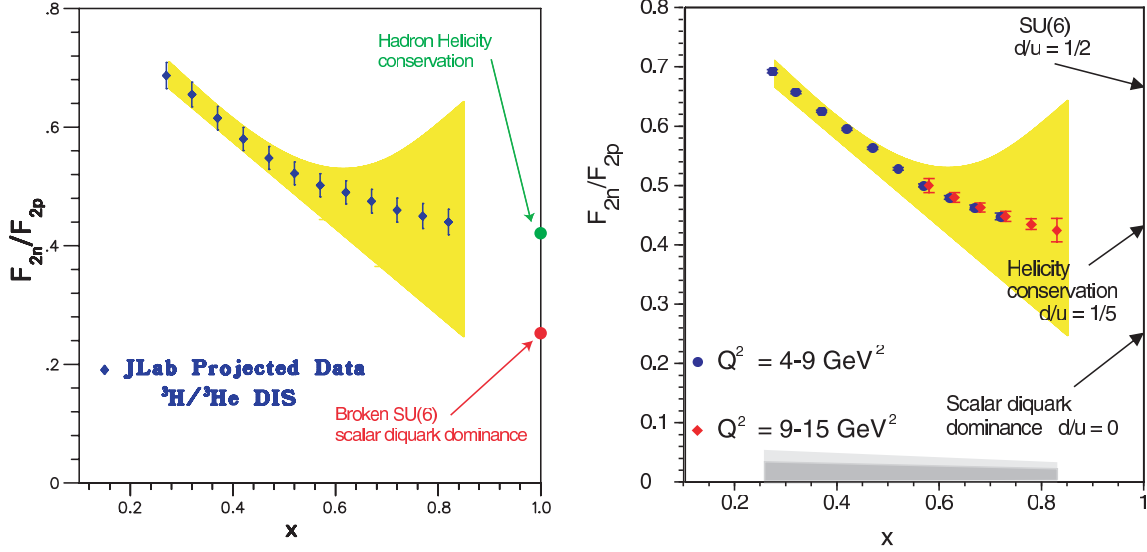


Figure 58: The ratio  $F_2^n/F_2^p$  versus  $x$  by two techniques. *Left figure:* Using the  ${}^3\text{He}/{}^3\text{H}$  ratio, with total (statistical, systematic, and theoretical) errors indicated. *Right figure:* Using spectator proton tagging from a deuteron target. Estimated systematic errors due to experimental and theoretical uncertainties are indicated by the bands at the bottom (light shade for total systematic error, darker shade for point-to-point error after normalization at low  $x$ ). The arrows indicate the different possible approaches to the limit  $x \rightarrow 1$ . The yellow shaded area indicates the range of uncertainty from existing data due to different treatment of nuclear effects (see Fig. 56).

exploiting the mirror symmetry of  $A = 3$  nuclei. Regardless of the absolute value of the nuclear EMC effect in  ${}^3\text{He}$  or  ${}^3\text{H}$ , the differences between the EMC effects in these nuclei will be small (on the scale of charge symmetry breaking in the nucleus). The advantage of this method is that by measuring a ratio of cross sections, most of the systematic and theoretical errors cancel.

In the absence of a Coulomb interaction, and in an isospin-symmetric world, the properties of a proton (neutron) bound in the  ${}^3\text{He}$  nucleus would be identical to those of a neutron (proton) bound in the  ${}^3\text{H}$  nucleus. If, in addition, the proton and neutron distributions in  ${}^3\text{He}$  (and in  ${}^3\text{H}$ ) were identical, the neutron structure function could be extracted with no nuclear corrections, regardless of the size of the EMC effect in  ${}^3\text{He}$  or  ${}^3\text{H}$  separately.

In practice,  ${}^3\text{He}$  and  ${}^3\text{H}$  are not perfect mirror nuclei (*e.g.*, their binding energies differ by some 10%) and the proton and neutron distributions are not quite identical. However, the  $A = 3$  system has been studied for many years, and modern realistic  $A = 3$  wavefunctions are known to rather good accuracy. Using these wavefunctions, together with a nucleon spectral function, the difference in the EMC effects for the  ${}^3\text{He}$  and  ${}^3\text{H}$  nuclei has been calculated [Uc88, Ci90, Af00b, Pa01, Sa01] to be less than 2% for  $x < 0.85$ . More importantly, the actual model dependence of this difference is less than 1% for all  $x$  values accessible experimentally with an 11 GeV beam.

By performing the tritium and helium measurements under identical conditions, the ratio of the deep inelastic cross sections for the two nuclei can be measured with 1% experimental uncer-

tainty in Hall A with the MAD (Medium Acceptance Device) spectrometer (SLAC Experiments E139 [Go94] and E140 [Da94, Ta96] have quoted 0.5% uncertainties for measurements of ratios of cross sections). Deep inelastic scattering with the proposed 11 GeV electron beam can therefore provide precise measurements for the  $F_2^{^3\text{He}}/F_2^{^3\text{H}}$  ratio, from which  $R^{np}$  can be extracted essentially free of nuclear corrections at the 1% level over the entire range  $0.10 \leq x \leq 0.82$ . The key issue for this experiment will be the availability of a high-density tritium target, comparable with the previously used Saclay [Am94] and MIT-Bates [Be89] tritium targets. The quality of the projected data is highlighted in Fig. 58.

**Longitudinal–transverse separation** While the relation between the  $F_1$  and  $F_2$  structure functions in Eq. (23) is exact for scattering off free, spin-1/2 quarks or anti-quarks, at finite  $Q^2$  small differences between these arise due to gluon radiation and multiparton correlation effects in QCD. These give rise to a non-zero value for the ratio of longitudinal to transverse cross sections,  $R = \sigma_L/\sigma_T$ . Unfortunately, the difficulty in separating the longitudinal and transverse components of the cross sections via the usual Rosenbluth separation method has resulted in a paucity of data on  $R$ , particularly at larger  $x$ . Current extractions of the  $F_2$  structure function are therefore hampered by poor knowledge of the longitudinal corrections, and often model-dependent assumptions must be made.

With a 6 GeV beam, the measurement of separated transverse and longitudinal structure functions is limited to  $Q^2 < 6 \text{ (GeV/c)}^2$ . With an 11 GeV beam, this range can be doubled and separated cross sections obtained out to  $Q^2 = 12 \text{ (GeV/c)}^2$ . Moreover, the precision possible for  $4 < Q^2 < 6 \text{ (GeV/c)}^2$  can be significantly improved by the larger beam energy available. Projected measurements of  $R$  with the HMS and SHMS Hall C spectrometers are shown in Fig. 59 for  $x = 0.8$  (in blue for 6 GeV and pink for 11 GeV). The surrounding lines indicate the total statistic and systematic uncertainties possible, a substantial improvement to the existing data set shown in red. Data of this quality would be obtained for numerous such bins in  $x$ , allowing for the experimental extraction of all unpolarized structure function moments out to  $Q^2 = 10 \text{ (GeV/c)}^2$ . This is of particular interest since these moments are now calculable from QCD using lattice techniques. In addition, the measurement of the  $Q^2$  dependence of  $R$  will be highly sensitive to gluons, and can provide another means for probing the gluon distribution in the nucleon.

**Moments of structure functions** A high luminosity 11 GeV beam complemented with well matched detectors will make accessible the broad kinematic region required to map out both the resonance and deep inelastic regimes requisite to precision structure function studies. The wide range of scattered electron energy and angle provided by the HMS and SHMS spectrometers in Hall C for instance will allow measurement of the  $F_1$  and  $F_2$  structure functions over a large range of  $x$  at a constant value of  $Q^2$ . In combination with the existing inclusive scattering data, typically emphasizing lower values of  $x$ , the 11 GeV data can be used to obtain moments of all unpolarized

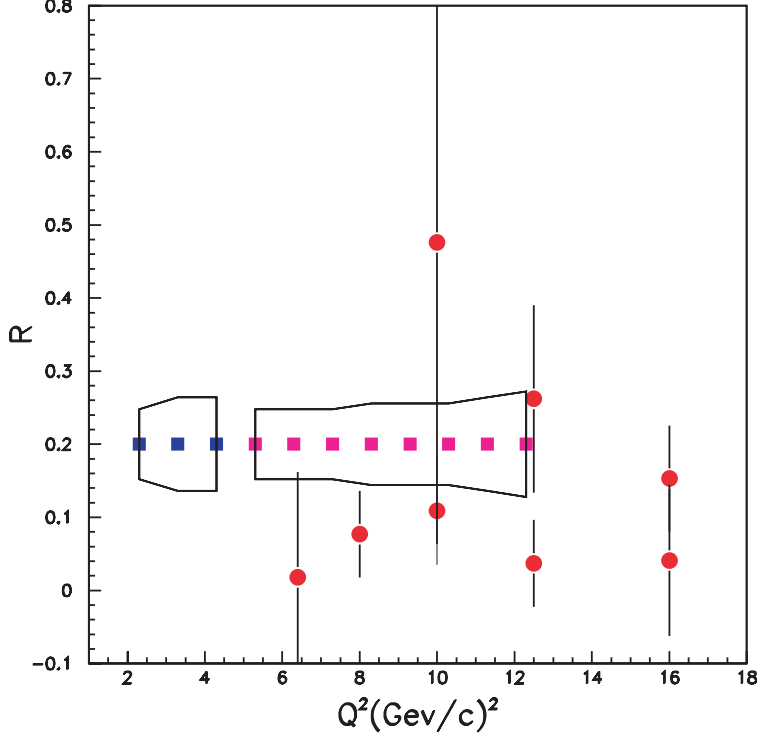


Figure 59: Projected measurements for  $R = \sigma_L/\sigma_T$  at  $x = 0.8$  (blue for 6 GeV, pink for 11 GeV). The surrounding lines indicate the total uncertainty, compared to the existing data (red).

structure functions, defined as

$$M_n^i(Q^2) = \int_0^1 dx x^{n-2} F_i(x, Q^2), \quad i = 1, 2, \quad (28)$$

with unprecedented precision, up to  $Q^2 \simeq 10 \text{ (GeV/c)}^2$ . The virtue of these moments is that they can be compared directly with first principles calculations in lattice QCD.

The operator product expansion in QCD allows the moments of structure functions to be expanded in powers of  $1/Q^2$ , with the coefficients of each of the terms given by matrix elements of local operators of a given twist (where “twist” is defined as the difference between dimension and spin of an operator), which can be calculated numerically on the lattice.

Figure 60 shows the quality of data for the lower moments of  $F_2^p - F_2^n$  that will be accessible in Hall C, compared with recent lattice QCD simulations [De02]. Note that because of the  $x^{n-2}$  weighting, the higher moments are more sensitive to the large- $x$  behavior of the structure functions, the currently poor knowledge of which will be significantly improved with the 12 GeV Upgrade. In particular, the technique of spectator proton tagging or  $^3\text{He}/^3\text{H}$  structure function measurements discussed above will lead to a dramatic improvement in the accuracy of the neutron structure function,  $F_2^n$ . The relatively large error bars on the calculated moments are associated with extrapolation of the lattice moments from the large values of quark mass at which they are currently calculated to the physical values [De01]. The realization of multi-Teraflops computing



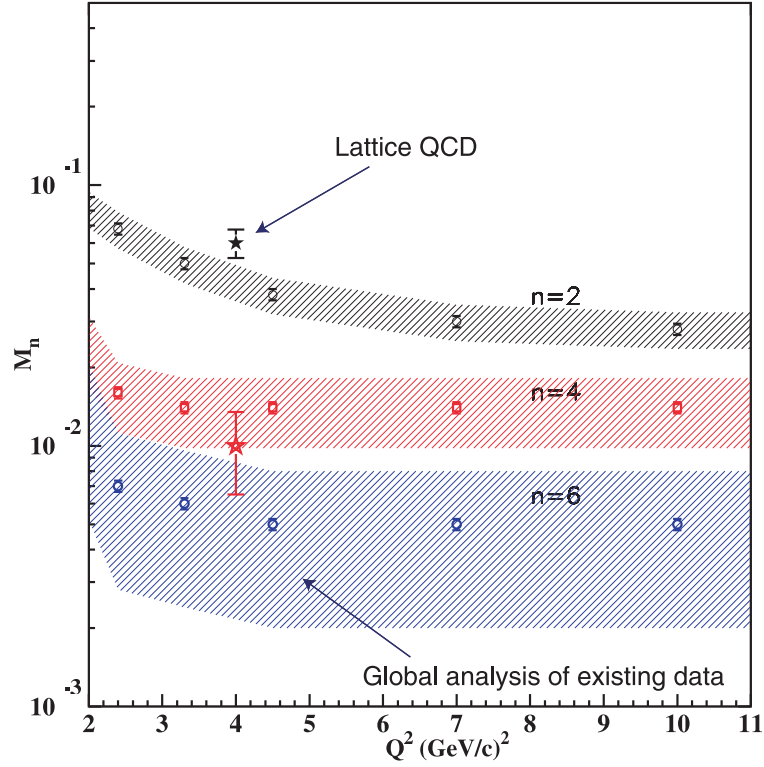


Figure 60: Lowest moments  $M_n(Q^2)$  of the proton-neutron  $F_2$  structure function difference, for  $n = 2$  (black), 4 (red), and 6 (blue), as a function of  $Q^2$ . Experimental moments without including JLab data are indicated as hatched areas. The 12 GeV program will obtain precise moments for  $Q^2 \leq 10$  (GeV/c) $^2$  for all structure functions. Lattice QCD calculations (stars) are shown at  $Q^2 = 4$  (GeV/c) $^2$  for  $n = 2$  (black) and 4 (red).

Table 8: Comparison of the figure of merit (FOM) for large  $x$  measurements of the  $A_1^n$  structure function at HERA, SLAC, and JLab.

Expt. name	$E_i$ (GeV)	$E'$ (GeV)	$\theta$ (deg.)	$x$ bin	$Q^2$ (GeV/c) <sup>2</sup>	$D$	$f$	Rate (Hz)	FOM (10 <sup>-4</sup> )
HERMES	35.0	17.0	5.2	0.60-0.70	9.1	0.22	0.3	0.05	7
SLAC E154	48.3	34.1	5.5	0.50-0.70	15	0.29	0.16	?	?
JLab	11.0	4.4	25	0.60-0.70	8.5	0.67	0.3	2.7	370

facilities in the next few years will allow the moments of the structure functions to be computed at the 5% level, providing critical benchmarks for the planned 12 GeV experiments [Ne00].

**The spin structure of the nucleon** While the behavior of the spin-averaged quark distributions at large  $x$  still awaits definitive resolution, our lack of understanding of the spin-dependent distributions at large  $x$  is even more striking.

**Neutron spin structure functions** Although data on  $R^{np}$  and  $A_1^p$  in Figs. 58 and 57 give some indication of the large- $x$  behavior of the valence quark distributions at  $x \lesssim 0.5$ , the experimental situation for the neutron  $A_1^n$  at large  $x$  is totally unclear. The statistical precision of the data available does not even allow a meaningful statement about the qualitative behavior of  $A_1^n$  for  $x > 0.4$ . The experiment proposed here will use the 11 GeV electron beam to perform a precision measurement of  $A_1^n$ , utilizing the Hall A polarized  $^3\text{He}$  target and the proposed MAD spectrometer. Because the neutron in  $^3\text{He}$  carries almost 90% of the nuclear spin, polarized  $^3\text{He}$  is an ideal source of polarized neutrons [Fr90].

The experiment involves measurement of the  $^3\text{He}$  polarization asymmetry,

$$A_1^{^3\text{He}}(x) \approx \frac{1}{D} \frac{d\sigma^{\uparrow\downarrow} - d\sigma^{\uparrow\uparrow}}{d\sigma^{\uparrow\downarrow} + d\sigma^{\uparrow\uparrow}}, \quad (29)$$

where  $d\sigma^{\uparrow\uparrow}$  ( $d\sigma^{\uparrow\downarrow}$ ) is the cross section for scattering polarized electrons from a polarized  $^3\text{He}$  target with the beam and target helicities parallel (antiparallel), and  $D$  is a kinematic factor relating the virtual photon polarization to that of the electron. The neutron asymmetry  $A_1^n$  is extracted from  $A_1^{^3\text{He}}$  after correcting for residual nuclear effects in  $^3\text{He}$  associated with Fermi motion and binding, using modern three-body wavefunctions [Wo89, Ci93a, Sc93, Bi01], similar to those used in correcting for nuclear effects in  $F_2^{^3\text{He}}$ . Furthermore, because the asymmetry is a ratio of nuclear structure functions, the nuclear effects on  $A_1^n$  will be considerably smaller than those associated with absolute structure functions. In addition to the use of the polarized  $^3\text{He}$  target, other polarized targets ( $\text{ND}_3$  and  $\text{NH}_3$ ) will be used for cross checks and for the investigation of the nuclear effects.

An example of the kinematics relevant for this experiment is given in Table 8. To illustrate the improvement of the projected results obtainable with JLab at 11 GeV compared with previously

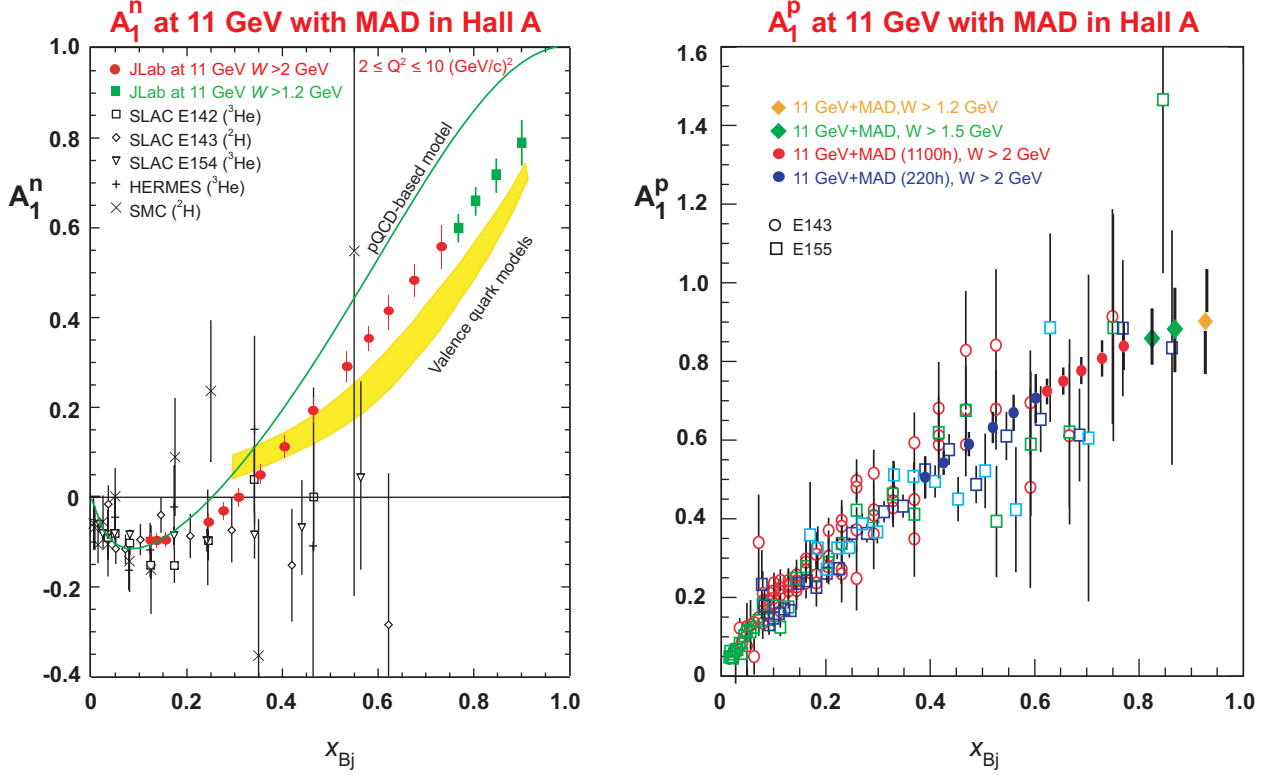


Figure 61: Projected errors for measurements of asymmetries  $A_1$  in the large- $x$  region made possible by the proposed 12 GeV Upgrade. *Left panel:* Neutron  $A_1^n$  in Hall A, compared with existing data from SLAC, HERMES and SMC. The red circles correspond to the DIS region ( $W > 2$  GeV), while the green squares illustrate the possibility of extending the measurement to higher  $x$  in the resonance region ( $W > 1.2$  GeV). *Right panel:* Proton  $A_1^p$  for Hall A (solid circles), compared with existing data from the SLAC E143 and E155 experiments (open symbols). Statistical errors only are shown. Extensions into the resonance region are denoted by diamonds. Theoretical  $x \rightarrow 1$  limits are indicated by red lines on the right side of the graph.

measured data from other facilities, we introduce a figure of merit  $(\text{FOM}) = D^2 \times \text{Rate} \times f$ , which allows a meaningful comparison between different laboratories. Here “Rate” takes into account the use of the proposed MAD spectrometer, and  $f$  is the dilution factor defined as the ratio of polarized nucleons to the total number of nucleons in the target. Table 8 shows the comparison between the relevant parameters at competitive existing laboratories at comparably large  $x$  and  $Q^2$ . Note that the depolarization factor is smaller at high beam energies; therefore the lowest beam energy that guarantees access to the large- $x$  region in the Bjorken limit is optimal. The anticipated data are shown in Fig. 61 (left panel). Jefferson Lab at 11 GeV would enable access to  $x \lesssim 0.8$  at  $W \approx 2$  GeV.

While the cut in  $W$  would allow the deep inelastic continuum to be cleanly accessed, one may extend the measurements of  $A_1^n$  to even larger  $x$  by using quark-hadron duality in the resonance region,  $W < 2$  GeV. If duality is observed to hold for the spin-dependent  $g_1$  structure function as well as it does for the unpolarized  $F_2$  structure function [Ni00], averaging over small regions of  $W$  will suppress the high twist ( $\sim 1/Q$ ) contributions associated with the low-lying resonances, and enable the dominant scaling component of  $A_1$  to be measured out to  $x \simeq 0.95$ . This will be discussed in more detail below.

In addition to providing unprecedented access to the spin structure of the neutron at large  $x$ , the 12 GeV Upgrade will allow significant improvements in our knowledge of the proton and deuteron spin structure. At low and medium  $x$  ( $x < 0.4$ ) the various data sets for  $A_1^p$  are consistent with each other and show a definite rise with  $x$ . At higher  $x$  ( $x > 0.4$ ), however, the errors become significantly larger, and the trend is no longer clear: the current data cannot distinguish between a pure SU(6) symmetric scenario, in which  $A_1^p \rightarrow 5/9$ , and the SU(6) breaking predictions in which  $A_1^p \rightarrow 1$ . With an 11 GeV beam, Jefferson Lab will provide a unique facility for closing this gap in our knowledge of  $A_1^p$ .

Figure 61 (right panel) illustrates the improvement in the measured proton asymmetry  $A_1^p$  at large  $x$  with the MAD spectrometer in Hall A. The precision that can be achieved for  $A_1^p$  with the CLAS<sup>++</sup> detector in Hall B is illustrated in Fig. 62 (left panel). These data will clearly distinguish between the SU(6) various models, and dramatically improve our knowledge of the proton’s spin structure at high  $x$ . The difference between these predictions is even more striking for the deuteron, where one will also be able to significantly improve on existing data, as shown in Fig. 62 (right panel) for CLAS<sup>++</sup> kinematics. The high precision data on all three targets (<sup>3</sup>He, proton and deuterium) that will be collected at fixed  $x$ , but in several bins in  $Q^2$ , will constrain the logarithmic and  $1/Q^2$  scaling violations of the spin structure functions  $g_1$ , and determine their higher moments, as well as allow duality for spin structure functions to be studied in detail. The accurate determination of the  $Q^2$  dependence of  $g_1$  at fixed  $x$  may also enable the poorly-known polarized gluon distribution,  $\Delta G(x)$ , to be constrained at large  $x$ .

One should note that in order to unambiguously extract the  $A_1$  asymmetry from data, two beam-target asymmetries must be measured: one with the target polarization oriented longitudi-

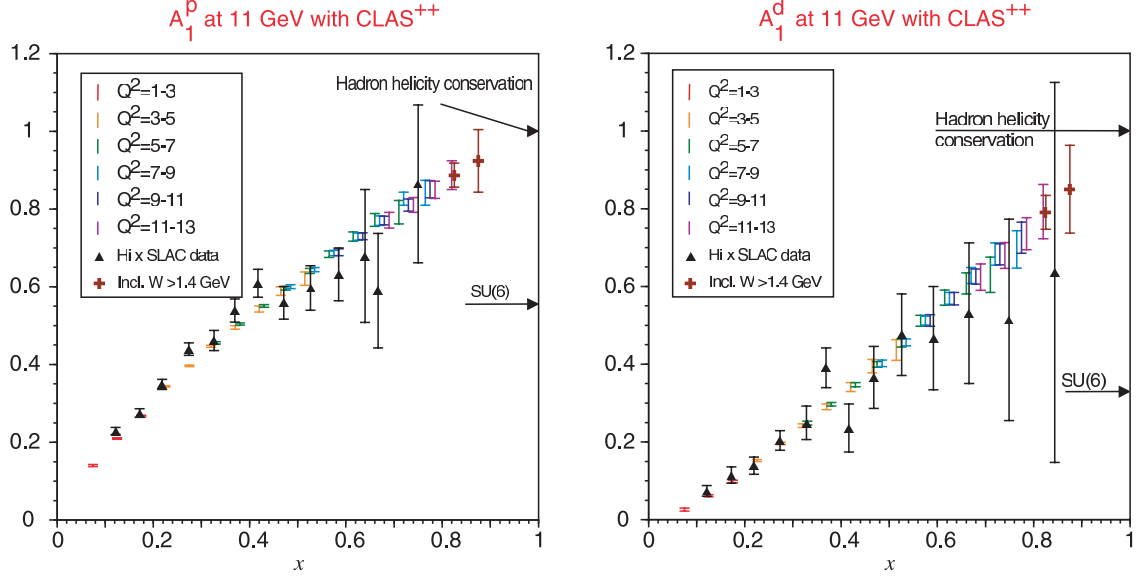


Figure 62: Expected data with CLAS<sup>++</sup> in Hall B for the polarization asymmetries of the proton (left panel) and deuteron (right panel) with statistical errors from 40 days of running. Several bins in  $Q^2$  (in units of  $(\text{GeV}/c)^2$ ) are indicated by slightly offset error bars. Existing SLAC data (from E130, E143 and E155) are shown for comparison. The predicted approach to the limit  $x = 1$  for two different models is indicated.

nally with respect to the electron beam ( $A_{\parallel}$ ) and one oriented transversely ( $A_{\perp}$ ):

$$A_{\parallel} = \frac{d\sigma^{\downarrow\uparrow} - d\sigma^{\uparrow\uparrow}}{d\sigma^{\downarrow\uparrow} + d\sigma^{\uparrow\uparrow}} \quad \text{and} \quad A_{\perp} = \frac{d\sigma^{\downarrow\rightarrow} - d\sigma^{\uparrow\rightarrow}}{d\sigma^{\downarrow\rightarrow} + d\sigma^{\uparrow\rightarrow}}, \quad (30)$$

where  $d\sigma^{\downarrow\rightarrow}$  ( $\sigma^{\uparrow\rightarrow}$ ) is the cross section for scattering an electron polarized parallel (anti-parallel) to the beam direction from a transversely polarized target. These observed asymmetries can then be related to the virtual photon-absorption asymmetries, and structure functions,  $g_1$  and  $g_2$ , the latter which is discussed below. Longitudinally and transversely polarized  $^3\text{He}$  targets have been used routinely in Hall A in many experiments, allowing the direct extraction of  $g_1$  and  $g_2$  from the measured spin-dependent cross sections. Transversely polarized targets can be used straightforwardly in Hall A and Hall C, and future installation of a transversely polarized target is also planned for CLAS<sup>++</sup>. An illustration of the quality of the data on the  $A_{\parallel}$  asymmetry for a proton target at  $Q^2 = 8$   $(\text{GeV}/c)^2$  is shown in Fig. 63, representing the results of a two-week experiment in Hall C. A measurement of  $A_{\perp}$  to minimize the uncertainty in  $A_1$  due to the  $A_2$  component of  $A_{\parallel}$  ( $= D(A_1 + \eta A_2)$ , where  $D$  and  $\eta$  are kinematic factors) requires only a small amount ( $\approx 10\%$ ) of this beam time.

**Higher-twist effects** Unlike the  $g_1$  structure function, which has a simple interpretation in the quark-parton model in terms of quark helicity distributions, and has been the focus of extensive experimental programs over the last decade, there have been few dedicated experimental studies of the  $g_2$  structure function. The  $g_2$  structure function is related to the transverse polarization of

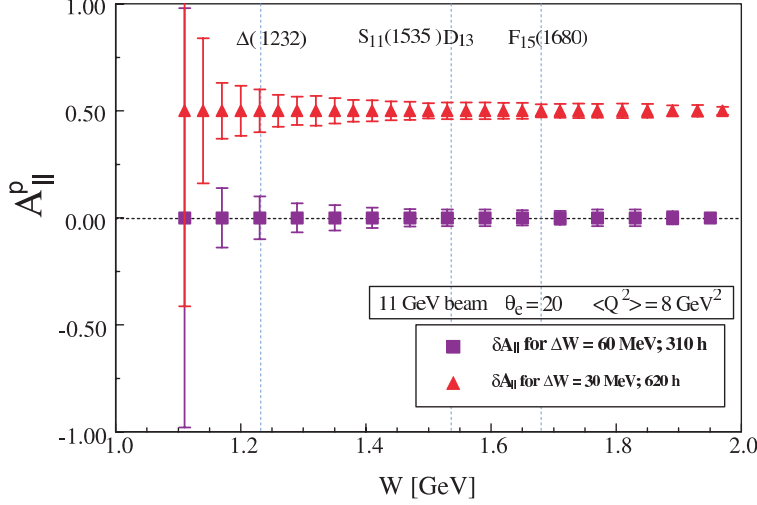


Figure 63: Longitudinal beam-target polarization asymmetry of a proton versus  $W$ , for an 11 GeV measurement at  $Q^2 = 8 \text{ (GeV/c)}^2$  in Hall C.

the nucleon, and although it does not have a simple quark-parton model interpretation, it contains important information about quark-gluon correlations within the nucleon.

In QCD the quark-gluon correlations are associated with higher twist operators, which are suppressed by additional factors of  $1/Q$  relative to the leading twist contribution (which corresponds to free quark scattering). At large values of  $Q^2$ , QCD allows one to relate moments of spin structure functions to the matrix elements of operators of given twist. The simplest twist-3 matrix element that contains information on quark-gluon correlations is given by:

$$d_2(Q^2) = \int_0^1 dx x^2 \left[ 2g_1(x, Q^2) + 3g_2(x, Q^2) \right]. \quad (31)$$

Note that because of the  $x^2$  weighting in the integral,  $d_2$  is dominated by the large- $x$  behavior of  $g_1$  and  $g_2$ . The physical significance of  $d_2$  is that it reflects the response of a quark to the polarization of the gluon color field in the nucleon,  $d_2 = (2\chi_B + \chi_E)/8$ , with  $\chi_B$  ( $\chi_E$ ) the gluon-field polarizability in response to a color magnetic (electric) field  $\vec{B}$  ( $\vec{E}$ ) [St95].

Published data for  $g_2$  were obtained from experiments E143-E155x at SLAC [Ab96, An03] and the SMC experiment at CERN [Ad93]. Using results from the most recent experiment at SLAC [An03], which measured  $g_2$  for the proton and deuteron, values for  $g_2$  are shown in Fig. 64 for the neutron (left panel) and proton (right panel). Note that the SLAC data vary in  $Q^2$  from 0.8–8.4  $\text{GeV}^2$  over the measured  $x$  range. The curve labeled “ $g_2^{WW}$ ” for the neutron represents the leading twist contribution to  $g_2$  [Wa77] at fixed  $Q^2 = 3 \text{ GeV}^2$ , calculated from a fit to world data on  $g_1$  [An03]. Using these data, a nonzero positive value for  $d_2^n$  has been extracted that is in disagreement with all of the theoretical calculations [Ba90, St93a, Ji94, Eh95, St95, So96, We97]. However, in most cases, the disagreement is less than  $1\sigma$ , and the size of the experimental error does not allow one to make a conclusive statement about the importance of higher-twist effects in

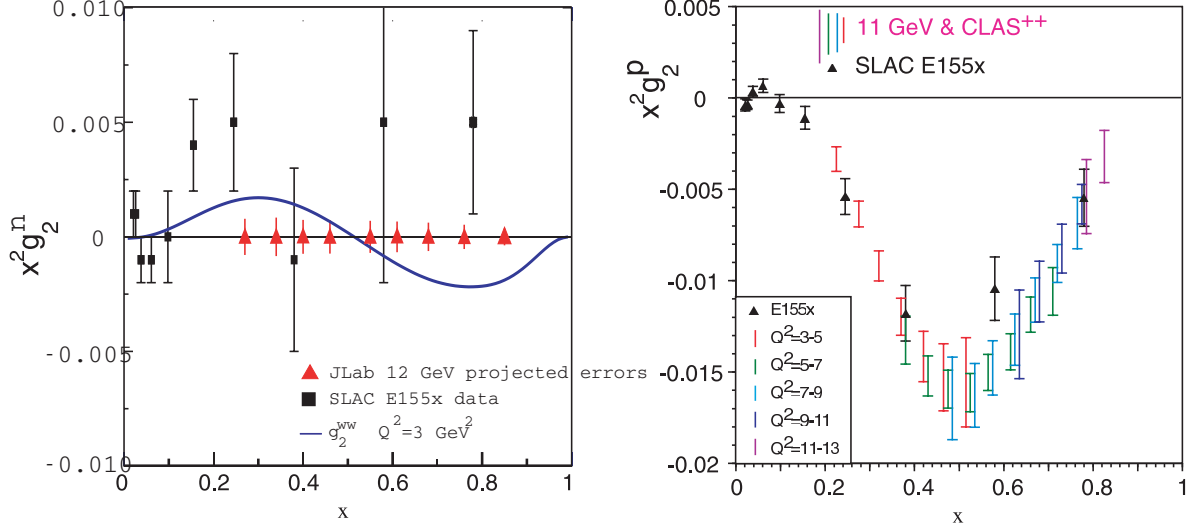


Figure 64: Projected errors for  $x^2 g_2(x)$  for the neutron (left panel) and proton (right panel) from 11 GeV JLab measurements, compared with values from the SLAC experiment E155x.

the nucleon. On the other hand, considerable progress has been made recently in calculating matrix elements from first principles in lattice QCD. The lattice results from the QCDSF Collaboration [Go01a] are in agreement with the better determined proton  $d_2^p$ , but underestimate somewhat the neutron data. For the neutron, the  $d_2^n$  lattice results have an error that is significantly smaller than the current experimental error, and will become even smaller with the next generation of lattice simulations which will be performed over the next 2–3 years [Ne00].

A 12 GeV JLab experiment will make a factor of 10 statistical improvement in the error on  $d_2^n$ , by taking advantage of the high-luminosity 11 GeV polarized beam and the large-acceptance MAD spectrometer. Precision data for  $g_1^n$  and  $g_2^n$  will be obtained by direct measurements of longitudinal and transverse polarized cross sections in the range  $0.15 < x < 0.9$  at fixed  $Q^2 = 3 \text{ GeV}^2$ , with special focus on the high- $x$  region which dominates  $d_2$ . Projected statistical errors for  $x^2 g_2^n$  and  $d_2^n$  are shown in Figs. 64 and 65. The expected statistical error on  $d_2^n$  for this experiment is  $2.5 \times 10^{-4}$  for 100 hours of beam. Precision data are also planned at fixed  $x$  values for several values of  $Q^2$  in the range  $2 \leq Q^2 \leq 10 \text{ (GeV/c)}^2$ .

Installation of a transversely polarized target in Hall B will improve significantly on the existing SLAC data for the proton  $g_2^p$  structure function, with smaller error bars and finer binning in  $x$  and  $Q^2$ . This will allow the  $Q^2$  dependence of  $g_2^p$  to be studied and  $d_2^p$  extracted with three times smaller statistical error than the current world data allow. In addition, the proposed 6 GeV experiment in Hall C with the BETA detector [Wa03] could improve the SLAC result by a factor of 2–3 in both statistical precision and resolution in  $x$ , which will improve even more at 11 GeV.

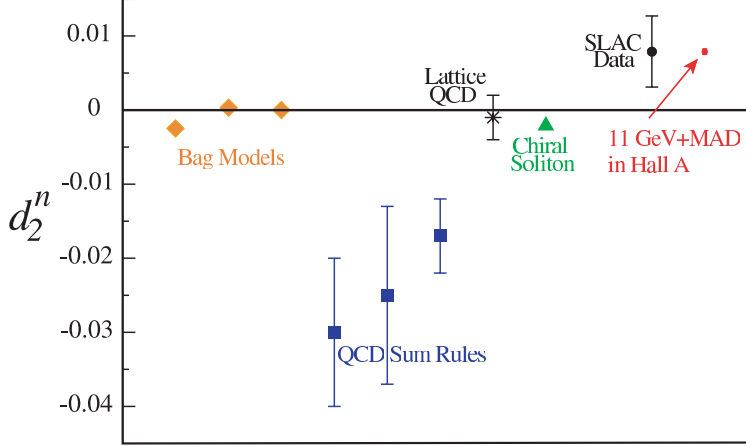


Figure 65: Neutron twist-3 matrix element  $d_2^n$ : projected error from a 12 GeV JLab measurement in Hall A compared with existing data from SLAC, and several theoretical calculations.

**Semi-inclusive scattering** The production of mesons ( $M$ ) in semi-inclusive electron scattering,  $eN \rightarrow e' M X$ , offers a tremendous opportunity for determining the spin and flavor structure of the nucleon, as well as extracting information on new distributions which are not accessible in inclusive scattering. At asymptotic energy the scattering and production mechanisms factorize into a parton distribution function and a quark  $\rightarrow$  meson fragmentation function,

$$\frac{d\sigma}{dx dz} \propto \sum_q e_q^2 q(x) D_q^M(z), \quad (32)$$

where  $D_q^M(z)$  gives the probability that a quark  $q$  hadronizes into a meson  $M$  with a fraction  $z$  of the virtual photon energy. The extent to which this factorization applies at lower energy is an open question (see the material on semi-inclusive duality below). Nonetheless, confirmation of factorization at lower energies would open the way to an enormously rich semi-inclusive program, allowing unprecedented spin and flavor decomposition of quark distributions.

The probability that the observed meson originated from the struck quark, and not from a  $q\bar{q}$  pair produced from the vacuum, can be maximized by restricting measurements to large values of  $z$ . In this way high momentum fragments of deep inelastic nucleon breakup statistically tag the underlying quark structure. On the other hand, semi-inclusive cross sections at large values of  $x$  and  $z$  are small, requiring the highest possible luminosity, while the detection of two particles in the final state requires an electron beam with a high duty cycle. These factors make the 12 GeV Upgraded CEBAF a unique facility for studying semi-inclusive electroproduction reactions.

The large  $x$  behavior of spin dependent distributions dictates the  $x \rightarrow 1$  limit of the inclusive polarization asymmetries  $A_1^n$  and  $A_1^p$ . As discussed above, measurements of the asymmetries  $A_1^n$  and  $A_1^p$  at  $x \leq 0.8$  at 11 GeV will enable one to clearly establish where the deviations from SU(6) symmetry appear. On the other hand, nonperturbative models which incorporate SU(6) breaking typically lead to a suppression of  $d$  quarks relative to  $u$  [Cl73, Ca75a, Is99]. Consequently, these



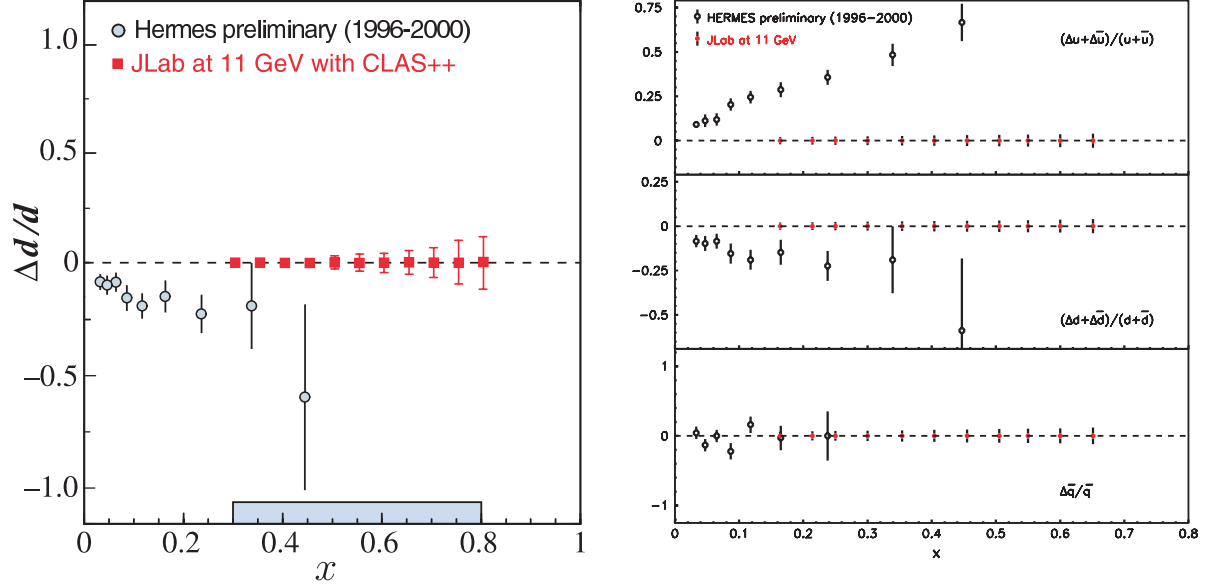


Figure 66: Projected errors for the ratio of polarized to unpolarized quark distribution functions at a 12 GeV CEBAF, compared with HERMES data. *Left panel:*  $d$  quark ratio from an 80 day measurement in Hall B. The solid curve uses wavefunctions from a constituent quark model, while the dashed uses pQCD-constrained fits to the world data. *Right panel:* Ratios for various flavors from 1000 hours of beam time on polarized  $\text{NH}_3$  and  $^3\text{He}$  targets in Hall A. Error bars are statistical only.

models also predict that  $A_1^{n,p} \rightarrow 1$  as  $x \rightarrow 1$ , making it difficult to discriminate for instance between the broken  $\text{SU}(6)$  and hadron helicity conservation (HHC) behaviors from inclusive measurements alone. This is unfortunate, since the behavior of the polarized  $d$  quark distribution is predicted to be qualitatively different:  $\Delta d/d \rightarrow 1$  in HHC, but  $\Delta d/d \rightarrow -1/3$  in broken  $\text{SU}(6)$  with hyperfine interactions, so that even the sign is unknown. By tagging  $\pi^\pm$  mesons in the final state at large  $z$ , one can disentangle the individual  $\Delta u$  and  $\Delta d$  distributions at large  $x$ . There are indications from HERMES data of a positive trend for  $\Delta u/u$  with increasing  $x$ , while  $\Delta d/d$  appears to stay below zero out to  $x \sim 0.4$ , as shown in Fig. 66. Semi-inclusive data will enable measurements to be extended to  $x \sim 0.8$ , and definitively test whether  $\Delta d$  stays negative, or turns positive as expected from HHC arguments.

The expected precision of the extracted  $\Delta d/d$  ratio for an 80 day measurement in Hall B is indicated in Fig. 66 (left panel). Using the MAD spectrometer in Hall A, the projected statistical errors for the individual polarized to unpolarized quark distribution ratios are shown in Fig. 66 (right panel), compared with the HERMES data [Ac99]. The errors are based on 1000 hour measurements with polarized  $\text{NH}_3$  and  $^3\text{He}$  targets.

The semi-inclusive scattering on unpolarized nucleons could provide an independent check on the methods for  $d/u$  extraction discussed above. Detection of  $\pi^+$  or  $\pi^-$  mesons produced from a hydrogen target at large  $z$  would preferentially tag  $u$  and  $d$  quarks in the proton, respectively

[Me98].

In addition to determining the large- $x$  behavior of the valence  $u$  and  $d$  flavor distributions, measurement of semi-inclusive cross sections will also allow an accurate reconstruction of the spin and flavor dependence of the  $q\bar{q}$  sea. One of the most important and exciting discoveries of the past decade concerning the structure of the nucleon came with the observation that the sea quarks in the proton are not symmetric, but that there is a significant excess of  $\bar{d}$  antiquarks over  $\bar{u}$  in the proton [Am91, Ba94, Ac98, Ha98]. Naive expectations from gluon radiation into  $q\bar{q}$  pairs, which is the dominant process of sea quark creation at high  $Q^2$ , were that this perturbatively generated sea would be equally populated by  $u\bar{u}$  and  $d\bar{d}$  pairs. The large asymmetry observed between  $\bar{u}$  and  $\bar{d}$  highlighted the crucial role played by nonperturbative physics in both the valence and sea structure of the proton. Many theoretical explanations of this effect focused on the role of dynamical chiral symmetry breaking and the associated pion cloud of the nucleon [Ku98, Sp98, Th00, Ga01].

On the other hand, the magnitude and  $x$  dependence of the  $\bar{d} - \bar{u}$  asymmetry is more difficult to understand from QCD, especially at larger  $x$  ( $x \sim 0.2 - 0.4$ ), where the asymmetry becomes smaller and the error bars larger. In particular, the downward trend of the  $\bar{d}/\bar{u}$  ratio observed in the Fermilab E866 Drell-Yan data [Ha98] in Fig. 67 presents a serious challenge to theoretical models [Pe98], and other mechanisms may be necessary to accurately describes the shape of the asymmetry [Me99]. For example, because there are more valence  $u$  quarks than  $d$  in the proton, the Pauli Exclusion Principle would suggest that creation of  $u\bar{u}$  pairs should be suppressed relative to  $d\bar{d}$  [Fi77, Sc91].

A study of the light quark sea flavor asymmetry in the high  $x$  region with precision significantly exceeding the Drell-Yan measurement is achievable with a 12 GeV CEBAF. Though the incident electron energy is lower than that available at HERMES, the larger scattering angle allows an exploration of a similar  $Q^2$  range with higher precision. The projected uncertainties in the extraction of  $\bar{d}/\bar{u}$  are shown in Figure 67, for a seventy-day measurement period in Hall A, compared with the existing Drell-Yan data.

To fully disentangle the pion cloud and Pauli blocking effects on the antiquark distributions one needs to consider the spin dependence of the  $\bar{d} - \bar{u}$  asymmetry. Since pions have spin zero, scattering from a virtual pion cloud of the nucleon will not contribute to the helicity distributions  $\Delta\bar{u}$  or  $\Delta\bar{d}$ . Effects of quark antisymmetrization, on the other hand, are expected to be as large or larger in the spin-dependent asymmetry  $\Delta\bar{u} - \Delta\bar{d}$  as in the unpolarized  $\bar{d} - \bar{u}$  asymmetry [Di97, Gl00, St02]. Preliminary data from HERMES [We02] shows that the distributions  $\Delta\bar{d}$  and  $\Delta\bar{u}$  are rather small, and consistent with zero within overall errors, suggesting that the dominant mechanism underlying the generation of the proton sea may be that associated with dynamical chiral symmetry breaking [Do77, Ro79, St97]. However, the errors on the difference  $\Delta\bar{u} - \Delta\bar{d}$ , which is most sensitive to nonperturbative effects such as meson clouds, are rather large, and better quality data in the range  $0.1 < x < 0.4$  would be crucial for drawing firm conclusions. The quality of the data on the antiquark polarization attainable with a 11 GeV beam in Hall A is illustrated in Fig. 66 (right

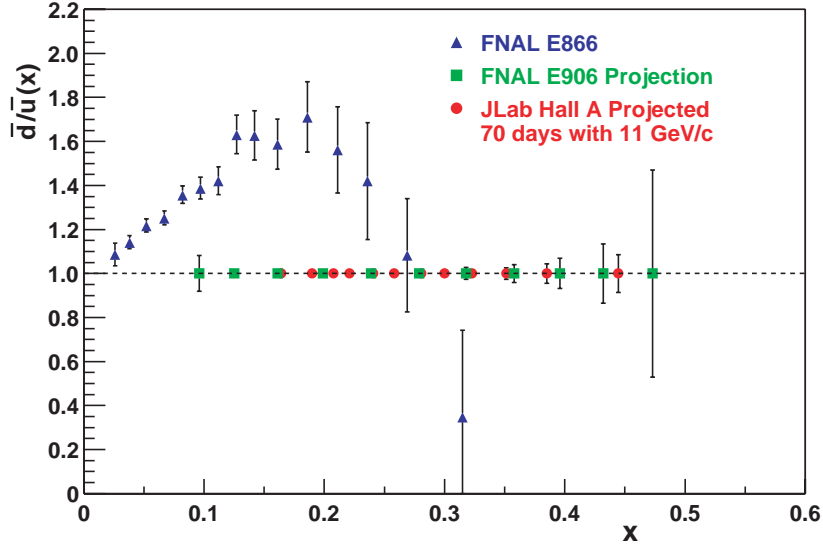


Figure 67: The projected precision of  $\bar{d}/\bar{u}$  extractions assuming factorization with strict  $Q^2$  and  $z$  cuts, and an 11 GeV JLab beam energy in Hall A, compared with the FNAL E866 Drell-Yan [Ha98] measurements. Statistical uncertainties are shown only.

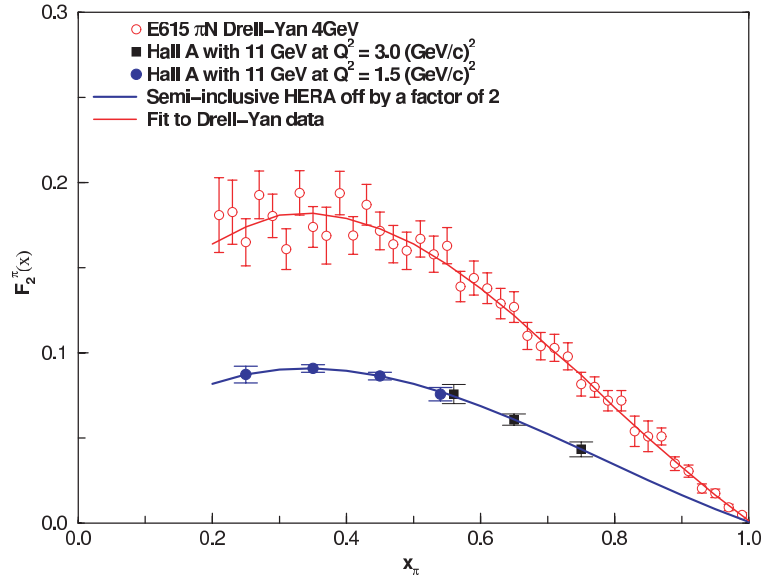


Figure 68: Simulated data for the pion structure function at  $Q^2 = 1.5$  (filled circles) and  $3.0$   $(\text{GeV}/c)^2$  (squares) using the MAD spectrometer in coincidence with a low energy neutron detector at 11 GeV beam in Hall A, for a 25-day run period. Existing data from the Fermilab E615 experiment [Co89] are shown for comparison (open circles).

panel). Clearly, measurement of semi-inclusive production of  $\pi^\pm$  with unpolarized and polarized electron beam and target at 11 GeV JLab kinematics will significantly improve our knowledge of the  $x$  dependence of both the flavor asymmetry  $\bar{d}/\bar{u}$  and the polarization asymmetries  $\Delta\bar{u}$  and  $\Delta\bar{d}$ .

Finally, a more direct test of the role of the pion cloud in spin-flavor asymmetries can be made by measuring the structure function of the pion in the semi-inclusive charge exchange reaction,  $ep \rightarrow en\pi^+$ , a technique that was recently used at HERA at small  $x$  [Le02]. These measurements revealed that the  $q\bar{q}$  sea in the pion was about 1/2 that which was expected based on current theoretical models. With the 12 GeV upgrade at Jefferson Lab measurements could be made in the valence region, and compared with existing pion Drell-Yan data, which would verify the technique used by the HERA experiments to measure the pion structure function. The key to the experimental technique is to measure the low-energy outgoing neutron in coincidence with the scattered electron. A simulation of a possible experiment in Hall A with the 11 GeV beam and the MAD spectrometer with an unpolarized beam is shown in Fig. 68.

### 2.B.3 The Generalized Parton Distributions as Accessed via Deeply Exclusive Scattering

**The Physics of the Generalized Parton Distributions** In the past five decades of electron-nucleon scattering, experiments dedicated to studying the substructure of the nucleon have mainly focused either on the measurements of electromagnetic form factors in exclusive processes or on measurements of deep inelastic structure functions in inclusive processes. Inelastic exclusive reactions, such as pion or eta electroproduction, played a role mostly in the study of nucleon resonances [Bu03]. This situation, however, is now changing. The 12 GeV upgrade at Jefferson Lab allows a first dedicated study of a whole new class of hard exclusive processes which are capable of probing the quark-gluon dynamics of the nucleon in unprecedented details.

Elastic processes measure the electromagnetic form factors as a function of the invariant momentum transfer  $t = -Q^2$ . The physical interpretation of the form factors is the simplest when the nucleon travels at the speed of light or in the infinite momentum frame (IMF): the Fourier transformation of the charge form factor with respect to  $t$  yields a two-dimensional distribution of electric charges in the transverse plane. Inclusive processes probe deep inelastic structure functions which again have a simple interpretation in the IMF: they are quark density distributions as a function of longitudinal momentum fraction  $x$ . Taking together, form factors and deep inelastic structure functions measure the proton structure in two orthogonal sub-spaces. While it is clear that the two pictures must be part of the big one, the actual framework unifying the two has only been discovered recently with the Generalized Parton Distribution (GPD) functions [Mu94, Ji97, Ra97]. The GPDs encode both the transverse spatial dependence and the longitudinal momentum dependence. A few review articles on the subject can be found in Ref. [Ji98, Go01b, Ra01].

A generalized parton distribution depends on three kinematic variables: the invariant momen-

tum transfer to the proton  $t = (p - p')^2$  just like the form factors do, the momentum transfer projected along the light cone:  $\xi = (p - p')^+ / P^+ \rightarrow x_{\text{Bj}} / (2 - x_{\text{Bj}})$  where  $P = (p + p') / 2$ , and finally the quark momentum fraction  $x$  as in the Feynman parton distributions. At the twist-2 level, for each quark species there are eight GPDs. The experiments at JLab can make a detailed study of at least four of them:

- $H(x, \xi, t)$ ,  $\tilde{H}(x, \xi, t)$  the helicity conserving and helicity flip, respectively, matrix elements of the vector current; and
- $E(x, \xi, t)$ ,  $\tilde{E}(x, \xi, t)$ , the helicity conserving and helicity flip, respectively, matrix elements of the axial-vector current.

The other four are related to the transverse polarization of quarks and are still under theoretical investigation. The first moments of the GPDs in  $x$  are related to the proton's form factors [Ji97],

$$\begin{aligned} \int dx H(x, \xi, t) &= F_1(t), & \int dx E(x, \xi, t) &= F_2(t), \\ \int dx \tilde{H}(x, \xi, t) &= G_A(t), & \int dx \tilde{E}(x, \xi, t) &= G_P(t) \end{aligned} \quad (33)$$

where  $F_1(t)$ ,  $F_2(t)$ ,  $G_A(t)$  and  $G_P(t)$  are Dirac and Pauli form factors of the vector current, and pseudo-vector and pseudo-scalar form factors of the axial current, respectively. At  $t = \xi = 0$ , the GPDs  $H$  and  $\tilde{H}$  reduce to the quark momentum  $q(x)$  and helicity distributions  $\Delta q(x)$ ,

$$\begin{aligned} H(x, 0, 0) &= q(x)\theta(x) - \bar{q}(-x)\theta(-x) \\ \tilde{H}(x, 0, 0) &= \Delta q(x)\theta(x) + \Delta \bar{q}(-x)\theta(-x) \end{aligned} \quad (34)$$

The forward limit of  $E(x, \xi, t)$  is related to the angular momentum distributions of partons (see below).

As an example of the GPDs, a model of  $H(x, \xi, t)$  distribution with factorized  $t$ -dependence [Go01b] is shown in Fig. 69. At  $\xi = 0$ , we have the usual parton distribution, and thus at very small  $x$ , the distribution becomes singular. The distribution is negative at negative  $x$  because the antiquark distribution is positive. For non-zero  $\xi$ , the distribution in  $|x| > \xi$  is markedly different from that in  $|x| < \xi$ . The former is a smooth continuation of the ordinary parton distributions, whereas the latter describes the amplitude for the proton to emit or absorb a meson, mimicking the meson light-cone distribution amplitude.

The joint probability distribution, represented by the GPDs, contains much more of the physics of partons than forward parton distributions and form factors. Mapping out the GPDs will allow,

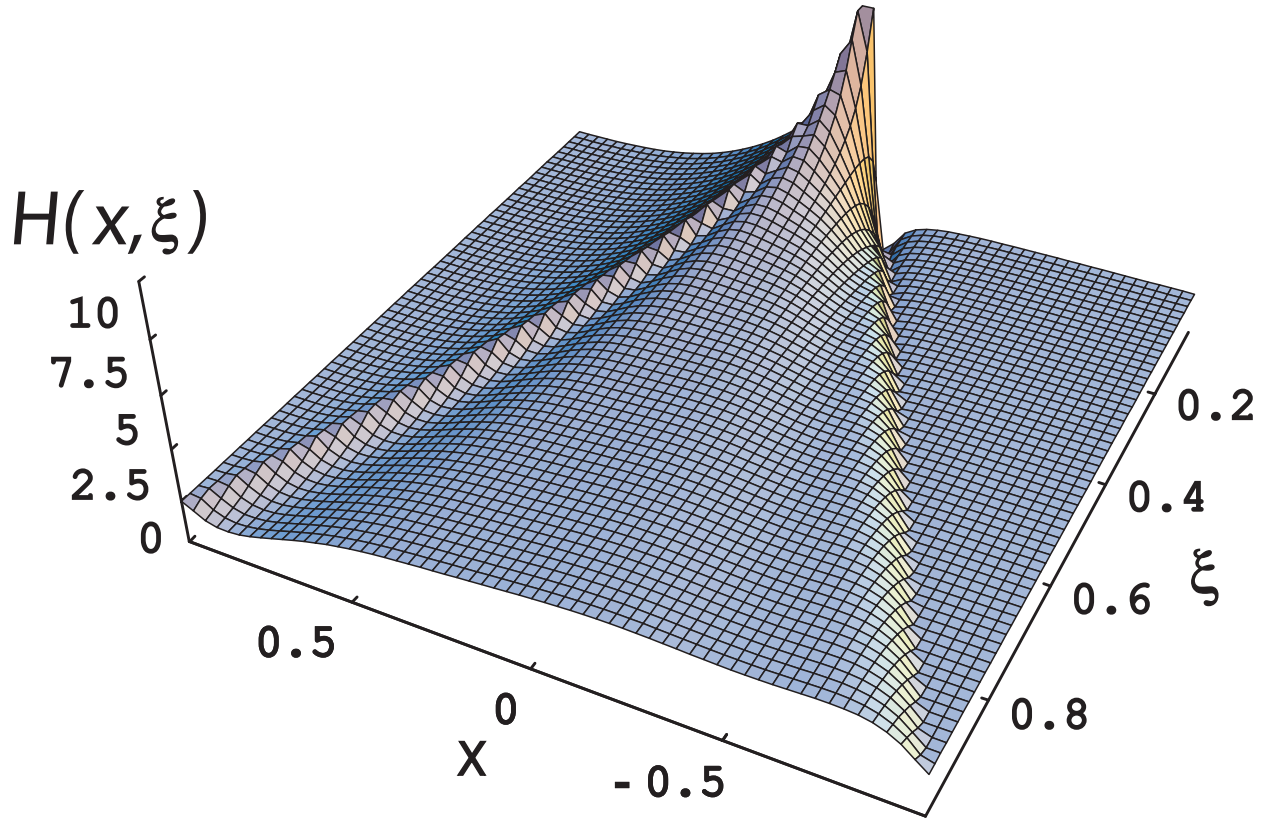


Figure 69: Two dimensional image of  $H(x, \xi, t)$  from a model with factorized  $t$ -dependence. The dramatic change in the shape of the surface reflects the change in the underlying physics. As  $\xi$  increases, the correlations between the quarks and anti-quarks increase leading to meson-like distributions at large  $\xi$ .

for the first time, to construct “tomographic” images of the nucleon’s charge and quark helicity distributions in transverse impact parameter space [Be02, Bu00, Ra02], in some analogy to the way tomographic images of macroscopic objects are assembled. Some highlights of the *new physics* involved in GPDs are as follows:

**Spin Structure of the Nucleon** In the simple quark model of Gell-Mann and Zweig, the spin of the nucleon comes just from the spin of the three valence quarks which carry no orbital angular momentum. This picture has been challenged recently by the data from polarized deep-inelastic scattering. Through a global analysis of the EMC, SMC, E142, E143, E154, E155, and HERMES data, it has been found that the fraction of the nucleon spin carried by the quark is about 25%, falling far short of the quark model prediction [Fi01]. The remaining part of the nucleon spin must be carried by the quark orbital motion and the gluon angular momentum.

Indeed, a quark having a momentum fraction  $x$  also carries some angular momentum. The angular momentum distribution  $J_q(x)$  can be obtained from the GPDs [Ho99]:

$$J_q(x) = \frac{1}{2}x[H_q(x, 0, 0) + E_q(x, 0, 0)] , \quad (35)$$

which involves the forward limit of  $E$ . After integrating over the momentum fraction, we have the fraction of the nucleon spin carried by quarks [Ji97]

$$J_q = \frac{1}{2} \int_{-1}^1 x dx [H_q(x, \xi, 0) + E_q(x, \xi, 0)] . \quad (36)$$

Given the result of the polarized DIS, an experimental determination of  $J_q$  allows extraction of the quark orbital angular momentum. Here an extrapolation of the GPDs from finite  $t$  to the  $t = 0$  point is needed.

**Gravitational Form Factors** If gravitons were available in the laboratory just like photons, they could be used to measure the mass and momentum distributions in the nucleon. [The notion of these distributions is usually considered only for macroscopic systems.] With GPDs, one can obtain the gravitational form factors without graviton scattering! Indeed, the second  $x$ -moment of the GPDs [Ji97a],

$$\begin{aligned} \int dx x H(x, \xi, t) &= A(t) + \xi^2 C(t) , \\ \int dx x E(x, \xi, t) &= B(t) - \xi^2 C(t) , \end{aligned} \quad (37)$$

where  $A(t)$ ,  $B(t)$  and  $C(t)$  are gravitational form factors. In the infinite momentum frame, the Fourier transformation of  $A(t)$  gives the mass distribution in the transverse plane and that of

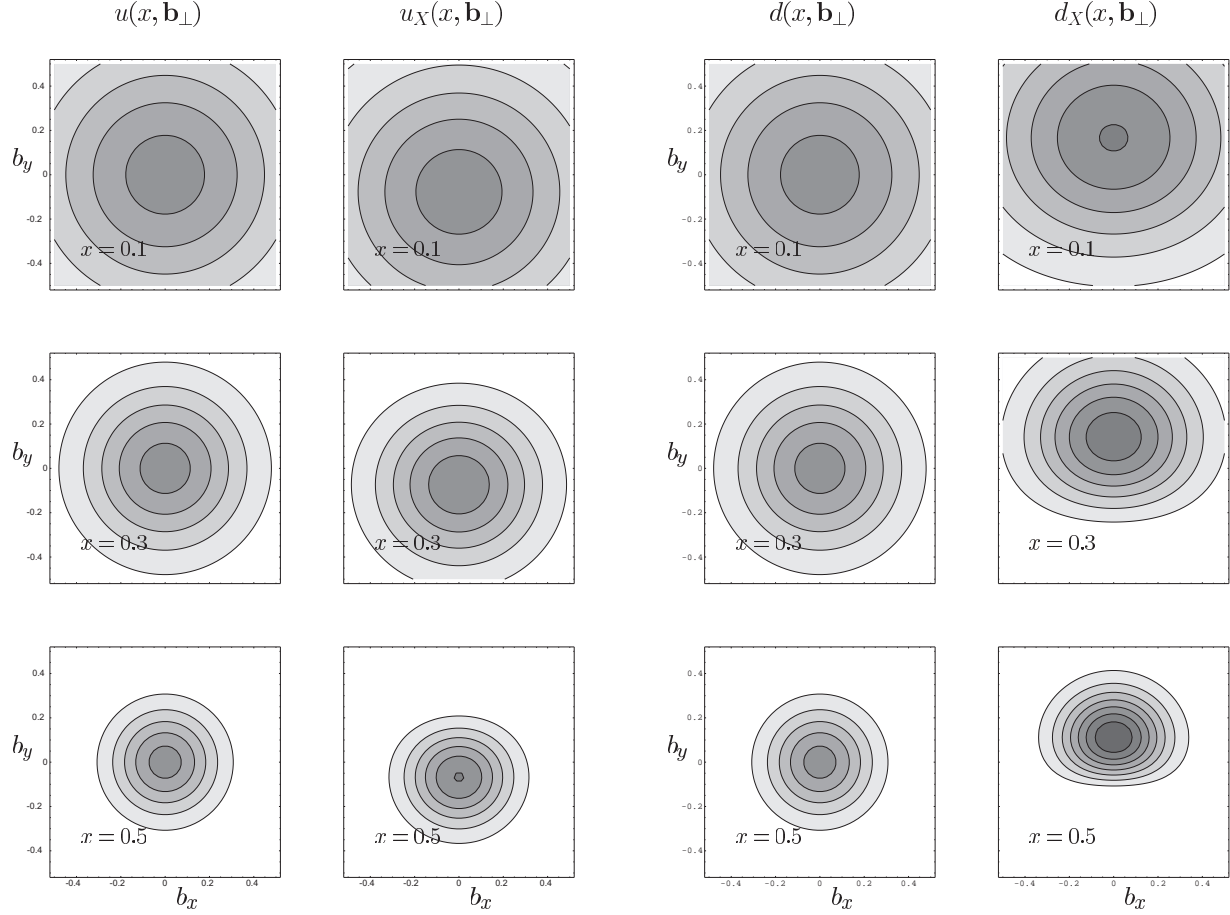


Figure 70: Model “tomographic” images of quarks in the transverse plane in an unpolarized and polarized nucleon in the IMF. The left panels show the  $u$  quark distribution at fixed  $x$  in unpolarized and polarized proton, and the panels on the right show the corresponding images for the  $d$  quarks. The right columns in each panel show the quark distributions in a transversely polarized proton.  $u$  and  $d$  quarks exhibit a strong and opposite spatial asymmetry generating a strong spin-flavor polarization, especially prominent at high  $x$ .

$t(A(t) + B(t))$  the momentum distribution. It would be very interesting to compare these distributions with electromagnetic charge and current distributions.

**“Tomographic” Images of the Nucleon** Knowledge of the  $x$  and  $t$  dependence of GPDs for specific quark flavors provides the basis for the construction of a 3-dimensional representation of the proton’s quark content in the transverse plane and in longitudinal momentum space [Bu00, Be02, Ra02]. This may be seen in some analogy to the way images of macroscopic objects can be assembled in tomography.

In GPDs, we expect that  $t$  and  $x$  dependences are correlated. The physical significance of these correlations at finite  $\xi$  is discussed in [Di02]. At  $\xi = 0$ , a particularly simple interpretation



is possible [Bu00]. A simple model of  $H$ , incorporating the general properties of the correlations between  $t$  and  $x$  is as follows [Bu00].

$$H_f(x, 0, t) \sim q_f(x) e^{-a|t|(1-x)\ln\frac{1}{x}}$$

where  $q_f(x)$  is the forward parton distribution of flavor  $f$  and  $a$  is a scale parameter characterizing the transverse size. Figure 70 illustrates these correlations in this model. The graphs show a strong correlation between the  $t$ -dependence (its Fourier conjugate is the transverse size, or impact parameter  $b_\perp$ ) and the  $x$ -dependence (longitudinal momentum). According to the uncertainty principle,  $t$  is related to  $b_\perp$  approximately through  $b_\perp \sim 1/\sqrt{-t}$ . For a spin-averaged nucleon, the panels show the dramatic change in transverse profile as a function of  $x$ , while the image remains isotropic.

For small  $x$ , the proton has a large transverse size, and it becomes very dense at large  $x$ . A strong spatial anisotropy is observed for the quark density in a polarized proton. The tomographic image shows the very strong spin-flavor polarization between the  $u$  quarks and  $d$  quarks for a proton polarized in the transverse plane, with the  $u$  and the  $d$  quark spin distribution spatially separated from each other, especially in the valence quark domain at high  $x$ . This regime can be accessed in deeply exclusive processes at JLab beginning at 6 GeV, and will be more fully accessible after the 12 GeV upgrade. Thus, *the knowledge of GPDs will provide the most fundamental insights into the internal quark-gluon dynamics of the nucleon, unimaginable just five years ago.*

**Modeling GPDs** Theoretical studies of the GPDs fall in two categories. In the first category, the nucleon models are used to calculate the GPDs. For example, the MIT bag model was used first to calculate GPDs [Ji97a]. Later the chiral soliton model was also used to compute the new distributions [Go01b, Pe00a]. In these calculations, the constraints on the GPDs are automatically satisfied. In the second category, GPDs are parameterized and the parameters are fitted by the constraints of the GPDs from the elastic form factors and parton distributions [Go01b]. Moreover, the moments of the GPD as a function of  $\xi$  must satisfy the polynomial condition [Ji98, Ji97a]. This later condition can be satisfied if one models the double distributions directly [Ra01, Ra99]. Additional constraint on the GPDs come from bounds derived from various inequalities [Po02].

**Probing GPDs Through 12 GeV Upgrade** One of the striking findings associated with GPDs is that they can be measured through a new class of "hard" exclusive processes: Deeply Virtual Compton Scattering (DVCS) and Deeply Virtual Meson Production (DVMP), both are part of deep inelastic scattering with special exclusive final states [Ji97, Ra97, Co97]. The basis for getting access to GPDs is the "handbag" mechanism for deeply virtual exclusive process shown in Fig.71. The electron knocks a quark out of the proton by exchanging a deeply virtual (massive) photon. The quark then emits a high energy photon and is put back into the proton (DVCS). Alternatively, a  $q\bar{q}$  pair is created, and a quark is returned into the proton while the  $\bar{q}$  recombines with the struck quark to form a meson. At sufficiently high energy and virtuality of the exchanged photon (Bjorken

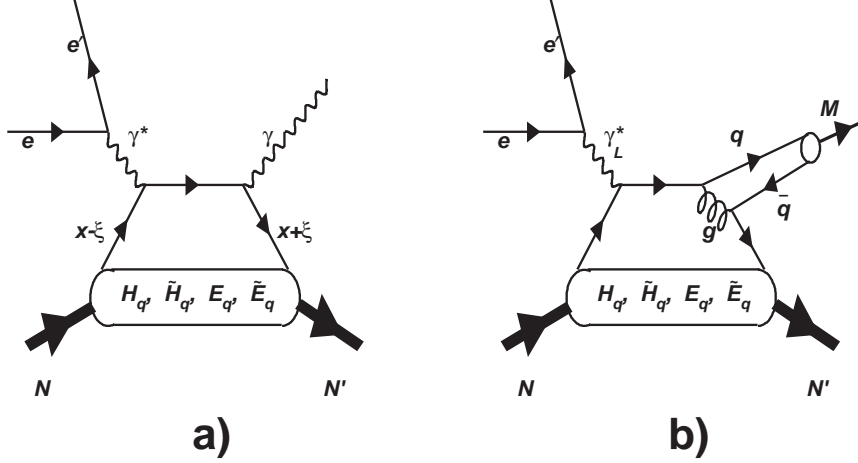


Figure 71: Representative handbag diagrams for deeply virtual Compton scattering a), and for deeply virtual meson production b).

regime) these hard processes can be described by perturbative QCD, and the cross section can be used to extract the “soft” information of the nucleon which is just the GPDs.

In the handbag approximation the cross sections for DVCS and for meson production at fixed  $t$  follow a  $1/Q^4$  and  $1/Q^6$  dependence, respectively. Predicted cross sections are shown in Fig. 72 for deeply virtual productions of photons, pseudoscalar mesons, and vector mesons at  $t = t_{min}$  [Go01b].

In the scaling regime, the production of photons will dominate over the production of  $\pi^0$ 's and  $\eta$ 's already at relatively low  $Q^2$ , and become the dominant exclusive channel at very high  $Q^2$ . Due to the absence of any gluon propagator, DVCS is likely to enter the Bjorken regime at relatively low photon virtuality,  $Q^2$ . This expectation has to be quantified experimentally. Until recently, the main evidence in support of this expectation came from the CLEO data on the  $\gamma\gamma^*\pi^0$  transition form factor measurement [Gr98]. The pQCD predictions for  $F_{\gamma\gamma^*\pi^0} \sim 1/Q^2$  seem valid for  $Q^2 > 2 \text{ GeV}^2$ . With additional quark transverse momentum corrections, this limit may even be as low as  $1 \text{ GeV}^2$  (see Fig. 74).

The  $\gamma\gamma^*\pi^0$  vertex (for a virtual pion) can also be measured on a fixed-target machine, in which case it is just part of the DVCS amplitude corresponding to the  $\tilde{E}(x, \xi, t)$  GPD. Hence, CLEO data indicate that DVCS may be handbag dominated for  $Q^2$  as low as  $1 - 2 \text{ GeV}^2$ .

At the energies currently available at JLab, the DVCS process is masked by the more copious production of photons from the Bethe-Heitler (BH) process. However, using polarized electron beams allows to isolate the DVCS/BH interference term, which gives direct access to the imaginary part of the DVCS amplitude  $T^{DVCS}$ . The BH term depends only on the well known electromagnetic form factors, and is used here to “boost” the much smaller DVCS term which depends on the unknown GPDs. The asymmetry, which is due to the DVCS/BH interference term, has recently been measured at CLAS [St01] and at HERMES [Ai01]. Figure 73 shows the CLAS result. The

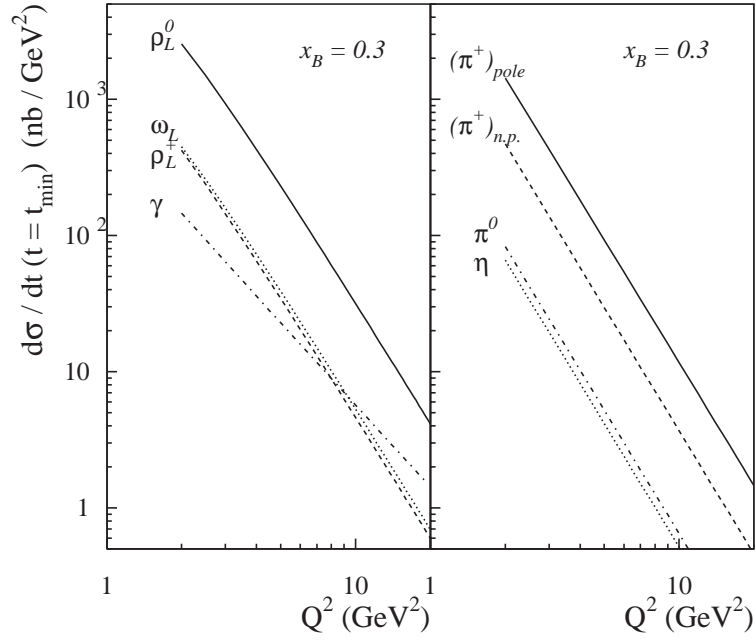


Figure 72: Scaling cross sections for the production of photons (DVCS), pseudoscalar mesons, and vector mesons. For meson production, the longitudinal cross sections are shown. For charged pion production there are two contributions, one related to the pion form factor(pole), the second one is due to knock out of quarks from the nucleon's quark core.

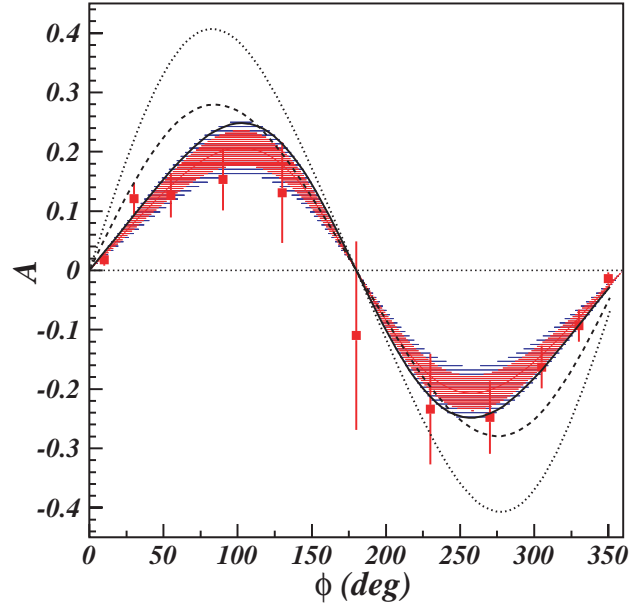


Figure 73: Beam spin asymmetry measured with CLAS. The shaded band shows the systematic uncertainties. The dashed and dotted curves are early predictions, while the solid curve is a more recent calculation.

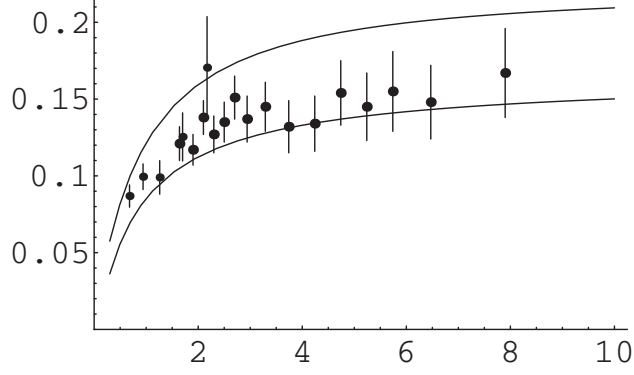


Figure 74: Comparison of data on the  $Q^2$  dependence of the  $\gamma\gamma^*\pi^0$  form factor with quark transverse momentum power-corrected pQCD predictions using asymptotic shape for the pion distribution amplitudes (lower-curve) and the Chernyak-Zhitnitsky model (upper curve). The quantity  $Q^2 \cdot F_{\pi^0\gamma\gamma^*}$  is plotted versus  $Q^2$  ( $\text{GeV}^2$ ).

asymmetry data have been predicted within the GPD framework using cross section data from HERA [Ad01, Sa03] measured at very small  $x_B$  values as input [Fr03]. Excellent agreement with the CLAS data is obtained in LO, lending strong support to the assumption of dominance of the handbag diagram.

Despite these recent successes, a direct demonstration of “scaling” of the DVCS amplitude is currently lacking, and is one of the objectives of two experiments currently in preparation at JLab. A set of new detectors for a complete measurement of all final state particles (e,  $\gamma$ , p) are currently under construction for CLAS and Hall A, which will also be used for DVCS experiments after the Upgrade. These experiments will directly measure the  $Q^2$  dependence of the  $\Im(T_{DVCS})$  as well as the  $\xi$  and  $t$  dependences.

**DVCS at JLab with 12 GeV Electrons** At the energies achieved with the Upgrade the DVCS and BH cross section become comparable in size in a broader kinematics domain, as shown in Fig.75. This will allow measurement not only of beam asymmetries but access to the DVCS cross section will also be possible. Beam asymmetries give access to the imaginary part of the DVCS amplitude, and are especially sensitive to the GPD  $H(\xi, \xi, t)$ . The DVCS cross section determines the  $x$ -integral, and is sensitive to the real part of a combination of GPDs, therefore providing independent information.

The energy Upgrade, in conjunction with the unprecedented luminosity that will be available, will allow a much broader kinematic coverage to be accessed in deeply virtual exclusive processes. Figure 76 shows the expected coverage in  $Q^2$  and  $x_B$ . Although the energy is lower for JLab experiments than for HERMES or COMPASS, the luminosity that can be utilized is several orders of magnitudes greater than for the higher energy experiments. This makes exclusive experiments at JLab competitive to the higher energy experiments in kinematics for which there is kinematic

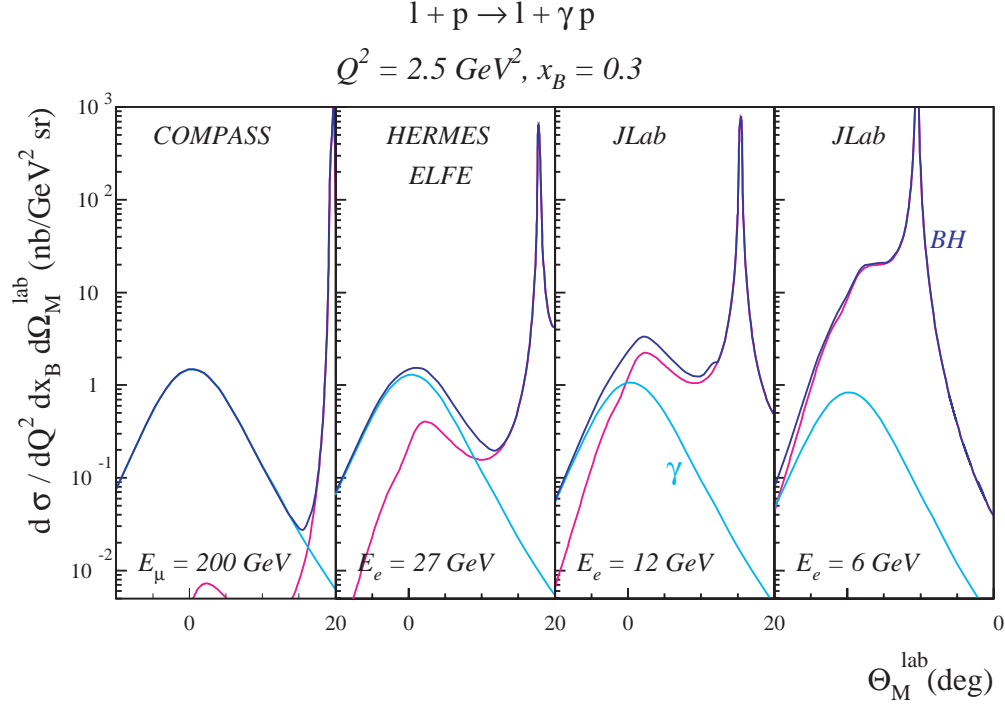


Figure 75: DVCS (cyan) and Bethe-Heitler (magenta) cross section for different beam energies.

overlap, i.e. at  $x_B = 0.1 - 0.3$ , and unique in the range  $x_B > 0.3$ . For processes requiring  $Q^2 > 4 - 5 \text{ GeV}^2$  to reach the Bjorken regime, e.g. vector mesons or pseudoscalar meson production, they can only be accessed efficiently with the high luminosities achievable with the 12 GeV Upgrade.

*DVCS using polarized electrons* Use of polarized beams at 11 GeV will be the most effective way of extracting information on the GPD  $H$  which is kinematically favored in the cross section difference. For  $Q^2 \gg -t, 4x_B^2 M^2$ , the beam helicity dependent cross section difference is [Be02a]:

$$\frac{\Delta^5 \sigma}{dx_B dQ^2 dt d\phi_e d\phi_{\gamma\gamma}} \rightarrow \frac{\sin \phi_{\gamma\gamma}}{-s' u'} \frac{\alpha^3}{\pi^2} \frac{2-y}{-t} \frac{\sqrt{1-x_B} \sqrt{t_{\min} - t}}{\sqrt{Q^2}} \left[ F_1(-t) H + \frac{x_B}{2-x_B} G_M(-t) \tilde{H} + \frac{t}{4M^2} F_2(-t) E \right], \quad (38)$$

where  $y = p \cdot q / p' \cdot k$  is the electron inelasticity and  $-s' u' = -4(q' \cdot k)(q' \cdot k')$  is the product of the  $\phi_{\gamma\gamma}$ -dependent BH propagators. The GPD's in Eq. 6 are  $H(\xi, \xi, t) - H(-\xi, \xi, t)$ ,  $E(\xi, \xi, t) - E(-\xi, \xi, t)$  and  $\tilde{H}(\xi, \xi, t) + \tilde{H}(-\xi, \xi, t)$ .

At small to modest values of  $x$  and  $t$  both  $\tilde{H}$  and  $E$  are kinematically suppressed, allowing direct access to the GPD  $H(\xi, \xi, t)$ . An operating luminosity of  $10^{35} \text{ cm}^{-2} \text{ sec}^{-1}$  is anticipated for CLAS<sup>++</sup>. Figure 77 shows the projected coverage of the beam spin asymmetry measurement. These measurements will produce high precision DVCS data for  $Q^2 = 1.0 - 7.5 \text{ GeV}^2$ ,  $x_B = 0.1 - 0.65$ , and  $-(t - t_{\min}) < 1.5 \text{ GeV}^2$ . Figure 78 shows the  $\sin \phi$  moments for the projected CLAS data; the beam helicity dependent cross section differences will be extracted simultaneously.

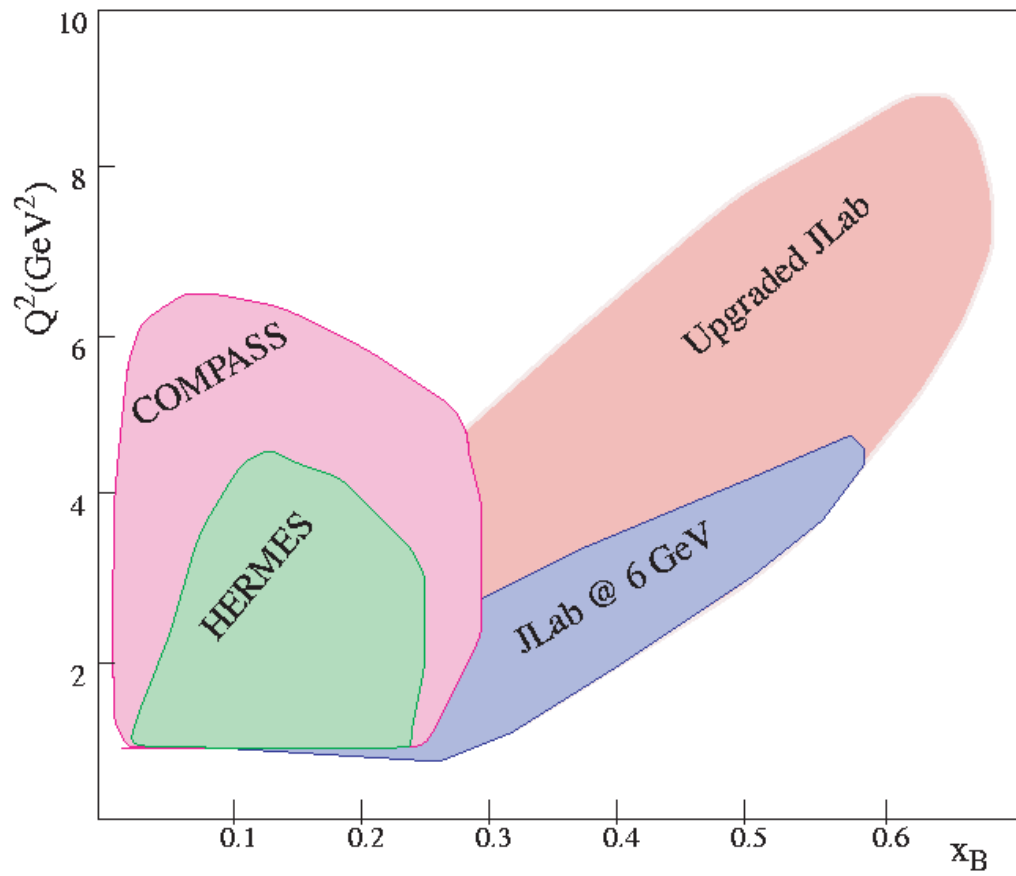


Figure 76: Kinematics coverage for deeply virtual exclusive processes for experiments at various laboratories. Not shown are the HERA experiments which cover a domain at very small  $x_B$  values.

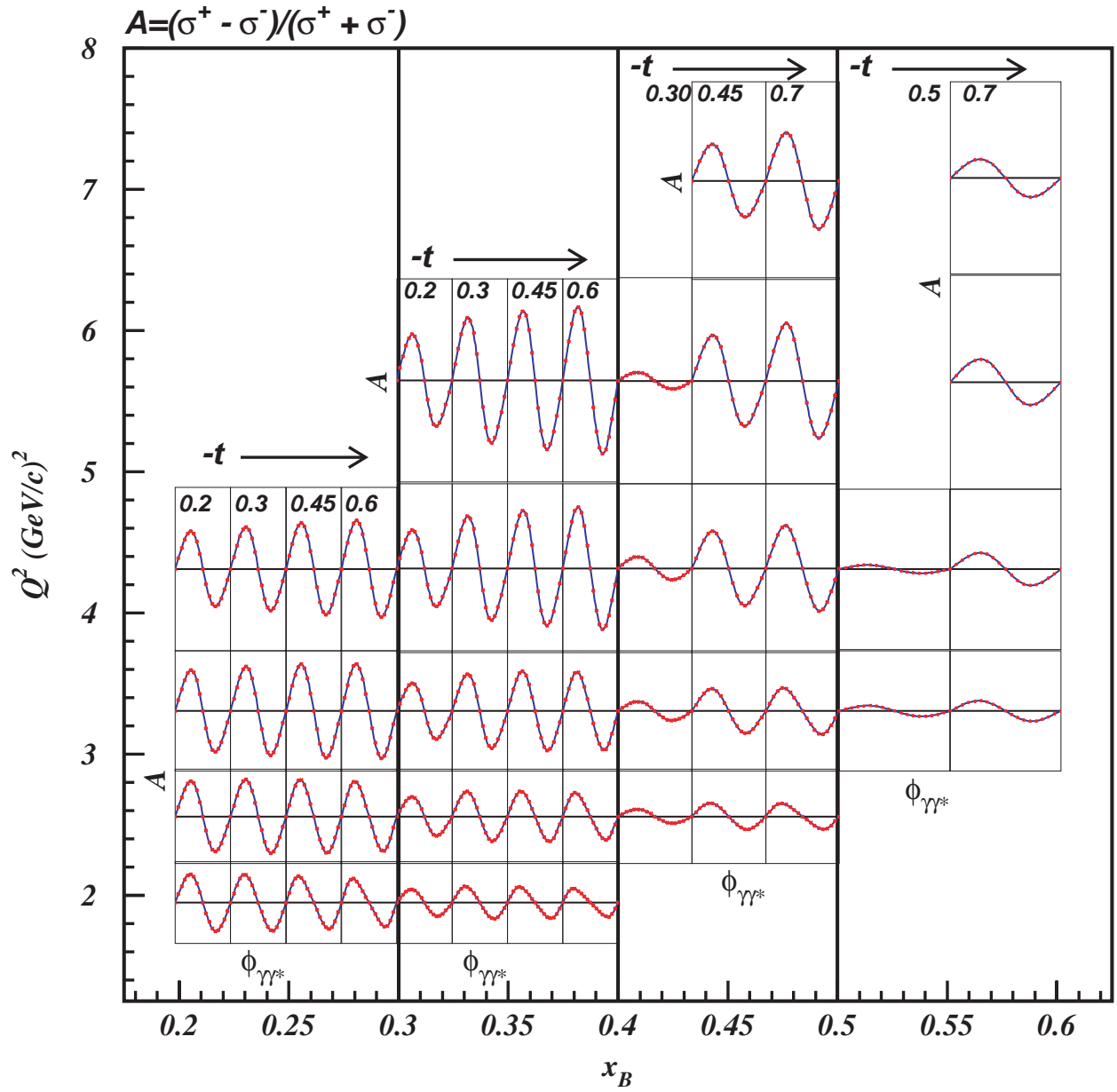


Figure 77: Kinematics for DVCS beam asymmetry measurements at 11 GeV. Only the bins for lower  $t$  values are shown. With CLAS<sup>++</sup> all bins will be measured simultaneously.

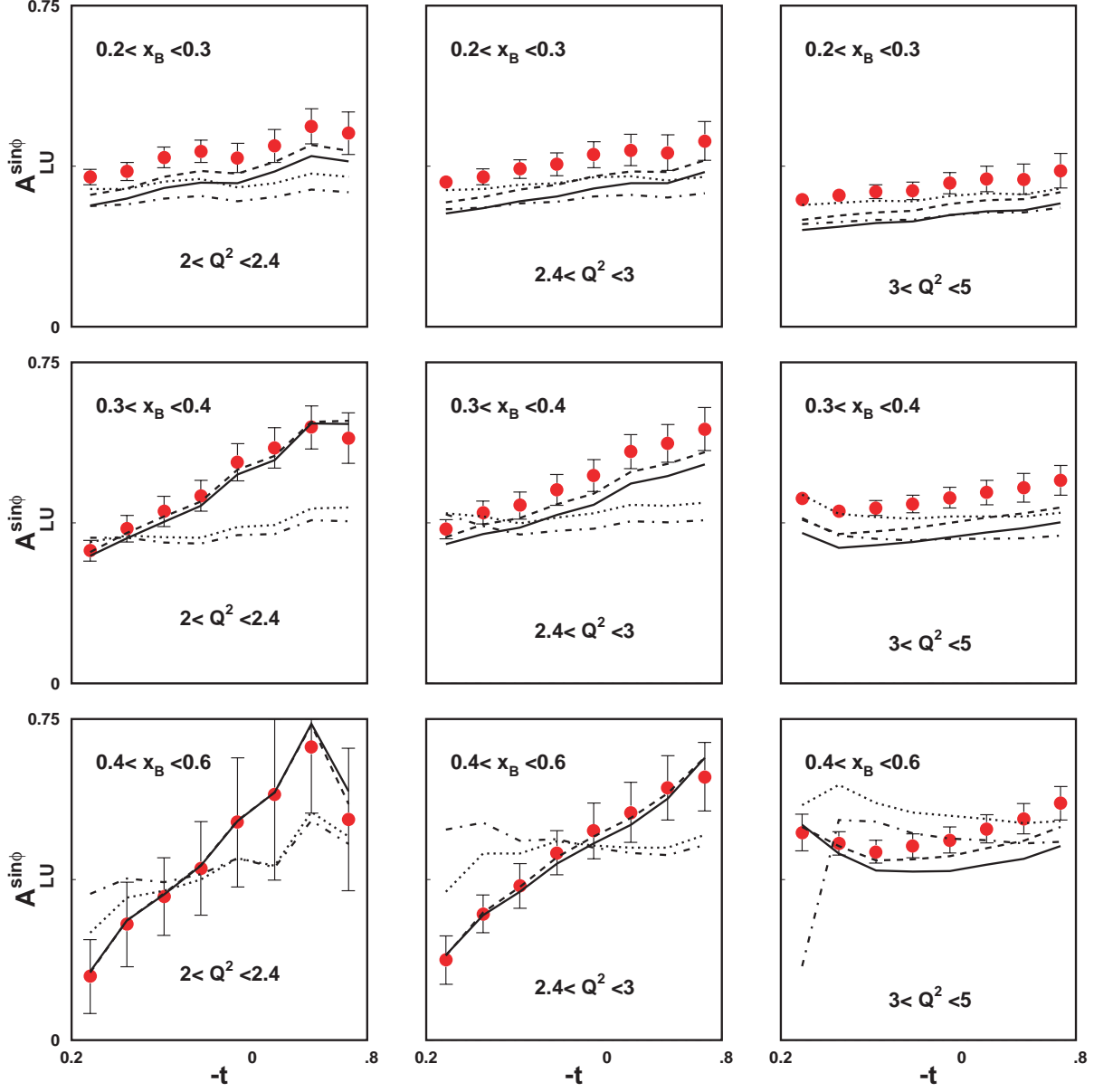


Figure 78: Projected data for the  $\sin\phi$  moment  $A_{LU}^{\sin\phi}$  of the DVCS/BH asymmetry. The curves and data points represent predictions of the GPD model with five different input parameter sets.



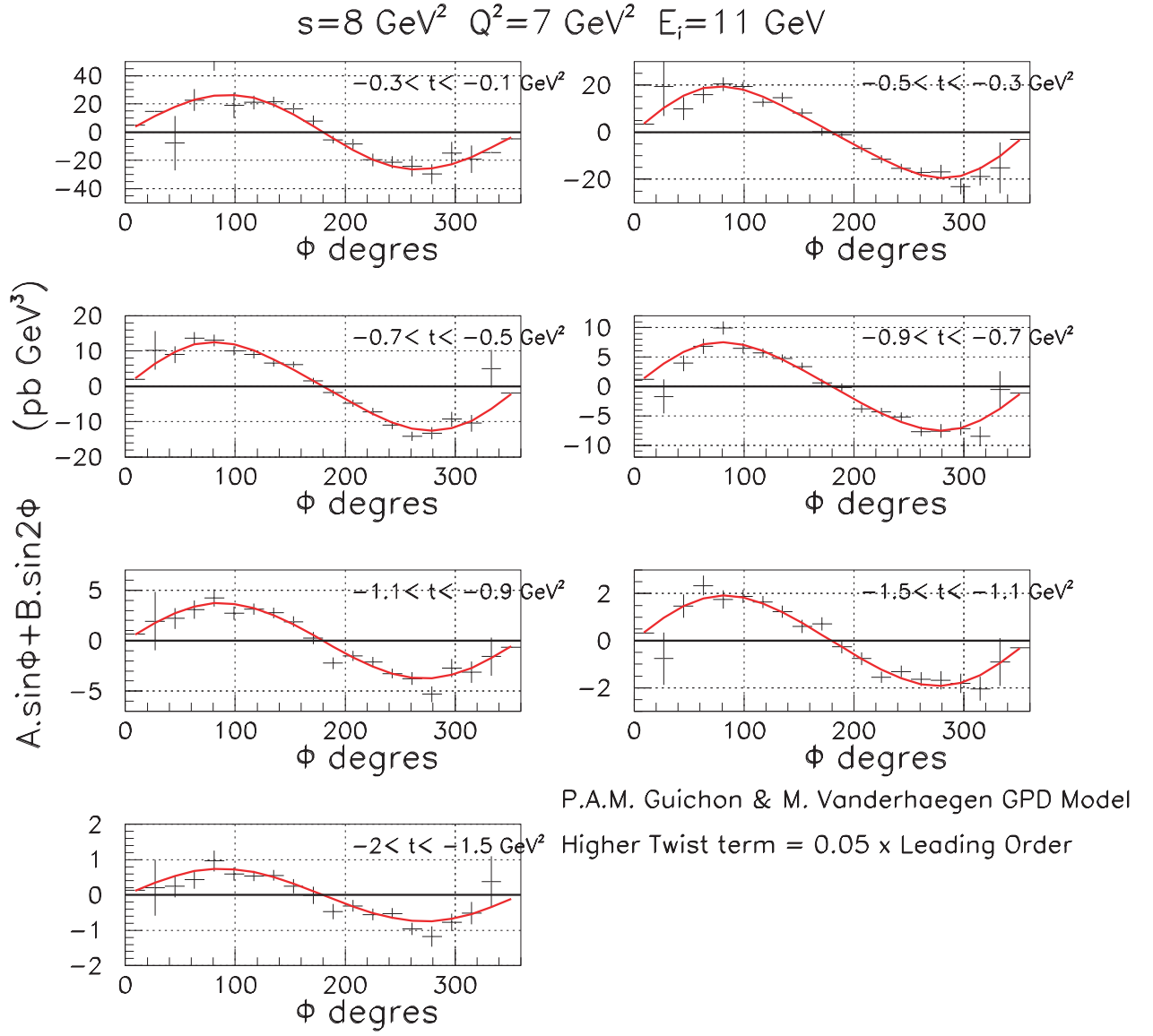


Figure 79: Projected Hall A data for the beam-helicity dependent cross section weighted by Bethe-Heitler denominator:  $-(k \cdot q')(k' \cdot q')\Delta\sigma$  at  $Q^2 = 7 \text{ GeV}^2$ .

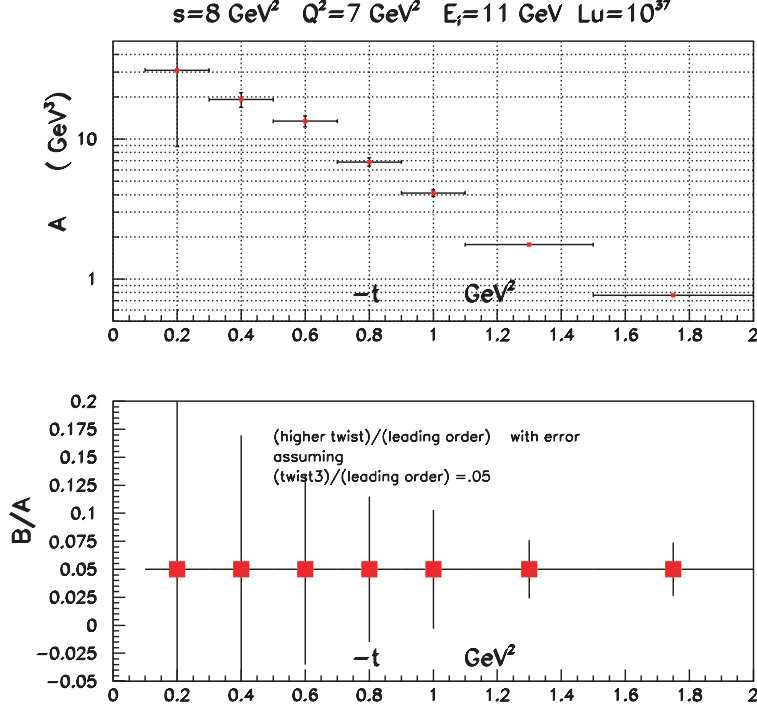


Figure 80: Projected results for the separation of  $\sin \phi$  and  $\sin(2\phi)$  terms in Fig. 79.

A complementary DVCS program in Hall A will focus on measurements of the helicity-dependent cross section difference at the highest  $Q^2$ . Projections of a 400 hours measurements of  $\Delta\sigma$  at a luminosity of  $10^{37}\text{cm}^{-2}\text{sec}^{-1}$  are shown in Fig. 79 at  $Q^2 = 7 \text{ GeV}^2$ . The projected data were fitted to a form  $\Delta\sigma = A \sin \phi + B \sin(2\phi)$ , where A and B correspond to the twist-2 and twist-3 terms, respectively. The size of the twist-3 term will give an indication of the convergence of the series, but it also contains information on the twist-3 GPDs which are of interest in their own rights. Figure 80 shows projections of the errors on the twist-2 and twist-3 contributions extracted from fitting the cross section differences.

*DVCS with polarized targets* The use of polarized nucleon targets will provide independent information on the GPDs. The longitudinal polarized target polarization dependent cross section is (in the same kinematic limits as Eq. 6 [Be02a]:

$$\frac{\Delta^5 \sigma}{dx_B dQ^2 dt d\phi_e d\phi_{\gamma\gamma}} = \frac{1}{-s'u'} \frac{\alpha^3}{\pi^2} \frac{2 - 2y + y^2}{y} \frac{\sqrt{1 - x_B} \sqrt{t_{\min} - t}}{(-t) \sqrt{Q^2}} \left[ \frac{x_B}{2 - x_B} G_M(-t) \left( H + \frac{x_B}{2} E \right) + F_1(-t) \tilde{H} + \frac{x_B}{2 - x_B} \left( \frac{x_B}{2} F_1(-t) + \frac{t}{4M^2} F_2(-t) \right) \tilde{E} \right], \quad (39)$$

As in Eq. 6, the GPDs are evaluated at  $x = \pm \xi$ .

In contrast to the beam asymmetry (6),  $\tilde{H}$  is not kinematically suppressed, but  $H$ ,  $E$ ,  $\tilde{E}$  are.

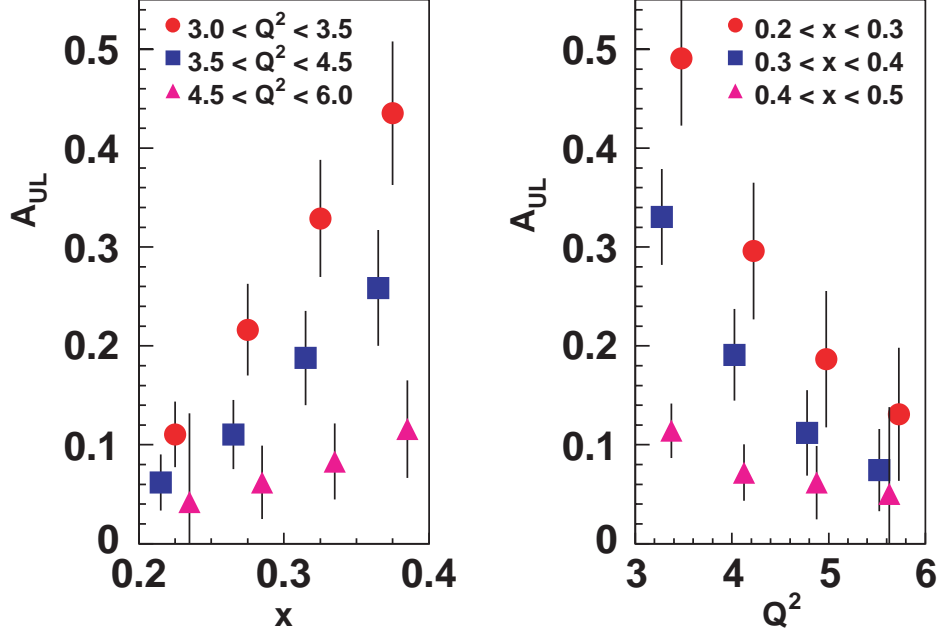


Figure 81: Projected data for longitudinal target asymmetry measured in CLAS<sup>++</sup> for a 2000 hrs run at a luminosity of  $10^3 5\text{cm}^{-2}\text{sec}^{-1}$ . The  $t$ -dependences will be obtained simultaneously.

The longitudinal target asymmetry will give the most direct information on the GPD  $\tilde{H}(\xi, \xi, t)$  in the lower  $x$  and lower  $t$  range where  $H$ ,  $E$  and  $\tilde{E}$  are kinematically suppressed. Figure 81 shows projections of the target asymmetry for the CLAS<sup>++</sup> detector for different models of  $\tilde{H}$ .

*DVCS on Neutron Targets* DVCS on protons is the most promising and cleanest way of accessing GPDs. However, photons have no flavor sensitivity and the observables contain contributions of both  $u$ -quarks and  $d$ -quarks. In DVCS on protons, the GPDs for each flavor enter in the combination

$$H_{DVCS}^p = \frac{4}{9}H^u + \frac{1}{9}H^d + \frac{1}{9}H^s \quad (40)$$

and similarly for  $\tilde{H}$ ,  $E$ , and  $\tilde{E}$ . For neutrons one has different weighting factors for the different flavors:

$$H_{DVCS}^n = \frac{1}{9}H^u + \frac{4}{9}H^d + \frac{1}{9}H^s \quad (41)$$

and similarly for  $\tilde{H}$ ,  $E$ , and  $\tilde{E}$ . This, in principle, opens up the possibility of studying the flavor dependence of the dominant GPD  $H$ . Unfortunately, the form factor  $F_1$  is small for the neutron, and Eq. (6) shows that this causes a suppression of the GPD  $H$ , which makes the flavor separation very difficult. However, this may open up the possibility to access the GPD  $E$ . DVCS measurements on neutrons can, in principle, be done using  $^2\text{H}$  or  $^3\text{He}$  targets. These possibilities of DVCS measurements at 11 GeV on neutrons are currently being evaluated.

*Double Deeply Virtual Compton Scattering (DDVCS)* The DDVCS process is the extension of

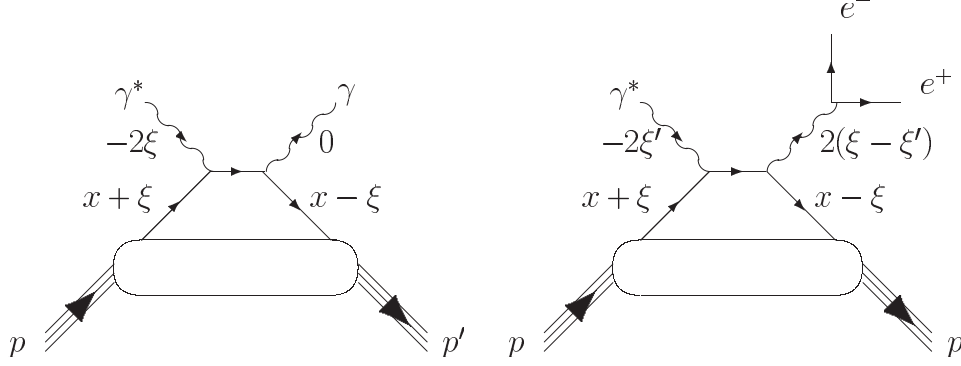


Figure 82: The handbag diagrams for DVCS (left) and DDVCS (right). The presence of two kinematic quantities  $\xi$  and  $\xi'$  in the case of DDVCS allows to access the kinematic region outside of  $x = \xi$  directly.

DVCS to the regime where the final state photon is time-like and decays into a lepton pair (Fig. 82).

This process gives *direct* access to the GPDs in a wider kinematic range. While DVCS with real photons gives access to GPDs integrated over  $x$ , or to GPDs at fixed kinematics  $x = \xi$ , DDVCS accesses GPDs directly in a large kinematic range as the kinematics of the two photons is now described by two variable  $\xi$  and  $\xi'$  that can be independently varied. The beam asymmetry depends on both variables and the GPD is measured at  $H(2\xi', \xi, t)$ . Since  $\xi$  and  $\xi'$  can be varied independently this allows to map out an extended area on the surface in Fig. 69 rather than a line. The rates for this process are suppressed by a factor of two to three orders of magnitude compared to DVCS. Any measurement of DDVCS will therefore be restricted to a much smaller number of bins and will yield larger statistical errors. Nevertheless the process has been seen in CLAS data taken at 4.3 GeV, showing the feasibility of the measurement. With the higher luminosity available with the upgraded equipment, these processes will become accessible with modest statistical accuracy.

*DVCS in  $N \rightarrow \Delta$  and Resonance Transitions.* Inelastic deeply virtual Compton scattering can provide a new avenue of resonance studies at the elementary quark level. The process of interest is  $ep \rightarrow e\gamma\Delta^+(N^{*+})$ . Varying  $\xi$  and the momentum transfer  $t$  to the recoil baryon probes the “transition” GPDs from the ground state nucleon to the excited  $\Delta$  or  $N^*$ . The handbag diagram is shown in Fig. 83.

That this process is indeed present at measurable levels can be seen in the preliminary data from CLAS [Gupc] shown in Fig. 84. The recoiling baryon system shows the excitation of resonances. Besides the  $\Delta(1232)$ , the  $N^*(1520)$  and  $N^*(1680)$  are seen. While these are well known s-channel resonances, they are here excited in t-channel processes. This has the advantage that the photon virtuality  $Q^2$  is decoupled from the momentum transfer to the baryon system. As in the case of elastic DVCS,  $Q^2$  can be chosen sufficiently high, such that the virtual photon couples to an elementary quark, while the momentum transfer to the baryon system can be varied from small to large values, allowing to access the resonance transition GPDs as a function of  $t$ . Similar to the

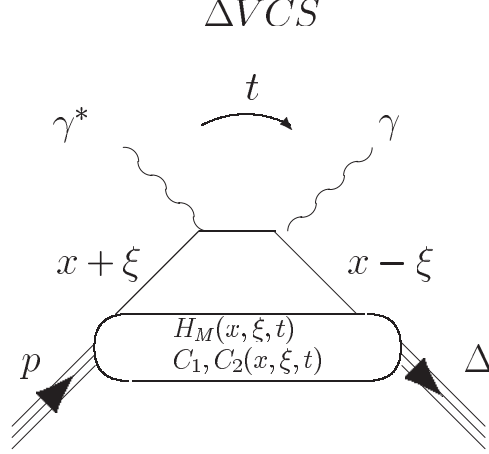


Figure 83: The handbag diagram for  $\Delta$ DVCS

elastic DVCS, the Bethe-Heitler process interferes with the DVCS process producing an asymmetry for the  $N\Delta(1232)$  transition. In general the beam asymmetry for the Delta production is expected to be smaller than for the elastic process as shown in Fig. 85

**Deeply Virtual Meson Production at JLab with 12 GeV Electrons** DVCS is the most promising and cleanest way of accessing GPDs, however, as discussed earlier, it is difficult to perform a flavor separation. Moreover, a separation of the spin-dependent GPDs from the spin-independent GPDs requires use of a polarized target, and may be limited to accessing the GPD  $\tilde{H}$ . Vector meson and pseudoscalar meson production, in principle, allow to accomplish both objectives. Measurements of exclusive vector mesons isolates the helicity-independent GPDs. If one measures both  $\rho$ 's and  $\omega$ 's production one can separate the  $u$ -quark and  $d$ -quark contributions in the GPDs. The electroproduction amplitudes for  $\rho^0$  and  $\omega$  contain terms with a different sign:

$$\rho : e_u H^u - e_d H^d \quad \omega : e_u H^u + e_d H^d \quad (42)$$

Measurement of pseudoscalar meson production isolates the helicity-dependent GPDs  $\tilde{H}$  and  $\tilde{E}$ . However, there is a price one pays for using the meson channel in the study of GPDs. Compared to DVCS, higher values of the photon virtuality  $Q^2$  are required to reach the domain where the GPD formalism is controlled by pQCD. The exact  $Q^2$  value where this will be the case is not currently well understood and needs to be studied experimentally in more detail. It will depend also on the specific kinematics being studied. This aspect is currently under intense investigation.

*The  $ep \rightarrow epp^0$  Channel* An experimental program to study GPDs in hard meson production must begin by identifying the longitudinal part of the cross section for which the factorization theorem applies and the connection with the GPD formalism can be made. Longitudinal  $\rho_L^0$ 's can be identified through the angular distribution of the vector meson decay. Assuming s-channel helicity conservation (SCHC), the desired cross section:  $\gamma_L^* p \rightarrow p \rho_L^0$  can be extracted by analyzing

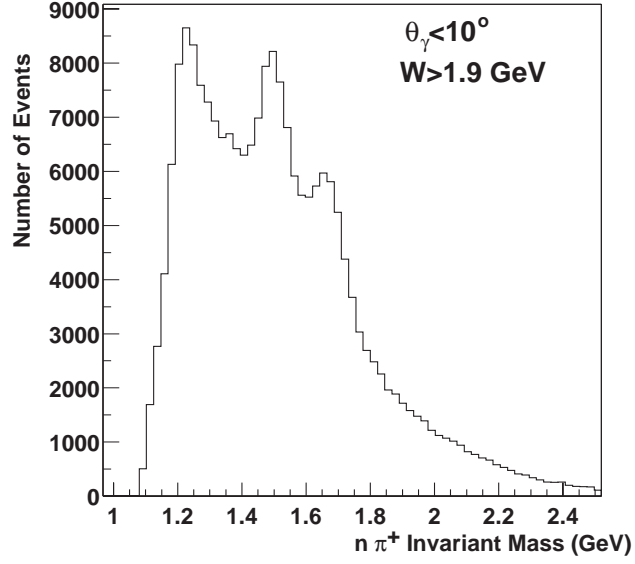


Figure 84: Inelastic DVCS as measured at 4.3 GeV. The scattered electrons,  $\pi^+$ , and neutron are detected. The recoil system clearly shows the excitation of the  $\Delta(1232)$  and higher mass states. Single  $\gamma$  and  $\pi^0$  events were not fully separated in this measurement.

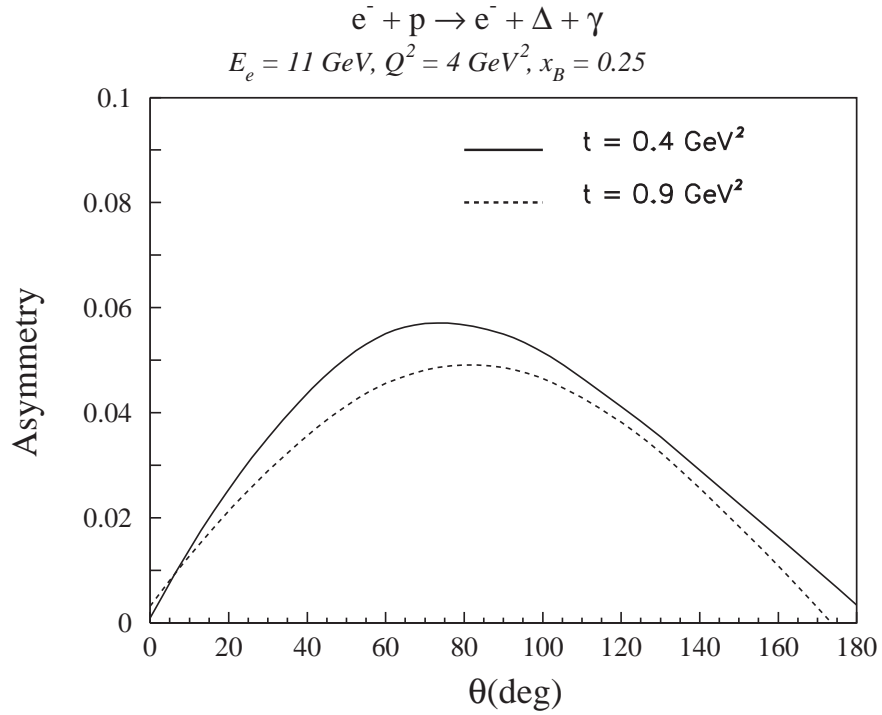


Figure 85: Asymmetry predicted for the  $\Delta$ DVCS at 11 GeV.

the angular distribution <sup>3</sup> of the  $\rho \rightarrow \pi^+\pi^-$  decay distribution, which reflects its polarization state. Assuming the outgoing electron and proton are detected, measurement of only one decay pion is sufficient to determine the decay angular distribution. The decay pion defines an angle,  $\theta_{cm}$ , which is the polar angle relative to the direction opposite to the recoiling target in the  $\rho$  center-of-mass frame. The  $\cos(\theta_{cm})$  distribution follows the form:

$$W(\cos(\theta_{cm})) = \frac{3}{4}[1 - r_{00}^{04} + (3r_{00}^{04}) \cos^2(\theta_{cm})]. \quad (43)$$

The matrix element  $r_{00}^{04}$  depends on  $Q^2$  and  $W$ , and is linked to the longitudinal polarization state of the  $\rho$ . For example,  $r_{00}^{04} = 1$  (0) correspond to pure longitudinal (transverse) polarization of the  $\rho$ , respectively, and, in terms of angular distribution, to  $\frac{3}{2} \cos^2 \theta_{cm}$  ( $\frac{3}{4} \sin^2 \theta_{cm}$ ), respectively. Using SCHC, the  $\rho$  polarization can be linked to the virtual photon polarization by defining:

$$R = \frac{\sigma_L}{\sigma_T} = \frac{1}{\epsilon} \frac{r_{00}^{04}}{1 - r_{00}^{04}},$$

where  $\epsilon$  defines the degree of longitudinal polarization of the virtual photon.  $R$  has been measured at low and at high  $Q^2$ , but only recently at moderately high  $Q^2$ . Figure 86 shows the world data including preliminary CLAS data. For  $W > 2$  GeV, the data show a consistent pattern of  $R$  rising steeply with  $Q^2$  in, what appears, an approximately linear fashion. Should  $\sigma_L$  become strongly dominant, an L/T separation may not be necessary at high  $Q^2$ , and one might be able to use  $\sigma_{tot}$  to extract information on GPDs by simply applying corrections for  $\sigma_T$ . This will only be possible as long as  $\epsilon$  is sufficiently large that the contribution of  $\sigma_L$  is dominant.

Recent results from CLAS and HERMES on  $\rho$  production indicate that modestly high  $Q^2$  values may be sufficient for the GPD formalism to be applicable. Figures 87 and 88 show preliminary CLAS and HERMES data, respectively, for  $\rho^0$  production with longitudinal photons compared with calculations in the GPD framework using a “frozen”  $\alpha_s$  [Gupc]. The various curves correspond to different assumption on the input GPDs. The quite good agreement with the data in the range  $x_B < 0.4$  gives some indication that the handbag diagram dominance may set in for longitudinal  $\rho^0$  production at  $Q^2 > 2 - 5$  GeV<sup>2</sup>, dependent on the exact kinematics being probed. These recent findings provide support for the GPD program with vector meson final states with the Upgrade.

While these data support the expectation that the handbag mechanism may become dominant already at modestly high photon virtualities, such expectations need to be tested at higher energies. Some of this can already be achieved at JLab using the 6 GeV [Ga99] beam.

At the energy of the upgraded CEBAF significantly higher  $Q^2$  will be achieved. In meson production, only the longitudinal component can be used for the direct extraction of GPDs. In the case of vector meson production the longitudinal contribution can be isolated by analyzing the decay distribution of the  $\pi^+\pi^-$  system for the  $\rho^0$ , or the 3-pion system in the case of  $\omega$  production,

---

<sup>3</sup>The SCHC hypothesis can actually be tested by considering the interference response functions  $R_{TT}$  and  $R_{TL}$ , which are accessible with a large-acceptance detector such as CLAS<sup>++</sup>.

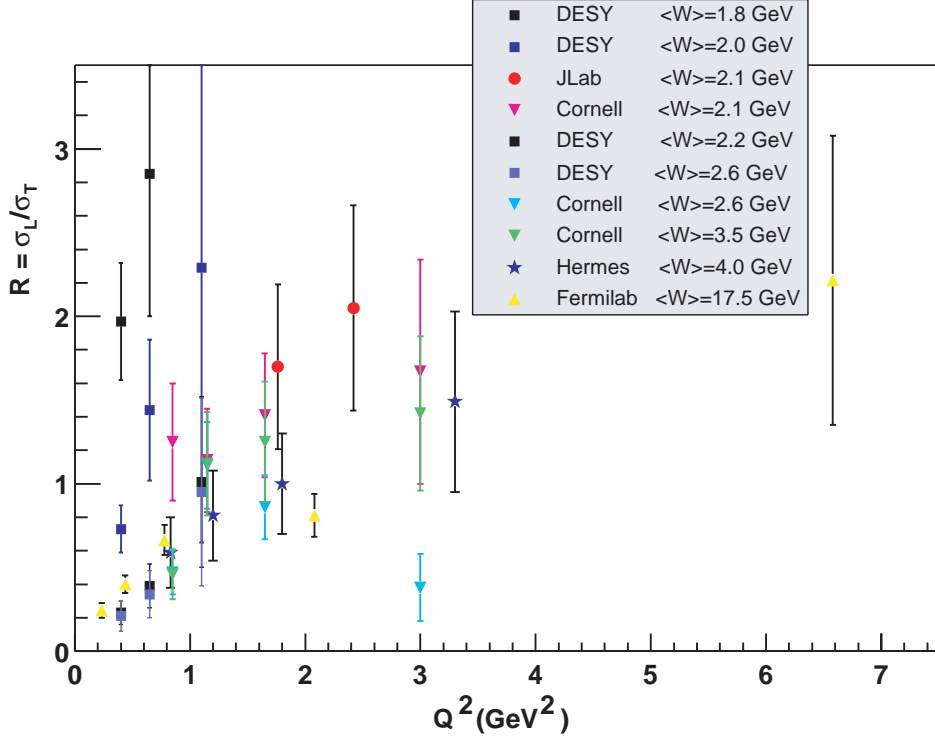


Figure 86: World data for  $R = \sigma_L/\sigma_T$  as a function of  $Q^2$  (assuming SCHC).

by using the s-channel helicity conservation for small- $t$  vector meson production. Figure 89 shows the projected data for the total  $\rho^0$  cross section and for the longitudinal and transverse pieces separately. The longitudinal cross section can be extracted for  $Q^2$  up to 7 GeV $^2$  at this particular  $x_B$  and  $t$  kinematics. Other kinematics will be measured, simultaneously.

*Hard pseudoscalar meson electroproduction* Production of pseudoscalar mesons  $\pi^{\circ\pm}$ ,  $\eta$ ,  $K^{\circ\pm}$  access the helicity-dependent GPDs  $\tilde{H}^{u,d,s}$  and  $\tilde{E}^{u,d,s}$ . The neutral channels are generally expected to reach the Bjorken regime earlier than the charged channels, and asymmetries or ratios of cross sections may even scale at a relatively low  $Q^2$  value. However, it is still important to study the charged channels as well. They can usually be more easily accessed experimentally. The process  $ep \rightarrow e\pi^+n$  is of special interest as it contains two contributions, one related to the well known pole-term scattering of the nucleon's pion cloud, and has sensitivity to the pion form factor  $F_\pi$ , the second relates to the usual handbag diagram in Fig. 71. Both terms should exhibit the same asymptotic  $Q^2$ -dependence, however they have different dependences on the kinematic quantities  $x_B$  and  $t$ . In order to separate the longitudinal contribution a Rosenbluth separation is necessary. This can be accomplished using the combination of HMS-SHMS spectrometers in Hall C for parallel kinematics ( $t = t_{min}$ ). Figure 90 shows projected data of a Rosenbluth separation for the  $n\pi^+$  channel. A maximum  $Q^2$  can be achieved using the Hall C spectrometers for this kinematics allowing to test the  $Q^2$  dependence to the highest possible values. With CLAS $^{++}$  a somewhat lower  $Q^2$  is achieved with access to a broad  $t$ -range allowing to map out the entire transverse impact parameter space, simultaneously. This allows to have different sensitivity to the two contributions in the cross section.



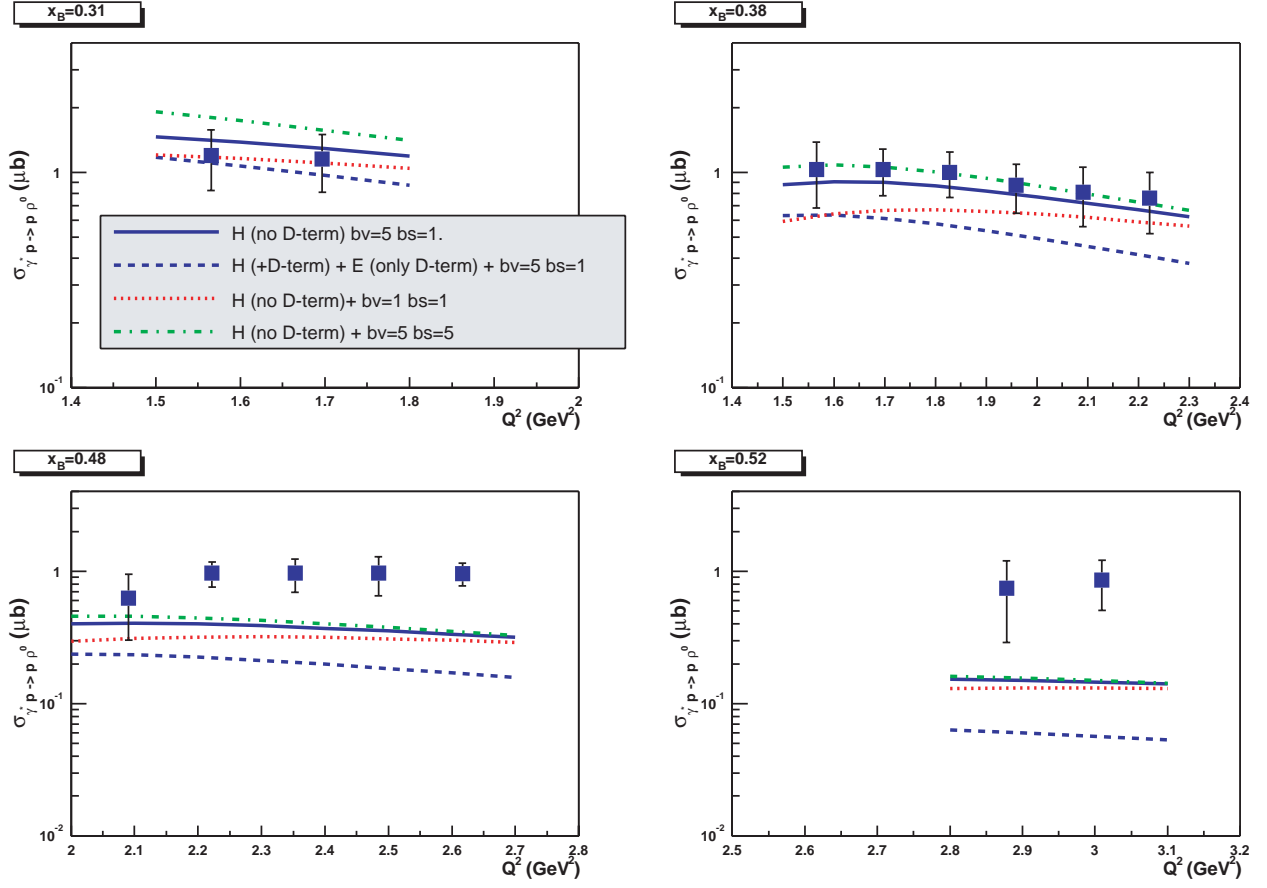


Figure 87: Preliminary data from CLAS on the longitudinal cross section for  $\rho$  production at 4.3 GeV beam energy. The curves represent predictions based on the GPD formalism with “frozen”  $\alpha_s$ . Different GPD ingredients are used as input.

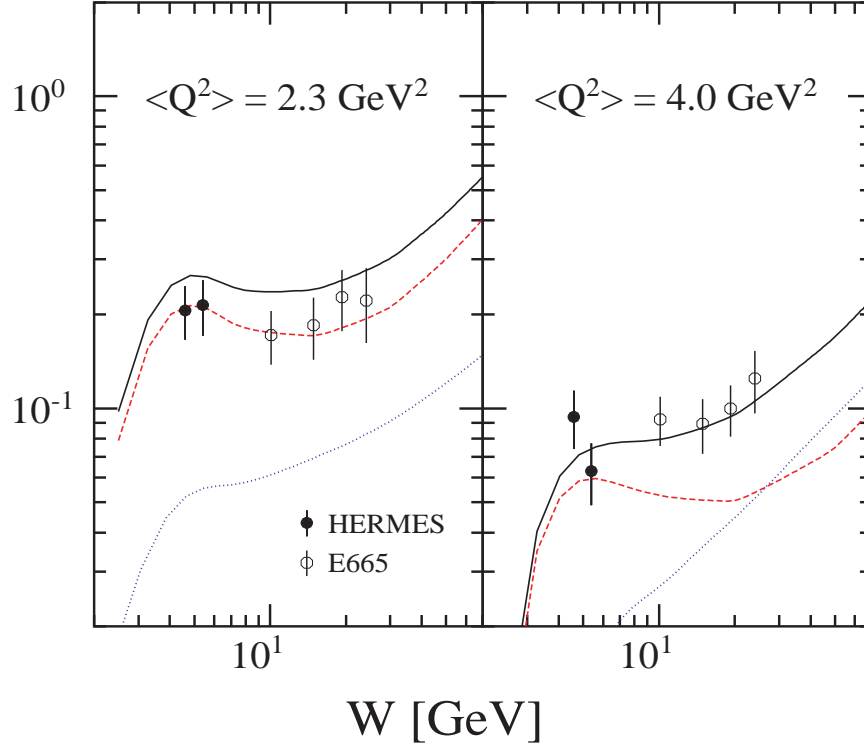


Figure 88: Data from HERMES [Ai00] and data from E655 at Fermilab [Ad97] on longitudinal cross sections for  $\rho^0$  production from protons at a beam energy of 27 GeV. The curves represent predictions based on the GPD formalism with “frozen”  $\alpha_s$ . Different GPD models are used as input.

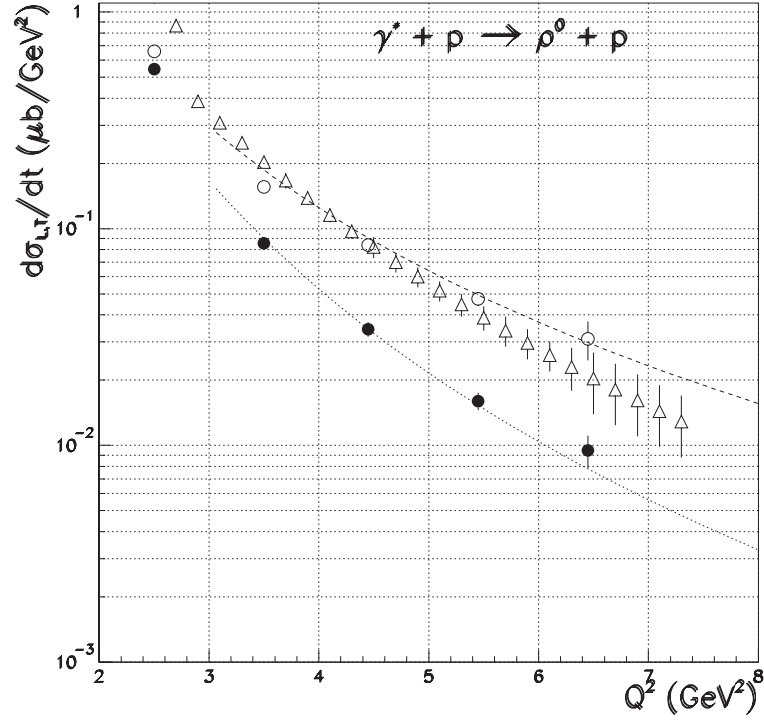


Figure 89: Projected data on  $\rho^0$  production from protons using CLAS<sup>++</sup>. The projected errors for the unseparated cross section and the separated longitudinal and transverse pieces are shown for the 2000 hours of data taking at a luminosity  $L = 10^{35} \text{cm}^{-2} \text{sec}^{-1}$ . Kinematic bins of  $x_B = 0.3-0.4$ ,  $-t = 0.2-0.4 \text{ GeV}^2$  were chosen. Other bins in  $x_B$  and  $t$  will be measured simultaneously, and with similar statistics.

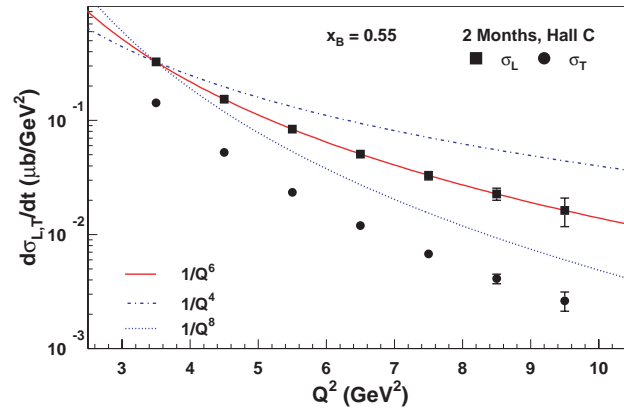


Figure 90: Projected data for a Rosenbluth separation of  $ep \rightarrow en\pi^+$  in Hall C at  $t = t_{\min}$ ,  $x_B = 0.55$ .



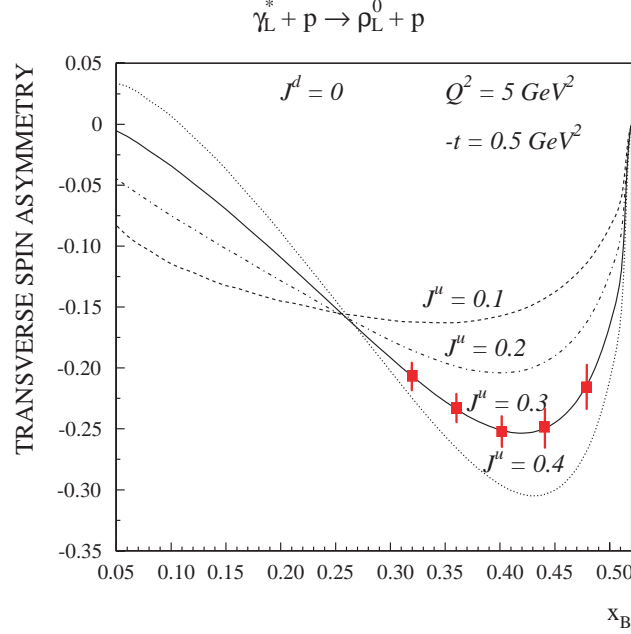


Figure 92: Projected CLAS<sup>++</sup> data on the transverse target asymmetry for  $\rho^0$  production on protons.  $\sigma_L$  dominance in the cross section is assumed.

give unambiguous results. However, one can make use of important constraints given by form factors as well as the parton distribution functions measured in DIS experiments. Moreover, the GPDs are strongly constraint by certain polynomial conditions.

Currently, at least three avenues are being investigated on how to obtain most direct information on the GPD content of exclusive reactions.

(1) Approximations may be made for certain kinematics allowing one to directly extract individual GPDs from asymmetry or from cross section differences at  $x = \xi$ . For example, the GPD  $H$  may be extracted from the beam asymmetry measurements for  $x_B < 0.25$  values [Do02]. Similar approximations are possible for the GPD  $\tilde{H}$  using asymmetry data from longitudinally polarized targets. The GPD  $E$  may be accessible in polarized beam measurements on neutrons.

(2) Global information on GPDs can be obtained from fits to large sets of data where constraints from elastic form factors, meson distribution amplitudes, forward parton distributions, and polynomiality conditions are imposed [Fr03, Be02b]. With increasing experimental information, this method may provide the strongest constraints on GPDs in the future.

(3) A new technique has recently been proposed [Po03] that makes use of partial wave analysis techniques where the GPDs are expanded in infinite sums over  $t$ -channel exchanges. The range of convergence of such a procedure still remains to be explored. In summary, GPDs uniquely connect the charge and current distributions of the nucleon with the forward quark distributions measured in DIS, in a fundamental and hitherto experimentally unexplored way. Recent results demonstrate

the applicability of the GPD framework at currently achievable values of  $Q^2$  for DVCS and possibly for  $\rho$  meson production. A broad program of DVCS and DVMP has been proposed for the 12 GeV Upgrade, that will provide a solid basis for the extraction of GPDs from exclusive processes.

## 2.B.4 Other Topics in Hadron Structure

**Transverse parton distributions** The origin of the spin of the proton has become a topic of considerable experimental and theoretical interest ever since the EMC [As88] measurements implied that the constituent quarks account for only a fraction of the nucleon spin. The gluon polarization and the orbital momentum of partons have been of central interest.

Transverse momentum of quarks is a key to orbital angular momentum. In recent years parton distribution functions were generalized to contain information not only on the longitudinal but also on the transverse distributions of partons in a fast moving hadron. Much of the interest in Generalized Parton Distributions (GPDs) [Ji97, Ra96] has been triggered by their potential to help unravel the spin structure of the nucleon, as they contain information not only on the helicity carried by partons, but also on their orbital angular momentum (OAM).

The transverse momentum dependent (TMD) parton distributions [Ra79, Mu96, Ko95] are another important class of nonperturbative functions that are complementary to the GPDs and carry information on both longitudinal and transverse hadron structure. They provide rich and direct information on the orbital motion of quarks. If the transverse momentum  $k_T$  of partons is included into consideration, the number of independent distribution functions at leading twist (see Table 9) increases to eight [Mu96]. While distribution functions describe the *confinement* of partons inside hadrons, another analogous set of non-perturbative functions describe the transition of partons to hadrons or *hadronization*. Three diagonal elements (in bold),  $f_1, g_1$  and  $h_1$  reduce to well known one dimensional, longitudinal momentum dependent parton distribution functions  $q(x), \Delta q(x)$  and  $\delta q(x)$  when integrated over  $k_T$ . This new degree of freedom makes possible studies of transitions of nucleons with one polarization state to a quark with another. Off diagonal elements of table 9 describe those transitions. In particular the  $f_{1T}^\perp$  known as the Sivers function [Si91, An98, Br02, Co02, Ji03b, Be03] describes unpolarized quarks in the transversely polarized nucleon. It is *time-reversal odd* (T-odd) and requires final state interactions and interference between different helicity states. The counterpart of the Sivers function in the hadronization process is the Collins T-odd fragmentation function  $H_1^\perp$  [Co93] describing fragmentation of transversely polarized quarks to unpolarized hadrons. As shown recently in Ref.[Be03], the interaction between the active parton in the hadron and the target spectators [Br02, Co02, Ji03b] (see Fig.93) leads to gauge-invariant TMD parton distributions. Furthermore, the factorization for semi-inclusive scattering with hadrons in the current fragmentation region detected at low transverse momentum was verified to one-loop order in perturbative QCD [Ji04].

The interference of wavefunctions with different orbital angular momentum responsible for

Table 9: Leading twist transverse momentum dependent distribution functions. The U,L,T stand for transitions of unpolarized, longitudinally polarized and transversely polarized nucleons (rows) to corresponding quarks (columns).

N/q	U	L	T
U	$\mathbf{f}_1$		$h_1^\perp$
L		$\mathbf{g}_1$	$h_{1L}^\perp$
T	$f_{1T}^\perp$	$g_{1T}$	$\mathbf{h}_1, h_{1T}^\perp$

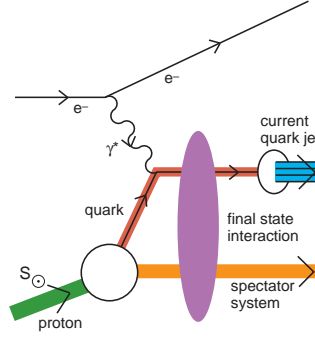


Figure 93: Interaction of struck quark and the target spectators[Br02].

the non-zero Sivers functions [Si91, An98, Br02, Co02, Ji03b, Be03] also yields the helicity-flip Generalized Parton Distribution (GPD)  $E$  [Br02a, Ji03a] which enters Deeply Virtual Compton Scattering [Ji97, Ra96] and the Pauli form factor  $F_2$ . Relations of GPDs and TMDs become particularly intuitive after a Fourier transform from transverse momentum transfer to impact parameter, both for GPDs [Bu03a, Di02a] and TMDs [Di02a]. GPDs at nonzero longitudinal momentum transfer  $\xi$  correlate hadronic wave functions with both different momentum fractions and different transverse positions of the partons. However, the difference in transverse positions is a *global* shift in each wave function; the *relative* transverse distances between the partons in a hadron are the same before and after the scattering. In contrast to impact parameter dependent GPDs in TMD distributions describing the correlation in transverse position of a single parton, the struck quark has a different transverse location *relative* to the spectator partons in the initial and the final state wave functions, in addition to the overall shift of the proton center of momentum [Di02a]. Finally the phase-space Wigner distributions were introduced [Be04] containing most general one-body information of protons. After integration over the spatial coordinates, they reduce to TMDs and after integration over the transverse momentum and a specific Fourier transform they recover the GPDs.

It was recognized long ago that non-zero transverse momenta of partons (a consequence of being confined by strong interactions) is accessible in measurements of azimuthal distributions of final state hadrons [Ge78, Ca78, Be80]. Combined with spin asymmetries, which were a major

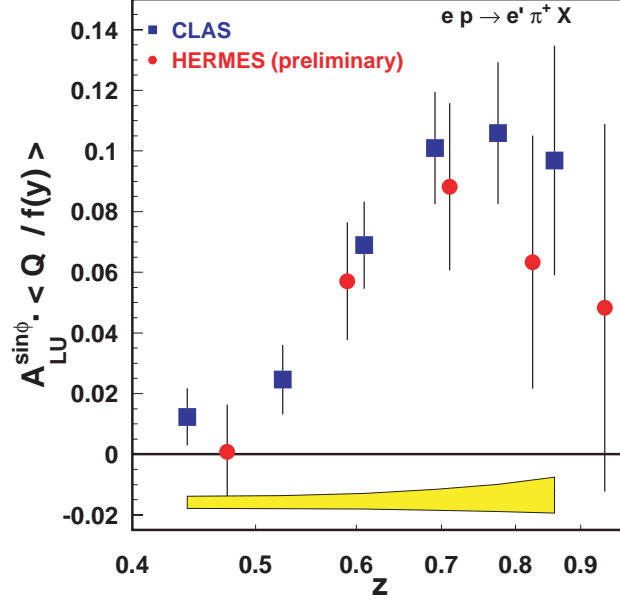


Figure 94: Beam SSA: HERMES vs CLAS. Analyzed in fragmentation terms  $A_{LU}(z)$  depends on the ratio of the Collins function and unpolarized fragmentation function. The  $f(y)$  is the kinematic factor, depending on the fraction of the initial energy of electron carried by the virtual photon.

testing ground for QCD, measurement of azimuthal distributions of final state particles provides a new important class of measurements: so-called spin-azimuthal asymmetries.

Both TMDs and impact parameter dependent GPDs are sensitive to the orbital momentum of partons and lead to predictions of spin-azimuthal asymmetries in hard scattering processes [Si91, Co93, Mu96, Ko95, Br03, Bu03a]. The connection between Single-Spin azimuthal Asymmetries (SSAs) and GPDs has also been discussed in terms of the transverse distribution of quarks in nucleon [Bu03a].

Measurement of asymmetries in azimuthal distributions of final state photons and hadrons in semi-inclusive DIS thus allows access to the transverse momentum distributions of quarks [Co93, Br02, Bu03a] providing a window to the physics of final and initial state interactions at the parton level. It is also argued that in both semi-inclusive [Ba02] and in hard exclusive [Fr99, Fr00a] pion production, scaling sets in for cross section ratios and, in particular, for spin asymmetries at lower  $Q^2$  than it does for the absolute cross section. There are quite a few examples of remarkable agreement between spin asymmetries measured at different beam energies over a wide  $Q^2$  range. Very good agreement was observed in single-spin asymmetries in  $ep$  scattering at HERMES [Mi02a] and CLAS [Av02, CLAS03], both for target and beam SSA measurements. Figure 94 shows that beam SSA measurements performed at very different energies are in fact consistent. All this makes spin-asymmetries a major tool for the measurement of different parton distribution functions (GPDs, TMDs) in the  $Q^2$  domain of a few  $\text{GeV}^2$ .



SSA in semi-inclusive DIS are recognized now as a major tool to measure the leading twist TMD distributions and in particular Collins function and quark transversity [Co93]. The chiral-odd transversity distribution,  $\delta q(x)$ , which, in combination with the number density  $q(x)$  and the helicity distribution  $\Delta q(x)$ , completes the list of leading-twist parton distribution functions is essentially unexplored.

For polarized target, several SSAs arise at leading order [Co93, Mu96, Ko95, Br02, Ji03b, Ko96]:

$$\sigma_{UT}^{\sin\phi} \propto S_T(1-y+y^2/2)\sin(\phi-\phi_S)\sum_{q,\bar{q}}e_q^2x\delta q(x)H_1^{\perp q}(z), \quad (46)$$

$$+ S_T(1-y)\sin(\phi+\phi_S)\sum_{q,\bar{q}}e_q^2xf_{1T}^{\perp q}(x)D_1^q(z), \quad (47)$$

$$\sigma_{UL}^{\sin 2\phi} \propto S_L 2(1-y)\sin 2\phi\sum_{q,\bar{q}}e_q^2xh_{1L}^{\perp q}(x)H_1^{\perp q}(z), \quad (48)$$

where  $\phi_S$  is the azimuthal angle of the transverse spin in the photon frame,  $S_L$  and  $S_T$  are longitudinal and transverse components of the target polarization with respect to the direction of the virtual photon,  $D_1^q(z)$  is the spin-independent fragmentation function,  $f_{1T}^{\perp q}(x)$  and  $H_1^{\perp q}(z)$  are T-odd Sivers and Collins functions, and  $h_{1L}^{\perp}$  is the Mulders distribution function [Mu96] describing transversely polarized quarks in the longitudinally polarized nucleon.

Contributions to transverse SSAs from T-odd distributions of initial quarks (or Sivers effect) and T-odd fragmentation of final quarks (or Collins effect) could be separated by their different azimuthal and  $z$ -dependences. The program of transverse asymmetry measurements is under way at HERMES[Mi02a] and COMPASS[CO96]. The effect of transversity is a valence quark effect and JLab measurements at 12 GeV will provide unique access to transverse spin effects at large  $x$  (see Fig. 95).

The interpretation of these experiments, and extraction of transversity in particular, will require a detailed knowledge of the Collins fragmentation function,  $H_1^{\perp}(z)$ . To reveal the source of SSA and separate the Collins and Sivers contributions, measurements with different target polarizations and with different final state particles may be required. One important, unique feature of Collins mechanism is the presence of a leading twist  $\sin 2\phi$  dependent SSA, the ‘‘Kotzinian-Mulders asymmetry’’ [Ko96a], for longitudinally polarized targets (see Eq. 48). Measurement of the  $\sin 2\phi$  SSA thus allows to study the Collins effect to leading order with no contaminations from other mechanisms. A large effect is predicted only at large  $x$ , the region well covered by JLab at 12 GeV (see Fig. 96). Figure 97 shows the prediction for the SSA arising exclusively from the Collins mechanism. Recent measurements at JLab with a longitudinally polarized target [Av03] demonstrate the feasibility of such a measurement (see Fig. 96). Measurements at 12 GeV will pin down the corresponding transverse momentum distribution function, describing the transition of a longitudinally polarized nucleon to transversely polarized quarks.

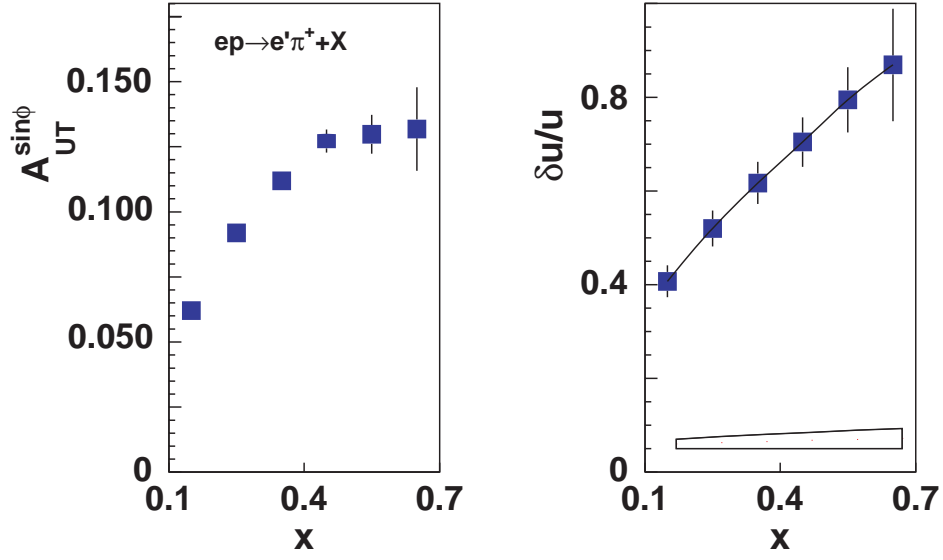


Figure 95: Projected transverse spin asymmetry ( $A_{UT}^{\sin\phi}$ ) in single  $\pi^+$  production with CLAS at 12 GeV (left plot) and expected precision of the extracted  $\delta u/u$  (right plot). The line is the Monte Carlo generated  $\delta u/u$ .

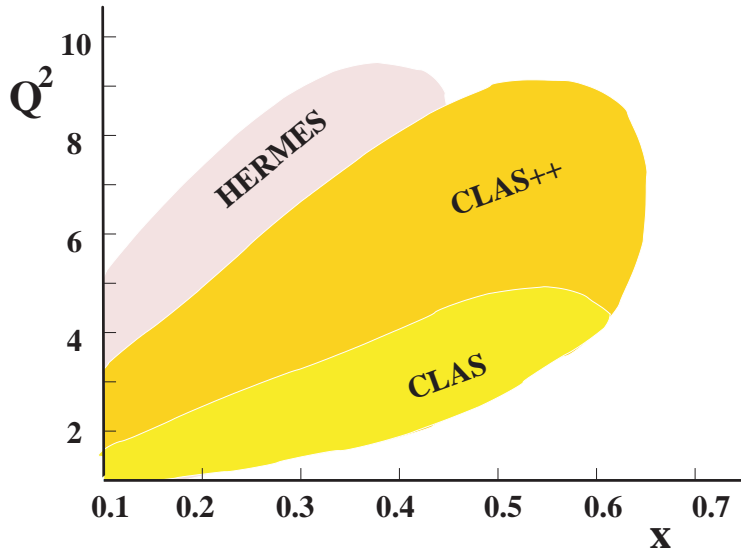


Figure 96: Kinematic coverage at JLab at 12 GeV.

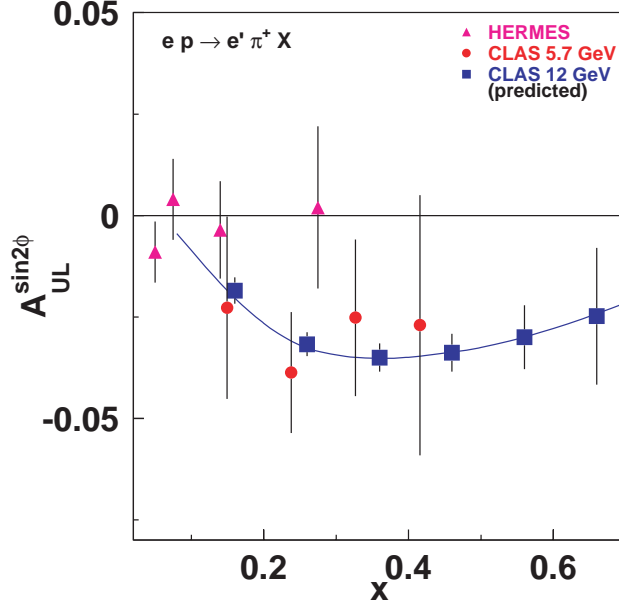


Figure 97: Target SSA: The shape of the  $A_{UL}^{\sin 2\phi}(x)$  measured with a longitudinally polarized target depends only on the ratio of the TMD distribution  $h_{1L}^\perp$  and  $f_1$ , providing a direct access to  $h_{1L}^\perp$ . The curve is the theory prediction based on the Collins mechanism [Ef01]

The SSA measured at JLab already at 4-6 GeV [Av02, CLAS03, Av03] are consistent with partonic picture and can be described by a variety of theoretical models. The significantly higher statistics of JLab at 12 GeV data, in simultaneous measurements of SSAs for the different final state particles as shown in Table 2, especially in the large  $x$  region, will enable the extraction of the  $x$  and  $Q^2$  dependences for different azimuthal moments in a wide kinematical range. The key goal of this program will be the study of transitions between the nonperturbative and perturbative regimes of QCD in measurements of spin-azimuthal asymmetries with unpolarized, longitudinally polarized, and transversely polarized targets enabling access to the orbital motion of quarks.

**The extended GDH integral and sum rule** The extended GDH integral,  $I(Q^2)$ , is a quantity that can be measured from arbitrarily small  $Q^2$ , where behavior is dominated by hadronic degrees of freedom, to arbitrarily large values of  $Q^2$ , where behavior is dominated by quark degrees of freedom. As such, the extended GDH integral provides a window on the transition from perturbative to non-perturbative regimes. The integral involves a sum over energy loss  $\nu$  from the pion threshold to infinity, however, so there will always be a limit to the range over which the integral can be measured. Existing measurements at JLab have made accurate measurements of  $I(Q^2)$  through the resonance region, but not much higher [Am02]. An upgraded JLab will be capable of measurements at much higher  $\nu$  over a wide range of  $Q^2$  values. Among the exciting new possibilities will be studying the high energy piece of the extended GDH integral.

Table 10: CLAS<sup>++</sup> Program Summary - Quark Transverse Momentum and Nucleon Orbital Angular Momentum in Semi-inclusive DIS

REACTIONS	OBSERVABLES	REQUIREMENTS
$\vec{e}p \rightarrow e\pi^+X$		
$\vec{e}p \rightarrow e\pi^0X$		
$\vec{e}p \rightarrow e\gamma X$		
$\vec{e}p \rightarrow eK^+X$		
$\vec{e}\vec{p} \rightarrow e\pi^+X$	PDF, TMD, $\bar{d}$ , $\bar{u}$	Large $t$ coverage
$\vec{e}\vec{p} \rightarrow e\pi^0X$	Frag. distribution fun.	Low $L \rightarrow$ large acc.
$\vec{e}\vec{p} \rightarrow e\gamma X$	Transversity	pol. targets
$\vec{e}\vec{p} \rightarrow eK^+X$		Improved Particle ID
$\vec{e}p^T \rightarrow e\pi^+X$		
$\vec{e}p^T \rightarrow e\pi^0X$		
$\vec{e}p^T \rightarrow e\gamma X$		
$\vec{e}p^T \rightarrow eK^+X$		

The extended GDH integral can be written[Dr00]

$$I(Q^2) = \int_{\nu_0}^{\infty} \frac{d\nu}{\nu} (1-x) \left[ \sigma_{1/2}(\nu, Q^2) - \sigma_{3/2}(\nu, Q^2) \right] = 2 \int_{\nu_0}^{\infty} \frac{d\nu}{\nu} (1-x) \sigma'_{TT} \quad , \quad (49)$$

where  $\sigma_{1/2(3/2)}(\nu, Q^2)$  is the total *virtual* photoabsorption cross section for the nucleon with a projection of  $\frac{1}{2}$  ( $\frac{3}{2}$ ) for the total spin along the direction of photon momentum,  $\nu_0$  is the pion production threshold,  $x = Q^2/2M\nu$  is the Bjorken scaling variable,  $M$  is the mass of the nucleon, and  $\sigma'_{TT}$  is the transverse-transverse interference cross section. Stringent theoretical constraints make  $I(Q^2)$  a quantity that can be used to test our understanding of hadronic structure. At  $Q^2 = 0$ ,  $I(Q^2)$  is anchored by the GDH sum rule[Ge66, Dr66]:

$$I(0) = -\frac{2\pi^2\alpha}{M^2}\kappa^2, \quad (50)$$

where  $\alpha$  is the fine structure constant and  $\kappa$  is the nucleon's anomalous magnetic moment. At small values of  $Q^2 > 0$ ,  $I(Q^2)$  can be computed using chiral perturbation theory[Ji01, Be93a, Ji00, Be02d]. At high  $Q^2$ ,  $I(Q^2)$  is related to the moments of the spin structure functions, and is thus constrained by various results from OPE techniques including the Bjorken sum rule[Bj66, El74]. The extended GDH integral can even be related to the forward virtual Compton amplitudes, thus establishing a true extended GDH sum rule[Ji01].

With the 12 GeV upgrade, an important door will be opened to new kinematic windows that, among other possibilities, will make accessible the high-energy piece of the extended GDH integral. Recent results from Mainz on the original GDH sum rule have made it clear that the high-energy piece of the integral is critical to convergence[Ah01]. We remark more generally that with the upgrade, high- $\nu$  low- $Q^2$  physics will become accessible, and the high-energy piece of the extended

GDH integral may well be the first of a new class of measurements[Ba01]. The upgrade is thus very central to both GDH physics, as well as to exploring a kinematic regime that is certain to provide important new insights.

**Quark-Hadron Duality** While at present we cannot describe the structure and interactions of hadrons directly utilizing the quark and gluon degrees of freedom of QCD, we know that in principle it should just be a matter of convenience in choosing to describe a process in terms of quark-gluon or hadronic degrees of freedom. This fact is referred to as *quark-hadron duality*, and means that one can use either set of complete basis states to describe physical phenomena. At high energies, where the interactions between quarks and gluons become weak and quarks can be considered asymptotically free, an efficient description of phenomena is afforded in terms of quarks; at low energies, where the effects of confinement make strongly-coupled QCD highly non-perturbative and the final state is guaranteed to be made of hadrons, it is more efficient to work in terms of collective degrees of freedom, the physical mesons and baryons. The duality between quark and hadron descriptions reflects the relationship between confinement and asymptotic freedom, and is intimately related to the nature of the transition from non-perturbative to perturbative QCD.

Although the duality between quark and hadron descriptions is formally exact in principle, how this reveals itself specifically in different physical processes and under different kinematical conditions is the key to understanding the consequences of QCD for hadronic structure. The phenomenon of duality is in fact quite general in nature and can be studied in a variety of processes, such as  $e^+e^- \rightarrow$  hadrons, or semi-leptonic decays of heavy quarks. Duality in electron-nucleon scattering, historically called Bloom-Gilman duality, links the physics of resonance production to the physics of deep inelastic scaling.

It has been said that (short of the full solution of QCD) understanding and controlling the accuracy of the quark-hadron duality is one of the most important and challenging problems for QCD practitioners today [Sh01]. Jefferson Lab at 11 GeV is uniquely poised to provide a wealth of data which can accurately answer where duality works, in what structure functions, in what reactions, and at what kinematics. While duality has been well-verified for the proton  $F_2$  structure function, significant progress can be made in a variety of experiments, for instance in the longitudinal and transverse separated unpolarized structure functions, on nucleons and in nuclei, in polarized structure functions, and in semi-inclusive reactions.

Measuring the complete set of unpolarized structure functions ( $F_L$ ,  $F_1$ ,  $F_2$ ,  $R$ ) in inclusive electron nucleon scattering requires a separation of the cross section into longitudinal and transverse strengths. The cleanest way to do this separation experimentally is via the Rosenbluth technique, where the cross section is measured at multiple values of  $\epsilon$ , or relative longitudinal virtual photon polarization, for fixed  $x$  and  $Q^2$ . The precision obtainable for measuring the longitudinal structure function depends on both the precision of the individual data points and the range in  $\epsilon$  over which the measurements are made. Given the typical point-to-point systematic uncertainties on precision

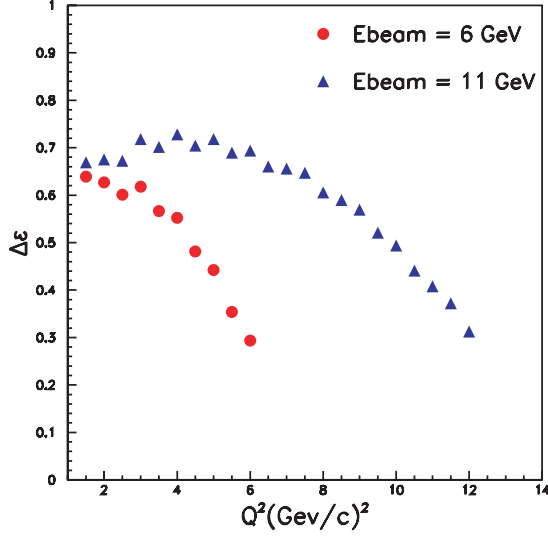


Figure 98: The  $\Delta\epsilon$  range (left) accessible at  $x = 0.8$  in Hall C as a function of  $Q^2$  for beam energies of 6 GeV (red circles), and 11 GeV (blue diamonds).

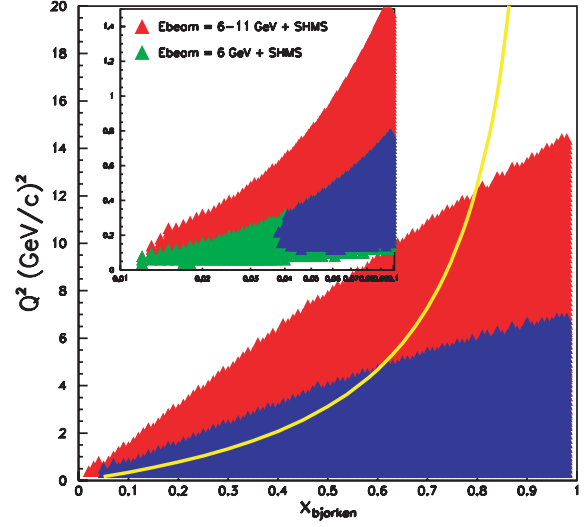


Figure 99: The  $(x, Q^2)$  ranges available with the SHMS and HMS spectrometers for  $\Delta\epsilon$  ranges above 0.3. The yellow line represents fixed  $W^2 = 4 \text{ GeV}^2$ .

cross section measurements in Hall C of  $\approx 1.2\%$ , the minimum  $\epsilon$  range required to perform a separation of the cross section is  $\Delta\epsilon \approx 0.3$ . Figure 98 shows the  $\epsilon$  range versus  $Q^2$  which is accessible at  $x = 0.8$  for a maximum JLab beam energy of both 6 GeV (red squares) and 11 GeV (blue diamonds). For a 6 GeV beam, the measurement of separated structure functions is limited to  $Q^2 < 6 \text{ (GeV/c)}^2$ , but with an 11 GeV beam this range can be doubled. In addition, with the higher beam energy, the precision possible for  $4 < Q^2 < 6 \text{ (GeV/c)}^2$  can be significantly improved due to the extended  $\epsilon$  range which is opened up at the higher energy.

Figure 99 depicts the substantial kinematic range enhancement made possible by the SHMS spectrometer and the 11 GeV beam over a range in  $x$ . This data will serve a variety of purposes, including addressing for instance long-standing questions regarding structure function behavior at low  $Q$ . Perhaps most importantly, the range of the data will allow for accurate moments of the structure functions to be obtained. To obtain a structure function moment, it is necessary to integrate over the full range in  $x$  at a fixed value of  $Q^2$ . These moments are calculated in lattice QCD without higher twist contributions. If duality is shown to hold, the proposed structure function moment data may be directly compared to lattice QCD calculations.

Bloom-Gilman duality can be formulated in the language of an operator product expansion (OPE) of QCD moments of structure functions, in which contributions are organized according to powers of  $1/Q^2$ . The leading terms are associated with free quark scattering, and are responsible for the scaling of the structure function. The  $1/Q^2$  terms involve interactions between quarks and gluons and hence reflect elements of confinement dynamics. Duality measurements have been explained in terms of a weak  $Q^2$  dependence of the low moments of  $F_2$ . This is interpreted within

the OPE as indicating that the non-leading,  $1/Q^2$ -suppressed, higher twist interaction terms do not play a major role even at low  $Q^2$  ( $\approx 1 \text{ GeV}^2$ ). It is this interpretation that facilitates comparison to lattice calculations.

Large  $x$  (resonance region) data become increasingly important for higher order moments. At  $n=6$ , for example, the resonance and large  $x$  region above  $x = 0.7$  make up 70% of the Cornwall-Norton moment of  $F_2$  at  $Q^2 = 10 \text{ (GeV/c)}^2$ . There exist little to no inclusive spectra in the resonance region above  $Q^2 \approx 8 \text{ (GeV/c)}^2$ , data which will be easily obtainable in Hall C at 11 GeV where cross sections can be measured to  $Q^2 > 15 \text{ (GeV/c)}^2$  and L/T separated data will be available at least out to  $Q^2 = 12 \text{ (GeV/c)}^2$ . This latter can be used to obtain moments of all unpolarized structure functions.

While the OPE formalism allows us to organize hadronic observables in terms of an asymptotic expansion, it does not tell us *a priori* why certain matrix elements are small or cancel. This can only be addressed via numerical solutions of QCD, or from experiment. Since the details of quark-hadron duality are process dependent, there is no reason to expect the accuracy to which it holds and the kinematic regime where it applies to be similar for different observables. In fact, there could be qualitative differences between the workings of duality in spin-dependent structure functions and spin-averaged ones, or for different hadrons — protons compared with neutrons, for instance.

Because of the absence of free neutron targets, deuterons are typically employed as effective neutron targets. However, at large  $x$ , theoretical uncertainties in the treatment of nuclear corrections has led to substantial ambiguity in extracted neutron structure functions. In particular, inclusion of Fermi motion and nuclear off-shell corrections in the deuteron can lead to  $F_2^n$  values which differ by 50% at  $x = 0.75$ . These differences are even greater if  $F_2^n$  is extracted on the basis of a nuclear density model. Therefore, while there exists a large body of data on nucleon structure functions over a wide range of  $x$  and  $Q^2$ , the region above  $x = 0.6$  is poorly explored. This is precisely both the regime necessary to duality studies and the regime which an 11 GeV beam at Jefferson Lab can optimally explore.

To overcome this problem, a program is proposed in Hall B to measure the inclusive electron scattering cross section on an almost free neutron using a novel recoil detector with low momentum threshold for protons and high rate capability. This detector will allow tagging of slow backward-moving spectator protons with momentum as low as 70 MeV/c in coincidence with the scattered electron in the reaction  $D(e, e'p_s)X$ . This will ensure that the electron scattering took place on an almost free neutron, with its initial four-momentum inferred from the observed spectator proton spectrum. This technique will allow for measurements in the neutron resonance region up to  $x > 0.95$  and  $Q^2 \sim 14 \text{ (GeV/c)}^2$ .

Close and Isgur [Cl01a] suggest that the onset of duality may occur later for the neutron as higher  $W$  states are averaged than the proton. Furthermore, the existing lattice QCD calculations are for non-singlet only, and therefore the proton-neutron difference moment is the best entity for

comparison (given the minimal or cancelling higher twists from duality) with experiment. In all, the proposed 11 GeV neutron measurements will provide an “acid test” for duality.

While the phenomenon of quark-hadron duality has been precisely determined in the  $F_2$  structure function, it has not yet been established for the spin-dependent structure functions. The structure function  $g_1$ , for example, is an intriguing case; the workings of duality may be more intricate for  $g_1$  than for the spin-averaged structure functions. It is given by a difference of cross sections, which need not be positive. Unlike the unpolarized case, spin 1/2 and 3/2 resonances contribute with opposite phase. For fixed  $Q^2$  values less than 1 (GeV/c)<sup>2</sup> the  $\Delta(1232)$  resonance pulls the  $g_1$  structure function from its large and negative value at  $Q^2 = 0$  (where it is related to the GDH sum rule) to a positive value at large  $Q^2$  (where it is related to the deep inelastic sum rules such as the Bjorken sum rule). Duality may yet be realized at low  $Q$  in this case and for other polarized structure functions if one averages over a complete set of resonances or performs a moment analysis. It is vital for our understanding of duality and its practical exploitation that both the spin and flavor dependence of duality be established and carefully quantified empirically. There are robust programs of spin structure function measurements proposed for Halls A, B, and C at 11 GeV, which will provide the extensive kinematic range necessary to precise quark-hadron duality tests.

It is important to point out that a revolutionary application of duality, if one understands the workings of the resonance—deep-inelastic interplay, would be to allow access to the region of very high  $x$ , which has not been possible in any other experiment. The region of  $x \approx 1$  is an important testing ground for mechanisms of spin-flavor symmetry breaking in the valence quark distributions of the nucleon. In addition, with nuclear targets it would permit measurement of the nuclear medium modification of the nucleon structure function (nuclear EMC effect) at large  $x$ , where the deviation from unity of the ratio of nuclear to nucleon structure functions is largest, and sensitivity to different nuclear structure models greatest.

While the phenomenon of duality in inclusive scattering is under investigation, duality in the related case of semi-inclusive meson electroproduction has not been experimentally tested. Here, the reaction is typified by  $\gamma + p \rightarrow \pi + X$ , where the photon may be real or virtual. One can substitute a kaon for a pion, with a loss in rate of order 10. The interesting kinematic region for this purpose is one where the pion is directly produced at short range and exits the reaction in kinematic isolation from other exiting particles. The cross section for hard pion photoproduction can be written as a kinematic factor times a scaling function, where the latter is a function that in general depends on several variables but in the limit of large  $t$  and large  $m_X$  depends only on the variable  $x$  (up to logarithmic corrections). A goal here is to see what happens at smaller recoiling mass  $m_X$ , particularly in the resonance region. The scaling curve will become bumpy at low  $m_X$ , and we may ask, Will the resonances averaged over their own width reproduce the scaling curve already (by that time) established? Will the resonance peak to background ratio remain constant for a given resonance as  $|t|$  increases?



The scaling region where  $m_X$  is large and direct pion production is dominant must be defined. One problem when the energy or transverse momentum is not high is a background coming from soft processes, which can be estimated using vector meson dominance (VMD) ideas. One can reduce the VMD background by having the photon off shell. For an 11 GeV incoming beam, preliminary estimates based on earlier work indicate that, with photons spacelike by  $1 \text{ GeV}^2$ , there is a significant scaling region with  $m_X$  between 2 and 3 GeV and with direct pion production dominating both fragmentation or VMD processes. There is also a resonance region with  $m_X$  between 1 and 2 GeV. Thus, an 11 GeV beam in Hall C, using the HMS / SHMS for electron and pion identification in coincidence, would undeniably allow this category of semi-inclusive duality experiment to be performed.

Semi-inclusive deep inelastic scattering in parallel kinematics can also be measured. Here, a parton exits the fundamental reaction, and then at some distance fragments into a jet of hadrons, one of which is the observed pion. This is in contrast to the process described above, where, at very high transverse momentum, short-range direct production dominates. Here again duality would manifest itself with an observed scaling in the meson plus resonance final state. Assuming one is in a kinematics region that mimics single-quark scattering, in analogy with the inclusive scattering case, the question is whether the remaining part of the process can be described in terms of a process where the struck quark hadronizes into the detected meson. Assuming such a factorization approach, where the cross section decomposes into a part,  $f_i(x, Q^2)$ , dependent on the photon-quark interaction, and another part described by the quark fragmentation functions  $D_{q_i}^h(z, Q^2)$  (or the probabilities that a quark of flavor  $q_i$  hadronizes into a hadron  $h$ ). This approach is strictly valid at asymptotic energies only, as at low energies there may not be clear separation of target and current fragmentation regions. However, as in the inclusive case where the nucleon resonances average at low energies to the scaling curve, the nucleon resonances remaining in the final state after having produced a fast meson may average to the fragmentation function.

The importance of understanding the onset of factorization for our understanding of the flavor content of the nucleon can not be underestimated. Should factorization (and duality) hold at JLab energies, unprecedented spin-flavor decomposition of the nucleon will become possible.

## 2.C The Physics of Nuclei

A great deal of nuclear properties and reactions over a wide energy range — from the few keV of astrophysical relevance to the MeV regime of nuclear spectra to the tens to hundreds of MeV measured in nuclear response experiments — can be quantitatively understood by describing nuclei as assemblies of individual nucleons interacting among themselves via effective interactions.

The dominant two-body interaction has a component at large inter-nucleon distances ( $\geq 2 \text{ fm}$ ) due to pion exchange, which is theoretically well understood. The main feature of this one-pion-exchange component is its tensor character, which leads to a strong coupling between the nucleons'

spatial and spin degrees of freedom. Indeed, these spin-space correlations make nuclei markedly different from other systems where the dominant interaction is independent of the particles' internal degrees of freedom (spin and isospin), such as the Coulomb interaction in atoms and molecules or the van der Waals interaction in liquid Helium. At short inter-nucleon distances, the two-body interaction is presumably influenced by heavy-meson and quark-exchange mechanisms, and the excitation of nucleon resonances. It is, in fact, poorly understood, although it is well constrained phenomenologically, at least below the pion production threshold, by the large body of  $pp$  and  $np$  elastic scattering data. It is predominantly characterized by a strong repulsion.

The interplay between these two outstanding aspects of the nucleon-nucleon interaction—its short-range repulsion and long-range tensor character—have profound consequences for the spatial and spin structure of nuclei [Fo96]. For example, the deuteron, the simplest nucleus consisting of a proton and neutron bound together, has a toroidal shape when the proton's and neutron's spins are opposite, and a dumbbell shape when their spins are aligned. This picture of the deuteron has been confirmed experimentally, in its broad outlines, by the recent measurement of the deuteron tensor polarization at Jefferson Lab [Ab00].

These short-range and tensor correlations are reflected in many nuclear properties. For example, the density distributions in nuclei of two-nucleon states with deuteron-like quantum numbers are very small at small inter-nucleon separations and exhibit strong anisotropies depending on the relative orientation of the two nucleons' spins; in the region  $r \leq 2$  fm, they are found to differ from those in the deuteron only by an overall scale factor depending on the mass number of the nucleus (e.g. [Fo96]). Another example of the impact of correlations is the increase in the relative probability of finding, within the nucleus, a nucleon with very large momenta.

As mentioned above, the nucleon-nucleon interaction is mediated at large distances by pion exchange. There were attempts to describe the nucleon-nucleon interaction at short and intermediate distances by an exchange of heavier (vector) mesons, with phenomenologically determined couplings and short-range cut-offs. Although this method described some set of experimental data, there is a paradox in the fact that QCD justifies only the existence of pseudoscalar (Goldstone) meson exchange as a result of spontaneously broken chiral symmetry of the QCD Lagrangian.

While the description of nuclei using the nucleon-meson picture outlined above provides a description of nuclear properties at average internucleon distances in nuclei, our lack of the knowledge of strong interaction dynamics at short and intermediate distances raises important questions:

- How much is the quark substructure of nucleons and mesons modified in the nuclear medium?
- To what distance scale does the short-range structure of nuclei based on the nucleon-meson degrees of freedom remain valid?
- How does the transition from the nucleon-meson to the quark-gluon based description of nuclei occur and what are its signatures?

A large portion of the experimental program of the 12 GeV upgrade is aimed at an understanding of the structure of isolated hadrons through a comprehensive study of their form factors, valence quark distribution functions, and generalized parton distribution functions. The 12 GeV upgrade will also provide unique opportunities for the investigation of possible modifications of this structure in the nuclear medium and the identification of the QCD mechanisms responsible for these modifications, through studies of the phenomenon of color transparency in exclusive processes, color van der Waals-type interactions in  $J/\psi$ -meson photoproduction, and quark propagation and hadronization in the nuclear medium.

Our current knowledge of nuclear structure and reactions in terms of interactions and rearrangements of unperturbed nucleons has been derived by probing nuclei “gently”, namely by measuring their response to hadronic and electroweak probes at low and moderate energies. However, an obvious question to ask is what happens when very high energies (comparable to or larger than the nucleon mass) are transferred to a nucleus and when nucleons are emitted at large angles. This must involve short-range mechanisms where nucleons overlap and where interactions between their constituents become relevant—the regime of short-range correlations. In this regime one expects that the notion of meson exchanges breaks down and direct constituent interactions like quark exchanges between nucleons, or “kneading” of the constituents of bound nucleons, becomes important. Clearly, the distance scale at which this occurs and the dynamical mechanisms responsible for short-range correlations need to be identified experimentally.

The nature of the hadron to parton transition region is another interesting and important open question in nuclear physics. Very little is known about the transition between these two regimes, in particular there are no clear indications from theory as to the energy range in which it should occur. Thus it must be mapped out by experiment.

An important search for this elusive transition region will be carried out with the 12 GeV Upgrade envisioned for Jefferson Lab. The strategy outlined below is to search for it in the simplest systems, i.e. in the pion and nucleon, since these are the hadronic building blocks of nuclei at low energy, and in the deuteron and helium isotopes, since these nuclei are particularly amenable to theoretical interpretation. Some proposed signals for the transition region are observation of scaling, hadron helicity conservation, color transparency and nuclear filtering. The proposed high-current 12-GeV electron beam coupled with relatively large acceptance detectors will be essential tools in searching for these exotic effects.

### **2.C.1 Hadron Structure in the Nuclear Medium**

One of the key goals of modern nuclear physics is to connect the properties of hadrons to their underlying degrees of freedom. Hadrons are bound states of quarks and gluons, whose interactions are described by QCD. While QCD describes well the weak interactions of quarks at short distances (perturbative QCD) and standard meson-nucleon models are successful in reproducing the overall

picture of hadrons interacting at large distances, our understanding of the connection between these regimes is extremely limited. While QCD is well established in the perturbative regime, properties of hadrons cannot be calculated perturbatively. Lattice QCD allows calculations of simple bound systems and is making significant progress in providing glimpses of the nucleon structure, but we are far from being able to calculate more complicated systems (e.g. nuclei or even nucleons) or the interactions of hadrons in terms of the underlying strong interaction of quarks and gluons. What we do know is that QCD leads to confinement of the fundamental constituents within hadrons, and that it is possible to describe nuclear structure in terms of these effective hadronic degrees of freedom at least in the limited energy range explored so far at Jefferson Lab.

The 12 GeV upgrade will allow us to probe in great detail the structure of nuclei, both in terms of the meson-nucleon model and the underlying quark structure. The upgrade also makes it possible to use the nucleus as a laboratory to study some of the central features of QCD which do not appear in traditional hadronic descriptions of nuclei. Studies of the strong interaction at short distance scales, where the meson-exchange model should break down, can help us understand how hadronic interactions are built up from the underlying interactions of quarks. Modification of nucleon structure as we approach the phase transition connected to chiral restoration and deconfinement at high densities will allow us to start mapping out the transition from hadronic degrees of freedom to the underlying quark degrees of freedom in the intermediate region between confinement and asymptotic freedom. We can also look for color transparency, a prediction of QCD that is related to the underlying color degrees of freedom, which is absent in traditional nuclear physics models.

With the energy upgrade we will cross the charm production threshold (8.3 GeV on free nucleons). The large mass of the charmed quark guarantees a perturbative treatment of its interaction with nuclear matter which may reveal 'exotic configurations' at short distances:  $J/\psi$ -N or  $J/\psi$ -A bound or quasi-bound states, as well as multi-quark, gluonic, or hidden color correlations in nuclei. The study of threshold and sub-threshold  $J/\psi$  production will also allow us to probe the creation mechanism and hadronic interactions of an exotic, intrinsically small-sized hadron. This allows us to study the interaction of a small color dipole object, providing yet another window on the microscopic (QCD) origins of hadronic interactions. Finally, because of the lack of  $c$ -quarks in nucleons, the production is dominated by multi-gluon exchanges, allowing access the Van der Waals part of the color interaction.

While these may appear to be largely unrelated topics, they all use the nuclear medium to look for effects absent in purely hadronic models of nuclear physics to establish QCD as the underlying theory of nuclear physics. They also give additional insight into the behavior of QCD in the non-perturbative regime. Currently, we study the non-perturbative behavior using effective degrees of freedom in QCD-inspired models and compare the predictions of these models to our knowledge of hadronic structure. As in the search for hybrid mesons, the goal is to probe the structure and interactions of new 'exotic' (non-hadronic) bound states of QCD to give us new windows on the

non-perturbative behavior. The ultimate goal is to answer the fundamental question: How are the structure and interactions of hadrons built up from their underlying constituents?

**Nuclear Matter at High Densities** High energy studies of hadrons in the nuclear medium will provide important opportunities to study the structure of nuclear matter at high density and characterize the nucleon-nucleon interaction at sub-fermi separations. The proton electromagnetic radius is  $\sim 0.86$  fm, and in the ground state of infinite nuclear matter the average spacing of nucleons is  $\sim 1.7$  fm. In dense nuclei, nucleons are closely packed and nearly overlapping. As the nucleons are not at rest, and in fact have strong interactions that generate significant momenta, there will be fluctuations in the nucleon separations. Thus, the nucleus is a natural place to investigate several questions regarding nuclear structure at high densities:

- What happens during the brief time intervals when two or more nucleons overlap in space?
- What is the mechanism of the exchange forces in sub-fermi distances? Can one continue to account for the interactions using meson-exchanges or will explicit quark-exchange forces start to play a dominant role?
- Does new physics emerge in these states where the densities can be several times the standard nuclear density as one approaches the phase transition from hadronic to quark matter?

If there is some modification to the confinement for overlapping nucleons, then a nucleus should deviate from a collection of closely packed nucleons. These deviations should increase for heavier nuclei, where the average density is larger and where there should be a larger component of overlapping nucleons. This should manifest itself in a density-dependence of the nucleon, or nuclear, structure beyond those predicted in meson-nucleon models. Such density-dependent effects have been seen in the past and these studies can be extended with the energy upgrade, in order to better understand their origins. More significantly, the upgrade will allow a new avenue of investigation into the behavior of matter at high densities. If we can isolate high density fluctuations in nuclei, we can probe these high density configurations, rather than just measuring the influence of this small component of the nuclear wavefunction on the overall structure of nuclei.

Investigating these questions will help us address the more general question of what is the role of quantum chromodynamics in the microscopic structure of nuclei. Figure 100 shows the phase diagram for hadronic matter. The high-density configurations in nuclei can have instantaneous densities several times higher than ordinary nuclear matter. Such densities approach the phase transition to a quark-gluon plasma, and effects from the onset of deconfinement and chiral restoration may significantly modify hadronic structure. These studies of high-density matter will provide complementary information to RHIC studies of the same phase transition at high temperature. In addition, these high-density fluctuations are the only forms of super-dense matter accessible in

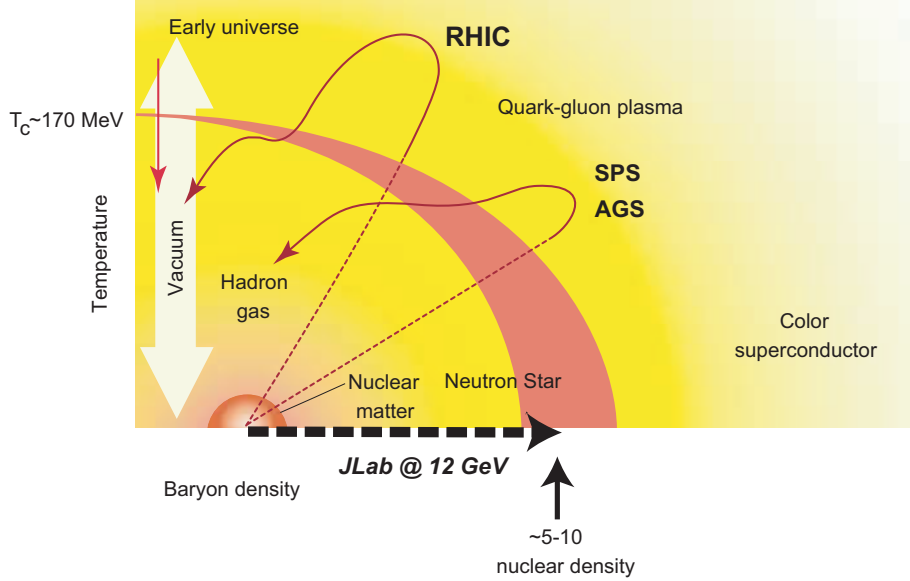


Figure 100: Phase diagram for hadronic matter.

terrestrial laboratories, and what we learn in nuclei may provide additional insight into matter at similar densities in neutron stars and other compact astronomical objects.

**Modification to Hadron Structure in Nuclei** The EMC collaboration first measured the nuclear dependence of the  $F_2$  structure function by comparing DIS scattering from heavy nuclei to deuterium. While these and subsequent measurements provided a clear observation of density-dependence to nuclear structure, there is not yet an accepted explanation of the effect. Some have tried to explain the effect within meson-nucleon models while others require modification to the hadronic structure. The exact origin of the nuclear dependence of the structure function is not known, although recent works [Sm02] indicate that a non-hadronic component is required to explain the data.

The  $x$ -dependence of the heavy nucleus to deuterium  $F_2$  structure function ratio is nearly independent of  $A$  and fairly well known for heavy nuclei, while the magnitude of the modification depends on the nucleus, and can be parameterized in terms of either  $A$ - or  $\rho$ -dependence. With the 12 GeV upgrade, Jefferson Lab can improve data at large  $x$  and in light nuclei. Data on  $^3\text{He}$  and  $^4\text{He}$  will allow us to determine if the EMC effect scales with  $A$  or with  $\rho$ , since while they are both very light nuclei,  $^4\text{He}$  has an anomalously large density ( $\rho_{^4\text{He}} \approx \rho_{^{12}\text{C}}$ ). If the EMC effect is related to a two-body effect (e.g. modification to nucleon structure in overlapping nucleons), then the EMC effect may have a very different  $x$ -dependence in few-body nuclei than in heavy nuclei [Sm99, Be99]. Measuring the EMC effect in light nuclei, especially at large  $x$ , will clearly differentiate such models from those which have a fixed  $x$ -dependence.

One other possibility is to determine the EMC ratio for the separated structure functions  $F_1$  and

$F_2$ . While existing DIS data show no nuclear dependence to  $R = \sigma_L/\sigma_T$ , the uncertainties are too large to determine if the separated structure functions might have different nuclear dependence, especially in the region where the EMC effect is large. While coverage in the DIS region limited for separated structure functions, coverage to larger  $x$  is possible in the resonance region. Even with 4 GeV beam, we see that the nuclear dependence in the resonance region (for  $Q^2 \gtrsim 4 \text{ GeV}^2$ ) is identical to the EMC effect observed in the DIS region. At larger beam energies, any deviation from this behavior due to the (much smaller) resonance contributions should be greatly reduced. The difficulty may be in extending the measurements to adequately large  $Q^2$ , as the ratio of  $\sigma_L/\sigma_T$  is expected to become quite small at large  $Q^2$ .

**High-Density Configurations in Nuclei** As discussed earlier, scattering from nuclei at  $x > 1$  can provide a great deal of information about the high momentum components of the nuclear wave function which are sensitive to short-range correlations (SRC's) in the nucleus. These correlated nucleons are an important part of nuclear structure and represent local high-density nuclear configurations. The minimum separation of the nucleons is determined by the short-range repulsive core of the N-N potential (at  $\sim 0.4 \text{ fm}$ ). By measuring at the highest  $Q^2$  values possible, we can isolate and probe the quark structure of these high-density configurations. This will allow us to look for new physics at high matter density (several times nuclear matter densities in the region where two nucleons overlap). At high enough densities, as at high temperatures, hadrons should be deconfined and hadronic matter undergoes a phase transition to a quark-gluon plasma. While these high-density fluctuations in nuclei will not lead to deconfinement, the structure of hadrons may be dramatically changed during the brief periods when the nucleons have significant overlap. The observations of the EMC effect as well as more recent measurements that indicate the form factors of a nucleon are modified [St02] in a bound nucleus, already hint that confinement may be weakened at densities found inside of a nucleus. By probing the quark structure of correlated nucleons, we can look directly for modification to hadron structure at high density.

The energy upgrade will allow us to expand the  $Q^2$  range for inclusive scattering at  $x > 1$ . This provides access to the DIS regime, even for  $x > 1$ , allowing us to probe the internal structure of two-nucleon correlations. A measurement in the DIS regime at  $x > 1$  would lead to a determination of the distributions of super-fast quarks in nuclei, where the momentum carried by the struck quark is greater than what one would expect for an entire nucleon. These quark distributions are related to the quark structure of the two-nucleon correlations which dominate for  $x \gtrsim 1.1$  and large  $Q^2$ . The EMC effect demonstrates that the quark structure of a nucleus is more than just a convolution of the quark structure of its nucleons. If this comes from density-dependent modifications to nucleon structure, then similar, but much larger, effects should be seen when one examines the quark distributions at large  $x$ , where the strength comes almost entirely from pairs of overlapping nucleons. The  $x$ -dependence from a convolution of the nucleon momentum distribution with the nucleon parton distribution functions will be very different from the quark distribution (*e.g.* 6-quark bags or nucleon deformations in the region of overlap). Such an exotic configuration would



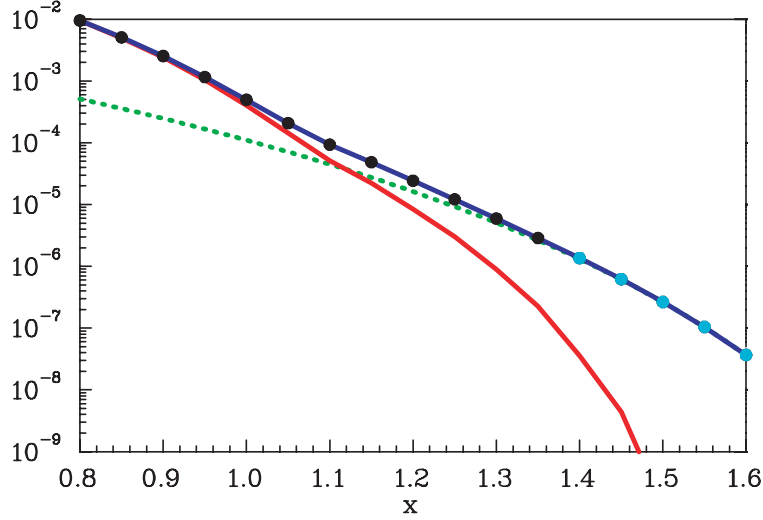


Figure 101: Distribution of super-fast quarks for deuteron assuming just two nucleons (red curve), or including a 5% contribution from a 6-quark bag (green dashed curve). The sum of the two contributions is shown as the blue curve. The expected uncertainties including a systematic uncertainty of 3-5% are smaller than the points shown. We expect that for  $x$ -values below 1.4 (black circles) the data should be in the DIS scaling regime.

allow the quarks in the two nucleons to share momentum directly, rather than sharing momentum just by nucleon interactions. The direct interaction of quarks in the two nucleons will lead to a dramatically increased probability of finding quarks at  $x > 1$ , and such an observation will give a clear indication of deviations from a purely hadronic picture of nuclear structure.

There is little data available for structure functions of nuclei at  $x > 1$ . Measurements of muon scattering from Iron [Be94] have only upper limits above  $x = 1.1$ , and show a rapid falloff in the structure function near  $x = 1$  ( $F_2(x) \propto \exp(-16.5x)$ ). Measurements of neutrino scattering from Carbon [Va00] also have a limited  $x$  range ( $x < 1.2$ ), but indicate significantly more strength at large  $x$  ( $F_2(x) \propto \exp(-8.3x)$ ). With the increase in  $Q^2$  possible with the JLab energy upgrade, high precision measurements of the structure function can be made over a wide range in  $x$ , allowing us to cleanly map out the distribution of super-fast quarks. The energy upgrade will allow us to reach  $Q^2 > 20 \text{ GeV}^2$ , where the inelastic contributions dominate the cross section up to  $x = 1.4$ . Figure 101 shows the difference in the distribution of super-fast quarks in deuterium in the presence of a small (5%) six-quark bag component to the deuteron. Measurements on deuterium will allow us to look for deviations from the purely hadronic model, without the need to model the effects of multi-nucleon correlations. Measurements on heavier nuclei (*e.g.* Carbon) will have much larger signals from two-nucleon SRC's, which can be separated from the effects of multi-nucleon correlations, as described in section 2.C.2.

The second step in understanding the structure of high-density configurations will be to study tagged structure functions [Fr81, Fr88, Ci93] in order to compare directly the parton structure of



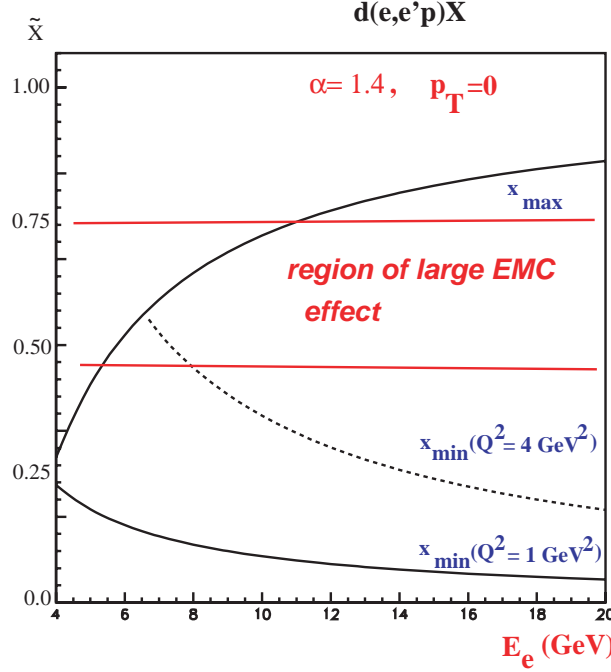


Figure 102: The scaling window for  $\alpha = 1.4$ , where  $\alpha$  is the light-cone fraction of the knocked-out nucleon. The upper curve is defined by the requirement that the mass of the produced final hadronic state  $W \geq 2$  GeV.

the bound and free nucleon. This will start with the  $e + {}^2\text{H} \rightarrow e + \text{backward nucleon} + X$  reaction in the kinematics where the momentum fraction carried by the struck quark in the moving nucleon ( $\tilde{x}$ ) is sensitive to the EMC effect [ $0.3 \leq \tilde{x} \leq 0.7$  (CEBAF at 11 GeV covers all of this region; see Fig. 102)] and continue to a similar reaction with  ${}^3\text{He}$  and the tagging of two backward nucleons to consider deformations in the three-nucleon correlations. In contrast to the case of the inclusive EMC effect, different models predict [Fr88, Ca91, Ca95, Me97] a qualitatively different dependence of the experimental results on the modifications of the bound nucleon wavefunction, which range from a complete absence of modification to an effect comparable to the EMC effect for heavy nuclei in the color screening model, for tagged nucleon momenta  $p_N \geq 300$  MeV/ $c$ . If the EMC effect for the bound nucleon is observed, one would be able to check whether the theoretical account of such deformations together with a realistic light-cone nucleon density (measured in the  $A(e, e'p)$  processes) would reproduce  $F_{2A}(x, Q^2)/F_{2D}(x, Q^2) > 1$  in the scaling region.

The two-step strategy described above requires related studies that are important to cross-check all aspects of these studies:

- *Investigation of the reaction dynamics at  $Q^2 \geq 4$  GeV<sup>2</sup>.* The reaction dynamics of  $(e, e'p)$  at GeV energy and momentum transfers have only just begun due to limited beam energy. These dynamic will be quite different from low energy, due to the diffractive nature of the high-energy  $NN$  interaction and the role of relativity. With the energy upgrade, one can

study, for example, the reaction  $e + {}^2\text{H} \rightarrow e + p + n$  in parallel kinematics for recoil nucleon momenta  $p_N = 400 - 500 \text{ MeV}/c$  up to  $Q^2 \approx 8 \text{ GeV}^2$ . A study of this type is essential for our understanding of the baseline color transparency calculations and of short-range structures in the nucleus.

- *A test of the binding models of the EMC effect*, by measuring the position of the quasielastic peak at large  $Q^2$ . In these models, a shift of the nucleon spectral function to  $\alpha < 1$  is expected, leading to a significant asymmetry in the cross section of the  $(e, e'p)$  process in parallel kinematics near the quasielastic peak [Fr92].
- *Studies of special modes of deuteron breakup at high  $Q^2$  using the upgraded CLAS* would be sensitive to meson-exchange currents, *e.g.*,  $e + {}^2\text{H} \rightarrow \text{two forward protons} + \text{leading } \pi^-$ , and processes such as production of backward  $\Delta$ 's off the deuteron and  ${}^3\text{He}$  that are especially sensitive to the presence of  $\Delta$ -isobar-like color-singlet clusters and six-quark clusters.
- *Probing quark degrees of freedom in large-angle electrodisintegration of the deuteron* will be a natural extension of the CEBAF photodisintegration experiment [Bo98]. This was the first case of a high-energy nuclear physics reaction for which descriptions based on the quark degrees of freedom and on the assumption that *the short-range NN forces are due to quark exchange* quantitatively agree with the data, while all theoretical descriptions invoking hadronic degrees of freedom qualitatively disagree with the data [Fr00]. Study of deuteron electrodisintegration and similar exclusive real photon reactions at high energies will allow a significant extension of the range of the observed energy scaling. A crucial prediction of the quark-exchange picture is that for a wide range of photon virtualities the cross section should depend on the photon virtuality as the point-like Mott cross section.

In summary, the increase of electron energy to 11 GeV will significantly expand the possibilities for systematic studies of high-momentum-transfer processes with nuclei. The ultimate result will be a detailed understanding of the hadronic and quark degrees of freedom in nuclear matter at extremely high densities.

**Color Transparency** While color transparency (CT) as a direct consequence of QCD in hard exclusive processes is not questionable, its applicability and its manifestation in specific processes remain open problems. Indeed, a non-ambiguous evidence of CT not only requires the selection of a small size configuration but also a clear signature of the subsequent reduced interaction. The main parameter that governs the CT phenomenon is the momentum transfer of the virtual photon that controls the transverse size and part of the coherence length of the mini-hadron. The latter corresponds to the distance required for the mini-hadron to evolve from its minimal valence state toward its asymptotic wave function. There are several ways to look for CT effects:  $A(e, e'p)$  reactions in both heavy and few-body nuclei, and meson electro- and photo-production.

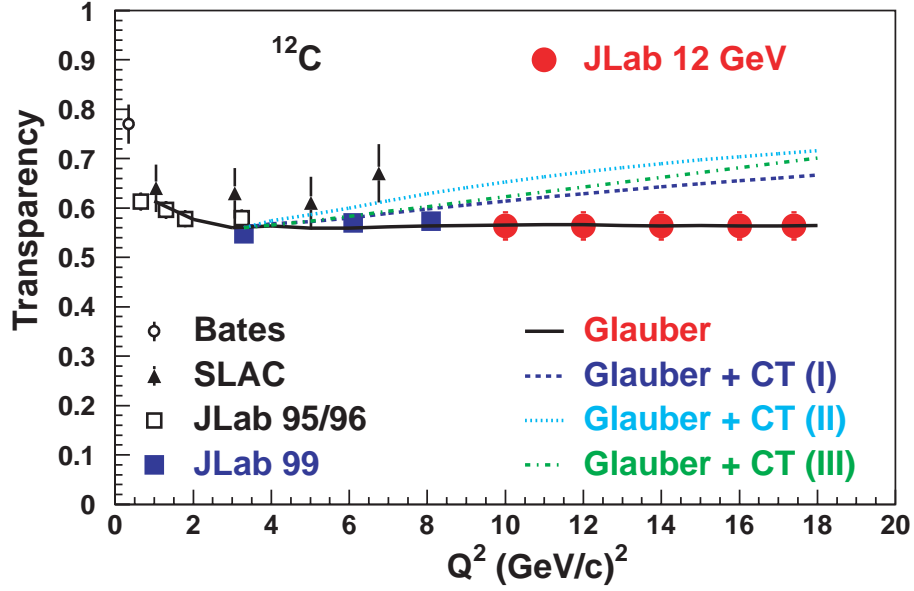


Figure 103: The  $Q^2$ -dependence of nuclear transparency. The data are from Refs. [Ga92, Ne95, Ab98, Ga02], while the circles are projected uncertainties for a one week run at 12 GeV.

**Color Transparency in  $A(e,e'p)$**  The study of quasiexclusive hard reactions  $A(p,2p)$  and  $A(e,e'p)$  can shed light on the range of  $Q^2$ s necessary for the wavefunctions of nucleons to be dominated by point-like configurations (PLC) [Br82, Mu82]. If  $Q^2$  is large enough, one expects both the scattered particle and the projectile (for  $(p,2p)$ ) to travel through the nucleus in point-like configurations. A straightforward way to look for CT is to determine the transparency ratio  $T = \sigma_{exp}/\sigma_{PWIA}$  in  $A(e,e'p)$  reactions as a function of  $Q^2$  and various nuclei  $A$ . Experiments at SLAC [Ne95] and JLab [Ab98, Ga02] exclude sizable CT effects up to  $Q^2 = 8.1 \text{ GeV}^2$ . The 12 GeV upgrade will improve the situation by more than doubling the accessible  $Q^2$  region. This will allow measurements to be made where the CT predictions diverge appreciably from the predictions of conventional calculations. In addition, the Brookhaven  $(p,2p)$  data establish a definite increase in transparency for nucleon momenta above  $7 \text{ GeV}^2$ . If this is a signature of CT, then  $A(e,e'p)$  measurements at  $Q^2 > 12 \text{ GeV}^2$ , corresponding to comparable momenta of the ejected nucleon, would also be expected to show CT. Figure 103 shows both the present status and projected uncertainties of CT in the measurements feasible with 11 GeV beams.

**Color Transparency in Few-Body Systems** A more sensitive way to observe the onset of CT in nuclei, feasible only with higher beam energies, is to look for processes where the ejectile interacts with other nucleons after the interaction with the virtual photon [Fr91, Eg94, Fr95b, La98a]. A large portion of the  $(e,e'p)$  cross section beyond  $p_m \geq 300$  MeV/c originates from recoil nucleons with lower momenta rescattering. With the onset of CT, this rescattering should decrease as a function of increasing  $Q^2$ , and produce a more significant effect than just measuring the transparency ratio  $T$ , even at low values of  $Q^2$ . Another important advantage of studying this reaction process is that the effect can be studied even in the lightest nuclei ( $^2H, ^3He, ^4He$ ) for which wave functions are known much better and the eikonal approximation, which accounts for all orders of rescattering [Eg94, Fr95, La98a], can provide a reliable base line calculation.

A suitable measure of this effect can be studied in the  $(e,e'p)$  reaction as a ratio  $R$  of the cross section in kinematics where this rescattering term is dominant ( $p_{recoil} \sim 400$  MeV/c) to the cross section in kinematics where single scattering is dominant and Glauber screening is important ( $p_{recoil} \leq 200$  MeV/c). Figure 104 shows these regions clearly in the  $^3He(e,e'p)d$  reaction cross section as a function of the missing momentum [E89044] for a low value of  $Q^2 = 1.55$  GeV<sup>2</sup>. The predicted value of this ratio  $R = \sigma(p = 400 \text{ MeV/c})/\sigma(p = 200 \text{ MeV/c})$  for the case of D( $e,e'p$ ) and the effect of color transparency is quite dramatic even at low values of  $Q^2$  (Fig. 105). In all cases, the CT effects are estimated within the quantum diffusion model (QDM) of Ref. [Fa88] utilizing two values for the expansion parameter  $\Delta M^2 = 0.7$  and  $1.1$  GeV<sup>2</sup>, which characterize the time development of the PLC during the propagation in the nuclear medium. These two values of  $\Delta M^2$  give the upper and lower limit of CT predictions within the QDM model. The predicted signal is much larger than in the attenuation measurement, and by measuring the  $Q^2$ -dependence of the *ratio*, uncertainties in the reaction mechanism become much less important.

**Color Transparency in Meson Production** Meson production should provide an even clearer process for observing CT phenomenon. Intuitively, one expects an earlier onset of CT for meson production, as it is much more probable to produce a small transverse size in a  $q\bar{q}$  system than in a three quark system. Direct measurements of nuclear transparency can be performed with pion and rho-meson electroproduction, as well as pion photoproduction. As in the case of the direct measurements of nuclear transparency in proton knock-out reactions, the increased beam energy will allow for a significant increase in the momentum transfer of these reactions compared to the measurements that can be made with 6 GeV beams. Figures 106 and 107 show projected uncertainties for measurements of  $\rho$  and  $\pi$  electroproduction. Color transparency in pion photoproduction is also discussed in a later section, along with the closely related topic of nuclear filtering, whereby the formation of a small size hadron configuration reduces not only the interaction of pions as they traverse the nucleus, but also the long-distance amplitudes which may lead to oscillations in the pion photoproduction cross section.

With the availability of high energy and high intensity electron beams, one can combine the advantages of rescattering measurements with those of meson production. Such experiments will

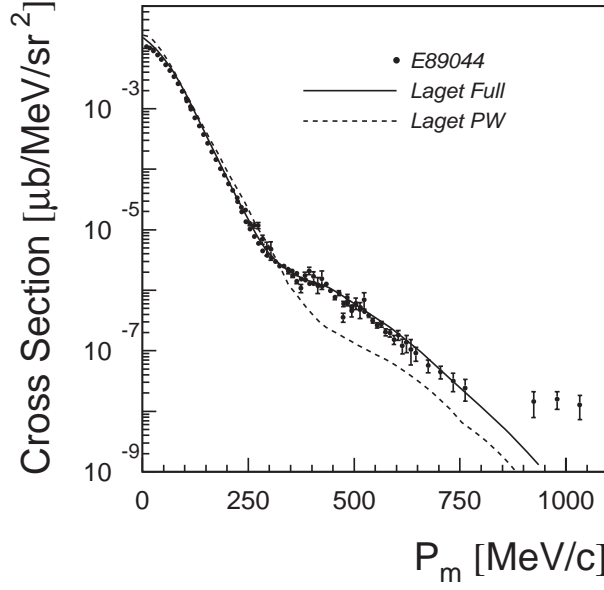


Figure 104: Data from the Hall A  $^3\text{He}(e, e'p)d$  experiment [E89044] shown with the calculations of Jean-Marc Laget show that the region around 400 MeV/c is dominated by FSI.

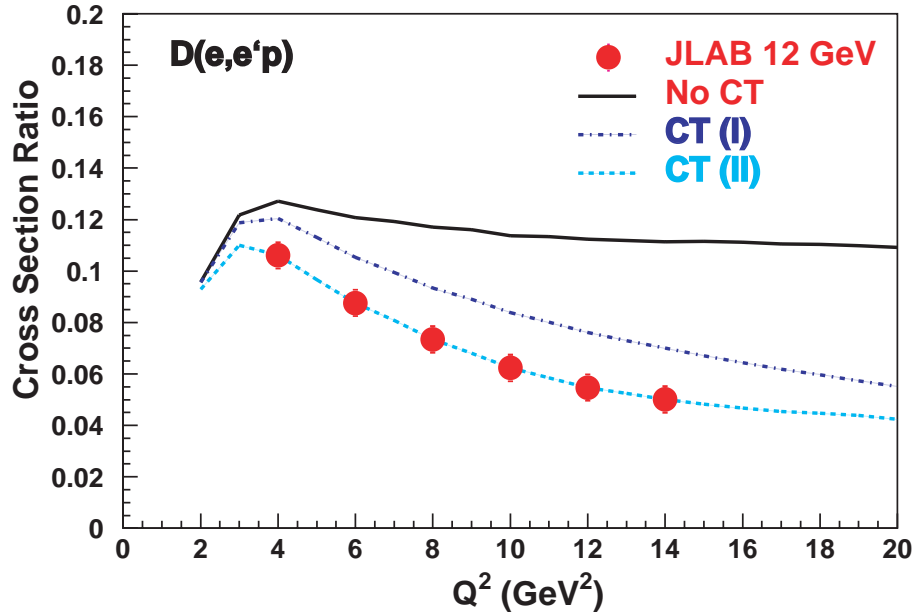


Figure 105: Ratio  $R = \sigma(p_m = 400 \text{ MeV}/c) / \sigma(p_m = 200 \text{ MeV}/c)$  for  $D(e, e'p)$  reaction. CT(I) and CT(II) corresponds to Color Transparency calculations with  $\Delta M^2 = 0.7$  and  $1.1 \text{ GeV}^2$  respectively in the QDM Model [Fa88, Sape]

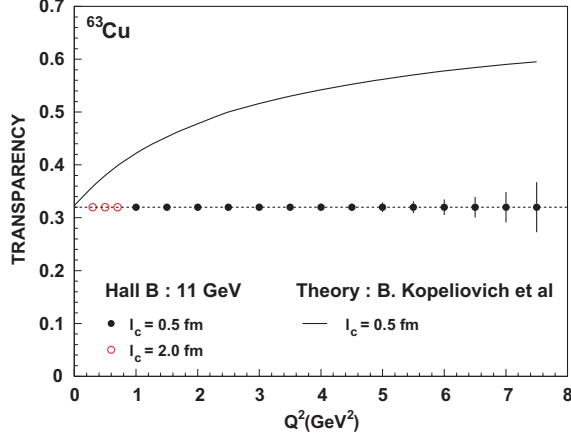


Figure 106: Projected uncertainties for a measurement of transparency in  $\rho$ -electroproduction in Hall B .

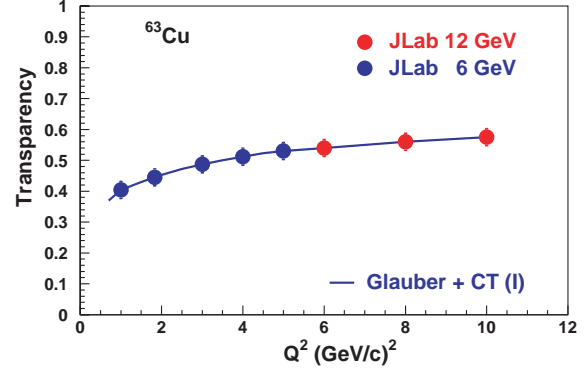


Figure 107: Projected uncertainties for measurement of transparency in pion electroproduction in Hall C.

be less sensitive to the formation of the PLC and its subsequent evolution back to a normal hadron, and should provide the cleanest test for color transparency. Electroproduction of vector mesons off a deuteron in a fully exclusive reaction is one such reaction:

$$e + d \rightarrow e' + V + d' \quad (51)$$

where “ $V$ ” is the  $\rho$ ,  $\omega$ , or  $\phi$  vector meson. The electron, recoiling deuteron, and decay products of the vector meson are all detected in the final state.

Coherent production of vector mesons off deuterium can be described by single- and double-scattering mechanisms. In the single-scattering case, only one nucleon participates in the interaction and so the  $t$ -dependence will follow the deuteron form factor. In the double-scattering (rescattering) mechanism, dominant at  $-t > 0.6 \text{ GeV}^2$ , the photon interacts with one nucleon to form an intermediate hadronic state that subsequently rescatters from the second nucleon before forming the final state vector meson. This process has a harder  $t$ -dependence than the first one, and this is where evidence of CT will manifest itself.

The key point in the investigation of CT phenomena is measuring the re-interaction process at different  $Q^2$  values. The reduction of the transverse size of the intermediate hadronic state with increasing  $Q^2$  will lead to a diminished reinteraction, and thus a change in the  $t$ -dependence at high  $t$ . Differential cross sections will be measured at the same  $Q^2$  and coherence length,  $l_c = 2\nu/(m_V^2 + Q^2)$ , but at different  $t$  values. At low  $-t$ , the single scattering process dominates, while at high  $-t$ , the rescattering dominates. The ratio of these cross sections, with and without the inclusion of CT effects, is plotted in Fig. 108. This ratio is sensitive to the effects of CT while being insensitive to systematic uncertainties.

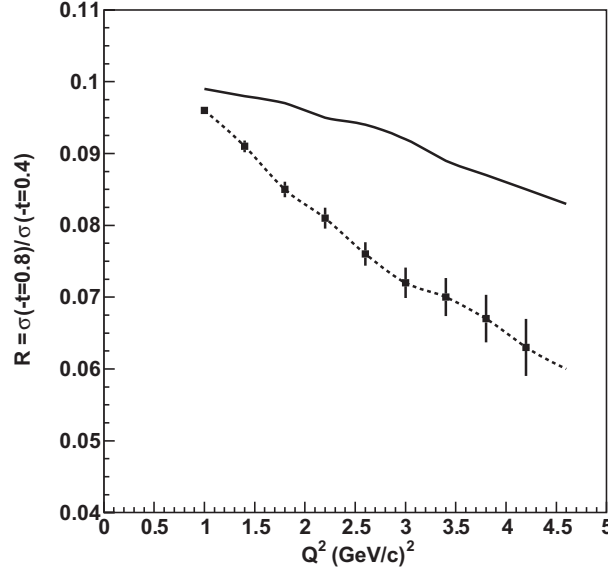


Figure 108: Projected uncertainties on the ratio of cross sections at transferred momenta  $0.4 \text{ GeV}/c^2$  and  $0.8 \text{ GeV}/c^2$  for 2000 hours of running on CLAS with  $11 \text{ GeV}$  beam. The solid curve assumes no color transparency effects, the dotted curve is with color coherent effect. Events in each point are integrated in the bins of  $\Delta Q^2 = 0.4 \text{ GeV}/c^2$  and  $\Delta l_c = 0.2$ .

The above series of attenuation and rescattering measurements for both protons and mesons will allow us to separate the necessary ingredients: formation of the small sized configuration, the reduced color interaction of these configurations, and the evolution of these exotic configurations back into ordinary hadrons. The observation of color transparency and characterization of the non-perturbative evolution of a mini-hadron to its physical size will lead to a better understanding of the dynamics of confinement.

**$J/\psi$  Photoproduction Near Threshold** The threshold production of charmonium and open charm production opens up a new window into QCD dynamics; in particular, these reactions are sensitive to multiquark, gluonic and hidden color correlations in nucleons and nuclei. In contrast to diffractive charm production at high energy, which tests the behavior of the gluon structure functions at small  $x$ , charm production near threshold tests the structure of the target near  $x = 1$  and its short-range behavior.

This difference results from the kinematics of the reaction products. For  $J/\psi$  production on nucleon, the threshold energy is  $E_\gamma = 8.20 \text{ GeV}$ , and due to the large mass of the charmed quark ( $m_c \approx 1.5 \text{ GeV}$ ) the  $c\bar{c}$  fluctuation of the photon travels over the coherence length  $l_c \cong 2E_\gamma/4m_c^2 = 0.36 \text{ fm}$ . The large mass of the charmed quark also imposes a small transverse size  $r_\perp \sim 1/m_c = 0.13 \text{ fm}$  of this fluctuation as well as a small impact parameter  $b \sim 1/m_c = 0.13 \text{ fm}$ . All five valence quarks (the two heavy charm quarks in the probe and the three light quarks in the target) must be in the same small interaction volume. As a consequence, all the quarks must be

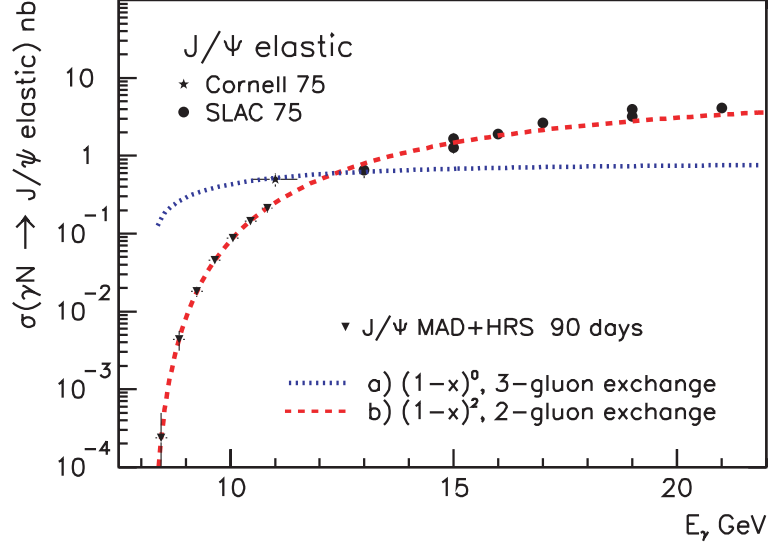


Figure 109: Variation of the cross sections of  $J/\psi$  photoproduction near threshold, for two or three gluon exchange mechanisms. The inverted triangles show the expected accuracy using the Hall A MAD and HRS spectrometers with 11 GeV beam.

involved in the reaction mechanism. For nucleon targets, this implies that three-gluon exchange may take over two-gluon and one gluon exchange, and open the way to the study of correlations between valence quarks [Br01]. As depicted in Fig. 109, such a conjecture is consistent with the limited data that are available [Ca75, Gi75, An77] on a nucleon target. Clearly higher energy beams from an upgraded CEBAF will allow a more comprehensive determination of the  $J/\psi$  photoproduction cross section between threshold and 12 GeV.

On few-body targets each exchanged gluon may couple to a colored quark cluster and reveal the hidden color part of the nuclear wave function, a domain of short-range nuclear physics where nucleons lose their identity. These hidden color configurations are predicted by the QCD evolution equations [Br83]. It is striking that in  $\gamma d \rightarrow J/\psi pn$  the  $|B_8 \overline{B}_8\rangle$  hidden color state of the deuteron couples naturally by two gluons to the  $J/\psi pn$  final state [La94] (see Fig. 110). Such a contribution may dominate subthreshold production, since the high momentum of the nucleon suppresses quasifree mechanisms. The threshold for  $J/\psi$  production on deuterium is 5.65 GeV, while on heavy nuclei the threshold approaches 3.1 GeV, the  $J/\psi$  mass.

Even though the  $c\bar{c}$  pair is created with rather high momentum at threshold, it may be possible to observe reactions where the pair is captured by the target nucleus, forming “nuclear-bound quarkonium” [Br90, Wa91]. This process should be enhanced in subthreshold reactions. There is no Pauli blocking for charm quarks in nuclei, and it has been estimated that there is a large attractive van der Waals potential binding the pair to the nucleus [Lu92]. The discovery of such qualitatively new states of matter would be a major achievement.



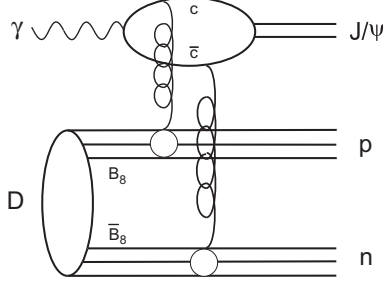


Figure 110: The simplest diagram to reveal hidden color state in deuterium [La94].

The formation length,  $l_F$ , over which the  $c\bar{c}$  pair evolves into a  $J/\psi$  after its interaction with a nucleon, is given by:

$$l_F \cong \frac{2}{m_{\psi'} - m_{J/\psi}} \left[ \frac{E_{J/\psi}}{2m_c} \right] \cong 0.22E_\gamma \quad (52)$$

Near threshold  $l_F$  is around 1 fm, closer to the size of the nucleon than the size of the nucleus. This is the ideal situation for determining the scattering cross section of a full sized charmed meson on a nucleon, in contrast to the situation at higher energies, where the cross section is sensitive to the interaction of a compact  $c\bar{c}$  pair with the entire nucleus. The study of the  $A$ -dependence of the  $J/\psi$  photoproduction cross section at SLAC at 20 GeV [An77b] gave  $\sigma_{J/\psi} = 3.5 \pm 0.8 \pm 0.5$  mb. Unfortunately the need to subtract a large calculated background and the lack of information on the  $J/\psi$  kinematics makes it impossible to disentangle coherent and incoherent photoproduction in this experiment. The study [Ge92] of hadron production gave  $\sigma_{J/\psi} \approx 7$  mb. However, after correction [Hu98] for energy loss of the incoming hadron and for coherence effects this value went down to  $\sigma_{J/\psi} \approx 3.6$  mb. On the theoretical side, QCD calculations [Kr99] predict that  $\sigma_{J/\psi} \approx 0.3$  mb at 20 GeV, and that it falls rapidly as the energy is reduced. In contrast, a calculation by Brodsky [Br97] based on the van der Waals potential yielded  $\sigma_{J/\psi} \approx 7$  mb at low energies.

This situation calls for a new measurement of  $J/\psi$  photoproduction on several nuclei for  $E_\gamma \approx 10$  GeV, with a good identification and determination of the  $J/\psi$  momentum. The systematic error of such a measurement will be better than in the previous SLAC measurement [An77b]. The nuclear transparency  $T = \sigma_{\gamma A}/(A \cdot \sigma_{\gamma N})$  and the expected statistical accuracy are given in Table 11.

Besides possible applications in connected domains (for instance, the knowledge of the  $J/\psi$ - $N$  scattering in the search for signatures of Quark-Gluon plasma), all these studies select *gluonic exchange mechanisms between hadrons or quark clusters*. The observation of a gluonic potential between color neutral states is of utmost importance as it would open up the possibility to trace part of the nucleon-nucleon interaction at short range to such a color van der Waals force. Only the high intensity and duty factor of the beams that will be available from an upgraded CEBAF make it possible to realize the new experiments that are essential for the exploration of this frontier of our knowledge.

Table 11: The values of nuclear transparencies for  $J/\psi$  propagation, calculated in the model used by the SLAC measurement [An77b], for 3 values of  $\sigma_{\psi N}$ . The last column presents the expected statistical error,  $\delta\sigma(\sigma_{\psi N})$  for a  $\sigma_{\psi N}$  measurement at CEBAF using 11 GeV beam, assuming a statistical error of 3% for the yields on every target.

A	9	12	27	63	108	207	$\delta\sigma(\sigma_{\psi N})$ , mb
T for $\sigma_{\psi N}=1.0$ mb	0.982	0.980	0.974	0.963	0.952	0.929	0.28
T for $\sigma_{\psi N}=3.5$ mb	0.938	0.931	0.908	0.870	0.833	0.751	0.24
T for $\sigma_{\psi N}=7.0$ mb	0.876	0.863	0.816	0.740	0.665	0.502	0.17

**Space-Time Characteristics of Hadronization** Due to the property of confinement, a struck quark in a hard process will evolve in space-time to produce multiple hadrons through the complex process of hadronization. This behavior is a unique property of QCD. By studying the properties of the hadrons emerging from deep inelastic scattering (DIS) on a range of nuclei, important information on the characteristic time-distance scales of hadronization can be determined as a function of several variables.

The physical picture of hadronization in a nucleus begins with a hard interaction on a bound quark within the nuclear volume. This is illustrated in Fig. 111. For large  $Q^2$  and  $\nu$  the initial interaction is localized to a very small volume and results in an energetic quark propagating through the nuclear medium. Ultimately this quark emerges bound in a hadron, accompanied by other hadrons generated in the process. The time interval between the  $\gamma^*-q$  interaction and the hadron being fully reconstituted is often referred to as the *formation time*. If the formation time is much smaller than the nuclear transit time, then the hadron that carries the struck quark will strongly interact with the nuclear medium. This hadron will then be 'lost' in the sense that the event shifts to higher multiplicity and lower particle momenta relative to the same interaction on a smaller nucleus. If, on the other hand, the formation time is much longer than the nuclear transit time, then the formed hadron will not interact with the nuclear medium. In this way, hadron absorption by nuclei can be used to estimate the time scales of the hadronization process.

The observable that is used to quantify this absorption is the *hadronic multiplicity ratio*  $R_M^h$ . This quantity is defined as

$$R_M^h = \left\{ \frac{N_h(z, \nu)}{N_e^{DIS}(\nu)} \right\}_A / \left\{ \frac{N_h(z, \nu)}{N_e^{DIS}(\nu)} \right\}_D \quad (53)$$

In this expression,  $N_h$  is the number of hadrons produced in DIS events and  $N_e^{DIS}$  is the number of associated DIS electrons. The numerator corresponds to target nucleus A, and the denominator corresponds to deuterium.  $\nu$  is the energy transferred by the electron, and  $z$  is the hadron energy divided by  $\nu$  ( $0 < z < 1$ ). In the QCD-improved parton model,  $R_M^h$  is given by ratios of sums over products of the quark distribution functions with fragmentation functions.



Figure 111: Artist's concept of the hadronization process in the valence quark regime. In the upper left corner, a quark undergoes a hard interaction with a virtual photon; in the middle picture the struck quark separates rapidly from the other quarks, forming a region of high energy density in which several proto-hadrons begin to form; in the bottom left-hand corner the struck quark emerges as part of a newly-formed hadron. In the lower left corner of the figure, this process is visualized implanted in a nucleus; by varying the nuclear size, the distance scales involved can be probed, since the fully formed hadron will interact with the nuclear medium.

There are several scientific issues surrounding the hadronization distance scale studies. An important example is the fundamental process of gluon emission. The present understanding of gluon emission by the propagating quark is that it occurs both in vacuum and within the nuclear medium; within the nuclear medium it is additionally stimulated by multiple scattering from the nuclear partons. The propagating quark loses energy as a result. In a hot nuclear medium an additional dynamic of thermally stimulated gluon absorption and emission comes into play, while this is irrelevant in the cold nuclear medium. At some point the propagating quark evolves into a hadron, and the copious production of gluons ceases. The balance between gluon emission and hadronization, and the relationships between the two, are not established theoretically or experimentally, and this is a major theme addressed by the measurements identified here. Most experimental efforts, as will be discussed below, have focused on formation of either pions or protons; the proposed JLab measurements will address a much broader spectrum of nearly twenty hadrons.

Exploratory studies of  $R_M^h$  have been carried out at HERMES using 12 and 27 GeV positron beams on nitrogen and krypton targets; the higher energy nitrogen data have been published to date [Ai01a, Na02a]. These studies have been interpreted as being dominated by hadronization, and characteristic formation times for negative and positive pions, and protons, have been derived. The HERMES nitrogen analysis employed a phenomenological formalism [Bi83] that characterizes the hadronization process by a single time constant, the formation length, which is the characteristic parameter of a decaying exponential  $P_q(x_1 - x_2) = \exp[(x_1 - x_2)/\tau_f]$  representing the probability that the propagating object struck at coordinate  $x_1$  is still a quark at coordinate  $x_2$ . The probability that the object is a hadron is then  $1 - P_q$ . The propagating object interacts with a quark-nucleon cross section  $\sigma_q$  while it is a quark, and a hadron-nucleon cross section  $\sigma_h$  while it is a hadron. The  $\nu$ - and  $z$ -dependence of  $\tau_f$  is not known from a fundamental theory, and several have been proposed. The HERMES analysis tested three basic forms and was able to eliminate two of the three based on the observed  $z$ -dependence. Within the above phenomenological framework, the form that most closely represented their data was  $\tau_f = c_h(1 - z)\nu$ , where  $c_h$  is a constant depending on the hadron type. Figure 112 shows a schematic example of what the upgraded JLab would be able to measure.

While many assumptions necessarily go into such an analysis, the HERMES pioneering studies offer tantalizing hints concerning the nature of hadronization. There are still numerous outstanding questions. For instance, is this a mass effect or a size effect? Is there contamination from knocked-out protons or pions rather than particles created through a fragmentation process? Are there other reaction mechanisms contaminating the event sample? What is the flavor dependence of the formation time? How realistic is the relatively simple picture of hadronization within the nucleus on which these analyses are based?

These questions can be well-addressed by an upgraded JLab in a natural extension to an approved 6 GeV measurement [E02104]. The limited information available on the  $Q^2$ -dependence of  $R_M^h$  will be easily remedied by the high luminosity available after the upgrade. The issue concerning contamination from potentially knocked-out protons (or pions) can be addressed by

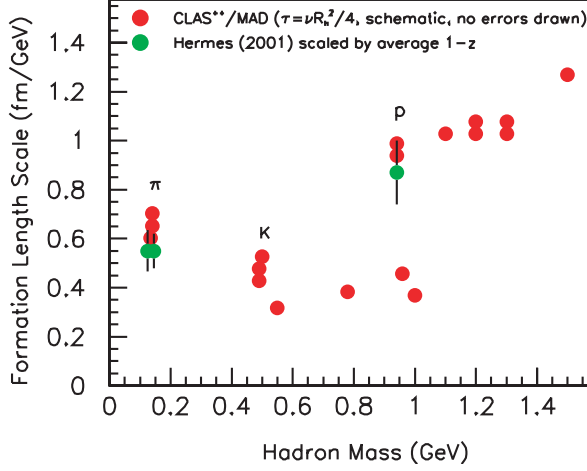


Figure 112: Schematic example of possible results for hadronization length scales. The meson band is in the lower half of the plot, the baryon band in the upper half.

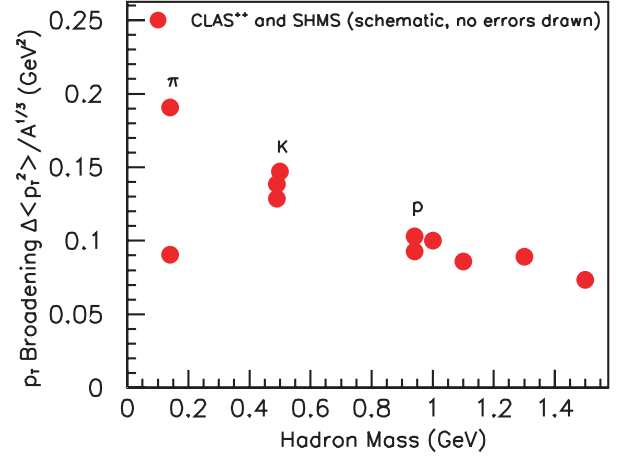


Figure 113: Schematic example of possible results for transverse momentum broadening. Many such plots will be available, in multivariable bins in, e.g.,  $Q^2$ ,  $\nu$ ,  $z$ , helicity.

studying particles of a similar mass which were not pre-existing in the nucleus, such as  $\Lambda$  particles or neutral kaons. The flavor and mass dependence can be further studied by using a wide array of particles that are known to be stable over a distance scale much larger than nuclear dimensions. Accessible hadrons include  $\pi^{+, -, 0}$ ,  $\eta$ ,  $\omega$ ,  $\eta'$ ,  $\phi$ ,  $K^{+, -, 0}$ ,  $p$  and  $\bar{p}$ ,  $\Lambda$  and  $\Lambda(1520)$ ,  $\Sigma^{+, 0}$ , and  $\Xi^{0, -}$ . A quite impressive advance in understanding formation lengths can be attained by systematically studying the production of all of these particles for a series of nuclei, providing strong constraints on model calculations.

The hadrons that decay into multiple particles will be measured by CLAS<sup>++</sup>. Measurements for the lowest-rate hadrons, or out to highest  $p_T$  or  $Q^2$ , can be performed by the SHMS and MAD. Because of the high luminosity, the dependence on multiple variables can be studied even for the particles that have a low production cross section or for which the acceptance is small. The ability to carry out studies on a number of different particles will help to evaluate if this simple picture of hadronization within nuclei is adequate. If a consistent picture emerges, then one can have confidence in that picture; if not, a more sophisticated framework can be developed.

In conclusion, the opportunity exists to thoroughly and systematically study the space-time characteristics of hadronization by determining the variable dependences of the formation length. The studies can be carried out as a function of  $Q^2$ ,  $\nu$ ,  $p_T$ ,  $z$ , helicity, hadron mass and size, and quark flavor. This large program is expected to yield a wealth of new insights into the nature of the gluon emission process and hadronization, which is a direct manifestation of confinement.

**Transverse Momentum Broadening** As a struck quark traverses the color field presented by a nucleus, it scatters off the partons in the medium, losing energy primarily by radiation of gluons.

The gluon emission, which is a fundamental prediction of QCD, may have a coherent character similar to that of the Landau-Pomeranchuk-Migdal (LPM) effect [Lan53, Mi56, An97] in the QED energy loss of charged particles passing through atomic matter. This coherence, in combination with the non-Abelian nature of QCD radiation, predicts that the energy loss will be *quadratic* in the distance the quark travels through a nuclear medium, in strong contrast to the energy loss in quantum electrodynamics.

A number of theoretical studies have linked the broadening of the transverse momentum to the energy loss due to gluon radiation [Ba00, Wa95]. Specifically, if the transverse momentum broadening through a nuclear medium of thickness  $L$  is expressed as  $\langle p_T^2 \rangle_L$ , then the energy loss per unit length  $-dE/dx$  is given approximately by

$$\frac{-dE}{dx} = \frac{\alpha_s}{\pi} N_c \langle p_T^2 \rangle_L \quad (54)$$

where  $N_c$  is the number of colors and  $\alpha_s$  is the strong interaction coupling constant. Further, the broadening is expected to be proportional to  $L$ , i.e., to vary for nuclei as  $A^{\frac{1}{3}}$ . As a result, the total energy loss is predicted to scale as  $L^2$ , a novel behavior quite unlike the QED energy loss of particles traveling through ordinary atomic matter. An observation of the quadratic energy loss would be a striking confirmation of the importance of coherence behavior in these processes, such as the LPM effect.

Transverse momentum broadening has also been theoretically linked to a correlation function between hard quarks and soft gluons [Gu00]. Therefore, these studies offer one avenue for studying partonic correlations. All of these simple interpretations depend on the assumption that the quark travels independently in the medium, which in turn requires an understanding of the hadronization time scales discussed in the previous section.

A further interest in this study is to gain a greater understanding of the ‘‘Cronin effect’’, the overabundance of high  $p_T$  events in heavier nuclei relative to light nuclei [Cr75, Kop02]. This effect, while seen most prominently in hadron-nucleus scattering, is also seen in DIS studies on nuclei [Mu01]. An advantage of DIS for these studies relative to hadron beam studies is that the probe does not multiple scatter or otherwise interact before undergoing the interaction being studied. The primary limitation of the study of this phenomenon in DIS to date is statistical accuracy, since the events of interest are for  $p_T > 0.5$  GeV, where the rate is correspondingly low. Since JLab brings high luminosity to these studies, it should be possible to determine the kinematic dependences that accompany the effect, such as the dependence on the coherence length [Kop02]. In general,  $p_T$  broadening will ultimately be predictable within the context of quark propagation models, and therefore will provide further discrimination power to differentiate among them. Experimentally, the determination of transverse momentum broadening for channels including only charged particles will be straightforward. A substantial body of new information will clearly become available from this data, as illustrated in Fig. 113.

### 2.C.2 Short-Range Correlations in Nuclei

Observing and characterizing short-range correlations (SRC's) in nuclei has been an important goal of experimental nuclear physics for decades [Be99, Be67]. Not that these correlations are small – calculations of nuclear wavefunctions with realistic  $NN$  potentials consistently indicate that in heavy enough nuclei about 25% of the nucleons have momenta above the Fermi surface [Pa97]. This corresponds to about 50% of the kinetic energy being due to SRC's. The experimental problem has been the unavailability of the high-momentum-transfer kinematics that could discriminate decisively between the effects of SRC's in the initial- and final-state interactions in detailed studies of the SRC's. Though the final-state interactions in nucleon knockout do not disappear at large  $Q^2$ , two important simplifications occur which make extraction of the information about the short-range nuclear structure possible. First, in high-energy kinematics a “hidden” conservation law exists – the light-cone momentum fractions of slow nucleons do not change if the ejected nucleon elastically scatters off slow nucleons [Fr97]. Second, the rescatterings of a high-energy nucleon can be described by the generalized Glauber approximation, which takes into account a difference in the space-time picture of proton-nucleus scattering (a proton coming from  $-\infty$ ) and the  $A(e, e'p)$  process (a proton is produced inside the nucleus) and also accounts for the nonzero Fermi momenta of rescattered nucleons [Fr97].

There is a general consensus that Glauber theory is the appropriate tool for describing final state interactions for proton kinetic energies  $\gtrsim 1$  GeV, which corresponds to  $Q^2 \geq 2$  (GeV/c)<sup>2</sup>. On the other hand, pushing to  $Q^2$  values that are too high is not optimal for the study of nucleon degrees of freedom in nuclei as at  $Q^2 \geq 4$  (GeV/c)<sup>2</sup> one may encounter new phenomena related to the EMC effect [Fr88, Fr96]. Hence the optimal range for probing nucleonic degrees of freedom is  $1.5 \leq Q^2 \leq 4$  (GeV/c)<sup>2</sup>. CEBAF at 6 GeV reaches the lower end of this range and can provide limited access to its upper part, but at the cost of low counting rates, especially at the higher missing momenta,  $p_m$ , crucial for observing SRC's. Studies of the  $(e, e'N)$  and  $(e, e'NN)$  reactions with 11 GeV will allow us to probe missing momenta up to 500–700 MeV/c, and will also provide information on how these momenta are balanced in nuclei: two- and three-nucleon short-range correlation contributions versus those of the mean field. Inclusive  $A(e, e')$  processes at deep inelastic kinematics are also sensitive to multi-nucleon correlations.

**Electrodisintegration of the Deuteron** Current  $NN$  interaction models, while tightly constrained by the large body of  $NN$  elastic scattering data, do not explicitly account for the quark-gluon substructure of the interacting nucleons. Indeed, it is an open question whether this rich substructure is correctly and/or adequately represented in these models at short internucleon separations. It is also unclear whether the short range structure in nuclei implied by these interactions is correct. The deuteron, being the simplest nucleus, is the nucleus of choice for carrying out the systematic study of these issues, with the possibility of extending these measurements at high missing momentum to other few-body systems (such as  $A=3$  and 4) amenable to accurate calculations.



The  $e + {}^2\text{H} \rightarrow e'pn$  reaction is ideally suited for this purpose, particularly in view of the fact that a high energy beam allows measurements to very high missing momenta ( $p_m$ ) where one is sensitive to the very short-range  $NN$  interaction. Though one has to rely on reaction models in order to extract information on the deuteron's structure, the kinematical flexibility afforded by beams of 8–11 GeV would allow extreme tests of the model assumptions. Finally, this same flexibility provides an opportunity to select kinematics where various reaction effects, which would otherwise frustrate the extraction of structure information, are likely to be small. Here we discuss two main components of the  ${}^2\text{H}(e, e'p)n$  program.

The first component of the  ${}^2\text{H}(e, e'p)n$  program would involve “perpendicular” kinematics at  $x_{bj} \approx 1$  where a separation of the  $R_{LT}$  interference response function would be carried out. This response function is predicted to be highly sensitive to relativistic effects and final state interactions. It should be pointed out that the  $NN$  potential models alluded to above were constructed from non-relativistic versions of 1-body and 2-body operators and based on relatively low energy data. The second component would involve measurements in parallel kinematics (where protons are detected along the three-momentum transfer direction) for  $x_{bj} > 1$ . In this configuration, non-nucleonic effects (virtual isobars and meson-exchange currents), as well as FSI, are expected to play a minimal role, whereas relativistic effects are expected to be quite large. This kinematics offers the greatest promise of constraining models of the deuteron structure, especially when combined with the  $R_{LT}$  measurements and resulting constraints on the relativistic aspects of the theory.

Although quite extreme kinematics can be accessed with 6 GeV beam energies, higher energies would reduce the beam time requirement significantly since the same  $Q^2$  could be reached with smaller scattering angles and commensurately larger cross sections. This can be seen from Fig. 114 which shows the statistical uncertainty per day of beam time as a function of beam energy for  $Q^2=6$  (GeV/c)<sup>2</sup> at various missing momenta. The kinematics are parallel with  $x_{bj}>1$ . The uncertainties are into each bin:  $\pm 50$  MeV/c in  $p_m$ ,  $\pm 1.0$  (GeV/c)<sup>2</sup> in  $Q^2$  and  $\pm 0.2$  in  $x_{bj}$ . For this analysis, the Hall C spectrometers, SHMS and HMS, were assumed for the detection of electrons and protons respectively. It is evident that a maximum beam energy of 11 GeV would allow measurements of the  ${}^2\text{H}(e, e'p)n$  reaction to very high  $Q^2$  and  $p_m$  (*i.e.* missing momentum). An analysis assuming the Hall A spectrometers, HRS and MAD, gives very similar counting rates for a beam energy of 8 GeV. Here, the maximum usable beam energy of 8 GeV is dictated by the momentum limits of these spectrometers. The relatively larger acceptances of the Hall A spectrometer pair very nearly compensate for the lower cross sections at the lower beam energy.

Given an 11 GeV beam energy, and the SHMS and HMS spectrometer configuration, Figure 115 shows the statistical uncertainty per day of beam time as a function of missing momentum for  $Q^2$  up to 12 (GeV/c)<sup>2</sup> (the bin sizes are the same as given above) for the high  $x_{bj}$  parallel kinematics case. For  $Q^2=12$  (GeV/c)<sup>2</sup>, a missing momentum of 500 MeV/c could be measured with 10% uncertainty with one week of beam time. For  $Q^2=8$  (GeV/c)<sup>2</sup>, the same uncertainty could be obtained in the same running time for a missing momentum of 800 MeV/c.



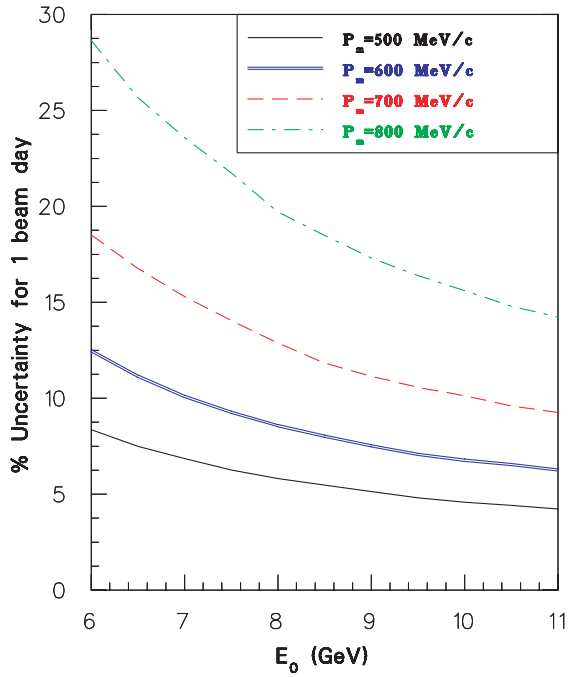


Figure 114: Statistical error per day of beam time as a function of beam energy for  $Q^2=6 \text{ (GeV/c)}^2$  at various recoil momenta. The kinematics are parallel with  $x_{bj}>1$ .

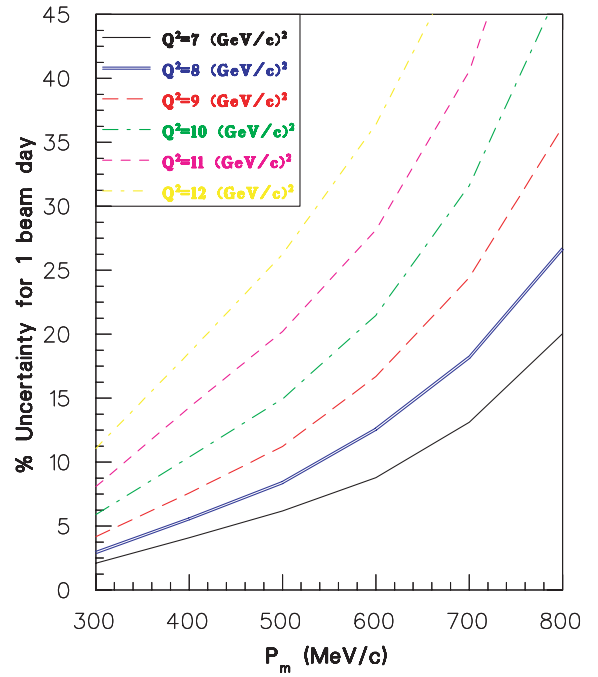


Figure 115: Statistical error per day of beam time for a beam energy of 11 GeV as a function of missing momenta for a variety of values of  $Q^2$ . The kinematics are parallel with  $x_{bj}>1$ . See the text for details.

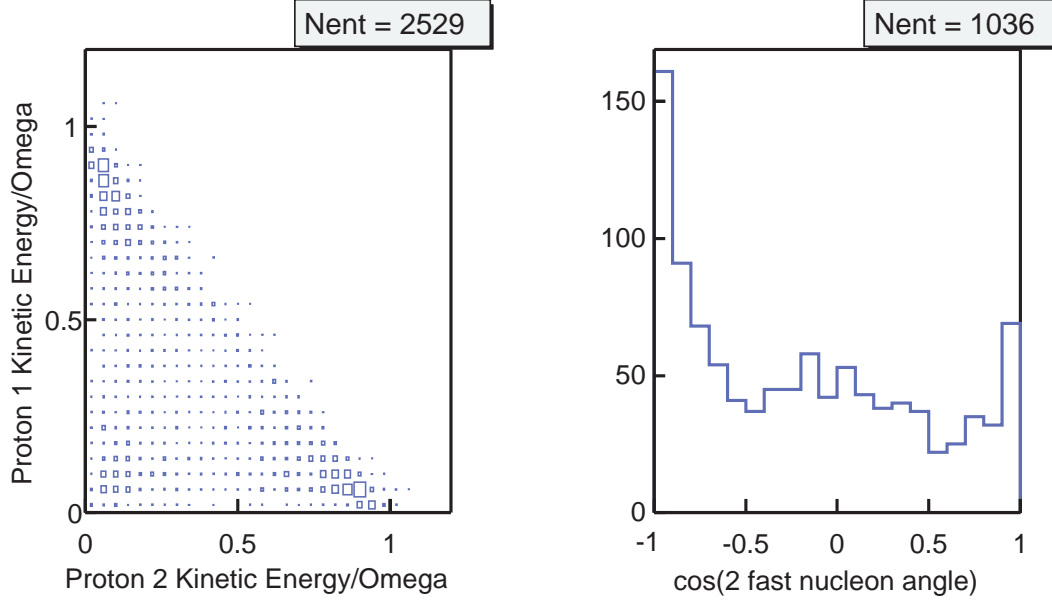


Figure 116:  ${}^3\text{He}(e, e'pp)n$  measured with CLAS in one day at  $E_0 = 4.4$  GeV. Left: Kinetic energy balance of the three nucleons for  $p_N > 0.25$  GeV/c (ie: a lab frame Dalitz plot). Note the large peaks in the corners where one ‘leading nucleon’ carries most of the kinetic energy the other two ‘fast nucleons’ share the remainder. Right: The cosine of the fast nucleon pair opening angle where the leading nucleon is a proton and the remaining  $p$  and  $n$  are ‘fast’. Note the very large back-to-back peak, indicative of the presence of short range correlations.

The progress in constructing tensor-polarized deuteron targets will make it feasible to study the same reaction using polarized targets at sufficiently large  $Q^2$ . In this case a separation of  $S$ - and  $D$ -wave contributions is possible. Since the  $D$ -wave is expected to play a key role over a wide range of nucleon momenta both in  ${}^2\text{H}$  and in heavier nuclei [Fr81, Fo96], this process will provide a crucial test of our understanding of the short-distance  $NN$  interactions.

**$A(e, e'pN)$  Processes** Triple coincidence experiments of the type  $A(e, e'pN)$  offer the opportunity to study directly short range correlations by measuring both ejected nucleons and directly determining the total ( $p_{tot}$ ) and relative ( $p_{rel}$ ) momenta of the final state  $NN$  pair and the excitation energy and momentum of the unobserved  $A - 2$  recoil. We then need to connect the  $NN$  pair final state with the  $NN$  pair initial state (within a model). We can do this either with theoretical guidance or, hopefully, through judicious choice of kinematics.

One possibility is to measure  $A(e, e'N_f N_b)$  with  $N_f$  the forward- and  $N_b$  the backward-going nucleons. If, as expected, the dominant contribution is from two-nucleon correlations,  $N_b$  should carry most of the excitation energy and the  $A - 2$  recoil should be almost at rest in a low energy state. Comparing  $(pp)$ ,  $(pn)$ , and  $(nn)$  cross sections will check the reaction mechanism and may allow us to compare the isospin zero and one  $NN$  SRC wavefunctions. However, the effects of FSI

and two body currents must be treated properly to extract any information about the wavefunction.

A much more promising technique for measuring  $NN$  momentum distributions is to study  ${}^3\text{He}(e, e'pp)n$  events in CLAS where one nucleon absorbs the virtual photon and the correlated pair is a spectator. This has been achieved in kinematics where all three nucleons have momenta  $p > 0.25$  GeV/c [We02a]. In this case, there are peaks in the kinetic energy distribution with one leading nucleon ( $T_N > 0.6 * \nu$ ) and two 'fast' nucleons ( $T_f < 0.2 * \omega$ ). These peaks in the kinetic energy distribution become much more pronounced at  $E_0 = 4.4$  GeV ( $1 \leq Q^2 \leq 2$  GeV<sup>2</sup>) than at  $E_0 = 2.2$  GeV ( $0.5 \leq Q^2 \leq 1$  GeV<sup>2</sup>) (Fig. 116). The opening angle of the two fast nucleons has a pronounced peak at  $180^\circ$  for both fast  $pn$  and fast  $pp$  pairs. This back-to-back peak is not due to kinematics (we do not see it in a fireball phase space simulation) or to the CLAS acceptance (since we see it for both  $pn$  and  $pp$  pairs).

Restricting the perpendicular momentum of the leading/struck nucleon (relative to  $\vec{q}$ ) to be less than 0.3 GeV/c (to minimize FSI) selects primarily  $NN$  pairs with very large opening angles. These pairs have the momentum component parallel to  $\vec{q}$ ,  $p_{tot}^\parallel \ll |\vec{q}|$ , and total momentum ( $\vec{p}_{tot} = \vec{p}_1 + \vec{p}_2$ ) smaller than their relative momentum ( $\vec{p}_{rel} = \frac{1}{2}(\vec{p}_1 - \vec{p}_2)$ ). The shape of the momentum distributions is very similar for  $pp$  and for  $pn$  pairs at both beam energies measured ( $E_0 = 2.2$  and 4.4 GeV). The shapes of the distributions are comparable to a Plane Wave Impulse Approximation calculation by M. Sargsian, but a factor of about 6 smaller. Calculations by Glockle [Gl97] at much lower energy indicate that the cross section is very strongly reduced by the continuum interaction between the nucleons of the fast pair and that meson-exchange currents (MEC) and final state interactions (FSI) of the leading nucleon are negligible. Calculations by Laget [La88] for leading proton and fast  $pn$  pair events at  $E_0 = 2.2$  GeV describe the data very well when he includes just the rescattering of the fast pair from each other. The FSI of the leading proton and MEC contributions are negligible.

Thus, these measurements appear to have measured distorted correlated  $NN$  momentum distributions in  ${}^3\text{He}$  by striking the third nucleon and observing the spectator pair. These measurements will benefit tremendously from CEBAF at 12 GeV:

- Cleaner signal: The peaks in the three-nucleon kinetic energy distribution are much more pronounced as  $Q^2$  increases.
- Larger momentum range: Since most of the events of interest have  $x_B \approx 1$ , increasing  $Q^2$  increases the average  $\omega$  and therefore increases the maximum relative momentum of the fast nucleon pair (since  $T_{fast} \leq 0.2 * \omega$ ).
- More data: increased CLAS<sup>++</sup> luminosity, smaller minimum scattering angle, fewer acceptance holes.

Although SRC's are expected to be predominantly two-nucleon, three or more-nucleon SRC's are also significant; they are likely to constitute  $\sim 20\%$  of all SRC's. Their probability can be

measured in the ratio of  $A(e, e')$  cross sections at  $x > 1$  and  $x > 2$  at large  $Q^2$ . They can be best measured through the  $A(e, e' N_f N_b)$  reaction and in processes with two backward-ejected nucleons [Fr88].

**Inclusive  $A(e, e')X$  Processes** The ‘EMC effect’ from measurements of the parton densities in nuclei ( $\bar{q}_A/\bar{q}_N$ , etc.), unambiguously demonstrated that on the parton level a nucleus cannot be viewed as merely a collection of nucleons. Practically all the mechanisms suggested to explain the EMC effect address the question of the quark-gluon structure of SRC’s and/or the origin of the nuclear forces. These include:

- a. Various patterns of mixing quarks (gluons) from different nucleons ranging from the deformation of the bound nucleon wavefunctions to “kneaded” (multiquark) states [Cl83, Ca83, Na84, Ja84, Fr85, Fr96].
- b. A loss of momentum by nucleons to some fields that bind *undeformed* nucleons together [Er83, Fr83, Be84, Ak85, Ku89, Du85, Ju88, Ci89, Ka90, Me93, Bi89, Me94, Ku94].
- c. The presence of  $\Delta$ -isobars and  $N^*$ ’s in nuclei, especially in the SRC’s [Fr83].

However, inclusive experiments at  $x \leq 0.8$  have not allowed us to discriminate between such models. The broad  $(x, Q^2)$  range available at 11 GeV and the feasibility of correlation experiments suggest a strategy that will work. Deep inelastic scattering off nuclei at  $x \geq 1$  in the scaling limit is a first step to establish in a model-independent way (*i.e.*, not sensitive to the final-state interactions) the presence of superfast quark components in nuclei – quarks that carry a larger momentum fraction than a whole nucleon.

Theoretical estimates indicate that for  $x \leq 1.5$  this will require  $Q^2 \leq 20$  (GeV/c)<sup>2</sup>, so experiments will be feasible with  $E_e = 11$  GeV. Several features of CEBAF and its experimental facilities (the good acceptance and high resolution of the CEBAF spectrometers, and the high intensity and small energy spread of the electron beam) are crucial for performing these measurements. Through a study of the  $Q^2$ -dependence of the cross section at fixed  $x$  it will be possible to observe for the first time the onset of scaling at  $x \geq 1$ , which will be the definitive signature for the existence of superfast quarks in nuclei.

Comparing the cross sections for  $A = 2, 3$ , and 4 and for heavy nuclei will allow the model-independent separation of contributions of two-, three-, or more-nucleon SRC’s. The two-nucleon correlations are expected to dominate for  $1.3 \geq x \geq 1$ , leading to quark structure functions for  $A \geq 12$  nuclei a factor of 5–6 larger than in the deuteron [Fr81, Fr88]. This ratio should be similar to the cross-section ratio for quasielastic scattering:

$$R_{A/D}(x, Q^2) \equiv \frac{2}{A} \frac{\sigma_{eA}(x, Q^2)}{\sigma_{e^2H}(x, Q^2)}$$

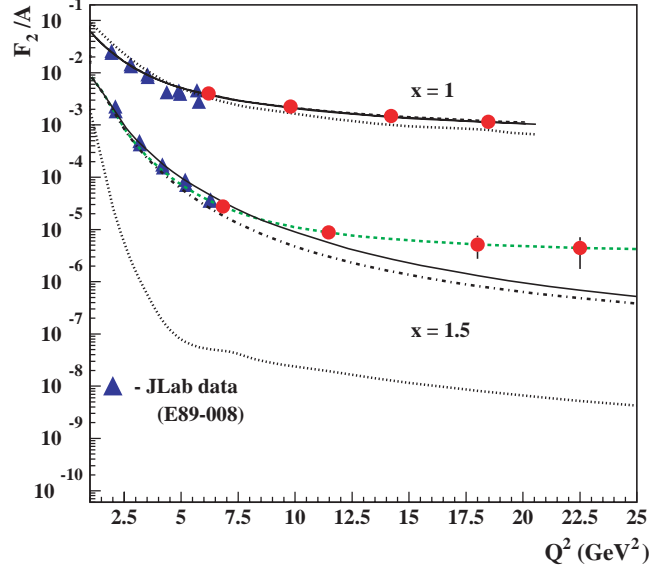


Figure 117: Prediction of the onset of scaling for the  $^{56}\text{Fe}(e, e')X$  reaction. The solid line and the dash-dotted line are predictions with 2 nucleon correlation, without and with the EMC modification of the nucleon elastic form factor, respectively. In both cases, one includes the EMC effect in the inelastic structure function to have agreement with EMC data at DIS for  $^{56}\text{Fe}$ . The dashed line is the prediction with multinucleon correlation with EMC effects included, and the dotted line is the prediction of mean-field approximation. The data shown are from Ref. [Ar99]

observed at  $x \sim 1.5$ ,  $4 \geq Q^2 \geq 1$  (GeV/c) $^2$  at SLAC [Fr93a]. Local nuclear densities probed in this case are several times larger than the average value,  $\rho_0 \sim 0.17 \text{ fm}^{-3}$ . For larger  $x \sim 1.5$  higher order correlations are expected to dominate, leading to an increase of  $R_{A/D}(x \sim 1.5, Q^2 \sim 50 \text{ (GeV/c)}^2)$  [Fr81]. At the same time the local nature of generating  $x \geq 1$  quarks will manifest itself experimentally through the same shape and probability per nucleon of the  $x \geq 1$  component in  $^4\text{He}$  and heavy nuclei. In this kinematics we expect to observe densities at least five times larger than  $\rho_0$ . Detailed studies of the  $A$ -dependence of  $q_A(x, Q^2)$  at  $1 \leq x \leq 1.5$  will provide important information about fluctuations of the local nuclear density as a function of average nuclear density as well as of the isospin of the correlations.

Measurement of the quark distribution at  $x \geq 1$ , in combination with the measurements of the light-cone nucleon density matrix ( $\rho_A^N$ ), will allow a check of whether  $F_{2A}(x, Q^2) > 1$  can be described as a convolution of  $\rho_A^N$  and the *free* nucleon structure function. At the same time these measurements will establish in a model-independent way the relative importance of two- and three-nucleon SRC's by comparing  $F_{2A}(x, Q^2)$  for light and heavy nuclei and show the dependence of SRC's on nuclear density. Figure 117 shows a prediction of the onset of scaling in the  $^{56}\text{Fe}(e, e')X$  reaction. The solid line and the dash-dotted line are predictions [Fr93a] with two nucleon correlation, without and with the EMC modification of the nucleon elastic form factor, respectively. In both cases, one includes the EMC effect in the inelastic structure function to have agreement with EMC data at DIS for  $^{56}\text{Fe}$ . The dashed line is the prediction with multinucleon correlation [Sa03a]

with EMC effects included, and the dotted line is the prediction of mean-field approximation. The data shown are from Ref. [Ar99]. With the 12 GeV upgrade data, measurements can be made to above  $Q^2 = 20 \text{ (GeV}/c)^2$ , where the two-nucleon and multi-nucleon calculations differ by more than an order of magnitude for  $x = 1.5$ .

### 2.C.3 The Parton-Hadron Transition in Nuclei

Mapping the transition from strongly interacting, non-perturbative Quantum Chromodynamics (QCD), where nucleon-meson degrees of freedom are effective, to perturbative QCD (pQCD), is one of the most fundamental and challenging tasks in nuclear and particle physics. Scaling<sup>1</sup> in the differential cross section  $d\sigma/dt$  and hadron helicity conservation have been pursued experimentally as signatures of this transition for decades.

Quark counting rules were originally obtained based on dimensional analysis [Br73], and were later confirmed by a short-distance pQCD approach up to calculable powers of the running coupling constant [Le80]. While global scaling behavior has been observed in many exclusive processes [An76], no experimental evidence supports hadron helicity conservation, which was predicted in the same approach, in similar energy- and momentum-transfer regions. Hadron helicity conservation arises from the vector coupling nature of the quark-gluon interaction, quark helicity conservation at high energies, and the neglect of the non-zero quark orbital angular momentum state in the nucleon. The parton orbital angular momentum was considered for the first time by Chernyak and Zhitnitsky [Ch77] for form factors. Recently, Ji, Ma and Yuan [Ji03] derived a generalized counting rule for exclusive processes at fixed angles involving parton orbital angular momentum and hadron helicity flip. This generalized counting rule opens a new window for probing the quark orbital angular momentum inside the nucleon. A natural connection between the study of the parton-hadron transition through exclusive processes and generalized parton distributions probed through deeply virtual processes is therefore established.

The elastic form factor of charged pions is extremely important since the pion has the simplest valence quark structure and is therefore amenable to both nonperturbative and pQCD calculations. Based on those calculations we know where to expect the transition to scaling – it should occur at relatively low momentum transfer. Measurements of the pion form factor will confirm our understanding and delineate the transition from nonperturbative to perturbative QCD. Measurements of the form factors of light nuclei at large momentum transfers provide analogous information on another important transition in nuclear physics – the transition from the traditional meson-nucleon description of nuclei to the underlying (and more fundamental) quark-gluon description.

Exclusive processes such as proton-proton elastic scattering, meson photoproduction, and deuteron photodisintegration have been measured extensively at many laboratories over the years in the search for such a transition, particularly at Jefferson Lab in recent years, taking full ad-

---

<sup>1</sup>Scaling in this context implies a dependence on a reduced set of kinematic variables.

vantage of the high luminosity capability of the CEBAF facility. Early onset of the transition from hadronic degrees of freedom to partonic degrees of freedom is also expected in nuclear transparency measurements due to nuclear filtering and color transparency. Nuclear filtering refers to the suppression of nonperturbative amplitudes involving large quark separations inside the nuclear environment. Nuclei are therefore often employed as laboratories in the search for this transition. While a coherent picture of this transition is on the verge of emerging, the Jefferson Lab 12 GeV energy upgrade will allow the exploration of this transition region with detail and precision. In the remaining section, we will discuss the planned measurements of the charged pion form factor, form factors of light nuclei, deuteron photodisintegration and photopion productions at Jefferson Lab with energy upgraded CEBAF and upgraded instrumentation.

**Elastic Form Factor of Charged Pion** A well known signature for the onset of pQCD is *constituent counting* scaling, where the cross sections are sensitive to short range valence quark distribution amplitudes. The reaction for which pQCD is expected to manifest itself at the lowest momentum transfers is in the elastic scattering from the charged pion, since the pion has the simplest valence quark structure. There have been a large number of calculations [Br00, Ja90, Ti92, It92, Ma00] of the pion form factor,  $F_\pi$ , which predict its magnitude and  $Q^2$  dependence. In one extreme the calculations involving purely perturbative mechanisms utilize simple valence quark distributions that have either their asymptotic shapes or those based upon QCD sum rules. Other calculations add higher non-leading configurations in various ways. The most recent theoretical studies of the charged pion form factor  $F_\pi$  seem to indicate that these hard exclusive processes may be expected to become important by  $Q^2 \sim 5 \text{ (GeV/c)}^2$ . To date, the most accurate measurement of  $F_\pi$  has been carried out in Hall C using the  $p(e, e\pi^+)n$  reaction to a maximum  $Q^2$  of around  $1.6 \text{ (GeV/c)}^2$  [Vo01]. Not surprisingly, these results do not exhibit the  $1/Q^2$  scaling predicted by pQCD. Thus it is crucial to measure  $F_\pi$  as accurately as possible to the highest  $Q^2$  possible to approximately  $6 \text{ (GeV/c)}^2$  with the CEBAF upgrade. The goal is to observe the transition to constituent scaling, and also to pin down the magnitude of the cross section, which constrains valence non-perturbative models and their higher twist corrections. Since  $F_\pi$  is manifested in the longitudinal cross section, one must carry out a Rosenbluth separation, and project as closely as possible to the *non-physical* pion pole. The combination of the SHMS and HMS spectrometers in Hall C is ideal for such a separation. High momentum pions will be detected at very forward angles by the SHMS spectrometer, in coincidence with electrons detected in the HMS spectrometer. Results of various theoretical calculations are shown in Fig. 118 together with the 12 GeV projection on the  $F_\pi$  measurement.

Due to its simplicity, the pion form factor provides our best hope for direct comparison with rigorous QCD calculations. As can be seen from Fig. 18, it is still dominated by non-perturbative effects at a few  $(\text{GeV/c})^2$ . An earlier onset to the scaling associated with pQCD may be seen by forming ratios of differential cross sections from exclusive processes. The simplest of such ratios is the charged pion photoproduction differential cross-section ratio,  $\frac{d\sigma}{dt}(\gamma n \rightarrow \pi^- p) / \frac{d\sigma}{dt}(\gamma p \rightarrow \pi^+ n)$ .

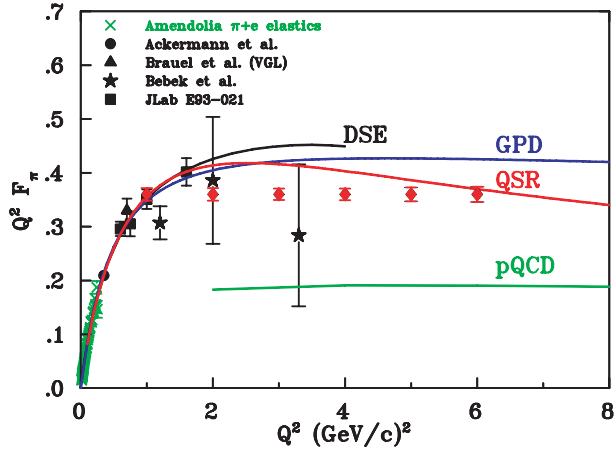


Figure 118: The  $\pi^+$  form factor, with recent Hall C data denoted by filled squares and previously obtained Cornell data indicated by filled stars. The curves are the results of theoretical calculations.

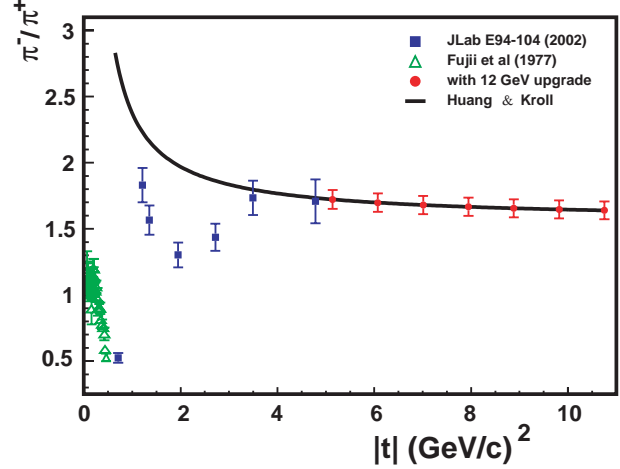


Figure 119: The charged pion photoproduction differential cross-section ratio at a C.M. angle of  $90^\circ$ , as a function of  $|t|$   $(\text{GeV}/c)^2$  from experiment E94-104 (blue) along with the projected measurements for JLab at 11 GeV (red). The solid curve is a prediction by Huang and Kroll [Hu00].

In such a ratio, non-perturbative effects may cancel and one may expect the  $\pi^-/\pi^+$  ratio to give the first indication of the onset of pQCD. Calculations of this ratio have been performed in the framework of handbag mechanism [Hu00, Hu03], in which the amplitude is factorized into a parton-level subprocess  $\gamma q_a \rightarrow P q_b$  and generalized parton distributions (GPD). The GPD part of the contribution describing the soft hadron-parton transitions indeed cancels in this ratio provided the assumption of negligible quark helicity flip contributions and the dominance of a helicity conserving amplitude of the parton-level subprocess  $\gamma q_a \rightarrow P q_b$  for pseudoscalar meson production [Hu03]. The most recent charged pion ratio data [?] from experiment E94-104 for momentum transfers up to  $5.0 (\text{GeV}/c)^2$  indicate that indeed one of the helicity conserving amplitudes dominates. This ratio measurement can be extended to a  $|t|$  value of about  $10 (\text{GeV}/c)^2$  with an 11 GeV beam. Figure 119 shows both the available data and projected results for this ratio at 11 GeV, together with a prediction of Huang and Kroll [Hu00].

**Few-Body Form Factors** Measurements of the elastic form factors of the deuteron and the helium isotopes are of crucial importance in understanding their electromagnetic structure and testing the “standard model” of light nuclei that is based on the meson-nucleon framework, the impulse approximation (IA), and meson-exchange currents (MEC) [Ca97]. Such measurements offer unique opportunities for studying the short-range nucleon-nucleon interaction, few-body wavefunctions, isobar and three-body force contributions, and effects from possible quark-cluster admixtures. Large-momentum-transfer measurements can also test “nuclear chromodynamics” predictions based



on quark dimensional scaling (QDS) and pQCD [Ca97].

The starting point of the conventional theoretical approach of elastic scattering from few-body systems is the impulse approximation, where the incident electron interacts with one of the nucleon constituents of deuterium or helium. The form factors of light nuclei are then convolutions of the nuclear wavefunction with the form factors of the constituent nucleons. At large momentum transfers the effects of relativity cannot be ignored, and either corrections must be made to the IA or fully relativistic approaches developed (as has been done in the case of the deuteron [Hu90]). It has long been understood and overwhelmingly supported by the available data that the few-body form factors are sensitive to the presence of meson-exchange currents and isobar configurations that augment the IA picture [Ca98].

At distances much less than the nucleon size, the underlying quark substructure of the nucleons cannot be ignored. This has led to the formulation of so-called hybrid quark models [Di89] that treat few-body nuclei as quark clusters when the internucleon separation becomes smaller than  $\sim 1$  fm. At sufficiently “large” momentum transfers, the few-body form factors are expected to be calculable in terms of only quarks and gluons within the framework of pQCD. The first attempt at a quark-gluon description of the few-body elastic form factors was based on the dimensional-scaling quark model (DSQM) [Br73], where the underlying dynamical mechanism during elastic scattering is the hard rescattering of the constituent quarks via exchange of hard gluons. The  $Q^2$ -dependence of this process is then predicted by simply counting the number  $n$  of gluon propagators ( $n = 5$  for deuterium, 8 for  $^3\text{He}$ , and 11 for  $^4\text{He}$ ), which implies that the elastic structure functions  $A(Q^2)$  of the few-body systems should follow the power law:  $\sqrt{A(Q^2)} \sim (Q^2)^{-n}$ . This prediction was later substantiated, for the deuteron case, in the pQCD framework, where it was shown [Br83] that to leading order:

$$\sqrt{A(Q^2)} = \left[ \alpha_s(Q^2) / Q^2 \right]^5 \sum_{m,n} d_{mn} \left[ \ln \left( \frac{Q^2}{\Lambda^2} \right) \right]^{-\gamma_n - \gamma_m},$$

where  $\alpha_s(Q^2)$  and  $\Lambda$  are the QCD strong coupling constant and scale parameter, and  $\gamma_{m,n}$  and  $d_{mn}$  are QCD anomalous dimensions and constants.

The 12 GeV energy upgrade of the JLab electron beam and the proposed spectrometer upgrades will be ideal for improving and extending the existing elastic structure function measurements of light nuclei to higher momentum transfers. These measurements will test the limits of the standard model of few-body nuclei, and may uncover a possible transition to a quark-gluon description of the few-body form factors, as predicted by quark dimensional scaling and perturbative QCD.

Figure 120 shows the recent JLab Hall A and older SLAC and Saclay data [Al99] on the deuteron form factor,  $F_d(Q^2) \equiv \sqrt{A(Q^2)}$ , multiplied by  $(Q^2)^5$ . It is evident that the data show an approach to a scaling behavior consistent with the power law of DSQM and pQCD. Although several authors have questioned the validity of QDS and pQCD at the momentum transfers of this experiment [Is84], similar scaling behavior has been reported in deuteron photodisintegration at moderate photon energies (see next section). It is extremely important to test this apparent

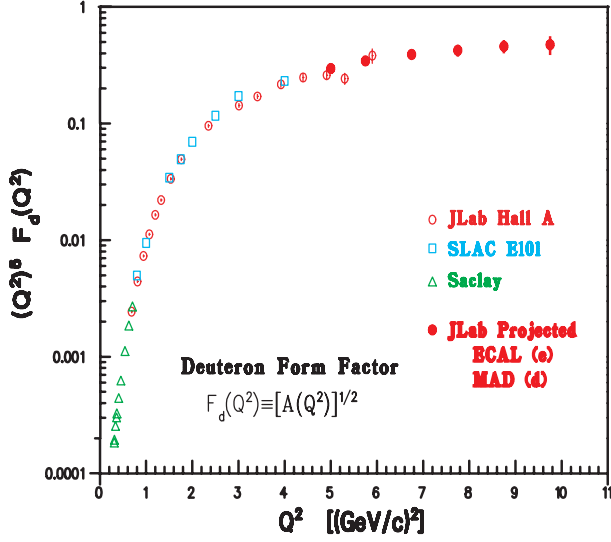


Figure 120: Projected data for the deuteron form factor  $F_d(Q^2)$  with an 11 GeV JLab beam. Also shown are existing JLab, SLAC, and Saclay data.

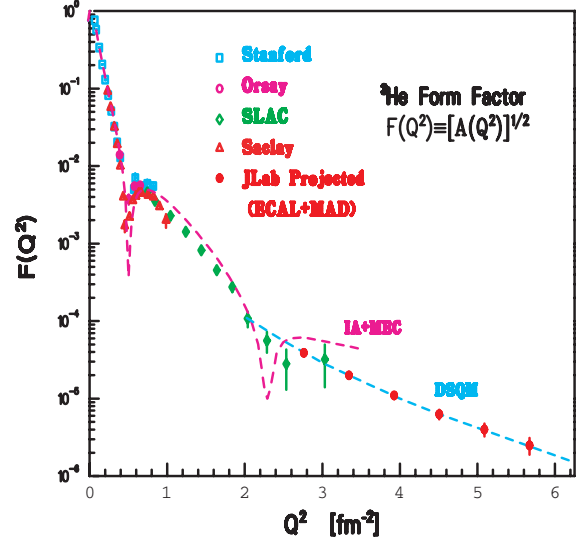


Figure 121: Projected data for the  $^3\text{He}$  elastic form factor  $F(Q^2)$  with an 11 GeV beam. Also shown are existing data and predictions of the standard model (IA+MEC) [Sc91] and the dimensional-scaling quark model (DSQM) [Ch78].

scaling behavior by extending the deuteron  $A(Q^2)$  measurements to higher momentum transfers. Higher JLab beam energies in the range of 9–11 GeV are essential for such measurements. To separate elastic from inelastic scattering and to suppress backgrounds, recoil deuterons should be detected in coincidence with scattered electrons. A possible scenario would be to use the proposed Medium-Acceptance Device (MAD) to detect recoiling deuterons and a segmented electromagnetic calorimeter (ECAL) to detect scattered electrons. Assuming a 20-cm-long liquid-deuterium target and beam current of 70  $\mu\text{A}$ ,  $A(Q^2)$  can be measured up to  $\sim 10 (\text{GeV}/c)^2$  in one month of beam time, as shown in Fig. 120. Such an experiment will double the  $Q^2$  range of the existing data, which have been acquired over a period of 40 years. The observation of a diffractive structure (which cannot be ruled out from the existing data) would settle in the negative the question of the applicability of the QDS ideas at moderate momentum transfers once and for all.

The existing data [Am94] on the  $^3\text{He}$  form factor,  $F(Q^2) \equiv \sqrt{A(Q^2)}$  (shown in Fig. 121), are in good agreement with the standard model (IA+MEC) calculations [Sc91] at low  $Q^2$  but are fairly inconclusive at the largest momentum transfers. They are consistent with a change in slope at  $\sim 2.1 (\text{GeV}/c)^{-2}$ , indicative of an onset of quark scaling [Ch78] (and consistent with the deuteron data), but, at the same time, cannot exclude the presence of a second diffraction minimum as predicted by conventional meson-nucleon theory. As in the case of the deuteron, more measurements at higher  $Q^2$  would be crucial in testing the quark-scaling prediction and a possible breakdown of the meson-nucleon framework. The energy upgrade of JLab will also allow

new  $^3\text{He}$  measurements that could double the  $Q^2$  range of the existing data (taken also over a period of 40 years) in a single experiment with a tenfold better sensitivity. As in the case of the deuteron, recoiling nuclei will be measured with the MAD spectrometer and scattered electrons with a calorimeter. Assuming a 20-cm-long  $^3\text{He}$  gas cryogenic target and an electron beam of 11 GeV with current of 70  $\mu\text{A}$ , the  $^3\text{He}$   $F(Q^2)$  can be measured up to  $\sim 5.8 (\text{GeV}/c)^{-2}$  in one month of beam time, as shown in Fig. 121. It is evident that this experiment will be able to show whether the apparent change in slope of the SLAC data can be attributed to a classical diffraction minimum, or a quark-scaling approach as argued in Ref. [Ch78].

**Deuteron Photodisintegration** The deuteron photodisintegration reaction,  $\gamma d \rightarrow pn$ , is one of the simplest reactions for studying explicit quark effects in nuclei. In recent years, extensive studies of deuteron photo-disintegration have been carried out at SLAC and JLab [Na88, Bo98, Sc01]. Figure 122 shows the scaled differential cross-section ( $s^{11} \frac{d\sigma}{dt}$ ) from deuteron photodisintegration as a function of photon energy. The data seem to show scaling at  $70^\circ$  and  $90^\circ$ , and suggest the onset of scaling at higher photon energies at  $52^\circ$  and  $36^\circ$ . The threshold for this scaling behavior corresponds to a transverse momentum slightly over 1 GeV/c. Also shown in Fig. 122 are the QCD rescattering calculation [Fr00] (shaded region), the quark-gluon string model calculation (dashed line) [Ko93, Gr01], and an estimate from Raydushkin [Ra01a] (dashed-dot line) based on a quark-exchange picture. While none of the theories agree with all of the data as well as one would like, they do indicate that quark models can approximately reproduce the cross section data, therefore establishing the importance of deuteron photodisintegration process in the study of the transition region.

A recent polarization measurement on deuteron photo-disintegration [Kr01] disagrees with hadron helicity conservation at kinematics where quark counting behavior is observed in the differential cross section. This is also supported by  $^1H(\vec{\gamma}, \vec{p})\pi^0$  [Kr02],  $d(e, e'\vec{d})$  deuteron tensor polarization  $T_{20}$  measurement [Ab00], and the  $p(\vec{e}, e'\vec{p})$  measurement of the proton electric to magnetic form factor ratio [Jo00].

At this point, it is extremely difficult to extend either the cross section or polarization measurements to higher energies at JLab with existing equipment. Experimental considerations for measurements of  $\gamma d \rightarrow pn$  are dominated by the small cross sections and by the high momentum of the outgoing proton. The increased solid angle of the proposed MAD spectrometer in Hall A would allow cross sections and polarization to be measured at higher energies, if backgrounds are low, as they have been for existing Hall A experiments. The MAD spectrometer will allow cross section measurements to photon energies near 8 GeV, which is a straightforward extension of the latest Hall C measurements [Sc01]. The Hall A polarization data can be extended to about 4 GeV. Figures 122 and 123 show the projected differential cross-section and induced polarization measurements for the deuteron photodisintegration with MAD together with existing data, respectively.

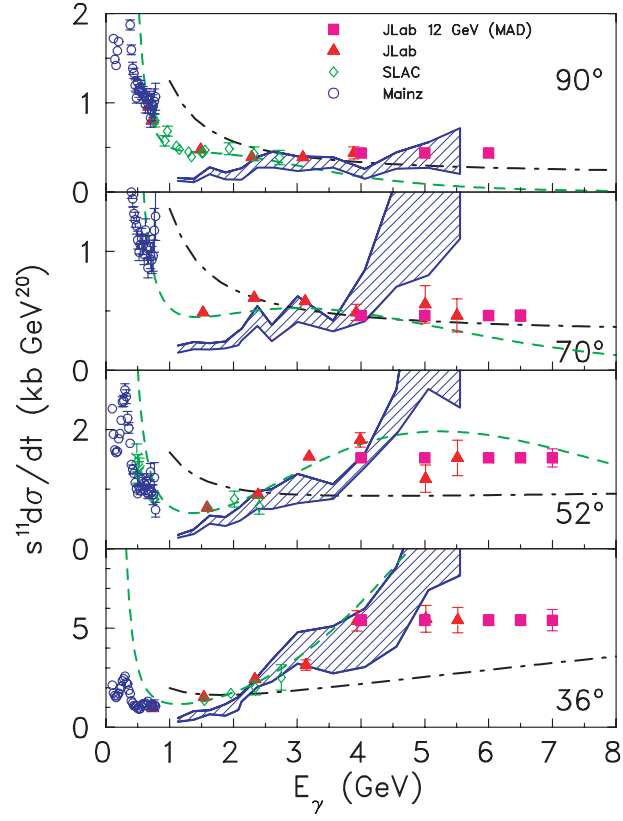


Figure 122: High energy deuteron photodisintegration differential cross sections scaled by  $s^{11}$ . The projected results with MAD are shown as purple solid squares.

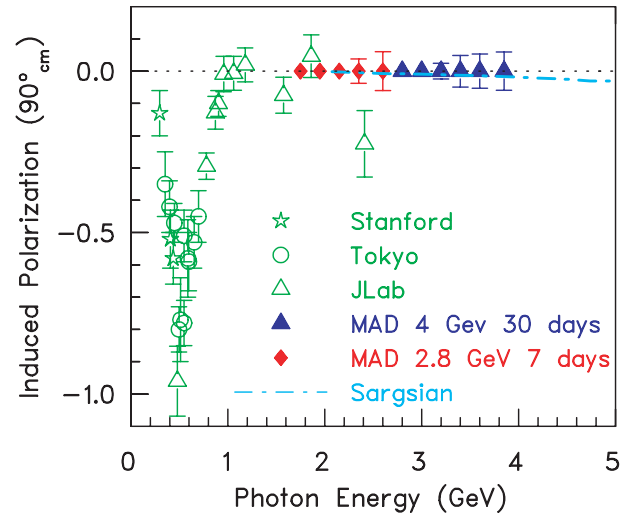


Figure 123: Projected results for deuteron photodisintegration polarizations with MAD.

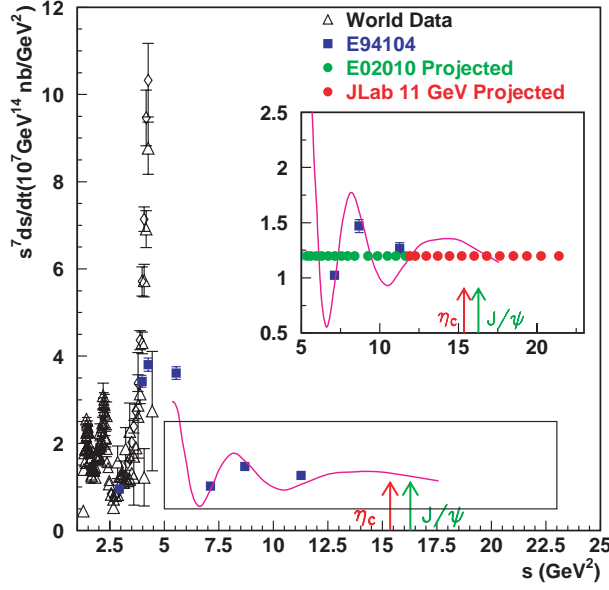


Figure 124: The scaled differential cross-section for the  $n(\gamma, \pi^- p)$  process at a C.M. angle of  $90^\circ$ , as a function of C.M. energy squared,  $s$ , in  $\text{GeV}^2$  along with the projected measurements for JLab at 11 GeV (red); we estimate that typical uncertainties will be  $\sim 2\%$  statistical and  $\sim 3\%$  systematic. The green points are the projected results from E02-010 and the blue points show the completed E94-104 data points.

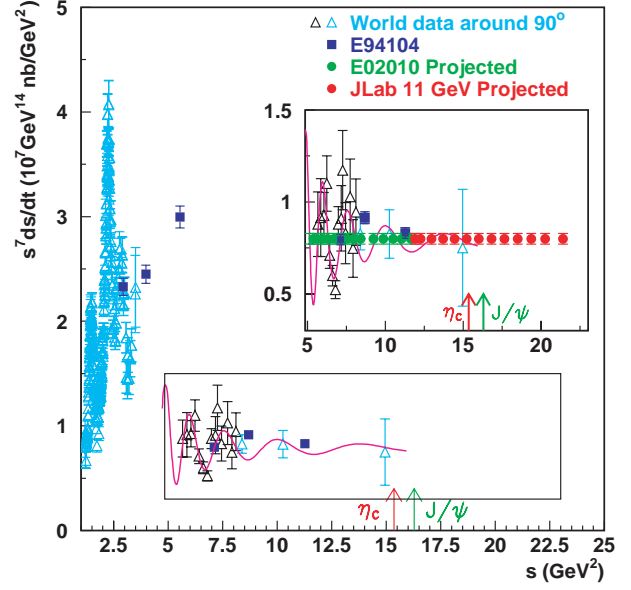


Figure 125: The scaled differential cross-section for the  $p(\gamma, \pi^+ n)$  process at C.M. angle of  $90^\circ$ , as a function of cms energy squared  $s$  in  $\text{GeV}^2$  along with the projected measurements for JLab at 11 GeV (red); we estimate that typical uncertainties will be  $\sim 2\%$  statistical and  $\sim 3\%$  systematic. The green points are the projected results from E02-010 and the blue points show the completed E94-104 data points.

**Nucleon Photopion Production** Because of the simple valence quark structure of the pion, its photoproduction from nucleon ( $\gamma n \rightarrow \pi^- p$ ,  $\gamma p \rightarrow \pi^+ n$ ,  $\gamma p \rightarrow \pi^0 p$ ) is an essential probe of the transition from meson-nucleon degrees of freedom to quark-gluon degrees of freedom. The relatively large cross-section at high energies (quark counting rule predicts a  $s^{-7}$ -dependence for the differential cross-section) not only will allow the investigation of the  $t$  and  $p_T$  dependence of the scaling behavior in addition to the  $s$  dependence, but also will allow studies of possible QCD oscillation<sup>2</sup>. In nuclei, photoreactions allow the search for QCD nuclear filtering of those oscillation as well as color transparency.

Apart from the early onset of scaling and departure from hadron helicity conservation rule, several other striking phenomena have been observed in  $pp$  elastic scattering –one of the prime cases establishing the experimental support of the constituent quark counting rule. This includes: the oscillation of the differential cross-section about the scaling behavior predicted by quark counting rules ( $s^{-10}$  for  $pp$  elastic scattering) and the anomalous spin correlation coefficient  $A_{nn}$  observed in  $pp$  elastic scattering [Cr78, Co86]. Theoretical interpretation for such an oscillatory behavior and the spin-correlation in  $pp$  elastic scattering was attempted [Br79] within the framework of quan-

<sup>2</sup>QCD oscillation refers to oscillatory scaling behavior around the quark counting rule prediction

tum chromodynamic quark and gluon interactions, where interference between hard pQCD short-distance and long-distance (Landshoff [La74]) amplitudes was discussed for the first time. This QCD process is analogous to the QED effect of Coulomb-nuclear interference observed in low energy charged particle scattering. Lastly, Carroll *et al.* [Ca88] reported the anomalous energy dependence of the nuclear transparency from the quasi-elastic  $A(p, 2p)$  process: the nuclear transparency first rises followed by a decrease. This intriguing result was confirmed recently at Brookhaven [Ma98a] with improved experimental technique. Ralston and Pire [Ra88] explained the free  $pp$  oscillatory behavior in the scaled differential cross section and the  $A(p, 2p)$  nuclear transparency results using the ideas of interference between the short-distance and long-distance amplitudes and QCD nuclear filtering. Carlson, Chachkhunashvili, and Myhrer [Ca92] have also applied such an interference concept to  $pp$  scattering and have explained the  $pp$  polarization data. On the other hand, Brodsky and de Teramond [Br88] proposed that the structure seen in  $s^{10} \frac{d\sigma}{dt}(pp \rightarrow pp)$ ,  $A_{nn}$  spin correlation [Cr78, Co86], and the  $A(p, 2p)$  transparency result can be attributed to new  $c\bar{c}uud\bar{u}ud$  resonant states.

Whether similar phenomena occur in pion production is an open problem. The results from E94-104, at  $90^\circ$  c.m. angle, suggest an onset of scaling behavior around a center-of-mass energy of 2.5 GeV and show very interesting hints of possible oscillation in the scaled differential cross-section for the  $\gamma n \rightarrow \pi^- p$  and  $\gamma p \rightarrow \pi^+ n$  channels. Precision measurements of these fundamental cross-sections would be a timely guide for theoretical efforts on this subject (see for instance [Is01, Zh03]) and would help understand the exact mechanism behind the scaling behavior observed in exclusive processes. An experiment (E02-010) to perform a fine scan of the region between  $2.3 \text{ GeV} < \sqrt{s} < 3.4 \text{ GeV}$  with photo-pion production from nucleons was recently approved. With the upgrade of JLab energy to 12 GeV, these measurements will be extended up to  $\sqrt{s} = 4.6 \text{ GeV}$ , above the charm production threshold.

Coincidence measurements from deuterium,  $d(\gamma, \pi^- p)$ , are necessary in order to study the fundamental  $\gamma n \rightarrow \pi^- p$  process. The combination of HMS and the planned Super-HMS spectrometers in Hall C makes this experiment feasible. Figure 124 shows the projected result as a function of  $s$  for the  $\gamma n \rightarrow \pi^- p$  process together with a 3% point-to-point systematic uncertainty and a 2% statistical uncertainty. For the  $\gamma p \rightarrow \pi^+ n$  process, the detection of the  $\pi^+$  particle alone is sufficient. Figure 125 shows the projected result as a function of  $s$  for the  $\gamma p \rightarrow \pi^+ n$  process together with a 3% point-to-point systematic uncertainty and a 2% statistical uncertainty, when the  $\pi^+$  is detected in the Hall A Medium Acceptance Spectrometer (MAD).

Polarization measurements can play a crucial role in understanding reaction mechanisms of wide angle meson photoproduction at high energy. The scattering amplitude at asymptotic energies is dominated by multi-gluon exchange within the minimal Fock-state of the nucleon and meson. The soft overlap process that likely dominates in Real Compton Scattering at energies below the asymptotic limit is also expected in the meson production case. These two mechanisms predict large, but opposite sign, polarization transfer observables.

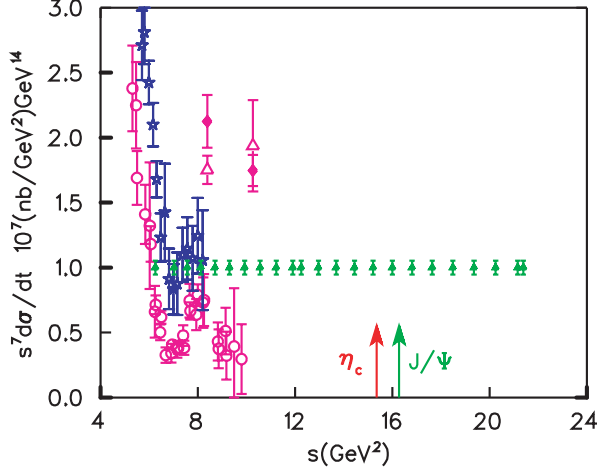


Figure 126: The scaled differential cross-section for the  $p(\gamma, \pi^0)p$  process at C.M. angle of  $90^\circ$ , as a function of cms energy squared  $s$  in  $\text{GeV}^2$  along with the projected measurements for JLab at 11 GeV (green).

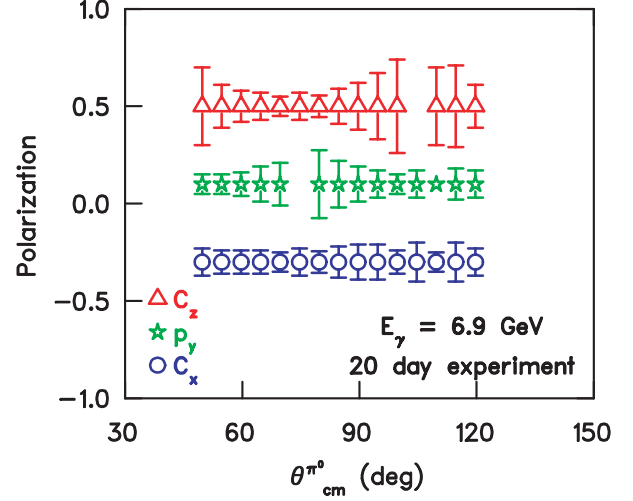


Figure 127: Estimated uncertainties for the induced polarization in  $\vec{\gamma}p \rightarrow \vec{p}\pi^0$  for  $E_\gamma = 6.9$  GeV, as a function of  $\pi^0$  angle. The value chosen for the polarizations is arbitrary. Three weeks of beam time is assumed. Similar quality angular distributions would be obtained at the same time for several additional 200 MeV bins in photon energy. See text for further details.

Recoil polarimetry of the proton, in neutral pion photoproduction, allows a determination of the induced polarization  $p_y$  and the polarization transfers  $C_x$  and  $C_z$ , for a longitudinally polarized electron beam. Recent Hall A experiments,  $G_E^p$  (E99-007) and RCS (E99-114), have demonstrated the feasibility of using a calorimeter for coincidence measurement of the two photons from the  $\pi^0$  decay, allowing a clean measurement of  $\vec{\gamma}p \rightarrow \vec{p}\pi^0$ . Fig. 126 shows the projected result for the differential cross section measurement for the  $\gamma p \rightarrow \pi^0 p$  process together with a 5% point-to-point systematic uncertainty and a 2% statistical uncertainty. Figure 127 shows estimated uncertainties for the recoil polarization that could be obtained with a polarimeter installed in MAD, and a coincident  $\pi^0$  detection to reduce background.

**Pion Photoproduction in the Nuclear Medium** In the nuclear medium, it has been suggested that long distance amplitudes are suppressed (nuclear filtering) by the strongly interacting nuclear environment [Ra90]: The oscillation phenomena arising from their interference with the short distance amplitude is expected to disappear in nuclear medium. The experimental manifestation of this effect is predicted to be in the form of oscillations in nuclear transparency<sup>3</sup>, which are  $180^\circ$  out of phase with oscillations in the scaled free differential cross-section. The nuclear filtering

<sup>3</sup>Nuclear transparency is defined as the ratio of the cross-section for a specified physical process from a nuclear target to a modeled cross-section based on the specified process from a free nucleon target within the plane-wave impulse approximation normalized by the number of nucleons in the nuclear target.



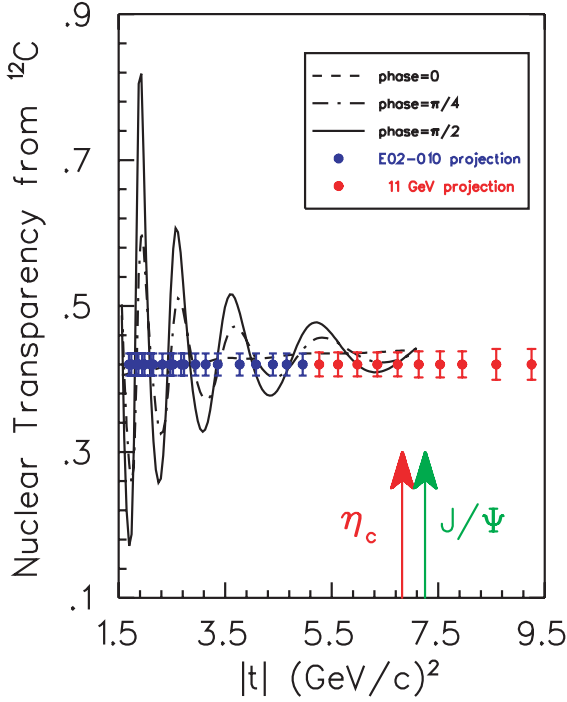


Figure 128: The projected results for nuclear transparency for photo-pion production from a  $^{12}\text{C}$  target. The lines are calculations from Ref [Ja02].

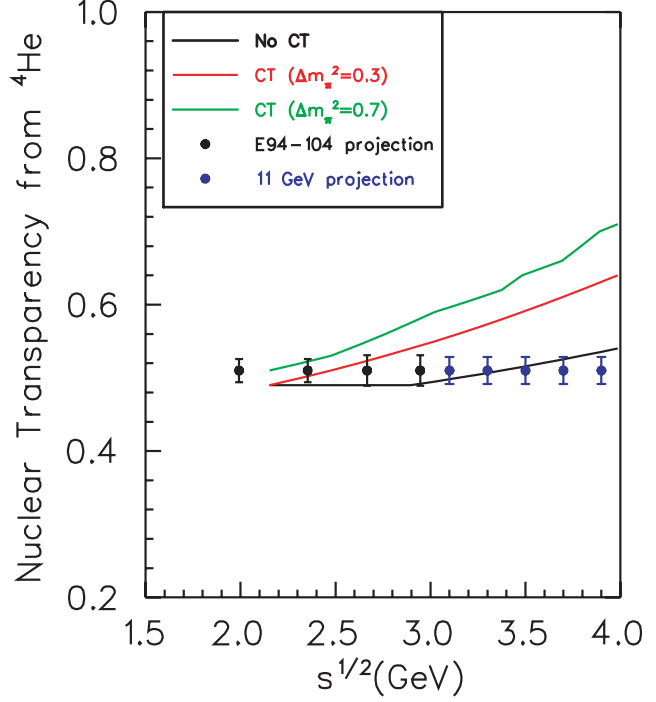


Figure 129: The projected results for nuclear transparency for photo-pion production from a  $^4\text{He}$  target. The lines are color transparency calculations from Ref [Ga96].

effect can be studied with photo-pion production from nuclei such as  $^{12}\text{C}$ . The preliminary results from the exploratory data taken on a  $^4\text{He}$  target during E94-104 demonstrated the experimental technique. With JLab at 12 GeV, search of nuclear filtering will be extended beyond the charm threshold. Figure 128 shows the projected results on the  $^{12}\text{C}$  nuclear transparency measurement of the  $\gamma n \rightarrow \pi^- p$  process, in which a 3% point-to-point systematic uncertainty along with a 2.0% statistical uncertainty are shown. Different curves shown in Fig. 128 correspond to different phase angles in the two-component model by Jain and Ralston [Ja02], which explains the Brookhaven A(p,2p) [Ca88, Ma98a] nuclear transparency data.

Color Transparency (CT), discussed previously in Section 2.C.1, is another phenomenon which will be studied with pion photoproduction in the nuclear medium. While nuclear filtering uses the nuclear medium actively, in CT large momentum transfers select out the short distance amplitude which are then free to propagate through the passive nuclear medium. The E94-104  $^4\text{He}$  nuclear transparency results from the  $\gamma n \rightarrow \pi^- p$  process at a  $90^\circ$  center-of-mass angle up to a center-of-mass energy of 3.0 GeV show a very intriguing momentum transfer dependence of the nuclear transparency. With a 12 GeV CEBAF and the upgraded detection system, the nuclear transparency of the  $\gamma n \rightarrow \pi^- p$  process from  $^4\text{He}$  can be extended to a  $|t|$  value of  $\sim 10$   $(\text{GeV}/c)^2$ . Such an extension allows detailed investigation of the onset of color transparency. The projected results are



shown in Fig. 129, in which a 3% point-to-point systematic uncertainty along with a 2.0% statistical uncertainty are shown.

With the 12 GeV energy upgrade and the planned upgrade of instrumentation, the transition region can be studied systematically using the simplest system: pion, nucleon, deuteron and helium with precisions, which allow definitive statements about the onset of the transition. This study is also important and coupled closely to other important nuclear physics questions which are discussed previously.

## 2.D Symmetry Tests in Nuclear Physics

Precision parity-violating electron scattering experiments made feasible by the 12 GeV Upgrade have the sensitivity to search for deviations from the Standard Model that could signal the presence of new gauge bosons  $Z'$ s, the existence of leptoquarks, or particles predicted by supersymmetric theories, *i.e.* physics beyond the Standard Model. Planned studies of the three neutral pseudoscalar mesons, the  $\pi^0$ ,  $\eta$  and  $\eta'$ , will provide fundamental information about low energy QCD, including certain critical low energy parameters, the effects of SU(3) and isospin breaking by the  $u$ ,  $d$ , and  $s$  quark masses, and the strengths of the two types of chiral anomalies. These two programs are described briefly below.

### 2.D.1 Standard Model Tests

Tests of fundamental symmetries have been an important area of study in nuclear physics for decades. Studies of parity-violation in  $\beta$ -decay and electron scattering, time-reversal violation in nuclear decays and electromagnetic interactions, and lepton number violation in neutrinoless  $\beta\beta$ -decay—to mention a few examples—have contributed in significant ways to our understanding of the structure of the Standard Model of the electroweak interaction. Now, attention is focused on what may lie beyond the Standard Model (SM). There exist numerous theoretical and phenomenological reasons for believing that the SM is only part of a larger, more fundamental framework. Uncovering the structure of the “new” Standard Model will require a concerted effort involving both experiment and theory. On the experimental side, important information will be gleaned from both high-energy collider studies as well as highly precise, low-energy measurements. In this respect, precision electroweak nuclear physics will continue to play an important role. Indeed, this fact was highlighted in the April 2002 NSAC Long Range Plan [NS02], which identified “What is to be the new Standard Model?” as one of the five scientific questions that would drive nuclear science for the next decade.

Tests of fundamental symmetries are also helping to elucidate presently poorly understood aspects of the strong interaction in the non-perturbative domain. The parity-violating electron scattering (PVES) program currently underway at Jefferson Lab represents an excellent example of using a symmetry violation to study novel aspects of non-perturbative nucleon structure. The

parity-violating weak, neutral current electron-quark interaction provides one of the only tools we have for probing the  $s\bar{s}$  sea over distance scales where a valence quark description of the nucleon has been assumed to be adequate. It remains a mystery as to why the valence quark model should work so well, given what we know about the role played by sea quarks and gluons in high-energy scattering processes. The use of parity-violation in electron scattering is shedding new light on this fundamental problem.

There exists a powerful synergy between these two uses of symmetry violation in nuclear physics. For example, the use of parity-violation to study nucleon structure requires that one have a sufficiently clear understanding of the weak interaction at a fundamental level. Conversely, the search for a new SM through precision parity-violation experiments involving nuclei depends upon having a sufficiently reliable understanding of non-perturbative QCD effects. In this respect, the Q-Weak experiment, to which Jefferson Laboratory has made a substantial commitment, provides an illustrative example. This experiment will provide a probe of new physics at the TeV scale. It will be able to do so, however, only because the present program of PVES measurements will reduce the uncertainty associated with non-perturbative QCD effects in the PV asymmetry to an acceptably small level. To the extent that both the strange quark and Q-Weak endeavors are successful, Jefferson Lab will have made substantial contributions to both nuclear and particle physics by exploiting the opportunities provided by PVES.

The proposed up-grade of CEBAF will amplify these opportunities. Below, we discuss two types of PVES experiments that will build on the successes of the present programs: parity-violating Møller scattering and PV deep inelastic electron-deuteron scattering. At present, a PV Møller experiment is being performed at SLAC. With the 12 GeV upgrade and the luminosity provided by the accelerator, one could perform a future version of the SLAC experiment with considerably smaller uncertainties. As discussed below, precision which could be achieved would allow one to probe various aspects of supersymmetry, such as the existence of a viable supersymmetric candidate for cold dark matter.

The second prospective experiment—PV deep inelastic scattering (DIS) with a deuteron target—could be envisioned either as a probe of new physics or as a tool to study higher-twist structure functions. The motivation in either case is strong. From the perspective of new physics, a study of PV DIS would complement the recent work of the NuTeV collaboration [Ze01], which studied deep inelastic  $\nu$  ( $\bar{\nu}$ )-nucleus scattering from iron. The results of the NuTeV experiment may be interpreted as a determination of the  $Q^2$ -dependence of the weak mixing angle, and indicate a  $3\sigma$ -deviation from the SM prediction for this quantity. It is difficult to accommodate such a sizeable discrepancy through the most widely-considered new physics models, so the NuTeV anomaly could be particularly important in this context. However, a debate has emerged as to the size of possible non-perturbative QCD contributions that may reduce the significance of the anomaly. A study of PV DIS could provide a complementary probe of the  $Q^2$ -dependence of  $\sin^2 \theta_W$  in the deep inelastic domain. As it would involve different systematic and non-perturbative QCD effects, it would help

determine whether or not a deviation from the SM exists in this regime. Alternatively, one could study the  $Q^2$ -dependence of the PV asymmetry in this domain in order to extract information on higher-twist structure functions. In this respect, PV DIS would represent a continuation of the strange quark program, wherein parity-violation is being used to study non-perturbative nucleon structure.

The ongoing SLAC E158/Møller experiment [Ca97a] is in the process of measuring  $Q_{\text{weak}}^e$ , with their final run taking place in the summer of 2003. This is a very important measurement, and the SLAC E158/Møller collaboration is doing an excellent job. It will be possible to achieve half of the anticipated uncertainty of the SLAC E158/Møller experiment with a 12 GeV experiment at Jefferson Laboratory, as discussed below.

A new measurement with twice the precision of SLAC E158 would be a powerful tool in the search for “new physics”, and at this precision, even a result in agreement with the Standard Model would have significant consequences. For example, such a result would severely constrain the viability of SUSY models that lack a candidate particle for dark matter, the non-luminous and unexplained source of 90% of the mass of the universe [Ku02]. This is illustrated in Fig. 130, which plots  $\delta Q_{\text{weak}}^e$  against  $\delta Q_{\text{weak}}^{\text{proton}}$  for 3000 possible SUSY parameter configurations, with the expected experimental uncertainties from Jefferson Lab’s Q-Weak, SLAC E158 and a 12 GeV Jefferson lab experiment superimposed. The large shaded truncated ellipse represents an area, in which if  $Q_{\text{weak}}^e$  and  $Q_{\text{weak}}^{\text{proton}}$  are found to lie, there is R-parity violation and no SUSY dark matter. Clearly a second generation Møller experiment would significantly restrict the available parameter space. This is only one example of the impact of a more precise measurement of  $Q_{\text{weak}}^e$ , others are described in reference [Ra99a].

The parity violating asymmetry in Møller scattering measures the weak charge of the electron,  $Q_{\text{weak}}^e$ . Observables like the weak electron and proton charges, proportional to  $1 - 4 \sin^2 \theta_W$ , are very sensitive to the value of  $\sin^2 \theta_W$  since the latter is close to 1/4. For

$$A = f(1 - 4 \sin^2 \theta_W) + D$$

where  $f$  is a kinematic factor and  $D$  is an experimental dilution factor, the uncertainty in  $\sin^2 \theta_W$  is given by

$$\frac{\delta \sin^2 \theta_W}{\sin^2 \theta_W} = -\frac{\delta A}{A} \frac{1}{4} \frac{(1 - 4 \sin^2 \theta_W + D/f)}{\sin^2 \theta_W}, \quad (55)$$

with  $\delta \sin^2 \theta_W / \sin^2 \theta_W \approx 0.05 \delta A / A$  for  $D = 0$ . The near-vanishing of the tree-level asymmetry makes such observables sensitive to  $\sin^2 \theta_W$ , new physics at tree-level (*e.g.*, a  $Z'$ ), and new physics via loops. Radiative corrections, not all of which are suppressed by factors of  $(1 - 4 \sin^2 \theta_W)$ , reduce the tree-level Møller asymmetry by about 40%.

At tree level the parity violating Møller asymmetry is [De79]

$$A_{\text{Moller}} = \frac{4m_e E G_F}{\sqrt{2}\pi\alpha} \frac{\sin^2 \theta_{\text{cm}}}{(3 + \cos^2 \theta_{\text{cm}})^2} (1 - 4 \sin^2 \theta_W) \quad (56)$$

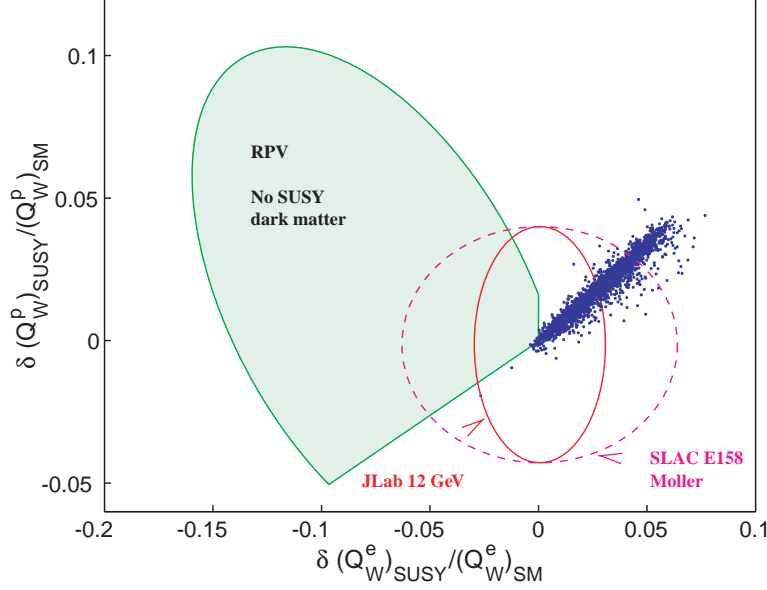


Figure 130: Relative shifts in  $Q_{\text{weak}}^e$  and  $Q_{\text{weak}}^{\text{proton}}$  from SUSY effects. The blue dots indicate MSSM loop corrections for approximately 3000 SUSY-breaking parameter choices. The interior of the green truncated ellipse shows possible shifts due to R-parity violation. In this region, SUSY dark matter is excluded [Ku02]. The dashed magenta ellipse illustrates the expected uncertainty from SLAC E-158 Møller and JLab Q-Weak, while the red ellipse represents what could be achieved with a 12 GeV Møller experiment at Jefferson Laboratory.

where  $E$  is the electron beam energy. The center-of-momentum cross section is

$$\frac{d\sigma}{d\Omega} = \frac{\alpha^2}{2m_e E} \frac{(3 + \cos^2 \theta_{\text{cm}})^2}{\sin^4 \theta_{\text{cm}}} \quad (57)$$

and hence the Figure-of-Merit (FOM) defined as  $A^2 d\sigma/d\Omega$  is simply proportional to the beam energy,  $E$ . All other things being equal, a measurement at 48 GeV has 4 times the FOM of a measurement at 12 GeV.

The design of the ongoing SLAC E158 is close to optimal for that facility. The 12 GeV Jefferson Lab facility can mount an improved measurement of  $Q_{\text{weak}}^e$  by employing an enormous integrated luminosity while maintaining ppb-level control of systematic uncertainties. Table 12 lists important parameters for the two experiments such as the cross section, asymmetry, and integrated luminosity. Small differences in the azimuthal acceptance and dilution have been ignored. In practical terms, the Jefferson Lab experiment would correspond to one year of running in one of the two high luminosity end-stations (32 weeks at 75% efficiency).

Table 13 compares the anticipated uncertainties for SLAC E158 and the potential Jefferson Lab 12 GeV measurement. For the Jefferson Lab measurement, systematic uncertainties are assumed to be limited to 1%-2% by the combination of  $Q^2$ , beam polarization, and corrections for residual helicity-correlated differences in beam parameters. The final projected uncertainty on  $\sin^2 \theta_W$

Table 12: Parameters for the SLAC E158 experiment from the proposal compared to those for a potential Jefferson Lab experiment at 12 GeV.

Parameter	SLAC E158	12 GeV JLab
$E$	48 GeV	12 GeV
$E'$	12-24 GeV	3-6 GeV
$\langle Q^2 \rangle$	$0.03 (GeV/c)^2$	$0.008 (GeV/c)^2$
$\theta_{cm}$	$90^\circ$ - $120^\circ$	$90^\circ$ - $120^\circ$
$\theta_{lab}$	$0.26^\circ$ - $0.46^\circ$	$0.53^\circ$ - $0.92^\circ$
$\langle A_{PV} \rangle$	161 ppb	40 ppb
$\sigma$	16 $\mu$ barns	64 $\mu$ barns
Polarization	80%	80%
Current	9.1 $\mu$ A	100 $\mu$ A
$LH_2$ Target Length	150 cm	75 cm
Luminosity $cm^{-2}s^{-1}$	$4.0 \times 10^{38}$	$2.2 \times 10^{39}$
Time	1445 hours <sup>a</sup>	4000 hours <sup>b</sup>
Luminosity $\times$ Time	$2.1 \times 10^{45} cm^{-2}$	$3.2 \times 10^{46} cm^{-2}$

<sup>a</sup>20 weeks at SLAC at 43% efficiency

<sup>b</sup>32 weeks at 75% efficiency: effectively, one year of JLab running

of  $\pm 0.0004$  would be competitive with the best measurements of  $\sin^2 \theta_W$  at the  $Z^0$  pole.<sup>4</sup> More importantly, this would be the best measurement of the electron's weak charge at low energy scales.

To put such an effort in context, all previous, ongoing, and approved Standard Model tests which employ parity violating electron scattering, along with the 12 GeV Jefferson Lab measurement under discussion are shown in Fig. 131. Since the original measurement by Prescott *et al.* [Pr78, Pr79], the difficulty of Standard Model tests employing PV electron scattering has been increasing. A 12 GeV Møller experiment would be the logical next step following successful completion of the Q-Weak (proton) experiment which is currently in preparation.

As with any precision Standard Model test, the interpretability of a 12 GeV Møller experiment is critical. The major limitation to the interpretability arises from hadronic loops in the  $\gamma Z$  mixing diagrams [Cz96] which are also the dominant correction. If the 12 GeV Møller experiment were done today, the 3% experimental uncertainty on the measured asymmetry would be comparable to the uncertainty in the theory. Fortunately, it is likely that forthcoming results from the SLAC E158 experiment will stimulate further work in this area.

Figure 132 gives a schematic representation of the experiment. The laboratory scattering angles are quite small,  $\sim 0.7$  degrees, and can be conveniently expressed in units of the average multiple scattering angle in the thick target. To focus the Møller electrons of such small angles (momentum  $4.5 GeV/c \pm 33\%$ ) in an azimuthally symmetric manner, we first plan to drift the

<sup>4</sup>Since there are no longer any  $e^+e^-$  colliders operating near the  $Z$  pole, there will be no further high energy precision neutral current measurements until construction of some version of the Next Linear Collider.

Table 13: Projected uncertainties for ongoing SLAC E158 (from the proposal) and for a potential Jefferson Lab measurement at 12 GeV.

Uncertainties	SLAC E158	12 GeV JLab
Statistical:		
$\delta A$	10 ppb	1 ppb
$\delta A/A$	6%	3%
$\delta \sin^2 \theta_W$	0.00071	0.00036
Systematic:		
$\delta A$	4 ppb	0.4 - 0.8 ppb
$\delta A/A$	2.7%	1% - 2%
$\delta \sin^2 \theta_W$	0.00032	0.00012 - 0.00024
Combined:		
$\delta A$	11 ppb	1 ppb
$\delta A/A$	6.6%	3.2% - 3.6%
$\delta \sin^2 \theta_W$	0.00079	0.00038 - 0.00043

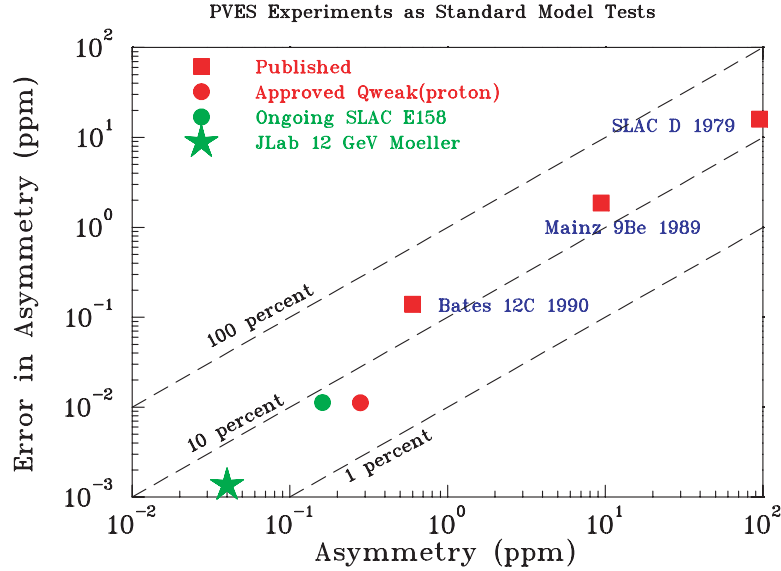


Figure 131: There has been a steady progression with time in the difficulty of Standard Models tests which employ parity violating electron scattering. (The 12 GeV Møller experiment is denoted by a star.) A new generation of experiments based on DIS might be an exception to this trend.

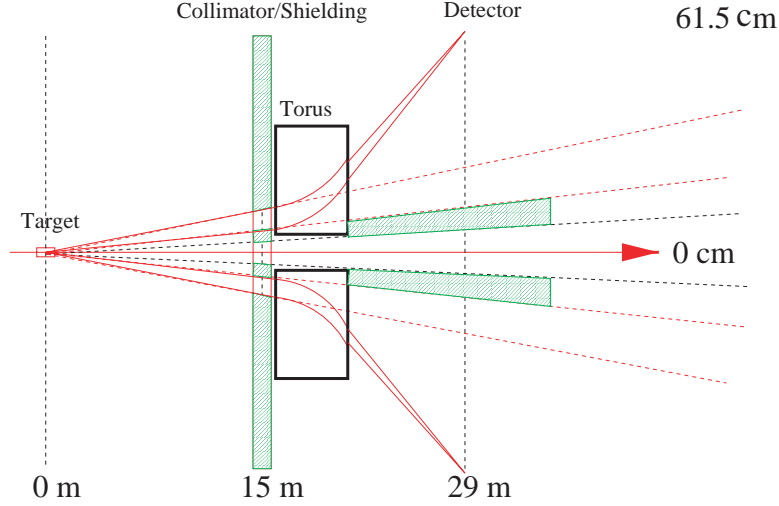


Figure 132: Schematic of a 12 GeV Møller experiment. The vertical scale is artificially magnified for visibility since the actual vertical/horizontal ratio is roughly 1:50.

scattered electrons to a collimator. The  $Q^2$  determination then depends only on geometry and the well-known beam energy. The electrons then enter a resistive toroidal magnet that provides a field integral tailored to the  $E'$  versus  $\theta$  correlation from Møller kinematics. The  $1/R$  field profile of a toroidal magnetic is well suited to this application, providing large field integrals at small radii with 75% azimuthal acceptance. Correction coils in the torus may be needed. Finally, the electrons drift to a focus on a ring of Čerenkov detectors where the Møller electron signals are integrated. Detectors at smaller and larger radii will monitor the asymmetry of backgrounds.

Despite the relatively low PV asymmetry of Møller scattering at 12 GeV, an improved measurement of  $Q_{weak}^e$  with half the proposed SLAC E158 uncertainty is achievable. This small improvement, however, is very important, when considered in terms of the allowable SUSY parameter space and SUSY dark matter.

Another PVES experiment utilizing the 11 GeV beam is a measurement of parity violation in deep inelastic scattering (DIS parity) from a deuterium target. This asymmetry is also sensitive to  $\sin^2 \theta_W$ . While the interpretation of DIS parity violation is not as clean as it is for Møller scattering due to higher twist contributions to the asymmetry, the experiment itself is literally several orders of magnitude easier, with an asymmetry of approximately  $10^{-4}$ . DIS parity violation from a deuterium target was first observed by Prescott *et al.* [Pr78, Pr79] in the mid-1970's and established the Weinberg-Salam model. This measurement can be repeated at 11 GeV with the precision necessary to once again confront the Standard Model. This measurement is made more interesting by the recent report from the NuTeV collaboration, using neutrino scattering on iron, of  $\sin^2 \theta_W^{\text{on-shell}} = 0.2277 \pm 0.001(\text{stat}) \pm 0.0009(\text{syst})$ , three standard deviations above the Standard Model predictions [Ze01]. This difference has been interpreted in terms of physics beyond the Standard Model (new propagator or couplings, dimension six operators, extra U(1) gauge bosons,

etc.) [Da01]. However, there are also more conventional explanations, including nuclear effects in the iron target [Mi02b] and QCD effects [Da01]. DIS-Parity violation using an 11 GeV beam electron beam could quite quickly achieve the statistical sensitivity needed to investigate the NuTeV result at  $Q^2$  near that of NuTeV. Using a deuterium target, it will not suffer from the uncertainties in nuclear effects and nuclear parton distributions that were present in the NuTeV iron measurement.

The parity-violating asymmetry for scattering longitudinally polarized electrons from an unpolarized isoscalar target such as a deuteron (assuming charge symmetry) is given by [Ca78a]

$$A_d = \frac{\sigma_L - \sigma_R}{\sigma_L + \sigma_R} = - \left( \frac{3G_F Q^2}{\pi \alpha 2\sqrt{2}} \right) \frac{2C_{1u} - C_{1d} [1 + R_s(x)] + Y(2C_{2u} - C_{2d})R_v(x)}{5 + R_s(x)}. \quad (58)$$

The  $C_{1u(d)}$  represents the axial  $Z$ -electron coupling times the vector  $Z$ - $u$  quark ( $d$  quark) coupling, and the  $C_{2u(d)}$  are the vector  $Z$ -electron coupling times the axial  $Z$ - $u$  quark ( $d$  quark) coupling. Taking  $\sin^2 \theta_W \approx 0.231$ ,

$$\begin{aligned} C_{1u} &= -\frac{1}{2} + \frac{4}{3} \sin^2 \theta_W \approx -0.192, & C_{1d} &= \frac{1}{2} - \frac{2}{3} \sin^2 \theta_W \approx 0.346, \\ C_{2u} &= -\frac{1}{2} + 2 \sin^2 \theta_W \approx -0.038, & C_{2d} &= \frac{1}{2} - 2 \sin^2 \theta_W \approx 0.038. \end{aligned}$$

Also

$$Y = \frac{1 - (1 - y)^2}{1 + (1 - y)^2 - y^2 R / (1 + R)} \text{ with } y = \nu/E.$$

Here,  $\nu = E - E'$  is the energy lost by an incident electron of energy  $E$  scattering to an electron of energy  $E'$ , and the ratio  $R = \sigma_L / \sigma_T \approx 0.2$  depends on  $x$  and  $Q^2$ . The ratios  $R_s(x)$  and  $R_v(x)$  depend on the quark distribution functions:

$$R_s(x) = \frac{s(x) + \bar{s}(x)}{u(x) + \bar{u}(x) + d(x) + \bar{d}(x)} \quad \text{and} \quad R_v(x) = \frac{u_v(x) + d_v(x)}{u(x) + \bar{u}(x) + d(x) + \bar{d}(x)}.$$

At high  $x$ , where sea quark contributions vanish,  $R_v = 1$  and  $R_s = 0$ , we find

$$A_d \approx 10^{-4} Q^2 (0.73 + 0.11Y).$$

The sensitivity to  $\sin^2 \theta_W$  is approximately given by

$$\frac{d \sin^2 \theta_W}{\sin^2 \theta_W} \approx \frac{dA}{A} \frac{0.95 + 0.15Y}{1.0 + 1.8Y}. \quad (59)$$

The dependence of the asymmetry on  $Y$  will allow for the extraction of  $2C_{1u} - C_{1d}$  and  $2C_{2u} - C_{2d}$  separately. The sensitivity to the  $2C_{2u} - C_{2d}$  makes the experiment quite unique. Since “new” physics may affect each of these coefficients in a different way, the ability to separate these coefficients may provide an additional tool to understand how “new” physics contributes [Ra99a].

To have the best sensitivity to  $\sin^2 \theta_W$  while minimizing systematic uncertainties imposes several conditions on experimental conditions. These include requiring  $x > 0.2$  to minimize uncertainties from parton distributions, and using a deuterium target where the  $d(x)/u(x)$  ratio is known. At the same time, to minimize effects from higher twist,  $x \lesssim 0.4$ . In addition, the experiment



must be run in the DIS region to ensure that the scattering is from quarks, with  $Q^2 > 1 \text{ GeV}^2$  and  $W^2 > 4 \text{ GeV}^2$ . It is also important to keep  $E'/E > 0.3$  to avoid large rates of pions and pair-symmetric backgrounds in the detectors. Given these constraints, a possible set of running conditions for an 11 GeV beam would be a scattering angle of  $12.5^\circ$  with spectrometer central momentum of 5.5 GeV, corresponding to  $\langle x \rangle = 0.28$ ,  $\langle Q^2 \rangle = 2.9 \text{ GeV}^2$ ,  $\langle W^2 \rangle = 8.3 \text{ GeV}^2$  (well above the resonance region), and  $\langle Y \rangle = 0.62$ .

With these kinematics, a beam current of  $90 \mu\text{A}$  with 80% polarization and a 60 cm liquid deuterium target, the experiment could be completed in an extremely modest amount of time. Using a set of spectrometers with a total acceptance of 12 msr and a momentum bite of  $\pm 10\%$ , a relative statistical uncertainty on the deuterium asymmetry of 0.6% and a corresponding uncertainty of 0.26% in  $\sin^2 \theta_W$  can be achieved in only 275 “ideal” hours of beam time. In this configuration, a rate of less than 1 MHz of DIS electrons is expected, with a similar rate from pions.

The spectrometer solid angle and momentum bite assumptions are matched to the combination of the HMS and SHMS spectrometers in Hall C or the HRS/MAD combination in Hall A, allowing the experiment to be performed in either of these Halls. At these event rates, the wire chamber and time-of-flight information would not be used—events would require a coincidence between the Čerenkov counters and lead glass calorimeters in the spectrometers. Flash ADCs, similar to those planned for Hall D, will be required on the counters to run in “event mode”. The Čerenkov counters will have to be adjusted (gas mixture, pressure) to have a threshold about 6 GeV for pions. The overall target length of 60 cm is limited by the desire to keep radiative corrections down and is well matched to the optical acceptance of the spectrometers under consideration. With  $90 \mu\text{A}$  of current, this then requires roughly 2 kW of cooling power, equivalent to that needed by the Q-Weak experiment [Ca01] in Hall C.

Given the relatively large asymmetry the statistical uncertainty may be made small in a short amount of beam time, and systematic effects will be the dominant source of uncertainties in this experiment. The largest of these uncertainties in  $A_d$  is expected to be from the beam polarization measurement (of order 1%). The uncertainty in  $A_d$  due to radiative corrections should be well under 1%, and the uncertainty due to the determination of the average  $Q^2$  should be under 0.5%. The uncertainty propagated from the parton distributions [Pu02, Ma02a] is less than 0.1% in  $A_d$ . The uncertainty in  $R = \sigma_L/\sigma_T$  is also well known and will contribute less than 0.4% in  $A_d$ . Because the asymmetry is several orders of magnitude larger than the Q-Weak and G0 experiments, control of helicity-correlated beam parameters should be adequate if they can be maintained at G0 levels when the beam energy is upgraded. Possible breaking of charge symmetry could lead to corrections. Fortunately, these effects are small—a large 0.5% charge symmetry violation would only contribute 0.1% to  $A_d$ . Charge symmetry violation effects, nuclear shadowing, and the “EMC Effect” in the deuteron can also be addressed by measuring the asymmetry with a proton target, if the  $d/u$  quark ratio is sufficiently well known at the desired kinematics from other experiments. These systematic uncertainties are summarized in Tab. 14. Combining these uncertainties, the deuterium asymmetry

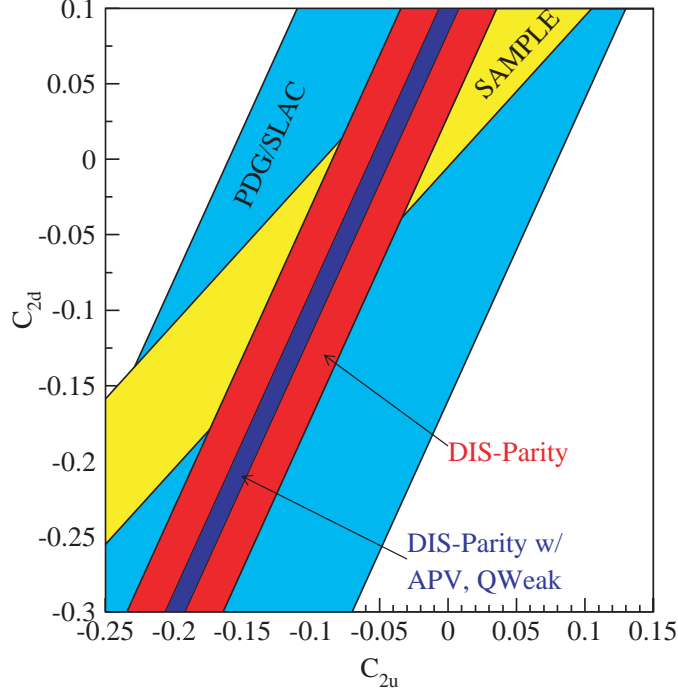


Figure 133: The limits on  $C_{2u}$  and  $C_{2d}$  listed by the particle data group [PDB], by the SAMPLE experiment [Ha01, Bepc] and by the proposed experiment (DIS-Parity) [Bo94a].

Table 14: This table lists possible sources of systematic uncertainty in the measurement of  $A_d$ . The dominate uncertainty is the knowledge of the beam polarization, and the influence of higher twist effects. Recall that  $\delta \sin^2 \theta_W / \sin^2 \theta_W \approx 1/2 \delta A_d / A_d$ .

Effect	$\delta A_d$ (%)	Effect	$\delta A_d$ (%)
Polarization	1.0%	$\delta \langle Q^2 \rangle$	0.5%
$\delta R_s, \delta R_v$	0.1%	$\delta R = \delta \sigma_L / \sigma_T$	0.4%
Charge Sym. Violation.	0.1%	Higher Twist	?

will be measured to  $\delta A_d = \pm 0.6\%$  (stat.)  $\pm 1.2\%$  (syst.), or  $\delta \sin^2 \theta_W \approx \pm 0.3\%$  (stat.)  $\pm 0.6\%$  (syst.), excluding higher twists effects as discussed below. This uncertainty is shown in Fig 134. With the successful completion of the Jefferson Lab Q-Weak experiment,  $C_{1u(d)}$  will be known to an absolute uncertainty of  $\delta C_{1u(d)} = 0.005$ . This will allow the proposed experiment to place an absolute uncertainty of  $\delta(C_{2u} - \frac{1}{2}C_{2d}) = 0.019$ . When taken together with the results from the SAMPLE experiment [Ha01] much tighter bounds are placed on  $C_{2u}$  and  $C_{2d}$  than were previously available [PDB] as illustrated in Fig. 133.

A more difficult uncertainty relates to the interpretation, because higher twist effects may not be negligible at the relatively low  $Q^2$  of about  $3 \text{ GeV}^2$ . This may be partially addressed by making an additional measurement at lower  $Q^2$ , and another at higher  $Q^2$  and  $x$ . Although the lever arm available to look for  $1/Q^2$  effects is limited with a maximum beam energy of 11 GeV, these

measurements would be able to determine if sizable effects are present. In addition, measurement at other laboratories, such as the proposed SLAC measurement of  $A_d$  at  $Q^2 \approx 20 \text{ GeV}^2$  [Bo03] will greatly help in the understanding of higher twist effects. Higher twist effects may also be minimized by selecting a kinematic region in which  $x < 0.4$ , which unpolarized DIS data have already shown smaller higher twist effects. (This is consistent with the kinematics given above.) Within the context of the bag model, Castorina and Mulders [Ca85] have calculated the effect of twist-four corrections on  $\sin^2 \theta_W$  as measured by DIS parity violation on deuterium and find that  $\delta_{HT} \sin^2 \theta_W \approx -6.5 \times 10^{-4}/Q^2$ . Fajfer and Oakes [Fa84] calculate a slightly smaller effect; although Brodsky [Br00b] comments that these calculations may yield too small of an effect at high- $x$ . Clearly, significant theoretical support will be needed to control all of these uncertainties to the desired level. It should be pointed out that the study of parity-violating higher twist effects is quite interesting in its own right, and that a comparison with higher- $Q^2$  data (*e.g.* the SLAC LOI) would, by itself, be a worthwhile study.

DIS parity violation offers Jefferson Lab the opportunity to perform a measurement of  $\sin^2 \theta_W$  to an 0.6% relative uncertainty by measuring a relatively *large* asymmetry of  $10^{-4}$ . This measurement would serve as a much needed check on the recent  $\sin^2 \theta_W$  results from NuTeV. At the same time by measuring the  $C_{2u} - \frac{1}{2}C_{2d}$ , the proposed experiment is complimentary to both the Møller and Q-Weak experiments in its sensitivity to extensions of the Standard Model.

The upgrade of CEBAF to 12 GeV will allow us to continue to build on the success of previous parity violating electron scattering experiments. Two complementary, 11 GeV PVES experiments have been outlined here, Møller scattering and DIS parity violation from deuterium. Within the Standard Model, both of these experiments will measure  $\sin^2 \theta_W$ , as shown in Fig. 134, but they are sensitive to different possible Standard Model extensions. The Møller experiment, while much more difficult, has a much cleaner interpretation and could have a significant impact on the understanding of dark matter within the context of SUSY. The asymmetry in DIS parity violation from deuterium is much larger than the Møller asymmetry and is also sensitive to  $\sin^2 \theta_W$ . The interpretation is somewhat less clean, however, due to possible higher twist contributions to the measured asymmetry. It is important to remember that the experiments measure different couplings, and as such, are sensitive to *different* possible extensions to the Standard Model. “New” physics may present itself in some but not all of these measurements, thus requiring the complementarity presented by a broad program of measurements.

### 2.D.2 Properties of Light Pseudoscalar Mesons via the Primakoff Effect

The future availability of high quality, high duty factor 12 GeV electron beams at Jefferson Lab will enable unprecedented new opportunities to perform precise measurements of meson decay widths and electromagnetic transition form factors. In particular, the high energy electro- and photoproduction of pseudoscalar mesons in the Coulomb field of a nucleus, the Primakoff effect, can be exploited to study the two photon decay widths,  $\Gamma_{\gamma\gamma}$ , and the transition form factors,

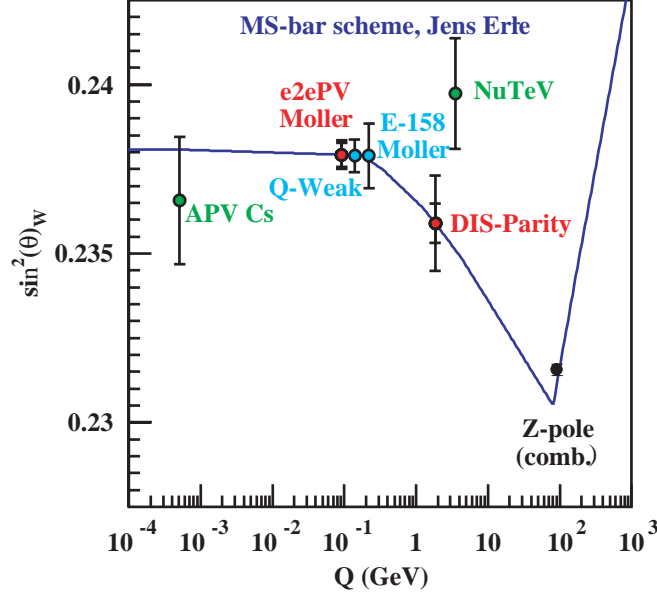


Figure 134: The running of  $\sin^2 \theta_W$  in the  $\overline{MS}$  scheme [Erpc], showing the two measurements discussed here (e2ePV/Møller and DIS-Parity). The inner error bars represent the statistical uncertainty and the outer represent the statistical and systematic uncertainty combined in quadrature. Also shown are the existing measurements from Cs Atomic Parity Violation [Wo97, Be99b, Mi02c], NuTeV  $\nu$ DIS [Ze01], a combined Z-pole measurement [Erpc]. The proposed measurements of Q-Weak (proton) [Ca01], SLAC E-158 Møller scattering [Ca97a] are also shown with their expected uncertainties. Given the different couplings measured by the individual experiments, “new” physics may present itself by a deviation from the running curve in some but not all of these measurements.

$F_{\gamma\gamma^*P}$ , where  $P$  represents the  $\pi^0$ ,  $\eta$ , and  $\eta'$  pseudoscalar mesons. This comprehensive program will provide fundamental tests of both QCD as well as QCD inspired models. In addition to the proposed 12 GeV upgrade to the CEBAF accelerator, a high energy photon tagging facility and an upgraded PrimEx calorimeter for detection of multiphoton states and scattered electrons will be required.

The three neutral pseudoscalar mesons,  $\pi^0$ ,  $\eta$  and  $\eta'$ , represent one of the most interesting systems in strong interactions. This system contains fundamental information about the effects of chiral,  $SU(3)$  and isospin breaking by the  $u$ ,  $d$ , and  $s$  quark masses as well as about effects driven by chiral anomalies. Precise experimental and theoretical study of these mesons is therefore necessary for extracting and understanding that information. The QCD Lagrangian is invariant under an enlarged group of flavor symmetry transformations in the limit of massless quarks (chiral limit). This group is  $SU_L(3) \times SU_R(3) \times U_A(1) \times U_{baryon}(1)$ . In the full quantum theory, these symmetries are realized differently. The  $U_A(1)$  symmetry turns out to be broken explicitly by the axial anomaly involving the associated Noether current  $j_A^\mu = \bar{q}\gamma^\mu\gamma_5 q$  and the gluon fields (see for instance [Do92]). This implies that QCD at the quantum level has a smaller symmetry, namely  $SU_L(3) \times SU_R(3) \times U_{baryon}(1)$ . The condensation of quark-anti-quark pairs in the QCD vacuum

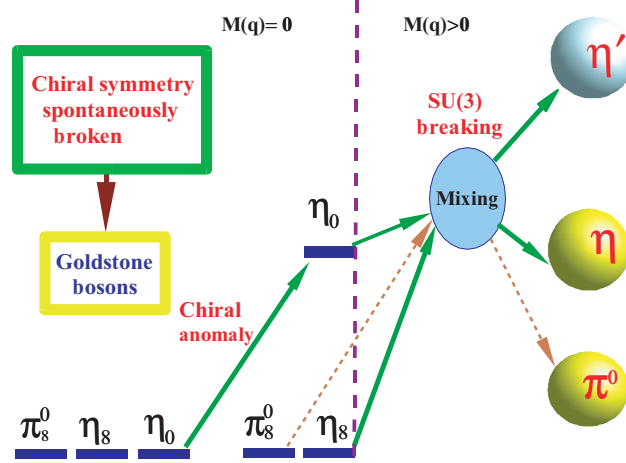


Figure 135: Symmetry breaking and quark mass effects for the light pseudoscalar mesons.

gives rise to a phenomenon of spontaneous breaking of this chiral symmetry down to the flavor  $SU(3)$  symmetry, which is the symmetry of the vacuum. As a result, there are eight massless Goldstone Bosons (GBs) corresponding to the eight spontaneously broken symmetry generators. The eight GBs are identified with the octet of pseudoscalar mesons ( $\pi^0$ ,  $\pi^\pm$ ,  $K^\pm$ ,  $K^0$ ,  $\bar{K}^0$ , and  $\eta$ ). In reality, the quark masses are non zero (albeit small), thus breaking the chiral symmetry explicitly and giving rise to masses for the GBs. (See Fig. 135.)

The  $\eta'$  is prevented from being a GB of spontaneously broken  $U_A(1)$  symmetry by the axial anomaly, which gives the  $\eta'$  a good fraction of its rather large mass. It is, however, important to note that in a certain limit in QCD, the  $\eta'$  does become a GB. This is the limit in which the number of colors,  $N_c$ , is large. In this limit the axial anomaly, which is proportional to  $\alpha_s \sim 1/N_c$ , vanishes. This limit has been recently exploited to build a highly predictive theoretical framework for studying the  $\eta'$ . There is a second type of anomaly that emerges when electromagnetism is turned on. This leads to a similar non-vanishing divergence of the axial currents:

$$\partial_\mu j_{Aa}^\mu \big|_{\text{em Anomaly}} = \frac{C_a \alpha_{\text{em}}}{4\pi} \epsilon^{\mu\nu\rho\sigma} F_{\mu\nu} F_{\rho\sigma}, \quad (60)$$

where  $a = 0, 3, 8$  labels the  $U(3)$  generator,  $C_0 = \sqrt{8/3}$ ,  $C_3 = 1$  and  $C_8 = \sqrt{1/3}$ , and  $F$  is the electromagnetic field. These EM anomalies play a crucial role in the physics of the  $(\pi^0, \eta, \eta')$  complex, being directly responsible for the decays of the three mesons into photon pairs. In the chiral limit, they lead to a rigorous prediction of the  $\pi^0$ ,  $\eta$  and  $\eta'$  decay amplitudes into two photons:

$$A(P \rightarrow \gamma\gamma) = A_{P\gamma\gamma} \epsilon^{\mu\nu\rho\sigma} \epsilon_\mu \epsilon'_\nu k_\rho k'_\sigma, \quad (61)$$

where  $P$  is one of the pseudoscalar mesons ( $\pi^0, \eta, \eta'$ ),  $\epsilon$  and  $k$  represent photon polarizations and momenta respectively, and  $A_{\pi^0\gamma\gamma} = -i \frac{\alpha_{\text{em}}}{8\pi F_\pi}$ ,  $A_{\eta 8\gamma\gamma} = -i \frac{\alpha_{\text{em}}}{8\sqrt{3}\pi F_{\eta 8}}$ , and  $A_{\eta 0\gamma\gamma} = -i \frac{\alpha_{\text{em}}}{\sqrt{24}\pi F_{\eta 0}}$ . The  $F$ 's are the corresponding meson decay constants. While in the chiral limit  $SU(3)$  symmetry implies that  $F_\pi = F_{\eta 8}$ ,  $F_{\eta 0}$  is not constrained by symmetries. However, in the limit of large number of colors (large  $N_c$  limit), one has  $F_{\eta 0} = F_\pi$ . Thus, in the chiral and large  $N_c$  limits the two-photon

decays can be predicted. The important question is then what are the effects of the quark masses and the corrections due to the fact that  $N_c = 3$ .

Indeed, the relatively straightforward situation of the chiral limit becomes much more complex when the quark masses are non-vanishing. In the real world the current quark masses are estimated to be  $m_u \sim m_d/2 \sim 5$  MeV and  $m_s \sim 150$  MeV at the renormalization QCD scale of about 1 GeV. These masses make the  $\pi^0$  and the  $\eta$  massive and shift the mass of the  $\eta'$  due to explicit breaking of chiral symmetry, while SU(3) and isospin breaking induce mixings among the three mesons. The mixings are expressed in terms of three mixing angles [Go02]. Writing the eigenstates in the chiral limit on the left, they are expressed in terms of the physical states by:

$$\begin{aligned}\pi_8^0 &= \pi^0 - \epsilon\eta - \epsilon'\eta' \\ \eta_8 &= \cos\theta (\eta + \epsilon\pi^0) + \sin\theta (\eta' + \epsilon'\pi^0) \\ \eta_0 &= -\sin\theta (\eta + \epsilon\pi^0) + \cos\theta (\eta' + \epsilon'\pi^0).\end{aligned}\tag{62}$$

A recent global analysis [Go02] has been performed that uses as input the two-photon decay widths of the  $\eta$  and  $\eta'$  and includes next to leading order chiral corrections as well as  $1/N_c$  corrections. It gives:  $\epsilon \sim 0.8^\circ$ ,  $\epsilon' \sim 0.3^\circ$  and  $\theta \sim -12^\circ$  for these mixing angles. The angles  $\epsilon$  and  $\epsilon'$  play an important role in the lifetime of the  $\pi^0$ , decreasing it by approximately 4% [Go02, Mo95].

Recently, a framework that implements the chiral and  $1/N_c$  corrections was developed [Go02, He97, Ka00]. This framework is a faithful representation of low energy QCD, relying only on the validity of the chiral expansion in the strange quark mass and the expansion in  $1/N_c$ . In particular, this implies the assumption that the  $\eta'$  can still be considered as an approximate GB. The framework predicts that the two-photon decays involve two mixing angles (two-mixing angle scenario [Kr98]). The decay constants of the  $\eta$  and  $\eta'$  associated with matrix elements of the two axial currents  $j_{A8}^\mu$  and  $j_{A0}^\mu$  are given by:

$$\begin{aligned}F_\eta^8 &= \cos\theta_8 F_8 & F_\eta^8 &= \sin\theta_8 F_8 \\ F_\eta^0 &= -\sin\theta_0 F_0 & F_\eta^0 &= \cos\theta_0 F_0.\end{aligned}\tag{63}$$

There is also a new low energy constant,  $t_1$ , to be taken into account at next to leading order in the chiral expansion. It can be estimated using QCD sum rules ( $t_1 = -F_\pi^2/m_\rho^4$ ). With this, the decay amplitudes into two photons defined in equation 61 become:

$$\begin{aligned}A_{\eta\gamma\gamma} &= \alpha\left(\frac{1}{24\pi F_0 F_8} \sec(\theta_0 - \theta_8)(\sqrt{3}F_0 \cos\theta_0 - 2\sqrt{6}F_8 \sin\theta_8)\right. \\ &\quad \left. - \frac{\pi}{18\sqrt{3}F_\pi} t_1((4M_K^2 - 7M_\pi^2) \cos\theta + 2\sqrt{2}(M_K^2 + 2M_\pi^2) \sin\theta)\right) \\ A_{\eta'\gamma\gamma} &= \alpha\left(\frac{1}{8\sqrt{3}\pi F_0 F_8} \sec(\theta_0 - \theta_8)(2\sqrt{2}F_8 \cos\theta_8 + F_0 \sin\theta_0)\right. \\ &\quad \left. + \frac{\pi}{18\sqrt{3}F_\pi} t_1(2\sqrt{2}(M_K^2 + 2M_\pi^2) \cos\theta + (-4M_K^2 + 7M_\pi^2) \sin\theta)\right)\end{aligned}\tag{64}$$

Here,  $\theta$  is the state mixing angle defined earlier in equation 63.

The fact that there is a well defined theoretical framework makes it very important to study the  $\eta$  and  $\eta'$  with high precision as a means to further understand fundamental aspects of QCD. In particular, more precise measurements of  $\Gamma(\eta \rightarrow \gamma\gamma)$  and  $\Gamma(\eta' \rightarrow \gamma\gamma)$  are crucial to the understanding of the mixing of the two mesons and their decay constants. Indeed, given the shortage of other observables that could be measured with a precision close to that of the two-photon partial widths, these are natural inputs that should be determined with good precision. It should be emphasized that more precise inputs at this level will imply a corresponding improvement in the determination of other important observables such as the decays  $\eta \rightarrow \pi\pi\pi$ .

Measurements of the  $\eta$  width have been carried out using the Primakoff effect [Br74] and  $\gamma - \gamma$  fusion in  $e^+ - e^-$  colliders [PDB]. These determinations are in clear disagreement. The  $\eta'$  width, on the other hand, has only been measured in  $e^+ - e^-$  colliders [PDB]. The current results for the widths, as listed in the Particle Data Book are:

$$\Gamma(\eta \rightarrow \gamma\gamma)_{\text{Primakoff}} = 324 \pm 46 \text{ eV}$$

$$\Gamma(\eta \rightarrow \gamma\gamma)_{\text{Collider}} = 511 \pm 26 \text{ eV}$$

$$\Gamma(\eta' \rightarrow \gamma\gamma)_{\text{Collider}} = 4.27 \pm 0.19 \text{ keV}.$$

Using these inputs, a recent analysis [Go02] determines  $\theta = -12^\circ$ ,  $\theta_8 \sim -20^\circ$ ,  $\theta_0 \sim \pm 3^\circ$ ,  $F_8 \sim 122 \text{ MeV}$ , and  $F_0 \sim 116 \text{ MeV}$ . These have, however, rather large errors. A new high quality Primakoff measurement of the  $\eta$  decay and a first Primakoff measurement of the  $\eta'$  can lead to a much more precise determination of these quantities.

One important question to ask is: What would be the impact of a more precise measurement of the two-photon partial widths? Right away, it would imply a corresponding improvement in the determination of the rest of the partial widths, as these are determined using the two-photon widths and the corresponding branching fractions. This would therefore have wide ranging implications. One set of decays that is particularly important is  $\eta \rightarrow \pi\pi\pi$  (two different final states), which is driven by isospin breaking, and thus gives access to the quark mass ratio  $(m_u - m_d)/m_s$ . Over time, the theoretical analysis of this decay has progressed to the point that now rather definite predictions can be made [An96]. However, substantial discrepancy remains with the corresponding partial widths determined in the fashion just mentioned, with the theoretical width being smaller than the experimental one. One important issue to be clarified here is whether the quoted experimental width  $\Gamma(\eta \rightarrow \gamma\gamma)$  is too large, or whether the convergence of the chiral expansion is not as good as expected. A more precise measurement would thus clarify this issue. Note that the decay  $\eta \rightarrow \pi\pi\pi$  plays a crucial role in determining the quark mass ratio  $m_u/m_d$ . In reference [Le96], the ratio  $Q$  given by:

$$Q^2 = \frac{m_s^2 - \hat{m}^2}{m_d^2 - m_u^2}, \quad (65)$$



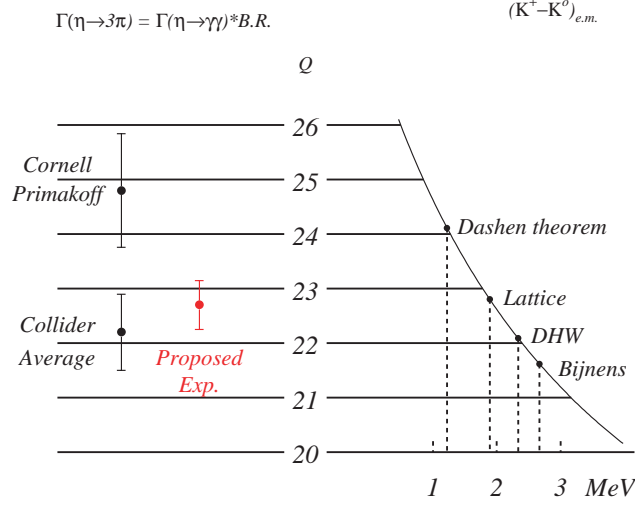


Figure 136: The importance of  $\Gamma_{\eta \rightarrow \gamma\gamma}$  in the measurement of  $\mathcal{Q}$ . The l.h.s. indicates the values of  $\mathcal{Q}$  corresponding to the Primakoff and collider experimental results for the  $\Gamma_{\eta \rightarrow \gamma\gamma}$  as well as what could be obtained with 12 GeV at Jefferson Lab. The r.h.s. shows the results for  $\mathcal{Q}$  obtained with four different theoretical estimates for the electromagnetic self energies of the kaons. Taken from Ref. [Le96].

where  $\hat{m} = (m_u + m_d)/2$ , was studied in detail. This ratio is sensitive to isospin breaking and it can be determined by the following ratio involving meson masses:

$$\mathcal{Q}^2 = \frac{M_K^2}{M_\pi^2} \frac{M_K^2 - M_\pi^2}{(M_{K^0}^2 - M_{K^+}^2)_{QCD}} [1 + O(m_{quark}^2)] \quad (66)$$

The difficulty in extracting  $\mathcal{Q}$  from this relation arises from the uncertainties in the electromagnetic contributions to the  $K^0 - K^+$  mass difference. Another way to extract  $\mathcal{Q}$  is by means of  $\eta \rightarrow \pi\pi\pi$  decays which have negligibly small electromagnetic corrections due to chiral symmetry. The second approach thus represents a more sensitive probe of the symmetry breaking generated by  $m_d - m_u$ , and has the potential to deliver accurate quark mass ratios. As emphasized in [Le96], the main errors in the determination of  $\mathcal{Q}$  using  $\eta \rightarrow \pi\pi\pi$  decays is due to the experimental uncertainty in the partial width  $\Gamma_{\eta \rightarrow \pi\pi\pi}$  which is determined by the two-photon width  $\Gamma_{\eta \rightarrow \gamma\gamma}$  and the branching ratio. The two different methods of measuring  $\Gamma_{\eta \rightarrow \gamma\gamma}$  (photon-photon collisions and Primakoff effect) yield conflicting results, as is shown in Fig. 136. This is one important example of the impact that a more accurate measurement of the  $\eta$  and  $\eta'$  two-photon widths would have for determining fundamental parameters of QCD. One of the most interesting questions has to do with the nature of the  $\eta'$ : is it, after all, an approximate GB or not? More precise measurements together with the theoretical framework we have in place would help answer that question via a global analysis of the different processes involving the  $\eta$  and  $\eta'$ . For instance, if such an analysis shows that the size of the  $1/N_c$  corrections is natural, this would imply that it is consistent to think about the  $\eta'$  as an approximate GB. As such, it is clear that a more precise experimental knowledge of the two-photon partial widths will have an important impact in our understanding of fundamental issues in QCD.



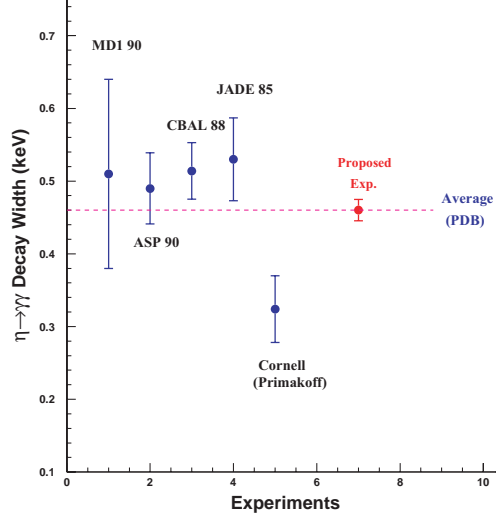


Figure 137: Two-photon decay width for the  $\eta$  meson. Points 1 through 4, are the results of  $e^+e^-$  collisions (for references, see[PDB]), point 5 is the result of a Primakoff experiment[Br74]. The dashed line indicates the Particle Data Book average based on these five points. Point 7 is the expected error for Jefferson Lab with 12 GeV, arbitrarily plotted to agree with the Particle Data Book average value. The plotted uncertainties combine the statistical and systematic errors in quadrature.

The present experimental knowledge of the  $\eta$  meson width is presented in Fig. 137[PDB], along with the projected measurement which could be made with 12 GeV at Jefferson Lab. Most of the measurements in the figure have been performed using two photon interactions in  $e^+e^-$  collisions. One exception is the Cornell measurement of the  $\eta$  width[Br74] via the Primakoff effect. This gives a width which is significantly lower (at the  $3\sigma$  level) than those from  $e^+e^-$  collisions. Using the same apparatus, the Cornell group measured the  $\Gamma(\pi^0 \rightarrow \gamma\gamma) = 7.93 \pm 0.39$  eV, in good agreement with the world average value of  $7.74 \pm 0.55$  eV. As such, the  $\eta$  width should be remeasured by the Primakoff process using state-of-the-art experimental techniques to resolve this discrepancy. The  $\eta'$  two photon width, in contrast, has been only measured in collider experiments which have provided an internally consistent data set. In view of the inconsistency between the two methods for the  $\eta$ , we also plan to measure the  $\eta'$  width with the Primakoff technique.

Figure 138 shows the mixing angle,  $\theta$ , based on the Cornell Primakoff measurements and the collider experiments. In the figure, the mixing angles were calculated in the three mixing angle scenario of reference [Go02], (see equation 63), and the resulting angle  $\theta$  is plotted. The rightmost (red) point shows the expected precision which could be obtained with 12 GeV at Jefferson Lab, projected to the Particle Data Book Average. As demonstrated in the figure, these new measurements would not only resolve the discrepancy between the previous measurements, but would greatly increase the experimental precision of this important mixing angle.

We propose to use a tagged photon beam obtained from the 11 GeV electrons to measure the widths of the  $\eta, \eta' \rightarrow \gamma\gamma$  decays via the Primakoff effect in which pseudoscalar mesons are produced

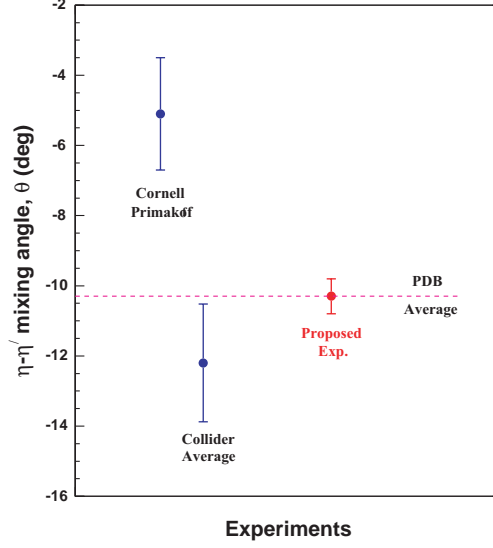


Figure 138: The  $\eta - \eta'$  mixing angle as determined by a previous Primakoff measurement,  $\gamma - \gamma$  collisions, and the projected result with the Jefferson Laboratory 12 GeV upgrade.

by the interaction of a real photon with a virtual photon from the Coulomb field of the nucleus. The formation of mesons will be identified through the invariant mass of two decay photons from the  $\eta/\eta' \rightarrow \gamma\gamma$  reaction, and the meson production angles will be reconstructed by detecting the  $\eta/\eta'$  decay photons along with the additional constraint provided by a precise knowledge of the incident photon energy.. The production of mesons in the Coulomb field of a nucleus by real photons is essentially the inverse of the decay  $\eta, \eta' \rightarrow \gamma\gamma$ , and the cross section for this process thus provides a measure of the  $\eta, \eta'$  two-photon decay widths.

For unpolarized photons, the Primakoff cross section is given by[Be70]:

$$\frac{d\sigma_P}{d\Omega} = \Gamma_{\gamma\gamma} \frac{8\alpha Z^2}{m^3} \frac{\beta^3 E^4}{Q^4} |F_{e.m.}(Q)|^2 \sin^2 \theta_m \quad (67)$$

where  $\Gamma_{\gamma\gamma}$  is the decay width of the  $\eta$  or  $\eta'$ ,  $Z$  is the atomic number,  $m$ ,  $\beta$ ,  $\theta_m$  are the mass, velocity and production angle of the mesons,  $E$  is the energy of the incoming photon,  $Q$  is the momentum transferred to the nucleus, and  $F_{e.m.}(Q)$  is the nuclear electromagnetic form factor, corrected for final state interactions of the outgoing  $\eta$  or  $\eta'$ .

In addition to the Primakoff effect, mesons are coherently produced in the nuclear hadronic field. There is also an interference between the strong and Primakoff production amplitudes. The cross section for the Primakoff effect to produce an  $\eta$  on  ${}^4\text{He}$  is presented in Fig. 139 where these effects can be seen. The classical method of extracting the Primakoff amplitude from the measured differential cross sections in the forward direction relies on the different characteristic behaviors of the production mechanisms with respect to the production angle. The Primakoff cross section is zero for mesons emitted along the incident photon direction, has a sharp maximum at a very small angle, and falls at larger angles as shown in the figure. It is proportional to  $Z^2$ , and its peak value

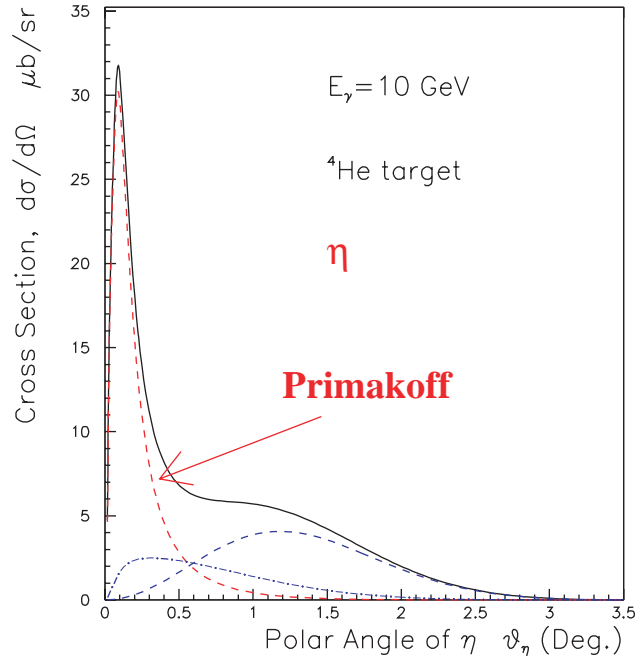


Figure 139: Differential cross sections (electromagnetic and nuclear) for the  $\gamma + {}^4\text{He} \rightarrow \eta + {}^4\text{He}$  reaction at small angles at 10 GeV. The solid line is the total differential cross section from all the processes, the red dashed line is from Primakoff process, the blue dashed line is from the nuclear coherent process, and the blue dot-dash line is from the interference of the Primakoff and nuclear coherent processes.

is roughly proportional to  $E^4$ . The nuclear coherent cross section for spin zero nuclei is also zero in the forward direction, but has a broad maximum outside the angular range of the Primakoff effect, and falls at larger angles as shown in Fig. 139, where the amplitudes are normalized to the Cornell data[Br74]. However, there are still two types of contributions under the Primakoff peak—the extended tail of the nuclear coherent mechanism, and the interference term between the two amplitudes as described above. The interference term amounts to a relatively large contribution and is also more difficult to identify since in addition to the knowledge of both amplitudes, it also requires knowing the relative phase between them. Therefore, a high precision determination of the contribution from the background amplitudes under the Primakoff peak requires good experimental information on the nuclear amplitude outside of the Primakoff region. This can be experimentally achieved by using very light spin zero nuclei as production targets. Since form factors for light nuclei fall slowly with momentum transfer, such targets are well suited for measuring the nuclear part at large angles, thereby determining the contribution under the Primakoff peak.

Compared to the Primakoff effect to produce a  $\pi^0$ ,  $\eta$  production has a significantly smaller cross section and peaks at relatively larger production angles. This is a consequence of the much larger mass of the  $\eta$  which increases the momentum transfer at a given production angle. As a result, the Primakoff peak is harder to distinguish from the nuclear coherent peak. There are two ways to ameliorate this problem. One is to go to higher photon energies, which, in addition to increasing the Primakoff cross section ( $\sigma_P \propto E^4$ ), will push the Primakoff peak to smaller angles ( $\theta_{Primakoff} \sim m^2/2E^2$ ) as compared to those of the nuclear coherent effect ( $\theta_{NC} \sim 2/EA^{\frac{1}{3}}$ ). As such, the proposed 12 GeV upgrade to the CEBAF accelerator is vital to these measurements. Another improvement is to use lighter targets such as  $^1H$ ,  $^4He$  or  $^{12}C$ , which are more bound compared to heavier nuclei, thereby enhancing coherency. In addition, due to the  $A$  dependence just mentioned, one would expect the nuclear coherent mechanism to peak at larger angles for lighter nuclei. By simultaneously going to higher photon energies and using lighter Primakoff production targets, one can make clean measurements of the widths.

We propose a measurement of the differential cross sections at forward angles on two targets: the proton and  $^4He$ .  $^4He$  has advantages over other targets: 1) it is a very compact nucleus (with a nucleon threshold of  $\sim 20$  MeV), which will greatly enhance coherent production; 2) its form factor is very well known and falls slowly with momentum transfer; and 3) it is a spin zero nucleus, which will suppress the spin flip amplitude contribution close to zero degrees. The nuclear coherent amplitude in principle can be expressed in terms of the single-nucleon photoproduction amplitudes, properties of the nuclear ground state, and the interaction of mesons in nuclei[En64].

The use of hydrogen and helium targets will greatly help to solve the difficulties of the Cornell  $\eta \rightarrow \gamma\gamma$  experiment to extract the coherent contribution under the Primakoff peak. As a production target, hydrogen is especially promising because it makes possible the selection of exclusive  $\pi^0 p$  events through a missing mass cut. In principle this can be done with the many-body nuclear targets, but in practice there is the complication due to inelastic transitions and breakup channels

at low excitation energy. For the nuclear targets, dynamical considerations (*i.e.* momentum transfer and the nuclear form factors) are usually invoked to ensure that coherency is satisfied to a high degree, whereas for the proton target it will be possible to guarantee coherency through kinematic cuts. The missing mass resolution that can be expected in a 12 GeV experiment, and how that resolution can be optimized, is presently under study.

The cross section calculations that are needed for a proton target are in progress. In the proton case, it is important to consider both charge and magnetic scattering from the target [Ha89], unlike the situation for a spin zero nucleus such as  $^4\text{He}$  where there is no magnetic contribution. For the coherent background amplitude, which is expected to be dominated by  $\rho$  and  $\omega$  exchanges, calculations based on the Regge model developed by Vanderhaeghen, Guidal, and Laget [Va98] will be performed. This formalism has been successfully used in extractions of the pion electromagnetic form factor from pion electroproduction data. Finally, it should be noted that a proof-of-principle exists for doing a Primakoff experiment on the proton. In the early 1970's a group at DESY measured forward  $\pi^0$  photoproduction on the proton [Br70]. Their data clearly exhibit a Primakoff peak at forward angles, and the pion lifetime obtained from the data agrees, within quoted errors, with the accepted value.

In addition to these radiative width measurements, we plan a related program to study the  $\gamma\gamma^*P$  vertex, where  $P$  represents the  $\pi^0$ ,  $\eta$ , or  $\eta'$  pseudoscalar mesons and  $\gamma^*$  is a virtual photon. Such measurements will enable one to study the transition regime from soft nonperturbative physics to the hard processes of perturbative QCD. We propose to measure the photon momentum dependence of the form factors  $F_{\gamma\gamma^*P}(Q^2)$  and thereby map out an extension to the axial anomaly to provide a clean test of QCD predictions for exclusive processes. Measurements of the  $\pi^0$ ,  $\eta$  and  $\eta'$  transition form factors at very low  $Q^2$  ( $\sim 0.001\text{--}0.5\text{ GeV}^2$ ) are particularly important to allow a model independent extraction of the slope of the transition form factor, which measures the size of the meson's electromagnetic interaction radius. Currently, there is no first principles theoretical determination of the form factors. In ChPT there are two sources of contributions [Bi88]. One is the long distance contribution from meson loops, and the other is a counterterm or short distance contribution. ChPT pins down the first, and for the second a model is needed. The long distance contributions are small, as they only provide a small fraction of the fall off of the form factor. The simplest model is to neglect the long distance contributions and assume a vector meson dominance (monopole) type form factor,

$$F_\pi = \frac{1}{1 + Q^2/m_V^2}, \quad (68)$$

where  $m_V$  is the mass of the vector meson. Using such a model, the available data at high  $Q^2$  fit very well with a scale  $m_V \sim 0.75\text{--}0.85\text{ GeV}$ . The vector meson dominance (VMD) model therefore provides an excellent fit to the current data ( $Q^2 > 0.6\text{ GeV}^2$ ).

A determination of the slope of the  $\pi^0$  form factors at low  $Q^2$  would allow one to uniquely fix a low energy constant  $\mathcal{O}(p^6)$  in the effective chiral Lagrangian [Bi88, Mo95]. By limiting the range

of extrapolation to the photon point, measurements of the  $\pi^0$ ,  $\eta$  and  $\eta'$  transition form factors at very low  $Q^2$  ( $\sim 0.001\text{--}0.5\text{ GeV}^2$ ) are particularly important to measure the size of the meson's electromagnetic interaction radius in a model independent manner. With a measurement of the  $\eta$  and  $\eta'$  form factor slopes one could also have a clear test of how good the U(3) flavor symmetry implied by the large  $N_c$  limit holds. In addition, one important reason to better understand the transition from factors of  $\pi^0$ ,  $\eta$  and  $\eta'$  is that pseudoscalar exchange is the major contribution to the hadronic light-by-light scattering part of the muon anomalous magnetic moment[Ma02], and is thus clearly crucial for measurements of  $a_\mu$  that search for “new physics” beyond the Standard model.

A number of experiments have been performed to measure these transition form factors. Existing data in the low and intermediate regions, however, are quite poor. The CELLO collaboration at PETRA has measured  $F_{\gamma^*\gamma P}$  in the space-like region at large momentum transfers using the reaction  $e^+e^- \rightarrow e^+e^- P$ [Be91]. In this experiment, two photons are radiated virtually by the colliding  $e^+e^-$  beams. One of the virtual photons is close to real and the other has a larger  $Q^2$  and is tagged by the detection of an  $e^+$  or  $e^-$ . Measurements were taken at momentum transfers ranging from 0.62 to 2.17  $(\text{GeV}/c)^2$ , and the value of  $a$  was deduced by extrapolation under the assumption of vector meson dominance. The authors quote values of  $a_{\pi^0} = 0.0325 \pm 0.0026$ ,  $a_\eta = 0.428 \pm 0.063$ , and  $a_{\eta'} = 1.46 \pm 0.16$ . Only statistical errors have been taken into account in these results, with systematic errors estimated to be of the same order as the statistical error. The results of these measurements, along with projected low  $Q^2$  results from Jefferson Lab, are shown in Fig. 140 for the  $\pi^0$  and in Fig. 141 for the  $\eta^0$ , with the corresponding fits to  $F_{\gamma^*\gamma P}$ . From the plots, it is clear that any extraction of the slope parameter at  $Q^2 = 0$  which relies on the experimental data at relatively large  $Q^2$  is highly model dependent. Data covering the higher  $Q^2$  region from 2 to 20  $\text{GeV}^2$  on these mesons have also been reported by the CLEO collaboration[As95]. Nevertheless, despite the theoretical interest in pseudoscalar meson form factors, the experimental situation remains incomplete. The low and intermediate momentum transfer region for these mesons is largely unexplored experimentally. While the L3 Collaboration has some results (with very poor  $Q^2$  resolution) in the low  $Q^2$  region for the  $\eta'$ , low and intermediate  $Q^2$  data on the  $\pi^0$  and  $\eta$  are totally lacking. The advent of 12 GeV electrons at Jefferson Lab, however, will make such studies possible.

In the time-like momentum transfer region, a number of experiments aimed at measuring the form factor slope  $a$  have been performed utilizing the  $\pi^0$  and  $\eta$  Dalitz decay  $\pi^0/\eta \rightarrow e^+e^-\gamma$  reaction [PDB]. The amplitude for this process involves the  $F_{\gamma^*\gamma P}$  form factor which, in the usual linear expansion

$$F(x = \frac{m_{e^+e^-}^2}{m_P^2}) \approx 1 + a \frac{m_{e^+e^-}^2}{m_P^2}, \quad (69)$$

where  $m_P$  is the pseudoscalar meson mass. Such experiments suffer from small kinematically accessible ranges and significant backgrounds, and they require large final-state radiative corrections. The Particle Data Book quotes a value of  $a = 0.032 \pm 0.004$  for the  $\pi^0$ , in agreement with vector meson dominance. The small error is surprising since the published values for the slope range from

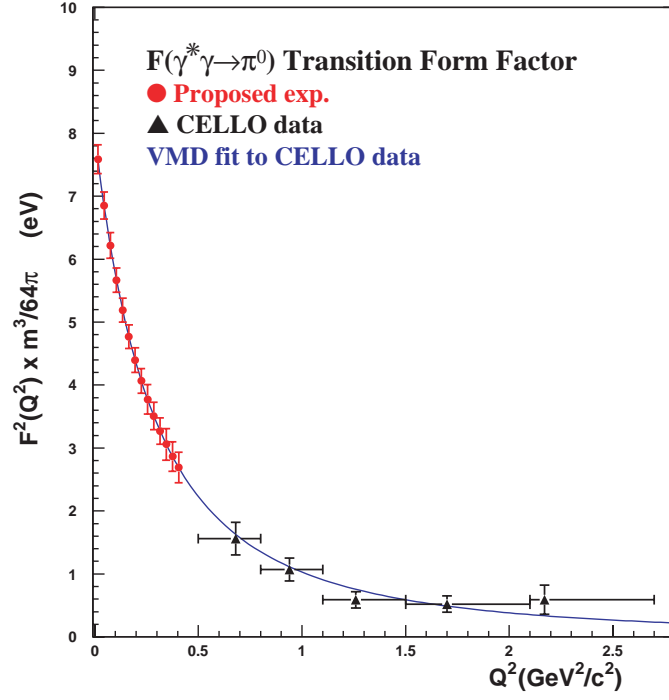


Figure 140: The  $\pi^0$  transition form factor. The proposed points are projected to the VMD prediction with expected total errors. CELLO data are from reference[Be91].

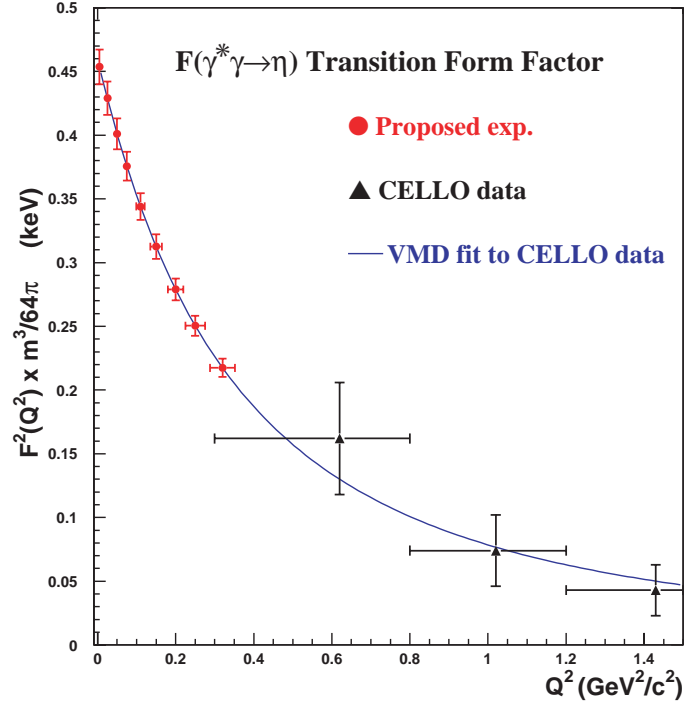


Figure 141: The  $\eta$  transition form factor. The proposed points are projected to the VMD prediction with expected total errors, in comparison with CELLO data[Be91].

$-0.24$  to  $+0.12$  and it would appear that even the sign of the form factor slope has not been well determined.

In 1989, Hadjimichael and Fallieros[Ha89] suggested that the virtual Primakoff effect could access additional fundamental information about the pion, as the cross section is proportional to  $|F_{\gamma^*\gamma\pi^0}(Q^2)|^2$ . They examined the sensitivity of the  $\pi^0$  Primakoff cross section to  $a$  for energy transfers up to 1.6 GeV. They saw only moderate sensitivity and noted that the cross section is optimized for  $\theta_e \rightarrow 0$  and  $\theta_\pi \rightarrow 0$  whereas pion energies above 2 GeV are favored for probing the  $\gamma^*\gamma\pi^0$  vertex. We have extended these calculations to kinematical ranges available with the proposed 12 GeV electron beam at Jefferson Lab and note that good sensitivity to the  $\gamma^*\gamma P$  form factor is present. The quality of data one can expect with a 12 GeV electron beam and a state-of-the-art electromagnetic calorimeter at Jefferson Lab is shown in Figs. 140 and 141.

In summary, we have described a comprehensive program to measure the two photon decay widths and transition form factors of the pseudoscalar mesons ( $\pi^0, \eta, \eta'$ ) which would be possible with the advent of 12 GeV CW electron beams at Jefferson Lab. The radiative width measurements will have a significant impact on the experimental determination of fundamental parameters of QCD, namely the light quark masses ( $m_u, m_d, m_s$ ) and on the magnitude of  $\eta - \eta'$  mixing. At a more general level, these measurements impact the issue of spontaneous chiral symmetry breaking in QCD, and the intriguing question of whether the  $\eta'$  meson can be considered as a GB in the combined chiral and large  $N_c$  limits. The proposed measurements of the  $\pi^0, \eta$  and  $\eta'$  transition form factors at very low  $Q^2$  ( $\sim 0.001\text{--}0.5 \text{ GeV}^2$ ) would provide information on the spatial distribution of the axial anomaly for each of the mesons. A determination of the slope of the  $\pi^0$  and  $\eta$  form factors would allow one to uniquely determine a low energy constant  $\mathcal{O}(p^6)$  in the effective chiral Lagrangian[Bi88] [Mo95]. With a measurement of the  $\eta'$  form factor slope, one could also have a clear test of how good the U(3) flavor symmetry, implied by the large  $N_c$  limit holds. In this limit, the same low energy term determines all three transition form factor slopes. One important additional reason to better understand the transition form factors of the  $\pi^0, \eta$  and  $\eta'$  is that pseudoscalar exchange is the major contribution to the hadronic light-by-light scattering part of the muon anomalous magnetic moment[Ma02]. It is thus important for measurements of  $a_\mu$  that search for “new physics” beyond the Standard model.



### 3 EXPERIMENTAL EQUIPMENT FOR THE 12 GeV UPGRADE

The equipment planned for the Upgrade project takes full advantage of apparatus developed for the present program. In each of the existing halls, new spectrometers are added and/or present equipment upgraded to meet the demands of the 12 GeV program. Then a new hall, Hall D, will be added to support the meson spectroscopy program.

In Hall A, the Upgrade will add a large angular- and momentum-acceptance, moderate-resolution magnetic spectrometer (to be called the Medium-Acceptance Device, or MAD) and a high-resolution electromagnetic calorimeter. The spectrometer will provide a tool for high-luminosity, high- $x$  studies of the properties of nucleons with an 11 GeV beam, and will also be used for selected investigations of the GPD's, where high luminosity and good resolution are needed. Details are provided in Section 3.A below. In Hall B, the CEBAF Large Acceptance Spectrometer (CLAS), which was designed to study multi-particle, exclusive reactions with its combination of large acceptance and moderate momentum resolution, will be upgraded to CLAS<sup>++</sup> and optimized for studying exclusive reactions (emphasizing the investigation of the GPD's) at high energy. It will also be used for selected valence quark structure studies involving neutron “tagging” or polarized targets capable of supporting only very low beam current. Most importantly, the maximum luminosity will be upgraded from  $10^{34}$  to  $10^{35}$  cm<sup>-2</sup> s<sup>-1</sup>. The present toroidal magnet, time-of-flight counters, Čerenkov detectors, and shower counter will be retained, but the tracking system and other details of the central region of the detector will be changed to match the new physics goals. Details are provided in Section 3.B. In Hall C a new, high-momentum spectrometer (the SHMS, Super-High-Momentum Spectrometer) will be constructed to support high-luminosity experiments detecting reaction products with momenta up to the full 11 GeV beam energy. This feature is essential for studies such as the pion form factor, color transparency, duality, and high- $Q^2$   $N^*$  form factors. The spectrometer will be usable at very small scattering angles. See Section 3.C for details. In the new hall, Hall D, a tagged coherent bremsstrahlung beam and solenoidal detector will be constructed in support of a program of gluonic spectroscopy aimed at testing experimentally our current understanding that quark confinement arises from the formation of QCD flux tubes. This apparatus is described in detail in Section 3.D. Finally, we describe in Section 3.E the apparatus required for the Primakoff effect experiments that will investigate the properties of light pseudoscalar mesons. This apparatus builds on experience being gained in a related experiment now underway in Hall B.

#### 3.A Hall A and the Medium Acceptance Device (MAD)

With the Jefferson Lab 12 GeV upgrade a large kinematics domain becomes accessible in deep inelastic scattering. The high luminosity and high polarization of beam and targets allow a unique contribution to the understanding of nucleon and nuclear structure, and the strong interaction in the high  $x$  region (which is dominated by the valence quarks). To fully utilize the high luminosity

Table 15: The design characteristics of the MAD spectrometer shown along with the HRS performance.

Parameter	MAD design	HRS performance
Central momentum range	0.4 - 7.5 GeV/c	0.2 - 4.3 GeV/c
Scattering angle range	6° - 130°	6° - 150°
Momentum acceptance	±15%	±5%
Momentum resolution	0.1%	0.02%
Angular acceptance	28 msr ( $\geq 35^\circ$ ) 4-6 msr ( $5^\circ - 12^\circ$ )	6 msr (standard) 12 msr (forward)
Angular resolution (hor)	1 mrad	0.5 mrad
Angular resolution (ver)	1 mrad	1 mrad
Target length acceptance (90°)	50 cm	10 cm
Vertex resolution	0.5 cm	0.1 cm
Maximum DAQ rate	20 kHz	5 kHz
e/h Discrimination	$0.5 \times 10^5$ at 98%	$1 \times 10^5$ at 98%
$\pi$ /K Discrimination	1000 at 95%	1000 at 95%

available at CEBAF (up to  $10^{39}$  e · nucleons/cm<sup>2</sup>/s), a well-matched spectrometer, given the name Medium-Acceptance Device (MAD), has been designed as the instrumental upgrade for Hall A.

The design of the MAD spectrometer has resulted in a versatile instrument. The main components are two warm-bore combined-function (dipole and quadrupole) superconducting magnets. Its maximum central momentum is 7.5 GeV/c with a momentum acceptance of  $\pm 15\%$  which makes it possible to accept particles with momenta above 8.5 GeV/c. It is expected that even higher momenta can be accommodated for specific experiments by decreasing the deflection of the second magnet. MAD has a momentum resolution of better than  $10^{-3}$  and an angular resolution of better than 1 mrad. A pointing accuracy of better than 0.5 mrad, required for an accurate L/T separation, can be obtained. The angular acceptance is 28 msr at angles larger than  $35^\circ$  and decreases linearly to 6 msr at an angle of  $12^\circ$ . An angle as small as  $5^\circ$  can be reached by using one of the existing septum magnets. This design has resulted in the characteristics shown in Table 15.

A detector package has been designed for the detection of electrons and hadrons. The standard electron detection system consists of four planes of scintillators for triggering, two drift chambers and a multi-wire proportional chamber for tracking and a gas Čerenkov counter and an electromagnetic calorimeter for particle-identification purposes. For hadron detection two aerogel Čerenkov counters or a focal plane polarimeter are additionally available. Both packages provide excellent ( $e^\pm, \pi^\pm, K^\pm$  and p) identification over the full momentum range. Pion rejection as good as a few times  $10^{-5}$  will be provided. The data acquisition system is designed with a new generation of pipeline digitizing front-end electronics to be able to handle event rates up to 20 kHz.

In combination with the MAD spectrometer, a 100 msr lead-glass calorimeter is available for studies of nucleon form factors and of Real Compton Scattering. A large acceptance, high granularity calorimeter with 1296 element array of PbF<sub>2</sub> crystals is proposed to optimally study

Generalized Parton Distributions through Deep Virtual Compton Scattering. It will also benefit other experiments, such as photo-production of neutral mesons at large transverse momenta.

With the cross section dropping rapidly with increasing  $Q^2$ , both a high luminosity and a large acceptance spectrometer are crucial for precision measurements. In combination with the existing HRS in Hall A MAD will open up a window to a rich program, including measurements of:

- Polarized and unpolarized quark distributions up to large  $x$ , using polarized proton and  $^3\text{He}$  targets. Values of  $x$  larger than 0.8 can be probed once spin duality has been established.
- Semi-inclusive  $\pi^\pm$  and  $K^\pm$  electroproduction in order to separate the spin and flavor components of the sea quark distributions up to  $x \approx 0.65$ ,
- Nucleon form factors to significantly larger  $Q^2$ -values, over 5  $(\text{GeV}/c)^2$  for  $G_E^n$  and over 14  $(\text{GeV}/c)^2$  for  $G_E^p$ ,
- Real Compton Scattering up to  $s \approx 20 (\text{GeV}/c)^2$  and  $|t| \approx 15 (\text{GeV}/c)^2$  and Deep Virtual Compton Scattering up to  $Q^2 \approx 7 (\text{GeV}/c)^2$  and  $x \approx 0.5$ ,
- Deuteron photo-disintegration up to photon energies of 7 GeV over a large range of CM angles, with recoil polarization up to a photon energy of 4 GeV,
- Few-body elastic form factors to  $Q^2$ -values of over 10  $(\text{GeV}/c)^2$ ,
- Parity violation in deep inelastic scattering with very high accuracy to probe possible extensions of the Standard Model,
- Threshold  $\psi$  photoproduction to study the color Van der Waals-type component of the  $NN$  force.

### 3.A.1 Design Characteristics of the MAD Spectrometer

In order to perform the experimental program, the Medium Acceptance Device (MAD) spectrometer has been designed. MAD is a 7.5 GeV/c super-conducting spectrometer with a moderately large acceptance of up to 30 msr. This device consists of two 4 m long super-conducting combined-function magnets, each with a 120 cm warm bore. These magnets and the shield house are supported by a welded steel structure with steel drive wheels. The shield house is a composite of concrete, steel, and lead. The cryogenics are proven systems using standard JLab components. A schematic drawing of the MAD spectrometer is shown in Fig. 142.

The MAD spectrometer requires two similar combined-function super-conducting magnets. The first magnet, MAD-1, simultaneously produces a 1.9 T dipole field and a 4.2 T/m quadrupole field while the second magnet, MAD-2, simultaneously produces a 3.7 T dipole field and a 3.3 T/m

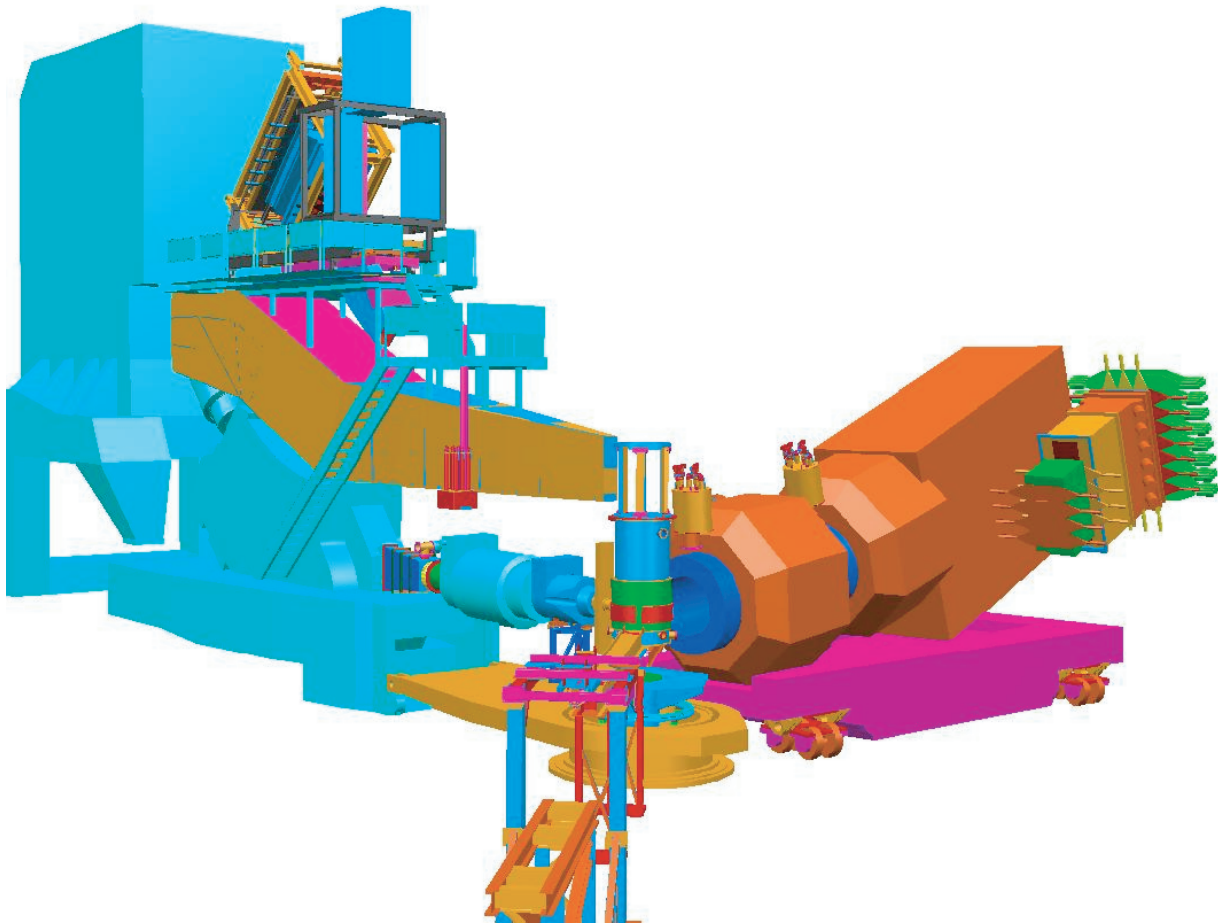


Figure 142: Three-dimensional CAD drawing of Hall A showing the MAD Spectrometer on the right along with one of the present high resolution spectrometers on the left.

quadrupole field. A magnetic design using TOSCA-3D has been performed to establish the basic magnetic requirements, provide 3D field maps for optics analysis and produce basic engineering information. A two-sector nested  $\cos\theta/\cos 2\theta$  design with low current-density coils (5140/5750 A/cm<sup>2</sup> for MAD-1 and 5125/5250 A/cm<sup>2</sup> for MAD-2), warm bore and warm iron has been selected and analyzed. These low current densities are within the limits for a cryostable winding. Coils of this type are the most conservative that can be built and the large size and modest field-quality requirements ( $\delta B/B = 3 \times 10^{-3}$ ) insure that construction tolerances (1-2 mm) are easily achievable. Other relevant parameters of the magnets are listed in Tables 16 and 17.

The magnetic design uses TOSCA-generated  $\cos\theta$  type coils with “constant perimeter” ends. These coils closely approximate the ideal cosine geometry that is well established as a “perfect” generator of high purity fields. Practical considerations, finite current distributions, and a limited number of sectors all contribute to higher-order field errors in the design. The yoke is modeled with the nominal properties of 1010 steel. This steel is a commonly available alloy with properties suitable for the simple return-yoke function of a cosine style magnet. The present design yoke has an elliptical outside shape to permit a closer approach to the beam line and a circular inner shape to fit the cryostat. Table 17 contains the designed yoke dimensions. Modifying the yoke shape to improve the smallest angles attainable by MAD does not have a significant effect on field quality, rather the effect is felt most in the integral strength. The MAD magnets have significant stability margins so small increases in current to make up for iron that is removed to provide access to small scattering angles can be easily accommodated without sacrificing reliability.

The combined-function magnets produce peak fields of 5.6 T in the warm bore of MAD-1 and of 6.4 T in the windings of MAD-2. These fields are comparable to those achieved in large-bore magnets produced 20 years ago for MHD research, although the stored energy and average forces of the present magnets are typically less, even though the field volumes are comparable. This is due to the fact that the superposed quadrupole field produces significantly less stored energy for a given maximum field. The combined fields also produce a very asymmetric field and force distribution. The fields add on the bottom of the magnet and subtract on the top, so that the fields across the bore range from -0.6 T to 4.4 T for MAD-1. Similarly, the fields in the windings are highest where the fields add giving 6.5 T winding fields and nearly -2 T where they subtract. The MAD magnets must operate in both relative polarities so the magnets must be designed accordingly. The peak linear force densities are 23,000 N/m for MAD-1 and 33,600 N/m for MAD-2.

The cryogenics for the MAD combined-function magnets are based on the successful thermal syphon cooling that has been incorporated in nearly all the SC magnets at JLab. The high (100 g/s) internal flow rates and simple reservoir level control insure reliable operation with simple controls. These magnets have approximately 100 liters of helium in a reservoir over the magnet coils and thus are capable of about 1 hour of isolated operation during a refrigerator shutdown.

Internally the magnets will have thermal syphon circulation from helium and nitrogen reservoirs. The magnets will have liquid level control and valves to permit independent warm up or cool

down using a local heat exchanger. The cryogenic supply will use the existing Hall A transfer lines, septum adapter box, vacuum jacketed return lines, flex gas lines, and cool-down heat exchanger. The MAD cryogenic system requires a new cryogenic distribution box that rides on the back of MAD and a flexible transfer line similar to that constructed for the G0 experiment. The magnets will be connected by JLab standard u-tubes similar to those used on HMS/HRS quads. A set of gas manifolds installed on the back of the MAD will collect and return cryogenic gases to the existing Hall A gas system. A stand to hold the new equipment and a platform are required for support and personnel access. The system is completed by automated cool down valves and actuators identical to those used on HMS.

The heart of this system is a somewhat complex control reservoir that contains JT valves, bayonet connections, phase-separating reservoirs, current leads, relief valves and instrumentation including level sensors. There are six of these control reservoirs at JLab and one more being delivered. The standardization of design and function and use of standardized components insures compatibility, reliability, and cost and operational savings. The control reservoir will be mounted on the downstream ends of the MAD magnets and will be located on the side to keep the overall profile of the MAD magnets low enough to fit through the truck access door. The cryogenic valving allows for top and bottom fill of helium and nitrogen for level operation and cool down, respectively. There will also be a separate valve for variable temperature cool down gas made in a LN2 to He gas heat exchanger (also standard design). This will be used to minimize thermal stresses and increase the overall efficiency of cryogenic operations during cool down and warm up of the MAD magnets.

During normal operation and liquid level control the MAD magnets are fed helium gas at 4.5 K and 3 atm. This gas is JT expanded at each magnet by a valve that is controlled by the MAD magnets control system to maintain liquid level. Boil-off gas and JT flash are returned to the local refrigerator cold at 1.2 atm and 4.2 K. Nitrogen is fed to the MAD at 85 K and 4 atm where it is expanded into the N2 reservoir by a local valve under local control. Boil-off N2 is vented outside. Vapor-cooled current leads are controlled by local valves that servo on current in the MAD magnet and adjust the helium gas flow accordingly. No burnout current leads are specified. The helium gas from the vapor cooled leads (VCL's) is returned warm to the ESR compressor suction. The cool down gas return and N2 gas return lines are vacuum jacketed to prevent ice and water from accumulating near the magnets.

Separate flow control and measurement for each current lead is a normal part of this design. Finally, the reservoirs contain dual relief devices, an ASME coded mechanical relief and a rupture disc, set at a 25% higher pressure. Exhaust lines for relief separate from cool down lines are used so that there is no chance of a contamination blockage in these all important pressure relief paths. The reservoirs contain temperature sensors, liquid level sensors and voltage taps. Generally all internal instrumentation is routed to the reservoir to a set of vacuum feed-throughs. Strain gauges in the cold to warm support system will be essential due to the force between yoke and coil, especially considering the asymmetry of these forces. Vacuum gauging and system pressure sensors will also



be located in the control reservoir. JLab owns the design for the installed and to be delivered control reservoirs, all of which were built commercially.

The MAD magnets will have a control system that is self-contained and able to be operated by an EPICS control screen. The internal controls will take care of interlocks, operating valves by PID, and processing information from the magnet. The EPICS system will allow user operation from GUI screens, archival data logging, and graphic display. A dual processor PLC of a type produced by Mitsubishi for critical fail safe process control will be used. These dual processor PLCs can switch the process control from primary to secondary in 50 ms in the event that the primary processor fails. These processors can also be switched manually or by software for routine software maintenance. Liquid-level control is by commercial AMI units and cryogenic thermometry is by commercial Lakeshore electronics modules. Readouts of magnet voltages, pressures, strain gauges, and valve position LVDTs is by standard PLC plug-ins. These systems are in wide use and all PLCs support them.

The DC power for the MAD magnets will be provided by four independent power supplies. These supplies will be 12 pulse SCR supplies with a final stage transistor regulator and stability of 10 ppm. These devices are readily available from Danfysik and others. The power supplies will provide 10 V for ramp up or down, have polarity switches and the possibility of NMR control for the dipole coils. The energy dump systems will consist of a 10 V ramp down, a slow dump and a fast dump resistor. The fast dump will apply a voltage of 150 V to the dipole coils and 250 V to the quad coils to reduce the current to zero in 150 s. These voltages may increase as the design progresses to maintain a reasonable final coil temperature near 80 K. The dipoles and quadrupoles have dump resistances such that the time constants are equal so that both coils discharge equally. The design of the MAD magnets is such that in the event of a discharge of one coil the second coil will see a voltage which will mimic a quench and a discharge of the second coil will be initiated.

The very large cold mass and low current density insure that sufficient material is available in the cold mass to absorb a large fraction of the stored energy at a low temperature during a quench discharge resulting in a safer overall magnet. Cryostable magnets are in general extremely safe and reliable but the presence of liquid helium in the windings is essential. The open windings characteristic of a cryostable coil exposes the coil to the risk of high temperature during a quench if the windings are uncovered due to the small residual heat conduction through the insulated spacers. The MAD coils would not be self-protecting and therefore a reliable fast discharge system is essential. Twelve of the thirteen large super-conducting magnets presently at JLab are cryostable. These systems all have dual quench detection systems and fail-safe energy dump switches.

The graphs in Fig. 143 display the field vs. current for the MAD-1 (top) and MAD-2 (bottom) combined-function magnets. The dashed curves display the short sample critical currents and the solid lines are the load line curves for the magnets where the  $B$  used is the maximum  $B$  found in the coil. The load line curves measure the current and field margins and the margin along the load line of the respective coil relative to the short sample curve at the operating temperature (4.4 K

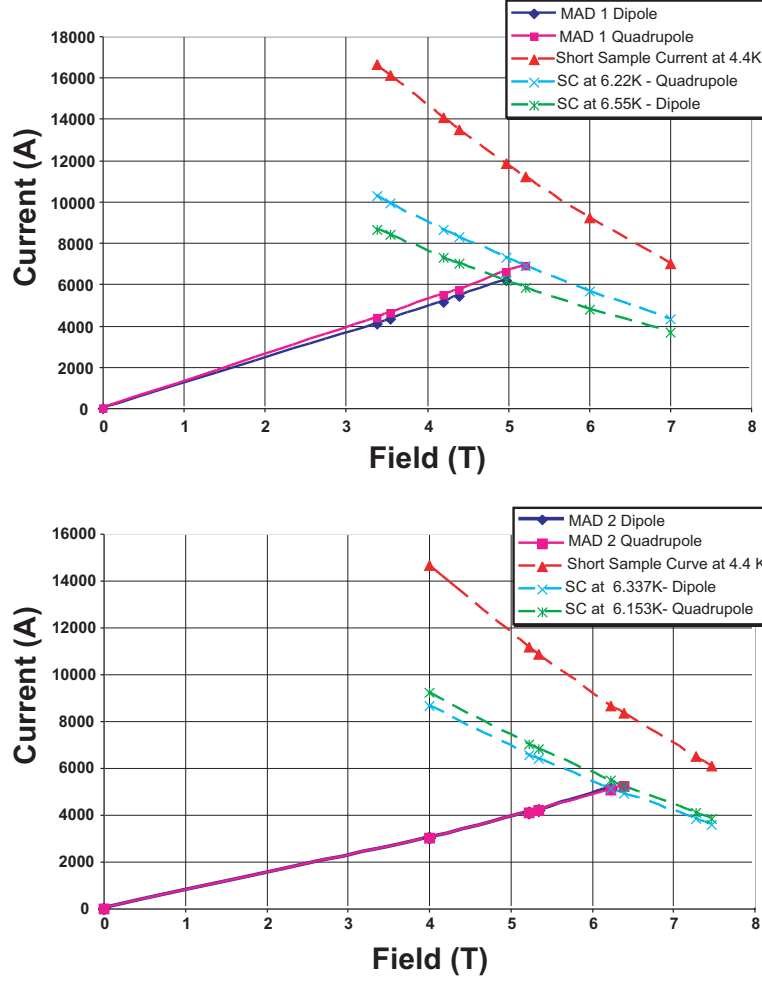


Figure 143: The field vs. current for the MAD-1 (top) and MAD-2 (bottom) combined-function magnets

dashed curve). The two intersecting dashed SC curves show the behavior in the MAD dipole and quadrupole at their respective critical temperatures. These curves measure the critical temperature margin ( $\sim 2$  K) relative to the operating temperature of 4.4 K.

Table 16 lists the parameters of the evaluation of the Steckly criteria ( $\alpha$ ) for cryogenic stability where  $\alpha$  is the ratio of Joule heating in an adiabatic unit length of conductor to the heat removed by surface conduction from the same unit length:

$$\alpha = I^2 \times \rho / (\text{area} \times \text{perimeter} \times \Gamma \times (T_c - T_o) \times H_c). \quad (70)$$

The condition of stability ( $\alpha < 1$ ) means that the velocity of spread of the normal zone is negative, therefore a normal zone will always shrink. This evaluation of  $\alpha$  ignores heat that is conducted along the conductor so this criteria is satisfied by an arbitrary length of conductor as long as the surface is wetted by liquid helium. Thus the magnets must be protected from operation when the helium liquid level is low and there is risk of exposed (non-wetted) coils. Therefore, in addition to



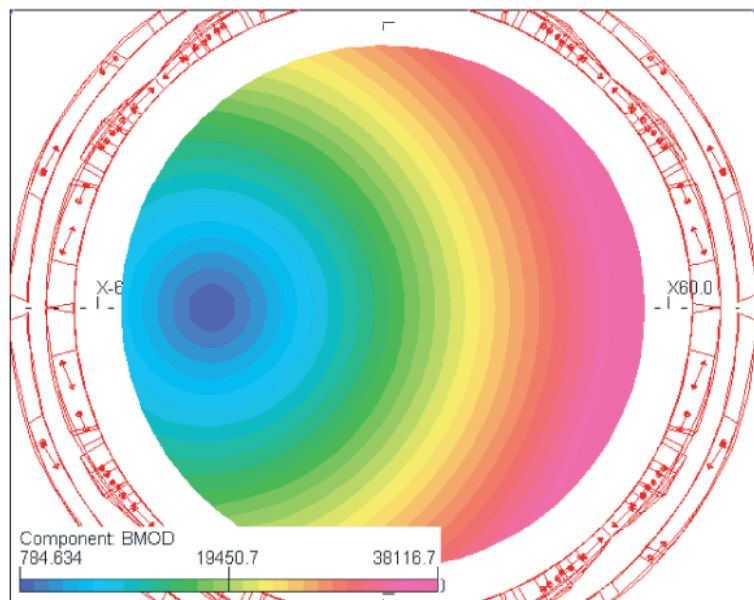


Figure 144: A TOSCA plot of the magnitude of the magnetic field in the warm bore of the combined-function MAD magnet. The bullseye pattern is typical of the superimposed quadrupole and dipole fields.

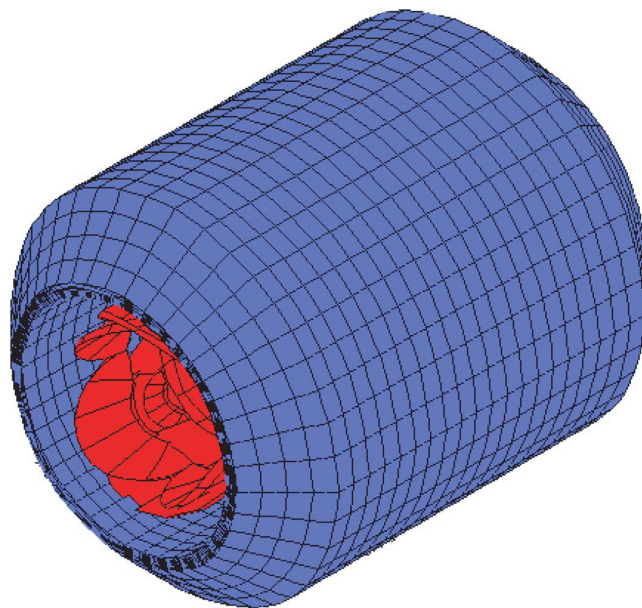


Figure 145: Exterior view of one of MAD's combined function magnets.

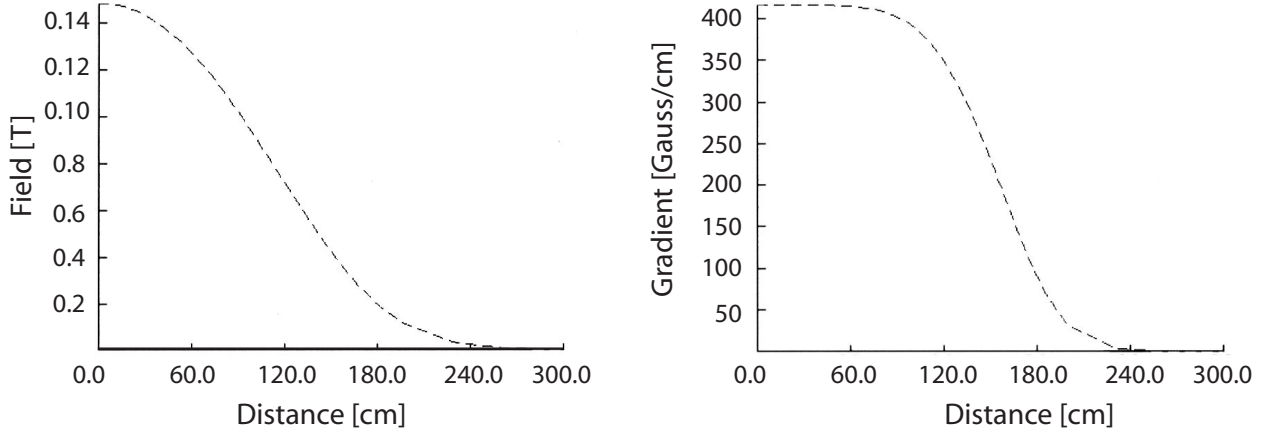


Figure 146: Plot of the dipole component ( $B_y$ ) and of the field gradient of the MAD-1 magnet along the centerline from the magnet center to 300 cm along the axis.

Table 16: The parameters necessary to evaluate the cryogenic stability by the Steckly criteria are listed.  $B_{max}$  is the maximum conduction field, area the conductor cross section, perimeter the fraction exposed to helium,  $\Gamma$  the percent of the perimeter that is covered with liquid helium,  $\rho$  the resistivity corrected for the magnetic field via the Kohler Plot,  $H_c$  the surface nucleate boiling heat transfer,  $(T_c - T_o)$  the temperature difference between the current sharing and the operating temperature, and  $I_{max}$  the maximum design operating current.

	MAD-1 Dipole	MAD-1 Quadrupole	MAD-2 Dipole	MAD-2 Quadrupole
$B_{max}$	4.2 T	4.4 T	6.24 T	6.39 T
area	1 cm <sup>2</sup>	1 cm <sup>2</sup>	1 cm <sup>2</sup>	1 cm <sup>2</sup>
perimeter	5 cm	5 cm	5 cm	5 cm
$\Gamma$	0.6	0.6	0.6	0.6
$\rho(273)$	$1.60 \times 10^{-6} \Omega \text{ cm}$	$1.60 \times 10^{-6} \Omega \text{ cm}$	$1.60 \times 10^{-8} \Omega \text{ cm}$	$1.60 \times 10^{-6} \Omega \text{ cm}$
$\rho(4.4\text{K})$	$8.00 \times 10^{-9} \Omega \text{ cm}$	$8.00 \times 10^{-9} \Omega \text{ cm}$	$8.00 \times 10^{-8} \Omega \text{ cm}$	$8.00 \times 10^{-9} \Omega \text{ cm}$
$\rho(5\text{T}, 4.4\text{K})$	$2.82 \times 10^{-8} \Omega \text{ cm}$	$2.91 \times 10^{-8} \Omega \text{ cm}$	$3.87 \times 10^{-8} \Omega \text{ cm}$	$3.87 \times 10^{-8} \Omega \text{ cm}$
$H_c$	0.21 <sup>2</sup>	0.21 <sup>2</sup>	0.21 <sup>2</sup>	0.21 W/cm <sup>2</sup>
$T_c$	7.39 K	7.10 K	6.33 K	6.15 K
$T_o$	4.42 K	4.42 K	4.42 K	4.42 K
$I_c(B, 4.2\text{K})$	14739 A	14115 A	9087 A	8722 A
$I_c(B, 4.4\text{K})$	14078 A	13481 A	8671 A	8331 A
$I_{max}$	5140 A	5750 A	5125 A	5250 A
$\alpha$	0.40	0.57	0.83	0.98

Table 17: Properties of the large-acceptance spectrometer magnets.

MAD-1	Combined-function quadrupole-dipole
Nominal Bend	10 °
Aperture	120 cm warm bore
NI dipole	$2.33 \times 10^6$ A turns, 5140 A/cm <sup>2</sup> , 2 sector - $\cos\theta$
NI quad	$4.92 \times 10^6$ A turns, 5750 A/cm <sup>2</sup> , 2 sector - $\cos 2\theta$
Bend strength,Bo,EFL	4.46 Tm, central field 1.87 T, effective length dipole 2.4 m
Quad strength,Go,EFL	12.8 (T/m)m, gradient 4.19 T/m, effective length quad 3.07 m
Field Homogeneity	$3 \times 10^{-3}$
Length	4.0 m
Yoke	1010 steel 140 ton warm iron, 3.2 m OD, 2.0 m ID, 3.0 m long
Coil and cryostat	28 ton stainless steel, 1.99 m OD, 1.20 m ID, 4.0 m long
Stored Energy	16.9 MJ
Peak linear force density dipole coil	21,600 N/m
Peak linear force density quad coil	23,000 N/m
MAD-2	Combined-function quadrupole-dipole
Nominal Bend	22 °
Aperture	120 cm warm bore
NI dipole	$5.89 \times 10^6$ A turns, 5125 A/cm <sup>2</sup> , 2 sector - $\cos\theta$
NI quad	$4.08 \times 10^6$ A turns, 5250 A/cm <sup>2</sup> , 2 sector - $\cos 2\theta$
Bend strength	10.2 Tm central field, 3.66 T, effective length dipole 2.78 m
Quad strength	9.79 (T/m)m gradient, 3.30 T/m, effective length quad 2.96 m
Field Homogeneity	$3 \times 10^{-3}$
Length	4.0 m
Yoke	1010 steel 205 ton warm iron, 4.0 m OD, 2.0 m ID, 3.2 m long
Coil and cryostat	28 ton stainless steel, 1.99 m OD, 1.20 m ID, 4.0 m long
Stored Energy	44.9 MJ
Peak linear force density dipole coil	32,000 N/m
Peak linear force density quad coil	33,600 N/m

quench voltage detection, a low liquid level condition is also cause for a fast discharge.

The MAD support structure is a welded steel frame riding on steel wheels. It will be fabricated from pre-fabricated sections that must be welded together in the Hall. The steel structure will have a main beam section that will carry the entire spectrometer. The steel fabrications will be hollow welded structures similar to ship hull sections. As such they will have internal access to permit complete welding of all seams and joints. The entire beam and spectrometer will ride on large steerable steel wheel bogies that permit radial motion and scattering angle changes. The wheel sections will be driven by motors and reducers with variable frequency drives. The wheels are planned to be flat cylindrical wheels that are steered while in motion to control the radius of rotation.

The MAD rotates and translates as a free body, without pivot connection. The wheels can be steered over 90° and then used to position the spectrometer radially for the lower acceptance small angle regime (12°-35°), the regime with a septum magnet (6°-12°), and the large acceptance (greater than 35°) regime. Pointing is achieved by slewing the front wheels relative to the rear

wheels and using a laser retro-reflector system to achieve the desired pointing accuracy. The retro-reflector is mounted on a reference circular stage on the scattering chamber. The distance off the pivot is determined by the same system.

The motion of the MAD spectrometer is coordinated by a stand-alone PLC that integrates the drive wheel motion, laser system read-back, proximity sensors and the laser scan (light curtain) obstacle detection. The rotation motion is limited to a preprogrammed range set in EPROM in the PLC and by the proximity detection. The slew drive system is a maximum  $\pm 1$  cm and a minimum  $\pm 1$  mm jog type system that acts on the front drive wheels only. Shaft encoders on the drive wheels are used to control the motion. A scale etched into the floor at the radius of the rear drive wheels and viewed by a video camera with a graticule lens is used to confirm the scattering angle setting. A sieve slit will provide angular calibrations of better than 0.5 mrad. Pointing accuracy is confirmed by the laser retro-reflector system with the spectrometer at rest. The final distance off the pivot is measured when all angle adjustments have been made.

The MAD spectrometer shield house is a reinforced cast-concrete structure that is built on the steel carriage. The concrete is confined by a steel housing that is up to 10 cm thick. The concrete thickness varies to optimize the shielding in all directions. The concrete is 80 cm thick in the sides towards the beam, back, and bottom. The sides away from the beam and the top are 40 cm thick and the front toward the target is 70 cm thick. The concrete is formed and poured in place including the two door sections. The concrete is a conventional mix with borate added to absorb thermal neutrons. The interior walls, floor, and ceiling will have a minimum 1 inch thick lead lining except for the front wall which has 3 inches of lead. The MAD detectors will be mounted on a transverse rail system so that the detectors may be moved sideways for servicing and relocated accurately. The shield house will be accessed by doors that are hinged to open outward on the side away from the beam.

The MAD spectrometer has three vacuum systems dedicated to the operation of the magnets, the MAD spectrometer vacuum, and the Čerenkov detector. The MAD cryogenic system is presumed to be leak-tight and cryo-pumping so a dedicated vacuum system is not included. The magnets are also assumed to be leak-tight but a vacuum system tailored to leak testing, commissioning, and bi-annual vacuum servicing is included as a dedicated vacuum system. This system can be used to commission and service the cryogenic system as needed. This system is assumed to be portable, self-contained, and fully instrumented. The spectrometer vacuum system and the Čerenkov vacuum systems are dedicated to these two systems and are permanently installed on the MAD.

### 3.A.2 Optical Characteristics of the MAD Spectrometer

The quadrupole components of the MAD provide the focusing necessary to achieve the desired solid angle while the dipole components provide the dispersion needed for momentum resolution. The

Table 18: The table shows the estimated performance parameters based on TRANSPORT calculations of the optical properties. The error estimates assume a 0.5 mrad angle determination and 100  $\mu\text{m}$  position determination.

Configuration	35°	20°	12°	6°
Central Momentum	7.5 GeV/c	7.5 GeV/c	7.5 GeV/c	7.5 GeV/c
$\Delta p/p_0$	$\pm 15\%$	$\pm 15\%$	$\pm 15\%$	$\pm 15\%$
$y_0$	$\pm 25$ cm	$\pm 25$ cm	$\pm 25$ cm	$\pm 25$ cm
$\theta_0$	$\pm 198$ mrad	$\pm 138$ mrad	$\pm 68$ mrad	$\pm 50$ mrad
$\phi_0$	$\pm 35$ mrad	$\pm 32$ mrad	$\pm 23$ mrad	$\pm 20$ mrad
$\Delta\Omega$	$\sim 28$ msr	$\sim 18$ msr	$\sim 6$ msr	$\sim 4.5$ msr
$\delta y_0$	2.6 mm	3.6 mm	4.6 mm	4.6 mm
$\delta\theta_0$	1.9 mrad	1.3 mrad	0.6 mrad	0.6 mrad
$\delta\phi_0$	0.5 mrad	0.5 mrad	0.5 mrad	0.5 mrad
$\delta\sigma$	$1.3 \times 10^{-3}$	$1.0 \times 10^{-3}$	$0.7 \times 10^{-3}$	$0.7 \times 10^{-3}$

maximum central momentum is 7.5 GeV/c. The total bend angle is 32° with a 10° bend in the first magnet and a 22° bend in the second. The larger bend in the second magnet was chosen to prevent direct line of sight between the target and the detectors while keeping the dispersion reasonably small thereby reducing the size requirements on the detector package. Extra versatility can be achieved by varying the drift distance to the first magnet. Larger drift distances allow smaller scattering angles at the cost of reduced acceptance. Depending on the details of the detector package, scattering angles as small as 12° are possible, which can be extended to 6° with a septum magnet. The overall performance expected of the spectrometer is summarized in Table 18.

The optics is very much that of a quadrupole pair. The large acceptance is achieved by keeping the magnets as short as possible and as close together as possible. The first-order transfer matrices for the 35° and 20° configurations are shown in Table 19. In both cases  $\langle x|\delta\theta \rangle \sim 17$ , which drives the expected momentum resolution at  $\delta \pm 15\%$ . The first-order transfer matrix for the 12° configuration is also shown in Table 19; in this case,  $\langle x|\delta\theta \rangle \sim 25$ . The extreme particle trajectories for the MAD optics are shown in Fig. 147.

A working model of MAD was developed using the ray-tracing code SNAKE. The magnetic fields in the magnets were based on TOSCA-generated maps. Two maps were created by running TOSCA with only the quadrupole coil energized and with only the dipole element energized; these maps were then added with scale factors to simulate tuning the various elements. Once the first-order properties expected from the TRANSPORT studies were obtained, a large number (appr. 2000) of random trajectories spanning the full acceptance of the spectrometer were traced through the spectrometer using SNAKE. These trajectories were then used as input to a fitting program (MUDIFI) that determines the best-fit polynomials reconstructing the target parameters ( $\delta$ ,  $\theta_0$ ,  $y_0$ , and  $\phi_0$ ) of the trajectories based on their positions and angles ( $x_f$ ,  $y_f$ ,  $\theta_f$ , and  $\phi_f$ ) in the detectors. The sensitivity to measurement errors in the detectors can then be explored in a Monte-Carlo

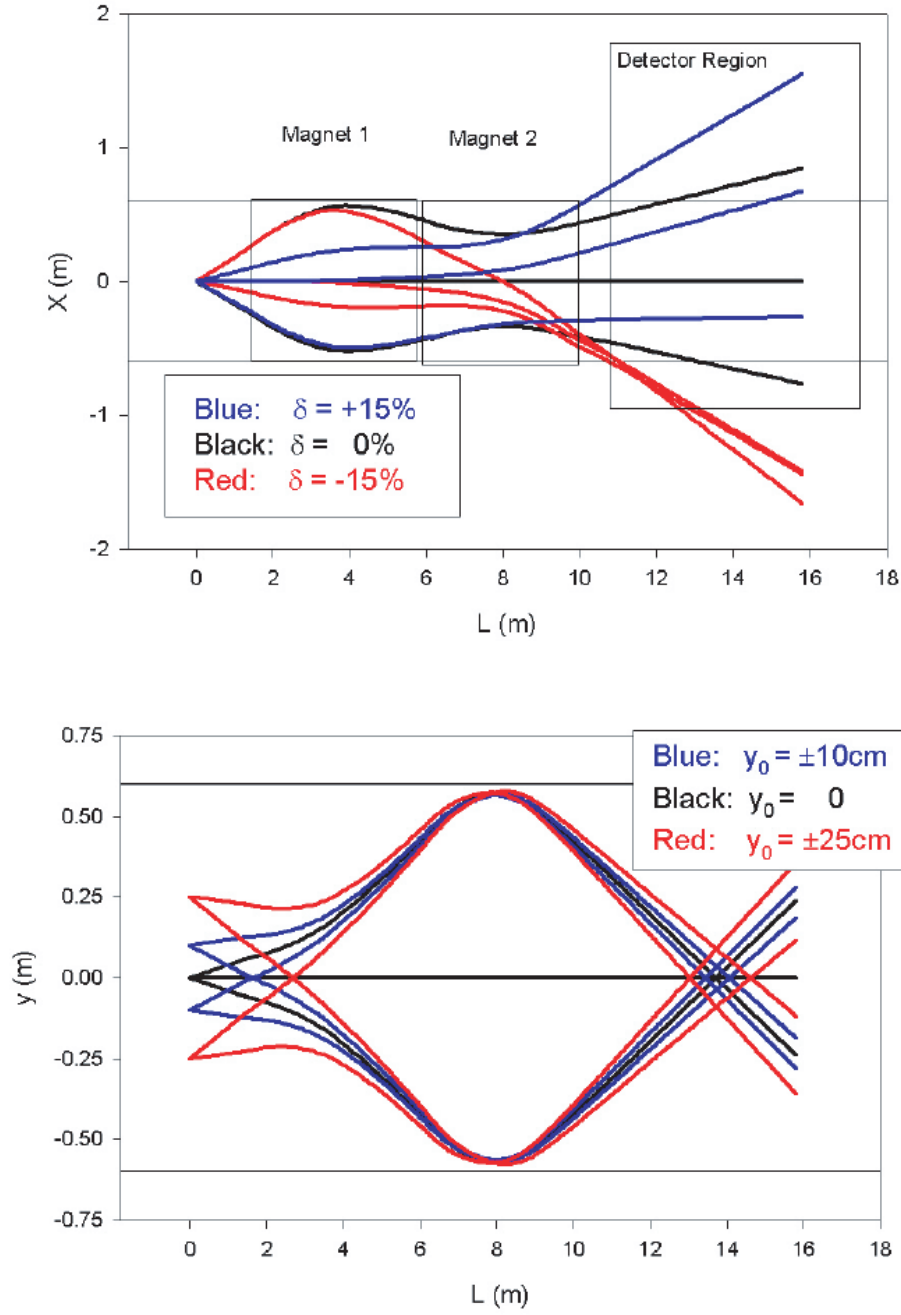


Figure 147: The top plot shows the distribution of extreme trajectories in the bend plane for  $\delta$  of +15%, 0%, and -15%. The bottom plot shows the distribution of the extreme transverse rays at  $\delta=0$  for different values of  $y_0$ .

Table 19: The first-order TRANSPORT matrices in natural units (m) for various configurations of the MAD spectrometer

For the 35 degree configuration:

$$\begin{bmatrix} x_{fp} \\ \theta_{fp} \\ y_{fp} \\ \phi_{fp} \\ \delta_{fp} \end{bmatrix} = \begin{bmatrix} -3.72 & 0.00 & 0.00 & 0.00 & 3.54 \\ -1.03 & -0.27 & 0.00 & 0.00 & 103.0 \\ 0.00 & 0.00 & 1.00 & 5.15 & 0.00 \\ 0.00 & 0.00 & -1.05 & -4.43 & 0.00 \\ 0.00 & 0.00 & 0.00 & 0.00 & 1.00 \end{bmatrix} \begin{bmatrix} x_{tg} \\ \theta_{tg} \\ y_{tg} \\ \phi_{tg} \\ \delta \end{bmatrix} \quad (71)$$

For the 20 degree configuration:

$$\begin{bmatrix} x_{fp} \\ \theta_{fp} \\ y_{fp} \\ \phi_{fp} \\ \delta_{fp} \end{bmatrix} = \begin{bmatrix} -2.51 & 0.00 & 0.00 & 0.00 & 3.29 \\ -0.70 & -0.40 & 0.00 & 0.00 & 90.2 \\ 0.00 & 0.00 & 1.00 & 7.10 & 0.00 \\ 0.00 & 0.00 & -0.79 & -4.58 & 0.00 \\ 0.00 & 0.00 & 0.00 & 0.00 & 1.00 \end{bmatrix} \begin{bmatrix} x_{tg} \\ \theta_{tg} \\ y_{tg} \\ \phi_{tg} \\ \delta \end{bmatrix} \quad (72)$$

For the 12 degree configuration:

$$\begin{bmatrix} x_{fp} \\ \theta_{fp} \\ y_{fp} \\ \phi_{fp} \\ \delta_{fp} \end{bmatrix} = \begin{bmatrix} -1.22 & 0.00 & 0.00 & 0.00 & 3.29 \\ -0.37 & -0.82 & 0.00 & 0.00 & 90.2 \\ 0.00 & 0.00 & 1.00 & 12.4 & 0.00 \\ 0.00 & 0.00 & -0.53 & -5.51 & 0.00 \\ 0.00 & 0.00 & 0.00 & 0.00 & 1.00 \end{bmatrix} \begin{bmatrix} x_{tg} \\ \theta_{tg} \\ y_{tg} \\ \phi_{tg} \\ \delta \end{bmatrix} \quad (73)$$

fashion using a new set of trajectories generated in the same manner as those used in the fitting. Figs. 148a)-d) show the resolutions  $\delta$ ,  $\theta_0$ ,  $y_0$ , and  $\phi_0$  generated in the Monte Carlo analysis. There is a reasonable match between the Monte-Carlo analysis and the TRANSPORT based predictions, with some degradation particularly at large positive  $\delta$ 's. This is most likely a consequence of higher order aberrations not accounted for in the TRANSPORT analysis.

The overall performance shown is for a generic tune that roughly meets the needs of the proposed experiments. Alternate tunes are possible. Better momentum resolution in the positive delta region could be achieved at the cost of momentum resolution in the negative delta region, and trade-offs sacrificing acceptance for resolution, in momentum and angles, are possible.

### 3.A.3 Simulations of the MAD Spectrometer

Three different software packages were used to simulate the MAD spectrometer. The first two, MCEEP and SIMC, were employed mainly to simulate physics results such as counting rates and distributions. Results of these simulations can be found in the various physics sections of this document. The third software package, GEANT, was used to simulate the spectrometer performance in terms of backgrounds and resolution. Results of the GEANT simulations are given below.

MCEEP [Ulp] and SIMC [Abpc] are standard simulation programs for the existing pair of Hall A high resolution spectrometers. They are designed to simulate (e,e'X) experiments by averag-

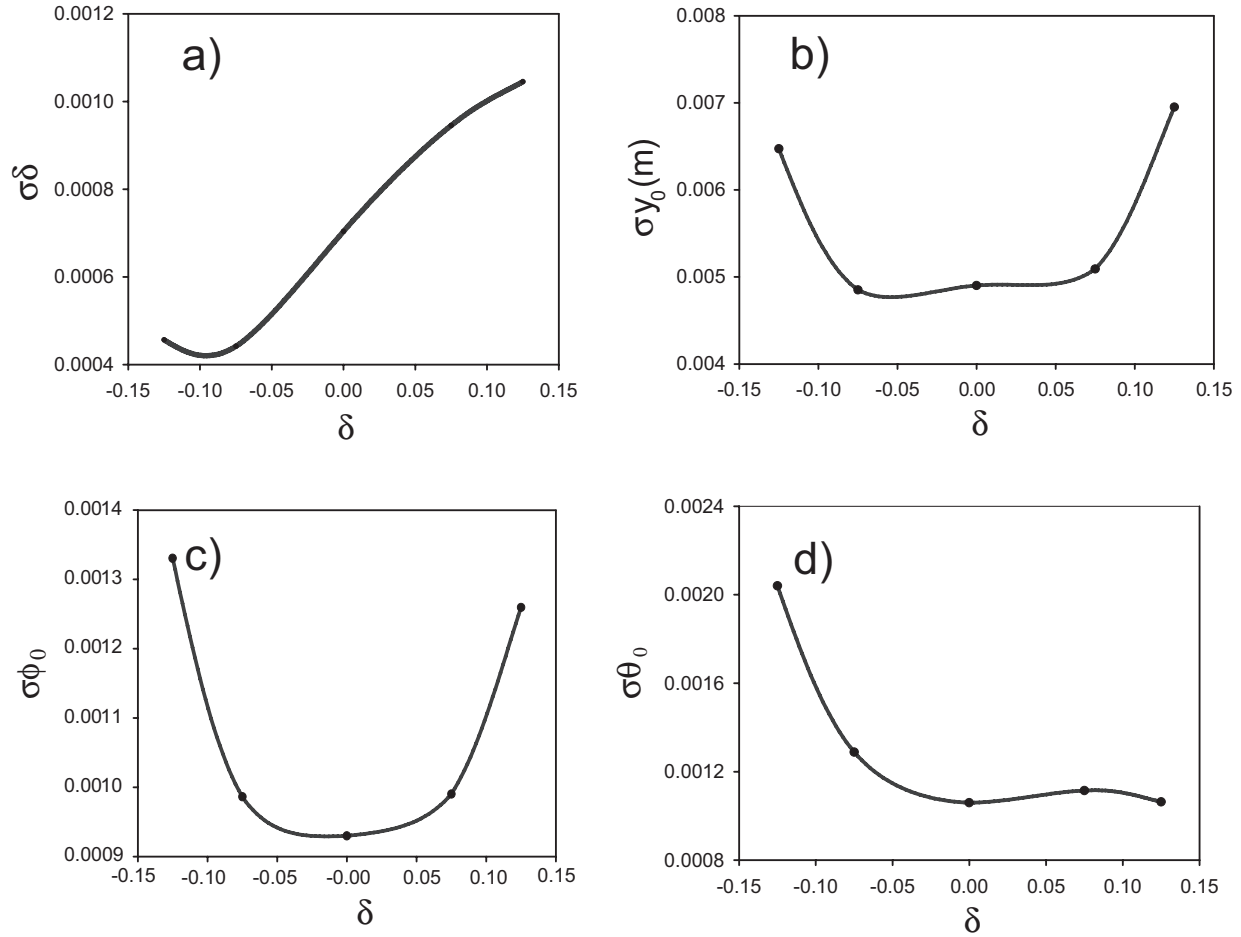


Figure 148: The MAD spectrometer's a) momentum, b)  $y_0$ , c)  $\theta$ , and d)  $\phi$  resolution. The calculations include the effects of multiple scattering in a polarized  $^3\text{He}$  target and a 10 m helium bag, and the effects of the intrinsic resolution of the detectors.



ing theoretical models over an experimental acceptance. The current version includes cross-section models for the proton, deuteron, triton,  $^3\text{He}$ ,  $^4\text{He}$ ,  $^{12}\text{C}$ ,  $^{56}\text{Fe}$ ,  $^{197}\text{Au}$  and  $^{208}\text{Pb}$ . Single-arm experiments can also be simulated. Internal and external radiative effects and multiple scattering can be simulated. Spin transport and precession inside magnetic elements of the spectrometer can be taken into account. MAD is described within MCEEP and SIMC via a set of transfer functions, which are essentially TRANSPORT matrices generalized to higher orders. Both forward and reverse functions have been incorporated in MCEEP. Coefficients up to 5th order and sometimes higher were included.

A thorough simulation of the expected backgrounds in MAD detectors is particularly important because of its large aperture and momentum acceptance. A simulation was used to optimize the optics and collimators in order to reduce the backgrounds. The background consists of high-energy particles, like electrons from DIS and pions from photoproduction by quasi-real photons, as well as a low-energy photon background stemming from cascades of electromagnetic interactions of electrons in the target and windows. The latter background was simulated using GEANT 3.21. The geometry used included the target vacuum chamber with all relevant details of the construction, the windows and the target cell, as well as the MAD geometry including the distribution of the materials and magnetic field maps. The beam interaction with the material on its way and the interactions of the secondary particles was done with GEANT, which includes the most important electromagnetic reactions, such as Møller scattering, bremsstrahlung, Compton scattering, etc. The main source of background is a cascade of processes involving low energy photons going inside the spectrometer aperture, scattering (via Compton scattering) one or more times on the walls of the spectrometer chamber, and finally impacting on the detector. There are several ways to reduce this background:

- a) *Increase the bending angle of the spectrometer.* It turns out that increasing the bending angle from  $20^\circ$  to  $32^\circ$  reduces the background by a factor of 5.
- b) *Place collimators inside the spectrometer in its focal areas.* The spectrometer optics accepts particles crossing the entrance to the first magnet of MAD in a relatively narrow vertical band. A collimator (COL1) with a rectangular opening 30 cm wide and 100 cm high does not affect the acceptance while reducing the background. Additionally, a collimator (COL3) close to the target chamber and leaving only the particles coming directly from the target, helps. In the vertical projection, MAD focuses the particles at about the center of the second magnet. A collimator (COL2) 30 cm upstream of the center of the second magnet with a hole about 30 cm high and as wide as the magnet bore helps to reduce the background. All three collimators reduce the soft photon background by a factor of 3.
- c) *Trap the photons on a special profile of the spectrometer chamber surface.* The hole in COL2 is in the direct line of sight from the target. Nearly half of the background left is formed by photons passing directly from the target through this hole and rescattering on the bottom side of the magnet chamber behind the collimator. A periodic structure on the surface of the chamber can reduce the background by a factor of about 1.5.

Table 20: MAD detector parameters

	Scintillators	Drift Chamber	Gas Čerenkov	Calorimeter
sensitive area	$0.5(0.6) \times 2.0(2.5) \text{ m}^2$	$0.5 \times 2.5 \text{ m}^2$	$0.6 \times 2.5 \text{ m}^2$	$1.0 \times 3.0 \text{ m}^2$
depth used	10, 10, 20 cm	100 cm	250 cm	100 cm
segmentation	16 paddles, 4 planes	1200	12 PMTs	192 PMTs
resolution	0.15 ns	$75 \mu\text{m}$	$> 7.5 \text{ ph.electrons}$	$10\%/\sqrt{E}$

With MAD positioned at  $25^\circ$ , with a  $50 \mu\text{A}$  beam impinging on a 15 cm liquid hydrogen target the calculated photon flux in the detector area is about 100 MHz with an average energy of  $\sim 0.7 \text{ MeV}$ . The photon energy spectrum is well described by the function  $\frac{dN}{dE} \propto e^{-\alpha E}$ , where  $\alpha = 1.5 \text{ MeV}^{-1}$ . This flux was taken into account in the detector design.

### 3.A.4 MAD Spectrometer Detector Systems

With a maximum central momentum of  $7.5 \text{ GeV}/c$  for the spectrometer and a momentum bite of  $\pm 15\%$  a wide range of momenta ( $0.4\text{--}9 \text{ GeV}/c$ ) must be considered in the design of the detector package. The proposed detector package for the spectrometer has three major functions: triggering, tracking, and particle identification. These are accomplished by using scintillator counters, multi-wire drift chambers (MWDC), gas and aerogel Čerenkov counters, and an electromagnetic calorimeter. Figure 149 shows the side view of the detector package in the configurations for electron and for hadron detection. The trigger will be formed from the signals of scintillators, Čerenkov counters, and the electromagnetic calorimeter. Two MWDCs separated by 100 cm will provide tracking information for momentum and angle reconstruction. A multi-wire proportional chamber (MWPC), installed between MWDCs, will improve the high-rate capability of the tracking system. The main parameters of the detector package are presented in Table 20 (without aerogel Čerenkov counters and Focal Plane Polarimeter).

Particle identification in the electron configuration utilizes the gas Čerenkov counter and the electromagnetic calorimeter. A variable refraction index is achieved by using a mixture of helium and nitrogen. The required pion rejection factor is dictated by the  $\pi/e$  ratio in inclusive electron scattering, which varies from less than  $10^3$  at high momentum up to  $10^5$  at low momentum and forward angles. The pion rejection factor, the product of rejection by the electromagnetic calorimeter (100) and gas Čerenkov counter (200), is sufficient to reduce the pion contamination to the 1% level in inclusive electron scattering experiments. A higher rejection factor, required at lower momentum settings, will be achieved by using gas with a higher index of refraction.

Two aerogel Čerenkov counters and a short (100 cm), high-index, gas Čerenkov counter will be used in the hadron configuration. The Čerenkov counters for the hadron configuration will use the same space as the low-index gas Čerenkov counter in the electron configuration. Expected rates in the spectrometer are shown in Table 21. They were calculated for a beam energy of 11 GeV and a

Table 21: Single rates in MAD detector (kHz) with  $E_{beam} = 11$  GeV ,  $I_{beam} = 70 \mu\text{A}$ , and a 15 cm long liquid hydrogen target.

p(GeV/c)	$\theta = 15^\circ$				$\theta = 25^\circ$				$\theta = 35^\circ$			
	e	$\pi^-$	$\pi^+$	p	e	$\pi^-$	$\pi^+$	p	e	$\pi^-$	$\pi^+$	p
1.5	1	780	830	360	500	290	300	290	0.1	21	120	330
3.0	3	90	90	170	0.4	5	100	270	0.02	0.04	130	270
4.5	4	9	70	170	0.1	0.03	30	280	—	—	—	—

beam current of  $70 \mu\text{A}$  on a 15 cm liquid hydrogen target (the luminosity is  $2.5 \times 10^{38}$  Hz/cm<sup>2</sup>).

The following paragraphs present the details of proposed detectors and their expected performance. The detector package does not need to be moved when the magnets are moved away from the interaction point to accommodate more forward scattering angles.

**Scintillators** The trigger package for the MAD detector system consists of four segmented planes of scintillators, designated  $S_0$ ,  $S_1$ ,  $S_2.V$ , and  $S_2.H$ . The  $S_0$  and  $S_1$  planes are located immediately before and after the drift chambers, respectively. The  $S_2$  package will consist of two planes ( $S_2.V$  and  $S_2.H$ ), oriented orthogonal to each other in a hodoscope configuration, and located just before the electromagnetic calorimeter. The primary DAQ trigger is formed by a coincidence between the  $S_1$  and  $S_2$  planes, with timing set by  $S_2.V$ . The  $S_0$  plane will be used primarily for trigger efficiency studies and can be removed when multiple scattering degrades the angular resolution of the spectrometer. Each plane will be segmented into 16 elements to keep the total rate in a given paddle at an acceptable level.

Based on GEANT simulations, the background rate due to low-energy photons will be approximately  $10^8$  Hz under typical running conditions. The fraction of these photons that interact is 4% in  $S_0$  and  $S_1$ , and 30% in each plane of  $S_2$ . Using discriminator thresholds of 0.5 MeV for  $S_0$  and  $S_1$ , and 5 MeV for  $S_2$  provides high efficiency for electron detection while reducing the background singles rate per paddle to approximately 50 kHz in  $S_0$  and  $S_1$ , and 100 Hz in each plane of  $S_2$ . Requiring a coincidence between  $S_1$  and one of the  $S_2$  planes yields a background trigger rate of approximately 10 Hz. Requiring  $S_1$  and both planes of  $S_2$  in coincidence makes the background trigger rate negligible.

The scintillator elements in the  $S_0$  and  $S_1$  planes will be stacked horizontally (segmentation in the dispersive direction). The thickness of each element is 0.5 cm for  $S_0$  and  $S_1$ , with a 1 cm overlap between adjacent elements. Each of the  $S_2$  planes will contain 16 scintillator elements, with one plane oriented vertically and the other horizontally. The scintillator elements in  $S_2$  are 5 cm thick to provide good timing resolution ( $\sigma < 150$  ps). Approximate geometrical dimensions for each element are given in Table 22.

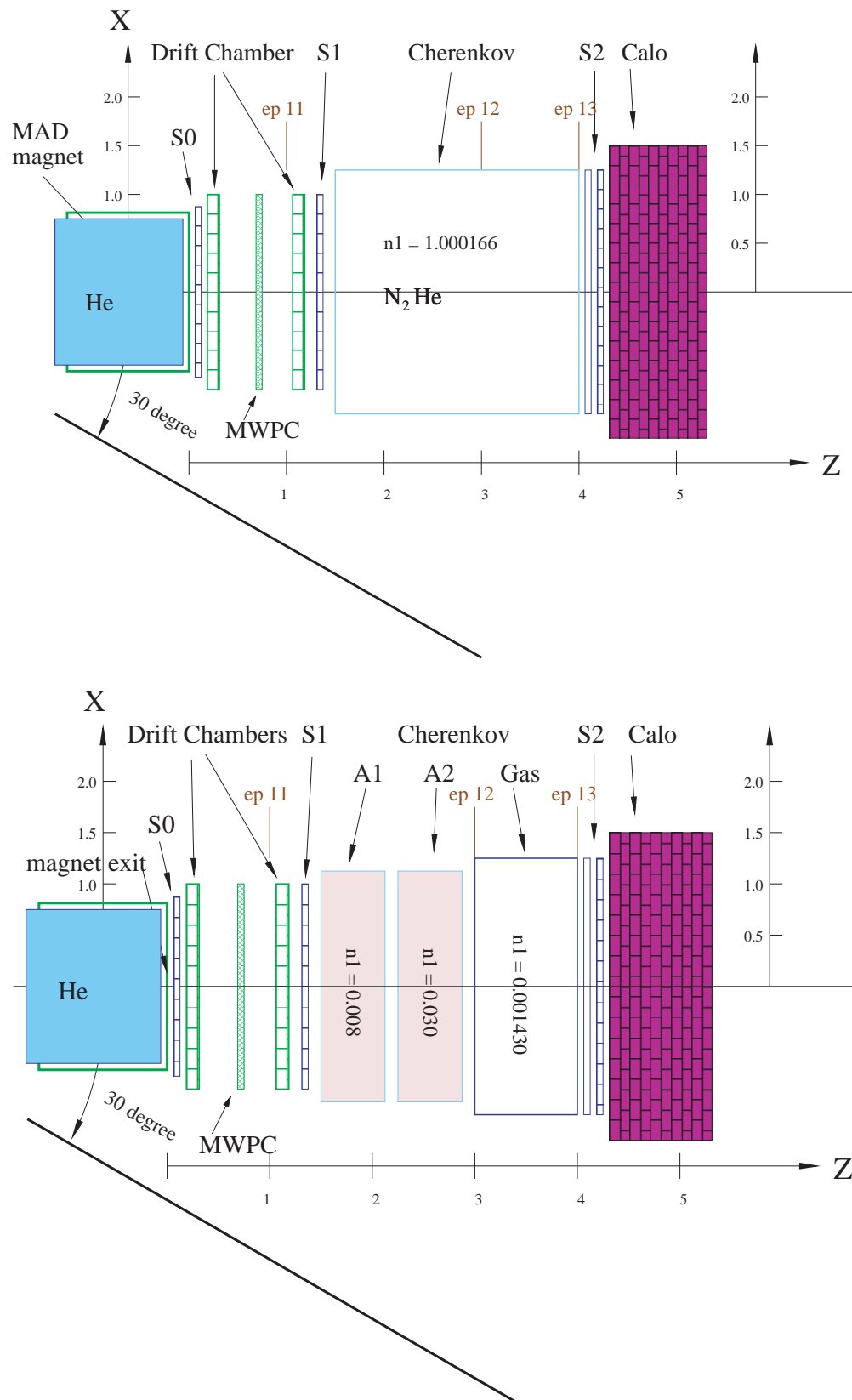


Figure 149: Configuration of the detector package for electrons (top) and hadrons (bottom).

Table 22: Geometrical specifications for scintillator planes.

Plane	Location (z)	Active Area (H x V)	Number of Elements	Element Dimensions, cm (L x W x T)
$S_0$	0.0-0.1 m	0.50 m x 2.0 m	16	50 x 13.5 x 0.5
$S_1$	1.3-1.4 m	0.50 m x 2.0 m	16	50 x 13.5 x 0.5
$S_2.V$	4.1-4.2 m	0.60 m x 2.5 m	16	60 x 16 x 5
$S_2.H$	4.2-4.3 m	0.64 m x 2.5 m	16	4 x 250 x 5

The detectors will be built of Bicron BC-408 or Eljen Technologies EJ-200 with a typical pulse width of FWHM  $\sim 2.5$  ns and long attenuation lengths. Each scintillator will have light guides attached to both ends which will channel the light onto 2 inch diameter photomultiplier tubes (PMTs). For  $S_0$  and  $S_1$ , a high gain PMT such as the Photonis XP2262 is appropriate. For  $S_2$ , the light output is expected to be high and a fast, 8-stage tube such as the Photonis XP2282B is suitable.

**Drift Chambers** A system of two drift chambers and a multi-wire proportional chamber is proposed to instrument the MAD focal plane. The first drift chamber is located at 0.1 m from the exit of the last MAD magnet, the second drift chamber 1 m further down-stream. The MWPC will be located at the mid-point between the chambers. Simulations of particle tracks through the MAD spectrometer indicate that the active area of the second chamber needs to be only about 20% larger than the active area of the first chamber. Design and construction considerations make it more cost-effective and convenient to make all three chambers with the same dimensions, 0.6 m  $\times$  2.5 m. The two drift chambers are proposed to have identical design, each with three groups of wire planes with wires oriented at  $+45^\circ$  ( $u$ ),  $-45^\circ$  ( $v$ ), and  $+90^\circ$  ( $x$ ). Each group of wire planes consists of four planes separated by 1 cm each. The four planes in each direction are essential to reconstruct good tracks in a high-rate environment. Furthermore, the four planes provide high resolution and high efficiency: single-wire plane resolutions of roughly 100 – 150  $\mu\text{m}$  have been achieved in the past, having four planes will improve this resolution to the required 75  $\mu\text{m}$  value. In case of inefficiencies, at least two wire planes in the same direction are required to resolve the left-right ambiguity of drift times. With the single-wire inefficiency for a drift chamber usually very low ( $< 3\%$ ), the inefficiency for a chamber with four planes, resulting from the absence of two out of four planes, is extremely small. The low-energy photon background at the MAD focus is estimated to be 100 MHz. Assuming a conversion efficiency of 0.1% we can estimate a low-energy electron rate of 0.1 MHz at the drift chambers. Some of these electrons will give random hits in the wire planes while others will make tracks through one or both drift chambers. The dead-time per drift cell, mainly arising from the drift of positive ions away from the region around the sense wire, electronic dead-time and pulse-widths, is usually limited to several hundred ns. As a result, the soft-photon background results in a negligible dead-time. Furthermore, four wire planes are combined in each direction and hence, the high timing resolution of the drift chamber can be used to suppress hits and tracks from

background electrons. The per-wire position resolution of roughly  $100\text{ }\mu\text{m}$  corresponds to a timing resolution of about 2 ns. Thus a comfortable  $5\sigma$  track reconstruction window of 10 ns can be used to select good tracks. This will easily separate the real track that registered the scintillator trigger from background tracks. The extra group of planes ( $x$ ) enhances high-rate operation and further improves resolution. In the rare case where two out of the four planes in a ( $u$ ), or ( $v$ ) group fail to fire, the hits on the ( $x$ ) planes can be used to ensure that the chamber has almost 100% efficiency. A wire spacing of 30 mm between sense wires is proposed to give a drift distance of 15 mm. This drift distance corresponds to a drift time of roughly 300 ns, and an extremely high limit on the rate *per wire* of around 3 MHz. For this inter-wire spacing, each plane will consist of 65 sense wires (about 1600 sense wires for the two chambers). Sensitive planes will contain alternating sense and field wires. Each sensitive plane will be between two field-shaping planes consisting of only field wires separated by 5 mm.

The chamber will be constructed out of planar frames. This design is popular in wire-chamber construction as it allows convenient wire stringing and easy access to each wire plane. The wire-chamber simulation package GARFIELD has been used for a complete simulation of the electric field configurations, drift parameters, and resolutions of the proposed drift chambers.

**Gas Čerenkov Counter** The gas Čerenkov counter is  $\sim 1.5$  m from the exit of the magnet, just after the  $S_1$  scintillator counter. In the electron configuration (Fig. 149) the counter is 2.5 m long. The mixture ratio of two gases (He and  $\text{N}_2$ ) will be used to adjust the index of refraction, so that the number of photo-electrons is maximized for the given momentum and length of the radiator while keeping the pion speed for the same momentum below the threshold of Čerenkov radiation. Figure 150 shows the parameters of the counter vs. particle momentum. At 6 GeV/ $c$  central momentum the fraction of  $\text{N}_2$  will be 60% resulting in approximately 8 photo-electrons.

In the hadron configuration the length of the counter will be reduced to 1 m. Here, the counter will be used to reject electrons. Depending on the needs of the particular experiment, the momentum threshold for pions can be adjusted by changing the partial pressure of Freon 114. In the momentum range above 2.7 GeV/ $c$  this detector can be used for positive identification of a pion.

The back surface of the Čerenkov counter is covered by 12 mirrors in a  $2 \times 6$  arrangement. Each mirror is tilted by  $15^\circ$  so that the reflected photons can be collected at the side wall of the chamber. Including the tilt, each mirror measures 62 cm $\times$ 50 cm. Since we need to allow a small overlap between mirrors, the size of the actual mirror will be a little larger than this, about 63 cm $\times$ 52 cm, which is still reasonable for manufacturing. Each mirror will have a spherical shape with a radius of 1 m (focal length of 50 cm). Figure 150 also shows the geometry of the Čerenkov counter with schematic diagrams for mirrors and phototubes.

Using the transfer functions of MAD, emission of photons, reflection on the mirror and collec-

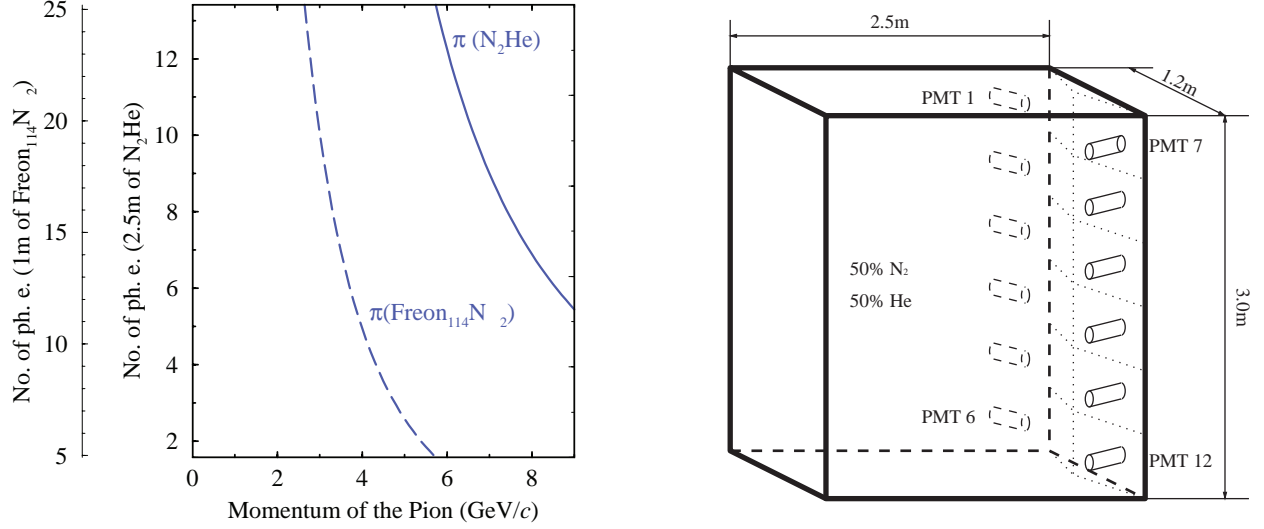


Figure 150: Number of photo-electrons expected for high-energy electrons in the gas Čerenkov counter. The solid line represents the  $N_2$ -He mixture and the dashed line the mixture of Freon 114 and  $N_2$ . Also shown a schematic diagram of the detector's geometry.

Table 23: Collection efficiency of photons for each phototube.

Tube Number	Efficiency(%)	Tube Number	Efficiency(%)
1	97.6	7	97.6
2	99.7	8	99.4
3	99.9	9	99.9
4	97.3	10	97.4
5	91.4	11	92.4
6	82.5	12	82.6
Average		96.3	

tion in the phototubes have been simulated. Except for the bottom four tubes, almost all of the photons reflected by each mirror will be collected by the 5" phototubes. For the bottom four tubes, "Winston Cones" are used to increase the collection efficiency. The photon collection efficiency has been quantified for each mirror in Table 23 and averages about 96%. With Winston cones, this efficiency will increase slightly.

**Aerogel Čerenkov Counters** Hadron identification, mainly  $\pi$ ,  $K$ , or  $p$ , will be accomplished by a combination of time-of-flight measurement and threshold Čerenkov counters. Two aerogel Čerenkov counters, with indices 1.008 and 1.030, are required to cover the full momentum range, as shown in Table 24 and Fig. 151.

A design similar to the current aerogel detectors in Hall A, A1 and A2, will be employed. All the inner surfaces of the detector are covered with millipore paper, including the inactive edge of the PMTs. The detector is constructed out of two separable assemblies for PMTs and aerogel.

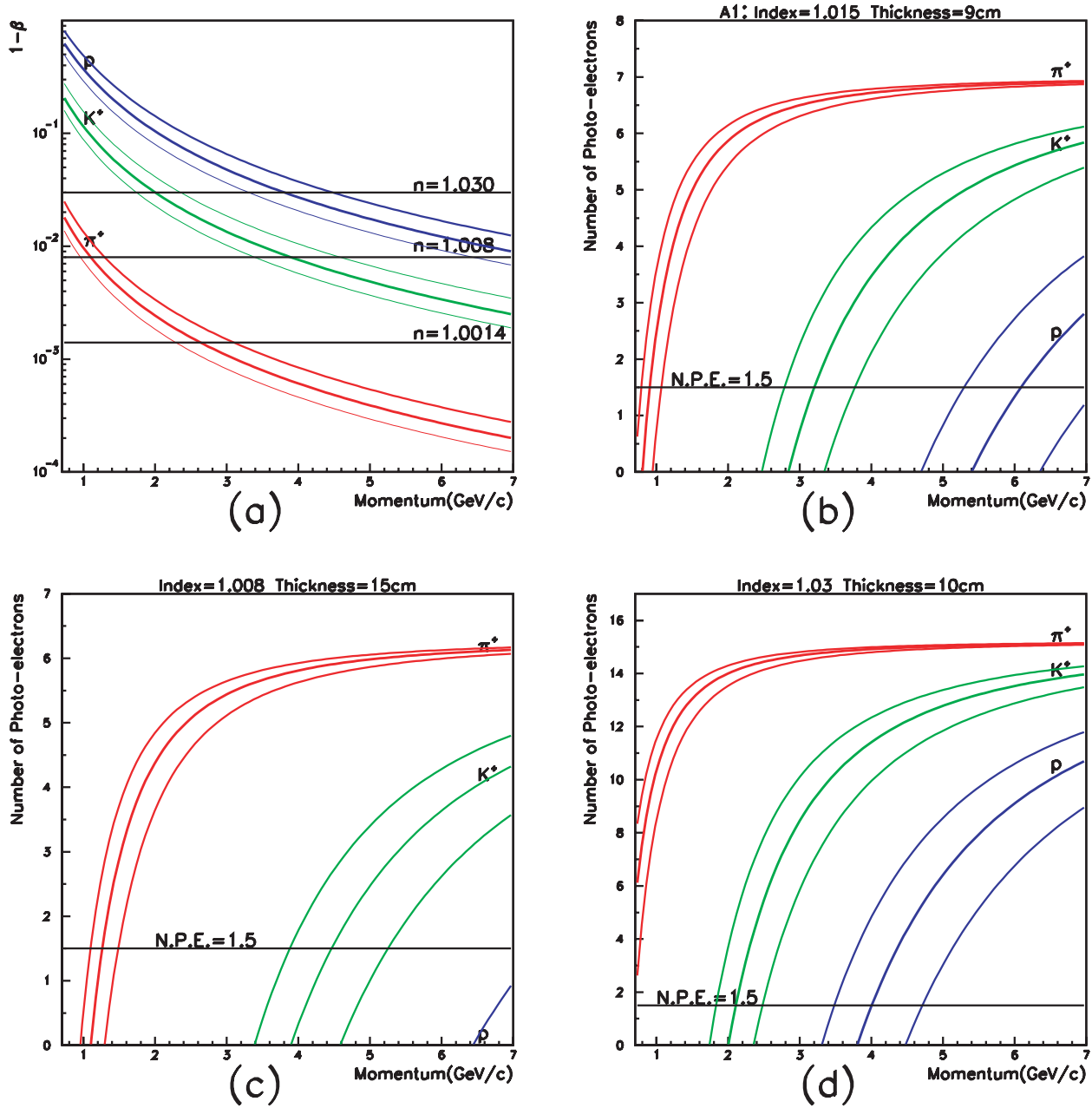


Figure 151: (a) The deviation of velocity from 1 vs. momentum for protons, pions and kaons. Dotted lines indicate the momentum bite of the spectrometer. (b) A1 performance with index of 1.015 and thickness of 9 cm. (c) Estimated number of photo-electrons vs. momentum for index of 1.008 and thickness of 15 cm. (d) Estimated number of photo-electrons vs. momentum for index of 1.030 and thickness of 10 cm.



Table 24: The momentum threshold to produce Čerenkov radiation.

Index	$p_\pi$ (GeV/c)	$p_K$ (GeV/c)	$p_p$ (GeV/c)
1.030	0.58	2.06	3.92
1.008	1.11	3.93	7.46
1.00143	2.61	9.24	17.6

However, some differences do exist:

- **Dimensions:** The MAD aerogel Čerenkov counters are 0.6 m(H)×2.5 m(V), significantly larger than the dimensions of A1 or of A2. Due to the wider horizontal dimension, the photons will be subject to more diffusion and losses on their way to the PMTs located on the sides of the detector. To compensate for the losses the height of the detector needs to be increased, which requires 2-3 layers of PMTs.
- **Magnetic field:** A magnetic shield is required as the magnetic field is at the level of 10 G. We will either add an enclosed shield for the whole detector, i.e. to insert an 0.50 mm iron planes before and after the aerogel detector with thicker iron on the sides or add individual shields for each PMT.
- **Aerogel thickness:** Fewer photo-electrons are expected when the refractive index gets closer to 1, which is nearly proportional to  $n - 1$ . To get enough photo-electrons, the aerogel thickness must be increased for index  $n=1.008$ . The number of photo-electrons will saturate at a thickness of approximately 15 cm due to absorption and scattering in the aerogel.

Based on the performance of A1( $n = 1.015$ ), shown in Fig. 151(b), the number of photo-electrons at different momenta was estimated for indices of 1.008 and 1.030, as shown in Fig. 151(c,d). The value of the rejection factor for a given momentum was estimated to be 30 based on experience with A1.

**Electromagnetic Calorimeter** An electromagnetic calorimeter is planned as the most downstream detector in the MAD detector stack. The main purpose of the calorimeter is to separate electrons and charged pions. Electrons, producing showers, have nearly all their energy absorbed in the calorimeter, whereas, only a small fraction of the energy of a hadron will be absorbed. Comparing the energy release in the calorimeter with the momentum of the particle provides pion/electron discrimination.

The size of the calorimeter was selected using the GEANT simulation of MAD at 25° and 35° and at a mean energy of 7.5 GeV. The initial particle was produced in a 10 cm long liquid hydrogen target with uniform angle and momentum distributions over the MAD acceptance. The

results depend considerably on the optics applied, in particular in y-projection (perpendicular to the dispersive direction), since the calorimeter is close to the transverse focus of MAD. Based on the simulation, a lead glass array of  $3.2 \times 1.0 \text{ m}^2$  is considered for the present purposes. Since most of the events in MAD will contain only one high-energy particle, only a coarse transverse segmentation of the calorimeter is required.

It is proposed to build a lead-plastic scintillator sandwich calorimeter, about 22 radiation lengths deep, divided along the dispersion direction in 32 bars. Each bar is 10 cm wide and 100 cm long. The bar is divided in three segments along its depth in order to improve the  $e^-/\pi$  separation. Since the light attenuation in the scintillator sheets along the bar length of 100 cm is considerable, each segment is read out by two PMTs from both sides of the bar. In total the detector will include 192 PMTs.

A similar design[Am01] is used in the calorimeters in the CLAS detector in Hall B; in this case with three projections read out from triangular-shaped detector modules, employing the same compensation of the attenuation losses. With longitudinal segmentation in two segments an energy resolution of about  $\sigma_E/E \sim 0.1 \text{ GeV}/\sqrt{E}$  and a  $e^-/\pi$  suppression factor of about 100 was obtained. The sandwich contained 2.2 mm lead sheets and 10 mm plastic scintillator sheets. The light was collected with the help of optical fibers. For the design proposed a similar result is expected.

**Focal Plane Proton Polarimeter** Conventional polarimeters measure an azimuthal asymmetry from the scattering of the protons in an analyzer to determine the polarization. The incoming trajectory is determined by the focal plane MWDCs, while the outgoing trajectory is determined by tracking chambers specific to the polarimeter. The polarimeter figure of merit,  $\epsilon A^2$ , is enhanced by a large efficiency for detecting scattered protons. This requires both large polarimeter chambers - the existing Hall A polarimeter can measure scatters up to about  $70^\circ$  - and thick analyzers, up to about 1 m, to increase the scattering efficiency. Because thick analyzers also absorb a significant fraction of the protons, up to about 50% at 3 – 4 GeV/c, it is further desirable to segment the polarimeter, alternating layers of analyzer with chambers. A double analyzer, as has been used in the Hall A RCS experiment, is a reasonable compromise between increased costs and increased efficiencies.

Due to the large beam envelope with MAD, an alternate detector stack to the conventional design is desirable. In the experiments considered so far, the only significant background is  $\pi^+$  mesons, which can be sufficiently reduced through the use of a single Čerenkov detector. Use of smaller tracking detectors further forward in the detector stack reduces the cost of the FPP. The layout of the focal plane polarimeter is shown in Fig. 152. Use of a  $\text{CH}_2$  analyzer with a density near  $1000 \text{ kg/m}^3$  leads to a total analyzer mass of 4500 kg. A carbon analyzer of similar volume would yield a similar figure of merit, with about 60 – 70% greater density. To capture scatterings from the analyzer with a good geometric efficiency, the tracking chambers would need to extend about  $\pm 50 \text{ cm}$  beyond the analyzer, leading to active areas near 2.5 m wide by 4 m high. We propose to

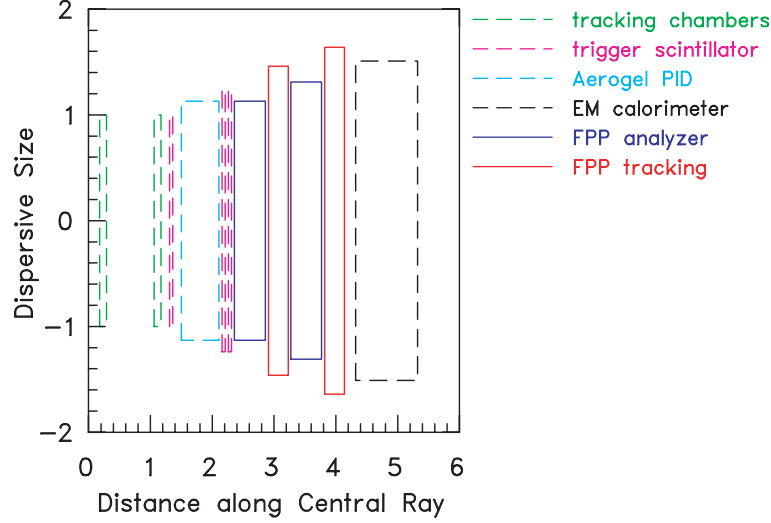


Figure 152: Layout of the MAD focal plane polarimeter.

construct a set of 4 multilayer straw-tube chambers, very similar in design to the existing Hall A FPP, to cover the above active area. With 2 cm drift cell diameter, the number of channels will be about 5000.

**Trigger Electronics** The proposed trigger electronics system will be built using commercially available components which follow VME, NIM and/or CAMAC standards. The described system will work as well with a DAQ system in a conventional environment or with a DAQ system based on Flash ADCs and Pipelined TDCs. To accomplish high singles rates in some of the detector subsystems, only modules capable of handling rates of 100 MHz or more are acceptable.

As described previously, the detector package of the MAD includes up to four scintillator planes, each made of 16 long scintillator paddles equipped with photo-multiplier tubes (PMTs) on each end. Although the main trigger will usually be formed by the signals of two planes only, all four planes will be built in the same fashion. Then, the trigger definition is very flexible and can be adjusted to the individual needs of each experiment.

The analog signal of each PMT will be split passively on the base of the tube. One signal will be fed into a pipeline Flash ADC, requiring no delay cable. The second signal will be fed into a leading-edge discriminator (e.g. CAEN V895 or C894). The specific modules mentioned parenthetically are examples of presently available off-the-shelf units. The discriminators listed above provide two copies of the logical signal. One will be used for timing purposes and put into a TDC. A programmable delay (e.g. CAEN C211) is used to adjust small timing differences within the different channels. A 16 channel mean-timer (e.g. CAEN C561 or V706) is used to combine the signals of the two PMTs of each scintillator paddle, and make this signal independent of the point of intersection. Finally the logical “or” of the 16 signals is formed in a logic module (e.g. CAEN C561

Table 25: Equipment needed for the triggering system of the MAD detector package

Device	Typical Module	Form Factor	Units (includes spares)
LE Discriminator	Caen C 894	Camac	15
Prog. Delay	Caen C 211	Camac	10
Mean-timer	Caen C 561	Camac	6
Gate and Delay	Caen C 469	Camac	4
PLU	Caen C 542	Camac	2
ECL-Nim-ECL	Caen C 467/468	Camac	6
Fan-Out	Caen C 211	Camac	5
Coinc Unit	Caen V 512	VME	4
Camac Crates			3
VME Crates			2
VME CPUs			2
Camac Controllers			3
Cables			

or V706). This signal is the trigger for each scintillator plane. Using Gate and Delay Generators (GDG, e.g. CAEN 469) and Programmable Logic Units (PLU, e.g. CAEN C542 or V495), the signals from the four scintillator planes can form various triggers, the definition of the trigger can be changed easily and other detectors, for example the Čerenkov detector, can be incorporated if needed. Some additional modules, Fan-in/Fan-Out modules, Level Converters and Coincidence Units, are needed to provide retiming signals, gates for the digitizing modules and scalers.

**Data Acquisition** The data acquisition system is built in VME using commercial components like scalers, ADCs, and TDCs where available, plus new custom-built modules that are presently under development by collaborators. The system will have a high performance that will exceed FASTBUS standards. Accommodating the detector design will require approximately 400 ADC channels, 2000 TDC channels, and 400 scaler channels. For the scintillators 60 ps resolution TDCs can be used, while for drift chambers and other detectors a resolution of 0.5 ns is adequate.

A new generation of pipeline digitizing front-end devices can be used for experiments that require speeds in excess of 5 kHz, up to 20 kHz. For pipelined ADCs, there are two foreseeable alternatives. One is a custom-built pipelined Flash ADC being prototyped by Indiana University, which might be manufactured at JLab. In the pipeline approach detector data are continuously digitized and stored in a pipeline, which is a dual-port memory. When a trigger condition is satisfied, the data are extracted from the pipeline and read out on the VME backplane. This scheme has two attractive features: 1) the pipeline approach introduces no deadtime; and 2) delay cables can be avoided. However, a possible disadvantage with respect to ADCs is that if the sampling frequency is not sufficiently high, one may suffer loss of resolution. In tests at Indiana University [IUpc], it was found that with 250 MHz and 8 bits resolution, the Flash ADC samples resulted in an energy resolution much better than the intrinsic resolution of lead glass.

Table 26: Comparison of Pb-Glass, PbF<sub>2</sub>, and PbWO<sub>4</sub> calorimeter properties.

	Pb-Glass TF-1	PbF <sub>2</sub>	PbWO <sub>4</sub>
Index of Refraction	1.65	1.85	1.85
Radiation Length $X_0$ (cm)	2.5	0.93	0.89
Moliere Radius $r_0$ (cm)	3.3	2.2	2.2
Density $\rho$ (g/cm <sup>3</sup> )	3.86	7.77	8.28
Photoelectrons/GeV	1100	1600	5000
Critical Energy (MeV)	15	8.6	

A new high-resolution pipelined VME TDC is being designed and prototyped by the Jefferson Lab DAQ group. This TDC has 60 ps resolution with 32 channels on a single slot 6U form factor, or 120 ps for 64 channels. The TDC can either run in a common start mode or a trigger matching mode. In the common start mode, a trigger starts and clears the hit counters, and a subsequent trigger initiates read-out of data since the start time. Of course, this mode will introduce deadtime. In the “trigger matching” or pipelined mode, a trigger is used to define a window in time to pull data out of a hit counter. The hit counter runs continuously even as the desired data is buffered in memory, and therefore produces very little deadtime.

### 3.A.5 High Performance Calorimeter

High intensity 11 GeV beams in Hall A offer unique possibilities for studying Real and Deep Virtual Compton Scattering (DVCS). These experiments require the construction of a large-acceptance and high-resolution electromagnetic calorimeter, capable of withstanding high levels of background. The photons need to be detected at angles as small as 10°, with a luminosity of at least 10<sup>37</sup>. This requires a calorimeter material that is radiation hard. It is also important to have a very fast time response to suppress pile-up and random coincidences.

PbF<sub>2</sub> is an attractive Čerenkov medium for electromagnetic calorimetry. Some basic properties of PbF<sub>2</sub> are listed in Table 26 and compared with Pb-Glass and PbWO<sub>4</sub>, which are commonly used in electromagnetic calorimeters.

The primary distinction of PbF<sub>2</sub> is its very high  $Z^2$  weighted density, resulting in much smaller individual element sizes. The transverse dimension of each element should be slightly larger than the Moliere radius, to optimize spatial resolution, and the longitudinal dimension should be 20 radiation lengths to fully contain the shower. High density PbF<sub>2</sub> will have lower background from hadrons (including neutrons) than Pb-Glass. The small size of the PbF<sub>2</sub> will also result in very narrow intrinsic time spread ( $< 0.6$  ns r.m.s.) in the collected light [Ap94]. The leading edge time resolution and the total pulse width are both critical parameters for suppression of accidental

coincidences and pile-up rejection. Small blocks make it practical to couple the crystals to very fast photo-tubes.

For radiation doses from 200 Gy (20 kRad) to 1 kGy (100 kRad) the radiation damage to PbF<sub>2</sub> is a factor of 10 less than SF5 Pb-Glass.[Ac98c] Radiation damage reduces the transmittance of the crystals, with the greatest effects at short wavelengths. The transmittance reduced by radiation damage to PbF<sub>2</sub> can be easily annealed with blue light as well as natural light.

Electromagnetic shower energy resolutions of  $(3 - 5.6)\%/\sqrt{GeV/E}$  and transverse position resolution of  $1\text{ mm}\sqrt{GeV/E}$  were reported for small test arrays for 1 to 6 GeV electrons [Ap94, Ac98c]. The spatial resolution may be degraded slightly with larger crystals, but it is clear that the very high spatial resolution will allow a PbF<sub>2</sub> array to be placed very near the target, without limiting the photon angular resolution.

The optimal angular coverage for DVCS experiments requires a calorimeter with a solid angle of 0.1 sr. To achieve a large solid angle coverage and high angular resolution, we propose a 1296 element array. In DVCS kinematics, with the calorimeter 3 m from the target, the design acceptance of 0.1 sr can be achieved with a photon angular resolution of 0.5 mrad.

Individual crystals will be 26x26x200 mm<sup>3</sup> rectangular blocks coupled to UV transmitting 25 mm fast PMT's. The EMI 9111WB 8-stage photomultiplier is chosen as a baseline solution. With a photo-cathode of 22 mm diameter, the PMT will cover 72% of the surface of the crystal. In addition, the PMT offers high quantum efficiency of about 28% and spectral response down to 180 nm. Simulations suggests light yields with the above solution to be about 2500 pe/GeV. The calorimeter will be arranged in a square matrix of 36x36 elements. However, the array will be flexible in design so that it can be easily reconfigured for a different geometry. A blue laser based light source coupled to each crystal will provide calibration, timing, and gain monitoring signal. Standard integrating ADC's for the readout and programmable high voltage supplies currently used in Hall A will be used.

### 3.A.6 The Hall A Beam Line

For the 12 GeV upgrade, the basic layout of the Hall A beamline and beamline instrumentation will remain the same. The quality of the beam will be somewhat compromised at the higher energies. Table 1 gives a comparison of the presently achievable beam parameters at 6 GeV and the expected beam parameters at 11 GeV.

No changes are envisaged regarding the primary diagnostic and beamline instrumentation [An03a, HallA]. This includes the present SEE Beam Position Monitors, the Hall A target OTR and the Scanners for beam profile measurements, the two RF cavity monitors (BCMs) and the Unser Monitor for beam current monitoring, the fast-feedback system to maintain the stability of the beam

Table 27: Key parameters of Beam Quality - present and with upgrade

Parameter	Present @6 GeV	With Upgrade @11 GeV
Horizontal emittance $\epsilon_x$	$2.9 * 10^{-7}$ m.rad	$9 * 10^{-6}$ m.rad
Vertical emittance $\epsilon_y$	$2.9 * 10^{-7}$ m.rad	$1.9 * 10^{-6}$ m.rad
Energy spread $\delta p/p$	$1 * 10^{-4}$	$2 * 10^{-4}$

in both position and energy, and the fast rastering system. The installation of a Synchrotron Light Interferometer for beam profile determination and the beam energy width monitoring, and a Silver Calorimeter for beam charge measurement are planned in near future (before the energy upgrade).

The beam optics and layout will also basically remain the same. Most of the modifications involved ensure that the various beam focusing and deflecting elements can reach the requisite higher fields. All the beamline magnets will remain resistive. The present plans for the dipoles (especially in the Hall A Arc section) will be modified from C-type magnets to H-type magnets by adding a return path to the yoke in order to reach the higher fields without saturation. The present beamline quadrupoles have enough margin that they are able to reach 170% of their design current (enough to reach 11 GeV) with acceptable field quality. Higher current power supplies for both will be needed for the upgrade.

The Hall A beam line is equipped with a Møller polarimeter to measure the longitudinal polarization of the electron beam. The analyzing power  $A$  depends on the scattering angle in the CM frame  $\theta_{CM}$  and has its maximum of  $7/9$  at  $\theta_{CM} = 90^\circ$ . A ferromagnetic foil, magnetized in an external magnetic field of about 0.03 T is used as the target. Both electrons, scattered close to the horizontal plane, are detected with the help of a spectrometer consisting of three quadrupole magnets, focusing the electrons onto two vertical slits in a dipole magnet, which provides a horizontal field. The dipole magnet deflects the electrons downward, away from the beam line, toward the detector. The beam also passes this dipole magnet, through an area shielded against the magnetic field. The polarimeter can measure the beam polarization in about 30 min with a relative error of about 0.2% statistical and 3% systematic.

Two factors limit the useful beam energy range of the polarimeter: a) the spectrometer acceptance, defined by the positions of the magnets and the available field strength, and also the positions of the collimators; b) the beam deflection in the Møller dipole caused by the residual field in the shielding insertion. At the moment, the first factor gives the lower limit of beam energy 0.8 GeV, the second the upper limit at about 6 GeV. In order to operate at 11 GeV an upgrade of the polarimeter is proposed, keeping the target and the dipole magnet at the same positions along the beam line by reducing the bend angle of the dipole from 11 to  $7.3^\circ$ , thereby reducing the maximum field needed in the dipole, lifting the detector by 10 cm, moving the 1-st quadrupole magnet 40 cm downstream, adding a 4-th quadrupole magnet at 70 cm from the Møller target, and adding a shielding pipe to the magnetic shielding insertion in the dipole magnet.



The four-quadrupole design provides a sufficiently large acceptance on the scattering angle  $\Delta\theta_{CM} \approx 20^\circ$ . The residual field in the beam area inside the dipole is reduced both by reducing the requirements for the magnetic field strength and by using additional magnetic shielding. The latter was optimized using a TOSCA simulation. The present diameter of the bore in the shielding insertion is 4.0 cm. The diameter of the electron beam line before and after the Møller polarimeter is 2.54 cm. It is possible to increase the attenuation of the shielding insertion by placing a coaxial magnetically isolated pipe with inner/outer diameters of 2.54/3.4 cm, made of magnetic steel AISI-1006, inside the bore. The shielding pipe is centered in the shielding insertion bore with an additional external isolating pipe of a non-magnetic material. The shielding pipe length should be 10 cm longer than the shielding insertion length in order to reduce the influence of the fringe field outside of the shielding insertion. The new design attenuates the dipole magnetic field to an acceptable level up to 14.8 kG, corresponding to a beam energy of 11 GeV and a dipole bending angle of  $7.3^\circ$ . This field can be provided with the power supply currently used for the dipole.

The Hall A Compton polarimeter determines the absolute polarization of the electron beam by measuring the Compton backscattering asymmetry of polarized light from polarized electrons. A detailed description of the existing Compton polarimeter can be found in Ref. [Ba96a]. In brief, the Compton polarimeter consists of a magnetic chicane made of 4 dipole magnets over about 15 m. The chicane displaces the beam downward by 300 mm where it interacts with polarized light confined in a High-Finesse Fabry-Perot cavity. The polarized light is injected from a 1064 nm infrared laser. The backscattered photons and the recoil electrons are detected in a  $\text{PbWO}_4$  electromagnetic calorimeter and silicon-strip detector, respectively. The Compton polarimeter chicane has been designed to operate up to a maximum beam energy of 8 GeV. This limit is due to the 1 m long dipoles in the chicane which have a maximum pole-tip field of 1.5 T.

To upgrade the maximum beam energy of the chicane to 11 GeV, the chicane displacement will be decreased to 218 mm. This requires raising the bottom two dipoles along with the optics cavity and the photon calorimeter by 82 mm.

There are at present two independent devices to measure the absolute energy of the beam in Hall A, the ARC and EP methods. The present EP design enables a measurement of the beam energy to about 6 GeV. A major redesign of the device would be necessary to implement it for energies above 6 GeV. To implement the ARC method at higher energies, the ARC dipoles, modified from C-type magnets to H-type magnets, will have to be remapped. The mapper for the 9th dipole will also have to be modified.



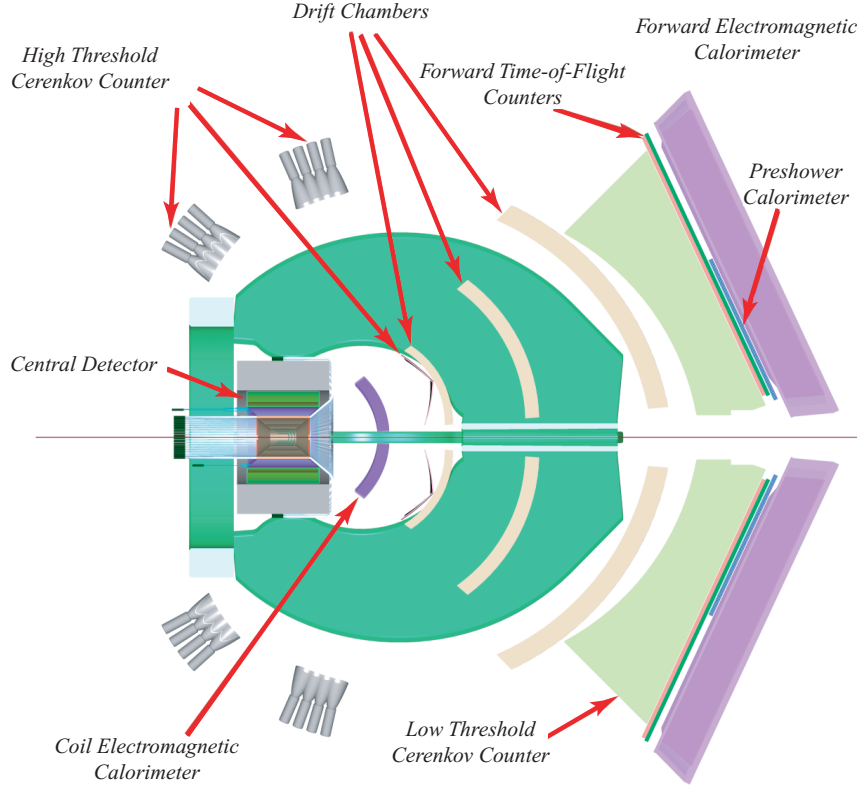


Figure 153: The upgraded CLAS<sup>++</sup> detector.

### 3.B Hall B Upgrade and the CLAS<sup>++</sup> Detector

#### 3.B.1 Overview

The CLAS<sup>++</sup> detector is shown in (Fig. 153). It has been designed to meet the basic requirements of the physics program currently anticipated for the 12 GeV Upgrade.

The main features of CLAS<sup>++</sup> are:

- High operating luminosity of  $10^{35} \text{cm}^{-2} \text{s}^{-1}$  for hydrogen targets, a ten-fold increase over current CLAS operating conditions.
- Improved detection capabilities for forward-going high momentum particles. Charged particles that bend outwards in the torus field can be reconstructed for angles as low as 5 degrees. Photon detection will be possible for angles as low as 3 degrees. Acceptances for electrons are momentum-dependent, and range from about 8 degrees to 40 degrees.
- Capability to detect the recoil baryons at large angles.

- Larger momentum range for the separation of electrons, pions, kaons, and protons. This is achieved with better resolution time-of-flight counters, and with the installation of a new gas Čerenkov detector.
- Improved hermeticity for the detection of charged particles and photons in regions where CLAS currently has no detection capabilities, achieved by instrumenting the coil regions and by extending the polar angle range for photon detection to 135 degrees.

CLAS<sup>++</sup> makes use of many of the components of the current CLAS detector.

- The torus magnet will be re-used in a slightly modified form.
- All large forward calorimeters will be used for electron, photon, and neutron detection.
- All gas Čerenkov counters will be used with adjustments in the optics and replacement of 1/3 of the mirrors.
- The time-of-flight scintillator material will be used to make smaller scintillator slabs for better timing.
- Part of the CLAS drift chamber electronics will be re-used as well.

A major new component in CLAS<sup>++</sup> is the Central Detector. Its main component is a superconducting solenoid magnet, which has a dual function: It replaces the existing mini-torus for shielding of the Møller electrons, and it provides the magnetic field for the momentum analysis of charged particles at large angles. Time-of-flight scintillators are used to provide particle identification at scattering angles greater than 40 degrees. Due to the limited space available excellent timing resolution is essential. Tracking at large angles is provided by a combination of drift chambers with cathode strip readout and a microstrip detector near the vertex. Since most charged tracks will have momenta of 1 GeV/c or less sufficient momentum resolution can be achieved even in the limited space available for tracking. A compact electromagnetic calorimeter based on tungsten powder and scintillating fiber technology provides photon detection capability for the angle range from 40-135 degree.

Much of the instrumentation of CLAS will be re-used in the CLAS<sup>++</sup> Forward Detector (FD). However, some modifications and additional detectors are needed in the Forward Detector as well. The main new component is a threshold gas Čerenkov counter for pion detection. The light collection is accomplished using a mirror system that focuses the Čerenkov light onto photomultipliers located sideways of the torus magnet. This area will be accessible after the removal of the CLAS drift chambers. The Čerenkov counter will allow electron and pion identification up to nearly 5 GeV/c. Beyond 5 GeV/c electrons are identified in the forward electromagnetic calorimeter.

There is also additional electromagnetic calorimetry placed in the area of the torus coils for improved hermiticity. Lead-tungstate crystals have emerged as a good choice for this detector.

A pre-shower detector will be inserted in front of the existing CLAS electromagnetic calorimeters. This detector will allow separation of single photons from  $\pi^0 \rightarrow \gamma\gamma$  events especially needed for deeply virtual Compton scattering.

All drift chambers in CLAS will be replaced by new ones that will cover a smaller angle range with a factor of two smaller cell sizes to reduce the accidental hit occupancy due to photon interactions allowing for a corresponding gain in luminosity.

The existing forward detection system will be modified to extend particle identification and reconstruction to higher momenta. This will be accomplished by several means: The timing resolution of the scintillation counters will be improved by using smaller scintillator slabs, and by adding an additional layer of scintillators, and by replacing the PMTs by new ones with better timing characteristics. This is expected to improve the timing resolution to about 60 psec. The existing gas Čerenkov counter will be modified for improved pion detection capabilities for momenta greater than 2.7 GeV/c. .

With these modifications and additions to the existing CLAS components, CLAS<sup>++</sup> will be able to carry out the core program for the study of the internal nucleon dynamics and hadronization processes by measuring exclusive, semi-inclusive, and inclusive processes. In the following sections the new components are discussed in some detail.

### 3.B.2 CLAS Torus Magnet

The CLAS<sup>++</sup> upgrade is based on using the original CLAS Torus with some modifications. The minimum modification required will be to replace all 72 out-of-plane (OOP) supports. These supports keep the coil centered in the vacuum case and support both magnet and gravitational loads. Experience gained from the original CLAS operation and detailed calculations have shown this to be a requirement for operating a high field solenoid inside the torus at full field. The CLAS Torus will also be modified to allow for the addition of the Central Detector, Solenoid Magnet, and iron flux return. This will require that the backward (upstream) end of the coils are moved out. After all modifications have been completed, the position and geometry will be surveyed, and the magnetic field will be mapped in the region where particle tracking will be done, i.e. up to about 40° in polar angle, and for all six sectors.

### 3.B.3 Central Detector

CLAS<sup>++</sup> consists of a forward detector system (FD), which is sensitive to charged and neutral particles emitted at lab angles between 5 and 40 degrees, and a central detector (CD), which covers

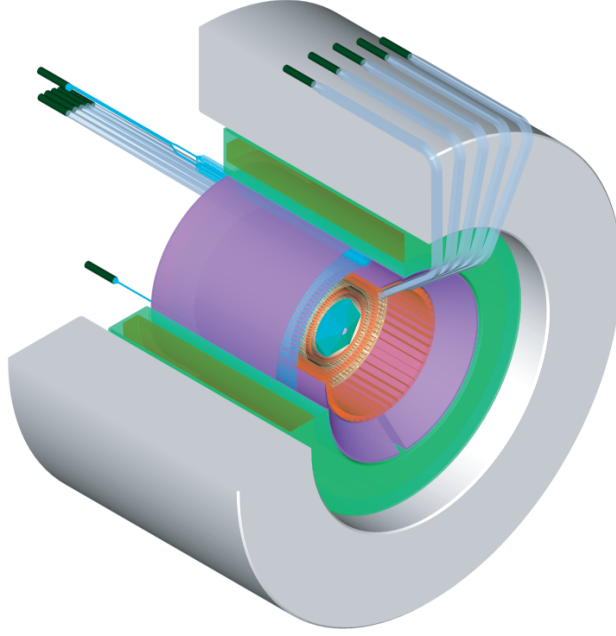


Figure 154: Central detector region showing (from the outside to the inside) the flux return iron, the super-conducting solenoid, and the layout of the central EC and TOF, the central tracker, and the microstrip detector assemblies.

the angular range from approximately 40 to 135 degrees. A layout of the central detector and its solenoid is shown in Fig. 154.

The central detector is located within a superconducting solenoidal magnet which performs a dual function: it curls emitted low-energy Møller electrons into tight spirals which are directed into a cylindrical absorbing tube, and it provides the magnetic field for particle tracking. An iron flux-return surrounding the magnet shields the torus coils from the strong magnetic field of the solenoid.

A major thrust of the experimental program will be measurements of deeply exclusive scattering (DES). DES events are characterized by the presence of the scattered electron and one or two hadrons in the forward spectrometer, and typically one recoil baryon in the central detector. Because we rely on the missing mass technique to identify reactions and to reject background we wish to optimize the missing-mass resolution and to maximize the multi-particle acceptance. This achieved by a combination of tracking devices covering the full angle in azimuth, and the polar angle range from  $40^\circ$  to  $135^\circ$ .

In addition to the tracking devices, the central detector consists of an array of scintillator paddles used to measure time-of-flight (CD-TOF) of the charged particles, and a central electromagnetic calorimeter (CD-EC) use to measure the energy of photons emitted in the central region. With the projected time resolution of 50psec the CD-TOF will be able to separate pions and protons up to 1.2 GeV/c, and kaons from pions up to 0.6 GeV/c. In addition it will be very important

in rejecting the out-of-time hadronic background. This can be accomplished with time resolutions on the order of 1 ns. The CD-EC will complement photon detection in the forward calorimeter, cover the full azimuthal angular range, and the polar angle range from  $40^\circ$  up to  $135^\circ$ . Most of the photons hitting the CD-EC will have energies from 50MeV to up to 1 GeV. The CD-EC has been designed to have sufficient “depth” to fully contain the energy deposition of 1 GeV photons, and allow detection of photons in this energy regime with approximately the same energy resolution as the forward angle calorimeter.

**Superconducting Solenoid Magnet** At the core of the central detector is a superconducting solenoid to provide a central longitudinal magnetic field of up to 5 Tesla. The solenoid magnet serves the following functions:

- determine particle momenta and charge via tracking in the central tracking devices.
- keep Møller scattered electrons from reaching the detectors by guiding them to a shielding pipe made of heavy metal. The maximum luminosity CLAS<sup>++</sup> can be operated at is limited by the degree to which tracking chambers are shielded from the Møller electrons and secondary particles. This technique has been used successfully during the CLAS eg1 runs, with the magnetic field provided by the 5 Tesla superconducting Helmholtz magnet that was used with the CLAS polarized target magnet.
- provide the magnetic field for a solid-state dynamically polarized target. This requires a 5 Tesla polarizing magnetic field with an inhomogeneity of  $\Delta B/B \leq 5 \times 10^{-4}$  for polarized  $NH_3$  material. The polarized target operation adds homogeneity constraints which will require additional correction coils.

**Magnet Design** A magnetic design using TOSCA<sup>(R)</sup> 3D has been performed to establish the basic magnetic requirements, provide 3D field maps for Møller background analysis and to produce basic engineering information about the magnet. A single layer, superconducting, warm iron yoke magnet was chosen as the optimal configuration. The field excitation ranges from 2T to 5T. The design constraints were as follows:

- reduce the fringe field in the proximity of the CLAS coils to minimize the CLAS’s out of plane forces.
- have a sufficiently large internal radius to house the central detectors, and
- an outer yoke radius to fit within the modified CLAS cryostat
- an opening in the forward region to allow detection of particles from  $5^\circ$  to  $40^\circ$ .

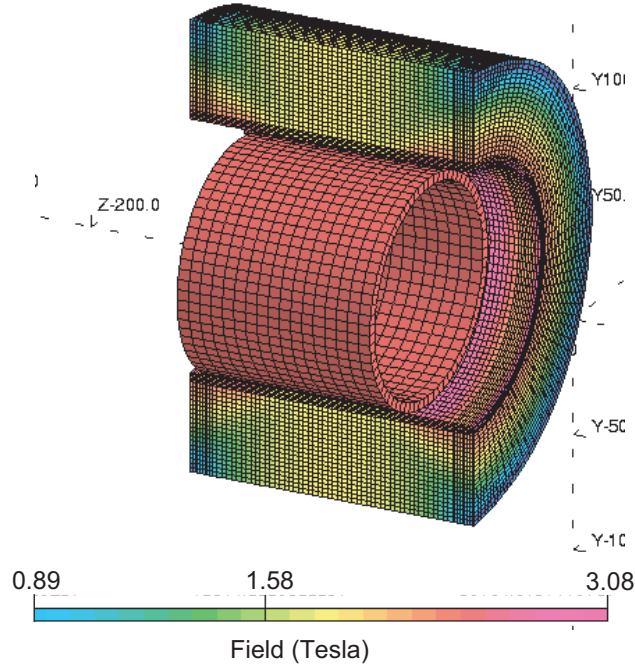


Figure 155: Field distribution in the solenoid magnet and the flux return yoke. The central field is 5 Tesla. The field in the iron yoke is typically less than 2 Tesla. Saturation field levels of up to 3 Tesla occur only in a few localized areas near the edges.

An important aspect of the iron yoke is to avoid magnetic interference with the toroidal magnet which may otherwise produce unacceptably high out-of-plane forces at the torus coils.

The magnetic design uses a TOSCA-generated solenoid coil. The yoke, which is a simple cylinder with an outer diameter of 1.96 m. and an inner diameter of 1.10, was modeled as a nonlinear iron (1006 steel). The length of the yoke is 1.18 m. The Superconducting coil is off centered within the yoke by 0.1252 m. The peak field produced within the yoke is 3.1 Tesla and within the coil windings of 6.4 Tesla. A projected view of the magnet in the cryostat and the flux return yoke is shown in Fig. 154.

The iron flux return reduces the total current required, increases the field homogeneity, and reduces the fringe field. An important aspect of the iron yoke is to avoid magnetic interference with the toroidal magnet which may otherwise produce unacceptably high out-of-plane forces at the torus coils. Since shielding the Møller electrons relies on the fringe field the geometry of the flux return has been optimized to avoid reducing the shielding effect.

Fig. 155 shows the magnetic field density distribution in the magnet bore and the flux return iron. The iron is sized to minimize saturation effects, while keeping its size and weight compatible with installation in the Torus magnet. At the bottom the distribution of the magnetic field density in the r-z plane is shown , where z is the axis along the beam line, and r is the radial distance from the solenoid symmetry axis. The distribution along the beam axis varies rapidly while the

Table 28: Central Electromagnetic Calorimeter parameters

Total Radiation Length	10 -12
Radial Space (radial thickness)	$\sim 10$ cm
Energy Resolution	$\approx 6\%/\sqrt{E}$
Angular Resolution, $\delta\theta = \delta\phi$	$\sim 1^\circ$
Timing Resolution, $\delta t$	few nsec
Energy Threshold, $E_\gamma^{min}$	$\leq 50$ MeV

variation along  $r$  is much more uniform. The extended fringe field is important for guiding the Møller electrons far enough away from the interaction region to a shielding pipe (not shown) where they can be absorbed.

## Central Electromagnetic Calorimeter

**Overview** The central electromagnetic calorimeter covers detection angles in the polar range of  $40^\circ \leq \theta \leq 135^\circ$  and in almost the entire azimuthal range  $0^\circ \leq \phi \leq 360^\circ$ . It is designed for the reconstruction of  $\pi^0$  and  $\eta$  by their neutral decays, therefore, for the detection of multi  $\gamma$  - events . The design parameters are defined to meet an operational luminosity of  $L \sim 10^{35} \text{ cm}^{-2} \text{ sec}^{-1}$ . The following sections describe the technical requirements, the detailed concept design and estimates for the calorimeter performance.

**Requirements** The available radial space for the calorimeter material, inside the magnet, is limited to  $\sim 10$  cm. The calorimeter must provide adequate energy and spatial resolutions to cleanly identify  $\pi^0$  and  $\eta$  . Typical energies of decay photons, produced under large angles ( $> 40^\circ$ ) at beam energies of 12 GeV, are up to  $E_\gamma \sim 1 \text{ GeV}$ . Reasonable energy resolutions with these size restrictions can only be achieved if very dense materials are used. Table 28 shows the main design parameters of the Central Calorimeter.

**Scintillating Fiber/Tungsten Powder Calorimeter Design** The overall view and basic dimensions of the central calorimeter mounted inside the solenoid magnet are shown on Fig. 156. Dense Tungsten metal powder is used as shower material. The calorimeter has a cylindrical shape: thin plastic scintillating fibers run in the direction parallel to the beam and are read out from the upstream end, see Fig. 157. Fibers are grouped in sectors of equal size. Each sector combines all fibers covering an azimuthal angle range  $\Delta\phi \approx \pm 0.6^\circ$  to a single photo-multiplier tube readout channel that provides energy,  $\phi$  and timing information. In the radial direction, there are one or two layers of fibers all bent at the same radius with both ends brought out of the sensitive volume. This circular layer of grouped fibers provides independent measurements of the polar angle  $\theta$  of the



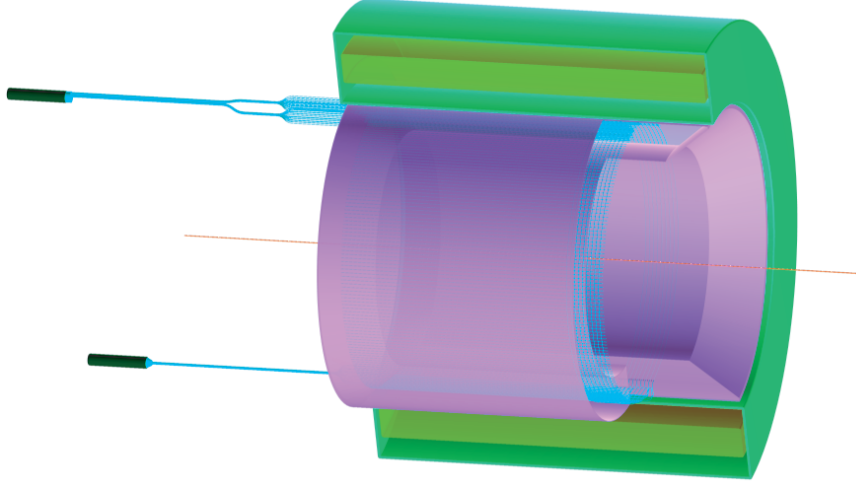


Figure 156: Perspective view of the central electromagnetic calorimeter inside the solenoid magnet.

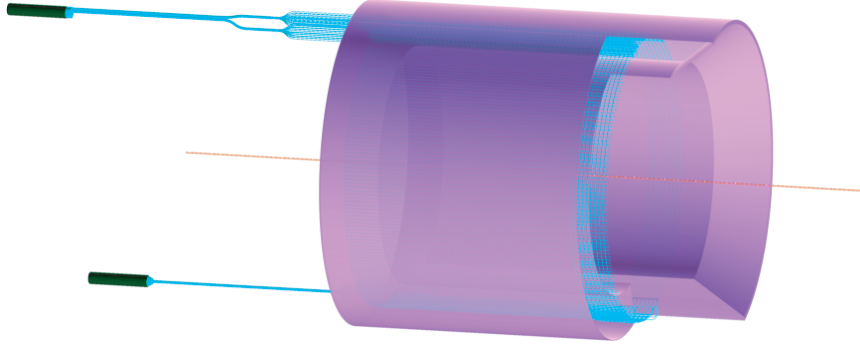


Figure 157: Central calorimeter. The tungsten powder volume and some of the axial readout fibers are shown at the left. Some of the radial fibers are indicated at the right side. The radial fibers are brought to the readout end through a slot at the bottom of the calorimeter.

shower. To have resolutions of  $\delta\theta \approx 1^\circ$  there will be a total of about  $\sim 50$  channels per polar angle measurement.

The implementation of such topology of scintillating fibers within essentially the same sensitive volume is only possible because of the powder technology, the volume is filled by loose tungsten powder. Since the so called “green density” of the Tungsten powder to be used as absorber is of about  $12 \pm 0.2 \text{ g/cm}^3$ , the whole structure becomes very efficient, especially providing high sampling ratios and frequencies with fibers as thin as 0.5 - 0.75 mm or even of smaller diameters. This particular feature allows matching two requirements, i.e. to have sufficient energy resolution and small overall dimensions at the same time.

**Expected Performance** To estimate the calorimeter response one can use parameterizations based on simulation and previous calorimeter data. We have used parameterizations during



the initial design phase for a fast estimation of the calorimeter basic dimensions and characteristics. The containment of the shower is parameterized using [Fa85]:

$$L(98\%) = 2.5 * [\log(\frac{E}{\epsilon}) + 1.2] * X_o(cm)$$

$L$  gives the length in centimeters that contains about 98% of the energy of the shower.  $E$  is the energy of the incoming photon,  $\epsilon$  the critical energy of the material and  $(X_o)$  the radiation length of the mix in centimeters. The material in the calorimeter is a mix of tungsten powder and scintillating plastic (Polystyrene) fibers. The radiation length for the mix  $(X_o)$  that contains a fraction  $y$  of scintillating plastic per volume and a fraction  $(1 - y)$  of tungsten powder absorber, is obtained using:

$$\frac{1}{(X_o)} = \frac{y}{X_{Sci}} + \frac{(1 - y)}{X_{Powder}}$$

For the powder with a fraction  $x$  of the pure tungsten density the radiation length is

$$X_{Powder} = X_{PureTungsten} / x.$$

The critical energy of the mix is obtained using:

$$\epsilon = y\epsilon_{Sci} + (1 - y)\epsilon_{Powder}$$

The results are shown in Fig. 158. The values of  $L$  are plotted versus the fraction of scintillating plastic by volume for three values of the powder density:  $x = 0.62$  (current loose powder),  $x = 0.8$  (cold pressed density currently obtained) and  $x = 1.0$ , pure tungsten. One can see that if the radial thickness of the calorimeter, using loose powder at  $x = 0.62$ , is limited by  $\sim 10$  cm, then the fraction of scintillating plastic should not exceed  $\sim 35\%$  per volume.

The other important figure-of-merit is provided by the sampling errors (in the energy measurements). For a given material ( $x = 0.62$ ), these sampling errors are a function of the fraction of scintillating plastic in the calorimeter  $y$  (sampling fraction), and the diameter of the fibers,  $\phi$  (sampling frequency). The corresponding parameterization for sampling errors are given by [Wi00]:

$$(\frac{\sigma}{E})_{sampling} = 0.02 * \sqrt{\frac{\phi(mm)}{f_{sampl}}}$$

where  $f_{sampl}$ , the sampling ratio for minimum ionizing particles (mip) is calculated using:

$$f_{sampl} = \frac{1}{1 + \frac{(1-y)}{y} * x * \frac{dE_W}{dE_{Sci}}}$$

where,  $dE_W$  and  $dE_{Sci}$  are the energy depositions by minimum ionizing particles in 1cm of tungsten (22.1 MeV/cm) and polystyrene (2.0 MeV/cm), respectively.

Figure 159 shows the sampling errors versus the fraction of scintillating plastic by volume for four different fiber diameters (0.25, 0.5, 0.75 and 1 mm), at a powder density of  $x = 0.62$ . One

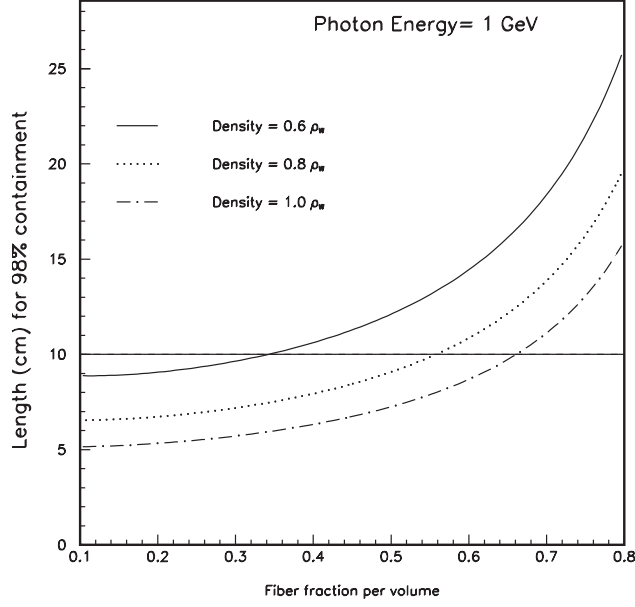


Figure 158: Containment versus fraction of plastic.

can see that for an absorber density of  $11.8 \text{ g/cm}^3$  ( $x=0.62$ ), a tungsten powder based sampling calorimeter built with fibers of 0.5 mm in diameter and with a fraction of scintillating fibers of 35% per volume can reach energy resolutions better than  $\sim 6\%$  at 1 GeV energies. These resolutions are similar to the one reached by the KLOE [An96b] and JETSET [He90] calorimeters using larger amount of scintillating fibers. In the same figure also is shown the value obtained by the KLOE collaboration [An96b] with a sampling calorimeter of 23 cm of radial thickness built at  $y=0.5$ , using lead absorber and 1 mm polystyrene fibers.

**Prototyping and Simulations** The proposed sampling calorimeter will use a new calorimetry construction technology. There are open questions that need to be answered, although some initial tests already have been successful. An important test will be to establish an efficient assembly procedure when fibers having different directions and shapes are installed in the same volume.

A prototype consisting of 12 modules is under construction to examine all basic properties of the calorimeter. The goal is to test the calorimeter in a photon or electron beam in the very near future. The prototype will have 10 cm thickness (12 radiation lengths) with a fraction of plastic of 35% by volume using polystyrene fibers of 0.75 mm in diameter.

**Central Time-of-Flight System** A conceptual view of the central TOF system is shown Fig. 160. The active scintillator area consists of a cylinder of radius 26 cm and length 50 cm. The thickness of the detector is 2 cm. It is located inside the solenoidal field and must therefore be able to operate in the high magnetic field. The design goal is to achieve timing resolution of  $\sigma=50 \text{ ps}$ . This timing resolution allows separation of pions from kaons up to 0.64 GeV/c and pions from protons up to

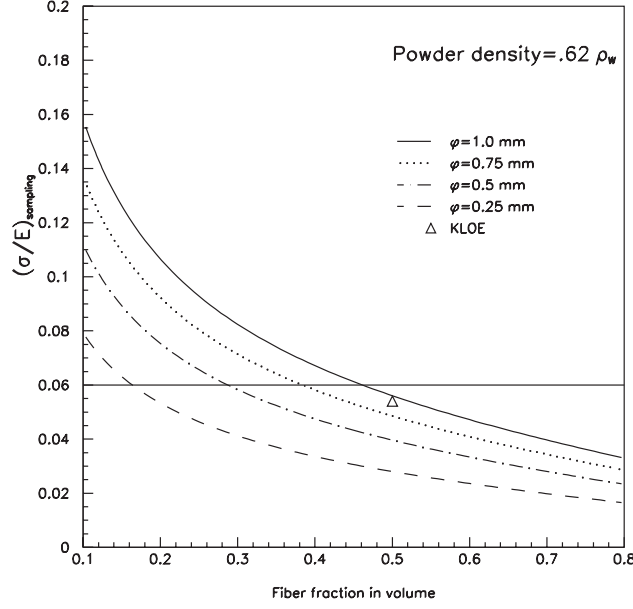


Figure 159: Sampling errors versus fraction of plastic.

1.25 GeV/c (Fig. 161). This assumes a “ $4\sigma$ ” difference in time between the two particles and allows identification of a signal in the presence of other particles with ten times higher rates.

**Expected Rates** The rates in the scintillators for the existing CLAS detector have been studied at two different beam currents and used to predict the counting rates at a luminosity of  $10^{35} \text{ cm}^{-2} \text{ s}^{-1}$  [Sm02a]. We summarize the results here for both the central and the forward detector systems. The rates are given in Table 3.B.3 at two thresholds. The expected integrated rates for the central and forward detectors are approximately equal. The current threshold setting for the counters is 20 mV, but efficient operation can be achieved at a threshold of 30 mV, which reduces the rate considerably (Fig. 162). The forward detector elements will have a typical rate per counter at 30 mV of about 750 kHz. At this threshold, the central detector has an integrated rate of 40 MHz. In order to keep the rates below one MHz per counter, we require approximately 50 channels of electronics.

**Options** The traditional scintillator detector array for TOF measurements in the central detector is challenging due to the magnetic field of the solenoid which may operate at several Tesla. Hybrid photomultipliers such as Hamamatsu R7100U-07 and DEP model PP0350G can operate in magnetic greater than 1.5 Tesla with no reduction in pulse height. The field in the region inside the solenoid near the ends of the scintillator is less than 1 T, so hybrid PMTs are an option for use with short light guides.

A second option is to use light guides to bring the light out of the high magnetic field to the region outside the yoke and use standard PMTs. The field surrounding the yoke is no less than

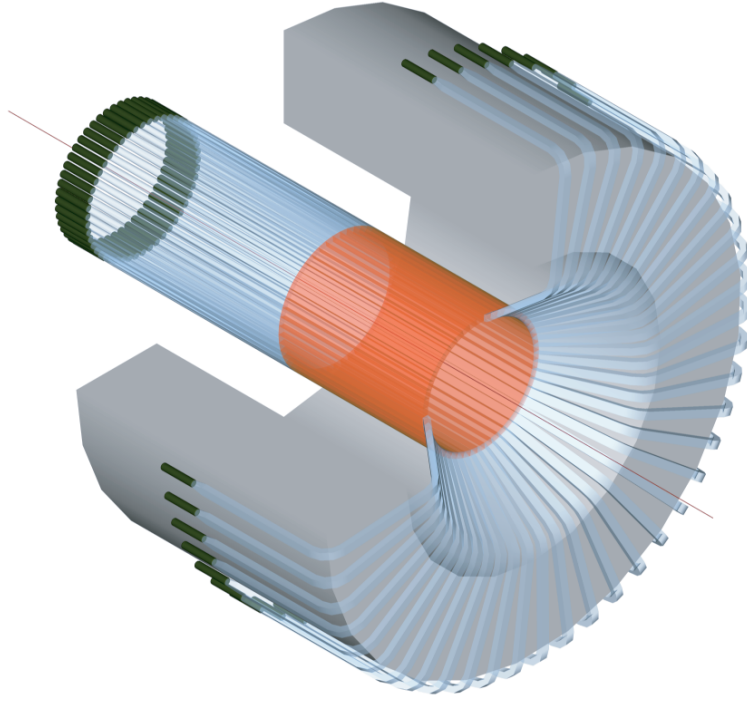


Figure 160: Perspective view of the central TOF system. Scintillator material shown in red color. In this option the scintillator light is transported to regions of reduced magnetic field using light guides (shown in translucent light blue color)

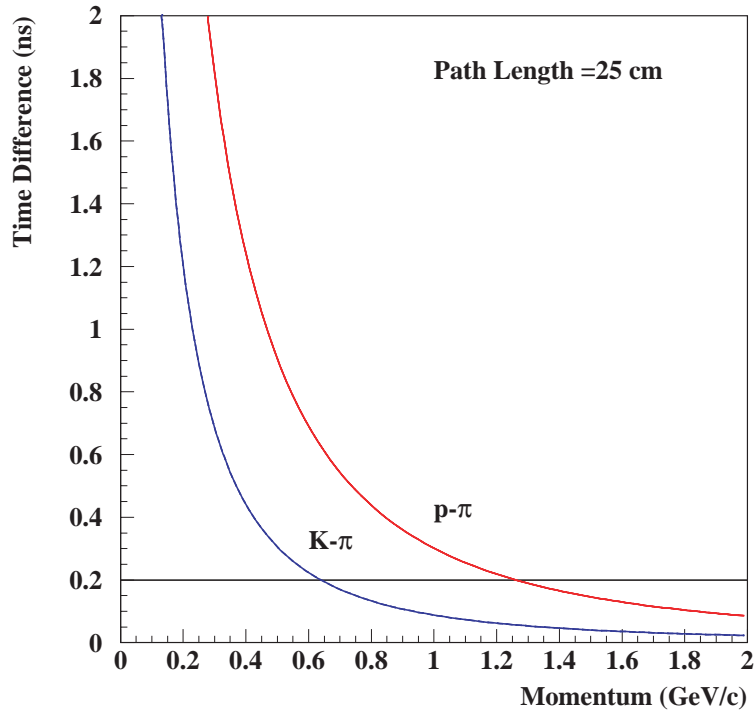


Figure 161: Time differences between protons and pions, and between kaons and pions over the 25 cm path length expected for the outer TOF system.

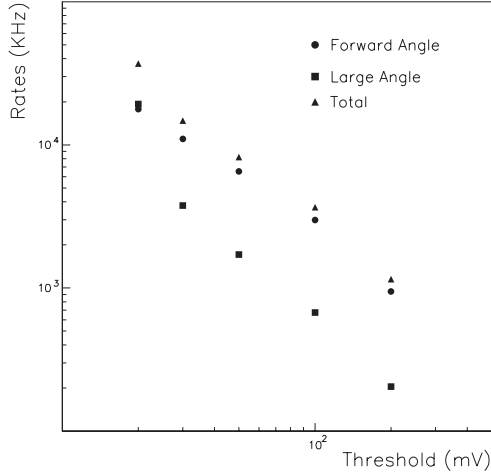


Figure 162: Rates summed over all six sectors as a at a luminosity of  $0.9 \times 10^{34} \text{cm}^{-2} \text{s}^{-1}$ . When the threshold is increased by a factor of two the count rates drop by a factor of between two to three.

The scalar rates in the CLAS scintillators extrapolated to a luminosity of  $10^{35} \text{cm}^{-2} \text{s}^{-1}$ . The rates are summed over all six sectors.

Angular Range	Threshold (mV)	Rate (MHz)
Forward	100	32
Central	100	8
Total	100	42
Forward	20	214
Central	20	243
Total	20	457

70-100 G, where standard magnetic shielding is challenging, though not impossible. We note that in the regions outside the solenoid, the magnetic field of the torus cannot be neglected, although it is not included in the present field tables.

**Central Tracker** The central tracker is located inside the central solenoid. Fig. 154 shows the layout of the entire area. A gas-filled wire chamber occupies the radial space from 12 to 25 cm. The radial space from 5 to 11.18 cm is occupied by a silicon strip detector.

The wire chamber design is cylindrical with axial anode wires arranged as four, 2-layer (staggered) superlayers with inside, inner and outside cathode foils. Foils reduce the need for additional field wires and lower the wire tension and thus, the thickness of the endplate. The endplates are angled such that the wires all subtend approximately the same range in scattered angle, from 40 to 135 degrees in the laboratory frame. A perspective view is shown in Fig. 163.

There are a total 2 super-layers, 2 layers each, 80 anode wires and 80 field wires per layer, with the drift distance varying from 0.22 to 0.91 cm. The anode wires provide the electric field to produce the avalanches and resulting gas gain. The anode wires will be read out to provide a precise time measurement as well as a phi measurement by converting the drift time into a drift distance. The z-position-sensitive readout is primarily via cathode pads; a drift-time measurement gives a measure of the azimuth, phi, while a charge measurement of several cathode pads gives theta information. When the anode avalanche multiplicity is one, the anode time information will be used for the phi measurement. In case of higher multiplicity on one anode wire, the time information will come from the cathode strips.

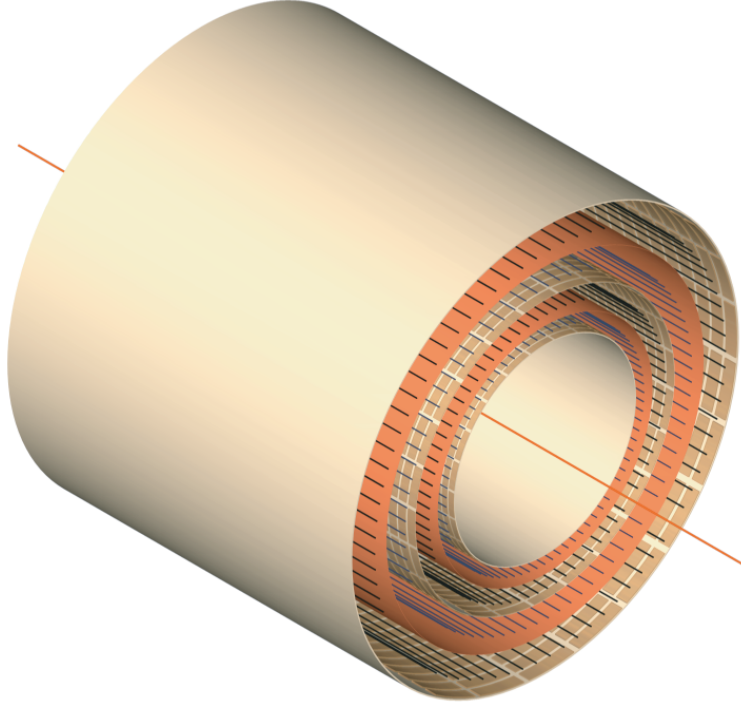


Figure 163: Cathode chamber view of two superlayers.

The accidental rate is proportional to the solid angle of the pads relative to background source times the time window. Compared to the present CLAS detector, we will have roughly the same number of channels per layer as Region 1; and a time window on the inner layer a factor of 10 smaller than Region 1. The major reduction in electromagnetic background comes from the solenoidal shielding scheme. Tests using a Helmholtz coil and cylindrical absorber showed that the dominant background was directed forward from the source (the mouth of the absorbing cylinder). We thus expect that the central tracker will be adequately shielded from any Møller background.

For  $B=3$  Tesla,  $P = 1$  GeV/c, 20 cm path and a  $100 \mu m$  accuracy  $\delta S$ , we estimate that

$$\frac{\delta P_{\perp}}{P_{\perp}} = 2.2\% .$$

The inner part of the central tracker consists of six layers of a silicon microstrip detector. In addition to providing tracking and vertex reconstruction (when combined with the gas chamber for polar angles from  $40^\circ$  to  $135^\circ$ ), the microstrip detector will provide tracking information and vertex reconstruction for the polar angle from  $5^\circ$  to  $40^\circ$ .

**Silicon Strip Detector** The limited radial space available in the Central Detector region for particle detection forces the charge particle tracking detectors to be located very close to the target in order to retain acceptable momentum resolution. Use of a small microstrip detector near the target can provide excellent position resolution, which will provide both position measurements

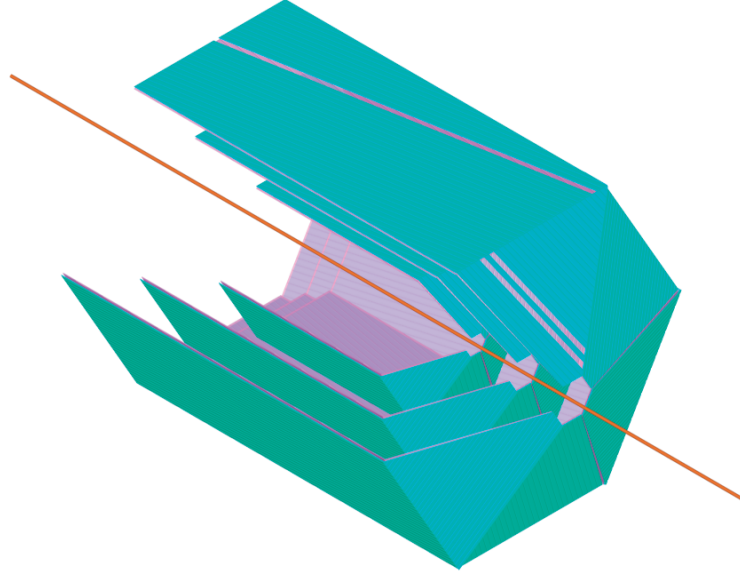


Figure 164: Concept of a Silicon Strip Detector covering the angular range from  $5^\circ$  to  $135^\circ$ . The orientation of the strips is indicated as well. We anticipate that the signal readout will be in the back. A total number of 50,000 readout channels are needed for full coverage. The signal readout will be at the back end.

close to the interaction point for excellent angle and vertex resolution, as well as providing good momentum determination for large angle tracks. These aspects are of particular importance in the detection of relatively low momentum protons and recoil hyperons, e.g.  $\Lambda \rightarrow \pi^- p$ , as well as in resolving the decays vertex of  $K_s \rightarrow \pi\pi$ . As mentioned earlier, the microstrip detector will also provide tracking at forward angles to aid in the reconstruction of high momentum tracks and in regions which are blocked by the torus coils. The track segments near the target can be linked up with tracks reconstructed in the forward angle tracking chambers to improve angle and momentum resolution. This is especially important for the CLAS<sup>++</sup> configuration where the first tracking chamber is located at a distance of about 2 meter from the target.

Fig. 164 shows a possible conceptual layout of a silicon strip detector, arranged in 6 layers around the target. The six layers (only the 3 superlayers are shown, each contains two stereo layers) provide 3 space points (x, y, z) for a given track. Alternating layers have strips at different angles to provide stereo readout and resolve ambiguities. In the large angle region the strips can be arranged to provide  $\pm 10^\circ$  readout. This will provide near optimal momentum resolution for tracks in the longitudinal solenoid field, while at the same time giving good polar angle resolution due to the excellent position resolution. In the forward region the strips are arranged to have a much larger crossing angle, giving excellent angle resolution for forward going tracks down to angles of  $5^\circ$ . The graph shows also a possible strip layout of the silicon wafers. A strip pitch of  $300\mu\text{m}$  is assumed which is expected to result in a position resolution of better than  $100\mu\text{m}$ . The first two layers may consist of  $100\mu\text{m}$  thick silicon wafers, while the four outer layers, which are considerably larger could be as thick as  $280\mu\text{m}$ . Using thinner wafers for the inner layers would allow detection

of recoil protons down to lower momenta. To limit the effect of multiple scattering, we consider the possibility of having strips on either side of the wafer for the outer four layers, which would reduce the multiple scattering effect considerably, and improve the momentum resolution. However, such design considerations will have to be carefully balanced against complications in the detector construction, and the reduction of the readout signal for minimum ionizing particles, among others.

**Instrumentation** The readout chips, in die form are attached to a substrate that is attached to the SSD. The substrate provides a pitch transition from the detector ( $300\text{ }\mu\text{m}$ ) to the readout chips ( $50\text{ }\mu\text{m}$ ), allows mounting the chip close to the strip, allows a certain degree of thermal matching and mechanical support, provides the routing for bias voltages and control signals and serves as a support for the output cable/fiber assemblies.

The substrate(s) may be FR-4 or polyimide High Density Interconnect (HDI) (a.k.a. flex interconnect). Ceramic substrates ( $\text{Al}_2\text{O}_3$ , BeO, AlN) are attractive for their thermal performance. For example, AlN has a coefficient of thermal expansion very similar to silicon. On the other hand, BeO has very high thermal conductivity. The wire bond pads must be gold-plated for reliable bonding.

The strips are wire bonded to pads on the substrate. These pads are routed to the appropriate chips and wire bonded to the pads on the chips. All chips' pads are wire bonded and routed out through bonded HDI assemblies.

The logic signals on the HDI assemblies are routed away from the detector along the support structure and connect to optical fiber driver boards. Multiplexing may be implemented through high-speed optical links (5 GHz) or by use of Wavelength Division Multiplexing (WDM) and multimode optical fibers.

**Prototyping** Silicon strip technology has matured during the past decade and is now widely used in high energy and nuclear physics applications. Yet, detectors have often very specific applications in experiments, are usually custom made, and require some prototyping effort. We are planning to construct one segment of the proposed detector with the help of the Brookhaven National Laboratory Instrumentation Group [Zepc], which would then be tested in Hall B in conjunction with the solenoid magnet currently planned for the DVCS experiment. The prototype work is expected to commence in the fall of 2003.

## Forward Detector

**Overview** The Forward Detector (FD) detects charged and neutral particles in the angular range between 5 and 40 degrees. The new detector is designed to provide extended particle iden-



tification, better charged particle tracking resolution, improved two-photon separation, nearly full azimuthal coverage for photon detection and greatly reduced sensitivity to background compared to the present CLAS. The FD consists of the following detector elements beginning with the one closest to the target:

- Forward angle part of the silicon microstrip detector (see Fig. 164)
- High threshold Čerenkov counter (HTCC)
- Coil calorimeter (coilEC)
- Tracking chambers (R1, R2, R3) with axial and stereo readout
- Low threshold Čerenkov counter (LTCC)
- Time-of-flight scintillator arrays (FTOF)
- Preshower electromagnetic calorimeter (preEC)
- CLAS forward electromagnetic calorimeter (FEC)

We give here a brief description of every element in the FD system. A more detailed description is provided in the sections following this overview.

*High threshold Čerenkov detector* The bulk of the FD provides active coverage in the azimuthal range not blocked by the main torus coils. Electron identification and pion rejection is accomplished using a new Čerenkov detector HTCC operated with a light radiator gas such as  $CO_2$ . This will provide pion rejection for momenta up to 4.9 GeV.

*Coil electromagnetic calorimeter* The coil electromagnetic calorimeter (coilEC) provides photon detection in the regions shadowed by the torus magnet coils. In conjunction with the microstrip detector it can discriminate photons from charged tracks.

*Tracking chambers* Forward tracking of charged particles is accomplished by three sets of chambers, analogous to the present CLAS drift chambers and named accordingly, Regions 1, 2 and 3 (R1, R2, R3). These chambers will cover less than one third the polar angular range of the present setup. By keeping the channel count constant, we are able to decrease the cell size and active time window by more than a factor of two, resulting in better spatial resolution and decreased sensitivity to backgrounds.

*Low threshold Čerenkov counter* The LTCC is the modified CLAS Čerenkov Detector operated with a higher density gas to allow pion identification for momenta above 3 GeV/c.

*Forward time-of-flight detector* The FTOF array consists of scintillator strips recycled from the existing CLAS TOF detector. The new array will consist of a double layer of 5cm thick

scintillator paddles each 5cm wide. This will provide a much improved timing resolution as the amount of light collected in the photomultipliers is increased by a factor of several.

*Preshower electromagnetic calorimeter* The forward electromagnetic calorimeter (FEC) currently used in CLAS will be augmented by a more highly segmented pre-shower electromagnetic calorimeter (preEC) located immediately in front of the FEC. It will provide better spatial resolution; especially needed for the detection of the two photons from high-energy  $\pi^0$  decays. The FEC will be used as is.

*Expected performance of the forward detector* The forward spectrometer will be able to detect all charged and neutral particles emitted in the polar angular range of 5 to 40 degrees; providing momentum resolutions of  $\delta P/P = 0.005 + 0.001 * P$  for charged particles and energy resolutions of  $\delta E/E \leq 9\% \sqrt{E(\text{GeV})}$  for photons. Particle identification is accomplished using time-of-flight information, Čerenkov counters, and electromagnetic calorimetry. In addition, kinematical fitting can be applied in some cases. Electrons and  $\pi^-$  can be separated for momenta up to 5 GeV/c using gas threshold Čerenkov counters, and above 5 GeV in electromagnetic calorimeters. Kaons(protons) can be separated from pions for momenta up to 3(6) GeV using the upgraded time-of-flight arrays, and above 3 GeV using the low threshold Čerenkov counter as a veto for kaons. Only the direction of the momentum vector can be measured for charged particles headed for the main torus coils. All of the detectors can operate in the background environment expected at luminosities of  $10^{35} s^{-1} cm^{-2}$ .

In the following sections we describe the new detector components of the FD in more detail.

**High Threshold Čerenkov Counter (HTCC)** The HTCC is the first active detector downstream of the microstrip tracker. Its main function is to aid in the identification of electrons and pions. A relatively light gas such as CO<sub>2</sub> will be used as radiator. This will provide a threshold for the detection of charged pions of 4.9 GeV/c. In combination with the CLAS FEC, this will provide highly efficient electron identification. A pion rejection factor of  $> 2000$  can be achieved this way for the entire momentum range up to 4.9 GeV.

The HTCC will also be used in combination with the LTCC for charged pion identification in the critical momentum range from 2.9 - 4.9 GeV. In this momentum range the HTCC does not detect pions while the LTCC does, this way providing identification of both electrons and charged pions. The HTCC is located in front of the Torus magnet and the first forward tracking chamber. A conceptual view is shown in Fig. 165.

The very limited space available for the HTCC puts serious constraints on the optics and the performance of the mirror system and the photon detectors. Figure 166 illustrates the optics of the HTCC. To optimize the light collection light produced at scattering angles less than about 20 degree is reflected towards large angles in the same Torus sector, while light produced at scattering angle greater than 20 degree is reflected towards the opposite Torus sector. The expected response in

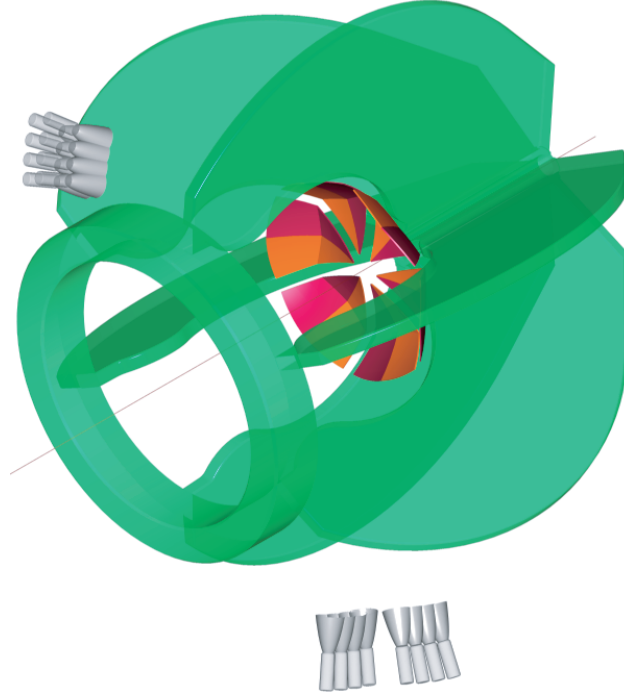


Figure 165: Concept of the High Threshold Čerenkov Detector located inside the Torus coil arrangement.

terms of the number of collected photoelectrons has been simulated using the measured properties of the mirror system in the CLAS Čerenkov counter, and photomultipliers with known photocathode sensitivities and quartz windows <sup>5</sup>. Figure 167 shows the projected distribution of the average numbers of photoelectrons ( $N_{pe}$ ) across the  $\phi - \theta$  plane. In the polar angle range from 6 to 35 degrees the  $N_{pe}$  is between 11 and 15, slightly dependent on the polar angle due to the varying pathlength in the radiator gas.  $N_{pe}$  is independent of the azimuthal angle  $\phi$ . Influence of the magnetic field of the solenoid on the particle trajectories is neglected as for the high momentum electrons (1 GeV/c) the solenoid field in first approximation will only produce a change in azimuthal angle. The main effect is a smearing of the photon distribution in the detector plane.

Most photons will directly hit the photocathode area in the 5" photomultiplier tubes, those outside are collected in Winston cone mirrors around the PMTs. The PMTs are located in the fringe field of the Torus magnet and will be magnetically isolated with a multi-layer magnetic shield. Such magnetic shields have been used successfully in the CLAS Čerenkov detector.

**Forward Tracking Chambers** The forward tracking chambers measure charged tracks which have polar angles between  $5^\circ$  and  $40^\circ$ . In order to use the missing mass technique effectively, the forward chambers must have excellent momentum resolution. The design we present here should allow momentum determination of  $\delta p/p = \sqrt{(0.1\% * p)^2 + (0.2\%/\beta)^2}$ . The spatial resolution

---

<sup>5</sup>The characteristics of the Burle 8854 photomultiplier have been used

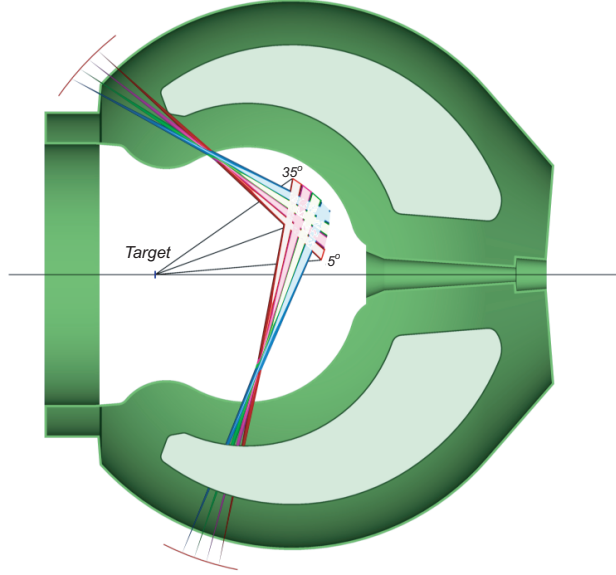


Figure 166: Optics of the High Threshold Čerenkov Detector. Čerenkov photons are generated in the gas volume beginning after the microstrip detector and the mirror system. The mirror system consists of 4 small angle segments which reflect the light towards the outside region of the torus magnet in the same sector. The 4 large angle mirrors reflect the light towards the PMTs located in the opposite sector. In order to avoid light obstruction due to the beam pipe the mirrors are tilted by about  $\pm 15^\circ$  left and right of the beam pipe.

portion of  $0.1\% * p$  is a factor of three better than the performance of the current CLAS tracking system. The chambers' intrinsic resolution is expected to improve from the present  $330 \mu m$  to  $200 \mu m$ , due to smaller cell size. We also expect to gain another factor of 1.5 by carefully controlling our knowledge of the B field and the chamber positions.

The forward tracking system consists of six microstrip layers, three sets of drift chambers: region 1, located immediately before the Torus magnet; region 2, located between the Torus coils, and region 3, just behind the Torus coils. The drift chamber arrangement is similar to the one currently used in CLAS, and optimizes the momentum resolution. The cell structure will be very similar to the current design, and will consist of a hexagonal cell geometry. Because the polar angular coverage will be much less than that of the current chambers, the cell size and hence the time window and the spatial resolution are expected to be roughly half that of the present chambers. The additional microstrip layers will provide much improved azimuthal angle information especially important at forward angles.

This design will provide precise measurements of the particle trajectory ( $100 \mu m$  accuracy per 12-layer chamber). They are also much less sensitive to background rates than the current chambers. The background rates for the R1 chambers will be reduced by an additional factor of two by using a special, high drift-velocity gas mixture such as  $He - CF_4$ .

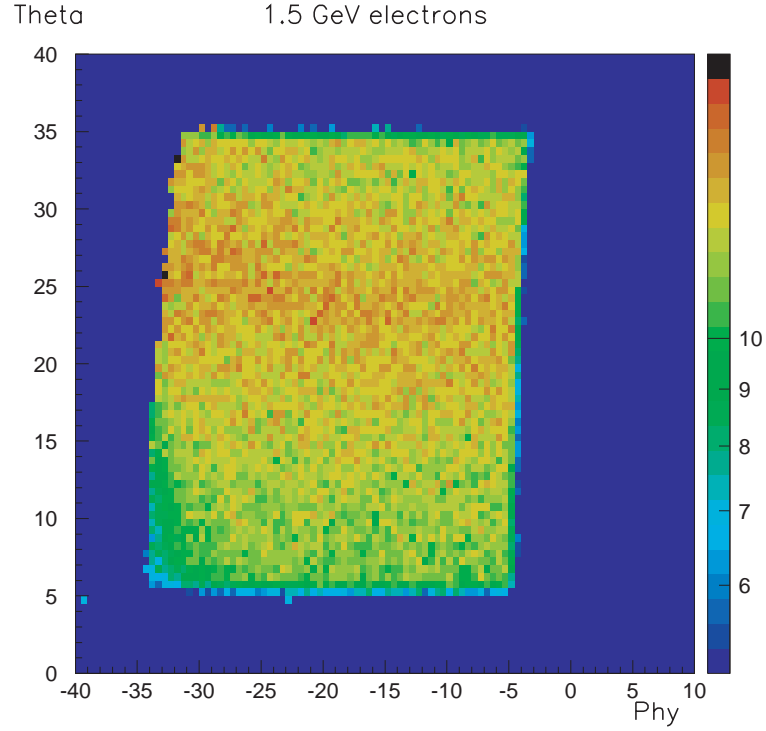


Figure 167: Left: Distribution of the number of photoelectrons  $N_{pe}$  for the HTCC in the  $\phi - \theta$  plane. The simulation was done for electrons of 1.5 GeV/c momentum. The solenoidal field was included in the simulation at full strength of 5 Tesla central field. The phi motion of the electrons in the solenoid field leads to a slight broadening of the photon distribution at the Winston cones and PMTs. Right: Average  $N_{pe}$  versus the polar angle (projection of the graph on the left onto the  $\theta$  axis). The  $\theta$ -dependence in  $N_{pe}$  is due to the different radiator gas length for different polar angles.

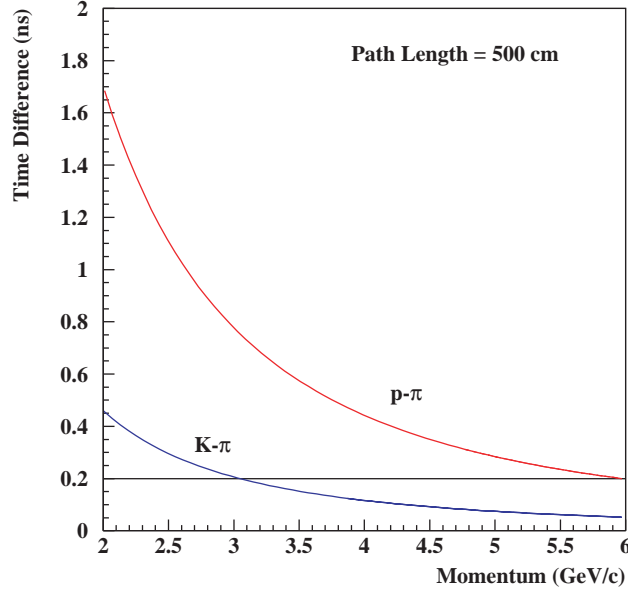


Figure 168: Time differences between protons and pions, and between kaons and pions over the 500 cm path length expected for the outer TOF system.

**Low Threshold Čerenkov Counter** The Čerenkov counter installed in the existing CLAS detector will be re-used to provide electron/pion separation for momenta up to 2.7 GeV/c and to identify  $\pi^+$  and  $\pi^-$  for momenta greater than 3 GeV/c. The radiator gas will be  $C_4F_{10}$  as in the current system. In CLAS the Čerenkov counter is exclusively used for electron/ $\pi^-$  separation. The mirror system in the CLAS Čerenkov counter was designed to be most efficient for inbending particles, while for outbending trajectories less than full efficiency for detection is obtained. At the higher energies after the upgrade the LTCC will be used to identify pions both inbending and outbending. In order to achieve full detection efficiency the optical system needs to be re-adjusted and the elliptical mirrors probably need to be replaced.

**Outer TOF System** The outer TOF system has the geometry of the existing CLAS detector [Ad02, Sm99a], but the detectors will be upgraded for improved timing resolution. The design goal is to achieve timing resolution of  $\sigma = 50$  ps for the shorter scintillators. This timing resolution allows separation of pions from kaons up to 3 GeV/c and pions from protons up to 6 GeV/c (Fig. 168). This assumes a “ $4\sigma$ ” difference in time between the two particles and allows identification of a signal in the presence of other particles with ten times higher rates.

The resolution of the counters in the present CLAS TOF system can be summarized as follows: The attenuation length of the forward-angle counters (15-cm wide) can be approximated by  $\lambda = 134 \text{ cm} + 0.36 \cdot L$ , where  $L$  is the length of the counter in cm. The large-angle scintillators (22-cm wide) have an approximate attenuation length of 430 cm. The time resolution of each counter has

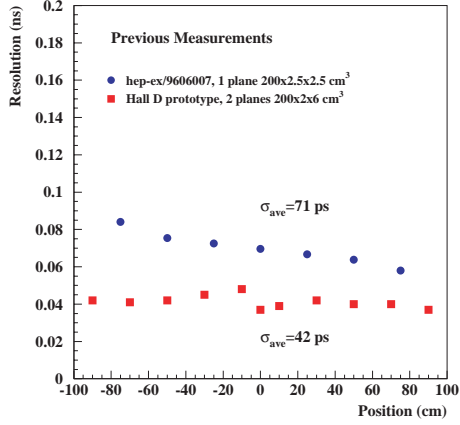


Figure 169: Previous measurements from two prototypes, 200 cm in length. The resolution of 50 ps is achieved using two scintillator planes which determine times with resolution of 70 ps.

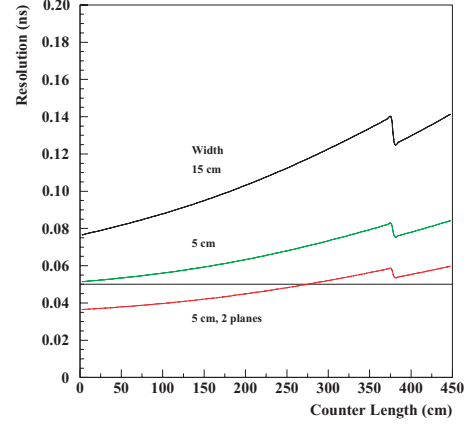


Figure 170: Expected resolution for the existing detectors (15 cm wide) with an intrinsic electronic resolution of  $\sigma_0 = 40$  ps. Also shown are predictions for 5 cm wide counters and for two planes of 5 cm wide counters.

been measured with cosmic-rays; it can then be parameterized with the following formula:

$$\sigma_{TOF}(ns) = \sqrt{\sigma_0^2 + \frac{\sigma_1^2 + (\sigma_P \cdot L/2)^2}{N_{pe} \cdot \exp(-L/2\lambda)}} \quad (74)$$

where  $\sigma_0 = 0.062$  ns represents the intrinsic resolution of the electronic measuring systems and other processes which are independent of light level,  $\sigma_1 = 2.1$  ns is the combined single-photoelectron response of the scintillator and PMT, and  $\sigma_P = 0.0118$  ns/cm corresponds to path length variations in the light collection.

Prototypes have achieved the desired resolution for counters 200 cm in length. Two examples are shown in Fig. 169 proving that a single plane of scintillators can achieve a resolution of 70 ps. The combined resolution of two measurements achieves the resolution of 50 ps. The prototypes used fast scintillator and XP2020 PMTS.

*Electronics* As a guide to necessary improvements in the time resolution of the system, we scale the parameterization of the CLAS system to narrow counters. The intrinsic resolution of the electronics system ( $\sigma_0$  in Eq. 74) must be reduced and we have measured it to be as small as 14 ps in various setups [Sm91]. There are many contributions to this term, and each electronic component will have to be selected carefully to insure that it meets our specifications. In order to achieve the rate capability at a luminosity of  $10^{35} \text{ cm}^{-2} \text{ s}^{-1}$  (see Section on Central TOF system), a pipeline TDC will be used to readout these detectors. The Jefferson Lab Fast Electronics group is developing such a TDC based on the COMPASS F1 chip which satisfies our requirements. Therefore, we assume that  $\sigma_0 = 40$  ps determined by the resolution of the TDC, which is 40 ps for the COMPASS F1 chip. The predicted resolution from Eq. 74 is 65 ps, assuming that the width of the counters is reduced to 5 cm, and is consistent with prototyping measurements of Fig. 169. The predictions are shown in Fig. 170.

Table 29: Rise time for various PMTs. The existing CLAS detector uses XP2262 PMTs.

PMT (2")	Rise Time (ns)
XP2262B	2.0
XP2020	1.5
XP2020/UR	1.4
R2083	0.7

Table 30: Properties of several scintillators. The existing CLAS detector utilizes BC-408 scintillator.

Scintillator	Bulk $\lambda$ (cm)	$\tau$ (ns)
BC-408	380	2.1
BC-404	160	1.8
BC-418	100	1.4

*Photomultiplier Tubes* The prototypes that have achieved the desired resolution have used XP2020 PMTs, which have faster rise times than our current CLAS detector. While detailed prototyping efforts should be performed to optimize the choice of components, we expect that a faster PMT will be required. In Table 29 we give the rise time of various common tubes. The XP2020 PMTs have 25% faster rise time than the XP2262 tubes used in the current detector which is achieved with improved transit time spread across the photocathode. Faster PMTs are available, but in practice should be matched to the decay times of the scintillator material for improved performance of the overall system.

*Scintillator* This parameterization is used to study the possible improvements in resolution based on a tradeoff between the decay time of the scintillator ( $\sigma_1$  in Eq. 74) and the number of photoelectrons arriving at the PMT which depends on the attenuation length  $\lambda$ . The bulk attenuation length and the scintillator decay times for three typical scintillators are listed in Table 30. In Fig. 171 the expected resolution is plotted as a function of counter length for the three scintillators listed in Table 30. For the figure we have used bulk attenuation lengths for BC-404 and BC-418, while we have used the measured values for BC-408. We have also plotted the resolution for BC-418 for half the bulk attenuation length. The plot indicates that, if the actual attenuation lengths approach the bulk attenuation of the material, the decay time dominates the performance for counters less than 200 cm in length. This is an option that should be explored experimentally for the shortest counters. Otherwise, we see that the existing material BC-408 is a good choice for scintillation material.



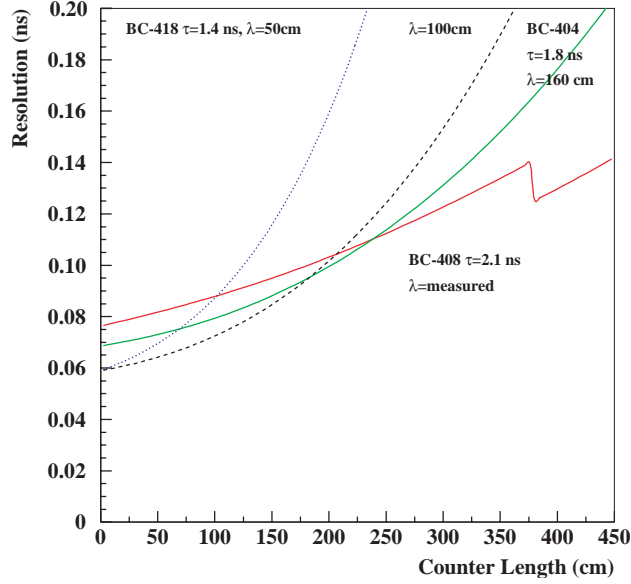


Figure 171: Resolution for various scintillators showing the tradeoff between attenuation length and scintillator decay time.

**Inner Calorimeter** In the present CLAS system, neutral particles heading for the coils are not detected. As is the case for charged particles, we would like to determine the direction and (to the extent possible) the energy of all photons. This requires coverage of the inside of the torus coils with photon detectors. Ideally, the detector should also give some information on charged particles, such as their energy deposition, range, etc.

The detector must be very compact since there is little space available in the angular range between  $5^\circ$  and  $40^\circ$  to complement the forward calorimeters. There is also a significant magnetic field in the region of the Torus coils that must be accommodated in the calorimeter design. A promising solution is to install short radiation length crystals. The currently most likely candidate is the scintillator crystal lead tungstate ( $PbWO_4$ ). To avoid problems with the magnetic field interfering with photomultiplier readout, the crystal light can be collected with avalanche photodiodes (APD). The signal will be further amplified in low noise preamplifiers and in post amplifiers, before digitization.

This technique is currently planned for use in the DVCS experiment with CLAS. The DVCS experiment has requirements very similar to the requirements for the CLAS upgrade. In particular the experiment will use a superconducting solenoid for shielding the detectors from the Møller electron background.

A conceptual design of a  $PbWO_4$  calorimeter for the Torus coil region is shown in Fig. 172

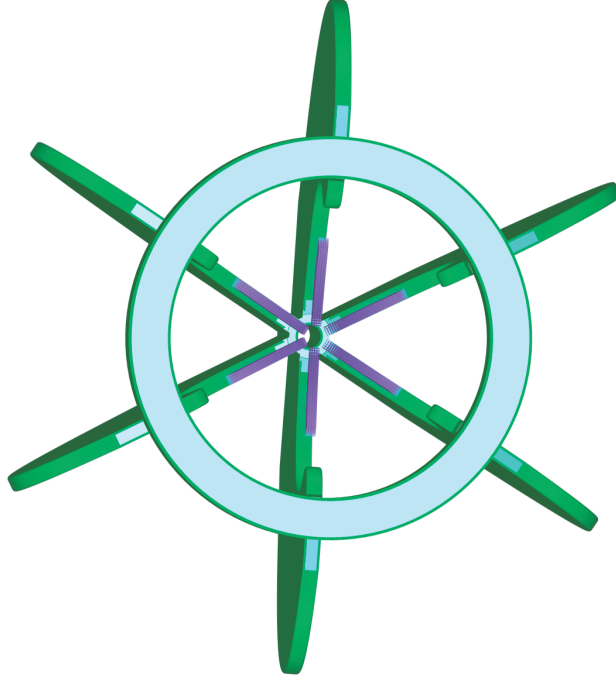


Figure 172: Arrangement of the Inner Calorimeter covering the regions of the torus magnet coils. The calorimeter consists of lead-tungstate crystals. The light is collected in Avalanche Photodiodes which are insensitive to magnetic fields. The APD signal is then amplified in low noise preamplifiers.

**Forward Angle Calorimeter** The CLAS forward electromagnetic calorimeter (FEC) will be reused in CLAS<sup>++</sup> without any modifications. In conjunction with the two threshold Čerenkov detectors the FEC provides electron identification up to the highest particle momenta, and efficient pion rejection with a rejection factor of  $> 2000$  at an electron detection efficiency of  $> 99\%$ . Above the pion threshold of the HTCC the FEC will continue to provide pion rejection, however with reduced rejection power ( $> 100$  at  $> 95\%$  electron detection efficiency).

**Pre-shower calorimeter** A major part of the physics program will require reliable detection of  $\pi^0$ s through their two-photon decays, in a wide range of momentum and angles. Forward-going photons in CLAS are detected in the forward electromagnetic calorimeter (FEC). FEC is a lead-scintillator sandwich with three stereo readout planes oriented at approximately  $120^\circ$  to each other. The transverse size of the readout module in a plane is about 10 cm. The energy of the photons is reconstructed using the fraction of the shower energy deposited in the scintillators. For the FEC this is about 30% of the total energy deposited in the calorimeter. The production angles of the photons are determined via the hit position on the FEC, reconstructed from three stereo readouts.

With 12 GeV beams  $\pi^0$ s will be produced with momenta up to 9 GeV/c. With increase of the pion energy the spatial distance between two photons at the calorimeter will decrease, Figure 173, and at pion momenta above 4 GeV/c the distance between two hits will be too small to allow

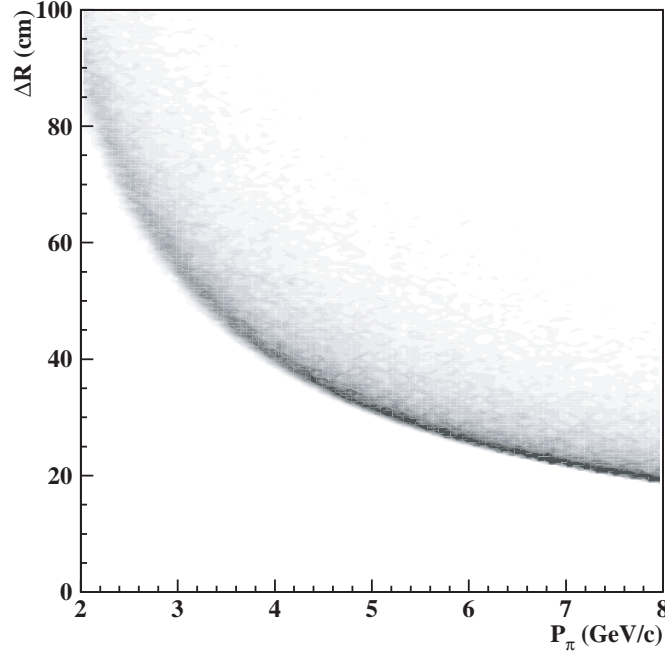


Figure 173: Distance between hit positions of the two photons from  $\pi^0$  decay at the FEC plane as a function of the pion momentum. At a pion momentum of 8 GeV/c the minimum distance between the two photons is 20 cm which does not allow a reconstruction of the two photons in the existing CLAS FEC.

unambiguous reconstruction as two separate hits. Most of high energy pions will be reconstructed as a single hit and can be misidentified as a single high energy photon. In Figure 174  $\pi^0$  detection efficiency of as a single hit (triangles) or as two hits (squares) in the forward calorimeter is shown as a function of pion momentum. Open symbols represent GEANT simulations with existing geometry. As one can see with increase of pion momentum the efficiency for reconstruction of two hits rapidly decreases, and two photons are mostly reconstructed as a single hit.

Finer transverse granularity of the readout plane is needed to resolve two photons from high energy pions. This can be done with a finer segmented pre-shower located in front of each FEC module. The pre-shower will be used for a more precise determination of the hit position. Most of the shower energy will still be absorbed and reconstructed in the FEC. In Fig. 174 full symbols are simulations with higher transverse segmentation of the calorimeter. Having two hits spaced more than 3 readout segments in a view will permit the separation of 2 photons from  $\pi^0$  decay up to 9 GeV/c.

The conceptual design for the pre-shower is similar to the existing FEC of CLAS. It is based on a lead-scintillator sandwich arrangement with the shape of an approximately equilateral triangle. Three stereo readout planes are oriented parallel to the sides of the triangle. There are 9 layers of scintillators, 3 alternating layers in each view. Each layer will consist of 3 cm wide and 0.5 cm thick scintillator strips. 2 mm thick lead sheets are interleaved between two scintillator layers.

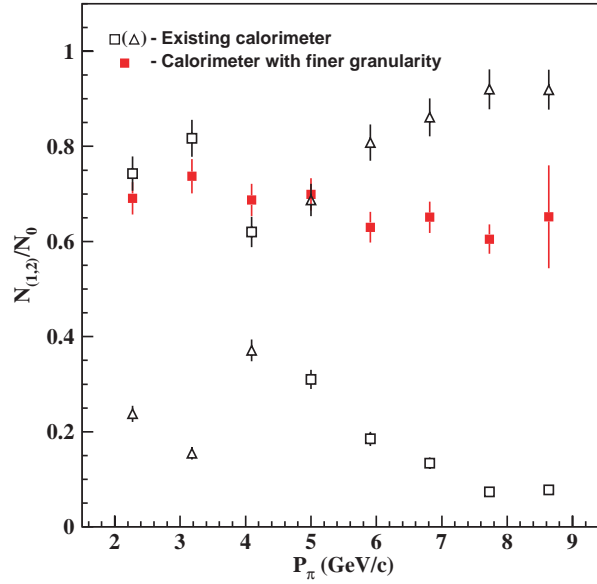


Figure 174:  $\pi^0$  reconstruction efficiency from the reaction  $ep \rightarrow ep\pi^0$  with beam energy of 11.5 GeV. Simulations are done with the CLAS FEC only. Open squares symbols indicate events when two hits are reconstructed, the invariant mass of the two photons is near the  $\pi^0$  mass, and the energy sum is about the energy of the pion. Open triangles show the frequency of single hit reconstruction with the energy corresponding to the  $\pi^0$  energy. For momenta of 4 GeV/c and higher most of the  $\pi^0$  events are misidentified as single photons. The full red squares show the results of a simulation when the preshower detector is used in the reconstruction. Pions are reconstructed over the full momentum range in this case.

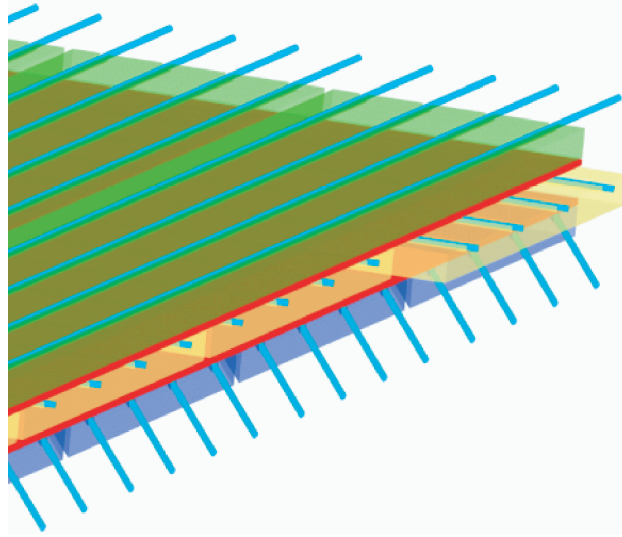


Figure 175: 3-d view of a corner of the pre-shower module. Three layers are shown only. Wavelength-shifting fibers are used to read out the light generated in the plastic scintillators. The scintillators and embedded fibers provide stereo information due to a geometry which is similar to the geometry of the CLAS FEC.

Light produced in the scintillator will be transported to the photo detector via four 1 mm radius waveshifting (WS) fibers embedded in the half-circular equally spaced grooves on the surface of the scintillator, as seen in Fig. 175. Photomultiplier tubes with  $\sim 1''$  green sensitive photocathode will be used for light detection. Corresponding strips from 3 layers of the same view will be read out with a single PMT. From studies using a prototype model we expect about 15 photoelectrons for 1 MeV energy deposition in the scintillator. With a sampling ratio of 0.3 this corresponds to 5 photoelectrons per 1 MeV deposited in the full calorimeter.

Simulations of exclusive,  $ep \rightarrow ep\pi^0$ , and semi-inclusive,  $ep \rightarrow e\pi^0$ , reactions showed that pions with momenta  $> 4 \text{ GeV}$  are produced at angles  $\theta < 25^\circ$ . Therefore, the pre-shower must provide coverage for straight tracks up to  $25^\circ$ . This corresponds to about half the size of the existing FEC. This implies that the height of the triangle, corresponding to the active area of pre-shower detector must be about 180 cm. The 64 scintillator strips in a layer with 3cm width cover the desired area. As described above, corresponding scintillator strips of the layers of a view are read out with a single PMT via four green WS fibers per strip, 12 fibers for each PMT. There will be 192 readout channels in each sector, making a total of 1152 channels for the entire system. Each read out channel will be furnished with trigger electronics, ADCs and TDCs.

### 3.B.4 Polarized Target Operation in CLAS<sup>++</sup>

**Longitudinally polarized Target in Solenoid Magnet** Part of the program for CLAS<sup>++</sup> requires a polarized solid state target polarized parallel or anti-parallel to the electron beam. In

CLAS<sup>++</sup> this can be accomplished by adding some correction coils to the superconducting solenoid to improve the field uniformity around the target. The correction coils are needed since the solenoid magnet alone may not produce a sufficiently uniform magnetic field in a large enough volume around the target to achieve highly polarized protons or deuterons (neutrons). With this option, the complete central detector could be used for polarized target experiments, allowing nearly full coverage for particle detection. This arrangement will allow measurement of multi-hadron final states in addition to the scattered electron. The target cryostat will have to be re-designed to allow for its operation in a warm bore magnetic field environment.

**Transversely Polarized Target.** At the higher energies achievable with the Upgrade there is a significant interest in semi-inclusive and exclusive processes involving transversely polarized targets. In the CLAS<sup>++</sup> configuration, and if the central detector is removed, the polarized target cryostat can be inserted from the top in between the torus coils which are no longer instrumented with tracking chambers. This provides a straight forward way of rotating the magnet by 90° to provide a transverse (to the beamline) polarization. As the magnetic field will deflect the incident beam vertically a magnetic chicane will be needed to compensate for that deflection. The chicane is to be inserted into the beamline upstream of CLAS<sup>++</sup>. The Helmholtz coil geometry will restrict the acceptance for particle detection to the forward region.

### 3.B.5 Beam Line

There are no major changes in the beamline necessary for the main 12 GeV operation. The bulk of the beamline equipment will operate as designed or better with an electron beam of higher energy and current. The items that should work without major upgrades include the three nA RF beam position and current monitors, beam profile harps, beam charge asymmetry monitors, beam halo monitors, beam viewers and beam raster magnets. One beamline element that is not-upgradable to 12GeV running is the tagger magnet. New beamline elements or existing equipment that needs modification for the upgrade are described in the following sections.

**Faraday Cup** The Faraday cup (FC) currently installed in the Hall B beamline contains no provision for water cooling. With the increase in beam energy by a factor of 2, and with the increase in luminosity by a factor 10, which will mostly come from an increase in beam current, the total power absorbed in the FC could increase by a factor of 20. This will either require the implementation of some cooling capability into the Faraday cup, or limit the duration during which the FC can be exposed to the beam. Another, though less desirable, possibility could be to limit use of the Faraday cup to short periods of time, e.g. for calibrating the upstream beam current monitors, and to move the FC out of the beam after the calibration is completed. This in turn would require installation of a low power beam dump located downstream of the FC that would dump the electron beam during routine operation.

**Møller Polarimeter** The Hall-B Møller polarimeter consists of a magnetized permadur target followed by two magnetic quadrupole magnets that deflect the electrons into scintillating fiber bundles. The maximum beam energy of the present polarimeter is given by the maximum field of the quadrupole magnets. This maximum is  $\sim 8.5$  GeV. In order to achieve operations with an 12 GeV beam energy the polarimeter will need to be reconfigured. A combination of increasing the distance separating the two magnets and relocating the detector bundles further from the magnets should be sufficient for 11 GeV operation. The determination of the optimum configuration for operation with any beam energy between 3 and 11 GeV is ongoing.

**Magnetic Chicane** Additional modifications will be needed when operating a polarized target in CLAS<sup>++</sup> when the magnetic field is oriented transverse to the beam line. A beam chicane<sup>6</sup> will be needed to compensate for the beam deflection of about  $3.2^\circ$  (at 12 GeV) in the polarized target field ( $\sim 2$  Tm integral). It will be inserted into the beam line upstream of CLAS<sup>++</sup>.

**Beam raster magnets** The installed beam raster system, which is used in conjunction with the polarized target, is dimensioned to allow full rastering over a polarized target a 1.5 cm diameter. The power supplies will be replaced with more powerful supplies.

### 3.B.6 Data Acquisition System and Trigger

The primary feature driving the redesign of the CLAS<sup>++</sup> Data Acquisition (DAQ) and triggering system is the higher data rates associated with the approximate factor of 10 increase in instantaneous luminosity that will be delivered to the experiments in Hall B.

**Design criteria for the system** The CLAS<sup>++</sup> DAQ must handle level1 trigger rates up to 20kHz at 10kByte/event event size with  $\leq 15\%$  dead time. High data transfer rates over the network will be handled by using gigabit Ethernet. The proposed DAQ system must assemble the event data from many front-end buffers to the Event Recorder (ER). The system must provide sufficient computing resources for executing physics algorithms which can substantially reduce the expected input rates. It must also provide continuous monitoring of the detector so that malfunctions may be readily identified and corrective measures taken. These functions will be performed by using a high performance readout network to connect the sub-detector readout units (ROC) via multiple event builders (EB) to the event filtering units (EFU, possibly implemented in computer farms). The flow of event data will be controlled by the triggering and timing system (TTS).

---

<sup>6</sup>The chicane is not part of the equipment complement for the upgrade, however it is part of a proposal currently under development for an experiment at 6 GeV, and may therefore exist before the energy upgrade

**System upgrade** CLAS<sup>++</sup> DAQ system design requirements are based on the rate estimates of the 12 GeV leading physics programs. The current system will be upgraded to meet the design requirements and to minimize the efforts, that will be invested to satisfy increased requirements of the 12 GeV physics programs. The following upgrade strategy will be used to achieve desired goal.

- Utilizing pipelined digitization hardware for the CLAS<sup>++</sup> new detector components.
- Replace the CLAS existing detector components: ADCs and high resolution TDCs with the equivalent pipelined digitization hardware, ready to function in the free-running DAQ mode.
- Keep existing low resolution TDC (TDC1877/1877S) in the system.

The mentioned hardware upgrades, with conjunction of the fast and optimized readout system, will guarantee fulfillment of the CLAS<sup>++</sup> DAQ design requirements. Using pipelined digitization hardware components in the system will provide most of the benefits, typical for the free-running DAQ systems. Gradual replacement of the remaining hardware (low resolution DC TDCs) with the pipelined equivalent will help us eventually implement full operational free-running DAQ system for future CLAS experiments.

Figure 176 shows possible data flow diagram of the CLAS<sup>++</sup> DAQ system. Here is a possible scenario of implementing higher level triggering algorithms, which demonstrates flexibility of the proposed system. In order to optimize the data flow, the event filtering computer farm performs event selection in two stages. First, a level2 filtering decision is made on a subset of the data from a programmable set of the detector components. This will help us to avoid system bandwidth saturation by reading out large volumes of tracking data at high level1 rates. The remainder of the full event data are only transferred to the filtering farm on a level2 accept, and a final level3 algorithm is then applied to the complete event. This activity is controlled by the Filtering Supervisor (FS) system.

### 3.B.7 Event Reconstruction and Offline Computing

The expected online data rate of 100 to 200 MByte/s cannot efficiently be handled when using the same procedures adopted by CLAS in the past: an efficient online event reduction is required to keep the data transfer rates to the Jefferson Lab tape silo within the bandwidth limits. Furthermore, the online event reduction and event processing will allow for a comparatively fast access to processed data for further analysis. We consider establishing a “grid-based” cluster of analysis and simulation centers to optimize the data processing.

**Data Reduction and Online Event Reconstruction** Major parts of data reduction will have to be performed online. The first stage of data reduction (noise reduction) will be performed at



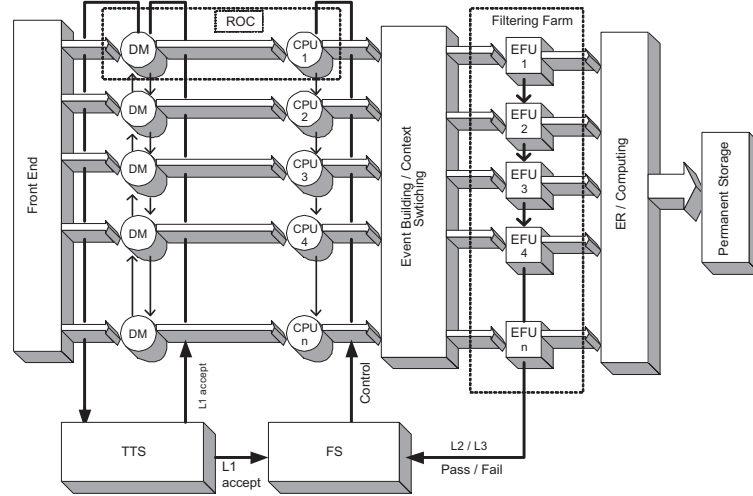


Figure 176: CLAS<sup>++</sup> DAQ bloc diagram. DM - Digitization Module, TTS - Triggering and Timing System, FS - Filtering Supervisor, EFU - Event Filtering Unit, ER - Event Recorder.

the crate level, the second stage in form of fast event filtering and tagging of events (Level 3) which will remove data which are not of interest for further analysis.

A fast online reconstruction will provide sufficient information on data quality and first-pass analysis of basic reactions. Depending on the available CPU power it is possible to perform a full event reconstruction of all events: using an online farm in the Hall-B Counting House and/or part of the JLab CUE farms which requires either a second output stream or large pre-silo stage disks. Taking into consideration the current achievements (7-10 ms/event) and the projected increase of CPU speed over the next 6 years, a full event reconstruction can be performed within 3-4 ms despite the more complex detector setup of CLAS<sup>++</sup>. The output will be written to disk in form of data summary files which contain all information required to perform a first-pass event analysis.

The (quasi-) online event reconstruction requires zero order calibration constants which have to come from analyses of previous run periods (and commissioning data) as well as the analysis of data taken during the first days in the specific run period. Additionally, small subsets of data will be selected for further analysis to perform a quasi-online calibration of all detector components. This continuous calibration process will provide a quick response to any changes in crucial detector parameters. In parallel, these subsets will be transferred to university-based analysis centers which will be responsible for a refinement of the online calibration.

The data summary files as well as the data subsets to be used for calibration purposes will be stored for several days on large RAID arrays to allow for fast access. We expect that the JLab Computer Center will provide the necessary infrastructure of fast network connections as well as short- and long-term storage media.

## 3.C Hall C and the Super High Momentum Spectrometer (SHMS)

### 3.C.1 Overview

Much of the physics outlined in Chapter 2 can be accessed only by a spectrometer system providing key features not available in the existing CEBAF facilities. It must have acceptance for very forward-going particles and analyzing power for particle momenta approaching that of the incoming beam. It must provide excellent particle identification even at these high energies. It must be capable of rapid, accurate changes to the kinematic settings with well understood acceptances allowing experiments to efficiently cover broad regions of phase space, enabling, for example, precise L/T separations. The basic design must be flexible so that specialized detector elements, such as polarimetry or additional particle ID, can be incorporated to satisfy the needs of particular experiments. And it must possess an efficient, highly time-resolved trigger system and a target and data-acquisition system suitable for running at high luminosity.

Our plan for meeting these needs consists of producing a new Super-High-Momentum Spectrometer (SHMS) and outfitting the existing HMS spectrometer with a compatible data-acquisition system. The SHMS will be capable of analyzing the higher energy particles produced by the upgraded CEBAF beam at scattering angles as low as  $4.5^\circ$  (central axis at  $5.5^\circ$ ). It will be designed as a companion to the HMS so that, taken together, the system will provide full momentum range single-arm capabilities as well as double-arm coverage over the entire kinematic region of interest to the proposed experiments. Thus, the SHMS will not be a replacement for the HMS, but rather a complementary partner to it just as the SOS (Short Orbit Spectrometer) functions as a partner to the HMS.

We present our plan by first reviewing the characteristics of the existing HMS in section 3.C.2. The physics demands developed in Chapter 2 of this report drive the proposed improvements to the HMS and determine the needed specifications for the companion SHMS. A summary of those specifications and a design for the SHMS which provides what the physics demands is given in section 3.C.3.

### 3.C.2 The High-Momentum Spectrometer

The HMS is a focusing spectrometer which can be tuned for central momenta from 0.4 to 7.3 GeV/c and production angles from 10.5 to 90 degrees relative to the beam direction. Its momentum acceptance is  $\pm 10\%$  and the angular coverage is  $\pm 32$  mr in-plane by  $\pm 85$  mr out-of-plane, achieved by the optical system consisting of three quadrupoles in a FDF arrangement followed by a dipole. The angular acceptance is defined by a collimator near the upstream end of the spectrometer.

The optical system is followed by a detector stack made up of two pairs of crossed scintillator hodoscopes, twelve planes of precision drift chambers, a gas Čerenkov counter which can operate

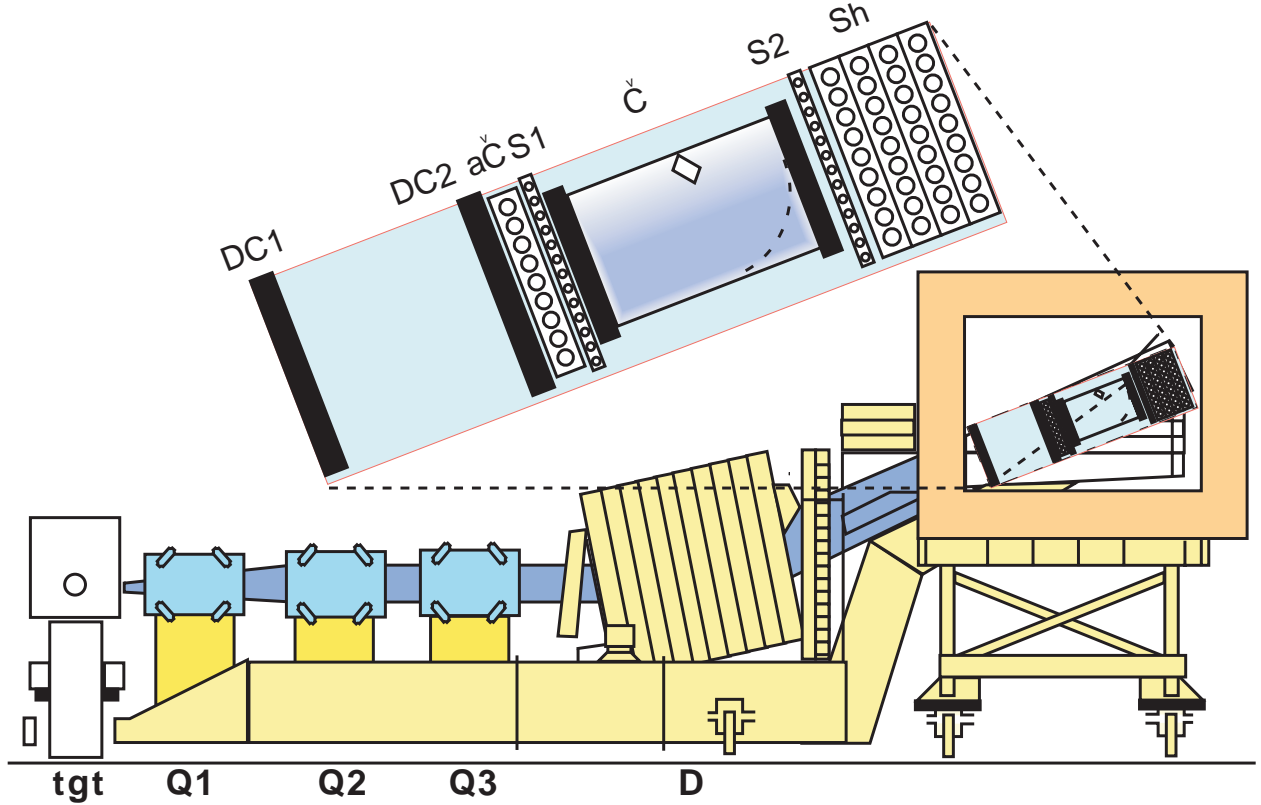


Figure 177: Sketch of the High-Momentum Spectrometer showing the Magnets, the Carriage, and an expanded block diagram of the Detector Stack.

from 0.3 to 2.5 atm., an aerogel Čerenkov counter, and a segmented lead-glass shower counter. A schematic diagram of the magnets and detector stack is shown in Fig. 177. The system is read out by a triggering and data-acquisition system providing full event readout of more than 2000 events/s with time-of-flight (TOF) and coincidence time resolution better than 200 ps.

Since the beginning of physics operation in Hall C, the HMS has provided precision tracking and particle identification for many experiments. Figure 178 shows some of the detector calibration results from these experiments which demonstrate its resolution and particle discrimination capabilities are summarized in Table 31.

Rotation of the whole spectrometer to the desired central scattering angle is accomplished remotely, without the need for access to the radiation enclosure, in about ten minutes. Angular setting accuracy is better than half a milliradian. Similarly, the central momentum may be adjusted remotely in about the same amount of time. These capabilities are crucial to experiments that must take data at a multitude of kinematic settings.

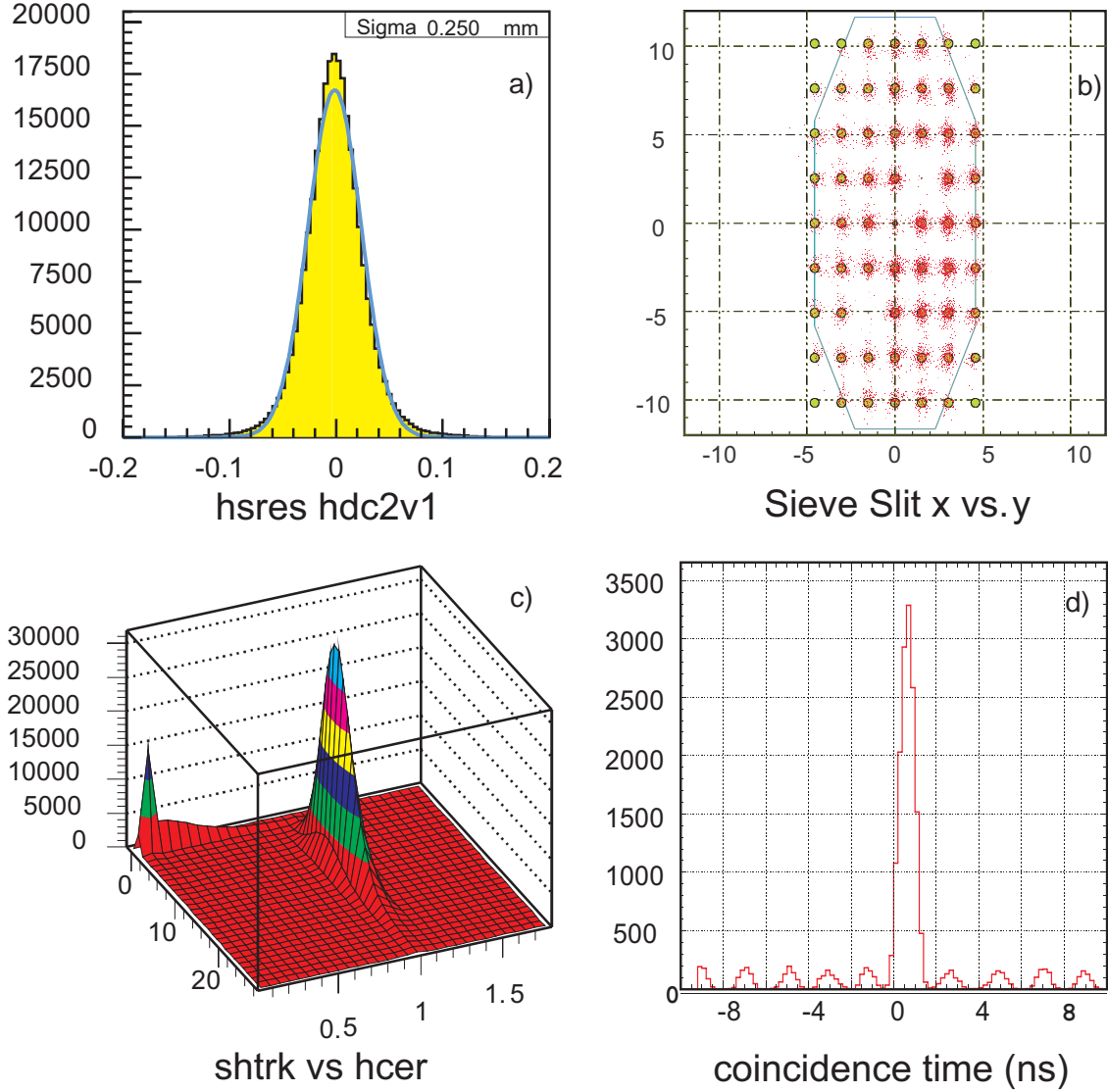


Figure 178: HMS Spectrometer Representative Data: Tracking capability is shown by a) Single-plane wire chamber resolution, and b) sieve slit reconstruction. Panel c) shows Shower Counter Energy vs. number of photons in the Čerenkov, demonstrating clear electron-hadron separation. Coincidence time resolution in the HMS-SOS hodoscope system is demonstrated in panel d) by the clear separation of particles from neighboring RF buckets.

Table 31: Summary of the HMS Performance and the Design Specifications for the SHMS.

<i>Parameter</i>	<i>HMS Performance</i>	<i>SHMS Specification</i>
Range of Central Momentum	0.4 to 7.3 GeV/c	2.5 to 11 GeV/c
Momentum Acceptance	$\pm 10\%$	-15% to +25%
Momentum Resolution	0.1% – 0.15%	< 0.2%
Scattering Angle Range	10.5 to 90 degrees	5.5 to 25 degrees
Target Length Accepted <sup>†</sup> at 90°	10 cm	50 cm
Horizontal Angle Acceptance	$\pm 32$ mrad	$\pm 18$ mrad
Vertical Angle Acceptance	$\pm 85$ mrad	$\pm 50$ mrad
Solid Angle Acceptance	8.1 msr	4 msr (LSA tune) 2 msr (SSA tune)
Horizontal Angle Resolution (yptar)	0.8 mrad	2-4 mrad
Vertical Angle Resolution (xptar)	1.0 mrad	1-2 mrad
Vertex Reconstruction Resolution (ytar)	0.3 cm	0.2 - 0.6 cm
Maximum DAQ Event Rate	2,000 events/second	10,000 events/second
Maximum Flux within Acceptance	$\sim 5$ MHz	$\sim 5$ MHz
e/h Discrimination	>1000:1 at 98% efficiency	1000:1 at 98% efficiency
$\pi/K$ Discrimination	100:1 at 95% efficiency	100:1 at 95% efficiency

<sup>†</sup> This length corresponds to what the spectrometer can “see” perpendicular to its optic axis.

The acceptable target length at any accesible scattering angle is, to first order, the projection of this length.

### 3.C.3 The Super-High-Momentum Spectrometer

**Overview** The Super-High-Momentum Spectrometer (SHMS) will play a vital role in the overall JLab physics program at 12 GeV. Short latency detector elements will minimize pileup and out-of-time events and, coupled with advanced data-acquisition components, will allow readout of 10,000 or more events per second. An inevitable consequence of relativistic kinematics is that much of the interesting physics at 12 GeV will only be accessible provided at least one of the spectrometers can achieve angles significantly below 10 degrees. The SHMS will achieve a minimum scattering angle of 5.5 degrees with acceptable solid angle and it will do so at high luminosity. The maximum momentum will be 11 GeV/c, well matched to the maximum beam energy available in Hall C. These three characteristics (high luminosity, small scattering angle, and high momentum) are essential for carrying out a program of electron-hadron coincidence experiments at large  $z = E_h/\nu$ , where  $\nu$  is the electron energy loss. (For orientation, in the limit of  $z \rightarrow 1$ , one approaches the exclusive limit.) At large  $z$  (*i.e.*  $z \approx 1$ ), sensitivity to the valence quark structure of the hadron is maximized and the reaction mechanism is simplified.

The HMS-SHMS spectrometer pair will be rigidly connected to a central pivot which permits both rapid, remote angle changes and reproducible rotation characteristics which simplify accurate measurements. From its inception, the SHMS momentum and target acceptances have been designed to be very flat, with performance similar to that of the HMS. This also simplifies making accurate measurements. These capabilities will facilitate experiments which rely on a large number of angle and momentum settings, such as L–T separations, for which accurate pointing as well as

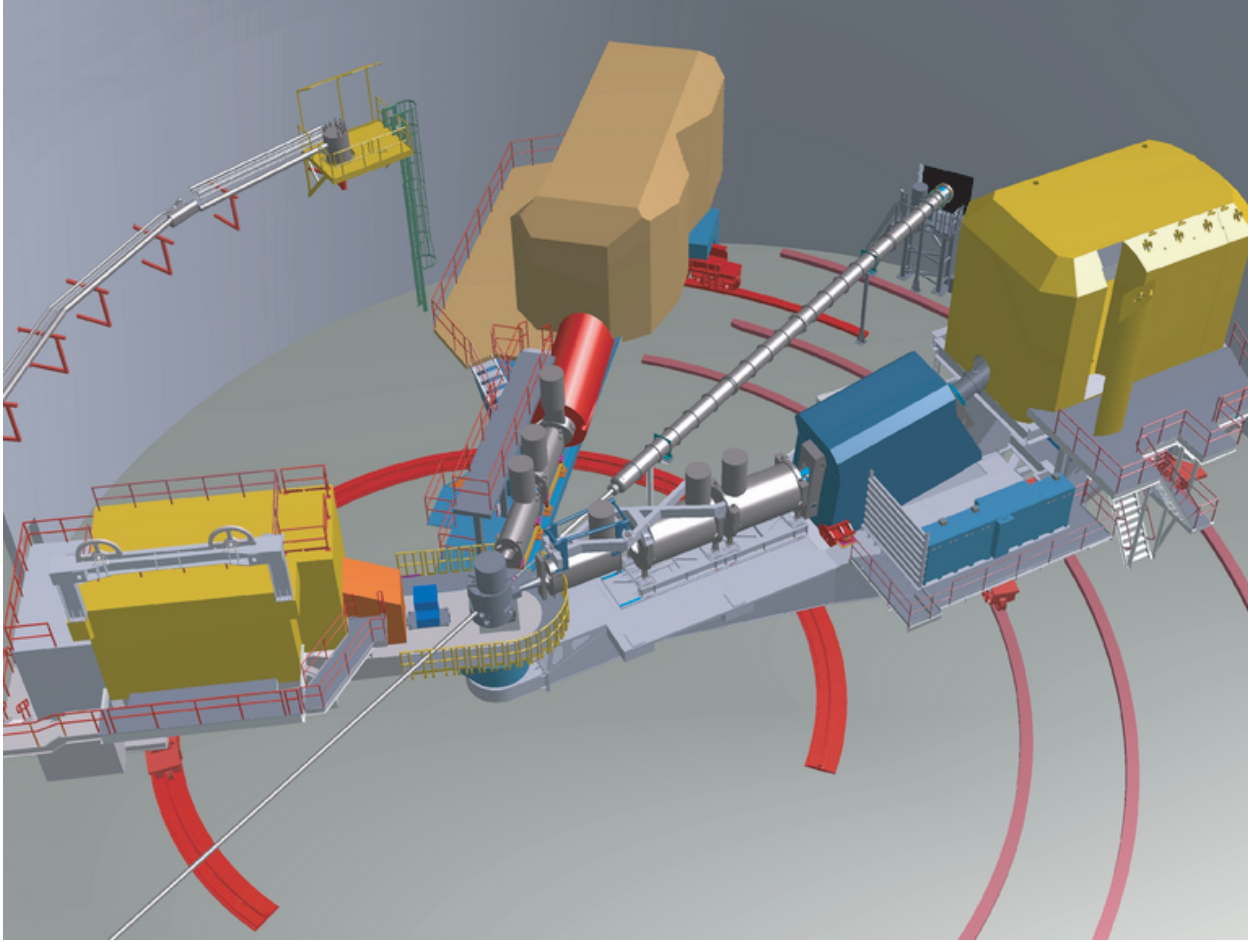


Figure 179: A CAD drawing of the new SHMS spectrometer installed in Hall C together with the existing HMS spectrometer (right) and the SOS spectrometer (left).

flat momentum and target acceptances are essential. Finally, for experiments which are willing to trade off small-angle performance for increased solid angle, this can be achieved by pulling the magnets and detectors forward and re-tuning the spectrometer. A CAD drawing of the new SHMS, together with the existing HMS and SOS spectrometers in Hall C, is shown in Fig. 179. In the remainder of this section we will address the design and performance details of the SHMS.

### The SHMS Magnets and Structural Design

**General** The SHMS is an 11 GeV/c superconducting spectrometer. The magnet system consists of two cold iron quadrupoles similar in design to the HMS Q1, and a combined-function warm bore magnet that is 5 m long. The cryogenics are proven systems using standard JLab components. The shield house is a composite of concrete, steel and lead. The magnets and the

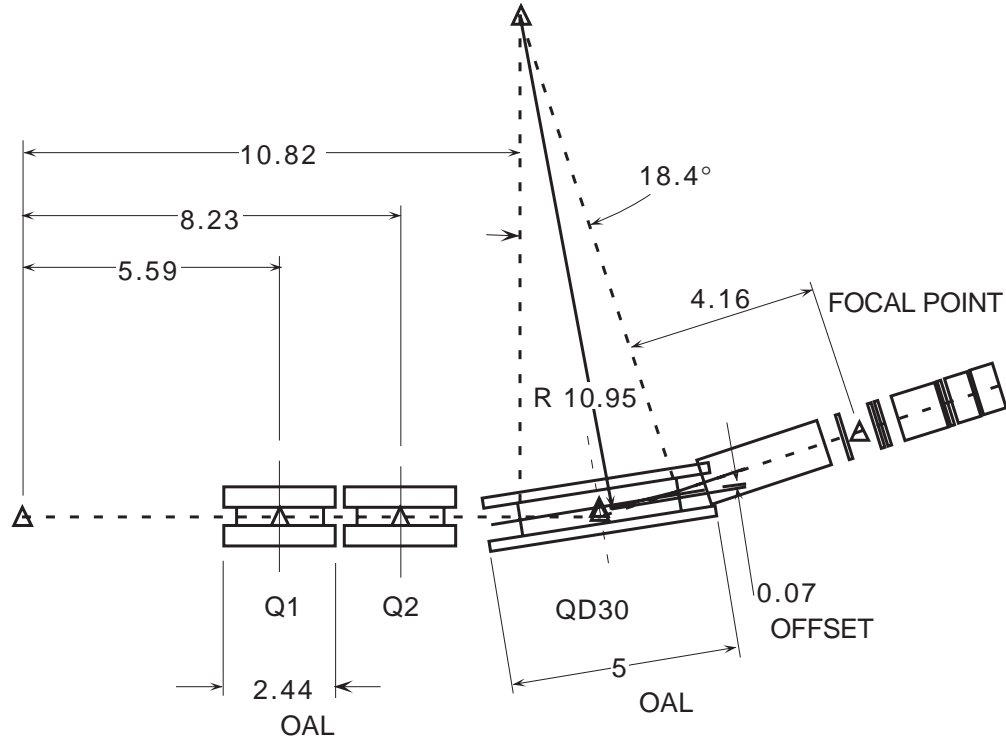


Figure 180: SHMS Spectrometer Key Dimensions (meters) showing the location of the two quadrupoles and the combined-function magnet relative to the target and the detector stack.

shield house are supported by a welded steel structure with steel drive wheels. Fig. 179 shows a perspective view of the spectrometer and Fig. 180 provides a line drawing of the layout.

**Q1 at 8.6 T/m** The SHMS spectrometer requires two quadrupoles with a gradient of 8.6 T/m and 40-cm aperture. The requirement to reach the scattering angle of 5.5 degrees means that the quads must be narrow. The existing HMS spectrometer Q1 magnet can just reach the required gradient due to the built in margin in operating current. The Q1 and Q2 magnets were designed by Oxford Instruments with a considerable operating margin so that the required gradients for HMS could be reached given some uncertainty in the yoke packing factor and the performance of the then new design of the large cold iron quads. The power supplies, for example, were sized at 1250 A even though the gradient was predicted to be reached at  $\sim 1050$  A. The cold iron quads worked as designed and the margin was never called into service. The margin in power supply current was matched by similar margins in the current leads, superconductor critical current, and force containment. Table 32 has the relevant Q1 parameters at the present maximum excitation and, for comparison, those required for SHMS. The forces at the 8.6-T/m gradient require further evaluation to determine if any internal structural modifications are required. The design margins in the present Q1 are very comfortable but much of this is lost at the higher excitation. Figures 181 and 182 show the gradient field quality and saturation at 8.6 T/m. Both are reasonable and meet the requirements.



Table 32: Q1 comparison between HMS at 1010 A and SHMS at 1291 A.

Parameter	HMS	SHMS	Change
Gradient (T/m)	7.11	8.59	20.8%
Current (A)	1010	1291	27.8%
Pole Tip Field (T)	1.78	2.15	20.8%
Field in Iron (T)	3.72	3.82	2.7%
Coil Forces <sup>†</sup>			
$F_x$ (N)	28,571	44,062	54.2%
$F_y$ (N)	7,465	-12,604	68.8%

<sup>†</sup>for Coil Stack 1

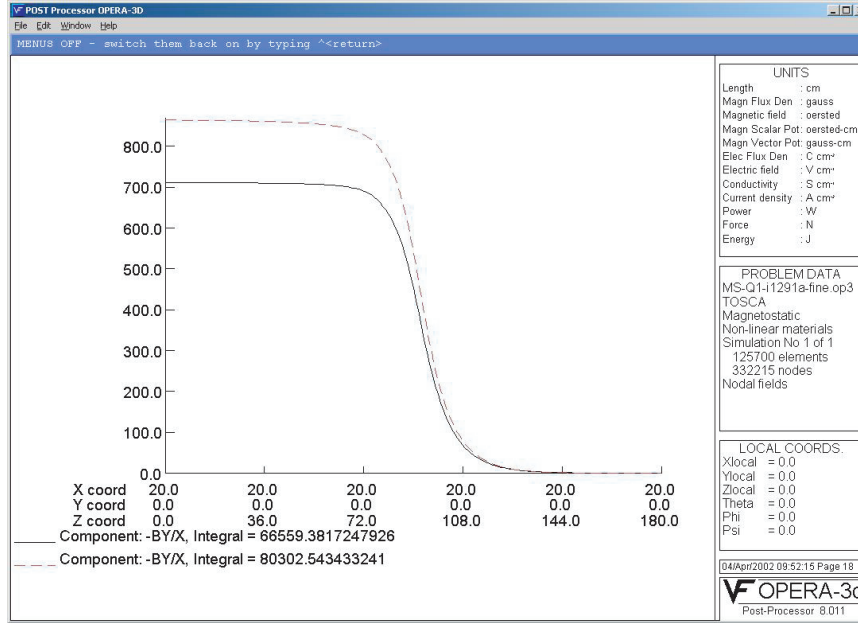


Figure 181: Comparison of the Q1 gradients along Z at 7.1 T/m and 8.6 T/m.

The project plan for SHMS is to procure, through competitive contracting, two Q1 magnet systems with a slightly thicker yoke shell to compensate for the  $\sim 50\%$  force increase. This modification will add a few centimeters to the overall size of the yoke/shell combination. The SHMS power supply will be rated for 1350 A, an increase of  $\sim 10\%$  over the present HMS Q1 supply. Similarly, the energy dump resistor will be designed to absorb a higher stored energy.

**QD30 Superconducting Magnet for the SHMS** The spectrometer requires a combined-function superconducting magnet that can simultaneously produce a 4.0-T dipole field and a 3.0 T/m quadrupole field inside a warm bore of 30 cm. A magnetic design using TOSCA 3-D[TOSCA] has been performed to establish the basic magnetic requirements, provide 3-D field maps for optics analysis, and produce basic engineering information about the magnets. A four sector cosine theta current distribution and a two sector cosine two-theta quad design with warm bore and warm iron has been selected and analyzed. A cut-away drawing is shown in Fig. 183.



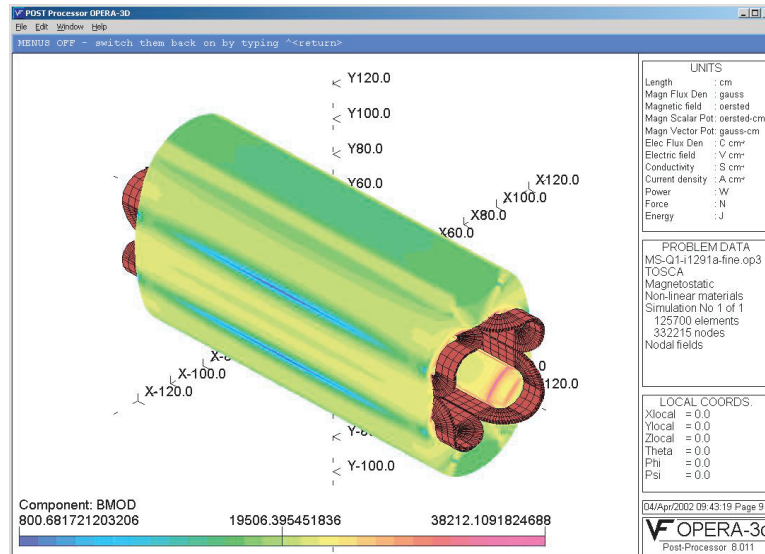


Figure 182: Magnetic Fields in Q1 at High Current.

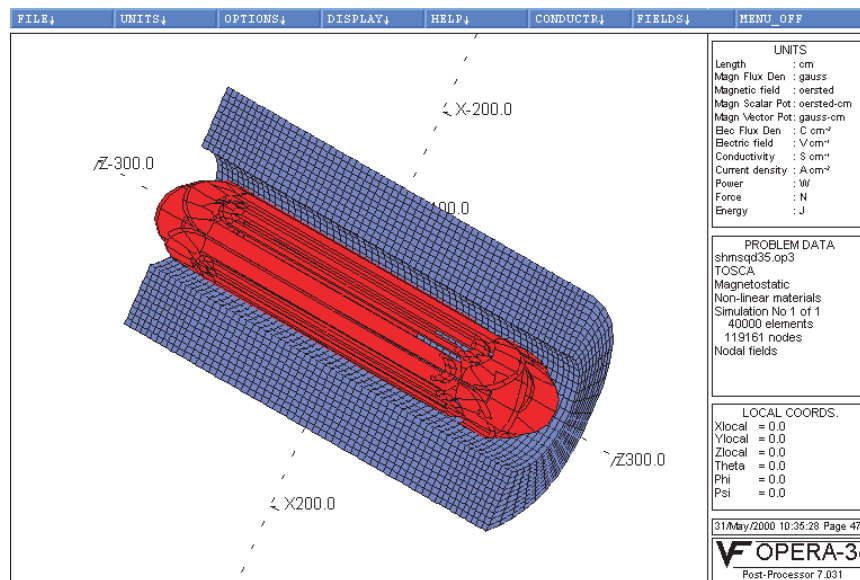


Figure 183: Cut-Away View of QD30 Magnet with beam-left side of yoke removed. Orientation is with bend field horizontal. Perspective angle is such as to make the image appear approximately as installed.

The magnetic design uses TOSCA-generated cosine theta type coils with “constant perimeter ends”. These coils closely approximate the ideal cosine geometry that would be a perfect generator of high purity fields. Practical considerations such as finite current distributions, a limited number of sectors, and TOSCA’s internal approximations, all contribute to deviations from the ideal geometry and are the sources of higher order field errors in the design. The yoke is modeled as non-linear iron with the nominal properties of 1010 steel. It is 4.2 m long with an outer elliptical shape having radii 120 cm 100 cm and a 60-cm inner circular radius. The detailed shape of the yoke is not very important in a cosine type magnet as the design requires an unsaturated yoke for good internal fields. The high field region is either on top or on the bottom depending on the relative sign of the dipole and quadrupole coils, therefore an elliptical yoke represents an ideal solution.

The QD30 combined-function magnet produces a peak field of 4.3-T in the bore and 5.4 T in the windings (see Figs. 184 – 187). These fields are comparable to those achieved in large bore magnets produced 20 years ago for MHD research, particle spectroscopy and coal sulphur separation. There are significant differences between the present magnet design and these prototypes. For example, the stored energy of the QD30 is somewhat less even though the field volumes are comparable. This is due to the fact that the superposed quadrupole field produces significantly less stored energy for a given maximum field. The combined fields also produce a very asymmetric resultant field and force distribution. The fields add on the bottom of the magnet and subtract on the top, so the fields across the bore range from  $\sim 0$  to  $\sim 5$  T. Similarly the fields in the windings are highest where the fields add (5.4 T) and nearly  $-2$  T where they subtract. Thus there is a net force between the yoke and coil that must be dealt with due to the asymmetry. The peak linear force densities are 40,000 pounds per inch for the dipole winding and 11,000 pounds per inch for the quadrupole winding. These forces add on one side and subtract on the other yielding peak pressures that range from 4680 psi to 2100 psi. Simple pressure vessel computations for 20-ksi material stress yields a 6.0-inch thickness for the cold mass force collar. Due to the large radial thickness of the windings (3.5 inches) and cryostat (11.8 inches), the required 6-inch pressure shell is easily accommodated without stressing the coil cold mass. Obviously in a real cold mass the stress will be distributed and the resulting stresses lowered. The large size of the cryostat will allow separate fluid pressure vessels in accordance with the ASME code. This will greatly simplify the final design and result in a much more conservative magnet. A fully clamped winding is planned for the final construction.

Cryogenic stability of the QD30 quadrupole and dipole has been evaluated against the Steckly criterion,  $\alpha$ . The condition of stability is that  $\alpha$  must be less than one, which means that the velocity of spread of a normal zone is negative. That is, a normal zone will always shrink. Analysis shows that  $\alpha$  is 0.79 and 0.48 for the dipole and quadrupole coil designs, respectively.

**Magnet DC Power and Energy Dump System** The DC power system for the SHMS magnets will consist of four independent power supplies. These supplies will be 12-pulse SCR supplies with a final stage transistor regulator providing stability of 10 ppm. They will be low-voltage high-current commercial units readily available from Danfysik and others. A DC current of

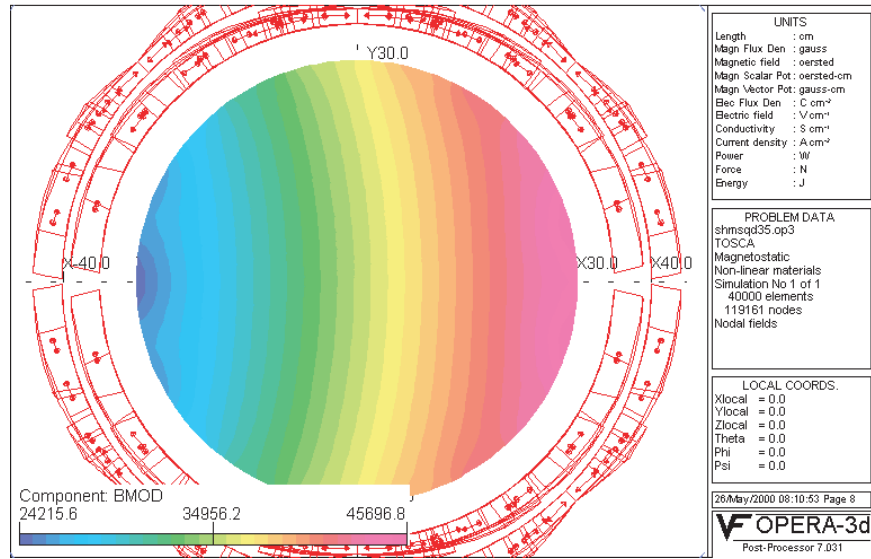


Figure 184:  $|B|$  in QD30 Midplane (G).

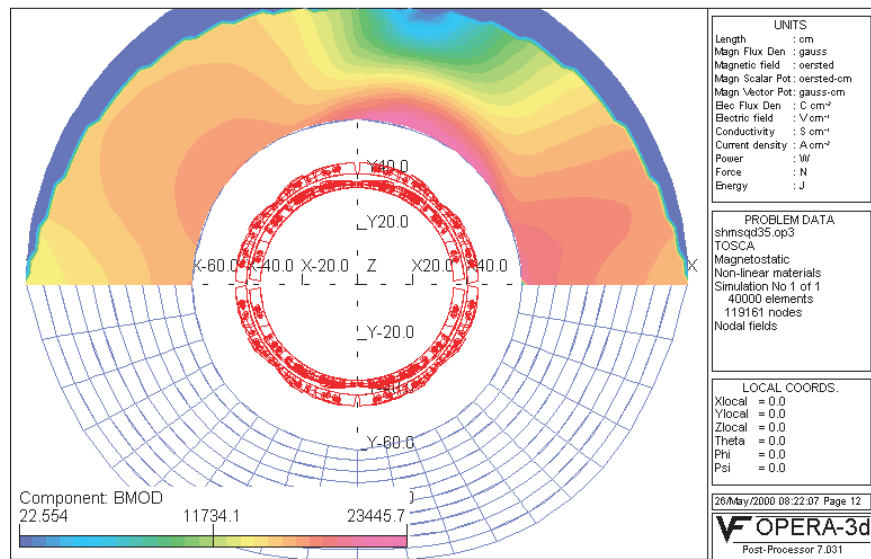


Figure 185: QD30 Yoke Saturation-  $|B|$  (G).

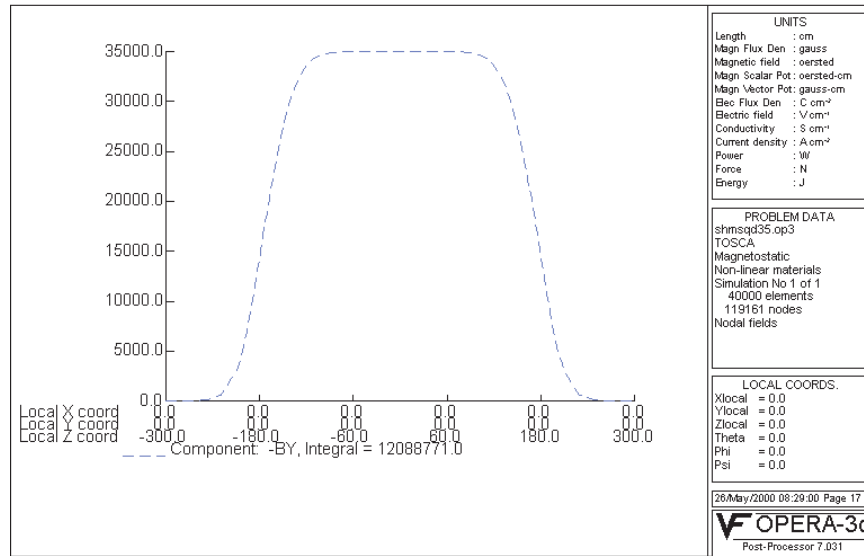


Figure 186: QD30 Dipole Field ( $B_y$ ) along the central axis  $x = y = 0$ .

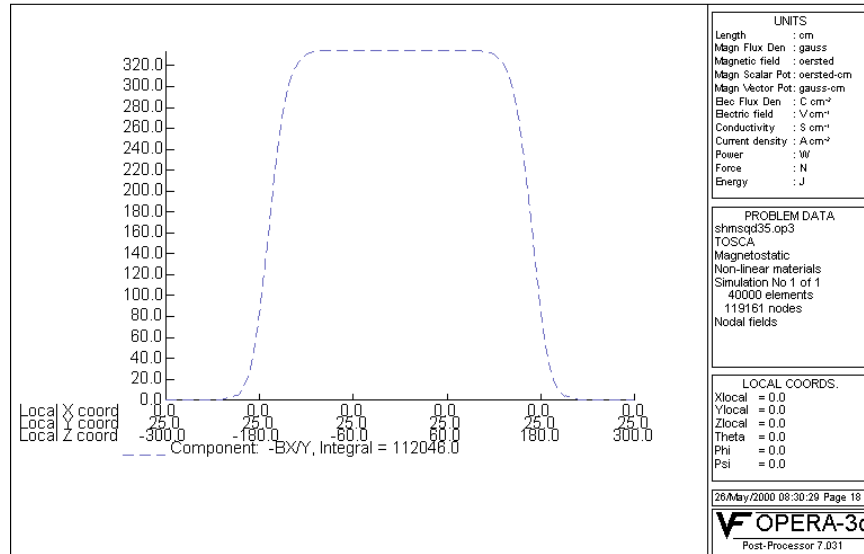


Figure 187: QD30 Field Gradient  $\partial B_x / \partial y$  along  $x = 0, y = 25$ .

Table 33: SHMS QD30 Magnet Parameters.

Function	Combined Quadrupole – Dipole	
Bore	30 cm Warm	
Overall Length	5.0 m	
Outer Diameter	3.2 m	
Yoke	240 kilopound (kip) warm 1010 steel. Length: 4.2 m. Outer envelope: ellipse with half-axes 1.2 m $\times$ 1.0 m. Inner envelope: 0.6 m radius circle.	
Coil and cryostat	40 kip St.Steel 5 m Long, 0.6 m (0.3 m) outer (inner) radius	
Stored Energy	13.0 MJ	
	Dipole	Quadrupole
Amp-Turns	$3.3 \times 10^6$	$1.8 \times 10^6$
Current Density	$5600 A/cm^2$	$5040 A/cm^2$
Coil Sectors	4	2
Winding	$\cos(\theta)$	$\cos(2\theta)$
Magnetic Strength	12.50 Tm	11.48 (T/m)m
Central	Field 3.58 T	Gradient: 3.63 T/m
Effective Length	3.45 m	3.4 m
Uniformity	$dB/B \sim 1 \times 10^{-3}$	$dG/G \sim 1 \times 10^{-3}$
Peak force density	40 kip/in	11 kip/in
Peak pressure	3390 psi	1290 psi

5000 A at 10 V would be a reasonable choice for SHMS dipole due to the relatively low inductance (0.72 H), and would provide a charge time under 30 minutes. The Quad power supplies will be identical to those in use on HMSQ1 and the QD30 magnet supply will be similar to the new HMS dipole power supply. All of the supplies will provide  $\sim 10$  V for ramp-up or ramp-down, have polarity reversal switches, and the possibility of NMR control for the dipole coils.

The energy dump systems will consist of a 10 V ramp-down, a slow dump and a fast dump resistor. The fast dump for the Quads will provide 450 V while the fast dumps for the QD30 magnet will apply a voltage of 150 V to the dipole coils and 250 V to the quad coils. These voltages may increase as the design progresses to maintain a reasonable final coil temperature near 80 K. The large cold mass and moderate current densities ensure that sufficient material is available to absorb a large fraction of the stored energy at a low final temperature during a quench discharge. The QD30 magnet circuits will have dump resistances such that the time constants are equal so that both coils will discharge at the same rate. The design is such that in the event of a discharge of one coil set, the second set will see a voltage which mimics a quench and a discharge of the second coil will be initiated. The possibility of a real second coil quench is also likely due to eddy current heating in the stabilizer material.

**Magnet Control System** The SHMS magnets will have a control system that is self contained and able to be operated remotely by EPICS. The magnets' internal controls will take care of interlocks, operating valves by PID, and converting information from the magnet into

engineering units. The EPICS system will allow operation from remote screens, archival data logging and graphic display. A dual processor PLC designed for critical fail safe process control will be used. Such PLCs can switch the process control from primary to secondary in  $\sim 50$  ms in the event that the primary processor fails. They can also be switched manually or by software for routine maintenance. The use of dual processor PLCs can reduce if not eliminate the nuisance of radiation induced local processor lockup. The PLC will use a combination of commercial electronics and PLC I/O modules for signal acquisition. Liquid level control and cryogenic thermometry is straightforward to provide using commercially available units. Readouts of magnet voltages, pressures, strain gauges and valve position LVDTs will be performed by standard PLC plug-ins.

**Support Structure** The SHMS support structure will be a welded steel frame riding on steel wheels and a center bearing. The structure will be built from prefabricated sections that must be welded together in the Hall. The steel structure will have a main beam section that will carry the entire spectrometer. The entire beam and spectrometer will ride on large hinged steel wheel bogies and floor mounted rails to allow precise scattering angle changes. This system is similar to that used in the HMS and SOS spectrometers. The steel fabrications will be hollow welded structures similar to ship hull sections. As such they will have internal access to permit complete welding of all seams and joints. The wheel sections will be driven by motors and reducers with variable frequency drives. The wheels are planned to be conical sections that are machined at the proper angle to control the radius of rotation. The use of the successful “Bertozzi” hinges on the wheel assemblies to eliminate the large radial forces that arise from even small misalignments is incorporated in the design.

**Spectrometer Motion System** The SHMS spectrometer has a required range of motion from 5.5 degrees to 25 degrees. These two orientations are shown in Fig. 190. Proximity detectors will ensure that the system always moves in a safe angular range and that obstacles are avoided. Positioning accuracy consists of three components: angular measurement, pointing control, and distance from pivot. The scattering angle positioning tolerance will be 0.01 degrees, the pointing tolerance will be  $\pm 0.5$  mm, and the distance off the pivot will be constant to within  $\pm 1$  mm. While it may be possible to measure these quantities more accurately, these are the spectrometer setting tolerances. Note that this is similar to what has been obtained with the HMS. The scattering angle will be measured by a shaft encoder that can detect an angle change of 0.003 degrees. A scale etched into the floor at the radius of the rear drive wheels and viewed by a video camera with a graticule lens will confirm the scattering angle setting. Pointing and distance from pivot will be controlled by a large central crossed roller bearing. The accuracy of such bearings is a few thousandths of an inch. A view of the pivot showing simultaneous connection of the SHMS, and SOS, and the HMS, is provided in Fig. 189.

The motion of the SHMS spectrometer will be coordinated by a stand-alone PLC that integrates the drive wheel motion, angle read-back, proximity sensors, and obstacle detection. The

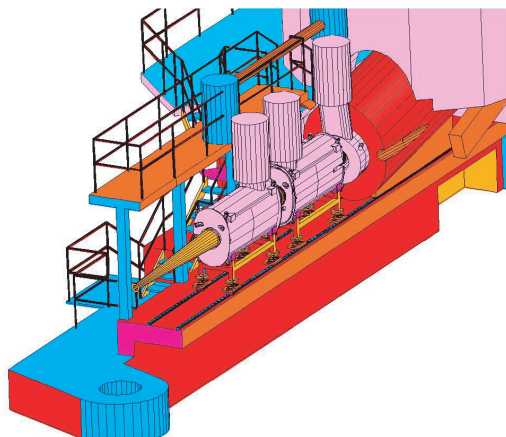


Figure 188: SHMS Pivot with Slider.

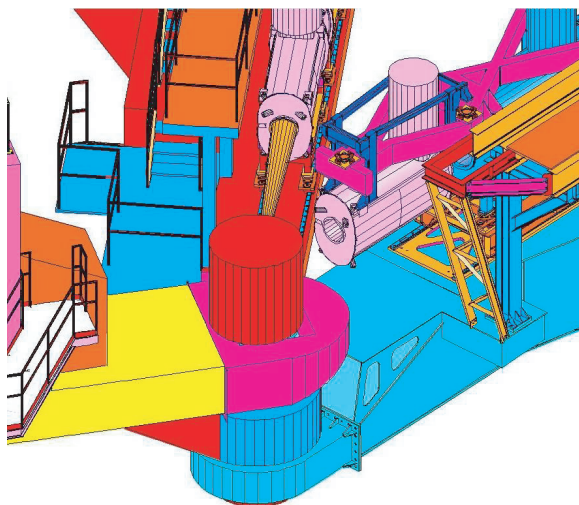


Figure 189: Hall C Pivot with (from left) SOS, SHMS, and HMS Attached.



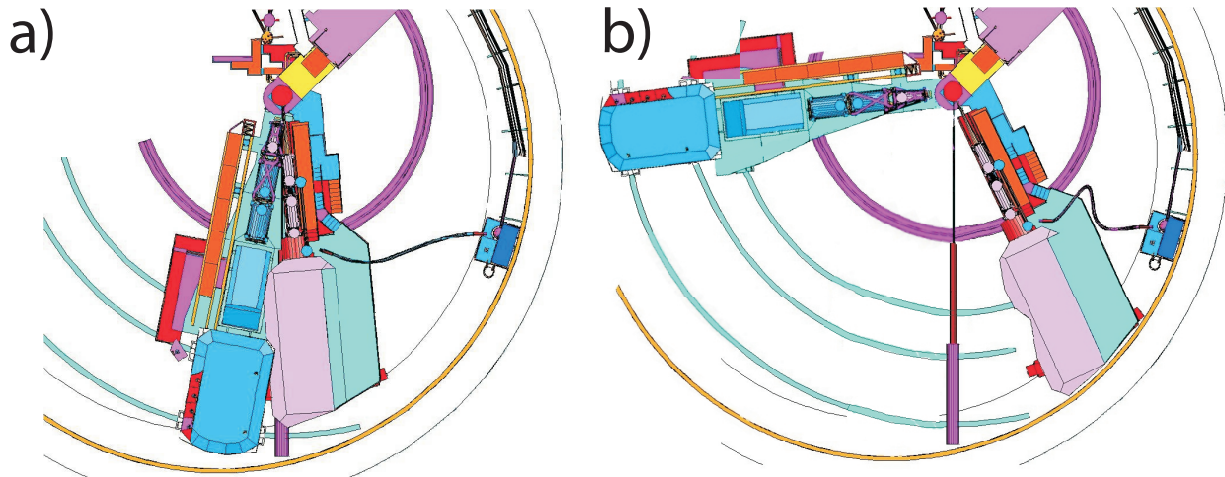


Figure 190: The SHMS-HMS spectrometer pair in two extreme configurations: a) the SHMS at  $5.5^\circ$  and the HMS at  $10.5^\circ$ ; and b) the SHMS at  $25^\circ$  and HMS at  $85^\circ$ .

rotation motion will be limited to a preprogrammed range set in EPROM in the PLC and by the proximity detection. This design is similar to the HMS rotation control system.

**Shield House** The SHMS spectrometer shield house will be a reinforced cast concrete structure that is built on the steel carriage. The concrete thickness will be 100 cm on all sides except toward the pivot where it will be 200 cm. The concrete is formed and poured in place. A conventional concrete mix will be used with added borate to absorb thermal neutrons. The interior walls, floor and ceiling will have a minimum 2-inch thick lead lining except for the front wall which will have 3 inches of lead. The lead will be covered and constrained by a system of aluminum plates and C channels. The SHMS detectors will be mounted on a transverse rail system so that the detectors may be easily removed for servicing and relocated accurately. The shield house will be accessed by a door that is hinged to open outward on the side away from the beam, and a removable block wall. There will be a limited amount of space inside the shield to allow a corridor access on both sides of the detector stack.

### SHMS Cryogenic System

*Description* The SHMS magnets will be designed with a cryogenic interface similar to the existing HMS magnets. Internally the magnets will have thermal siphon circulation from helium and nitrogen reservoirs. The reservoirs will contain dual relief devices: an ASME coded mechanical relief and a rupture disc set at a 25% higher pressure. Exhaust lines for relief which are separate from the cool-down lines will be used so that there will be no chance of a contamination blockage in these pressure relief paths. Temperature sensors, liquid level sensors, and voltage taps will be within the reservoirs. The magnets will have liquid level control and valves to permit independent



warm up or cool down using a local heat exchanger. The cryogenic valving will allow for top-fill and bottom-fill of helium and nitrogen for steady operation and for cool-down, respectively. Cold return and warm return shutoff valves will be included to allow a smooth transition from cool-down to regular closed cycle operation. The cryogenic supply will use the existing Hall C G0 transfer line including the G0 flex line, vacuum jacketed return lines, flex gas lines and cool-down heat exchanger. The SHMS cryogenic system will use a new cryogenic distribution box mounted on the back of SHMS and a flexible transfer line similar to that constructed for the G0 experiment. The magnets will be connected by JLab standard U-tubes similar to those used on HMS/HRS quads. A set of gas manifolds installed on the back of the SHMS will collect and return cryogenic gases to the existing Hall C cryogenics system. A stand and a platform are required for support of equipment and for personnel access. The system is completed by automated cool-down valves and actuators identical to those used on HMS.

*Operating modes* During normal operation the SHMS magnets will be fed helium gas at 4.5 K and 3 atm. This gas gets JT expanded at each magnet by a valve that is controlled by the SHMS magnet control system to maintain liquid level. Boil off gas and JT flash will be returned to the local refrigerator at 1.2 atm. and 4.2 K. Nitrogen will be fed to the SHMS at  $\sim 85$  K and 4 atm. where it is expanded into the  $N_2$  reservoir by a valve under local control. Boil off  $N_2$  will be vented outside. Vapor cooled current leads will be controlled by valves that servo on the SHMS magnet current and adjust the helium gas flow accordingly. Separate flow control and measurement for each current lead is a normal part of this design. Non burn-out current leads are specified. The helium gas from the leads will be returned warm to the End Station Refrigerator compressor suction. The cool-down gas return and  $N_2$  gas return lines will be vacuum jacketed to prevent ice and water from accumulating near the magnets.

Internally the SHMS magnets use thermal siphon circulation. An insulated supply line will feed helium to the bottom of the magnet cryostat and a return line will collect the slightly less dense fluid at the top of the cryostat and return it to the helium reservoir through a stand-pipe. The magnet heat leak will provide the energy to drive the circulation. The pipes are sized for 10 times the design heat load to ensure stable thermal siphon flow under all conceivable conditions. The  $LN_2$  system design is similar.

During cool down and warm up, 4-atm. helium gas at 300 K will be blended with a pre-cooled 80-K helium stream on the SHMS in a “cool-down heat exchanger” (CDHXR). This variable temperature source will be controlled by the SHMS magnet control system to provide a 70-K differential temperature for either warming or cooling, and will maintain an internal temperature difference in the SHMS magnet of no more than 50 K. This CDHXR will provide a precise method of warming and cooling the SHMS magnets independently in a manner which minimizes thermal stress due to relative contraction. This technique will also provide increased cryogenic efficiency.

**SHMS Vacuum Systems** The SHMS spectrometer will have three vacuum systems dedicated to the operation of a) the QD30 superconducting magnet, b) the SHMS spectrometer vacuum, and c) the Čerenkov detector. The SHMS cryogenic system is presumed to be made leak tight and cryo-pumping so a dedicated vacuum system is not included in the design. The QD30 magnet will also be leak tight, but a vacuum system tailored to leak testing, commissioning and biannual vacuum servicing will be included as a dedicated system. It can be used to commission and service the cryogenic system as needed. It will be portable, self contained, and fully instrumented. The spectrometer and Čerenkov vacuum systems will be dedicated to those devices and will be permanently installed on the SHMS.

The pumping system for the QD30 magnet will consist of a turbo pump backed by a direct drive roughing pump. A 1000 liter per second turbo pump with a full port gate valve, roughing bypass manifold and leak testing manifold will be required. The wheeled pump station will have a mechanical 30 – 0 – 30 vacuum gauge, high range and low-range thermocouple gauges, and a cold cathode ion gauge. A dedicated RGA for system commissioning will be needed. A large full port cold trap that can be piped in for system startup and mounted on a separate wheeled cart is included in the specification. Appropriate auxiliary vacuum hoses, valves and flanges to facilitate connecting to all the SHMS vacuum systems will be provided as well.

The SHMS will have thin aluminum entrance and exit windows. The windows will be hydro-formed spherical shapes similar to those in use on the HMS. The spectrometer vacuum between these windows will be maintained by a large mechanical pump and roots blower as a roughing system, and a 1000 l/s turbo pump.

The Čerenkov vacuum and gas system design is similar to the above but includes the capability of introducing other gases besides helium. This system will be dedicated to providing the correct Čerenkov atmosphere and will have differential pressure relief valves to limit the operating pressure range. Appropriate monitoring equipment to verify that the correct index has been achieved will be necessary. An arc cell system and a hygrometer will be used for quality control of the process. The Čerenkov system operates first with a nitrogen purge to dry the system, then the nitrogen is displaced with the detection gas. A small volume purge of the detection gas may be maintained to permit monitoring of gas quality.

## **SHMS Optics and Monte Carlo**

**SHMS Optics Design** The goal of the SHMS design was a compact, general purpose spectrometer similar in properties to the HMS, but with a higher maximum momentum setting for experiments that will use the 11 GeV beam available in Hall C from the CEBAF upgrade. The SHMS needs to be compact in order to fit into the forward-angle space now used by the SOS spectrometer, with angular range from 5.5 to 25 degrees, and a minimum angle with respect to the

HMS of 16 degrees. The design process also sought to minimize the cost. A summary of the design parameters is given in Table 31.

To achieve these goals, the SHMS was designed as a vertical bend, QQ(QD) spectrometer. Two quadrupole magnets are followed by a combined-function magnet that includes both quadrupole and dipole elements. This is similar to the HMS optical layout, except that the last quad and the dipole have been superimposed to make the spectrometer compact.

The first two quads are copies of the HMS Q1 magnet. Re-use of this design helps keep costs low, and the performance of these magnets is well known. The QD is a new design, the engineering details of which may be found in section 3.C.3. Because of the large fields required to bend 11 GeV electrons in a compact spectrometer, the QD must be superconducting, without iron pole-faces. The coils are enclosed in a cylindrical shell of iron, which serves as a flux return yoke. This configuration is very compact, and relatively inexpensive to build. However, it is not a true QD magnet. That would require a toroidal iron shell, and similarly curved coils. A true QD magnet would be very expensive to build, and the performance of the SHMS with a cylindrical QD is adequate.

The SHMS design is very flexible. The coils in the QD are separately excited, and the magnets and detectors will have adjustable positions, making many tunes possible. We consider two here: the original Small Solid Angle (SSA) tune used to design the spectrometer, and a Large Solid Angle (LSA) tune, with all magnets and detectors moved forward 2.32 meters as a rigid body.

Several tools were used in designing the SSA tune. The first of these is TOSCA[TOSCA], a finite-element, 3-D magnetostatics program. The results discussed here come from the ‘QD30’ TOSCA model of June 5, 2000. TOSCA calculated the field values on a 3-D grid inside the magnet, and a model was fit to the horizontal, or  $y$  field component on the  $y = 0$  plane (the vertical mid-plane, or symmetry plane of the magnet.) A ray-tracing program was then used to numerically integrate the equations of motion for an electron in the model’s field. This determines the trajectory of the central ray in the spectrometer.

Early in the design process, the total bend angle was fixed at 18.4 degrees. This is essentially the maximum that can be allowed without limiting the acceptance through the QD magnet. An important point to realize is that the quadrupole fields in the QD bend the central ray. Optimizing the spectrometer performance involved tuning the Q/D ratio, and this required compensatory changes in the dipole strength in order to preserve the correct bend angle.

It should also be noted that the central ray has to be offset from the exact center of the QD to avoid cutting off the acceptance by the magnet entrance and exit. Monte Carlo simulations showed that an offset of 7 cm in the center of the magnet combined with a beam-pipe transition at 200 cm from the QD center would optimize the acceptance. This layout is shown in Fig. 180. A complex transition pipe will join the QD to the neighboring quad magnet.

With a central trajectory specified through the QD, the optics of the spectrometer as a whole could be studied. The optics are defined by map functions that transform the trajectory of a particle at one location to its trajectory at a different location. We used the COSY [COSY] program to calculate 5th order Taylor series polynomial expansions of both the global map from target to detectors, and the individual sequential maps that transform from one significant aperture in the spectrometer to the next. The COSY calculations are based on a model of the spectrometer magnets that we describe below. Concurrent with the map calculations, COSY would track an ensemble of test rays through the spectrometer, and adjust the strength of the first two quads to produce the sharpest focus at the detectors. This process was iterated with manual adjustment of other parameters, such as focal plane position, to optimize the performance. The end result was the standard tune. Parameters of the standard tune are given in table 34, and the tracks of 27 test rays are shown in Fig. 191.

**COSY magnet model** Standard COSY quadrupole elements were used for the two quad magnets, as was done in the HMS optics model. There are no COSY standard elements corresponding to the QD magnet, and it had to be modeled using the general field-map element. Past experience has shown that this requires extremely smooth field-map data, such that the TOSCA field-maps could not be directly used. Instead, field values were calculated from a model fit to the data. The use of a model also allows changes to be made in the fields to simulate small changes in the dipole and quadrupole coil excitations for tuning purposes. This model was also used in the central-ray integrations mentioned above. The form of the model is:

$$B_y(x, z) = \sum_{i=0}^6 C_i(z) (x/r_0)^i \quad (75)$$

in which  $(x, y, z)$  are right-handed Cartesian coordinates with  $z$  the axis of the magnet pointing downstream,  $y$  is horizontal, and  $x$  is in the vertical plane, pointing upwards, with origin the center of the magnet;  $B_y$  is the  $y$ -component of the magnetic field in the plane  $y = 0$ ; and  $r_0 = 30$  cm is the radius of the beam-pipe. For each discrete  $z_j$  in the TOSCA data, polynomial coefficients  $C_{ij}^T$  were fit to the data using the method of singular value decomposition. Gaussian interpolation was then used to calculate coefficients at arbitrary  $z$ :

$$C_i(z) = \sum_j C_{ij}^T \exp(-[(z - z_j)/(s \Delta z)]^2)/(s \sqrt{\pi}) \quad (76)$$

where  $\Delta z$  is the 2-cm grid spacing.  $S = 2.5$  gives smooth results that accurately reproduce the TOSCA data.

As mentioned above, both the dipole and quadrupole coil excitations needed to be adjusted by small amounts to fine tune the bend angle and optimize the focus. In principle, this could be done by re-running the TOSCA model, but this was not practical. Instead, we use symmetry arguments

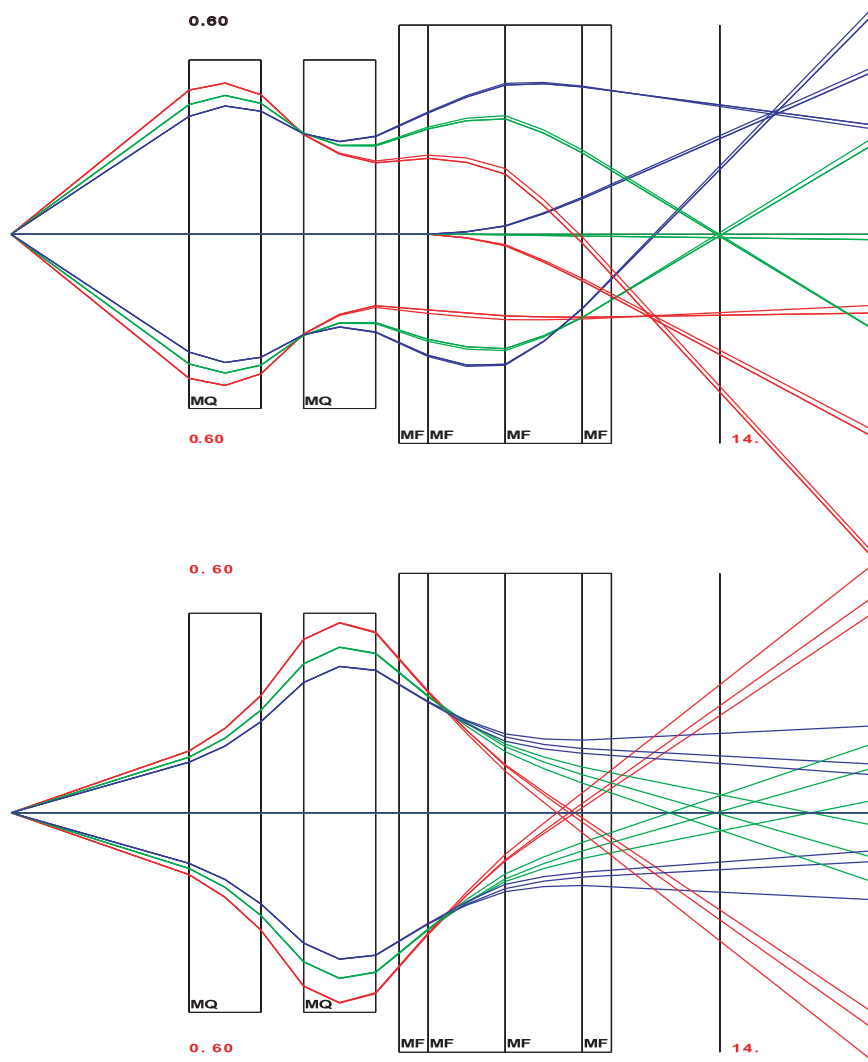


Figure 191: Rays Tracked through the SHMS by COSY for the SSA Tune. The top panel is the bend-plane projection (COSY  $(x, z)$  coordinates), while on the bottom is the transverse projection (COSY  $(y, z)$  coordinates). 27 rays are plotted for all combinations of 3 values of total momenta ( $\Delta p/p_0 = 0.1$  [blue], 0 [green],  $-0.1$  [red]), 3 values of  $p_x/p_0$  (0.4, 0,  $-0.4$ ), and 3 values of  $p_y/p_0$  (0.15, 0,  $-0.15$ ).

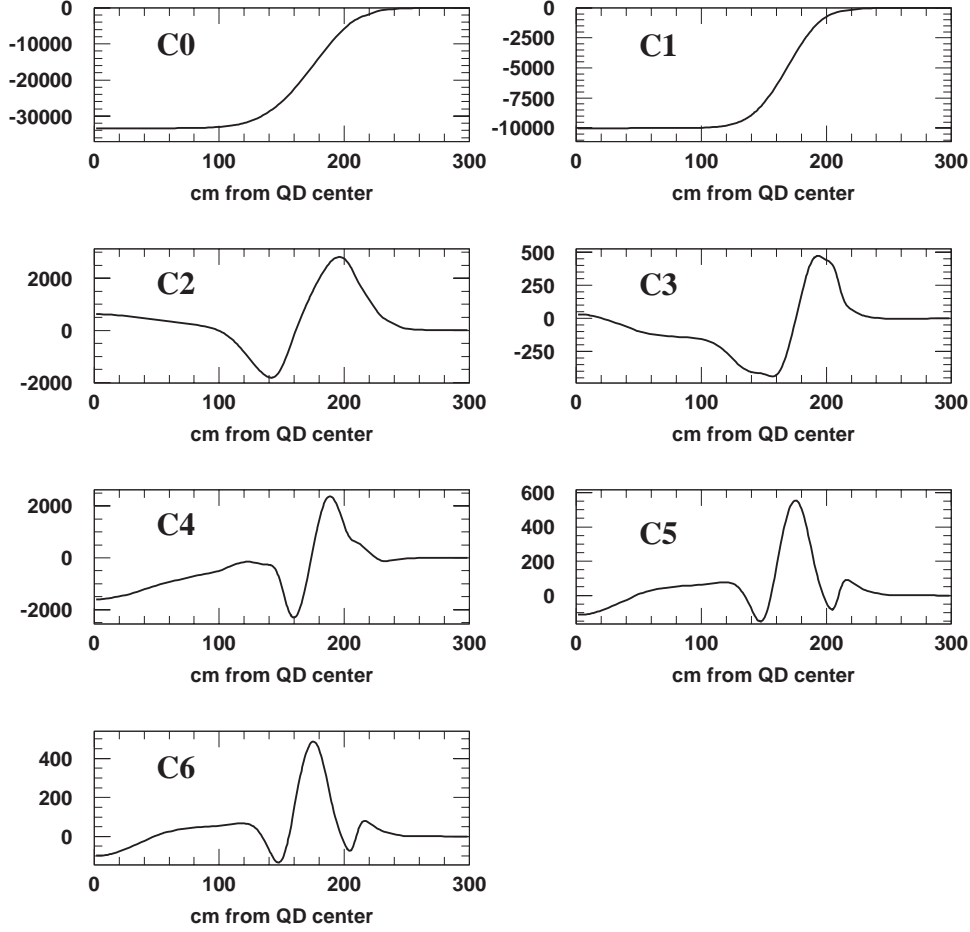


Figure 192: Polynomial Coefficients in the QD Magnetic Field Model as a function of  $z$ , the axial distance from the magnet center. (The functions are symmetric about  $z = 0$ .)  $C0$  is the dipole component,  $C1$  the quadrupole component, and the others are higher order contributions. The vertical axes are the contribution to  $B_y$  at  $x = 30$  cm, in gauss.

to treat all the terms in the model that are even-order in  $x$  as harmonics of the dipole coils, and the others as harmonics of the quad coils. Thus, we adjusted the dipole excitation in the model by simply scaling the even-order coefficients, and similarly adjust the quadrupole excitation by scaling the odd-order ones. This approximation neglects non-linear saturation effects in the iron and thus is only good for small corrections. The adjusted coefficients are plotted as a function of  $z$  in Fig. 192. One can see that there are significant higher order terms beyond about  $z = 120$  cm, with the  $C_2$  component dominant. Once the final tune is determined by this approximation, a full TOSCA calculation based on the tune values may be performed to verify the results.

**LSA tune** The LSA tune is closely related to the SSA tune. It is produced by sliding all the magnets and detectors forward by 2.32 m. The QD is operated with the same fields, so that the central ray follows the same path through the QD and the detectors. The fields in the two

Table 34: SHMS Optics Parameters for SSA and LSA Tunes. Coordinates are given as (horiz,vert) distance from nominal target center.

<i>Parameter</i>	<i>SSA tune</i>	<i>LSA tune</i>
Q1, Q2 mechanical length	189.0 cm	189.0 cm
Q1, Q2 magnetic length	187.9 cm	187.9 cm
Q1, Q2 pole-tip radius	25.0 cm	25.0 cm
Q1, Q2 beam-pipe inner radius	20.5 cm	20.5 cm
Length from target center to Q1 center	558.5 cm	326.5 cm
Length from target center to Q2 center	857.5 cm	625.5 cm
Q1 field gradient for 11 GeV	-7.7069 T/m	-10.7436 T/m*
Q2 field gradient for 11 GeV	8.6041 T/m	9.3790 T/m*
QD beam-pipe inner radius	30.0 cm	30.0 cm
Central ray path-length to middle of QD	1290.0 cm	1058.0 cm
Coordinates of QD center	(1288.2 cm, 20.8 cm)	(1056.2 cm, 20.8 cm)
QD rotation	9.200°	9.200°
Total bend angle	18.400°	18.400°
Layout bend radius	1079.8 cm	1079.8 cm
Coordinates of layout bend center	(1116.6 cm, 1079.8 cm)	(884.6 cm, 1079.8 cm)
Total length of central ray	1850.0 cm	1718.0 cm
Central ray coordinates at focal plane	(1824.3 cm, 177.3 cm)	(1687.2 cm, 208.8 cm)
Field at QD center for 11 GeV	3.3416 T	3.3416 T
Quad component at QD center, 11 GeV	3.3416 T/m	3.3416 T/m
Minimum spectrometer angle	5.5°	10°
Maximum spectrometer angle	25°	25°
Minimum separation from HMS	16°	25°

\* Maximum achievable quad gradient of 8.6 T/m limits central momentum to 8.8 GeV

quadrupoles were re-optimized by COSY in order to produce a good focus at the focal plane, which was shifted 1 meter farther back from the QD, as measured along the central ray, to avoid tipping the focal plane to too shallow an angle. By having the quads closer to the target, the solid angle acceptance is increased, as is evident from Fig. 193, in which we track the 27 standard test rays. However, this tune requires substantially higher quadrupole fields, as listed in Table 34. The values listed, corresponding to a central momentum of 11 GeV/c, exceed the capability of these magnets. The maximum central momentum that can be reached in this mode of operation is 8.8 GeV/c, for which Q1 operates at its maximum gradient of 8.6 T/m. Note that with a central momentum of 8.8 GeV/c the SHMS still accepts full energy (11 GeV/c) particles, albeit with somewhat poorer resolution. With the quads moved forward the minimum scattering angle becomes 10°.

**SHMS model in the ‘physics’ Monte Carlo** The field maps generated by COSY have been incorporated into a model of the spectrometer so that detailed simulations can be made of the SHMS acceptance, resolution, and distributions of events at the detectors. COSY-generated transformations are used to propagate particles from the target to each of the important apertures in the spectrometer. In addition, the particle trajectories can be evaluated at each detector package

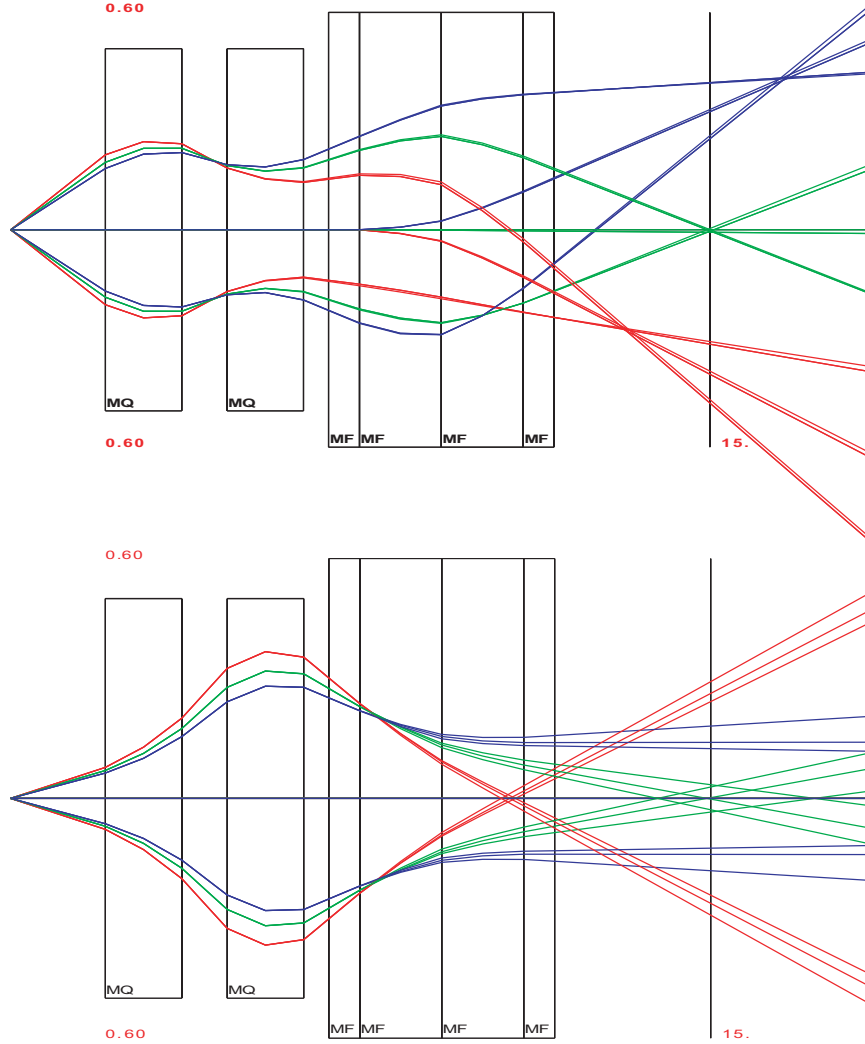


Figure 193: Rays Tracked through the SHMS by COSY for the LSA Tune. The top panel is the bend-plane projection (COSY  $(x, z)$  coordinates), while on the bottom is the transverse projection (COSY  $(y, z)$  coordinates). 27 rays are plotted for all combinations of 3 values of total momenta ( $\Delta p/p_0 = 0.1$  [blue], 0 [green],  $-0.1$  [red]), 3 values of  $p_x/p_0$  (0.4, 0,  $-0.4$ ), and 3 values of  $p_y/p_0$  (0.15, 0,  $-0.15$ ).



in order to determine the active region needed for each detector.

The SHMS model is of the same format as the existing HMS and SOS models, and so has been added to 'SIMC', the physics Monte Carlo used extensively in Hall C. This allows generation of various physics processes, taking into account the cross sections and event distributions, as well as multiple scattering and energy loss in target, spectrometer, and detector materials, and any relevant particle decays. The SHMS model includes the same level of detail as the models for the existing spectrometer, and so the simulation can be used for detailed and extremely realistic studies under a variety of conditions. In particular, it can be used to determine the acceptance and resolution as functions of target length, collimation scheme, and detector configuration.

### SHMS Performance (Resolution/Acceptance)

A stand-alone Monte Carlo has been used to investigate the properties of the SHMS design as developed in the previous section. The Monte Carlo was run with the spectrometer at  $90^\circ$  and a target length of 70 cm. Electrons were generated uniformly over the phase space and sent through the SHMS spectrometer with the central momentum ( $p_{\text{cent}}$ ) set at 7.5 GeV/c. Events were generated over the  $\delta = (p - p_{\text{cent}})/p_{\text{cent}}$  range of -40% to 40%, horizontal angle ( $y' = dy/dz$ ) range of  $\pm 100$  mr and vertical angle ( $x' = dx/dz$ ) range of  $\pm 100$  mr relative to the spectrometer axis. Studies were done with the large solid angle (LSA) tune (spectrometer moved forward by 2.32 m) and the small solid angle (SSA) tune.

Plots of the  $\delta$ ,  $Y_{\text{tar}}$ ,  $y'$  and  $x'$  acceptance are shown in Fig. 194 for the large solid angle (LSA) tune (solid black line) and the small solid angle (SSA) tune (solid red line). Both tunes have a large acceptance in  $\delta$  and  $Y_{\text{tar}}$ , the horizontal position. Both tunes have a flat acceptance in  $Y_{\text{tar}}$ . For the LSA tune, the  $\delta$  acceptance is flat for negative  $\delta$  and gradually decreases with increasing positive  $\delta$ . The SSA tune has a fairly flat acceptance with a drop-off above  $\delta = 10\%$ . Both tunes have a sharp drop off below  $\delta = -20\%$ . In designing the size of the detectors, cuts of  $-15 < \delta < 25\%$  and  $-25 < Y_{\text{tar}} < 25$  cm were used. The plots of  $y'$  and  $x'$  acceptance in Fig. 194 include these cuts. The LSA tune has about twice the  $x'$  acceptance of the SSA tune.

The beam envelope at  $z=0$  in the detector hut is plotted in Fig. 195 for the LSA tune with cuts of  $-15 < \delta < 25\%$  for target lengths of 0.5, 4, 30 and 50 cm. (Note that a 30 (50) cm target viewed at  $90^\circ$  roughly corresponds to a  $\geq 70$  (120) cm target at  $\leq 25^\circ$ .) We use the TRANSPORT[Br80a] coordinate system in which +X is down and +Y is beam left. For the 0.5-cm target, one can see the expected hourglass shape of the X versus Y distribution and with increasing target length the waist of the hourglass expands. The bottom plots in Fig. 195 (for target lengths of 30 and 50 cm) show that the detectors have to be increased by 1.4 times in the horizontal dimension to accommodate an increase of the target length by 1.7 times. The detectors will be built for  $-25 < Y_{\text{tar}} < 25$  cm, but, where appropriate, will initially only be instrumented for the 30-cm target. The beam envelope for the LSA tune is plotted in Fig. 196 at key points within the detector stack.

The effective solid angle was calculated by generating 100K events over a range of horizontal angle of  $\Delta x' = \pm 0.1$ , vertical angle of  $\Delta y' = \pm 0.1$ ,  $-15 < \delta < 25$  % and  $-25 < Y_{tar} < 25$  cm. The effective solid angle,  $\Omega$ , was calculated as  $\Delta x' \cdot \Delta y' \cdot \frac{\# \text{ accepted}}{\# \text{ thrown}}$ . The LSA tune has  $\Omega \approx 4.0$  msr, while the SSA tune has  $\Omega \approx 2.0$  msr.

The resolutions for the target quantities  $\delta$ ,  $Y_{tar}$ ,  $y'$  and  $x'$  for 7.5 GeV/c electrons are plotted as functions of  $\delta$  in Fig. 197 for the SSA tune. For these calculations, the assumption was that the pipe which could contain the gas and mirror for the first gas Čerenkov detector will be at vacuum. This Čerenkov detector is primarily intended for experiments in which high resolutions are not needed. The solid blue curve has no multiple scattering nor wire chamber resolution in the Monte Carlo and indicates the limitations of the optics matrix used in the model of the SHMS. The blue line is nearly at zero except near the edges of the  $\delta$  range, confirming that the optics matrix is adequate. The red dashed curve shows the effect of including wire chamber resolutions in the Monte Carlo. The solid black curve adds the effect of multiple scattering. For the Monte Carlo, the hydrogen target cell was a cylinder with radius 3.37 cm and a wall thickness of 0.005 inches. The combination of the scattering chamber window, air, and spectrometer entrance window was 0.6% radiation lengths. In the detector hut the material was the spectrometer's exit window ( taken as Mylar/Kevlar material of 0.020 inches thickness in the simulation), air, and the material of the drift chambers. The resolutions in  $y'$  and  $x'$  are relatively independent of  $\delta$ . The contribution to the resolution in  $y'$  and  $x'$  from wire chamber resolution and multiple scattering are about equal, while the  $Y_{tar}$  and  $\delta$  resolutions are dominated by wire chamber resolution with multiple scattering having almost no effect at this momentum. The  $Y_{tar}$  resolution has a fairly dramatic parabolic dependence on  $\delta$ . For the SSA tune, the  $\delta$  resolution is seen to have a slightly asymmetric parabolic dependence on  $\delta$  with a minimum at  $\delta \approx -1\%$ . For the LSA tune (not shown here), the  $\delta$  resolution has an asymmetric parabolic dependence with a minimum at  $\delta \approx -6\%$ . The average resolutions for  $\delta$ ,  $Y_{tar}$ ,  $y'$  and  $x'$  are about 0.05 %, 0.20 cm, 0.8 mr, 0.8 mr for both the SSA and LSA tunes, meeting or exceeding the requirements given in Table 31.

**SHMS Detector Systems** As the momentum range of a spectrometer changes, so also do the demands on the particle detector elements. At higher momenta, the degradation of angle and momentum resolution due to multiple scattering are reduced, and one can consider incorporating a low-mass detector in the upstream regions of the detector stack. The times-of-flight (TOF) of different particle species differ less, making trigger timing somewhat easier, but also making particle identification by TOF a less viable option. Particle identification using the Čerenkov effect also depends upon the relative speeds of particles, which means that Čerenkov counters must be more thoughtfully designed than at lower momenta, and that other identification techniques should be considered. Higher energy leads to larger fluctuations of the energy deposited in a total-absorption calorimeter, as there is a higher probability that some of the energy leaks out the back; this necessitates considering a thicker shower counter for the SHMS than is used in the HMS.

The above considerations lead us to a SHMS detector system design which would essentially be

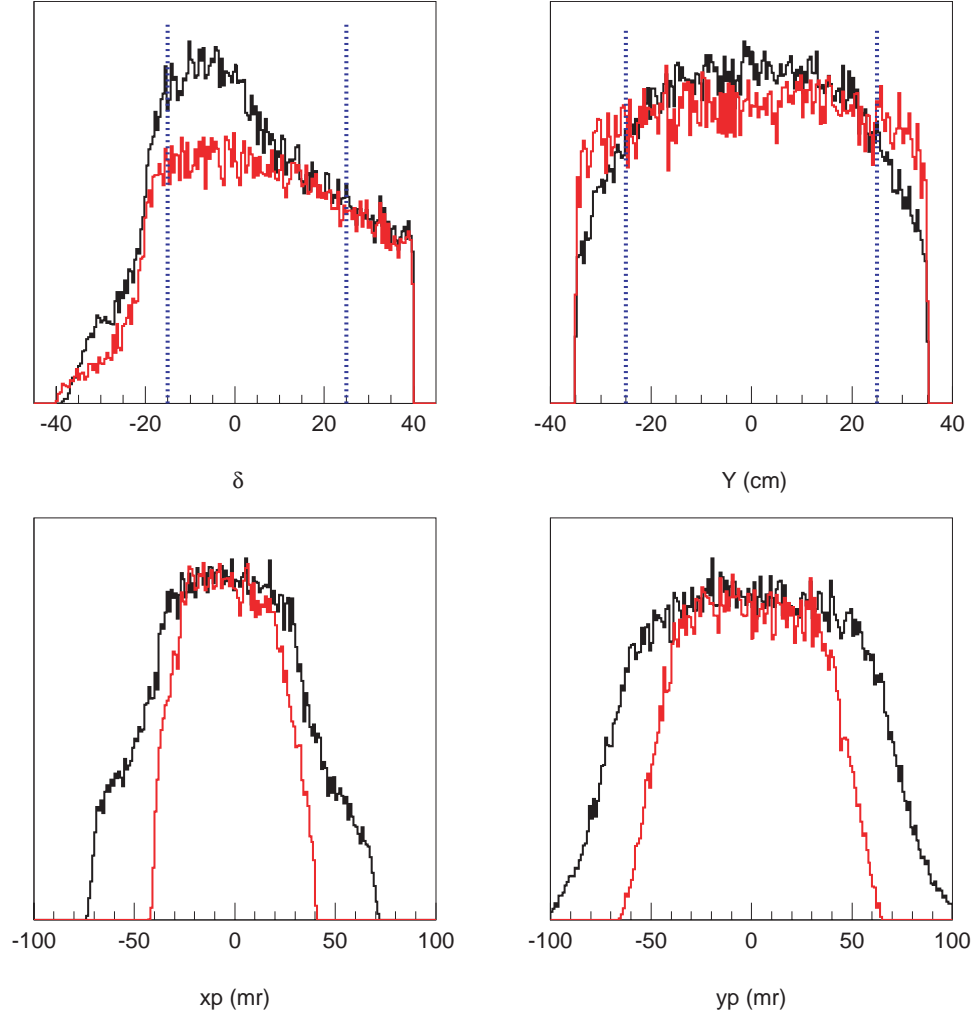


Figure 194: The Phase Space Acceptance plotted as function of  $\delta$ ,  $Y_{tar}$ ,  $y'$  and  $x'$  for the large solid angle (LSA) tune (black solid line) and the small solid angle (SSA) tune (red solid line). The y-axis is yield in arbitrary units and the LSA and SSA yields have been scaled to match each other at the maximum. The blue dotted lines indicate the limits of  $-15 < \delta < 25$  % and  $-25 < Y_{tar} < 25$  cm which were used in determining the detector size. The plots of  $y'$  and  $x'$  include the cuts of  $-15 < \delta < 25$  % and  $-25 < Y_{tar} < 25$  cm.

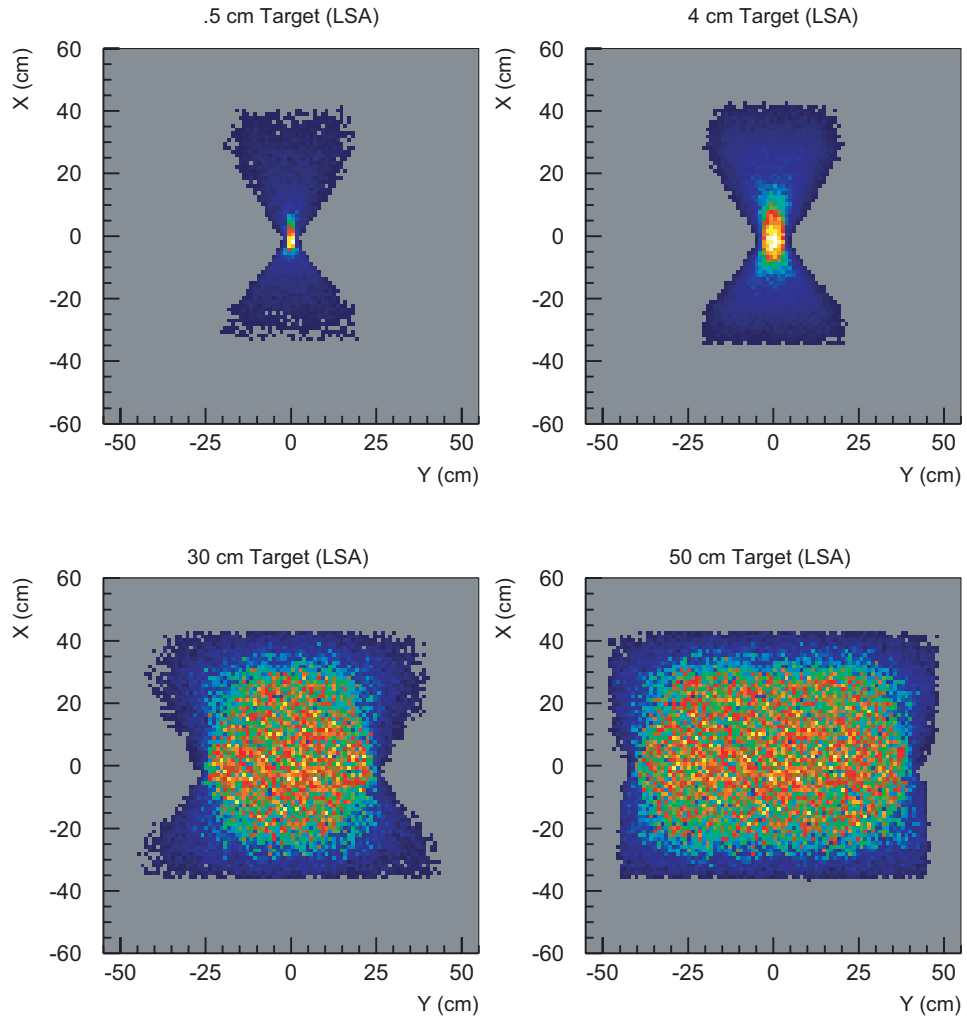


Figure 195: Plots of the Vertical ( $X$ ) versus the Horizontal ( $Y$ ) position at  $z=0$  cm in the detector hut for target lengths of 0.5 cm, 4 cm, 30 cm and 50 cm. Spectrometer set for large solid angle tune with a cut of  $-15 < \delta < 25$  %.

## LSA Tune

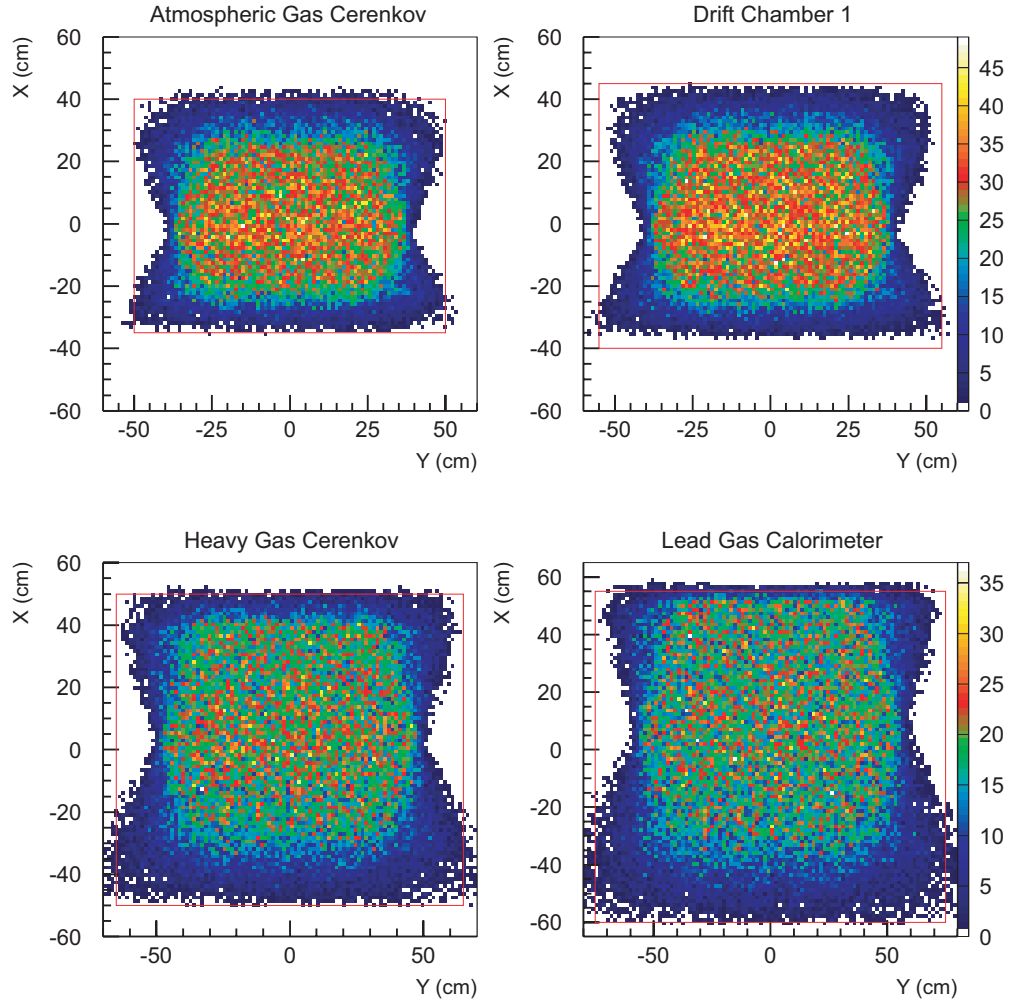


Figure 196: Plots of the vertical  $X$  versus the horizontal  $Y$  position at  $z=-60$  cm (*Atmospheric Čerenkov*),  $z=-40$  cm (*Drift Chamber 1*),  $z=160$  cm (*Heavy Gas Čerenkov*) and  $z=320$  cm (*Lead Glass Calorimeter*.) Spectrometer set for large solid angle tune with cuts of  $-15 < \delta < 25$  % and  $-25 < Y_{tar} < 25$  cm.

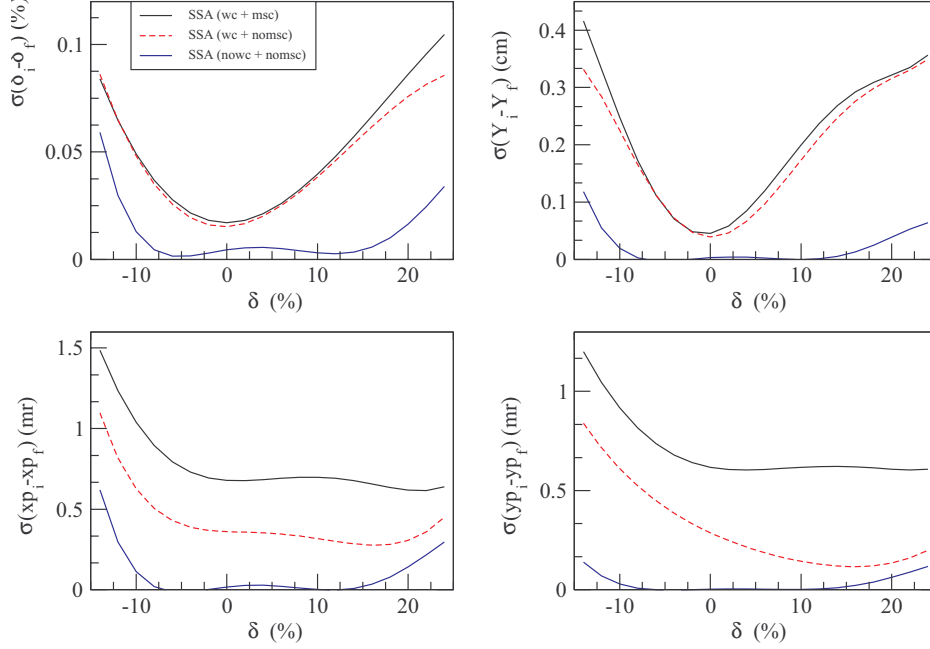


Figure 197: For the small solid angle (SSA) tune, plots of the resolutions in the target quantities  $\delta$ ,  $Y_{tar}$ ,  $y'$  and  $x'$  as a function of  $\delta$  for 7.5 GeV/c electrons. The solid black curve is the best estimate of real-world resolutions. Other curves explained in the text. The subscripts f and i refer to the reconstructed and originally generated variables.

a HMS stack modified for higher energies. However, new physics initiatives demand the inclusion of new capabilities. Measurement of the polarization of final state particles would require the inclusion of a polarimeter in the SHMS detector stack, for example. Experiments at higher rates or with low signal-to-background would benefit from improved electron/hadron discrimination, such as that provided by the addition of a transition radiation detector (TRD). Pion/kaon separation, primarily achieved by gas and aerogel Čerenkov counters, can be enhanced by recording  $dE/dx$  information in the tracking chambers and the TRD. Below, we describe an integrated system of detector components which are optimally matched to one-another and to the physics to be done in Hall C. A block diagram of the proposed detector system is shown in Fig. 198. The overall specifications for the spectrometer, developed for the physics, were summarized in Table 31.

The magnetic optics described above provides good resolution over a large acceptance. It also allows the possibility of performing experiments with a projected target length as large as 50 cm without giving up good resolution. To detect and measure this full acceptance will require that the detectors cover a large area. The required detector sensitive areas are given in Table 35. Our plan is to build the mechanical components of the detectors large enough to achieve full coverage of the 50-cm (projected) target over a 40% momentum bite ( $-15\% < \delta < +25\%$ ). However, until such time as the full acceptance is actually needed by an experiment, only the central regions of the detectors (covering a 30-cm projected target) will be instrumented.

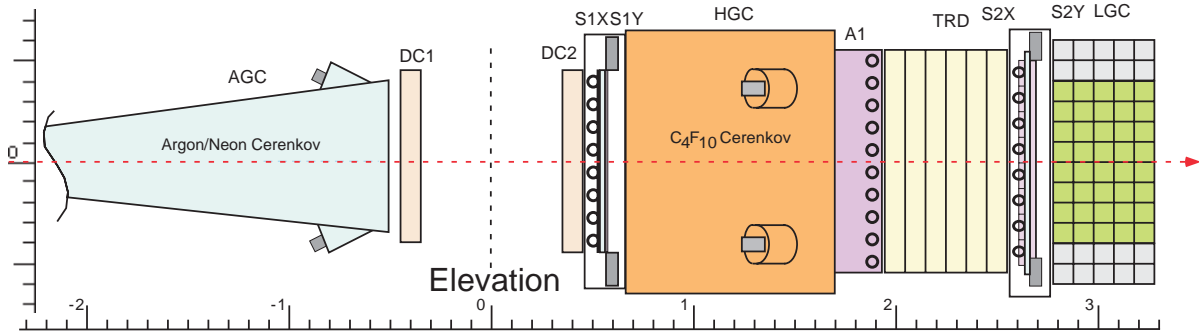


Figure 198: Block Diagram of SHMS Detector Arrangement.

Table 35: Sensitive Areas of the Detectors for Momentum Range  $-15\% < \delta < +25\%$  , for both 30-cm long and 50-cm long targets.

Detector	30-cm Target		50-cm Target	
	X size	Y size	X size	Y size
Atm. Gas Č	75	80	75	100
Drift Chambers	85	80	85	110
Scint. Hodo 1	90	90	90	110
Heavy Gas Č	100	95	100	130
Aerogel Č	110	100	110	140
TRD	110	100	110	140
Scint. Hodo 2	110	100	110	140
Shower Counter	115	120	115	150

**Wire Chambers** The SHMS tracking system will provide the only measurement of particle momentum and production angle in the spectrometer. Given an adequate description of the magnetic optics, the momentum and production angles are determined by measuring enough of the track to generate a track vector at the reference plane, then projecting it back to the target.

Although Multiple Coulomb Scattering is reduced at higher momentum, it is still a significant effect limiting momentum and angular resolution, even at 11 GeV/c. We have considered several alternatives to wire chambers for tracking in the SHMS, but conclude that gas drift chambers remain the best choice to simultaneously provide the necessary position resolution while keeping the detector mass low.

The particular design we have chosen is based upon the successful SOS drift chambers, with only minor modifications suggested by the different SHMS optical parameters and lessons learned from the original design. These chambers provide better than 180- $\mu\text{m}$  single-plane resolution and operate at rates of at least 1 MHz per wire, while placing only about 0.002 radiation lengths of material in the path of particles for a stack of six sense planes. The excellent performance of the SOS drift chambers is demonstrated by the distributions of track residuals shown in Fig. 199.

A simplified diagram of the chamber design is shown in Fig. 200. These chambers are constructed using the “open plane” technique, in which individual wire and cathode (foil) planes are fabricated on a work bench, then stacked up on a rigid frame to make the chamber assembly. This method of construction is relatively simple and robust, lending itself nicely to fabrication in a modest workspace.

As a baseline, we plan to use commercially available readout electronics of the same design as presently in use in the SOS, the HMS, and other wire chambers at JLab. However, we note that there is the possibility of enhancing the particle identification power of the SHMS spectrometer if we measure the energy loss distribution of particles traversing the wire chambers. To do so would require modified electronics at the chamber and the addition of analog readout for groups of wires. A study of the feasibility and usefulness of performing a maximum likelihood analysis of these Landau distributed  $dE/dx$  samples is ongoing. Figure 201 shows the results of a simulation of such a  $dE/dx$  system for identifying kaons and pions.

**Quartz Čerenkov Hodoscope** The existing scintillating hodoscopes in Hall C are used for a surprising number of essential functions: to provide a trigger which is approximately 100% efficient for minimum ionizing particles<sup>7</sup>, to reject accidental coincidences in multi-arm experiments, to help measure the efficiency of the tracking system, and to provide Particle Identification (PID) by time-of-flight (TOF).

While the first three functions listed above will still be critical for the SHMS, the PID function

---

<sup>7</sup>For common detector materials, this corresponds to  $\beta\gamma \simeq 3\text{--}4$ , so a “realistic worst case scenario” is the detection of protons of momenta 3-4 GeV/c.



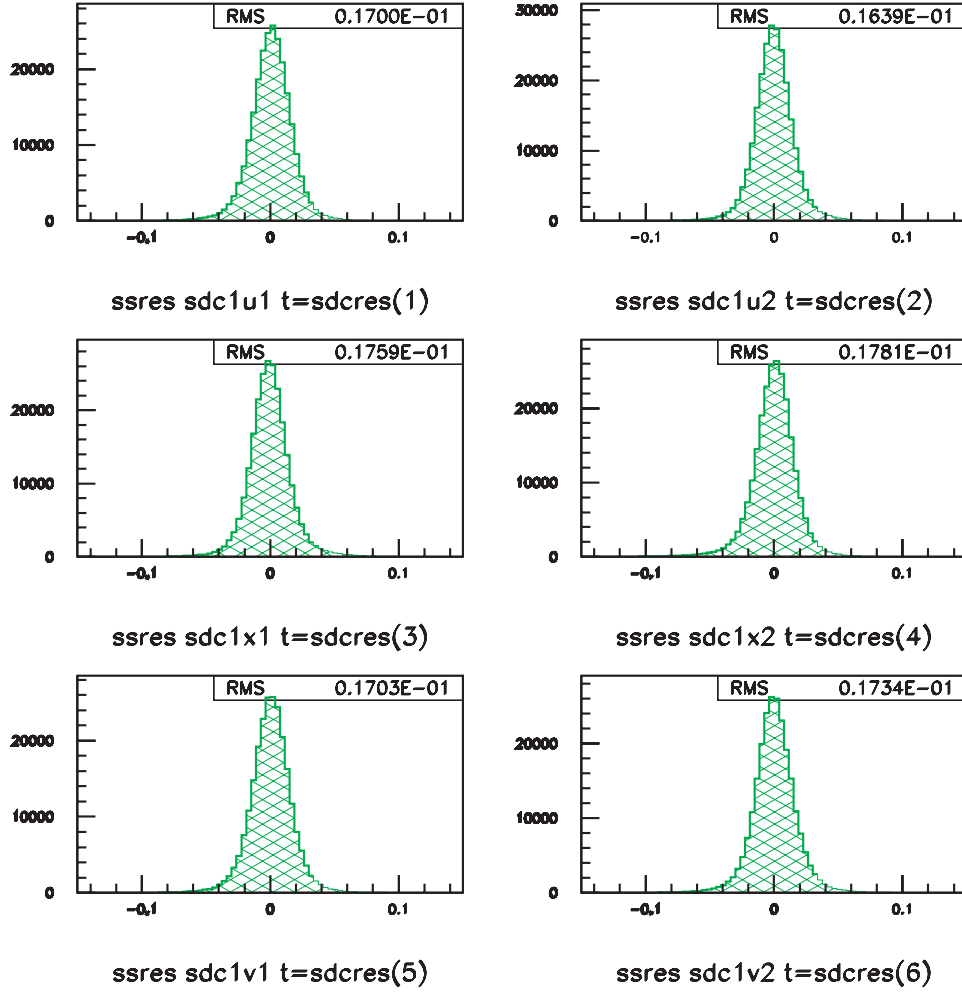


Figure 199: Measured Residual Distributions in the SOS Wire Chambers. The figures show the deviations (in centimeters) between measured hit locations in each wire chamber plane and the projected position of the associated fitted track as it passes through the wire plane. In each case track fits were performed without using the measurement from the wire plane under study. Typical residual widths are 170 microns (RMS).

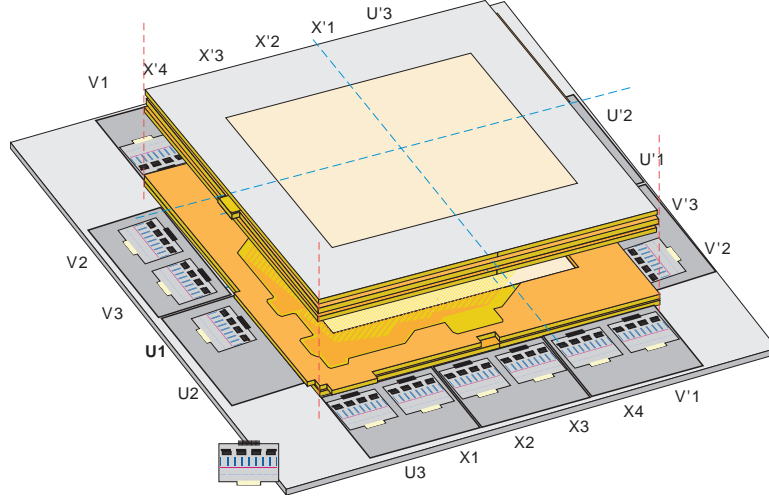


Figure 200: Block diagram of the SHMS Wire Chamber Assembly. The chamber is built by stacking individual wire and foil planes, each of which is fabricated separately using precision tooling.

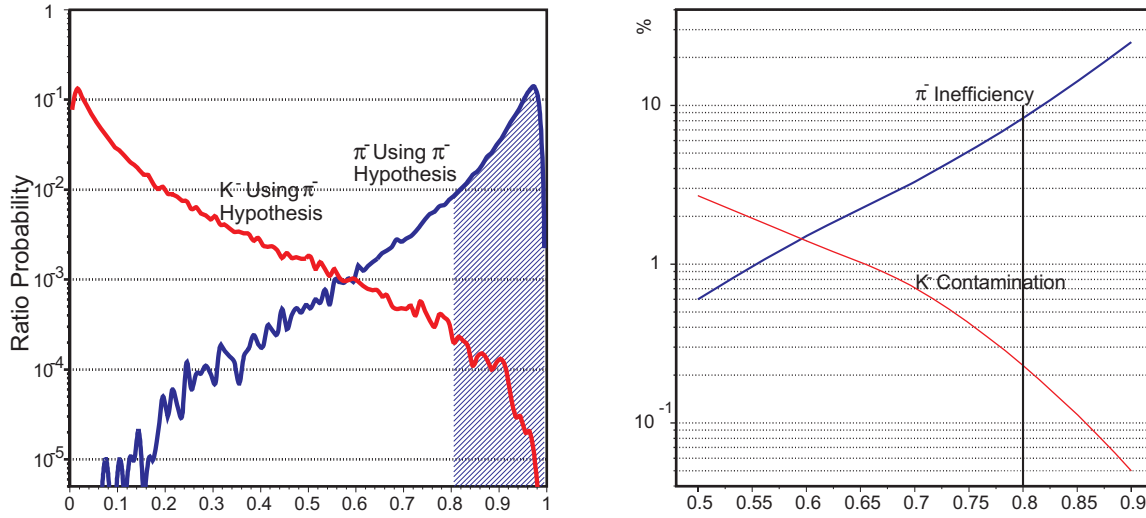


Figure 201: Pion/Kaon Discrimination using a Likelihood function applied to simulated energy loss distributions for 7 GeV/c particles in 12 wire chamber planes. For the (pion/kaon) hypothesis, only the eight (highest/lowest) measured energies are used. Left: the distribution of pion likelihood ratios  $R = \frac{L_{\pi}}{L_{\pi} + L_K}$  when the incident particle is a kaon or a pion. Right: the pion inefficiency and the kaon contamination as a function of the choice of cut, when equal numbers of pions and kaons are passed through the system.

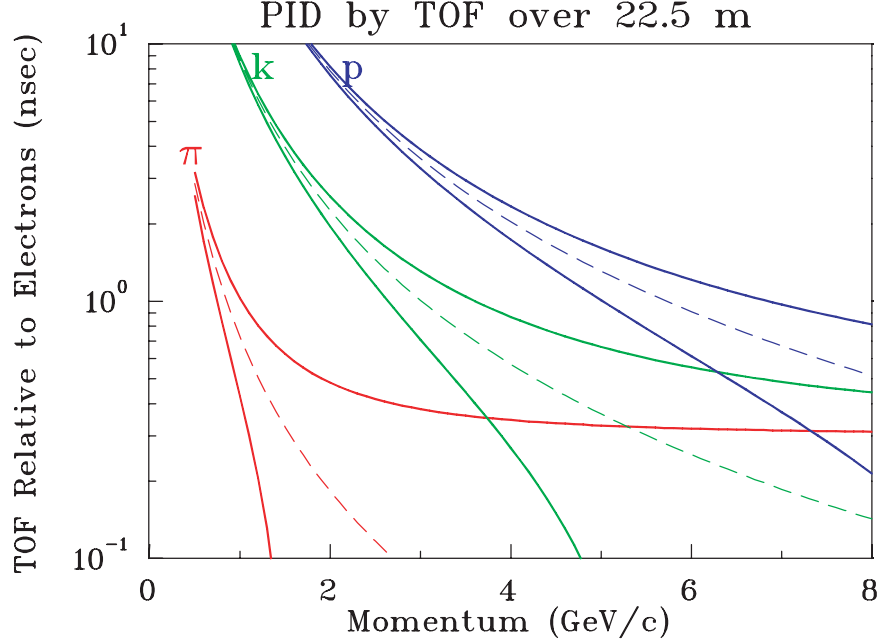


Figure 202: The dashed lines represent the time-of-flight (relative to electrons) versus momentum. The vase-shaped envelopes in solid lines demonstrate the limitations due to finite timing resolution ( $\pm 1.5\sigma$  with  $\sigma = 200$  ps assumed). At the points where the solid lines first intersect, the separation is only  $3\sigma$ .

by TOF over the short  $\simeq 2.2$ -m baseline inside the SHMS hut will be of little use at the higher average energies of the upgrade. Figure 202 shows that, even over a 22.5-m distance from the target to the detector stack, particle identification by TOF is of limited use. Generally speaking, efficient, high-confidence PID will require extensive use of other technologies such as Čerenkov detectors, and that the time resolution requirement for the hodoscope system may therefore be relaxed. This means that the front hodoscope array can be made thinner (5mm versus the present 10mm in the HMS and SOS) which will help reduce the production of knock-on electrons which would otherwise deteriorate the performance of downstream Čerenkov detectors. Meanwhile, the rear hodoscope array can be made quite thick (10mm-25.4mm) since it will be the last element before the electromagnetic calorimeter.

Taking into account the essential functions, and folding in our experience with the Hall C scintillating hodoscopes, we arrive at the following specifications for the SHMS hodoscopes:

- Trigger: Because it is the heart of the SHMS trigger, the hodoscope must have  $\geq 99.9\%$  trigger efficiency for minimum ionizing particles. To help ensure high efficiency, the pulse

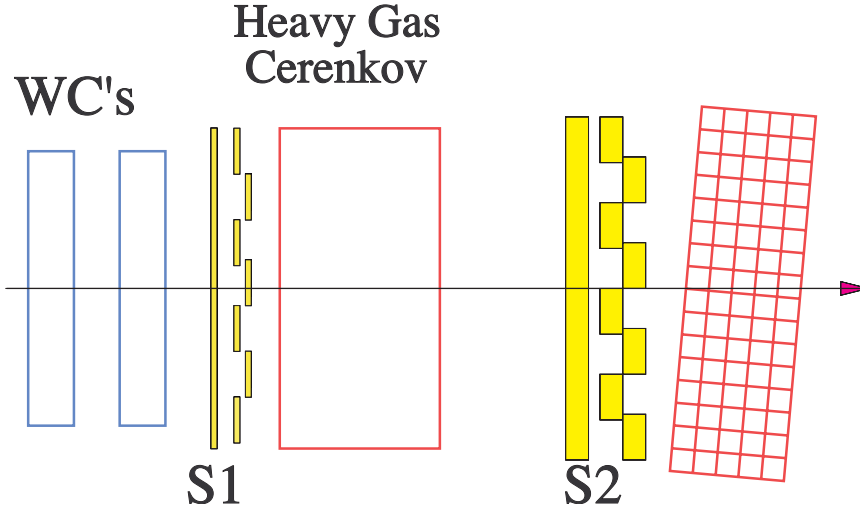


Figure 203: The thin S1 X and Y arrays will be located immediately after the wire chambers. The thicker S2 arrays will be located just before the electromagnetic calorimeter. (Drawing not to scale.)

height variation across an element should be less than 10%. There must also be sufficient redundancy such that an  $S_1 \cdot S_2$  coincidence is robust with respect to the inefficiency (or even loss) of a few channels. The detector should also be insensitive to background.

- **Rejection of Accidentals:** The mean-time resolution of the SHMS focal plane must be at least 100 ps (rms). This will easily permit a coincidence time resolution of 200 ps (rms) so that a  $\pm 1$ -ns cut (single beam bucket) on coincidence time would remove only the tails of the good event distribution beyond  $5\sigma$ .
- **Wire Chamber Tracking Efficiency:** The segmentation of the hodoscope X and Y elements has to be sufficiently fine to define a beam of particles which pass through the active region of the wire chambers.
- The hodoscope should have minimal adverse impact on downstream detectors.
- The hodoscope should have a 10-year lifetime before major overhaul.

The solution which meets all of the above specifications is two pairs of X-Y hodoscopes (Fig. 203), named  $S_1$  and  $S_2$ , similar to those currently installed in the HMS and SOS. The two arrays would be separated by roughly 2 m, with S1 following the Wire Chambers and S2 just before the Calorimeter. The new features which we would like to emphasize are that

- S1 will be made of “thin” (*e.g.* 5mm), scintillator elements with long attenuation length BC408,
- S2 will consist of a relatively “thick” (*e.g.* 2cm-3cm) quartz Čerenkov radiator elements, and

Table 36: Nominal dimensions for the hodoscope elements of each of the four arrays. There are eight elements per plane.

Element	Material	Width	Length
S1X	5 mm BC408	11.3 cm	110 cm
S1Y	5 mm BC408	14 cm	90 cm
S2X	2.5 cm Quartz <sup>9</sup>	14 cm	140 cm
S2Y	2.5 cm Quartz	18 cm	110 cm

- iii. standard 12-stage PMTs like the XP2262B will be employed, operated at low anode currents for extended lifetime.

Since the existing Hall C hodoscopes are made of scintillator, the most dramatic change listed above would be the use of a quartz Čerenkov for the S2 arrays. Simulations by Simicevic[Si01] for the  $Q_{weak}(proton)$  experiment indicate that it is reasonable to expect several hundred photoelectrons (p.e.) for a 1-meter length quartz radiator with a moderately good surface reflectivity. A quartz Čerenkov detector operated at a threshold of 100 p.e. could be essentially 100% efficient and blind to low-energy backgrounds, resulting in a much cleaner  $S_1 \cdot S_2$  trigger. This capability is critical for the clean detection (and accurate tracking efficiency determination) of protons in extremely low cross section measurements<sup>8</sup> at a CW facility.

Each of the four arrays will have eight rectangular bars of scintillator or Čerenkov radiator. The active area of the arrays is designed to have  $\simeq 100\%$  acceptance of the beam envelope for the full momentum bite and target acceptance of the large solid angle tune. The SHMS beam envelope simulations can be found in Section 3.C.3. A summary of the nominal hodoscope dimensions is given in Table 36. Finally, with one PMT on each end of a scintillator or Čerenkov radiator paddle, the total number of SHMS hodoscope channels will be 64.

## Particle Identification

*Overview* Hadron identification for momenta up to 11 GeV/c will be fundamentally different from that of the HMS-SOS detector systems. With increasing momentum it becomes more and more difficult to distinguish hadrons by time-of-flight measurements. With the 2.2-m flight path in the detector hut, kaon-pion separation by time-of-flight becomes infeasible at roughly 2 GeV/c. At 3.5 GeV/c also proton-kaon separation will no longer work. Coincidence timing with a hadron flight path in the SHMS of 22.5 m and a reconstructed coincidence time resolution of roughly 200 ps extends this to 4 GeV and 7 GeV, respectively. Note however, that particle identification by means of coincidence timing will in general not distinguish particles from accidental coincidences and therefore will lead to an irreducible background that must be subtracted. Therefore, at high

---

<sup>8</sup> *e.g.*,  $d(\gamma, p)n$  at high  $s$  and  $A(e, e'p)A - 1$  at high  $Q^2$ .

momenta one must rely on other means of particle identification, *e.g.* Čerenkov detectors,  $dE/dx$  measurements, and Transition Radiation Detectors (TRD).

As described in detail below, the Super-High Momentum-Spectrometer will draw upon a variety of techniques to achieve particle identification over its entire momentum range. A global outline of the scheme is shown graphically in Fig. 204, where the discrimination power is shown as the significance of the measurements (number of standard deviations) in the various PID detectors versus the particle momentum.

Electron identification can always be accomplished by use of energy measurements in the electromagnetic calorimeter, and optionally improved upon with a TRD. Over the SHMS momentum range, electrons will always radiate in Čerenkov counters, so these devices will also contribute to electron tagging. For extreme cases at high momentum and low signal to background, such as measurements at  $x > 1$ , we envision adding another Čerenkov counter in place of the last section of vacuum pipe just upstream of the first wire chamber. This device, using a Ne-Ar mixture at atmospheric pressure, can have its index of refraction tuned to enhance either electron-pion or pion-kaon discrimination at high momentum.

For hadron identification the following PID strategy can be employed:

**$\sim 1$  to  $\sim 3$  GeV/c:** Kaon-pion separation can be achieved with the appropriate choice of one aerogel Čerenkov. A time of flight path of 2.2 m with a TOF resolution of 200 ps still allows one to distinguish protons from kaons at the  $3\sigma$  level up to 2 GeV/c. At the high end of this range, proton PID can be improved with the use of an additional aerogel counter with  $n=1.02$ .

**$\sim 3$  to  $\sim 5.5$  GeV/c:** Pions will trigger a  $C_4F_{10}$  gas Čerenkov. The  $C_4F_{10}$  pressure will be adjusted such that kaons do not radiate. Kaons will trigger an  $n = 1.015$  aerogel Čerenkov.

**$\sim 5.5$  to 11 GeV/c:** Pions will still trigger the  $C_4F_{10}$  gas Čerenkov. An atmospheric pressure gas Čerenkov counter will be inserted upstream of the first wire chamber and filled with an Ar-Ne mixture to provide a pion tag or an additional electron tag. At these higher momenta the multiple scattering in this added detector will be tolerable.

Thus, an appropriate choice of combinations of detectors and techniques will allow the SHMS to provide useful particle identification over its entire momentum range. The remainder of this section will describe each of these detectors.

*Shower Counter* The SHMS magnetic spectrometer is aimed to cover small forward angles and higher momentum settings not available so far in Hall C[WP01]. When identifying electrons at these settings, good particle identification is needed to suppress high hadron background. Lead glass electromagnetic calorimeters are well suited to this purpose.

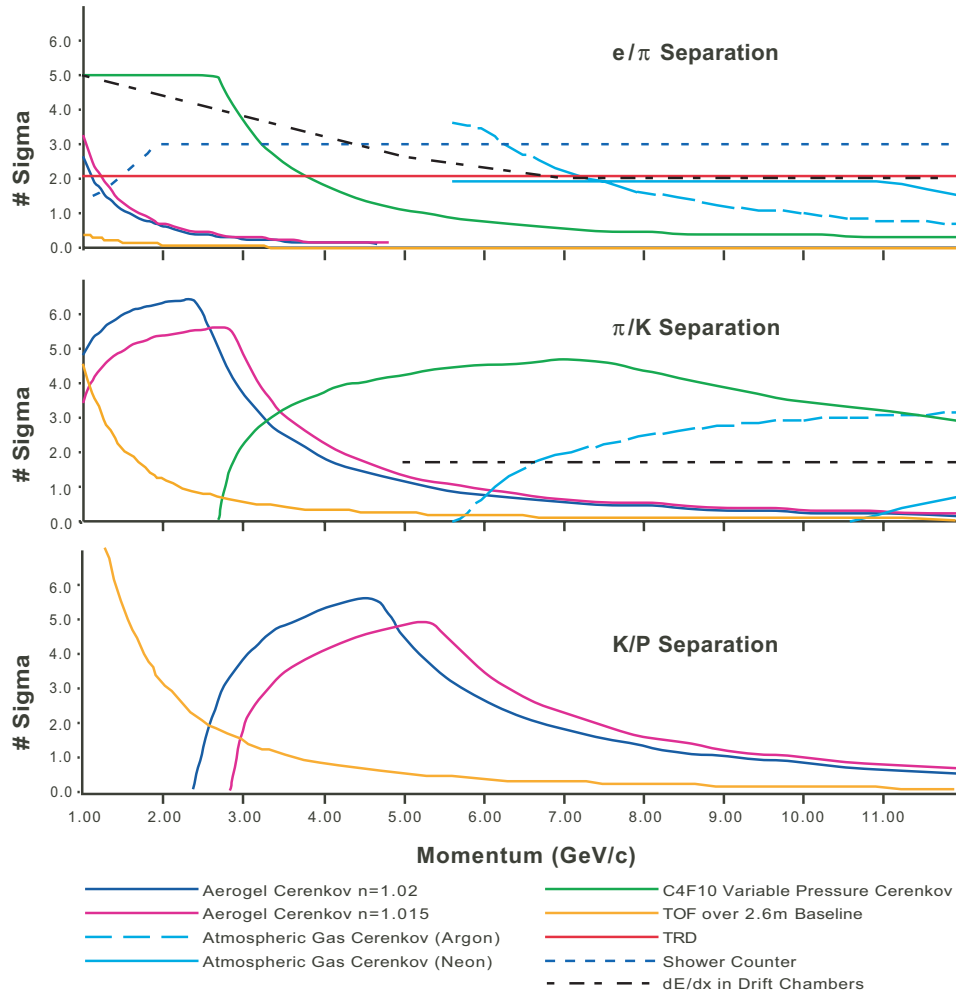


Figure 204: Particle Identification Resolving Power over the SHMS Momentum Range. The vertical scale in each graph is number of standard deviations which separate the two particle types shown, calculated for all of the relevant detectors in the system.

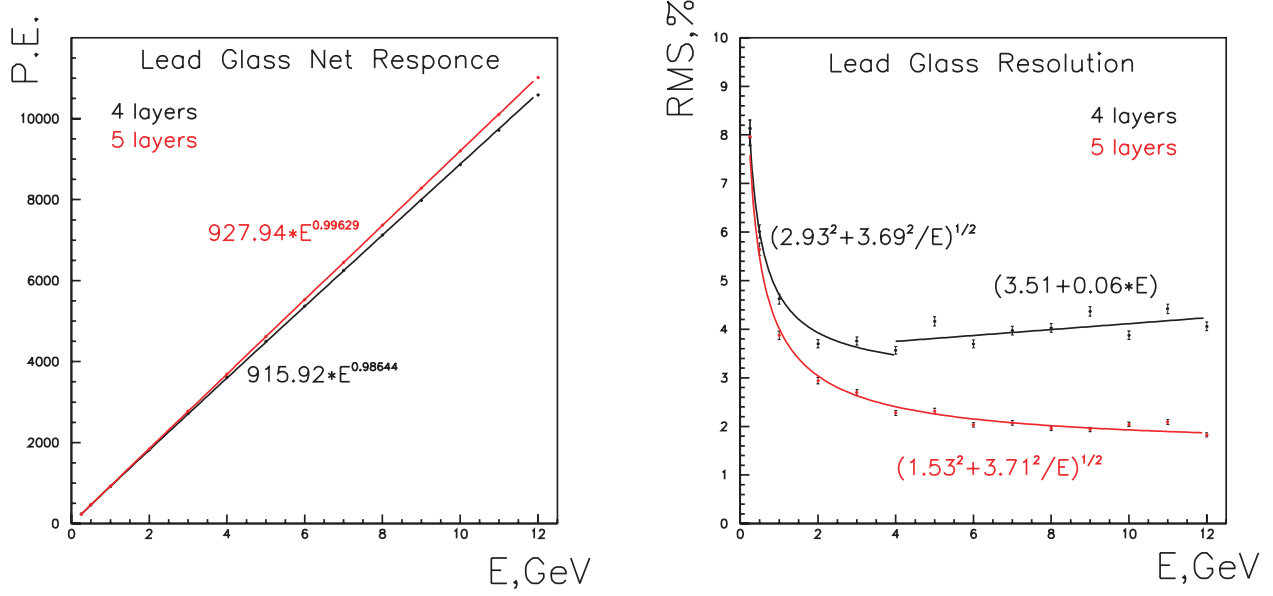


Figure 205: EGS4 Monte Carlo simulation of the linearity (left panel) and resolution (right panel) of a TF-1 Lead Glass modular calorimeter. The calibration, coordinate correction and electronic effects are not included.

The design of the SHMS electromagnetic calorimeter is similar to the existing HMS and SOS calorimeters in many respects. The HMS calorimeter consists of  $10 \times 10 \times 70 \text{ cm}^3$  TF-1 Lead Glass rectangular blocks wrapped in thin aluminized mylar and in tedlar film for optical tightness. The characteristics of the TF-1 lead glass are: density  $\rho = 3.86 \text{ g/cm}^3$ , refractive index  $n=1.65$ , radiation length  $R_L = 2.74 \text{ cm}$ . The blocks are arranged in four layers for a total thickness of 40 cm (14.6 radiation lengths). Photomultiplier tubes (Philips XP34462B) are mounted at both ends of each block in the first two layers and at one end for the remaining layers. The modules are equipped with ST-type fiber adapters for the gain monitoring system.

Figure 205 shows the results of a Monte Carlo simulation for the lead glass calorimeter. As can be seen from the left panel, the calorimeter is linear within 3.5% up to electron energies of 12 GeV. The energy resolution of the HMS calorimeter (PMTs mounted on one end of each block) measured in the energy range 0.5–4.0 GeV is given by

$$\frac{\Delta E}{E}(\%) = \frac{6.1}{\sqrt{E(\text{GeV})}} + 0.3 \quad (77)$$

and is comparable to the resolution of similar devices[PDB]. The SOS calorimeter is somewhat better in this respect[Ar98]. More details on the HMS and SOS calorimeter construction and performance can be found in Ref. [Ar98]. The performance of the calorimeters has not deteriorated significantly in the 7 years since they were first installed.

The observed  $\pi^-/e^-$  rejection factor of the HMS calorimeter is better than  $(1 - 5) \times 10^{-2}$  in the momentum range 0.5 to 2.0 GeV/c, with electron detection efficiency  $\geq 99\%$ . At these low momenta, pion rejection can be improved at the cost of electron efficiency by using a tighter cut



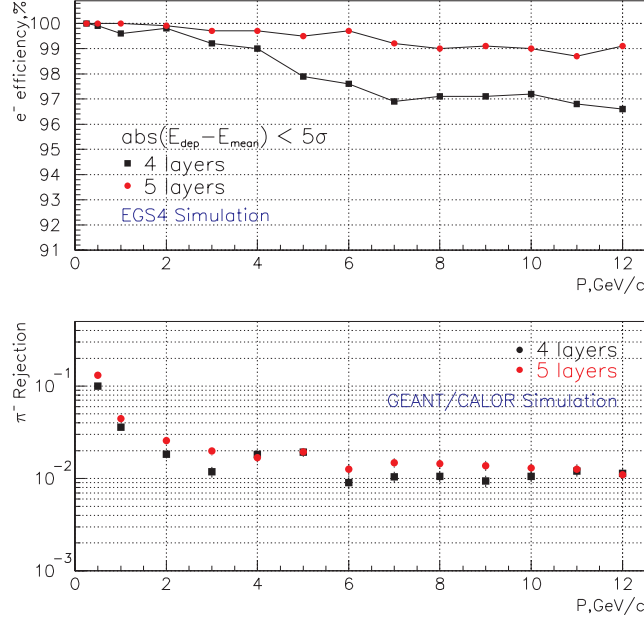


Figure 206: Electron detection efficiency (top panel) and pion rejection (bottom panel) obtained from the Monte Carlo simulation of the TF-1 Lead Glass Calorimeter. The calibration, coordinate correction and electronic effects are not included.

on the calorimeter energy. At higher momenta, the pion rejection is not significantly improved by a tighter cut.

The energy dependence of the resolution of the calorimeters indicates almost complete absorption of electromagnetic showers up to energies of  $\sim 4$  GeV. However, at higher energies the Monte Carlo simulation predicts a slow rise of the resolution, which is a clear indication of leakage (see Fig. 205, right panel). Adding an additional layer restores full absorption, hence improving both the resolution and linearity. Adding a fifth layer also improves the electron detection efficiency (see Fig. 206, top panel), but it does not change the pion rejection (Fig. 206, bottom panel). Exploiting the transverse and longitudinal spread of the deposited energy will improve pion rejection, and the contribution of a fifth layer may be valuable in this case.

Two side by side stacks of 12 blocks are needed to cover the whole acceptance of the spectrometer (see Fig. 196) and thus 120 modules would be required. As adjacent blocks will be optically decoupled, the light will be collected with PMTs on both ends of the calorimeter blocks. The calorimeter will be deflected by small amounts in both vertical and horizontal directions to avoid cracks in between the modules.

Alternatively one can construct a lower cost, 4-layer calorimeter using only 96 modules. It will still contain most of the electromagnetic shower and hence have hadron/electron rejection capability. The leakage of energy will not significantly affect the hadron rejection, but will hurt the electron efficiency (or the electron rejection when measuring pions).

Another low-cost alternative is an assembly of 132 short modules oriented along the beam direction. A preshower wall of 24 long modules before this assembly may be helpful for the separation of minimum ionizing hadrons from just developed electromagnetic showers. The deepness of the calorimeter should be optimized to get good rejection across the SHMS momentum range.

*Atmospheric Pressure Čerenkov* One of the typical uses of the SHMS will be to detect highly inelastic scattered electrons. At such kinematics the pion background can be significant, so a reliable method of electron identification is required. Threshold Čerenkov detectors are excellent tools to use when the particle velocity  $\beta$  is greater than phase velocity of light in the medium  $c/n$ . The minimum momentum at which a particle will exceed the phase velocity of light in the medium is given by:

$$P_{min} \cdot c = \frac{M \cdot c^2}{\sqrt{n^2 - 1}} \quad (78)$$

Thus, if we require 10 GeV/c pion to be under threshold, then  $n - 1$  must be 0.0001 or smaller, which can be achieved either by choosing low-pressure gases, or certain noble gases at STP. For example  $n - 1 = 0.000067$  for Ne,  $n - 1 = 0.000033$  for He.

The main characteristic of threshold Čerenkov detectors is the number of detected photons. For very low refractive-index gases the number of emitted photons is extremely small. At  $p > 9.0$  GeV/c a gas Čerenkov for electron-pion discrimination should be over 2.5-3 m long in order to have an adequate number of photoelectrons. A  $\beta=1$  particle traversing a 3 m long Ne radiator will produce about 30 photons in the visible light range (300-700nm). Most PMTs are not very sensitive below 300 nm. Since the production has a  $\lambda^{-2}$  dependence, and  $n(\lambda)$  goes to unity at short wavelengths, the Čerenkov light produced will be peaked in the ultraviolet (100-300nm). Using these photons will double the number of photoelectrons from the photocathode [Ar98, So99]. PMT windows coated with p-terphenyl, which absorbs UV light and retransmits it in the range of 390 nm, increase the PMT response by about 90% compared to the uncoated tubes[So99]. The expected number of photoelectrons will be  $\simeq 10 - 12$ .

The solution to adjust the refractive index by using the noble gases at STP appears more attractive than the use of a low-pressure tank. The low-pressure approach requires a 3 m long vacuum sealed volume. Having this volume under-pressurized tends to gradually take in O<sub>2</sub> and H<sub>2</sub>O which can change not only the threshold condition, but also absorb the ultraviolet part of the Čerenkov radiation. Further, using Ne and Ar at STP allows the windows of the Čerenkov tank to be made very thin (possibly from tedlar). This will aid in minimizing multiple scattering in front of the drift chambers.

The atmospheric Čerenkov tank we propose would replace the final 3 m of the vacuum pipe as it enters the SHMS detector hut. The diameter needs to be only about 60 cm at the upstream end, and cover 75×100 cm<sup>2</sup> at the downstream end. A vacuum window with the same scattering properties as the standard one would be installed upstream of the Čerenkov counter. The Čerenkov windows and mirrors and their supports will be made lightweight so as to keep multiple scattering

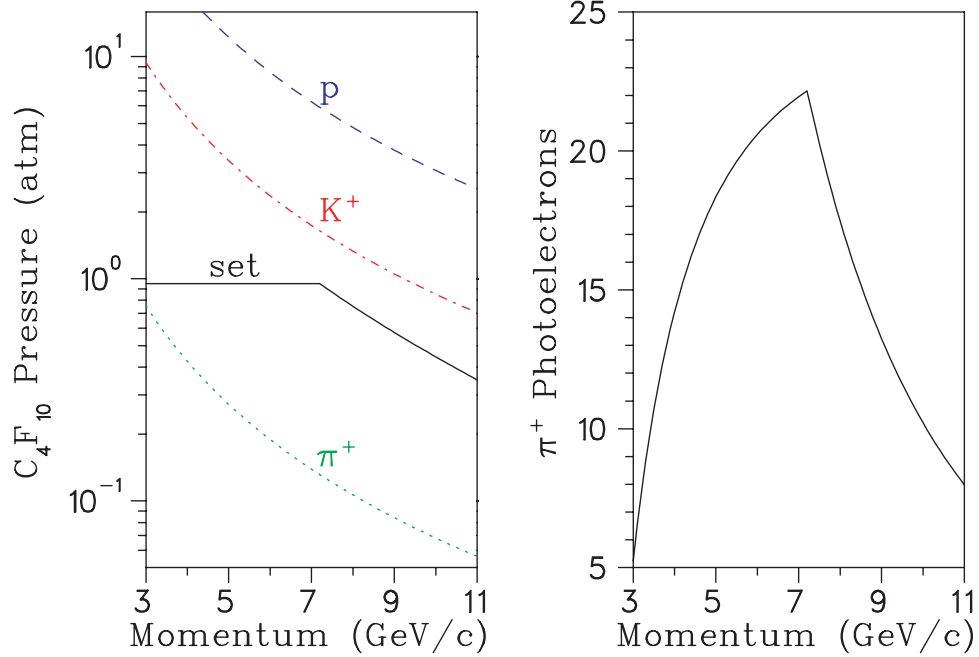


Figure 207: (Left) Threshold  $C_4F_{10}$  pressure required for Čerenkov light generation from the particles indicated. The solid curve indicates the operating pressure planned for the detector. (Right): Number of photoelectrons anticipated for the detector, taking into account the transmittance, reflectivity, and quantum efficiency functions of the detector components.

at a minimum. Even then, the detector would only be compatible at the high end of the SHMS momentum range.

*Heavy Gas Čerenkov* Above  $\sim 3$  GeV/c, hadron species cannot be reliably distinguished by time of flight over the 2.2-m baseline planned for the SHMS detector stack, and so information from Čerenkov detectors becomes increasingly relevant. An aerogel Čerenkov detector with  $n = 1.02$  will provide  $\pi^\pm/K^\pm$  discrimination only up to 2.4 GeV/c. Beyond this momentum, a gaseous Čerenkov detector is required. Based on the excellent operational experience at JLab and elsewhere, we propose to construct a threshold Čerenkov using the heavy perfluorocarbon (PFC) gas  $C_4F_{10}$  as a radiator. This gas has an index of refraction of 1.00143 at standard temperature and pressure, and so can be used here over a wide range of incident particle momenta.

The solid curve in the left panel of Fig. 207 indicates the gas pressure we propose to use at each SHMS central momentum setting. It is expected that the detector gas pressure will be remotely controlled from the counting room as the spectrometer momentum is changed. We assume 0.95 atm. pressure from 3.4 GeV/c to 7.0 GeV/c, and sub-atmospheric pressure at higher momenta. The gap between the ‘set’ and ‘ $K^+$ ’ curves above 7 GeV/c takes into account the +25%/-15% momentum bite of the SHMS, and a possible 0.1-atm error in the setting of the gas pressure regulator. We do not anticipate the detector being used for  $\pi^+/K^+$  separation at momenta below 3.4 GeV/c.

Figure 208 shows a schematic design for the heavy gas Čerenkov. The enclosure is a cylinder

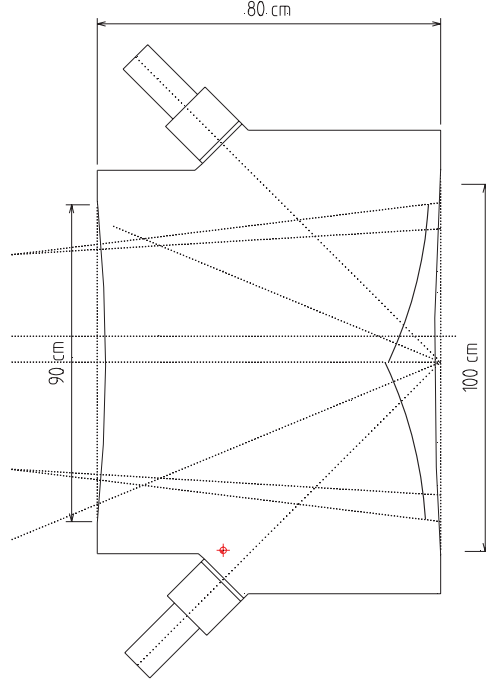


Figure 208: Schematic Design for the SHMS Heavy Gas Čerenkov Detector.

of nonmagnetic stainless steel, with the PMTs located outside, viewing through a 1-cm thick UV-grade fused silica window. This allows for better isolation of the pressurized cavity, and allows one to maintain proper PMT-mirror optical alignment should the PMT require servicing. Four mirrors and photomultipliers are required to cover the SHMS beam envelope; they should be of the highest possible quality. As a reference design, we have selected the Photonis[PHOT] XP4508B 5" photomultiplier tube. This is similar to the PMT currently used in Hall B, except that it has a flat face of fused silica, which allows for flush mating with the quartz window. A custom-design voltage divider with boosted voltage between the photocathode and the first dynode will be used to provide optimum focusing of the photoelectrons, and so minimize losses within the dynode chain. To minimize aberrations, the mirrors should be thin glass, which can be structurally reinforced outside of the beam envelope. Protected aluminum mirror coatings with  $> 90\%$  reflectivity down to 200 nm are commercially available[LAM10]. We propose to use 0.020" titanium for the particle entrance and exit windows, which is the same material used on the G0 spectrometer [Be02c].

$C_4F_{10}$  is very expensive, and so a recovery system is required.  $C_4F_{10}$  has excellent UV transmission characteristics (97%@170 nm) provided it is kept pure. A filter and cold trap may be desirable additions to the gas recovery system, to maintain the required gas purity. Both oxygen and water absorb strongly below 200 nm, and should be kept below 0.1%. Residual nitrogen has an effect on the refractive index, and should be kept constant and below  $< 1\%$ .

The right panel of Fig. 207 indicates the number of detected photoelectrons expected from a  $\pi^+$  for a 70-cm radiator length. The  $C_4F_{10}$  transmission, mirror reflectivity, quartz transmittance,

and PMT spectral characteristics, as well as possible optical misalignment, were all taken into account. The resulting  $\pi^+$  detection inefficiency, assuming that an off-line cut is placed at  $< 1.5$  photoelectrons to eliminate knock-on events, is less than 0.1% for all momenta between 3.4 and 10.3 GeV/c, and rises to a modest 0.3% at 11.0 GeV/c.

In conclusion, a heavy gas Čerenkov detector, utilizing a  $C_4F_{10}$  radiator with variable pressure between 0.4 and 0.95 atm., appears to be a practical way to obtain reliable  $\pi^+/K^+$  separation within the SHMS.

*Transition Radiation Detector* The purpose of the transition radiation detector (TRD) is to separate electrons from pions. This is possible because ultra relativistic charged particles emit *transition radiation* (TR) in the form of x-rays when they traverse a dielectric boundary[Gi46]. TRDs are composed of multiple modules stacked together where a single module contains a radiator and x-ray detector (*i.e.* multiwire proportional chamber). Each radiator is made up of many dielectric interfaces of low-Z material to increase the TR yield. TRDs typically have a threshold of  $\gamma = 1000$ , hence only electrons will produce TR photons in the momentum range of the SHMS. In general, particle identification is accomplished either by examining the total energy deposited in the detector or by cutting on the number of high energy clusters (typically above 5–7 keV) deposited along the track. It has been shown that there is improvement in the particle separation if cluster counting is performed[Lu81a, Fa81]. This is because the number of clusters obeys a Poisson distribution while the total energy has a long Landau distributed tail. The pion rejection factor (PRF), which is inversely related to the pion efficiency, is largely dependent upon the length of the detector, as shown in Fig. 209 with smaller effects coming from the type of radiator, chamber, electronics and particle identification method[PDB].

The detector will be located between the heavy gas Čerenkov and the back hodoscope planes and will be about 60 cm long. To maximize the PRF, uniformly spaced foils of polyethylene would be close to ideal (lithium foils being ideal), but due to the relatively large active area of the detector ( $110 \times 140 \text{ cm}^2$ ), carbon fibers or polyethylene foam will be considered. Using a fiber or foam radiator decreases the PRF by a factor of about 2 when compared to foils. The radiator will be 50 mm thick with a mean foil thickness of about  $17 \text{ }\mu\text{m}$  and a mean gap or pore size of about  $200 \text{ }\mu\text{m}$ . This corresponds on average to 230 foils per radiator which will produce about one detected TR x-ray per module. The x-ray detector will be a xenon filled longitudinal drift proportional chamber to facilitate cluster counting. Since xenon gas is expensive, the chamber gas will be recirculated and filtered. Figure 210 shows a sketch of a single TRD module and the pulse distribution. The longitudinal drift will be 20 mm and, if a 90% Xe/10%  $\text{CO}_2$  gas mixture is used (drift velocity  $\sim 25 \text{ mm}/\mu\text{s}$  for  $\mathcal{E} = 3 \text{ kV/cm}$ ), the maximum drift times will be about  $0.80 \text{ }\mu\text{s}$ . The proportional region will be  $8 \times 5 \text{ mm}^2$  (anode wires spaced by 5 mm). Monte Carlo simulations which include hadronic showers and  $\delta$ -ray production will be needed to determine if this segmentation is sufficient. Special attention must be paid to the exit cathode plane to reduce bulging due to pressure changes and the “hydrostatic” pressure inside the chamber. The electronics

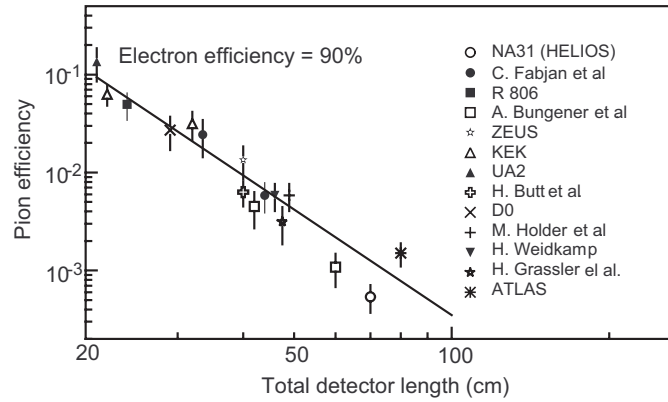


Figure 209: Pion Efficiency Measured (or Predicted) for different TRDs as a function of the detector length for an electron efficiency of 90%. (Figure from Ref. [PDB])

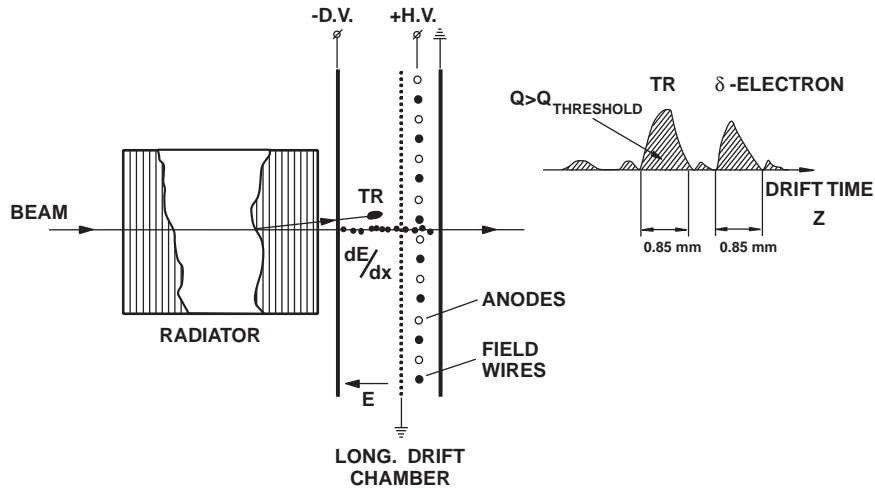


Figure 210: Single module with time expansion chamber (TEC) which includes a drift region and a proportional region. The output signals will consist of uniform  $dE/dx$  ionization with localized TR clusters and  $\delta$ -ray clusters.

on each anode wire will consist of a preamplifier, a shaping amplifier and an 8-bit flash ADC.

At least six modules will be used for the TRD with a total length of about 60 cm. At 90% electron efficiency, this will result in a PRF of about 200 - 300. At 95% electron efficiency, the PRF will reduce by a factor of 3 or 4, but if a higher rejection factor is needed, additional modules could be used and/or a foil radiator could be used. Off-line analysis which includes more sophisticated statistical methods (*i.e.* likelihood) and an intelligent cluster threshold will also improve the PRF. This intelligent threshold will vary the threshold with drift time, thus taking advantage of the energy dependence of the photon's range in the chamber. Since the TR yield tends to saturate at  $\gamma \sim 8000$ , the PRF will be flat over the SHMS momentum range. The combination of the TRD, shower counter and a Čerenkov will be more than adequate to suppress any hadronic background encountered in the SHMS. Additionally, having three particle identification detectors will provide a better mechanism for systematic studies of the detector efficiencies.

*Aerogel Čerenkov Counter* The aerogel detectors will be standard diffusion box type detectors consisting of a layer of silica aerogel in a diffuse reflective box, read out at the sides by large 5-inch PMTs. For the SHMS, a detector with a minimum active area of  $110 \times 140 \text{ cm}^2$  is needed for full coverage of the beam envelope at the anticipated detector location, 2.3 m downstream from the focal plane (see Fig. 196 and Ref. [WP01]). Thus, a detector could be 110 cm in  $x$  (bending or vertical) with 5 PMTs on each side and 140 cm in  $y$  (horizontal). Allowing for an up to 10 cm thick aerogel layer the entire box will be roughly 30 cm deep (in  $z$  direction).

The technology of aerogel detectors with a diffusion box and PMTs as light collectors is well established at Jefferson Lab. The Hall C detector with  $n = 1.034$  yielded 19.3 photoelectrons for  $\beta = 1$  particles [Mo99a]. The two Hall A detectors, A1 with  $n = 1.015$  (9 cm) and A2 with  $n = 1.055$  (5 cm), yielded 8 and 30 photoelectrons, respectively [Zh01a]. The significantly better performance of A2 is certainly due in part to the higher index of refraction. Additionally, it is believed to benefit from a higher photoelectron yield of the Photonis tubes used in this detector as opposed to the Burle tubes used in the A1.

Two more detectors are currently under design, one for the HMS and another for the hyper-nuclear spectrometer (HKS). The HKS detector explores the possibility of segmenting the detector along the focal plane and thus increasing the rate capability. This should also be considered for the SHMS detector, *i.e.* to ensure reliable performance at the very forward angle settings possible with this spectrometer. The design with 5 PMTs on each side would allow for 5 optically separated segments. Limiting individual segment rates to 1 MHz would result in a total rate capability of 5 MHz for particles above the Čerenkov threshold. To compensate for the dead areas introduced by segmentation, a second plane with the segments offset by half a segment width would be required.

As aerogel the materials SP15, SP30 and SP50 from Matsushita Electric Works is recommended. Matsushita's aerogel has a waterproof coating that makes it hydrophobic. This removes the need for baking (in fact baking will destroy the coating) and also increases transparency. A

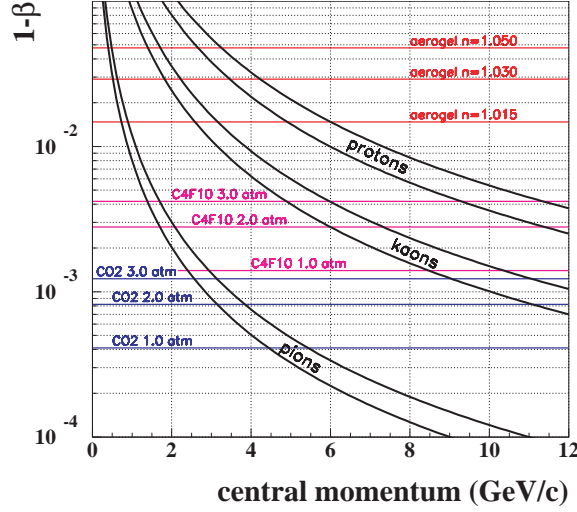


Figure 211: Hadron Velocity  $1 - \beta$  as a Function of Momentum. For each particle a band is shown corresponding to a momentum acceptance of  $\pm 10\%$ . The horizontal lines show thresholds for different Čerenkov radiators.

low-cost 5-inch PMT (Photonis XP4572) has been successfully employed in the Hall A A2 detector and should also be considered for the detector proposed here. Figure 211 shows the thresholds for these materials as a function of momentum.

The performance of the detector has been simulated with D. Higinbotham's Monte Carlo code [Hi98]. With the standard parameters and  $n = 1.015$  one gets 6 photoelectrons. This results in a detection efficiency of  $> 99\%$  for a 1 p.e. cut and 88% for left-right coincidence of  $\geq 1$  p.e. The experience with the Hall A A2 and the HKS prototype suggest that this simulation is a lower estimate. Therefore, it is expected that we will actually see closer to 10 photoelectrons and achieve a left-right coincidence efficiency close to 98%.

**Focal Plane Polarimeter** To measure the ratio of proton electric to magnetic form factor at  $Q^2 > 12 \text{ GeV}^2$  using the recoil polarization technique, the focal plane polarimeter (FPP) which is being built for the HMS will have to be moved to the SHMS. The FPP is in effect two polarimeters in series, so there is a  $\text{CH}_2$  analyzer followed by drift chambers and then an additional  $\text{CH}_2$  analyzer followed by drift chambers. A drawing of where the FPP would fit into the SHMS detector package is shown in Fig. 212. The 2nd Čerenkov and aerogel/TRD would have to be removed.

### Trigger, Data Acquisition, and On-line Computing

*Trigger* The focal plane trigger electronics used for the HMS and SOS has been designed to be flexible, fast and efficient at detecting particles. These triggers consist of requiring hits in a majority of the hodoscope planes combined with options to require or veto on signals from the various particle ID capable detectors in the focal plane hut. The SHMS trigger electronics will be



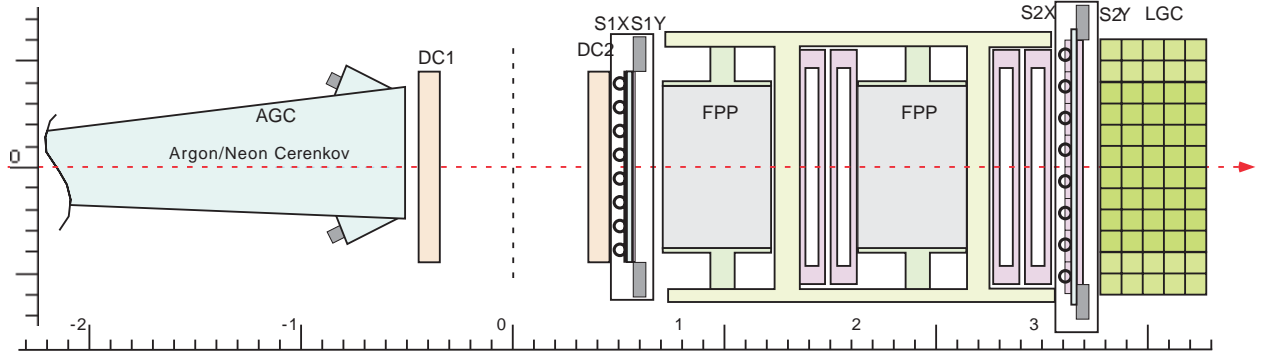


Figure 212: A Schematic of where the Focal Plane Polarimeter could fit into the SHMS Detector Package. There are two  $\text{CH}_2$  analyzers, each followed by a set of drift chambers.

similar to the HMS and SOS logic but there will be opportunities for increased sophistication in the trigger.

The design of the HMS and SOS triggers was in part driven by the desire to minimize the time to form the trigger, thus minimizing the amount of delay required for the TDC and ADC inputs from each PMT. With the use of common stop TDCs and ADCs such as those described below, triggers will not need to be formed as quickly. This will allow for the possibility of more sophisticated triggers and the use of computer controllable logic modules.

*DAQ Electronics* The fine resolution (0.5 ns) TDCs used for the Hall C drift chambers are multihit common-stop models that do not require long cables to delay the signals until a trigger arrives. The absence of delay cables greatly simplifies the physical layout of the experimental apparatus and electronics and also simplifies the commissioning of experiments. Such common-stop devices have not been available at the higher resolutions required for PMT based detectors, and no similar devices have been affordable for charge digitization. For PMT digitizers the inputs must be delayed by approximately 400 ns to wait for the formation of focal plane triggers and a coincidence between spectrometers. Recent advances, however, make it clear that multihit, buffered, common stop TDCs and ADCs of sufficient resolution will be available for the SHMS.

The JLab Physics Electronics Group is developing a 64/32 channel TDC based on the F1 chip [Br99a]. When used in the 32 channel mode this TDC will have a least count of 60ps, yielding sufficient time resolution for any PMT based detector. The effort to develop this TDC is already well advanced and it is expected that the VME module being developed will be used by some experiments at JLab within the next few years. The per-channel cost of this TDC is expected to be comparable to that of common-start high-resolution TDCs used now.

Standard ADCs operate by integrating the current on an input while a gate is present. Since this gate is generated by a trigger which can take many hundreds of nanoseconds to form, each ADC input must be delayed with long coaxial cables. The use of analog delay can be avoided by using a Flash ADC to continuously digitize the input and saving the data in memory while waiting

for the gate. When the gate arrives, the appropriate samples can be summed to produce a digital integration of the input. While this technique has been used, it is not in common use for situations with PMT pulses only a few tens of nanoseconds in width.

While affordable commercial Flash ADC modules are not available, indications are that either affordable modules will be available before the upgrade or that building suitable modules at JLab will be feasible. Flash ADC modules suitable for particle physics use, such as the Struck SIS3300, are available now. This 8 channel module which digitizes at 100MHz with a 12 bit Flash ADC would work well with detectors with wide PMT pulse shapes. However, the cost per channel is several times that of conventional ADCs, so the module would only be appropriate for prototyping and specialized applications.

As part of R&D efforts for the Hall D GlueX experiment, a single channel ADC prototype that uses a 250MHz 8bit Flash ADC chip has been designed. The key components of this design are inexpensive, so overall costs should be comparable to those of conventional ADC modules. Even though the 8 bit resolution is less than the 10 to 14 bits typically used in nuclear physics spectrometers, some resolution is recovered by the fact that a PMT pulse a few tens of nanoseconds wide will be sampled several times yielding better precision. An ADC based on this existing design is already good enough for the majority of the charge digitization required for the SHMS, but we note that higher resolution flash ADCs may be affordable at the time of the upgrade. The JLab electronics group is currently exploring development of a general purpose ADC module based on the GlueX flash ADC prototype.

A side-benefit of flash ADCs is that not only do they record pulse shape, but also pulse timing. Although it is unlikely that a flash ADC can obtain time resolutions as good as the 60ps of the F1TDC, sub nanosecond timing is feasible. This will allow moderate time resolution to be obtained for detectors such as Gas Čerenkov, Aerogel, TRD, and Lead Glass shower counters without additional discriminators or TDC modules.

*Data Acquisition and On-line Software* The philosophy of the data-acquisition system for Hall C with the SHMS is that the DAQ should not be the limiting factor in the event rates that can be handled. Experience in Hall C has shown that factors other than DAQ, such as accidentals rates or singles rates on individual detectors, generally limit overall trigger rates to less than 10K events/s. With the front end TDC and ADC electronics discussed above, a DAQ system can be constructed that can handle event rates in excess of 10K/s with minimal deadtime. Other than the front end electronics, no technology advances are required in order to obtain these data rates. Future improvements in the speed and cost of networking, CPUs, and disk drives will only help to simplify the design of the DAQ system.

Data acquisition will continue to be managed by CODA[CODA]. CODA development over the next few years will include an emphasis on an on-line analysis farm as a part of CODA. With the upgrade we plan to add a moderate analysis farm. This will have two uses:

1. Real-time accumulation of diagnostic histograms
2. Data compression (background filtering, sparsification)

**Stand-Alone (Third-Arm) Calorimeter** A large lead-glass calorimeter is planned to be used in experiments in Hall C with the present CEBAF 6 GeV machine. An approved experiment, GEP-III, will use the calorimeter to detect the scattered electron from the elastic  $\bar{e}p$  reaction. This experiment will measure the ratio of proton electric to magnetic form factor at  $Q^2 = 9 \text{ GeV}^2$  by measuring the ratio of the transverse to longitudinal polarization of the outgoing proton in the elastic  $\bar{e}p$  reaction. To cleanly identify elastic events, the scattered electron will be detected in a lead-glass calorimeter. This calorimeter is being constructed and is expected to be ready for the GEP-III experiment in 2005. The new calorimeter can be used in experiments to measure the ratio of proton electric and magnetic form factors at  $Q^2 = 9\text{--}14 \text{ GeV}^2$ , and to perform  $\gamma - \pi^0$  production experiments. This new calorimeter is also planned to be used in real Compton scattering (RCS) experiments with 11 GeV beam energy which are extensions of experiments done with 6 GeV beam.

The calorimeter will consist of 1600-1700 lead-glass blocks. Two sizes of lead glass are used in the calorimeter. One set (which was used in the RCS experiment which ran in Hall A) has a frontal area  $3.8 \times 3.8 \text{ cm}$  with length of 45 cm. The other set has a frontal area of  $4.0 \times 4.0 \text{ cm}$  with length of 40 cm. The expected position resolution is 3-5 mm. The lead-glass calorimeter will have a frontal area of  $2.7 \text{ m}^2$  and an aspect ratio of 2:1. The infrastructure for the calorimeter, such as platforms, cabling, and electronics, is planned to be usable for the experiments with 12 GeV beam. The electronics readout will be flexible. It will use active splitters for amplitude digitization of each channel and timing of the sums of 8 channels. The splitters will be designed to allow the full formation of a calorimeter trigger for experiments that need it, such as the RCS experiments.

### 3.D Hall D and the GlueX Experiment

#### 3.D.1 Introduction

The goal of the GLUEX experiment is to search for gluonic excitations of  $q\bar{q}$  pairs with masses up to  $2.5 \text{ GeV}/c^2$ . The identification of such states requires knowledge of their production mechanism, identification of their quantum numbers,  $J^{PC}$ , and measurement of their decay modes. These in turn require a partial wave analysis of exclusive final states. The decay products of produced mesons must be identified and measured with good resolution and with full acceptance in decay angles. In many cases, the decays of mesons involve a chain of particle decays. The GLUEX detector must therefore be hermetic (effective  $4\pi$  coverage) and have the capability of measuring directions and energies of neutral particles ( $\gamma$ ,  $\pi^0$ ,  $\eta$ ) and four-momenta of charged particles with good resolution. Clearly, particle identification is also required.

The partial wave analysis technique depends on high statistics and, in the case of incident photons, also requires linear polarization. The latter is needed to identify the production mechanism. The linear polarization is achieved by the coherent bremsstrahlung technique. The degree of linear polarization and flux of photons in the coherent peak fall dramatically as the photon energy approaches the endpoint energy. On the other hand, it is desirable to have photon energies high enough to produce the required masses with sufficient cross-section and with sufficient forward-boost for good acceptance. For a fixed incident momentum and a fixed resonance mass, it is also desirable to have a fairly constant  $|t|_{min}$  over the natural width of the resonance. This requirement demands a higher incident photon energy than expected by simple threshold production.

An operating photon energy of 9.0 GeV produced from a 12.0 GeV electron beam represents an optimization of beam flux, cross-section and degree of polarization. The GLUEX detector is optimized for this energy range. Extensive Monte Carlo simulations has been performed to optimize the detector's ability to reconstruct exclusive final states. Acceptances are nearly 90% for many complicated channels, and the detector resolutions have been balanced to facilitate excellent reconstruction of the events. This will allow kinematic fitting to reduce background contamination of events. Such backgrounds are known complications in partial wave analysis.

### 3.D.2 The Photon Beam and Polarization

Linearly polarized photons can be produced in the desired energy range by using the technique of coherent bremsstrahlung. A horizontal plan view of the photon beam line is shown in Fig. 213 with the major components labeled. The electron beam enters the figure from below ground at the left and is bent into the horizontal plane to enter the tagger building. There it passes through two small dipoles to impinge upon the bremsstrahlung radiator.

**The Photon Tagger and Beam Collimation** After its exit from the radiator, the electron beam passes into the tagger magnet where the primary beam is bent in the direction of the electron beam dump. The radiator crystal is thin enough that most of the electrons lose less energy in traversing the radiator than the intrinsic energy spread of the incident beam. Those electrons which lose a significant fraction of their initial energy inside the radiator do so by emitting a single bremsstrahlung photon. These degraded electrons are bent out of the primary beam inside the tagger magnet and exit the vacuum through a thin window, passing through air for a short distance to strike the focal plane of the spectrometer. The primary electron beam is contained inside vacuum all the way to the dump.

The tagging system used in the GLUEX experiment will consist of a dipole magnet spectrometer with two sets of plastic scintillation counters in the focal plane to tag photon energies: a precision set with 0.1% energy resolution and a broad-band set with a coarser energy resolution of 0.5%. The precision system will be composed of 64 narrow counters and will nominally tag photons from 70%

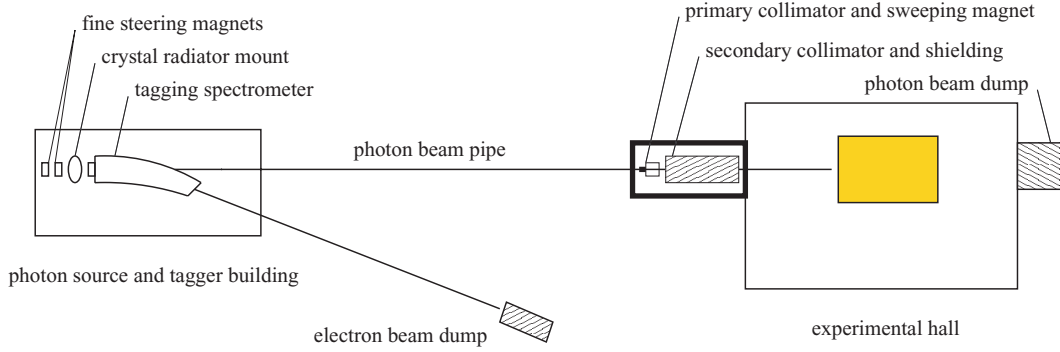


Figure 213: A schematic plan view of HALL D photon beam line for the GLUEX experiment, (shown in the horizontal plane as viewed from above). The objects in this figure are not drawn to scale.

to 75% of the electron beam, but will be movable allowing precision tagging of other energy bytes as well. The broad-band tagging system will tag photons between 25% and 92% of the electron beam energy using 128 fixed scintillation counters. The second system will be crucial for alignment of the radiator crystal and could also be used by other experiments that might be run in HALL D.

The tagger magnet will be similar to the existing tagger in Hall B of Jefferson Lab. The higher energy needed in GLUEX is largely compensated for by going to smaller bend angles, so the sizes of the magnets are comparable, although the HALL D system will bend in the horizontal rather than in the vertical plane.

The photons that are produced in the radiator pass through a small hole bored in the return yoke of the tagger magnet and exit the vacuum through a thin window in the forward direction. They then pass into a transfer pipe, which may either be evacuated or filled with helium to reduce photon beam degradation due to interactions, and travel to the experimental hall. Just before entering the hall the photon beam passes through a system of collimators and sweeping magnets. In Fig. 213 they are shown in a separate enclosure for shielding purposes. The primary collimator is first. It selects the part of the photon beam that is allowed to reach the target. Debris from interactions along the inside surface of the collimator bore forms a halo around the photon beam that exits the collimator. The charged component of the halo is deflected away from the beam axis by a dipole “sweeping” magnet just downstream of the collimator. A secondary collimator follows the sweeping magnet to stop the deflected shower particles and block the halo of secondary photons generated by the first collimator. This collimator is of a larger diameter than the primary and so sees a reduced rate of secondary interactions on the inner surface of the hole. Any new showers that are generated there are cleaned up by a second sweeping magnet. The beam then passes through a final collimating aperture into the experimental hall. This triple-collimation system was copied from the setup developed at SLAC [Ka75].

The collimated photon beam, now only a few mm in diameter, is delivered to the experimental target. After traversing the target (3% radiation lengths), the photon beam passes through the

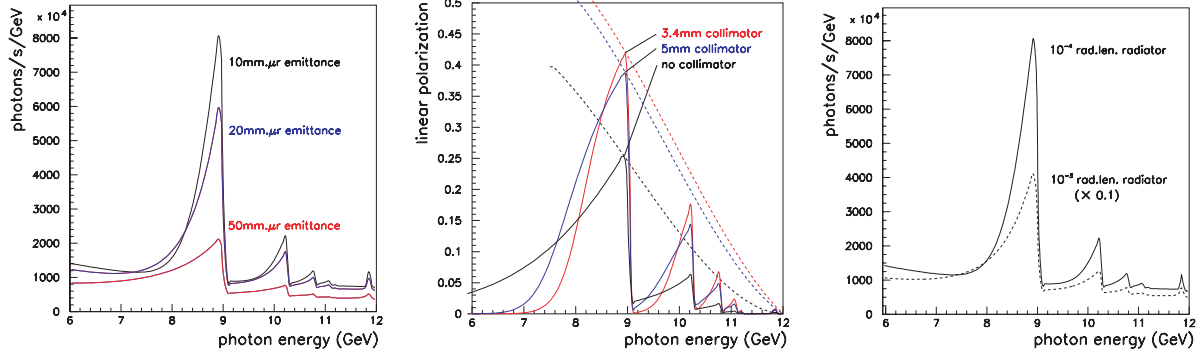


Figure 214: Left: The effect of collimation on the coherent bremsstrahlung spectrum, (various collimation diameters are given with the optimum value being 3.4 mm). Center: Plane polarization of the coherent bremsstrahlung. The dashed lines indicate the trajectory of the peak polarization. Right: Collimated coherent bremsstrahlung spectrum for 2 crystal radiator thicknesses.

detector and into the photon beam dump at the back of the HALL D building. Based upon a design upper limit of 60 kW (5  $\mu$ A at 12 GeV) being delivered to the electron beam dump, the total power in the photon beam is at most 1.5 W in the experimental Hall And at most 15 W in the collimator enclosure. The safety issues of such a beam have been reviewed by Jefferson Lab's RadCon group. As an additional safety constraint, permanent magnets will be installed in the photon beam down stream from the tagger building to prevent an accidental loss of the electron beam into HALL D. These magnets have been obtained as surplus from FermiLab.

**Polarization via Coherent Bremsstrahlung** The net polarization of the beam under different collimation conditions is shown in Fig. 214 (center panel). The dashed curves show how the maximum polarization in the peak varies as the peak energy is changed by rotating the crystal. The polarization in all cases is zero at the endpoint, but its dependence on the electron beam energy  $E$  and photon energy  $k$  is different. Without collimation it rises as  $(k - E)^2$ , one power coming from the intensity of the coherent peak relative to the incoherent component and goes linearly to zero at the endpoint, and the other from the intrinsic polarization of the coherent photons that also behave like  $(k - E)$  near the endpoint. Collimation allows one to essentially isolate the coherent component, so that the polarization available to the experiment rises from zero at the endpoint in a linear fashion. The dashed curves in Fig. 214 demonstrate this point.

In order to obtain the full polarization enhancement from collimation, it is necessary to have a distance between the radiator and collimator of about 80 m. This distance scale is set by the requirement that the collimator aperture must be large compared to the size of the electron beam spot on the collimator, but small compared to the actual photon spot size. Figure 215 shows the maximum polarization as a function of radiator-collimator distance for a coherent peak at 9 GeV. The collimator diameter was adjusted in this calculation to keep the collimation half-angle at  $0.5 m_e/E$ . At zero distance the collimator has no effect except to attenuate the beam, and so the uncollimated polarization from coherent bremsstrahlung is obtained. At 100 m separation distance

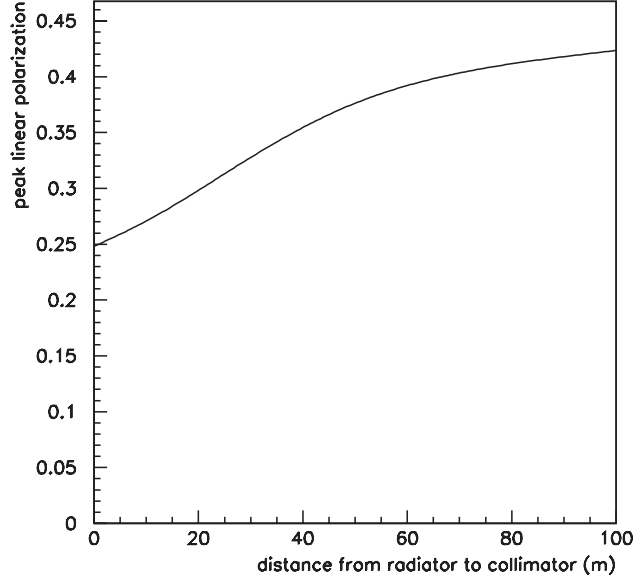


Figure 215: Maximum polarization *vs* radiator-collimator distance for a coherent peak at 9 GeV. The collimator diameter was held fixed in this calculation to keep a constant ratio between the sizes of the virtual electron spot and the collimator.

the polarization enhancement has saturated. The design for HALL D calls for a radiator-collimator distance of 80 *m* with a collimator diameter is 3.4 mm.

The range of permissible thicknesses for a crystal radiator is bounded from above by multiple scattering of the electron beam as it passes through the radiator; this causes the beam divergence to grow, thereby enlarging the photon beam spot on the collimator face and reducing the ability of collimation to discriminate the coherent component relative to the incoherent part. The minimum thickness is determined by the thickness necessary to achieve the full coherent gain. For a 12 GeV beam energy and a 6 GeV coherent photon the coherence length is 18 nm. The coherence length does not impose a practical limit on how thin the radiator should be. The effects of multiple scattering are best presented by showing the calculated spectra for various radiator thicknesses. The photon spectrum for a 20  $\mu\text{m}$  ( $10^{-4}$ ) and a 100  $\mu\text{m}$  ( $10^{-3}$ ) radiator is shown in Fig. 214 to demonstrate the effect. The 100  $\mu\text{m}$  spectrum is scaled down by a factor of 5 to facilitate the comparison, but it is clear that for a significant coherent gain, the crystal thickness must be near 20  $\mu\text{m}$ .

Synthetic diamonds are made using either vapor deposition (CVD) or high pressure high temperature (HPHT) techniques. CVD diamonds have an extensive mosaic and are unsuitable for coherent bremsstrahlung, but HPHT synthetics look very promising. The Glasgow group recently acquired a 5 mm  $\times$  5 mm synthetic diamond less than 18  $\mu\text{m}$  thick which has a [100] orientation. This diamond yielded a very good coherent bremsstrahlung spectrum and X-ray measurements showed rocking curve widths of less than 10  $\mu\text{r}$ , quite close to the ideal value for diamond.

A 30- cm-long liquid hydrogen target will be used. It will be contained in the same vacuum



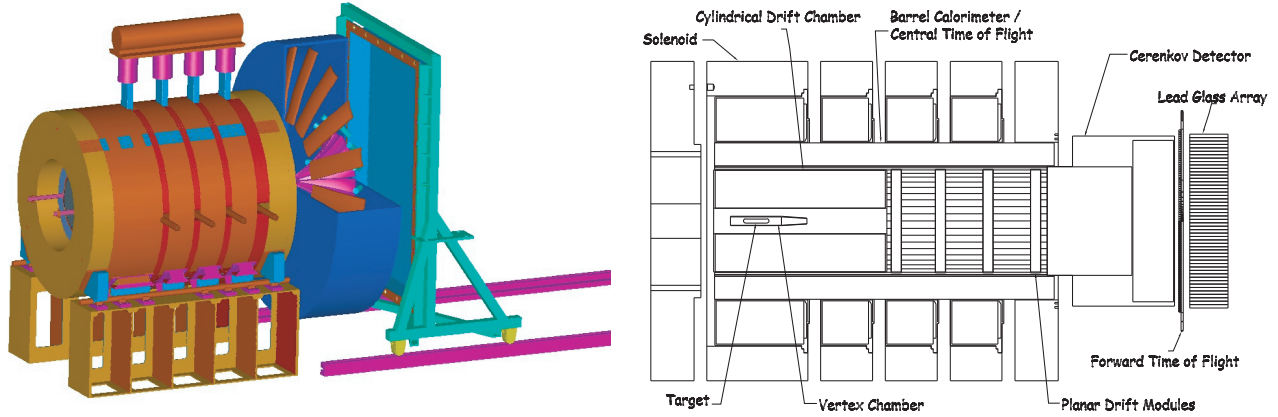


Figure 216: A 3D cutaway view of the GLUEX detector (left) and schematic diagram of its major subsystems (right)

jacket as the photon tagger radiator and will be constructed of low mass materials. The collimated photon beam will be contained within a radius of 2.5 cm from the beam axis. This will allow adequate space between the hydrogen vessel and the innermost detector element for insulation, a vacuum pipe and any plumbing and wiring required to instrument the target.

### 3.D.3 The GlueX Detector

The GLUEX detector has been optimized to provide nearly hermetic acceptance for both charged particles and photons. In addition, a combination of particle identification systems will allow very good  $K$ - $\pi$  separation. Design optimization will allow the detector to fully reconstruct exclusive many-body final states. In conjunction with high statistics, this will allow excellent partial wave analysis of many final states. Figure 216 is a schematic representation of the proposed detector with the individual subsystems discussed briefly below. A more detailed description can be found in the GLUEX Design Report [GX02].

**The Super-conducting Solenoid** Momentum analysis in GLUEX will be provided by a nominal 2 Tesla superconducting solenoid magnet. This solenoid was built at SLAC ca. 1970 for the LASS spectrometer [As87] and subsequently moved to LAMPF in 1985 for inclusion in the MEGA spectrometer. The MEGA Experiment and the solenoid were decommissioned in place in 1995. The MEGA experiment has since been removed from the solenoid and arrangements are underway to ship the solenoid from LANL to the Indiana University Cyclotron Facility (IUCF) for refurbishment and testing. This magnet was designed and built using standards that today would be considered ultra-conservative. The magnet employs a cryostatically stable design and uses cryostats that were designed to be easily opened for service with hand tools. A recent inspection [ML00] of the magnet at LANL revealed that it is still in excellent condition and worthy of the time and cost involved in relocation and refurbishment. Nevertheless, the magnet support systems are now 30 years out of



date so even though the magnet is in excellent condition it requires some maintenance, updating, and modifications for use as part of the GLUEX experiment.

The LASS/MEGA solenoid was inspected in April 2000 by a team from the GLUEX collaboration, JLab staff and two of the original designers of the magnet. This team met at Los Alamos with the MEGA staff and inspected the magnet installation and the fourth coil. Except for two small mechanical vacuum pumps the system was completely intact. The committee concluded that “the condition of the magnet is excellent and if cooled down in place would in all likelihood work!” Subsequently, Jefferson Lab formally transferred the solenoid system from Los Alamos to JLab as of October 2001. A Memorandum of Understanding (MOU) was negotiated with LANL to cover all disassembly aspects of the MEGA experiment. This work, performed by a JLab crew, began in November 2001 and was completed in February 2002. The solenoid is now at IUCF where testing and repairs are underway under the auspices of a MOU between JLab and IUCF. A detailed description of the work needed to bring the magnet systems up to date and have the magnet operational in the GLUEX experiment can be found in reference [GX02].

**Particle Tracking and Particle Identification** The system of tracking chambers in the GLUEX detector must cover as close to a  $4\pi$  solid angle as possible over a wide range of particle momenta, and have sufficient momentum resolution to be able to identify missing particles. In the solenoid region, the chambers are inside the barrel calorimeter. The location of the target, very near the entrance to the solenoid, coupled with the energies involved which force the reaction products into forward angles, result in an effective  $4\pi$  coverage in the center-of-mass of the produced particles, even though the geometrical coverage around the target is less than that. The chambers also must extend as close to the beam line as possible. Near the target, this will provide very accurate vertex information which will be important in identifying decaying particles (e.g.  $K_S$ ,  $\Lambda$ ,  $\Sigma$ , ...). In the forward region, this is needed to reconstruct very fast particles ejected at small angles (down to nearly  $0^\circ$ ). Finally, at large angles, the tracking must be able to separate  $\pi$ 's and  $K$ 's up to momenta of about  $0.5 \text{ GeV}/c$  — a regime where  $dE/dx$  measurements will work. To satisfy the tracking requirements, a starting point based on the LASS detector [As87] was used. A series of three different tracking elements will be implemented as shown in Fig. 216, with each element optimized for a particular region in the detector.

**The Vertex Detector** The Vertex System (VTX) surrounds the target and has several purposes. First it will be used to provide accurate tracking information very close to the target. These track elements must be sufficiently well defined to be connected to the other tracking chambers. Secondly, the VTX must provide a fast signal (start signal for the event) which can be used in the level -1 trigger of the experiment. Finally, it is a critical element of all time-of-flight systems. The vertex detector will consist of two detector packages. One will be optimized for timing purposes and the other one will provide fast tracking information (see Fig. 217).

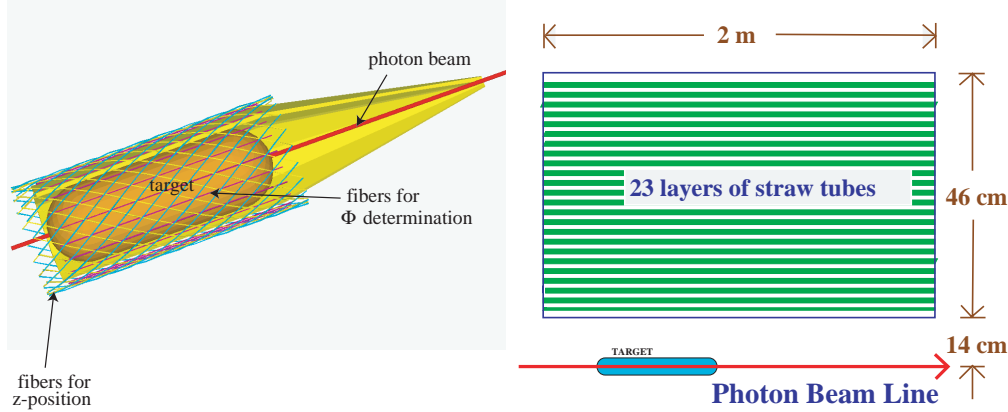


Figure 217: Left: The start counter/vertex chamber. Right: The straw tube chamber.

The timing detector will consist of a cylindrical array of 10 scintillator paddles. This will allow us to cover scattering angles between  $1^\circ$  and  $90^\circ$  for the full length of the target. The scintillators have a thickness of 5 mm which reduces to 2 mm in the forward direction. This will provide good light output and therefore a good timing signal. Using Bicron BC-404 scintillating material in combination with fast photo multipliers should result in an overall timing resolution better than 120 ps.

The fast tracking detector will consist of three super-layers of fibers, each containing two layers to minimize dead space. The central layer will be arranged around the target and parallel to the beam, and will determine the azimuthal angle. The  $z$  position is deduced from the two outer layers. They will be wound in two opposite helices around the first layer. In order to function in the high magnetic field, we are studying the possibility using Visible Light Photon Counters (VLPC) developed by Rockwell in collaboration with Fermilab [Pe89]. The spectral sensitivity of the VLPCs require us to use SCSF-3HF multi clad scintillating fibers from Kuraray which have a long attenuation length of 5.5 m and are also the least susceptible to radiation damage. One of the main advantages of using VLPCs is their large quantum efficiency of approximately 80% [Wa97] for the light produced by the fibers together with a very high rate capability of  $10^8$  single photoelectrons per second. The design of this detector system will closely follow the prototype system developed by the D0 collaboration at FNAL [Ba96]. The expected position resolution will be less than 1 mm.

**The Cylindrical Drift Chamber** The Cylindrical Drift Chamber (CDC) surrounds the VTX and provides very good  $r - \phi$  information and moderate-to-good  $z$  information. This chamber also provides  $dE/dx$  information for tracks which do not reach any time-of-flight detectors. The CDC is used to accurately track particles between polar angles of  $20^\circ$  and  $170^\circ$ . To minimize material in the forward end plate of the chamber, the chamber must be self-supporting. This leads to a straw chamber, where the straw walls support much of the wire tension. The disadvantage of this design is the difficulty of making  $dE/dx$  measurements in a circular straw tube, which requires

careful primary path-length corrections.

The straw-tube chamber will contain 3349 straws, each of which is 1.6 cm in diameter. They are arranged in 23 layers. Eight of the 23 layers will be stereo tilted by  $\pm 6^\circ$  from the straight tubes. Figure 217 schematically shows the arrangement of the tubes in the chamber. The tubes are assumed to have an  $r - \phi$  resolution of  $200\ \mu\text{m}$ , while resolution along the wire length will be obtained using the stereo layers. This will nominally yield a resolution along the length of the wire of about  $200\ \mu\text{m} / \sin(6^\circ)$  or about 1 mm. The chamber end plates are 0.95 cm thick, and constructed as eight separate *pie-shaped* pieces. The chamber plates extend between an inside radius of 14 cm and an outer radius of 60 cm. Current plans call for no inner shell, and an 8 mm thick outer fiberglass shell. The straw tubes consist of  $100\ \mu\text{m}$  thick aluminized kapton, and have  $20\ \mu\text{m}$  diameter gold-plated tungsten wires in them. In order to study the behavior of straw tube chambers, a 2 m long chamber with 2 cm diameter tubes has been acquired from the EVA experiment at Brookhaven.

In the construction of the straw-tube chamber, the most technically difficult to construct are the stereo tubes. A 1/3-scale model of the chamber has been built with the specific purpose of understanding the construction difficulties of the stereo layers, and has demonstrated the importance is the transition region from straight to stereo layers. A prototype of the end plate is currently being built to determine how accurately the plate can be built.

The choice of gas also plays a significant role in the chamber's performance due to the  $2.25\ T$  magnetic field in the detector. In order to study this, the GARFIELD program [Ga84] has been used to compute electrostatic properties of the straw tubes, both with and without the magnetic field. The chamber will require a *slow* gas in order to minimize the *Lorentz angle*. Calculations indicate that the maximum drift time will be on the order of  $500\ \text{ns}$  in such a mixture. Investigations are currently underway with mixtures containing larger fractions of  $\text{CO}_2$ , a slow gas known to work well in high magnetic fields.

**The Forward Drift Chambers** The Forward Drift Chambers (FDC) are disk-shaped drift chambers. The basic drift package is a plane of wires with  $150\ \mu\text{m}$  spatial resolution between two planes of cathode strips. The strips are arranged in a  $u$  and  $v$  geometry with respect to the wires, allowing the reconstruction of a 3-D space point from each hit. The chambers are arranged in packages of six, which results in a small track segment, so as to facilitate a later linking of the tracks. Given the number of spiraling tracks, it is critical that these chamber packages not only provide good spatial resolution, but also reasonable directional information. The basic chamber element is a disk with an outer radius of 60.0 cm and the wires strung as chords across the chamber. With a 1.0 cm wire spacing, each chamber will contain 119 wires. In addition, there will be an equal number of cathode strips on each face. These are arranged in a  $u-v$  pattern with respect to the wires. The wires that cross through the beam line will be deadened out to a radius of about 3.5 cm by placing material such as Styrofoam in the chambers.

Monte Carlo studies show that the combined tracking system provides very good momentum resolution for the event topologies in GLUEX. The system is sufficient to identify undetected particles by missing mass cuts. In particular, a missing neutron can be separated from a completely missing recoil  $\Delta$  for most kinematic regions. Detailed information on resolutions can be found in reference [GX02].

**Electromagnetic Calorimetry** The goal of the GLUEX calorimetry is to detect and measure photons from the decays of  $\pi^0$ 's and  $\eta$ 's, which, in turn, can come from the decays of produced mesons, or from an excited baryon ( $N^*$  or  $\Delta$ ). The positions and energies of the photons must be of sufficient accuracy to allow for a complete kinematic reconstruction of the event. Finally, for events with only charged particles, it is essential to be able to veto on neutral missing energy. Thus, nearly hermetic coverage is critical. For selected triggers, neutral energy requirements (or vetoes) are relatively easy to implement.

Calorimetry in the GLUEX experiment will be handled by three different detector systems. In the forward region ( $\theta > 14^\circ$ ), a circular array of lead-glass (Pb-Glass) crystals will be used. In the central region ( $14^\circ < \theta < 138^\circ$ ), a lead-scintillating-fiber matrix calorimeter will be deployed, and in the backward region ( $\theta > 138^\circ$ ) an iron-scintillator photon veto detector will be the likely choice. In the forward and central region, it is necessary to be able to accurately reconstruct the photon energy and direction for physics event, whereas, photons in the backward direction can only result from background events and only a veto system is necessary.

**The Forward Calorimeter** The Forward Calorimeter in the GLUEX experiment is a circular lead glass array (see Fig. 218). The crystals have been salvaged from an existing detector, the Brookhaven National Laboratory E852 lead glass calorimeter [Cr98], and are currently in storage at JLab. In order to be used in the GLUEX experiment, a new support structure will need to be constructed. This will allow the crystals to be stacked in a circular arrangement and the detector package to move in and out of the GLUEX detector region. Moreover, new Cockroft-Walton base similar to those used in the JLab Rad $\phi$  experiment will be used. Finally, the gated ADCs used in E852 will be replaced with 8 bit, 250 MHz FADCs to eliminate dead time and allow digital pipeline triggers.

The calorimeter has a measured resolution,  $\sigma_E/E$  in percent which can be parameterized as  $a + b/\sqrt{E [GeV]}$  where  $a = 1$  to 2 and  $b = 5$ . The average spatial resolution is 2 to 4 mm and decays with up to eight photons are routinely reconstructed.

Operating an electromagnetic calorimeter, like the LGD, near a high-intensity (a few  $\times 10^7$  photons per second) photon beam line could be a concern given the backgrounds one might expect with a tagged bremsstrahlung photon beam. For this reason, the experience with the LGD used in the Radphi experiment in the Hall B photon beam is of particular relevance. Because of the high

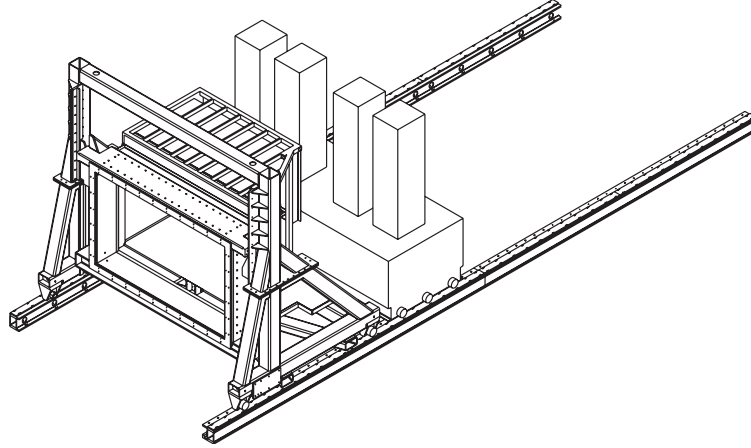


Figure 218: A sketch of the Pb-glass array as modified for the GLUEX detector. The glass is stacked in a circular arrangement to match the solenoid.

quality of the photon beam, beam-associated backgrounds were manageable, even when operating at an endpoint energy of 4 GeV. At higher energies the beam spot size will be even smaller and the LGD energy resolution will improve.

**The Barrel Calorimeter** The Barrel Calorimeter, shown schematically in Fig. 219, will utilize scintillating fibers embedded in a lead matrix to make a relatively high-resolution sampling calorimeter. Advantages include speed, cost, ease of readout, and the fact that it is based on a proven technology. This technology has been used in calorimeter design and operation for more than a decade. The ratio of the active scintillator to the passive high- $Z$  material, as well as the diameter of the fibers can be tuned to enhance resolution, to determine the radiation length, and to achieve uniformity in the electromagnetic to hadronic response (the  $e/h$  ratio). For high-resolution EM performance, the JetSet detector developed at Illinois [He90] was the first designed specifically to optimize EM resolution. The recipe produced a detector comparable to lead glass at a considerably lower cost and with approximately half the radiation length. Our design for GLUEX follows this concept but would be a full 12.5-15  $X_0$  thick at normal incidence and considerably longer. Realization of these changes fortunately can be based on the KLOE calorimeter at DAΦNE, a device of the same length as the barrel calorimeter but with an even larger inner diameter [An96]. The KLOE detector has achieved an excellent energy resolution parameterization of  $\sigma/E \approx 4.4\%/\sqrt{E}$  in a half-length prototype, using 1 mm-diameter scintillating fibers, and 0.5 mm-thick lead sheets.

For GLUEX, we will build 54 modules each 4.5 m in length and 20–25 cm deep, using the same diameter of fibers and thickness of lead sheets as for the KLOE detector, (see Fig. 219). The readout scheme takes advantage of the fact that all fibers run parallel to the axis of symmetry of the solenoid and therefore all light piped to the ends of the modules retains its azimuthal and radial information. Since this device is located near the central region of the solenoid, where the magnetic field is  $\sim 2$  Tesla, field-resistant readout must be employed. The most promising candidate is the

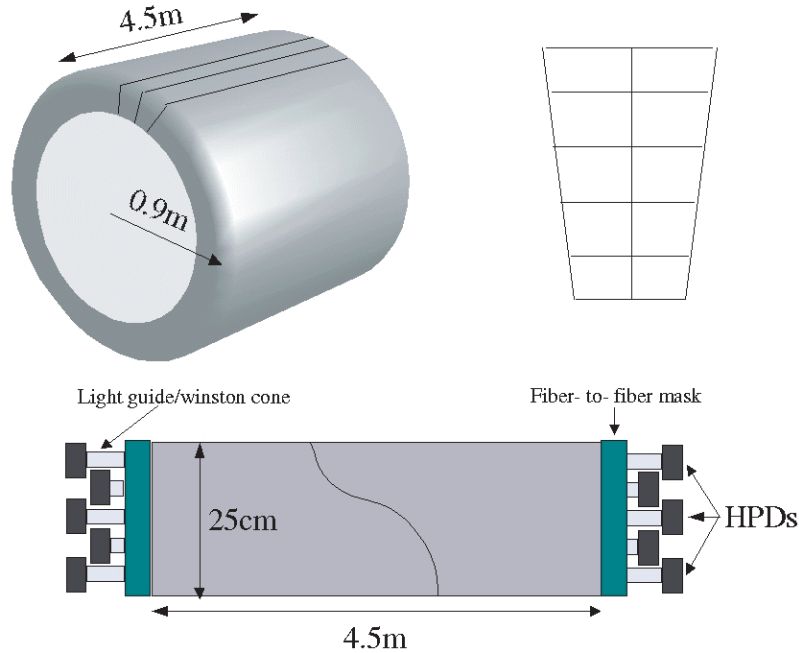


Figure 219: Sketch of the Barrel Calorimeter made from bars of Pb/SciFi material. Upper left: perspective view; upper right: close up of end with suggested readout segmentation for one of the 54 bars; Lower: side view showing approximate locations of the PMTs.

hybrid photo diode devices developed for CERN applications. They have a very fast rise time (6 ns or less), a fast fall time (less than 10 ns), and excellent energy resolution. They are immune to magnetic fields up to 2 T and their power supplies are very compact due to the fact that they draw virtually no current even under maximum bias. The polished ends of the lead, scintillating fiber matrix will be coupled to multiple independent light guides or to a fiber-to-fiber mask.

An important feature of these detectors is the signal rise-time and overall duration. Because fast plastic scintillator is used, integrated signal time can be kept below 100 ns with shorter times possible if deemed necessary for rate considerations. At the expected maximum luminosity no problems are anticipated. With short rise-times, very good timing can be expected for each of the PMTs involved in collecting the light from a shower. Time differences from the two ends produces the  $z$  coordinate of the hit. The mean light collection time of the two readout ends can be used to determine the particle time-of-flight (TOF). TOF coupled with the track length and momentum then yields particle mass. In the KLOE design, timing of  $\approx 250$  ps (RMS) was achieved, and improvements are possible.

In order to construct 4.5 m long modules, we have been studying the KLOE tooling development. Several visits of HALL D physicists to Frascati and Pisa have already taken place and their training in the use of the KLOE 15 cm-wide lead swagging machine is nearly complete. In May 2002, we successfully swagged 0.5 mm thick lead sheets, and glued 10 layers of lead and 1 mm opti-

cal fibers together, producing the first Pb/SciFi test module with dimensions 100 cm x 15 cm x 1.25 cm. This swaging machine is now located at Regina on loan from Frascati, where the construction of larger modules is well under way.

We have conducted several static tests at Regina and in-beam test at TRIUMF of several makes of single- and multi-clad SciFi strands have also been conducted, from Kuraray and Pol.Hi.Tech. The main features of the results were in close agreement with benchmark tests from KLOE. The Kuraray fibers showed a consistently superior performance as per the light attenuation coefficient. They also exhibited a better timing resolution. However, the Pol.Hi.Tech. multi-clad fibers performed better in terms of light yield, based simply on the observation that for the same bias and gain the mean of the ADC spectra for these fibers was higher. For this reason, multi-clad fibers have been ordered and their testing is in progress.

Finally, considerable R&D has gone into the investigation of the performance of the hybrid PMTs as well as toward the development of a suitable pre-amplifier electronic circuit. In our tests we used the DEP PP0350G hybrid PMT and its PP0100Z HV power supply. This device is powered by a HV supply which is typically set to -8 to -9 kV, and a bias of -60 to -80 V is applied across the diode. The gain response of the hybrid PMT at -8 kV is around 1600, which necessitates the use of a preamplifier. For our initial evaluation, we have used a Cremat<sup>10</sup> CR-101D charge sensitive pre-amplifier. Its rise time is 13 ns, its input capacitance is 20 pF and its power dissipation is 150 mW. These tests have pointed to the great care which must be exercised so as to electrically isolate the circuits. Much effort was expended in the avoidance of current (ground) loops in the circuit and in the shielding of the circuits from RF noise. Many parameters of the circuit were studied, such as rise time, signal amplitude, ADC response and photo-cathode positional sensitivity. All measurements were very promising and we are confident that we are close to a production design.

**The Upstream Photon Veto** The Upstream Photon Veto is needed to be able to detect and veto on photons traveling in the backward direction. Detailed Monte Carlo studies have shown that events in which a baryon resonance is recoiling against the meson system can produce photons, from the baryon decay, which are traveling in the backward direction. The detector is a soft-steel scintillator sandwich device located directly upstream of the target and in place of the solenoid's original field shaping mirror plate. In the current design, the mirror plate is modified by removing all of the soft iron within the inner solenoid radius. This modification effectively removes the upstream mirror plate leaving only a soft iron annulus the size of the magnet coils and has several benefits: it allows the addition of an upstream photon veto, and upstream access to the target region, cylindrical drift chamber, and the upstream end of the barrel calorimeter.

The photon veto consists of 18 layers of 1 cm thick scintillator alternating with first 12 layers 0.635 cm (0.36X<sub>0</sub>) thick steel sheets then 6 layers of 1.270 cm (0.72X<sub>0</sub>) thick steel sheets (see Fig. 220). Each scintillator layer consists of seven 34 cm x 238 cm paddles forming a plane. The

---

<sup>10</sup>Cremat Inc., 45 Union Street, Watertown, MA 02472, USA.



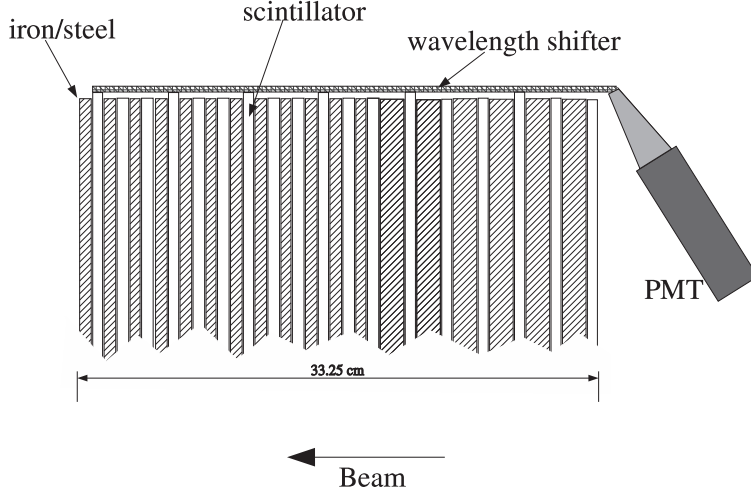


Figure 220: Sketch of a upstream photon veto segment. The 18 scintillator layers are arranged into three alternating orientations:  $x$ ,  $u$ , and  $v$ . Shown is the light collection for one such orientation. The light collecting ends of the scintillators are joined together via a wavelength shifter which is oriented perpendicular to the scintillators. The wavelength shifter is used to redirect the light through  $90^\circ$  and out the upstream end of the solenoid to photomultiplier tubes (PMT).

central paddle has a hole to allow for the passage of the beam and the target support and cryogenic system. The effective area of each plane is approximately  $238 \text{ cm} \times 238 \text{ cm}$ . The total counter thickness is  $33.25 \text{ cm}$  ( $8.91X_0$ ). The layers are arranged into three alternating orientations:  $x$ ,  $u$ , and  $v$  ( $\pm 45^\circ$  deg, respectively).

**Charged Particle Identification** Charged particle identification (PID) separates  $\pi^\pm$  from  $K^\pm$  from  $p$  (and the occasional  $\bar{p}$ ). (We do not consider  $e^\pm$  nor  $\mu^\pm$  identification explicitly, but they can be separated from hadrons at some level using the electromagnetic calorimeters.) Two detector systems will be constructed explicitly for this purpose, namely the time-of-flight hodoscope and the Čerenkov detector. Both of these address PID in the forward region, where velocities are close to  $c$  and the separation is the most difficult. In the solenoid, we expect to make use of  $dE/dx$  in the drift chambers and timing in the barrel calorimeter. Furthermore, constrained fitting is a generally useful tool for identifying the event topology as a whole.

If the particle momentum is not too high, time-of-flight is useful for PID in the forward region. For TOF scintillators that are 2 m long, RMS time resolutions on the order of 100-200 ps are typically achievable using well established techniques [Mo79, Be82]. With improvements in photomultiplier design, however, one can achieve 50 ps RMS for detectors with long, narrow geometry. Superior time resolution has also been achieved with mesh PMTs which will work well in a high magnetic field. In Fig. 221 shows range of relevant momenta for particle identification for both the time-of-flight system and the Čerenkov counter. Beam tests of prototype time-of-flight designs have been carried out and the results indicate we are well on track to achieving time resolutions below 100 ps.



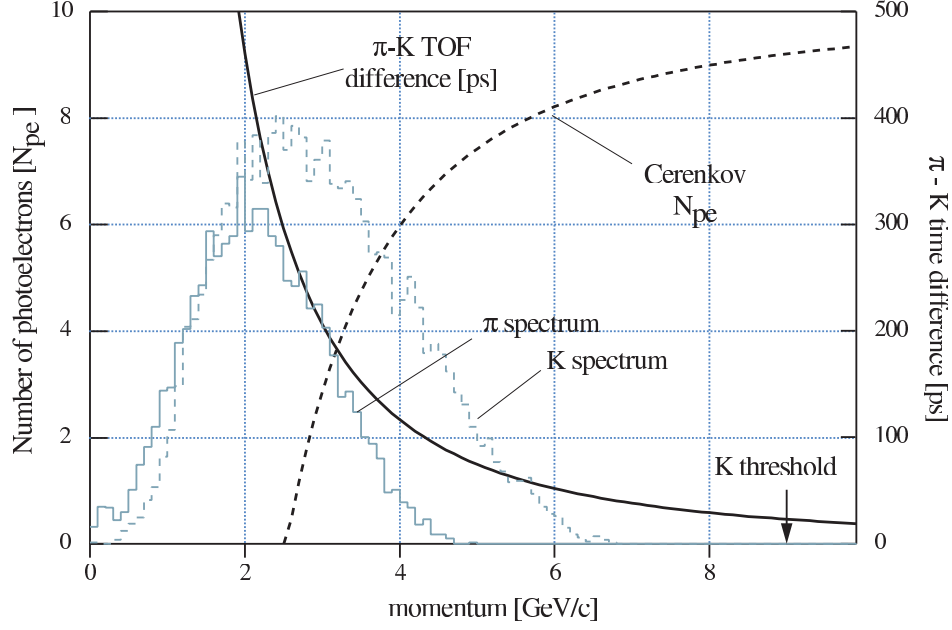


Figure 221: The time of flight difference between  $\pi$  and  $K$  mesons and the number of photoelectrons from the Čerenkov counter as a function of momentum. Also shown are expected  $\pi$  and  $K$  momentum spectra for  $K^*\bar{K}^*$  final states.

**The Time-of-Flight System** In the forward region the TOF system will consist of two walls of scintillation counters oriented perpendicular to each other and located downstream of the Čerenkov counter and just upstream of the lead glass detector (LGD). The scintillator bars need to be 2 m long to cover the active regions of the Čerenkov counter and LGD. The bars will be read out at both ends with photomultipliers. The width of the bars is set by the requirement that the overlap of charged particles from the same event at the TOF in any one bar be acceptably small ( $< 2\%$ ).

Extensive prototype studies have been carried out to optimize the TOF system design [De01]. Data on scintillation bars of various dimensions and manufacture and various phototubes were collected using a cosmic ray test facility at Indiana University and using hadron beams at the Institute for High Energy Physics (IHEP) in Protvino, Russia, . The first data run at IHEP was used to test 2-m long counters with square cross sections of  $2.5 \times 2.5 \text{ cm}^2$  and  $5.0 \times 5.0 \text{ cm}^2$ . The scintillator material was type EJ-200, produced by the Eljen Corporation. This scintillator has a decay time of 2.1 ns, a bulk attenuation length of 4 m, an index of refraction of 1.58, a peak in the emission spectrum at  $425 \text{ nm}$ , and a light output equal to 64% of that of Anthracene. The average time resolution measured for various combinations of scintillation bars was in the range of 100-180 ps for the 2.5 cm bars and sub-100 ps for the 5.0 cm bars, depending on the PMTs used. In a later data run 2 m-long bars of cross sections  $2.5 \times 6.0 \text{ cm}^2$  were tested using a 5 GeV/c beam. Using constant fraction discriminators the time resolution for two bars was measured to be less than 40 and 60 ps when particle cross 6.0 cm and 2.5 cm of scintillator respectively. Based on the results presented above, we have chosen the 2.5 cm thick, 6 cm wide bar for the TOF wall.

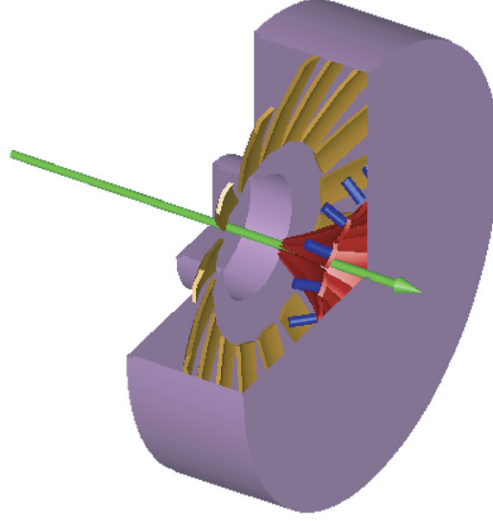


Figure 222: A schematic drawing of the GLUEX Čerenkov detector system. The beam direction is indicated with an arrow. The Čerenkov light is focused by ellipsoidal mirrors (red and orange) into phototube assemblies at the downstream side (blue cylinders).

**The Čerenkov Detector** The primary function of this detector is to signal the presence of pions over a large part of the expected momentum range. The Čerenkov Detector is planned to be a gas filled threshold detector running at atmospheric pressure. Current studies suggest that a  $\text{C}_4\text{F}_{10}$  filled Čerenkov detector ( $n = 1.0014$ ) will be a good match to the kinematics of GLUEX reactions. For individual tracks, the results of the Čerenkov detector coupled with the time-of-flight system are shown in Fig. 221.

The detector will be segmented into sixteen azimuthal regions, each housing a single mirror that focuses light onto its own photomultiplier tube. Light emitted into the region within 10 cm of the beam axis will not be collected in order to suppress accidental coincidences in the detector. The optical design of the detector (two ellipsoidal mirrors) was chosen to produce a strong focus at the photomultiplier tubes. This produces small linear magnification and allows good light collection from the wide range of particle trajectories exiting the solenoid. Prototype mirrors were constructed and tested for their focal properties. These were found to be mechanically and optically stable after being cut to shape. Having two mirrors in the design also offers flexibility as to the placement of the photomultipliers. This freedom will be used to place the axis of the tubes perpendicularly to the ambient magnetic field, in order to optimize the effectiveness of the passive magnetic shields surrounding the photomultipliers. A schematic drawing of the Čerenkov is shown in Fig. 222.

Because the GLUEX experiment will be reconstructing exclusive final states, perfect  $K$ - $\pi$  separation for all tracks is not necessary. Detailed Monte Carlo studies using the detector parameters and imposing additional constraints such as the total strangeness in an event and kinematic fitting have been performed. We find that combining all available information will make for a very efficient particle identification system for GLUEX events.

**Sub-system Installation and Integration** The assembly and integration of each of the detector subsystems into the GLUEX detector requires careful coordination and attention to many diverse issues.

The magnetic field configuration outside the magnet dictates the location and orientation of standard PMTs and/or use of hybrid PMTs. The field distribution can be affected by magnetic materials used for support structures such as iron and, therefore, care must be taken in choosing common materials for the various support systems.

The detectors in the forward direction (Čerenkov, TOF and LGD) are relatively isolated mechanically and operate independently of other systems. The detectors inside the magnet, however, are in close proximity and mounted on the same mechanical frames that are anchored either on the BCAL or the solenoid. Therefore, cabling, power consumption, and access for maintenance must be coordinated carefully. In general, care must be exercised in the design of the electrical circuits, so as to avoid ground loops and RF interference.

The mounting and assembly of detectors must allow for the delivery of services required for their operation, including cryogenics, electrical power, ventilation, gas connections for the Čerenkov and drift chambers, as well as high voltage and signal cables for all detectors. During installation and servicing, careful surveying must be carried out to ensure a precise (better than 100  $\mu\text{m}$ ) knowledge of the relative tracking element location. Moreover, access to each sub-system must be facilitated for purposes of maintenance or repair.

#### **3.D.4 Rates, Electronics, Trigger and Data Acquisition**

The goal of the GLUEX readout electronics system is to digitize and read out the detector signals for level 1 trigger rates of up to 200 kHz without incurring dead time. A pipelined approach is required. The digitized information will be stored for several  $\mu\text{s}$  while the level 1 trigger is formed. Multiple events must be buffered within the digitizer modules and read while the front ends continue to acquire new events.

Two basic types of readout electronics will be used in GLUEX, FADCs and TDCs. Detectors which measure energy will be continuously sampled with flash ADCs while detectors which require precise time measurements will use a multi-hit TDC. No currently available commercial solutions exist. These boards will be designed by our collaboration. Prototypes have been constructed, and are being tested.

The number of channels in the GLUEX detector is not large enough to justify the financially risky development of custom integrated circuits. Programmable logic devices are fast enough and available at reasonable cost. Programmable logic also allows for optimization of the data path without redesigning a printed circuit. ICs developed for other experiments could also be used.

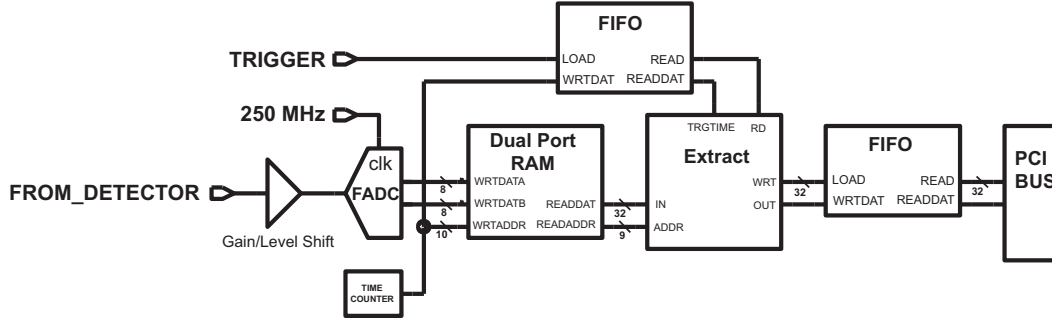


Figure 223: Block diagram of prototype FADC board.

Electronics technology is constantly evolving, and the optimum solution for the GLUEX detector depends on when funding becomes available and the construction schedule.

A single channel prototype of the calorimeter FADC has been designed and built at Indiana University. A block diagram is shown in Fig. 223. A differential amplifier inverts the negative PMT signal and shifts the voltage levels to match the input range of the digitizer integrated circuit. The digitization is performed by an SPT7721 integrated circuit manufactured by Signal Processing Technologies [Spt]. This IC costs about US\$25 each in small quantities. An 8-bit value is produced internally every 4 ns; two samples are output every 8 ns (125 MHz).

All digital functions are performed in a Xilinx [Xiln] XC2S50 programmable gate array. This IC costs about US\$15 each in small quantities. A dual port RAM configured as a circular buffer stores the data for 8 microseconds. Upon receipt of a trigger signal the data from the time window of interest is copied to an output FIFO which can buffer the data from multiple events. This FIFO is interfaced to a 32 bit, 33 MHz PCI bus. More information on this prototype is available [Sm02].

The Photon Tagger, Start Counter, Vertex Tracker, Forward Drift Chamber anodes, Čerenkov Detector, Barrel Calorimeter, and Time of Flight Wall will all be read out using multi-hit TDCs. Such a high resolution pipeline TDC module has been developed for use at Jefferson Lab, and is designed to meet the requirements of current experiments, as well as to serve as a prototype for future experiments, including GLUEX. The design is implemented as a VME-64x module. This bus standard was chosen because it is already in use at Jefferson Lab, has good (and evolving) data transfer capabilities, and reasonable channel densities are possible. A block diagram is shown in Fig. 224. The module is built around the TDC-F1 integrated circuit from Acam-Messelectronic GmbH [Acam], originally designed for the COMPASS experiment at CERN [Co99].

The prototype was outfitted with a single F1 chip. All channels were found to be operational and tested for performance. Timing signals were generated with a measured jitter of approximately 30 ps. The time calibration at low resolution was found to be 115.1 ps/count (120 ps/count nominal) and 57.5 ps/count in high resolution (60 ps/count nominal). Subtracting the contribution from the time generator we obtain 62 ps and 51 ps for the prototype performance in both the low

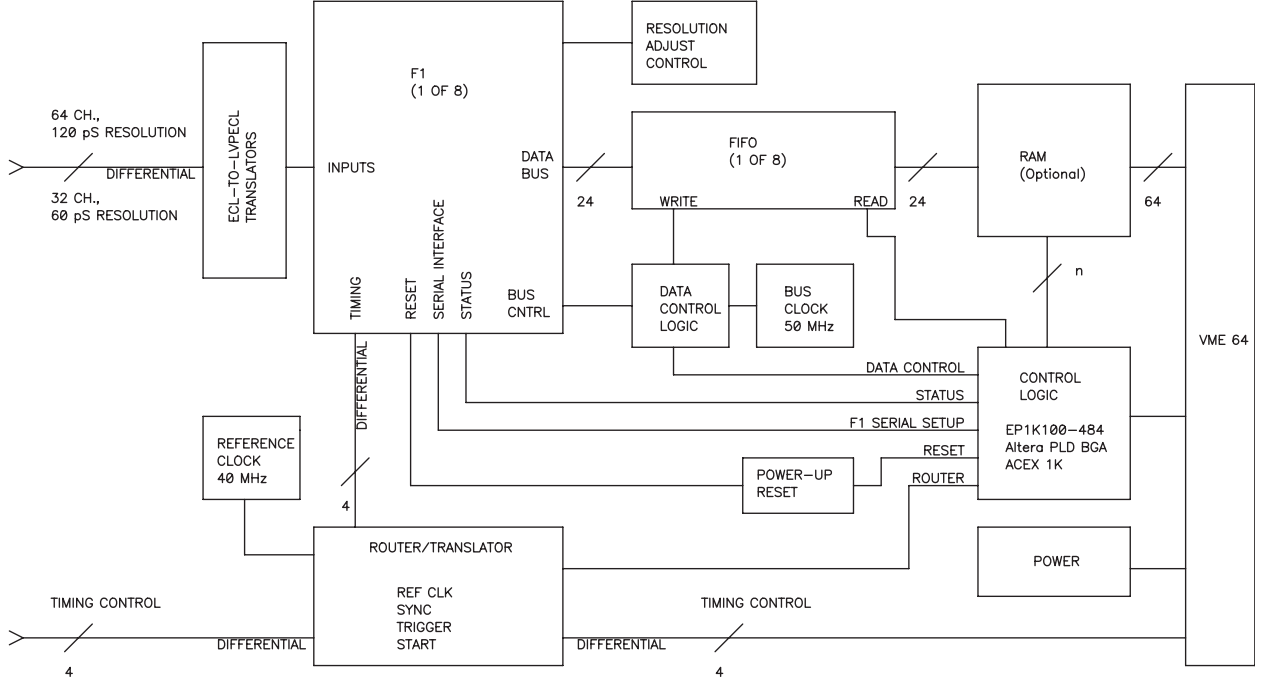


Figure 224: Block diagram of prototype TDC board.

and high resolution respectively. This is to be compared with the quoted rms resolution of the F1 chip of 40 ps.

Table 37 gives the total hadronic rate as well as the tagged hadronic rate for fixed electron beam conditions for various energies of the coherent peak. For  $E_\gamma = 9 \text{ GeV}$  and  $10^8 \gamma/s$  in the peak, the experiment will have a total hadronic rate of 365 KHz and a tagged hadronic rate of 14 KHz. Initial operating conditions will be at about 10% of these values, ( $10^7 \gamma/s$ ), but as the trigger improves, and the detector is better understood, rates will be pushed up toward the  $10^8$  number.

In order to achieve the roughly 20-1 reduction in event rate, GLUEX will use a two-stage trigger, combining a hardware-based level 1 trigger with a software (reconstruction) based level 3 trigger. An essential feature of the GLUEX design is to build pipelining into the entire trigger, digitizer, and data acquisition systems at the outset. This has the twin virtues of allowing adequate time for the level 1 trigger to do its job, while eliminating signal degradation involved in delaying the signals while the trigger operates. Pipelining in this way also allows us to upgrade from initial photon fluxes of  $10^7$  photons/sec to eventual fluxes of  $10^8$  photons/sec without any significant changes to the trigger/DAQ architecture. Eliminating conversion dead times will allow us to acquire events which occur very close together in time.

The data acquisition goal for GLUEX is to accept the level 1 trigger rate without incurring any DAQ system dead-time. The high rate of level 1 triggers (70-180 kHz) drives the design of the trigger, the front-end electronics, and the DAQ system. When the level 1 trigger is asserted, a time

Table 37: Operating parameters for an experiment using the coherent bremsstrahlung beam. The calculation assumes a 12 GeV electron beam energy and a 3.4 mm collimator 80 m downstream from a radiator of thickness  $10^{-4}$  radiation lengths. The electron beam current is taken to be  $3\mu\text{A}$ . The rates in the detector (last two rows) are calculate for a 30 cm hydrogen target and an open hadronic trigger.

$E$ of peak	8 GeV	9 GeV	10 GeV	11 GeV
$N_\gamma$ in peak	185 M/s	100 M/s	45 M/s	15 M/s
peak polarization	0.54	0.41	0.27	0.11
(f.w.h.m.)	(1140 MeV)	(900 MeV)	(600 MeV)	(240 MeV)
peak tagging efficiency	0.55	0.50	0.45	0.29
(f.w.h.m.)	(720 MeV)	(600 MeV)	(420 MeV)	(300 MeV)
power on collimator	5.3 W	4.7 W	4.2 W	3.8 W
power on target	810 mW	690 mW	600 mW	540 mW
total hadronic rate	385 K/s	365 K/s	350 K/s	345 K/s
tagged hadronic rate	26 K/s	14 K/s	6.3 K/s	2.1 K/s

slice of each ring buffer will be copied, compressed and stored. Buffering will occur in groups of at least 10 event fragments on each electronic board and then transferred first across a backplane to be built into crate-event fragments and then to a computer farm to be built into complete events. The farm will perform a quick analysis to reduce the event rate by approximately a factor of ten before recording to mass storage media. This design allows GLUEX to start running with a modest tagged photon rate and then to scale-up by an order of magnitude.

The goal of the level 3 trigger is to reduce the event rate given by the level 1 trigger to an acceptable on tape rate. In low intensity running ( $10^7$  tagged photons/s) the level 1 trigger rate is expected to be 15 kHz. Since the DAQ system is being designed to handle this rate to tape, the level 3 trigger farm will not have to cut any events, although it may be used to reduce the event rate somewhat. In high intensity mode where the level 1 rate is 70 to 180 kHz, the level 3 trigger must be able to reduce the event rate by a factor of ten.

Most of these unwanted events result from an untagged (mostly lower energy) photon interacting in coincidence with a tagged photon. Rejecting these events means that level 3 must be able to calculate, with reasonable accuracy, the energy of the photon which produced the event. This involves accurately reconstructing tracks, matching them with the calorimeter information, and adding additional energy deposited by neutral particles in the calorimeters.

Because of the accuracy requirements and the demands of linking information from different detectors, we have decided to use a processor farm architecture for level 3 instead of building a dedicated hardware processor. All events passing the level 1 trigger will be read into the level 3 processor farm where they will be reconstructed; events passing the cuts applied will then be written to tape. This approach allows for algorithmic flexibility and improvements, and the ability to cost-effectively adjust to higher rates, but it does put pressure on the DAQ system.

Table 38: Rates, sizes, and processing requirements for the level 3 trigger.

	Low Rate	High Rate
Event Size	5 KB	5 KB
Event Rate to Farm	20 KHz	200 KHz
Data Rate to Farm	100 Mbytes/s	1000 Mbytes/s
Num Links to Farm	1	10
Data Rate per Link	100 Mbytes/s	100 Mbytes/s
Link Technology	Gigabit Ethernet	Gigabit Ethernet
Events/s per Link	20000	20000
SPECints/ev for L3	0.1	0.1
Num SPECint/link	2000 SPECint	2000 SPECint
Num SPECint/link x 2	4000 SPECint	4000 SPECint
Num 200 SPECint processors/link	20	20
Total Num 200 SPECint processors	20	200

We estimate the processing power required as follows. The Hall B on line hit-based event reconstruction system obtains 3% momentum resolution using  $\sim 5$  ms of cpu time on a 20 SPECint processor (about 0.1 SPECint/event); full reconstruction with better than 1% resolution takes about 45 ms. Assuming the same for GLUEX gives 20000 SPECint total for the full level 3 farm at 200 KHz event rate. Assuming 50% processor utilization (due to I/O overhead, etc.), approximately 40000 SPECint (200 processor boxes at 200 SPECint each) are needed. 150 SPECint boxes are currently running in the JLab farm system, and, depending on the improvement in cpu performance over the next few years, it is likely that far fewer boxes will be required, perhaps 1/4 as many.

### 3.D.5 Computing and Partial Wave Analysis

GLUEX will be the first Jefferson Laboratory experiment to generate petabyte scale data sets on an annual basis (One petabyte =  $1\text{ PB} = 10^{15}$  Bytes). In addition, the need to generate physics results in a timely fashion has been identified as a primary goal of our collaboration since its inception. For these reasons, a well-designed, modern, and efficient computing environment will clearly be crucial to the success of the experiment.

Currently, there are a number of particle physics projects world wide which also will produce very large data sets, and which will function with large dispersed collaborations. It seems quite reasonable to expect that over the coming years many new tools will be developed that will aid in effectively processing and managing these large volumes of data. As a collaboration, we will undoubtedly make effective use of these tools, which will include such things as grid middle ware, distributed file systems, database management tools, visualization software, and collaborative tools.



Nonetheless, it also is clear that the GLUEX collaboration will need to develop a suite of tools which are dedicated to this experiment. This will include data acquisition and trigger software, experiment monitoring and control software, data reduction tools, physics analysis software, and tools dedicated to the partial wave analysis (PWA) effort.

The primary goal of GLUEX is the systematic identification and categorization of short-lived meson states, unraveled from the raw, multi-particle reaction data using the techniques of PWA. Achieving this goal requires simultaneous access to two large and independent data sets, namely the actual reduced experimental data and the simulated Monte Carlo data, each sorted for the particular multi-particle reaction(s) under consideration. It is quite probable that these data sets will be distributed physically over multiple locations, and that the access will be from other separated sites, associated with the group which has undertaken that particular analysis.

This not only impacts the structure of the data grid, but also implies that new analysis tools need to be developed. This especially includes visualization tools, as one searches for the appropriate combination of partial waves which best describe the reaction. That is, as one fits the parameters associated with a certain set of partial waves, some visual inspection mechanism is needed to evaluate how well the fit reproduces distributions in angles and invariant mass, for the many possible combinations. A universal set of tools is important in order to come to a more or less standard set of measures that would be applied by the analysis groups.

In order to identify the  $J^{PC}$  quantum numbers of a meson, it is necessary to perform a PWA. In the simplest terms, a partial wave analysis is an attempt to determine production amplitudes by fitting decay angular distributions. The fit may include information on the polarization of the beam and target, the spin and parity of the resonance, the spin and parity of any daughter resonances and any relative orbital angular momenta. The analysis seeks to establish both the production strengths and the relative phase motion between various production amplitudes. Phase motion is critical in determining if resonance production is present.

While the implementation of a PWA is in principle straight forward, there are both empirical and intrinsic difficulties. Empirically, instrumentation effects, such as detector acceptance and resolution, can conspire to make one distribution look like another. These similar distributions can lead to *leakage* from one wave into the other in the PWA. Here, cropping, smearing, or incorrect acceptance corrections of two physically different distributions may lead to distributions which are apparently indistinguishable. There is also the related problem of background in PWA. Backgrounds involve a different final state accidentally reconstructing as the channel under study. Either a particle is missed by the detector, or when putting the final state back together, multiple interpretations are possible. Both of these effects limit one's ability to measure phase motion, and can be particularly severe in a region of dense overlapping resonances. These difficulties can be minimized by properly designing the experiment. Full angular coverage in the distributions can be achieved by using a nearly  $4\pi$  detector with excellent resolution. In addition, high statistics are critical to be able to accurately separate these partial waves. A thorough PWA requires nearly  $4\pi$



coverage, excellent resolution, high statistics and a very good understanding of the detector.

The PWA method is subject to intrinsic mathematical ambiguities for certain final states. Two or more different choices of amplitudes lead to identical observables. Here there are at least two approaches. The first assumes some a priori physics knowledge that allows one to choose one solution over another. The second, and cleaner approach is to simultaneously examine several final states to which the resonance can decay. While the distributions may be confused in one final state, such as  $\eta\pi$ , they are likely to be absent or different in a second such as  $\rho\pi$ . This latter approach assumes that the detector has been optimized for many different final states, and that relative normalizations between these are understood.

This latter approach of looking at multiple final states not only allows the separation of different waves, but also yields key information about the relative decay rates of mesons. This information is critical to understanding the underlying wave functions of the mesons — their content, and mixing with other states. The ability to measure many final states accurately, and to perform a simultaneous PWA is a key feature of the GLUEX spectrometer for doing excellent spectroscopy.

The use of photon polarization will allow us to both simplify the analysis parameterization, as well as access additional information on the production of mesons. It will also provide key checks on the stability of the analysis itself. While circularly polarized light may yield some information in a few special cases, the true gain comes from linear polarization. Linear polarization defines a *new spatial direction* beyond the photon direction, while for circular polarization, the polarization and the momentum are in the same direction. Secondly, linearly polarized light is a coherent sum of circularly polarized light, which leads to new interference terms.

As part of the GLUEX design studies, the group has carried out a double-blind partial wave analysis on simulated data for the reaction:

$$\gamma p \rightarrow \pi^+ \pi^+ \pi^- n,$$

for 8.5 GeV photons. Studies have been done with photon polarizations ranging from 0% up to 100%. The simulated data correspond to a mix of seven waves including the  $a_1$ ,  $a_2$ ,  $\pi_2$  and the  $J^{PC} = 1^{-+} \pi_1$ , all of which decay via  $\rho^0 \pi^+$  to the  $3\pi$  final state. The data are assumed to proceed via purely one-pion exchange. Two different packages for partial wave analysis have been used, each using a different formalism for fitting the data. The results between the two agree. The use of more than one analysis package on real data will allow us to better access the systematics associated with the fitting of the data. The data used in these fits corresponds to a couple percent of one year's reconstructed sample using  $10^7$  photons per second. It should be noted that this channel has a large photoproduction cross section, while the goal of the experiment is to simultaneously study channels with much smaller cross sections.

Figure 225 shows the results of fits to the simulated data. The solid figures correspond to simple generated data, while the open figures are for data which has been run through the GLUEX

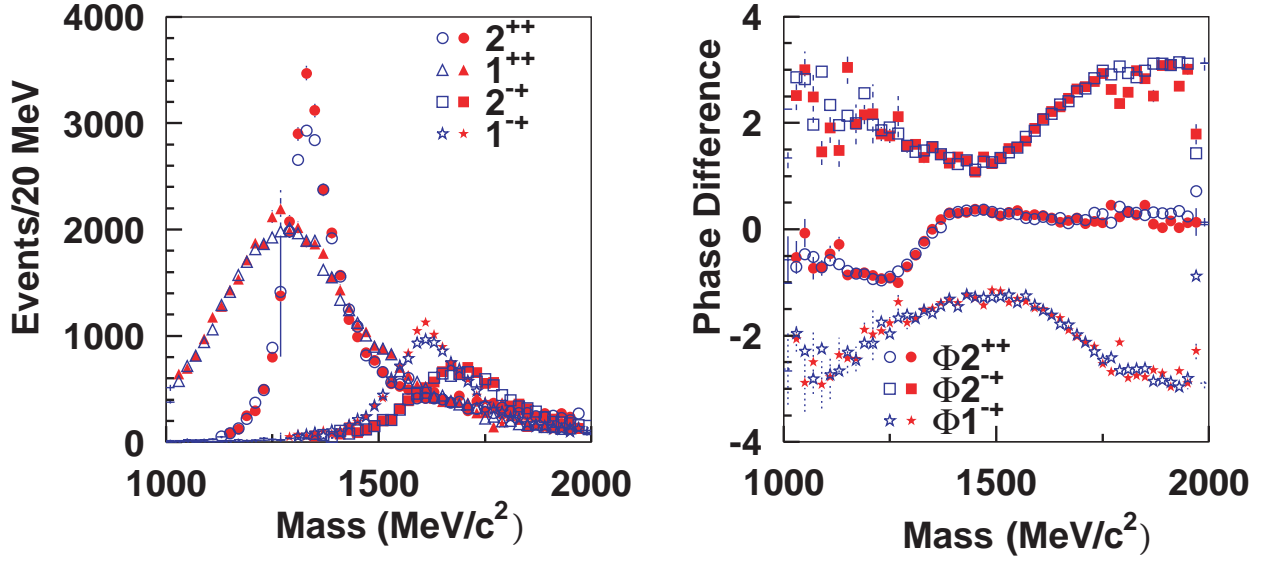


Figure 225: Partial Wave Analysis results for simulated  $3\pi$  data. The solid points correspond to generated data, while the open points correspond to events which have been run through the GLUEX Monte Carlo program. The left hand figure shows the intensities of several waves, while the right hand figure shows the phase difference from the  $1^{++}$  wave.

Monte Carlo program to simulate both acceptance and resolution effects. The small differences between the two curves are due mostly to resolution, particularly for the fast  $\pi$ 's in the events. It should be noted that the  $3\pi$  channel while one of the stronger photo production channels, is also one of the more difficult as far as resolution goes. The four curves correspond to the  $a_2(1320)$ , ( $J^{PC} = 2^{++}$ ), the  $a_1(1260)$ , ( $1^{++}$ ), the  $\pi_2(1670)$ ,  $2^{-+}$  and an exotic  $\pi_1(1600)$ , ( $1^{-+}$ ). The phase differences are plotted with respect to the  $a_1(1260)$  wave. A second PWA exercise was performed to assess the ability to extract an small exotic signal from mix of various non-exotic waves, ( this latter study used simple 4-vector smearing and cuts rather than the fast Monte Carlo). Figure 226 shows the results of this second study where the exotic wave was about 2.5 % of the total sample. The statistics shown correspond to several days of running and it is clear that one can easily extract this small signal from the data, and accurately reproduce the original resonance

Similarly, a study on the effect of linear polarization in determining the production mechanism has been undertaken. To do this, a second event generator was built that produced the same  $3\pi$  final states via  $\rho$  exchange, rather than  $\pi$  exchange. The naturality of these two exchange particles are opposite from each other, and in the absence of linear polarization, only the sum of the two intensities can be determined. With the addition of linear polarization, it is possible to disentangle the two contributions. Figure 227 shows this by examining the exotic  $1^{-+}$  wave produced via both these mechanisms. The upper curves in the figures correspond to fits to the sum of the two intensities, and are well fit for all polarizations. The lower curves correspond to fits to the differences between the two intensities. This is completely undetermined for the unpolarized data set, while it is separated for the polarized samples.

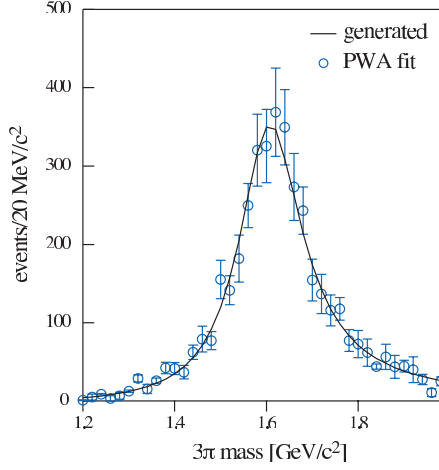


Figure 226: The results of a double-blind Monte Carlo exercise showing the  $J^{PC} = 1^{-+}$  exotic wave after fitting (open circles) and the exotic wave input (curve) into the mix of  $\gamma p \rightarrow \pi^+ \pi^+ \pi^- n$  events that were generated in this study. Details are given in the text.

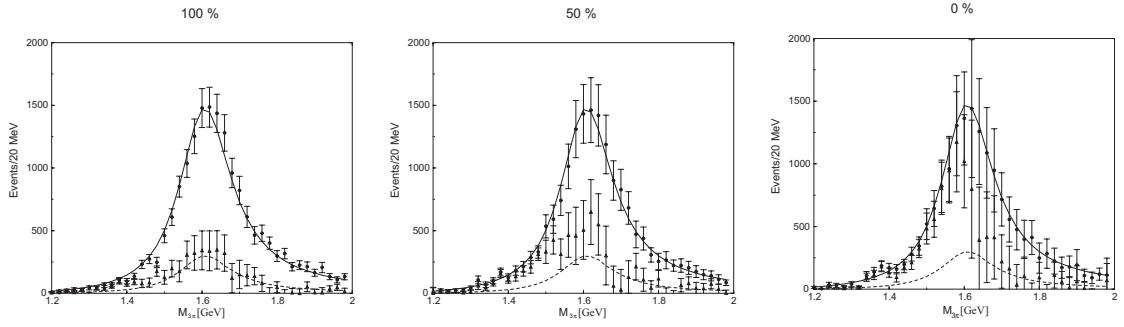


Figure 227: Partial Wave Analysis results for simulated  $3\pi$  data generated with a combination of natural and unnatural parity exchanges with 100%, 50% and 0% linearly polarized photons. The upper curves correspond to the sum of the two intensities, while the lower curves correspond to the differences between the two intensities.

A detailed *leakage* study has also been performed using the PWA tools [Za01]. In doing this, the geometry in the detector simulation for producing physics events and the detector simulation for performing the PWA were varied by several  $\sigma$  in the resolution parameters for the GLUEX detectors. A search was then made for signals that leaked into the exotic waves with the results that with the current detector geometry, it is extremely difficult to produce leakage into the exotic waves.

The GLUEX collaboration has organized a collaborative program with the CLEO-c experiment to develop advanced tools for PWA that would be useful for both groups. The initial efforts by GLUEX members have been to begin work on parallelizing existing PWA codes, and using these to analyze large existing data sets collected by the E852 collaboration. A sample of approximately 35-million  $3\pi$  events is being analyzed using the large computer facilities available at Indiana University. These efforts have made possible the PWA analysis of the largest data set ever.

In order to continue and expand these efforts, members of both the GLUEX collaboration and the CLEO-c collaboration submitted an NSF ITR proposal in February of 2003. This proposal would support a 4-year multi-pronged development and implementation of the next generation of PWA tool. Under this proposal, the CLEO-c contingent will develop data caching tools and interfaces to allow transparent access to large data sets. The GLUEX collaboration will work on visualization tools, parallelization of PWA code and improvements in minimization algorithms. In parallel with this, improvements in theory will be explored and implemented into the PWA tools. The tools will initially be applied to existing E852 data sets. Once CLEO-c spectroscopy data becomes available, they will be analyzed. At the end of the 4 year proposal, the goal is to have a robust set of tools that can be used to handle the GLUEX data.

### 3.D.6 Summary

The GLUEX beam and detector have been optimized to facilitate a robust PWA of mesons and baryons produced with an 8 to 9 GeV linearly polarized photon beam. Even with rates of only  $10^7 \gamma/s$ , the experiment will collect at least an order of magnitude more data than existing  $\pi$  beam experiments during its first year of running. Such an increase in statistics coupled with a new production mechanism will not only allow us to map out the gluonic excitations, but to measure their decay properties and production mechanisms as well.

## 3.E Experiment-Specific Equipment

### 3.E.1 Properties of Light Pseudoscalar Mesons via the Primakoff Effect

In addition to the 12 GeV upgrade to the CEBAF accelerator, the proposed program to perform high precision measurements of the electromagnetic properties of the light pseudoscalar mesons would

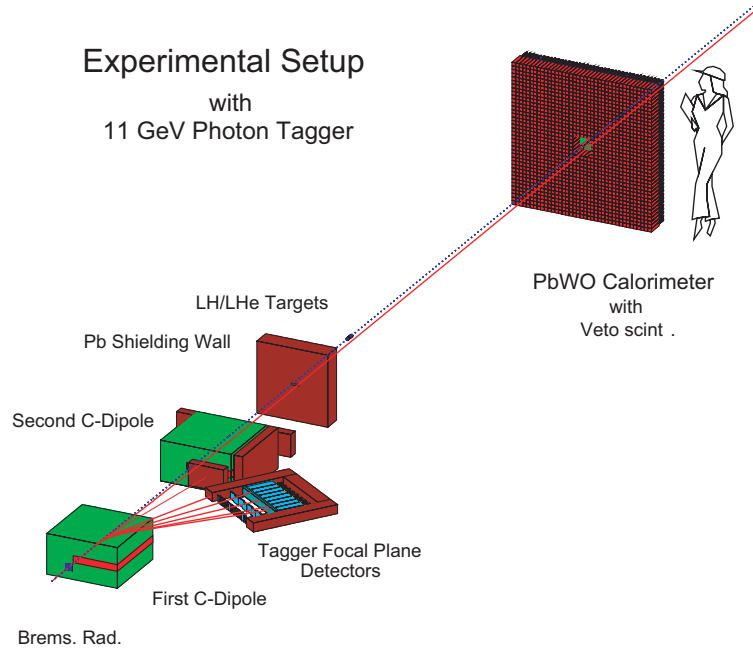


Figure 228: Side view of the experimental setup for  $\eta$  and  $\eta'$  two-gamma decay width measurements. It includes (1) a photon tagging system, and (2) a  $1.5 \text{ m} \times 1.5 \text{ m}$  multichannel calorimeter.

require a high energy photon tagging system and a multichannel calorimeter to detect photons from the meson decays. While the calorimeter is common to both the photo- and electroproduction measurements, the transition form factor measurements involve electroproduction, and would be performed with the same setup as the radiative width measurements but with the bremsstrahlung radiator removed and the photon tagger turned off. In such a configuration, the calorimeter would simultaneously detect both the two photons from the meson decay as well as the scattered electron.

The construction of a new tagging system is necessitated by the fact that the existing Hall B tagger is designed for a maximum energy of 6 GeV and at present there are no known plans to bring it to the capability to tag higher energy photons. While a high energy photon tagging system has been proposed by the Hall D Collaboration[HallD], its design is optimized to provide linearly polarized photon beams with high collimation of the bremsstrahlung photons. This requires a relatively long distance (approximately 90 meters) for photons from the bremsstrahlung radiator to the collimators, thus making this part of the photon beam line inaccessible. The experimental program proposed here simultaneously requires high precision in both photon flux control (at the 1% level) and angular resolution for forward meson production ( $\sim 0.3 \text{ mrad}$ ). This angular resolution requires the photon beam spot at the Primakoff production target to be minimized to about one millimeter. The optimal configuration for these measurements is thus one in which the physics target is relatively close to the bremsstrahlung converter and the photon beam is uncollimated. As such, the proposed Hall D tagging system will not simultaneously satisfy these two criteria.

We are proposing the construction of a photon tagging system based on a new approach

involving parallel transport of both the photon and primary electron beams through the beam line to the beam dump. Two identical 'C-type' dipole magnets will displace the initial electron beam and make it parallel to the photon beam, which is produced in the bremsstrahlung radiator just upstream of the first dipole (see figure 228). The displacement is determined by two parameters – the integrated field in the dipole magnets and the distance between them.

The following requirements for the design of this tagging system have been imposed. First, it should be a functional, relatively low cost system. Second, its size and design should allow flexibility to potentially incorporate it into any of several upgraded Halls currently being proposed at Jefferson Laboratory. Two standard C-dipole magnets (see Fig. 228) with a  $\int Bdl = 5$  kG meter placed 2 meters apart will provide a 5 cm parallel displacement of the electron and photon beams. Three centimeter diameter, 10 cm long liquid hydrogen and helium-4 targets will be placed downstream of the second dipole. To minimize beam backgrounds, a set of lead shielding walls (20 radiation lengths thick) surrounding the second dipole and one with a narrow hole (8 cm width, 2 cm in height) in the middle of a wall will be placed one meter downstream of the second dipole and just upstream of the physics targets. The post-bremsstrahlung electrons will be deflected in the first C-dipole and detected by the tagger focal plane detectors (see Fig. 229). Three layers of detectors are proposed. The first will be highly segmented scintillating detectors for energy definition of the post-bremsstrahlung electrons. The second plane of seven scintillators will provide fast timing for the tagger, while eight lead glass detectors ( $\sim 8.5 \times 8.5 \times 35$  cm<sup>3</sup>) in the third plane will significantly improve background suppression. A 2.5 cm thick aluminum absorber plate in front of the lead glass detectors will cut down the low energy charged particle background produced in the shower counters. This design emphasizes the tagging of high energy photons only, with a focal plane of length approximately 60 cm providing tagged photons of energy  $E_\gamma = 10.0 - 10.5$  GeV.

The decay particles from the forward produced neutral mesons will be detected in a high resolution electromagnetic calorimeter. We are proposing to upgrade the HYCAL detector, currently under construction for the Jefferson Lab PrimEx experiment, such that it is composed entirely of lead tungstate ( $PbWO_4$ ) modules with a total overall size of  $1.5 \times 1.5$  m<sup>2</sup>. This will consist of a  $75 \times 75$  matrix of crystals, with a central  $12 \times 12$  cm<sup>2</sup> hole ( $6 \times 6$  crystals removed) in the middle for the passage of the beams. This calorimeter will be placed at a variable distance (five to ten meters) downstream from the production targets to provide optimal acceptance for each experiment.

As is typical of all conventional tagging experiments, the beam backgrounds for the decay width measurements will be dominated by the post bremsstrahlung electrons which lose relatively little energy in the bremsstrahlung radiator and hit the tagger structure. Conventional taggers also have an additional source of background from the electron beam dump. Since in the high energy tagging system proposed here the electron beam will be dumped together with the photon beam far from the tagger, this setup should be largely free of this second type of background. Nevertheless, in this geometry a significant number of electrons will hit the shielding structure close to the beam line. The forward electromagnetic calorimeter will be centered on the beam line downstream of the

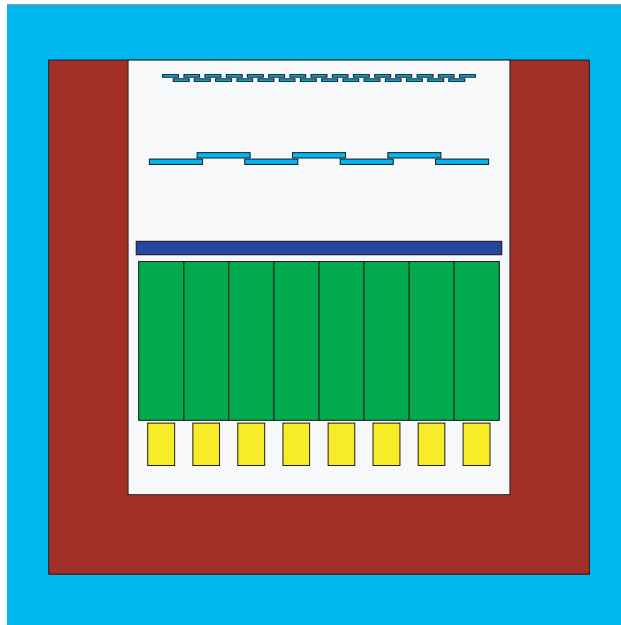


Figure 229: Focal plane detectors for the proposed high energy tagging system including two rows of segmented scintillators (top) and lead glass detectors (bottom). In the figure, the post-bremsstrahlung electrons enter from the top.

production target. As such, it will be very sensitive to the tagging setup configuration. There are two basic approaches to the geometrical design of the calorimeter. One is to remove a  $6 \times 6$  matrix of crystal modules from the center of the calorimeter for the beam to pass through. This maximizes the geometrical acceptance and simplifies its determination. The next option is to remove all the modules from several rows of the calorimeter in the dispersive plane of the electron beam (the horizontal plane for this design). Here we propose the first option, removal of a central hole in the calorimeter, for the reasons mentioned above.

To estimate the background levels and to optimize the experimental setup, we have performed a Monte Carlo simulation based on the GEANT package. The photoproduction experiments will typically run with an electron beam current of 75 nAmps, which will produce  $5 \times 10^7$  equivalent  $\gamma$ 's/sec on a  $10^{-4}$  radiation length thick gold radiator. We have simulated a total of  $10^8$  beam electrons through the setup with a 10 centimeter long liquid helium-4 target in the photon beam. This would be equivalent to approximately 200 microseconds of beam time in an experiment. The resulting distribution of background events on the calorimeter is shown in Fig. 230, projected onto the horizontal axis. The energy distribution of these events is shown in Fig. 231. Based on these simulations, the electromagnetic calorimeter will have a rate of approximately 200 kHz of particles with energy bigger than 0.5 GeV. The expected rate per detector module is 0.4 kHz on average. These numbers are quite favorable for the proposed tagging system.

A similar experimental setup will be used for the transition form factor measurements. For these experiments, the bremsstrahlung radiator will be removed and there will be no magnetic field

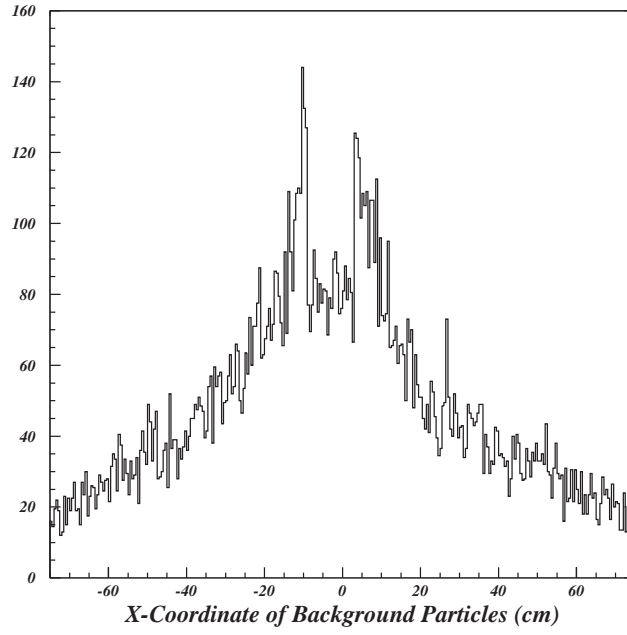


Figure 230: Background events in the calorimeter projected to the horizontal (dispersive) plane for a photon tagging (photoproduction) run.

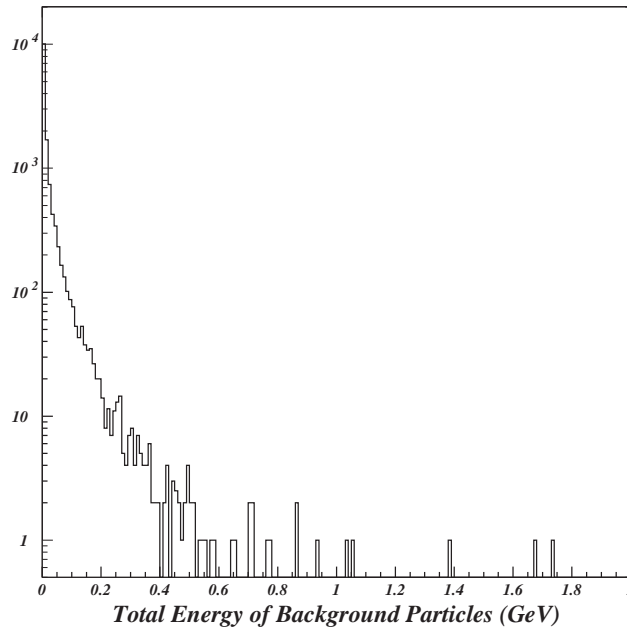


Figure 231: Energy distribution in calorimeter corresponding to the events in Fig. 230 (photon run).



in the tagger dipoles. We have simulated  $2 \times 10^7$  electrons through this setup, which is equivalent to 300 microseconds of running with an electron beam current of 100 nAmp. With a 0.5 GeV threshold, the total rate in the calorimeter is expected to be 80 MHz. The high segmentation of the calorimeter (5625  $PbWO_4$  modules) will bring this rate down to the level of 10 kHz per module, which is also quite favorable.

Photons resulting from  $\eta$  and  $\eta'$  decay, as well as scattered electrons in the transition form factor measurements will be detected in the highly segmented array of the shower calorimeter located downstream of the target. Currently, the PrimEx Collaboration is constructing a hybrid shower calorimeter for the  $\pi^0$  life time experiment in Hall B. This will be ready for commissioning in the Fall of 2003. We propose to use a somewhat larger version of this detector for these experiments. It will be  $150 \times 150 \text{ cm}^2$  in the dimensions transverse to the beam. The calorimeter is designed to measure both the position and the energy of electromagnetic showers using a two dimensional matrix of radiators ( $PbWO_4$  crystals). This will be accomplished by choosing the cross section of the individual counters to be small enough so that the energy leakage into adjacent counters can be used to determine the position of the shower axis.

The Primakoff cross section peaks at extremely small angles ( $\theta_\eta = 0.1^\circ$  at  $E_\gamma = 10 \text{ GeV}$ ) and therefore the experimental setup must have sufficient resolution for the  $\eta$  production angle in order to identify and extract the Primakoff amplitude. This resolution depends strongly on the decay photon energy and position resolutions of the calorimeter. As such, this detector will be constructed from lead tungstate crystals of size  $2 \times 2 \times 18 \text{ cm}^3$ . In our beam tests at Jefferson Lab in 2001 and 2002, crystal energy resolutions of  $\frac{\sigma_E}{E} = 1.2\%$  and position resolutions of  $\sigma_X = 1.2 \text{ mm}$  were obtained for 4 GeV electrons [Ga00], where the quoted value for position resolution is at the boundary between two lead tungstate crystal detectors. These results are consistent with those reported by the Mainz group for similar crystals operated at a stabilized temperature ( $8^\circ\text{C}$ ) where they attained:

$$\frac{\sigma_E}{E}(\%) = \frac{1.54}{\sqrt{E}} + 0.3, \quad (79)$$

with  $E$  given in  $\text{GeV}$  [Me00]. As compared to lead glass, use of these crystals will significantly improve the radiation hardness of the detector near the beam line where radiation doses can be high. Furthermore, a central  $12 \times 12 \text{ cm}^2$  hole will be left open to enable the photon beam to pass through. The modules contiguous with this region on the beam axis as well as the two outermost layers of modules will be excluded from the fiducial volume of the detector to control coordinate resolution and detection efficiency near the boundaries of the detector. To monitor and correct possible gain changes due to temperature and aging, a light monitoring system similar to that of the PrimEx experiment will be used.

In these experiments, the Primakoff amplitude will be extracted from the differential cross section measurements for forward angle meson production. As mentioned earlier, the different angular dependences will enable identification of the Primakoff amplitude from the background nuclear coherent and interference contributions. We propose to perform a high precision measurement of

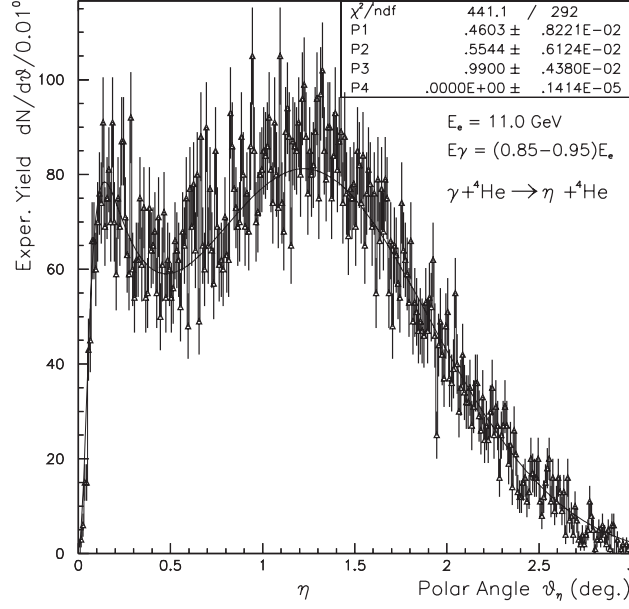


Figure 232: Monte Carlo simulation of expected yield as a function of angle for  $\eta\gamma\gamma$  events on  ${}^4\text{He}$ .

the differential cross sections on two different nuclei,  ${}^1\text{H}$  and  ${}^4\text{He}$ , over a range of angles ( $0 - 5^\circ$ ) as determined by the electromagnetic calorimeter. The  $1.5 \times 1.5\text{m}^2$  calorimeter placed at a distance of  $\sim 6\text{m}$  from the  $10\text{ cm}$  long liquid helium target will provide a high geometrical acceptance for the two decay photons, yielding detection efficiencies of about 70%. The expected experimental angular distribution from a Monte Carlo simulation of  $\eta \rightarrow \gamma\gamma$  events for a 30 day run is shown in Fig. 232. In this simulation, the experimental resolutions and all efficiencies of the setup are taken into account. The  $\eta \rightarrow \gamma\gamma$  rate for a  $10\text{ cm}$  long liquid  ${}^4\text{He}$  target and 75 nAmp electron beam incident on a  $10^{-4}$  radiation length thick gold bremsstrahlung target is  $\sim 23,300\text{events}/60\text{days}$ . Here, we have taken the upper 1 GeV energy range of the tagged photon beam only. The estimated experimental uncertainties for  $\Gamma(\eta \rightarrow \gamma\gamma)$  are listed in table 39. The total error for the  $\eta \rightarrow \gamma\gamma$  decay width has been estimated to be on the level of 3.1%, which includes 1.0% statistical error (for 60 days of beam time), and the estimated systematic errors are added in quadrature as is shown in the table.

The  $\eta' \rightarrow \gamma\gamma$  experiment has two major difficulties as compared with the  $\eta$  decay width experiment. The first and most important one is that the  $\eta' \rightarrow \gamma\gamma$  branching ratio is relatively small and poorly known. ( $2.12 \pm 0.14\%[\text{PDB}]$ ). The branching ratio directly effects the number of events in the experiment, necessitating more beam time for this measurement. The current experimental error on the branching ratio ( $\pm 6.6\%$ ) sets a lower limit on the total error of any new experiment. We expect this situation to be improved by the time we perform the  $\eta'$  measurements. If this is not the case, we plan to run a dedicated experiment with a similar setup but with an additional low momentum recoil detector. At the forward production angles, the kinetic energy of the recoiling  ${}^4\text{He}$  is in the range of 10-70 MeV, and the produced  $\eta'$ 's will be identified by recoil detection through missing mass reconstruction. At the same time, the decay photons will

Table 39: Estimation of the experimental uncertainties for  $\Gamma(\eta \rightarrow \gamma\gamma)$  measurement.

Error Source	Estimate (%)
statistical	1.0% (60 days)
photon flux	2.0%
target thickness	1.5%
acceptance, misalignment	0.5%
Physics background	0.4%
beam energy	0.2%
nuclear coherent contrib.	1.0%
distorted form factor	0.3%
branching ratio	0.8% (PDB)
Total	3.1%

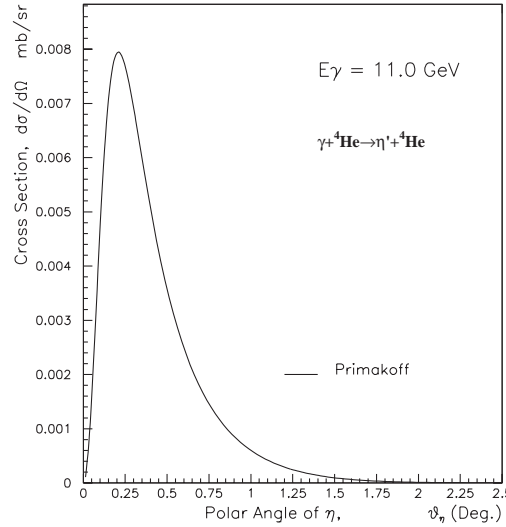


Figure 233: Coulomb photoproduction of the  $\eta'$  as a function of angle.

be detected by the downstream electromagnetic calorimeter. A preliminary conceptual design of the recoil detector includes a cylindrical multi-layer proportional chamber under  $\sim 5$  atm  ${}^4\text{He}$  gas pressure. The differential cross section at the forward angles for the  $\eta'$  meson is shown in Fig. 233. Only the Primakoff contribution is shown here, since there are no experimental data for the  $\eta'$  done with the fixed target technique. Our estimation is that with 90 days of beam time and using a 15 cm long liquid  ${}^4\text{He}$  target, we can reach a 3.0% statistical error for the  $\eta'$  decay width measurement. The systematic errors are basically the same as those for the  $\eta$  experiment shown in table 1, except for the branching ratio. Assuming that one can attain a  $\sim 3.0\%$  error in the knowledge of the branching ratio, we estimate the total error in the determination of the  $\eta' \rightarrow \gamma\gamma$  decay width to be on the level of 5%.

In summary, the proposed instrumentation to be constructed for this program, a highly seg-

mented electromagnetic calorimeter and a high energy photon tagger, will provide a new and powerful experimental window on QCD at Jefferson Lab. Furthermore, one can fully expect such instrumentation to be of general use for future high precision experiments.

## References

- [Ab84] K. Abe *et al.*, Phys. Rev. Lett., **53**:751, 1984.
- [Ab85] K. Abe *et al.*, Phys. Rev., **D32**:2288, 1985.
- [Ab96] K. Abe *et al.* Phys. Rev. Lett. **76**, 587 (1996).
- [Ab97] K. Abe *et al.* [SLAC E154], Phys. Rev. Lett. **79**, 26 (1997).
- [Ab98] A. Abele *et al.* [Crystal Barrel Collaboration], Phys. Lett. **B423**, 175, (1998).
- [Ab98a] D. Abbott *et al.*, Phys. Rev. Lett. **80**, 5072 (1998).
- [Ab98b] K. Abe *et al.* [SLAC E143], Phys. Rev. D **58**, 112003 (1998).
- [Ab99] H. Abramowicz and A. Caldwell, Rev. Mod. Phys. **71**, 1275 (1999).
- [Ab99a] K. Abe *et al.* [SLAC E155], Phys. Lett. **B463**, 339 (1999).
- [Ab00] D. Abbott *et al.*, Phys. Rev. Lett. **84**, 5053 (2000).
- [Abpc] “A-B-SIMC”, SIMC Primer, by J. Arrington, Argonne National Lab, unpublished (2001). Available from [http://www.jlab.org/~johna/SIMC\\_documents/simc.ps](http://www.jlab.org/~johna/SIMC_documents/simc.ps).
- [Ac98] K. Ackerstaff *et al.* [HERMES Collaboration], Phys. Rev. Lett. **81**, 5519 (1998).
- [Ac98a] M. Acciarri *et al.*, Phys. Lett. **B418**, 399 (1998).
- [Ac98c] P. Achenbach *et al.*, Nucl. Instr. and Meth. **A416** (1998) 357.
- [Ac99] K. Ackerstaff *et al.*, Phys. Lett. B **464**, 123 (1999).
- [Ac00] K. Ackerstaff *et al.*, hep-ex/0002016 (2000).
- [Acam] Details of the “F1” chip can be found at <http://www.acam.de>.
- [Ad93] B. Adeva *et al.*, Phys. Lett. **B302**, 533 (1993); D. Adams *et al.*, Phys. Lett. **B329**, 399 (1994); B. Adeva *et al.*, Phys. Lett. **B357**, 248 (1995).
- [Ad94] G. Adams, Workshop on CEBAF at Higher Energies, N. Isgur and P. Stoler, eds, CEBAF (1994), p. 65.
- [Ad94a] D. Adams *et al.* [SMC Collaboration], Phys. Lett. **B329**, 399 (1994).
- [Ad95] M. R. Adams *et al.* [E665 Collaboration], Phys. Rev. Lett. **74**, 1525 (1995).
- [Ad96] J. Adomeit *et al.* [Crystal Barrel Collaboration], Z. Phys. **C71**, 227 (1996).
- [Ad97] M. r. Adams *et al.* Zeit. Phys. **C74**, 237 (1997).

- [Ad98] G. S. Adams *et al.* [E852 Collaboration], Phys. Rev. Lett. **81**, 5760 (1998).
- [Ad01] C. Adloff, *et. al.* [H1 collaboration], Phys. Lett. B **517**, 47 (2001)
- [Ad02] G. Adams *et al.*, submitted to Nucl. Instr. and Meth., June (2002)
- [Af94] A. Afanasev, J. Gomez and S. Nanda, Workshop on CEBAF at Higher Energies, *op. cit.*, p. 184.
- [Af98] A. Afanasev and P. R. Page, Phys. Rev. D **57**, 6771 (1998).
- [Af99] A. Afanasev, hep-ph/9910565, “ Proceedings of the JALB-INT Workshop on Exclusive and Semi-Exclusive Processes at High Momentum Transfer”, C. Carlson and A. Radyushkin, World Scientific (200), May 1999.
- [Af00] A. Afanasev, C. E. Carlson, and C. Wahlquist, Phys. Rev. D **62**, 074011 (2000).
- [Af00a] A. Afanasev, C. E. Carlson, and C. Wahlquist, Phys. Rev. D **61**, 034014 (2000).
- [Af00b] I. R. Afnan *et al.*, Phys. Lett. B **493**, 36 (2000).
- [Af00c] A. V. Afanasev and A. P. Szczepaniak, Phys. Rev. D, **61**:114008, 2000.
- [Ah01] J. Ahrens *et al.* [The GDH and A2 Collaborations], Phys. Rev. Lett. **87**, 022003-1 (2001).
- [Ai00] A. Airapetian *et al.* Eur. Phys. J. **C17**, 389 (2000)
- [Ai01] A. Airapetian *et al.* [HERMES collaboration], Phys. Rev. Lett. **87**, 182001 (2001)
- [Ai01a] A. Airapetian *et al.*, Eur. Phys. J. **C20**(2001) 479-486. bibitem[Ai02]hermes HERMES Collaboration: A.Airapetian, *et al.*, hep-ex/0209072.
- [Ak85] S. V. Akulinichev, S.A. Kulagin and G.M. Vagradov, Phys. Lett. **B158**, 485 (1985)
- [Al76] M. J. Alguard *et al.* [SLAC E80], Phys. Rev. Lett. **37**, 1261 (1976); **41**, 70 (1978).
- [Al88] D. Alde *et al.*, Phys. Lett., **B205**:397, 1988.
- [Al90] D. M. Alde *et al.*, Phys. Rev. Lett. **64**, 2479 (1990).
- [Al98] M. Alford, K. Rajagopal and F. Wilczek, Phys. Lett. **B422**, 247 (1998).
- [Al99] L. C. Alexa *et al.*, Phys. Rev. Lett. **82**, 1374 (1999); and references therein.
- [Al00] S. I. Alekhin and A. L. Kataev, Nucl. Phys. **A666-667**, 179 (2000); and references therein.
- [Am91] P. Amaudraz *et al.*, Phys. Rev. Lett. **66**, 2712 (1991).
- [Am94] A. Amroun *et al.*, Nucl. Phys. **A579**, 596 (1994); and references therein.

- [Am95] C. Amsler and F. E. Close, Phys. Lett. **B353**, 385 (1995).
- [Am96] C. Amsler and F. E. Close, Phys. Rev. D **53**, 295 (1996).
- [Am98] M. Ambrogiani *et al.*, Nucl. Phys. B **61**, 384 (1998).
- [Am01] M. Amarian *et al.*, Nucl. Instr. and Meth. **A460** (2001) 239.
- [Am02] M. Amarian *et al.* [the JLab E94-010 Collaboration], Phys. Rev. Lett. **89**, 242301-1 (2002).
- [An71] R. L. Anderson *et al.*, Phys. Rev. **D4**, 3245 (1971).
- [An76] R. L. Anderson *et al.*, Phys. Rev. **D14**, 679 (1976); G. White *et al.*, Phys. Rev. **D49**, 58 (1994)
- [An77] R. Anderson *et al.*, SLAC-PUB-1741, *Invited talk presented at Int. Conf. on Production of Particles with New Quantum Numbers, Wisconsin U., Madison, Apr. 22-24, 1976.*
- [An77b] R. L. Anderson *et al.*, Phys. Rev. Lett. **38**, 263 (1977).
- [An93] P. L. Anthony *et al.* [SLAC E142], Phys. Rev. Lett. **71**, 959 (1993).
- [An95] V. V. Anisovich *et al.*, Phys. Lett. **B323**, 233 (1994).
- [An96] A. V. Anisovich and H. Leutwyler, Phys. Lett. B375 (1996) 335.
- [An96a] M. Anghinolfi *et al.*, Nucl. Phys. **A602**, 405 (1996).
- [An96b] M. Antonelli, *et al.*, NIM, 558, **A409**, (1996).
- [An97] L. Anthony *et al.*, Phys. Rev. **D56**, 1373 (1997).
- [An98] M. Anselmino and F. Murgia, Phys. Lett. **B442** (1998) 470.
- [An03] P. L. Anthony *et al.* [E155 Collaboration], Phys. Lett. B **553**, 18 (2003).
- [An03a] B.D. Anderson *et al.*, Basic Instrumentation for Hall A Beamline preprint.
- [Ao93] H. Aoyagi *et. al.*, Phys. Lett., **B314**, 1993.
- [Ap94] R. D. Appuhn *et al.*, Nucl. Instr. and Meth. **A350** (1994) 208.
- [Ar75] X. Artru *et al.*, Phys. Rev. D **12**, 1289 (1975).
- [Ar88] R. G. Arnold *et al.*, Phys. Rev. Lett. **61**, 806 (1988).
- [Ar97] R. Arnold and J. McCarthy, *A Proposal for Extension of E155 to Measure the Transverse Spin Structure Functions of the Proton and Deuteron* , SLAC E155x, September 1997.
- [Ar98] J. Arrington, Ph.D. thesis, California Institute of Technology, 1998.

- [Ar99] C. S. Armstrong *et al.*, Phys. Rev. D **60**, 052004 (1999).
- [Ar00] C. S. Armstrong *et al.*, submitted to Phys. Rev. D (2000).
- [As87] D. Aston *et al.*, *The LASS spectrometer*, Technical report, 1987, SLAC-Report-298.
- [As88] J. Ashman *et al.* [EMC Collaboration], Phys. Lett. **B206**, 364 (1988).
- [As89] J. Ashman *et al.* [EMC Collaboration], Nucl. Phys. **B328**, 1 (1989)
- [As89a] D. Aston *et al.*, SLAC-PUB-5145; Nucl. Phys. (Proc. Suppl.) **B8**, 32 (1989).
- [As95] D.M. Asner *et al.*, CLEO CONF95-24, EPS0188, 1995.
- [As99] D. Ashery [E791 Collaboration], Proceedings of the Int. Workshop on Physics with Electron Polarized Ion Colliders, Bloomington, 1999, p. 322.
- [At84] M. Atkinson *et al* (The Omega Collaboration) Nucl. Phys., **B231**:15, 1984.
- [At84a] M. Atkinson *et al* (The Omega Collaboration) Nucl. Phys., **B243**:1, 1984.
- [Au83] J. J. Aubert *et al.* [EMC Collaboration], *Phys. Lett.* **B123**, 275 (1983).
- [Au97] G. Audit *et al*, Nucl. Phys. **A614**, (1997) 461
- [Av00] T. Averett, Proceedings of the HiX2000 workshop, J.P. Chen and Z.E. Meziani, eds.
- [Av02] H. Avakian Proceedings of SPIN 2002.
- [Av03] H. Avakian Proceedings of X-th Workshop on High Energy Spin Physics, Dubna 2003.
- [Ba73] W. Bartel *et al.*, Nucl. Phys. **B58**, 429 (1973).
- [Ba77] Exotic hybrids were apparently first described in a bag model context by T. Barnes, Ph.D. thesis, California Institute of Technology, 1977 (unpublished).
- [Ba82] “The Role of Electromagnetic Interactions in Nuclear Science”, a report of the DOE/NSF Nuclear Science Advisory Committee (1982).
- [Ba83] G. Baum *et al.*, [SLAC E130] Phys. Rev. Lett. **51**, 1135 (1983).
- [Ba90] I. Balitsky *et al.*, Phys. Lett. **B242**, 245 (1990); **B318**, 648 (1993) (Erratum).
- [Ba93] G. S. Bali *et al.*, Phys. Lett. B **309**, 378 (1993).
- [Ba94] A. Baldit *et al.*, Phys. Lett. B **332**, 244 (1994).
- [Ba95] T. Barnes, F. E. Close, and E. S. Swanson, Phys. Rev. D **52**, 5242 (1995).
- [Ba96] B. Baumbaugh *et al.*, IEEE Trans. Nucl. Sci. **43**, 1146, (1996).



- [Ba96a] G. Bardin *et al.*, Conceptual Design Report of a Compton Polarimeter for Hall A at CEBAF, DAPNIA/CEA Report,  
<http://www.jlab.org/compton/Documentation/Technical/1996/proposal.ps>.
- [Ba97] G. Bali *et al.* [SESAM Collaboration], Nucl. Phys. Proc. Suppl. **63**, 209 (1997).
- [Ba98] G. Bali *et al.* (SESAM Collaboration) Nucl. Phys. Proc. Suppl., **63**:209, 1998.
- [Ba00] G. S. Bali *et al.* [SESAM/TCL Collaboration], Phys. Rev. D **62**, 054503 (2000).
- [Ba00] R. Baier, D. Schiff, and B. G. Zakharov, Annu. Rev. Nucl. Part. Sci. **50**, (2000) 37.
- [Ba01] S. D. Bass and A. De Roeck, Eur. Phys. J. **18**, 531 (2001).
- [Ba02] A. Bachetta *et al.*, Phys. Rev. D **65**, 94021 (2002).
- [Be67] H. A. Bethe, Ann. Rev. Nucl. Sci. **21**, 93 (1971).
- [Be69] J. S. Bell and R. Jaciw, Nuovo Cimento **60A**, 47 (1969); S. L. Adler, Phys. Rev. **177**, 2426 (1969).
- [Be70] G. Bellettini *et al.*, Il Nuovo Cimento, vol. 66, no. 1, (1970), 243.
- [Be75] C. J. Bebek *et al.*, Phys. Rev. Lett. **34**, 759 (1975); Phys. Rev. Lett. **37**, 1525 (1976); Phys. Rev. D **15**, 3085 (1977).
- [Be78] C. J. Bebek *et al.*, Phys. Rev. D **13**, 1693 (1978).
- [Be80] E. Berger, Z. Phys., **C 4**, 289 (1980).
- [Be82] B. Bengtson and M. Moszynski, Nuclear Inst. and Meth. **204**, 129, (1982).
- [Be84] E. L. Berger, F. Coester, and R. B. Wiringa, Phys. Rev. D **29**, 398 (1984).
- [Be89] D. Beck *et al.*, Nucl. Instr. Methods in Phys. Res. **A277**, 323 (1989).
- [Be91] H. J. Behrend *et al.*, Z. Phys. **C49**, 401 (1991).
- [Be93] G. M. Beladidze *et. al*, Phys. Lett., **B313**, 1993.
- [Be93a] V. Bernard, N. Kaiser, and Ulf-G. Meißner, Phys. Rev. D **48**, 3062 (1993); Int. J. Mod. Phys. **E4**, 193 (1995).
- [Be94] A. C. Benvenuti *et al.*, [BCDMS Collaboration], Z. Phys. **C 63**, 29 (1994).
- [Be95] V. M. Belyaev and A. Radyushkin, Phys. Lett. **B359**, 194 (1995).
- [Be96] O. Benhar, S. Fantoni, N. N. Nikolaev, J. Speth, A. A. Usmani and B. G. Zakharov, J. Exp. Theor. Phys. **83**, 1063 (1996);
- [Be97] C. Bernard *et al.* [MILC Collaboration], Phys. Rev. D **56**, 7039 (1997).

- [Be99] H. A. Bethe, Rev. Mod. Phys. **71**, S6 (1999).
- [Be99a] O. Benhar, V. R. Pandharipande, I. Sick, Phys. Lett. **B469**, 19 (1999).
- [Be99b] S. C. Bennett and C. E. Wieman, Phys. Rev. Lett. **82**, 2484 (1999).
- [Be00] O. Benhar, N. N. Nikolaev, J. Speth, A. A. Usmani and B. G. Zakharov, Nucl. Phys. **A673**, 241 (2000).
- [Be00a] P.Y. Bertin, C.E. Hyde-Wright, F. Sabatié (spokespersons), Experiment E-00-110.
- [Be01] A. Belitsky and D. Müller, Phys. Lett. B **153**, 349 (2001).
- [Be02] A. Belitsky and D. Müller, Nucl.Phys. **A711**, 118 (2002).
- [Be02a] A. V. Belitsky, D. Müller and A. Kirchner, Nucl. Phys. B **629**, 323 (2002) [arXiv:hep-ph/0112108]
- [Be02b] A. Belitsky and D. Müller, Nucl. Phys. A **711**, 118 (2002).
- [Be02c] D. Beck *et al.*, G0 Experiment, ([http://www.jlab.org/exp\\_prog/generated/apphallc.html](http://www.jlab.org/exp_prog/generated/apphallc.html) as viewed 26-JUN-2002)
- [Be02d] V. Bernard, T.R. Hemmert, and Ulf.-G. Meißner, hep-ph/0203167.
- [Be03] A. Belitsky, X. Ji and F. Yuan hep-ph/0208038.
- [Be03a] A. Belitsky, X. Ji, and F. Yuan, Phys.Rev.Lett. **91**, 092003 (2003).
- [Be04] A. Belitsky, X. Ji and F. Yuan, Phys. Rev. **D 69**, 074014 (2004).
- [Bepc] E. Beise, private communication
- [Bi83] A. Bialas and T. Chmaj, Phys. Lett. **133B** (1983) 241.
- [Bi88] J. Bijnens, A. Bramon and F. Cornet, Phys. Rev. Lett. **61**, 1453 (1988).
- [Bi89] R. P. Bickerstaff and A. W. Thomas, J. Phys. G **15**, 1523 (1989).
- [Bi95] A. Bianconi, S. Jeschonnek, N. N. Nikolaev, and B. G. Zakharov, Phys.Lett.**B343** (1995), 13.
- [Bi96] A. Bianconi, S. Jeschonnek, N. N. Nikolaev, and B. G. Zakharov, Nucl.Phys. **A608** (1996), 437.
- [Bi96a] A. Bianconi, S. Jeschonnek, N. N. Nikolaev, and B. G. Zakharov, Phys. Rev. C **53** (1996), 576.
- [Bi01] F. Bissey, A. W. Thomas and I. R. Afnan, Phys. Rev. C **64**, 024004 (2001); F. Bissey, V. Guzey, M. Strikman and A. W. Thomas, Phys. Rev. C **65**, 064317 (2002).

- [Bj66] J. D. Bjorken, Phys. Rev. **148**, 1467 (1966); Phys. Rev. D **1**, 465 (1970); Phys. Rev. D **1**, 1376 (1970).
- [Bl69] E. D. Bloom *et al.*, Phys. Rev. Lett. **23**, 930 (1969), and M. Briedenbach *et al.*, Phys. Rev. Lett. **23** 935 (1969)
- [Bl70] E. D. Bloom and F. J. Gilman, Phys. Rev. Lett. **25**, 1140 (1970); Phys. Rev. D **4**, 2901 (1971).
- [Bl97] G. R. Blackett *et al.* The Photoproduction of the  $b_1(1235)\pi$  System, Technical report, August 1997. hep-ex/9708032.
- [BNL00] A. Leksanov *et al.* [E850 Collaboration], Proc. of 7th. Conf. CIPANP2000, Quebec, p. 306.
- [BNL98] Y. Mardor *et al.*, Phys. Rev. Lett. **81**, 5085 (1998).
- [Bo81] A. Bodek and J. L. Ritchie, Phys. Rev. D **23**, 1070 (1981).
- [Bo83] A. Bodek *et al.*, Phys. Rev. Lett. **50**, 1431 (1983).
- [Bo94] G. D. Bosveld, A. E. L. Dieperink and A. G. Tenner, Phys. Rev. C **49**, 2379 (1994).
- [Bo94a] P. Bosted, *et al.*, “DIS-Parity: Parity Violation in Deep Inelastic Electron Scattering”, SLAC-PROPOSAL-E-149 (1993) (unpublished).
- [Bo98] C. Bochna *et al.* [E89-012 Collaboration], Phys. Rev. Lett. **81**, 4576 (1998)
- [Bo00] P. Bosted, “Spin Structure Functions of the Nucleon Measured at SLAC”, *Circum-Pan-Pacific RIKEN Symposium on High Energy Spin Physics* (Wako, Japan, November 1999), RIKEN Review 28 (May, 2000) (No. 13); P. Bosted, private communication.
- [Bo03] “DIS-Parity: Search for New Physics through Parity Violation in Deep Inelastic Electron Scattering”, SLAC Letter of Intent (2003) (unpublished)
- [Br70] M. Branschweig, *et al.*, DESY preprint, 70/1.
- [Br73] S. J. Brodsky and G. R. Farrar, Phys. Rev. Lett. **31**, 1153 (1973); V. A. Matveev, R. M. Muradyan and A. N. Tavkhelidze, Lett. Nuovo Cimento **7**, 719 (1973).
- [Br74] A. Browman *et al.*, Phys. Rev. Letts., vol. 33, no. 23,(1974)1400
- [Br79] E. L. Berger and S. J. Brodsky, Phys. Rev. Lett. **42** (1979) 940.
- [Br79] S. J. Brodsky, C. E. Carlson, and H. Lipkin, Phys. Rev. D **20**, 2278 (1979).
- [Br79a] S. J. Brodsky and G. P. Lepage, Phys. Lett. **B87**, 359 (1979).
- [Br80] S. J. Brodsky and G. P. Lepage, Phys. Rev. D **22**, 2157 (1980).

- [Br80a] K. L. Brown, “TRANSPORT, A computer program for designing charged particle beam transport systems”, CERN 80-04, Geneva, 1980.
- [Br82] S. J. Brodsky, in *Proceedings of the Thirteenth Int’l Symposium on Multiparticle Dynamics*, ed. W. Kittel, W. Metzger and A. Stergiou (World Scientific, Singapore, 1982) 963.
- [Br83] S. J. Brodsky, C. Ji and G. P. Lepage, Phys. Rev. Lett. **51** (1983) 83.
- [Br83a] Brodsky S J and Hiller J R 1983 *Phys. Rev. C* **28** 475 ; 1984 *Phys. Rev. C* **30** 412(E) .
- [Br88] S. J. Brodsky, and G. F. de Teramond, Phys. Rev. Lett. **60**, 1924 (1988).
- [Br88a] S.J. Brodsky and A.H. Mueller, Phys. Lett. **B 206**, 685 (1988).
- [Br90] S. J. Brodsky, G. F. de Teramond and I. A. Schmidt, Phys. Rev. Lett. **64** (1990) 1924.
- [Br92] S. J. Brodsky *et al.*, Nucl. Phys. **B369** (1992) 519.
- [Br97] S. J. Brodsky and G. A. Miller, Phys. Lett. **B412**, 125 (1997).
- [Br99] S. J. Brodsky, M. Diehl, P. Hoyer, and S. Peigne, Phys. Lett. **B449**, 306 (1999); A. Afanasev, C. E. Carlson, and C. Wahlquist, Phys. Rev. D **58**, 054007 (1998) and Phys. Lett. **B398**, 393 (1997); C. E. Carlson and A. B. Wakely, Phys. Rev. D **48**, 2000 (1993).
- [Br99a] G.Braun *et al.* “F1 - An Eight Channel Time-to-Digital Converter Chip for High Rate Experiments”, hep-ex/9911009.
- [Br00] V. M. Braun, A. Khodjamirian, M. Maul, Phys. Rev. D **61**, 073004 (2000).
- [Br00a] V. M. Braun, A. Khodjamirian, M. Maul, Phys. Rev. D **61**, 073004 (2000).
- [Br00b] S. J. Brodsky, “Dynamical higher-twist and high x phenomena: A window to quark quark correlations in QCD”, hep-ph/0006310 (2000).
- [Br01] S. J. Brodsky, E. Chudakov, P. Hoyer and J.-M. Laget, Phys. Lett. **B498**, 23 (2001).
- [Br02] S. Brodsky *et al.*, Phys.Lett. B **530**, 99 (2002).
- [Br02a] S. Brodsky et.al, hep-ph/0206259.
- [Br03] S. Brodsky et al., hep-ph/0104291
- [Bu98] V. Burkert, “Physics with CLAS at Energies up to 12GeV”, in *Physics & Instrumentation with 6-12 GeV Beams*, a Thomas Jefferson National Accelerator Facility report, S. Dytman, H. Fenker and P. Roos, eds., June 1998, p. 407.
- [Bu98a] V. Burkert, “Electromagnetic Calorimeter Upgrade Possibilities for CLAS”, in *Physics & Instrumentation with 6-12 GeV Beams* (ibid.) p. 425.

- [Bu00] M. Burkardt, Phys. Rev. D **62**, 071503 (2000).
- [Bu01] V. Burkert, L. Elouadrhiri, M. Garcon, S. Stepanyan (spokespersons), Experiment E-01-113.
- [Bu02] M. Burkardt, Nucl. Phys. **A711**, 127 (2002).
- [Bu03] For a recent overview see: V. Burkert, hep-ph/0207149
- [Bu03a] M. Burkardt, hep-ph/02091179.
- [Ca75] U. Camerini *et al.*, Phys. Rev. Lett. **35** 483 (1975).
- [Ca75a] R. Carlitz, Phys. Lett. **B58**, 345 (1975).
- [Ca78] R. Cahn, Phys.Lett., **B78**, 269 (1978); Phys.Rev., **D 40**, 3107 (1989).
- [Ca78a] R. N. Cahn and F. J. Gilman, Phys. Rev. **D17**, 1313 (1978).
- [Ca83] C. E. Carlson and T. J. Havens, Phys. Rev. Lett. **51**, 261 (1983).
- [Ca85] P. Castorina and P. J. Mulders, Phys. Rev. **D31**, 2760 (1985).
- [Ca88] A. S. Carroll *et al.*, Phys. Rev. Lett. **61**,1698 (1988).
- [Ca90] C. E. Carlson and N. C. Mukhopadhyay, Phys. Rev. D **41**, 2343 (1990).
- [Ca91] C. E. Carlson, K. E. Lassila, and U. P. Sukhatme, Phys. Lett. **B263**, 377 (1991).
- [Ca91a] C. E. Carlson and N. C. Mukhopadhyay, Phys. Rev. Lett. **67**, 3745 (1991).
- [Ca92] C. E. Carlson, M. Chachkhunashvili, and F. Myhrer, Phys. Rev. D **46**, 2891 (1992).
- [Ca95] C. E. Carlson and K. E. Lassila, Phys. Rev. C **51**, 364 (1995).
- [Ca95a] C. E. Carlson and N. Mukhopadhyay, Phys. Rev. Lett. **74**, 1288 (1995).
- [Ca97] C. E. Carlson, J. R. Hiller, R. J. Holt, Ann. Rev. Nucl. and Part. Sci. **47**, 395 (1997); and references therein.
- [Ca97a] R. Carr, *et al.*, “A Precision measurement of the weak mixing angle in Moller scattering”, SLAC-PROPOSAL-E-158 (1997) (unpublished).
- [Ca98] J. Carlson and R. Schiavilla, Rev. Mod. Phys. **70**, 743 (1998); and references therein.
- [Ca00] D. Cassel, F. Close, J. Domingo, W. Dunwoodie, D. Geesaman, D. Hitlin, M. Olson and G. Young, *Review of the Jefferson Laboratory “Hall D Project”*, January 2000, ([http://www.phys.cmu.edu/halld/halld\\_notes/Note\\_024/](http://www.phys.cmu.edu/halld/halld_notes/Note_024/)).
- [Ca00a] G. W. Carter and D. Diakonov, Nucl. Phys. B **582**, 571 (2000).

- [Ca00b] S. Catani *et al.*, hep-ph/0005025.
- [Ca01] R. Carlini, *et al.*, “The  $Q_{\text{weak}}$  Experiment: A Search for New Physics at the TeV Scale via a Measurement of the Proton’s Weak Charge”, JLab Proposal (2001) (unpublished).
- [Ca02] Jefferson Lab Experiment E02-013, G. Cates, K. McCormick, B. Reitz and B. Wojtsekhowski, spokepersons.
- [Ch77] V. L. Chernyak and A. R. Zhitnitsky, JETP Lett. **25**, 510 (1977); V. L. Chernyak, A. R. Zhitnitsky and V. G. Serbo, JETP Lett. **26**, 594 (1977).
- [Ch77a] V. L. Chernyak and A. R. Zhitnitsky, JETP Lett. **25**, 510 (1977).
- [Ch78] B. T. Chertok, Phys. Rev. Lett. **40**, 1429 (1978); S. J. Brodsky and B. T. Chertok, Phys. Rev. **D14**, 3003 (1976).
- [Ch96] E. Chen, M. Saulnier, W. Sun, and H. Yamamoto, *Tests of a high resolution time-of-flight system based on long and narrow scintillator*, hep-ex/9606007, (1996).
- [Ch99] E. Christova and E. Leader, Phys. Lett. **B468**, 299 (1999).
- [Ch01] E. Chudakov *et al.*, Letter of Intent for CEBAF12, JLab technical note: JLAB-TN-01-007, January 2001.
- [Chpc] E. Chudakov, private communication
- [Ci89] C. Ciofi degli Atti and S. Liuti, Phys. Lett. **B225**, 215 (1989).
- [Ci90] C. Ciofi degli Atti and S. Liuti, Phys. Rev. C **41**, 1100 (1990).
- [Ci93] C. Ciofi degli Atti and S. Simula, Phys. Lett. B **319**, 23 (1993); Few-Body Systems **18**, 55 (1995); S. Simula, Phys. Lett. B **387**, 245 (1996); Few-Body Systems Suppl. **9**, 466 (1995).
- [Ci93a] C. Ciofi degli Atti, S. Scopetta, E. Pace and G. Salme, Phys. Rev. C **48**, 968 (1993).
- [Ci02] C. Ciofi degli Atti and B. Z. Kopeliovich, Eur. J.Phys. J. A **17**, 133 (2003); B. Z. Kopeliovich, J. Nemchik and E. Predazzi, in *Proceedings of the ELFE Summer School on Confinement Physics*, eds. S. D. Bass and P. A. M. Guichon, Editions Frontieres, 1995, p. 391, Gif-sur-Yvette, hep-ph/9511214.
- [Cl73] F. E. Close, Phys. Lett. **B43**, 422 (1973); Nucl. Phys. **B80**, 269 (1974).
- [Cl79] F. E. Close, *An Introduction to Quarks and Partons* (Academic Press, 1979).
- [Cl83] F. E. Close, R. G. Roberts, and G. G. Ross, Phys. Lett. **B129**, 346 (1983).
- [Cl88] F. E. Close and A. W. Thomas, Phys. Lett. **B212**, 227 (1988).

- [Cl95] F. E. Close and P. Page, Nucl. Phys. **B443**, 233 (1995).
- [Cl95a] F. E. Close, private communication, advocates using the *positive* term “strong QCD” instead of the negative “nonperturbative QCD”.
- [Cl00] F. E. Close and A. Kirk, Phys. Lett. B **483**, 345 (2000).
- [Cl00a] Proposal for CLAS Upgrade at High Energies.
- [Cl01] F. E. Close and A. Kirk, Eur. Phys. J., **C21**:531–543, 2001.
- [Cl01a] F. E. Close and N. Isgur, Phys. Lett. B **509**, 81 (2001).
- [CLAS03] CLAS Collaboration (H. Avakian et al.) hep-ex/0301005.
- [Co86] G.R. Court *et al.*, Phys. Rev. Lett. **57**, 507 (1986), T.S. Bhatia *et al.*, Phys. Rev. Lett. **49**, 1135 (1982), E.A. Crosbie *et al.*, Phys. Rev. D **23**, 600 (1981).
- [Co89] J. S. Conway *et al.*, Phys. Rev. D **39**, 92 (1989).
- [Co93] J. Collins, Nucl.Phys.B396, 161 (1993)
- [Co93a] G. T. Condo, T. Handler, W. M. Bugg, G. R. Blackett, M. Pisharody and K. A. Danyo, Phys. Rev., D**48**:3045, 1993.
- [CO96] COMPASS Collaboration, “Common Muon and Proton Apparatus for Structure and Spectroscopy” CERN/SPSLC 96-14.
- [Co97] J. C. Collins, L. Frankfurt, and M. Strikman, Phys. Rev. D **56**, 2982 (1997).
- [Co98] C. Coriano, H-N. Li, and C. Savkli, J. High En. Phys. 9807, 008 (1998).
- [Co99] COMPASS experiment at CERN: <http://wwwcompass.cern.ch>.
- [Co02] J. Collins, hep-ph/0204004 (2002)
- [CODA] JLab Data Acquisition Group, CODA, (<http://coda.jlab.org>)
- [COSY] M. Berz, COSY INFINITY Version 7 Reference Manual, MSUCL-977 (1996), Michigan State University, East Lansing, MI 48824
- [Cr75] J. W. Cronin et al., Phys. Rev. D**11**, 3105 (1975).
- [Cr78] D. G. Crabb *et al.*, Phys. Rev. Lett. **41**, 1257 (1978).
- [Cr97] J. A. Crittenden [ZEUS Collaboration], presented at Photon '97, May 1997.
- [Cr98] R. R. Crittenden *et al.*, Nuclear Inst. and Meth. **387**, 377 (1998).
- [Cz96] A. Czarnecki and W. Marciano, Phys. Rev. **D53**, 1066 (1996).

- [Da73] M. Davier *et al.*, Nucl. Phys., **B58**:31, 1973.
- [Da93] Jefferson Lab Experiment E93-026, D. Day, G. Warren and M. Zeier, spokespersons.
- [Da94] S. Dasu *et al.*, Phys. Rev. D **49**, 5641 (1994).
- [Da01] S. Davidson, S. Forte, P. Gambino, N. Rius, and A. Strumia, JHEP **02**, 37 (2002).
- [De79] E. Derman and W. J. Marciano, Ann. Phys. **121**, 147 (1979).
- [De00] D. Debruyne, J. Ryckebusch, W. Van Nespen, and S. Janssen, *Phys. Rev. C* **62**, 024611 (2000).
- [De01] W. Detmold, W. Melnitchouk, J. W. Negele, D. B. Renner and A. W. Thomas, Phys. Rev. Lett. **87**, 172001 (2001).
- [De02] W. Detmold, W. Melnitchouk and A. W. Thomas, Phys. Rev. D **66**, 054501 (2002), and references therein.
- [Di88] M. Diemoz *et al.*, Z. Phys. **C39**, 21 (1988).
- [Di89] H. Dijk and B. L. G. Bakker, Nucl. Phys. **A494**, 438 (1989); Z.-J. Cao and L. Kisslinger, Phys. Rev. C **41**, 647 (1990), and references therein.
- [Di97] D. Diakonov, V. Yu. Petrov, P. V. Pobylitsa, M. V. Polyakov and C. Weiss, Phys. Rev. D **56**, 4069 (1997).
- [Di99] M. Diehl, T. Feldmann, R. Jakob and P. Kroll, Eur. Phys. J. C **8** 409 (1999). M. Diehl, T. Feldmann, R. Jakob and P. Kroll, Phys. Lett. B **460**, 204, (1999).
- [Di02] M. Diehl, Eur. Phys. J. C **25**, 223 (2002)
- [Di02a] M. Diehl, hep-ph/0205208.
- [Do77] J. F. Donoghue and E. Golowich, Phys. Rev. D **15**, 3421 (1977).
- [Do92] J. F. Donoghue, E. Golowich, and B. R. Holstein, Dynamics of the Standard Model, Cambridge University Press (1992).
- [Do97] J. F. Donoghue and E. S. Na, Phys. Rev. D **56**, 7073 (1997).
- [Do02] A. G. Korotkov and W. D. Nowak, Nucl. Phys. A **711**, 175 (2002)
- [Dr66] S. D. Drell, and A. C. Hearn, Phys. Rev. Lett. **16**, 908 (1966).
- [Dr99] D. Drechsel, O. Hanstein, S. S. Kamalov and L. Tiator, Nucl. Phys. A **645**, 145 (1999).
- [Dr00] See, for example, D. Drechsel, S. S. Kamalov, and L. Tiator, Phys. Rev. D **63**, 114010 (2001).



- [Du85] G. V. Dunne and A. W. Thomas, Nucl. Phys. **A446**, 437c (1985).
- [Du91] M. Dueren and K. Rith, *Polarized Electron Nucleon Scattering at HERA: The HERMES Experiment*, in “Hamburg 1991, Proceedings, Physics at HERA, vol. 1” 427-445.
- [E01004] JLab experiment E01-004: The Charged Pion Form Factor, extension to E93-021.
- [E02104] “Quark Propagation through Cold QCD Matter,” W. Brooks, spokesperson. Jefferson Lab proposal E02-104, (2002).
- [E89044] JLab experiment e89-044, preliminary results (Contact: A. Saha).
- [Ef80] A. V. Efremov and A. V. Radyushkin, Theor. Math. Phys. **42**, 97 (1980).
- [Ef01] A. Efremov K. Goeke, P. Schweitzer Phys. Lett. **B552**, 37 (2001).
- [Eg94] K. S. Egiyan, L. L. Frankfurt, W. R. Greenberg, G. A. Miller, M. M. Sargsyan, M. I. Strikman, Nucl. Phys. **A580**, 365 (1994).
- [Eh95] B. Ehrensperger and A. Schafer, Phys. Rev. D **52**, 2709 (1995).
- [Ei72] Y. Eisenberg *et al.*, Phys. Rev., **D5**:15, 1972.
- [Ei84] E. Eichten, I. Hinchliffe, K. Lane and C. Quigg, Rev. Mod. Phys. **56**, 579 (1984).
- [Ei99] M. Eides, L. Frankfurt, and M. Strikman, Phys. Rev. D **59**, 114025 (1999).
- [El74] J. Ellis and R. L. Jaffe, Phys. Rev. D **9**, 1444 (1974); Phys. Rev. D **10**, 1669 (1974).
- [En64] C.A. Engelbercht, Phys., Rev., 133, B988 (1964).
- [En00] R. Ent, C. E. Keppel, and I. Niculescu, Phys. Rev. D. **62**, 73008 (2000).
- [En00a] R. Ent, H. Mkrtchyan, and G. Niculescu, JLAB Proposal E00-004 (2000).
- [Er83] M. Erikson and A. W. Thomas, Phys. Lett. **B128**, 112 (1983).
- [Erpc] J. Erler, private communication.
- [Fa75] G. R. Farrar and D. R. Jackson, Phys. Rev. Lett. **35**, 1416 (1975).
- [Fa79] G. R. Farrar and D. R. Jackson, Phys. Rev. Lett. **43**, 246 (1979); and D. R. Jackson, Thesis, CALTECH, 1977 (unpublished);
- [Fa81] C. Fabjan *et al.*, Nucl. Instrum. Meth. **185** (1981) 119.
- [Fa84] S. Fajfer and R. J. Oakes, Phys. Rev. **D30**, 1585 (1984).
- [Fa85] C. Fabjan, Techniques and Concepts in High Energy Physics III, T. Ferbel, ed, Plenum Pub.(1985).

- [Fa88] G. R. Farrar, H. Liu, L. L. Frankfurt and M. I. Strikman, Phys. Rev. Lett. **61**, 686 (1988).
- [Fe72] R. P. Feynman, *Photon Hadron Interactions* (Benjamin, Reading, Massachusetts, 1972).
- [Fi77] R. D. Field and R. P. Feynman, Phys. Rev. D **15**, 2590 (1977).
- [Fi01] B. Filippone and X. Ji, Adv. Nucl. Phys. **26**, 1 (2001).
- [Fo96] J. L. Forest, V. R. Pandharipande, S. C. Pieper, R. B. Wiringa, and R. Schiavilla, Phys. Rev. C **54**, 646 (1996).
- [Fr81] L. L. Frankfurt and M. I. Strikman, Phys. Rep. **76**, 215 (1981).
- [Fr83] B. L. Friman, V. R. Pandharipande, and R. B. Wiringa, Phys. Rev. Lett. **51**, 763 (1983).
- [Fr85] L. L. Frankfurt and M. I. Strikman, Nucl. Phys. **B250**, 1585 (1985).
- [Fr88] L. L. Frankfurt and M. I. Strikman, Phys. Rep. **160**, 235 (1988).
- [Fr90] J. L. Friar *et al.*, Phys. Rev. C **42**, 2310 (1990).
- [Fr91] L. L. Frankfurt and M. Strickman, Prog. Part. Nucl. Phys. **27**, 135 (1991).
- [Fr92] L. L. Frankfurt, G. A. Miller and M. I. Strikman, Phys. Rev. Lett. **68**, 17 (1992).
- [Fr92a] L. L. Frankfurt, G. A. Miller, and M. I. Strikman, Comm. Nucl. Part. Phys. **21**, 1 (1992).
- [Fr93] L. L. Frankfurt, G. A. Miller and M. Strikman, Phys. Lett. **B304**, 1 (1993).
- [Fr93a] L. L. Frankfurt, D. B. Day, M. M. Sargsian and M. I. Strikman, Phys. Rev. C **48**, 2451 (1993).
- [Fr94] L. L. Frankfurt *et al.*, in Workshop on ‘CEBAF at Higher Energies’, Eds. N. Isgur and P. Stoler, Conf. Proc. p. 499 (1994).
- [Fr94a] B. Frois and P. J. Mulders, Workshop on CEBAF at Higher Energies, Thomas Jefferson National Accelerator Facility, Eds. N. Isgur, P. Stoler, p. 309 (1994).
- [Fr95] L. L. Frankfurt, E. J. Moniz, M. M. Sargsyan, M. I. Strikman, Phys. Rev. C **51**, 3435 (1995).
- [Fr95b] L. L. Frankfurt, W. R. Greenberg, G. A. Miller, M. M. Sargsian and M. I. Strikman, Z. Phys. **A352**, 97 (1995).
- [Fr96] M. R. Frank, B. K. Jennings and G. A. Miller, Phys. Rev. C **54**, 920 (1996); B. K. Jennings and G. A. Miller, Phys. Lett. **B318**, 7 (1993).
- [Fr97] L. L. Frankfurt, M. M. Sargsian and M. I. Strikman, Phys. Rev. C **56**, 1124 (1997).

- [Fr98] L. Frankfurt, G. Piller, M. Sargsian, and M. Strikman, Eur. Phys. J. **A2**, 301 (1998).
- [Fr98a] V. V. Frolov *et al.*, Phys. Rev. Lett. **82**, 45 (1998).
- [Fr99] L. Frankfurt *et al.*, Phys. Rev. **D60** 014010, (1999).
- [Fr99a] L. L. Frankfurt, V. Polyakov, M. Strikman and M. Vanderhaeghen, Phys. Rev. Lett. **84**, 2589 (2000).
- [Fr00] L. L. Frankfurt, G. A. Miller, M. M. Sargsian, and M. I. Strikman, Phys. Rev. Lett. **84**, 3045 (2000); and L. L. Frankfurt, G. A. Miller, M. M. Sargsian, and M. I. Strikman, Nucl. Phys. A **663**, 349 (2000); and Sargsian M M private communication.
- [Fr00a] L. Frankfurt, M. Poliakov, M. Strikman and, M. Vanderhaeghen, Phys. Rev. Lett., **84** 2589 (2000).
- [Fr01] A. Freund, M. McDermott, and M. Strikman, arXiv:hep-ph/0208160
- [Fr03] A. Freund, M. McDermott, and M. Strikman, arXiv:hep-ph/0208160
- [Ga71] S. Galster, H. Klein, J. Moritz, K.H. Schmidt, D. Wegener, Nucl. Phys. **B32**, 221 (1971).
- [Ga84] Rob Veenhof, *The GARFIELD Program, Simulation of Gaseous Detectors*, CERN, (1984),
- [Ga92] G. Garino *et al.*, Phys. Rev. C **45**, 780 (1992).
- [Ga96] H. Gao, R. J. Holt and V. R. Pandharipande, Phys. Rev. C. **54**, 2779 (1996), D. Dutta, H. Gao, private communication
- [Ga99] M. Garcon, M. Guidal, E. Smith (spokespersons), Experiment E-99-105
- [Ga00] A. Gasparian, Proceeding of the 10th international conference on the calorimeter, Pasadana, 2002.
- [Ga01] G. T. Garvey and J.-C. Peng, Prog. Part. Nucl. Phys. **47**, 203 (2001).
- [Ga02] K. Garrow *et al.*, Phys. Rev. C **66**, 044613 (2002).
- [Ge66] S. B. Gerasimov, Sov. J. of Nucl. Phys. **2**, 430 (1966).
- [Ge78] H. Georgi and H.D. Politzer, Phys.Rev.Lett., **40**, 3 (1978).
- [Ge92] C. Gerschel and J. Hufner, Z. Phys. **C56** (1992) 171.
- [Ge93] P. Geiger and N. Isgur, Phys. Rev. D **47**, 5050 (1993); D **44**, 799 (1991).
- [Ge95] D. F. Geesaman, K. Saito and A. W. Thomas, Ann. Rev. Nucl. and Part. Sci. **45**, 337 (1995).

- [Gi46] V. L. Ginzburg and I. M. Frank, JETP **16**, 15 (1946).
- [Gi75] B. Gittelman *et al.*, Phys. Rev. Lett. **35**, 1616 (1975).
- [Gi00] R. Gilman, Proceedings of the HiX2000 workshop, J.P. Chen and Z.E. Meziani, eds (ibid); P. Mulders, ibid; H. Gao, private communication
- [Gl97] W. Glöckle, proceedings of the “5<sup>th</sup> Workshop on Electromagnetically Induced Two-Hadron Emission”, Lund, Sweden, 2001.
- [Gl98] M. Glück, E. Reya, and A. Vogt, Eur. Phys. J. **C5**, 461 (1998).
- [Gl00] M. Gluck and E. Reya, Mod. Phys. Lett. A **15**, 883 (2000).
- [Go69] K. Gottfried and D. R. Yennie, Phys. Rev. **182** (1969) 1595.
- [Go94] J. Gomez *et al.*, Phys. Rev. D **49**, 4348 (1994).
- [Go01] K. Goeke, V. Polyakov and M. Vanderhaeghen, Prog. Part. Nucl. Phys. **47**, 401 (2001).
- [Go01a] M. Göckeler *at al.*, Phys. Rev. D **63**, 074506 (2001).
- [Go01b] K. Goeke, M. V. Polyakov, and M. Vanderhaeghen, Prog. Part. Nucl. Phys. **47**, 401 (2001).
- [Go02] J. L. Goity, A. M. Bernstein and B. R. Holstein, Phys. Rev. D **66** (2002) 076014.
- [Gr75] L. V. Gribov and L. Lipatov, Yad. Fiz. **20**, 181 (1975); G. Altarelli and G. Parisi, Nucl. Phys. **B126**, 298 (1977); Dokshitzer, Sov. Phys. JETP **46**, 641 (1977).
- [Gr94] W. R. Greenberg and G. A. Miller, Phys. Rev. C **49**, 2747 (1994).
- [Gr97] J. Gronberg *et al.* [CLEO Collaboration], Phys. Rev. D **57**, 33 (1998).
- [Gr98] J. Gronberg *et al.* [CLEO Collaboration], Phys. Rev. D **57**, 33 (1998).
- [Gr01] V. Yu. Grishina *et al.*, Euro. Journal of Phys. A **10**, 355 (2001).
- [Gu00] X. Guo, J.-W. Qiu, Phys. Rev. D **61**, 096003 (2000).
- [Gupc] M. Guidal “*Computer Code for DVCS and BH calculations*”, private communication.
- [GX02] The GLUEX Collaboration *The Gluonic Excitations experiment*, Design Report Version 4, September 2002, ([http://www.phys.cmu.edu/halld/cdr\\_v4/](http://www.phys.cmu.edu/halld/cdr_v4/)).
- [Ha89] E. Hadjimichael and S. Fallieros, Phys. Rev. C, vol. 39, no. 4(1989) 1438.
- [Ha98] E. A. Hawker *et al.*, Phys. Rev. Lett. **80**, 3715 (1998); R. S. Towell *et al.*, Phys. Rev. D **64**, 052002 (2001).
- [Ha01] R. Hasty, *et al.*, Science **290**, 2117 (2000).

- [HallA] Hall A Operational Manual (2000).
- [HallD] Hall D PCDR.
- [HD99] The Hall D Collaboration, *Photoproduction of Unusual Mesons: The Hall D Project at Jefferson Lab*, Design Report version 2, August 1999,  
(<http://www.phys.cmu.edu/halld/cdr/>).
- [He90] D. W. Hertzog *et al.*, Nucl. Inst. and Meth., **A294**, 446 (1990).
- [He97] P. Herrera-Siklody, J. I. Latorre, P. Pascual and J. Taron, Nucl. Phys. **B497** (1997) 345,  
and Phys. Lett. **B419** (1998) 326.
- [Hi98] D.W. Higinbotham, Nucl. Instrum. Meth. A **414** (1998) 332-339.  
( <http://www.jlab.org/~doug/cherenkov>)
- [Ho55] R. Hofstadter and R. W. McAllister, Phys. Rev. **98**, 183 (1955).
- [Ho97] P. Hoyer, Nucl. Phys. **A622**, 284c (1997).
- [Ho98] E.P. Venugopal and B.R. Holstein, Phys. Rev D **57** (1998) 4397.
- [Ho99] P. Hoodbhoy, X. Ji, and W. Lu, Phys. Rev. D **59**, 014013 (1999); **59**, 074010 (1999).
- [Hu90] E. Hummel and J. A. Tjon, Phys. Rev. Lett. **63**, 1788 (1989); Phys. Rev. C **42**, 423 (1990); J. W. Van Orden, N. Devine and F. Gross, Phys. Rev. Lett. **75**, 4369 (1995); D. R. Phillips, S. J. Wallace and N. K. Devine, Phys. Rev. C **58**, 2261 (1998); F. M. Lev, E. Pace and G. Salme, Phys. Rev. C **62**, 064004 (2000).
- [Hu98] J. Hufner and B. Kopelovich, Phys. Lett. **B426**, 154 (1998).
- [Hu00] H. W. Huang and P. Kroll, Eur. Phys. J. **C17**, 433 (2000); P. Kroll, hep-ph/0207118 (2002).
- [Hu03] H.W. Huang *et al.*, hep-ph/0309071.
- [In84] T. Inagaki *et al.*, Cryogenics **24**, 83 (1984).
- [Is81] N. Isgur, G. Karl, and D. W. L. Sprung, Phys. Rev. D **23**, 163 (1981).
- [Is84] N. Isgur and C. H. Llewellyn Smith, Phys. Rev. Lett. **52**, 1080 (1984); Phys. Lett. **B217**, 535 (1989); G. R. Farrar, K. Huleihel and H. Zhang, Phys. Rev. Lett. **74**, 650 (1995).
- [Is85] N. Isgur, and J. Paton, Phys. Rev. D **31**, 2910 (1985); N. Isgur, R. Kokoski and J. Paton, Phys. Rev. Lett. **54**, 869 (1985).
- [Is85a] N. Isgur, R. Kokoski, and J. Paton, Phys. Rev. Lett., **54**:869, 1985.
- [Is91] N. Isgur and M. B. Wise, Phys. Rev. D **43**, 819 (1991).

- [Is99] N. Isgur, Phys. Rev. D **59**, 034013 (1999).
- [Is99b] N. Isgur, Phys. Rev. D **60**, 114016 (1999).
- [Is01] N. Isgur, S. Jeschonnek, W. Melnitchouk, and J. W. Van Orden, Phys. Rev. D **64**, 054005 (2001); F. E. Close and N. Isgur, Phys. Lett. **B 509**, 81 (2001); S. Jeschonnek and J. W. Van Orden, Phys. Rev. D **65**, 094038 (2002); F. E. Close and Q. Zhao, Phys. Rev. D **66**, 054001 (2002).
- [It92] H. Ito, W. W. Buck, and F. Gross, Phys. Lett. **287B**, 23 (1992).
- [It97] H. Ito, S. E. Koonin and R. Seki, *Phys. Rev. C* **56**, 3231 (1997).
- [IUpc] Indiana University test results at <http://dustbunny.physics.indiana.edu/~paul/hallDrd>.
- [Iv01] E.I. Ivanov *et al.* (E852 Collaboration) Phys. Rev. Lett., **86**:3977, 2001.
- [Ja84] R. L. Jaffe, F. E. Close, R. G. Roberts, and G. G. Ross, Phys. Lett. **B134**, 449 (1984).
- [Ja90] O. C. Jacob and L. S. Kisslinger, Phys. Lett. **243B**, 323 (1990).
- [Ja90] O. C. Jacob and L. S. Kisslinger, Phys. Lett. **243B**, 323 (1990).
- [Ja92] R.L. Jaffe and X. Ji Nucl.Phys. **B375** (1992) 527.
- [Ja93] R. Jakob and P. Kroll, Phys. Lett. **315B**, 463 (1993).
- [Ja02] P. Jain, B. Kundu, and J. Ralston, Phys. Rev. D **65**, 094027 (2002).
- [Je99] S. Jeschonnek and T. W. Donnelly, Phys. Rev. C **59** (1999), 2676.
- [Je00] S. Jeschonnek, N. Isgur, W. Melnitchouk, and J. W. Van Orden, to be submitted to Phys. Rev.
- [Ji94] X. Ji and P. Unrau, Phys. Lett. **B333**, 228 (1994).
- [Ji95] X. Ji, e-print hep-ph/9509288 (1995)
- [Ji95a] X. Ji and P. Unrau, Phys. Rev. D **52**, 72 (1995).
- [Ji97] X. Ji, Phys. Rev. Lett. **78**, 610 (1997); Phys. Rev. D **55**, 7114 (1997).
- [Ji97a] X. Ji, W. Melnitchouk, and X. Song, Phys. Rev. D **56**, 1 (1997).
- [Ji98] X. Ji, J. Phys. G **24**, 1181 (1998).
- [Ji00] X. Ji, C. Kao, and J. Osborne, Phys. Lett. **B 472**, 1 (2000).
- [Ji01] X. Ji and J. Osborne, J. Phys. G **27**, 127 (2001).

- [Ji03] X. D. Ji, J. P. Ma, F. Yuan, hep-ph/0301141.
- [Ji03a] X. Ji, J.-P. Ma and F. Yuan, Nucl. Phys. **B652**, 383 (2003).
- [Ji03b] X. Ji, F. Yuan e-Print Archive: hep-ph/0206057.
- [Ji03c] X. Ji, hep-ph/0304037, to appear in Phys. Rev. Lett.
- [Ji04] X. Ji, J-P. Ma and F. Yuan, e-Print Archive: hep-ph/0404183.
- [Jo00] M. K. Jones *et al.*, Phys. Rev. Lett. **84**, 1398 (2000) ); O. Gayou *et al.*, Phys. Rev. Lett. **88**, 092301 (2002). .
- [Jo02] K. Joo *et al.*, Phys. Rev. Lett. **88**, 122001 (2002).
- [Ju88] H. Jung and G. A. Miller, Phys. Lett. **B200**, 351 (1988).
- [Ju97] K. Juge, J. Kuti, and C. J. Morningstar, Nucl. Phys. Proc. Suppl. **63**, 326, (1997).
- [Ju99] K. J Juge, J. Kuti and C. J. Morningstar, Phys. Rev. Lett. **82**, 4400 (1999).
- [Ju02] K.J Juge, J. Kuti and C. Morningstar, hep-lat/0209109, to be published in Proceedings of Lattice 2002.
- [Ka75] W. Kaune, G. Miller, W. Oliver, R. W. Williams, and K. K. Young, Phys. Rev. D **11**, 478 (1975).
- [Ka90] L. P. Kaptari *et al.*, Nucl. Phys. **A512**, 684 (1990).
- [Ka93] Kang Y, Erbs P, Pfeil W, and Rollnik H 1990 *Abstracts of the Particle and Nuclear Intersections Conference*, (MIT, Cambridge, MA); Kang Y 1993 Ph.D. thesis Bonn.
- [Ka00] R. Kaiser and H. Leutwyler, Eur. Phys. J. **C17** (2000) 623.
- [Ko93] L. A. Kondratyuk *et al.*, Phys. Rev. C **48** 2491 (1993).
- [Ko95] A. Kotzinian, Nucl. Phys. **B 441** (1995) 234.
- [Ko96] A. M. Kotzinian and P. J. Mulders, Phys. Rev. **D54** (1996) 1229; Phys. Lett. **B406** (1997) 373.
- [Ko96a] A. M. Kotzinian and P. J. Mulders, Phys. Lett. **B406**, 373 (1997).
- [Ko97] N. I. Kochelev, *Proc. of Workshop on Physics with Polarized Protons at HERA*, 1997, Hamburg, p. 225, hep-ph/9711274.
- [Kop02] B. Z. Kopeliovich, J. Nemchik, A. Schaefer, and A. V. Tarasov, Phys. Rev. Lett. **88** (2002) 232303.
- [Kopc] N. Kochelev, private communication.

- [Kr98] Th. Feldmann and P. Kroll, Eur. Phys. J. **C5** (1998) 327.  
Th. Feldmann, P. Kroll and B. Stech, Phys. Rev. **D58** (1998) 114006.
- [Kr99] D. Kharzeev, Eur. Phys. J. **C9**, 459 (1999).
- [Kr01] K. Wijesooriya, *et al.*, Phys. Rev. Lett. **86**, 2975 (2001).
- [Kr02] K. Wijesooriya *et al.*, Phys. Rev. C **66**, 034614 (2002).
- [Ku89] S. A. Kulagin, Nucl. Phys. **A500**, 653 (1989).
- [Ku94] S. A. Kulagin, G. Piller, and W. Weise, Phys. Rev. C **50**, 1154 (1994).
- [Ku98] S. Kumano, Phys. Rep. **303**, 183 (1998).
- [Ku00] S. Kuhlmann *et al.*, Phys. Lett. **B476**, 291 (2000).
- [Ku02] A. Kurylov, M. J. Ramsey-Musolf, and S. Su, “Parity-violating electron scattering as a probe of supersymmetry”, hep-ph/0205183 (2002).
- [La72] J.-M. Laget, Nucl. Phys. **A194**, 81 (1972).
- [La74] P. V. Landshoff, Phys. Rev. D **10**, 1024 (1974).
- [La88] J.M. Laget, J. Phys. G **14**, (1988) 1445.
- [La91] J.-M. Laget, in *Modern Topics in Electron Scattering*, edited by B. Frois and I. Sick (World Scientific, 1991) 290, and references therein.
- [La94] J.-M. Laget and R. Mendez-Galain, Nucl. Phys. **A581**, 397 (1995).
- [La94a] J.-M. Laget, Nucl.Phys. **579** (1994) 333.
- [La95] H. L. Lai *et al.* [CTEQ Collaboration], Phys. Rev. D **51**, 4763 (1995); H. L. Lai *et al.*, Eur. Phys. J. **C12**, 375 (2000).
- [La97] P. Lacock *et al.* [UKQCD Collaboration], Phys. Lett. **B401**, 308, (1997).
- [La98] J.-M. Laget, in *Proceedings of workshop on Jefferson Lab Physics & Instrumentations with 12 GeV Beams*, Newport News, 1998, p. 57.
- [La98a] J.-M. Laget, Proc. of the *Workshop on Color Transparency*, Grenoble (France), Edt. E. Voutier, (1998) 131 ; <http://isnwww.in2p3.fr/ct97>.
- [La00] B. Lampe and E. Reya, Phys. Rep. **332**, 1 (2000); S. D. Bass and A. W. Thomas, Prog. Part. Nucl. Phys. **33**, 449 (1994).
- [LAM10] Lambda/Ten Optics, 7A Stuart Road, Chelmsford, MA 01824.
- [Lan53] L. D. Landau, I. Y. Pomeranchuk, Dokl. Akad. Nauk SSSR **92**:535, 735 (1953).



- [Le80] G.P. Lepage, and S.J. Brodsky, Phys. Rev. D **22**, 2157 (1980).
- [Le92] Lee T-S H 1992 *Few Body Syst. Supplement* **6** 526 ; Lee T-S H 1991 *Argonne National Laboratory Preprint* PHY-6886-TH-91; Lee T-S H 1991 *Argonne National Laboratory Preprint* PHY-6843-TH-91.
- [Le96] H. Leutwyler, Phys. Lett. B378: 313-318, (1996).
- [Le02] G. Levman, J. Phys. G **28**, 1079 (2002).
- [Li00] S. Liuti, R. Ent, C. E. Keppel, and I. Niculescu, to be submitted to Phys. Rev. D.
- [Lu81] M. Luscher, Nucl. Phys. **B180**, 317 (1981).
- [Lu81a] T. Ludlam *et al.*, Nucl. Instrum. Meth. **180** (1981) 413.
- [Lu92] M. Luke, A. V. Manohar and M. J. Savage, Phys. Lett. **B288**, 355 (1992).
- [Lu93] A. Lung *et al.*, Phys. Rev. Lett. **70**, 718 (1993).
- [Ma91] A. V. Manohar, Phys. Rev. Lett. **66**, 289 (1991).
- [Ma93] Jefferson Lab Experiment E93-038, R. Madey and S. Kowalski, spokespersons.
- [Ma94] N. C. R. Makins *et al.*, Phys. Rev. Lett. **72**, 1986 (1994).
- [Ma94a] A. D. Martin, R. Roberts and W. J. Stirling, Phys. Rev. D **50**, 6734 (1994).
- [Ma98] A. D. Martin, R. G. Roberts, W. J. Stirling and R. S. Thorne, Eur. Phys. J. **C4**, 463 (1998).
- [Ma98a] Y. Mardor *et al.*, Phys. Rev. Lett. **81**, 5085 (1998); A. Leksanov *et al.*, Phys. Rev. Lett. **87**, 212301-1 (2001).
- [Ma00] P. Maris and P. C. Tandy, Phys. Rev. C **62**, 055204 (2000).
- [Ma00] P. Maris, P. C. Tandy, Phys. Rev. C **62**, 055204 (2000).
- [Ma02] Andrzej Czarnecki and William J. Marciano, Phys. Rev. D64, (2001), 013014.
- [Ma02a] A. D. Martin, R. G. Roberts, W. J. Stirling, and R. S. Thorne, “Uncertainties of predictions from parton distributions. I: Experimental errors”, hep-ph/0211080 (2002).
- [Me93] W. Melnitchouk and A. W. Thomas, Phys. Rev. D **47**, 3783 (1993).
- [Me94] W. Melnitchouk, A. W. Schreiber and A. W. Thomas, Phys. Rev. D **49**, 1183 (1994).
- [Me96] W. Melnitchouk and A. W. Thomas, Phys. Lett. **B377**, 11 (1996).
- [Me97] W. Melnitchouk, M. Sargsian, and M. I. Strikman, Z. Phys. **A359**, 359 (1997).

- [Me98] W. Melnitchouk, J. Speth and A. W. Thomas, Phys. Lett. B **435**, 420 (1998).
- [Me99] W. Melnitchouk, J. Speth and A.W. Thomas, Phys. Rev. D **59**, 014033 (1999).
- [Me00] K. Mengel, R. Novotny, R. Beck, *et al.*, "Detection of Monochromatic Photons Between 50 and 790 MeV with a PbWO<sub>4</sub> - Scintillator Array", to be published (1999).
- [Me00] Z.-E. Meziani, *Proceedings of the HiX2000 Workshop*, J.P. Chen and Z.-E. Meziani, eds.
- [Mi56] A. B. Migdal, Phys. Rev. **103**:1811 (1956).
- [Mi00] J. Mitchell, *Proceedings of the HiX2000 Workshop*, J.-P. Chen and Z.-E. Meziani, eds.
- [Mi02] G. A. Miller, Phys. Rev. C **66**, 032201 (2002).
- [Mi02a] A. Miller (HERMES Collaboration) Proceedings of SPIN2002 BNL, Upton NY 2002.
- [Mi02b] G. A. Miller and A. W. Thomas, "Comment on 'A precise determination of electroweak parameters in neutrino nucleon scattering'", hep-ex/0204007 (2002)
- [Mi02c] A. I. Milstein, O. P. Sushkov, and I. S. Terekhov, "Calculation of radiative corrections to the effect of parity nonconservation in heavy atoms", hep-ph/0212072 (2002).
- [Mkpc] H. Mkrtchyan *et al.*, JLab test run results, 1999 (private communication).
- [ML00] *Assessment of the MEGA/LASS Magnet at LANL, 20 March, 2000*,  
([http://www.phys.cmu.edu/halld/halld\\_notes/Note\\_026/](http://www.phys.cmu.edu/halld/halld_notes/Note_026/)).
- [Mo70] M. Morpurgo *et al.*, Particle Accelerators **1**, 255 (1970).
- [Mo79] M. Moszynski and B. Bengston, Nucl. Inst. and Meth., **158**, 1 (1979).
- [Mo79a] M. Morpurgo *et al.*, Cryogenics **19**, 411 (1979).
- [Mo95] B. Moussallam, Phys. Rev. **D51** (1995) 4939.  
B. Ananthanarayan and B. Moussallam, hep-ph/02052702.
- [Mo97] C. J. Morningstar and M. Peardon, Phys. Rev. D **56**, 4043 (1997).
- [Mo99] H. Morita, C. Ciofi degli Atti, and D. Treleani, Phys. Rev. C **60**, 034603 (1999).
- [Mo99a] R. Mohring, Ph.D. thesis, University of Maryland, 1999.
- [Mopc] M. Morlet and J. Van de Wiele, private communication.
- [Mu82] A. H. Mueller, in *Proceedings of the Seventeenth Rencontres de Moriond*, ed. J. Tran Thanh Van (Editions Frontieres, Gif-sur-Yvette, France, 1982) **Vol. I** 13.

- [Mu83] A. H. Mueller, in *Proceedings of the Seventeenth Rencontre de Moriond Conference on Elementary Particle Physics*, Les Arcs, France, 1982, edited by J. Tran Thanh Van (Editions Frontieres, Gif-sur-Yvette, France, 1982); S. J. Brodsky, in *Proceedings of the Thirteenth International Symposium on Multiparticle Dynamics*, Volendam, The Netherlands, 1982, edited by W. Kittel *et al.* (World Scientific, Singapore, 1983).
- [Mu94] D. Müller *et al.*, Fortschr.Phys.42,101 (1994)
- [Mu94] D. Müller *et al.*, Fortschr.Phys. **42**, 101 (1994)
- [Mu95] C. R. Munz *et al.*, Phys. Rev. C **52**, 2110 (1995).
- [Mu96] P.J. Mulders and R.D. Tangerman, Nucl.Phys.B461, 197(1996)
- [Mu01] V. Muccifora, hep-ex/0106088, (2001).
- [Mu02] A. Mukherjee, I.V. Musatov, H. C. Pauli, A. V. Radyushkin, hep-ph/0205315.
- [Na70] Y. Nambu, Univ. of Chicago Report No. 70-70 (1970) (unpublished); lectures at the Copenhagen Summer Symposium (1970) (unpublished).
- [Na84] O. Nachtmann and H. J. Pirner, Z. Phys. **C21**, 277 (1984).
- [Na88] J. Napolitano *et al.*, Phys. Rev. Lett. **61**, 2530 (1988); S.J. Freedman *et al.*, Phys. Rev. C **48**, 1864 (1993); J.E. Belz *et al.*, Phys. Rev. Lett. **74**, 646 (1995).
- [NA99] *Nuclear Physics: The Core of Matter, The Fuel of Stars*, The Committee on Nuclear Physics of the Board on Physics and Astronomy of the Commission on Physical Sciences, Mathematics, and Applications of the National Research Council, National Academy Press, Washington, D.C. (1999).
- [Na02] A. Nathan ( for the RCS Collaboration), *Workshop Proceeding for Exclusive Processes at High Momentum Transfer*, A. Radyushkin and P. Stoler , eds, World Scientific (2002), 225.
- [Na02a] Paul van der Nat, “Hadronization at 12 GeV,” Master’s thesis, vrije Universiteit Amsterdam/Nikhef, July 2002.
- [Ne77] R. Nieman *et al.*, IEEE Trans. on Magn., **13**, 632 (1977).
- [Ne95] T. G. O’Neill *et al.*, Phys. Lett. **B351**, 87 (1995).
- [Ne00] Lattice Hadron Physics Collaboration proposal, “*Nuclear Theory with Lattice QCD*”, J.W. Negele and N. Isgur principal investigators, <ftp://www-ctp.mit.edu/pub/negele/LatProp/>.
- [Ni94] N. N. Nikolaev, A. Szczurek, J. Speth, J. Wambach, B. G. Zakharov and V. R. Zoller, Phys. Rev. C **50**, 1296 (1994).

- [Ni99] I. Niculescu, C. Keppel, S. Liuti, and G. Niculescu, Phys. Rev. D **60**, 094001 (1999).
- [Ni00] I. Niculescu *et al.*, Phys. Rev. Lett. **85**, 1186 (2000).
- [Ni00a] I. Niculescu *et al.*, Phys. Rev. Lett. **85**, 1182 (2000).
- [NS96] “Nuclear Science: A Long Range Plan”, a report by the DOE/NSF Nuclear Science Advisory Committee, February, 1996.
- [NS02] “Opportunities in Nuclear Science: A Long-Range Plan for the Next Decade”, a report by the DOE/NSF Nuclear Science Advisory Committee, April, 2002.
- [Os99] M. Ostrick *et al.*, Phys. Rev. Lett. **83**, 276 (1999). C. Herberg *et al.*, Eur. Phys. J. A **5**, 131 (1999).
- [Pa97] V. R. Pandharipande, I. Sick, and P. K. A. deWitt Huberts, Rev. Mod. Phys. **69**, 981 (1997).
- [Pa99] I. Passchier *et al.*, Phys. Rev. Lett. **82**, 4988 (1999).
- [Pa00] E. Pace, G. Salme and S. Scopetta, to appear in *Proceedings of the XVII-th European Few-Body Conference*, Evora, Portugal (2000).
- [Pa01] E. Pace, G. Salme and S. Scopetta, Nucl. Phys. A **689**, 453 (2001); E. Pace, G. Salme, S. Scopetta and A. Kievsky, Phys. Rev. C **64**, 055203 (2001).
- [PDB] Particle Data Book, Phys. Rev., D66, (2002),01001.
- [Pe89] M. D. Petroff and M. Atac, IEEE Trans. Nucl. Sci. **NS-36**, 163 (1989).
- [Pe98] J.-C. Peng *et al.*, Phys. Rev. D **58**, 092004 (1998).
- [Pe00] G. Petratos, *Proceedings of the HiX2000 Workshop*, J.-P. Chen and Z.-E. Meziani, eds.
- [Pe00a] V. Petrov *et al.*, Phys. Rev. D **57**, 4325 (1998); M. Penttinen, M. V. Polyakov, and K. Goeke, Phys. Rev. D **62**, 014024 (2000).
- [PHOT] Photonis Imaging Systems, [www.photonis.com](http://www.photonis.com).
- [Pi01] S.C. Pieper, R.B. Wiringa, Ann. Rev. Nucl. Part. Sci. **51**, 53 (2001).
- [Po99] M. V. Polyakov and C. Weiss, Phys. Rev. D **60**, 114017 (1999).
- [Po02] P. V. Pobylitsa, Phys. Rev. D **66**, 094002 (2002).
- [Po03] M.V. Polyakov and A.G. Shuvaev. hep-ph/0207153
- [Pr78] C. Y. Prescott, *et al.*, Phys. Lett. **B77**, 347 (1978).
- [Pr79] C. Y. Prescott, *et al.*, Phys. Lett. **B84**, 524 (1979).

- [Pu02] J. Pumplin, *et al.*, JHEP **7**, 12 (2002).
- [Ra77] A. V. Radyushkin, JINR report P2-10717, Dubna, 1977 (unpublished).
- [Ra79] J. Ralston and D. Soper, Nucl. Phys. **B152**, 109 (1979)
- [Ra88] J. P. Ralston and B. Pire, Phys. Rev. Lett. **61**, 1823 (1988).
- [Ra90] J. P. Ralston and B. Pire, Phys. Rev. Lett. **65**, 2343 (1990); B. Kundu, J. Samuelsson, P. Jain and J. P. Ralston, Phys. Rev. D **62**, 113009 (2000).
- [Ra91] V. A. Nesterenko and A. V. Radyushkin, Phys. Lett. B **115**, 410 (1982); and A. V. Radyushkin, Nucl. Phys. A **532** 141c (1991).
- [Ra92] J. P. Ralston and B. Pire, Phys. Rev. Lett. **61**, 1823 (1988); C. E. Carlson, M. Chachkhunashvili, and F. Myhrer, Phys. Rev. D **46**, 2891 (1992).
- [Ra96] A. V. Radyushkin, Phys. Lett. **B380**, 417 (1996); Phys. Lett. **B385**, 333 (1996); Phys. Rev. D **56**, 5524 (1997).
- [Ra97] A. Radyushkin, Phys.Lett.B380.417 (1996); Phys. Rev. D **56**, 5524 (1997).
- [Ra98] R. Rapp, T. Schafer, E. V. Shuryak and M. Velkovsky, Phys. Rev. Lett. **81**, 53 (1998)
- [Ra98a] A. V. Radyushkin, Phys. Rev. D **58**, 114008 (1998).
- [Ra99] A. V. Radyushkin, Phys.Rev.D **59**, 014030 (1999).
- [Ra99a] M. J. Ramsey-Musolf, Phys. Rev. **C60**, 015501 (1999).
- [Ra01] A. V. Radyushkin, in *At the frontier of particle physics/Handbook of QCD*, vol. 2, ed. M. Shifman, World Scientific (2001).
- [Ra01a] Radyushkin A (private communication).
- [Ra02] J.P. Ralston and B. Pire, Phys. Rev. D **66**, 111501 (2002)
- [Ra03] J. P. Ralston and P. Jain, hep-ph/0302043.
- [Rapc] Radyushkin A (private communication).
- [Ri98] G. Ricco *et al.*, Phys. Rev. C **57**, 356 (1998).
- [Ro79] D. A. Ross and C. T. Sachrajda, Nucl. Phys. **B149**, 497 (1979).
- [Ro82] S. Rock *et al.*, Phys. Rev. Lett. **49**, 1139 (1982).
- [Ro99] D. Rohe *et al.*, Phys. Rev. Lett. **83**, 4257 (1999).
- [Ru75] A. de Rújula, H. Georgi and H.D. Politzer, Ann. Phys. **103**, 315 (1975).

- [Sa69] J. J. Sakurai, Phys. Rev. Lett. **22**, 981 (1969).
- [Sa01] M. M. Sargsian, S. Simula and M. I. Strikman, Phys. Rev. C **66**, 024001 (2002).
- [Sa03] P.R. Saull [ZEUS collaboration] arXiv:hep-ex/0003030
- [Sa03a] M. Sargsian, L. Farnkfurt and M. Strikman in progress.
- [Sapc] M. M. Sargsian, private communication.
- [Sc91] R. Schiavilla and D. O. Riska, Phys. Rev. C **43**, 437 (1991); R. Schiavilla, V. R. Pandharipande and D. O. Riska, Phys. Rev. C **41**, 309 (1990); and references therein.
- [Sc93] R. W. Schulze and P. U. Sauer, Phys. Rev. C **48**, 38 (1993).
- [Sc01] E.C. Schulte, *et al.*, Phys. Rev. Lett. **87**, 102302 (2001).
- [Se95] J. Sexton *et al.* [IBM Collaboration], Phys. Rev. Lett. **75**, 4563 (1995).
- [Sh79] M.A. Shifman, A.I. Vainshtein, V.I. Zakharov, Nucl. Phys. **B147**, 385 (1979).
- [Sh79a] M. A. Shupe *et al.*, Phys. Rev. D **19**, 1921 (1979).
- [Sh01] M. Shifman, Handbook of QCD, Volume 3, 1451, World Scientific (2001)
- [Si91] D.Sivers, Phys.Rev. **D43**, 261 (1991).
- [Si93] A. F. Sill *et al.*, Phys. Rev. D **48**, 29 (1993).
- [Si01] N. Simicevic, “Design of a Čerenkov Counter for the Q-Weak Experiment”, LATECH-CAPS-01-03A, March 12, 2001. Available in Public Access Papers area of <http://www.jlab.org/qweak/>.
- [Sl88] T. Sloan, G. Smadja, and R. Voss, Phys. Rep. **162**, 45 (1988).
- [Sm91] E. S. Smith and R. Jacobs, “Photomultiplier Tests for the CLAS TOF,” CLAS-NOTE 91-003, Feb 1, 1991.
- [Sm99] G. I. Smirnov, Eur. Phys. J. C **10**, 239 (1999); V. V. Burov, A. V. Molochkov, G. I. Smirnov, Phys. Lett. **B466**, 1 (1999).
- [Sm99a] E. S. Smith *et al.*, Nucl. Instr. and Meth. **A432** (1999) 265.
- [Sm02] J. R. Smith and G. A. Miller, Phys. Rev. C **65**, 055206 (2002).
- [Sm02a] E. S. Smith, “CLAS TOF Rates in an Electron Beam,” CLAS-NOTE 2002-004, Mar 8, 2002.
- [So96] X. Song, Phys. Rev. D **54**, 1955 (1996).
- [So99] L. Sorrel, E155 Technical note 81. SLAC. 1999

- [So00] P. Souder, *Proceedings of the HiX2000 Workshop*, J.-P. Chen and Z.-E. Meziani, eds.
- [Sp98] J. Speth and A. W. Thomas, *Adv. Nucl. Phys.* **24**, 83 (1998).
- [Spt] Signal Processing Technologies: <http://www.spt.com>.
- [St93] P. Stoler, *Phys. Rep.* **226**, 103 (1993).
- [St93a] M. Stratmann, *Z. Phys* **C60**, 763 (1993).
- [St95] E. Stein *et al.*, *Phys. Lett.* **B343**, 369 (1995).
- [St97] F. M. Steffens and A. W. Thomas, *Phys. Rev. C* **55**, 900 (1997).
- [St00] N.G. Stefanis, W. Schroers and H.-Ch. Kim, *Phys. Lett. B* **449**, 299 (1999); and *Eur. Phys. J. C* **18**, 137 (2000).
- [St01] S. Stepanyan, et al. [CLAS collaboration], *Phys. Rev. Lett.* **87**, 182002-1 (2001)
- [St02] F. M. Steffens, *Phys. Lett. B* **541**, 346 (2002).
- [St03] P. Stoler, e-Print Archive: hep-ph/0307162
- [STARpc] The STAR TOF Working Group, "Proposal for a Large Area Time of Flight System for STAR, STAR-TOF," May 15, 2002.
- [Sz01] A. P. Szczepaniak and M. Swat, *Phys. Lett.*, **B516**:72, 2001.
- [Ta96] L. Tao *et al.*, *Z. Phys. C* **70**, 387 (1996).
- [tH76] G. 't Hooft, *Phys. Rev. Lett.* **37**, 8 (1976); and *Phys. Rev. D* **14**, 3432 (1976).
- [Th84] A. W. Thomas, *Adv. Nucl. Phys.* **13**, 1 (1984).
- [Th97] D. R. Thompson *et al.* (E852 Collaboration) *Phys. Rev. Lett.*, **79**:1630, 1997.
- [Th97] D. R. Thompson *et al.*, *Phys. Rev. Lett.* **81**, 5760, (1997).
- [Th00] A. W. Thomas, W. Melnitchouk and F. M. Steffens, *Phys. Rev. Lett.* **85**, 2892 (2000).
- [Th01] R. Thompson *et al.*, *Phys. Rev. Lett.* **86**, 1702 (2001).
- [Ti92] P. C. Tiemeijer and J. A. Tjon, *Phys. Lett.* **277B**, 38 (1992).
- [Ti92] P. C. Tiemeijer and J. A. Tjon, *Phys. Lett.* **277B**, 38 (1992).
- [TOSCA] 3-D Non-linear magnetostatics computer program, SCARPIA pre-processor and OPERA post-processor, Vector Fields, Oxford, U.K.
- [Uc88] T. Uchiyama and K. Saito, *Phys. Rev. C* **38**, 2245 (1988).

- [Ulp] “MCEEP — Monte Carlo for Electro-Nuclear Coincidence Experiments”, User Manual, version 3.6, by P.E. Ulmer, Old Dominion University, unpublished (2001). Available from <http://www.physics.odu.edu/~ulmer/mceep/mceep.html>.
- [Va00] M. Vakili *et al.*, [CCFR Collaboration], Phys. Rev. **D 61**, 052003 (2000).
- [Va98] M. Vanderhaeghen, M. Guidal, J.-M. Laget, Phys. Rev. C **57**, 1454 (1998).
- [Va99] M. Vanderhaeghen, P. A. M. Guichon, and M. Guidal, Phys. Rev. D **60**, 094017 (1999).
- [Vap] M. Vanderhaeghen, private communication. The calculations were done using the double distribution of Radyushkin [Ra99] with and without the  $D$ -term of Polyakov and Weiss [Po99].
- [Ve87] P. Verner, RPAC (II), CEBAF, January 1987, p. 615.
- [Vi92] M. Virchaux and A. Milzstajn, Phys. Lett. **74B**, 221 (1992).
- [Vo88] M. B. Voloshin and M. A. Shifman, Sov. J. Nucl. Phys. **47**, 511 (1988); N. Isgur, Phys. Rev. D **40**, 101 (1989); Phys. Lett. **B448**, 111 (1999).
- [Vo01] J. Volmer *et al.*, Phys. Rev. Lett. **86**, 1713 (2001).
- [Wa77] S. Wandzura and F. Wilczek, Phys. Lett. **B72**, 195 (1977).
- [Wa80] S. T. Wang *et al.*, Adv. in Cryogenics Engineering **25**, 19 (1980).
- [Wa82] S. T. Wang *et al.*, Cryogenics **22**, 335 (1982).
- [Wa91] D. A. Wasson, Phys. Rev. Lett. **67**, 2237 (1991).
- [Wa95] X.-N. Wang, M. Gyulassy, and M. Plumer, Phys. Rev D **51**, 3436 (1995).
- [Wa97] M. R. Wayne, Nucl. Inst. and Meth. **A386**, 278 (1997).
- [Wa03] G. Warren *et al.*, “Spin Asymmetries on the Nucleon Experiment (SANE)”, Jefferson Lab Proposal P03-002.
- [We71] G. B. West, Phys. Lett. **B37**, 509 (1971); W. B. Atwood and G. B. West, Phys. Rev. D **7**, 773 (1973).
- [We94] D. Weingarten, Nucl. Phys. **B34** (Proc Suppl.), 29 (1994).
- [We96] G. West, hep-ph/9612403.
- [We97] H. Weigel *et al.*, Phys. Rev. D **55**, 6910 (1997).
- [We02] J. Wendland [HERMES Collaboration], <http://www-hermes.desy.de/notes/pub/trans-public-index.html>.



- [We02a] L.B. Weinstein and R. Niyazov, proceedings of the conference ‘Electron-Nucleus Scattering VII’, Elba, June 26, 2002. nucl-ex/0209014.
- [Wh92] L. Whitlow *et al.*, Phys. Lett. **B282**, 475 (1992).
- [Wi00] R. Wigmans, Calorimetry, Oxford Science Pub. (2000).
- [Wo81] R. C. Wolgast *et al.*, IEEE Trans. on Magn. **17**, 195 (1981).
- [Wo89] R. M. Woloshyn, Nucl. Phys. **A496**, 749 (1989).
- [Wo97] C. S. Wood, *et al.*, Science **275**, 1759 (1997).
- [Wopc] B. Wojtsekhowski and C. Hyde-Wright, private communication; K. Abe *et al.*, Phys. Lett. **B404**, 404 (1997); P. L. Anthony *et al.*, Phys. Lett. **B458**, 529 (1999).
- [WP01] “The Science Driving the 12 GeV Upgrade of CEBAF”, an internal report of the Thomas Jefferson National Accelerator Facility, Newport News, VA (2001)
- [Xiln] Xilinx: <http://www.xilinx.com>.
- [Yu95] Yu. Prokoshkin, S. A. Sadvski, Phys. Atom. Nucl., **58**:606, 1995.
- [Za01] B. Zaroukian, J. Kaditz, C. A. Meyer and P. Eugenio, *A Study of leakage in Partial Wave Analysis for the HallD Detector at Jefferson Lab*, July 2001, ([http://www.phys.cmu.edu/halld/halld\\_notes/Note\\_051/](http://www.phys.cmu.edu/halld/halld_notes/Note_051/)).
- [Ze01] G. P. Zeller, *et al.*, Phys. Rev. Lett. **88**, 091802 (2002).
- [Zepc] Z. Li, Brookhaven National Laboratory, private communications (2002)
- [Zh01] H. Zhu *et al.*, Phys. Rev. Lett. **87**, 081801 (2001).
- [Zh01a] L.Y. Zhu, Hall A data analysis workshop, Dec. 11-12, 2001. (<http://www.jlab.org/~lyzhu/work/dec01.ps.gz>)
- [Zh03] Q. Zhao and F. Close, private communication.
- [Zh03a] L.Y. Zhu *et al.*, Phys. Rev. Lett. **91**, 022003 (2003).

## List of Figures

1	QCD predicts a confining flux tube is formed between distant static charges. . . . .	3
2	Evidence for flux tubes and linear potentials from lattice QCD. . . . .	4
3	Model-independent spectrum of the glue (flux tube) of Fig. 1. . . . .	5
4	The results of a double-blind Monte Carlo simulation of the GlueX experiment. . . .	6
5	The relative splittings of the $Q\bar{d}$ states and the $Q\bar{Q}$ states, both shown from the heaviest to the lightest. . . . .	7
6	A model of the Generalized Parton Distribution (GPD) $H(x, \xi, t = 0)$ in two dimensions. . . . .	10
7	Representations of the proton properties probed in elastic scattering, deeply inelastic scattering, and deeply exclusive scattering. . . . .	11
8	The result of the JLab measurement of $G_E^p/G_M^p$ and the range of the projected measurements, both compared to a variety of theories. . . . .	12
9	A projected measurement of the neutron polarization asymmetry $A_1^n$ , determined by the spin structure of the valence quarks, made possible by the proposed 12 GeV Upgrade. . . . .	14
10	The ratio of polarized to unpolarized valence down quark distribution functions measured in semi-inclusive deep inelastic scattering . . . . .	14
11	A projected measurement of the ratio of momentum distributions of valence $d$ quarks to $u$ quarks made possible by the proposed 12 GeV Upgrade . . . . .	14
12	The “handbag” diagrams for deeply virtual Compton scattering and deeply virtual meson production. . . . .	16
13	Projected data for the DVCS beam spin asymmetry from JLab at 11 GeV . . . . .	17
14	A model $u$ -quark phase space charge distribution in 3D coordinate space for three Feynman momentum fractions. . . . .	18
15	The quark spatial and spin distributions in the transverse plane from model calculations. . . . .	20
16	Phase diagram for nuclear matter. . . . .	25

17	Available data projected results for a differential cross-section measurement of deuteron photodisintegration. . . . .	27
18	Projected measurements of the pion elastic form factor . . . . .	29
19	Projected measurements of the charged pion photoproduction cross section at a C.M. angle of $90^\circ$ . . . . .	29
20	Relative shifts in $Q_{\text{weak}}^e$ and $Q_{\text{weak}}^{\text{proton}}$ from SUSY effects . . . . .	31
21	The importance of $\Gamma_{\eta \rightarrow \gamma \gamma}$ in the measurement of the quark mass ratio . . . . .	32
22	The $\eta - \eta'$ mixing angle as determined by a previous Primakoff measurement, $\gamma - \gamma$ collisions, and the projected result with the Jefferson Laboratory 12 GeV Upgrade .	32
23	The configuration of the proposed 12 GeV CEBAF Upgrade. . . . .	35
24	Three-dimensional CAD drawing of the MAD spectrometer . . . . .	37
25	Three dimensional CAD drawing of the CLAS <sup>++</sup> detector. . . . .	39
26	A CAD drawing of the new SHMS spectrometer installed in Hall C together with the existing HMS and SOS spectrometers. . . . .	44
27	The proposed detector for the study of the photoproduction of mesons in the mass region around 2 GeV. . . . .	47
28	Level diagram for mesons and exotics . . . . .	53
29	The $q\bar{q}$ spectrum . . . . .	54
30	Field lines associated with forces. . . . .	56
31	Lattice calculation of energy density . . . . .	56
32	$3\pi$ mass distributions . . . . .	58
33	Intensities distributions in the $3\pi$ system. . . . .	59
34	Intensity in the exotic wave. . . . .	59
35	Breit-Wigner fit results. . . . .	60
36	Production of Hybrid Mesons . . . . .	61
37	Photoproduction cross sections . . . . .	62

38	$3\pi$ spectrum from SLAC data. . . . .	64
39	Photproduction of particles . . . . .	66
40	$ t $ distributions. . . . .	66
41	Schematic diagrams of form factor reactions that can be expressed in terms of the GPD formalism . . . . .	74
42	Form factor reactions that can be expressed in terms of the valence pQCD formalism	75
43	The GPD $H(x, b_\perp) = u(x, b_\perp)$ obtained from the GPD $H(x, 0; \Delta_\perp)$ . . . . .	78
44	The $\pi^+$ form factor . . . . .	80
45	The proton magnetic form factor . . . . .	82
46	The status of the JLab measurement of $G_E^p/G_M^p$ and the range of the projected measurements . . . . .	82
47	The current status of the data for $G_M^n$ , and the projections for the Hall B program with the 12 GeV upgrade . . . . .	83
48	The neutron electric form factor $G_E^n$ . . . . .	84
49	Kinematic coverage of the planned RCS experiments with the 12 GeV upgrade . . .	86
50	The recoil polarization observable $K_{LL}$ measured in the recent real Compton scattering experiment with projected data for a proposed experiment . . . . .	86
51	The statistical accuracy of $R_A^{\pi^0}(t)$ anticipated in the Hall B measurement of the exclusive $\pi^0$ electroproduction. . . . .	87
52	The Delta resonance transition form factor $G_M^*$ , as compared to the dipole $G_D$ . . .	88
53	The $E_{1+}/M_{1+}$ (or - $G_E^*/G_M^*$ ) ratio for Delta excitation. . . . .	88
54	Existing JLab data for $S_{1+}/M_{1+}$ and JLab Hall B 12 GeV projections. . . . .	88
55	The JLab data for the $N \rightarrow S_{11}$ helicity amplitude $Q^3 A_{1/2}$ . . . . .	91
56	Ratio $R^{np}$ of neutron to proton structure functions as a function of $x$ , extracted from the SLAC data on the deep inelastic proton and deuteron structure functions. . . . .	93
57	Sample of large- $x$ data for $A_1^p$ and $A_1^n$ . . . . .	96
58	The ratio $F_2^n/F_2^p$ versus $x$ . . . . .	98

59	Projected measurements for $R = \sigma_L/\sigma_T$ at $x = 0.8$ . . . . .	100
60	Lowest moments $M_n(Q^2)$ of the proton–neutron $F_2$ structure function difference, for $n = 2, 4$ , and $6$ , as a function of $Q^2$ . . . . .	101
61	Projected errors for measurements of asymmetries $A_1$ in the large- $x$ region made possible by the proposed 12 GeV Upgrade . . . . .	103
62	Expected data with CLAS <sup>++</sup> in Hall B for the polarization asymmetries of the proton and deuteron . . . . .	105
63	Longitudinal beam-target polarization asymmetry of a proton versus $W$ , for an 11 GeV measurement at $Q^2 = 8$ (GeV/c) <sup>2</sup> in Hall C. . . . .	106
64	Projected errors for $x^2 g_2(x)$ for the neutron and proton from 11 GeV JLab measurements . . . . .	107
65	Neutron twist-3 matrix element $d_2^n$ data and projected errors for a 12 GeV JLab measurement . . . . .	108
66	Projected errors for the ratio of polarized to unpolarized quark distribution functions at a 12 GeV CEBAF, compared with HERMES data . . . . .	109
67	The projected precision of $\bar{d}/\bar{u}$ extractions compared with the FNAL E866 Drell-Yan [Ha98] measurements. . . . .	111
68	Simulated data for the pion structure function at $Q^2 = 1.5$ and $3.0$ (GeV/c) <sup>2</sup> . . . .	111
69	Two dimensional image of $H(x, \xi, t)$ from a model with factorized $t$ -dependence . . .	114
70	Model “tomographic” images of quarks in the transverse plane . . . . .	116
71	Representative handbag diagrams for deeply virtual Compton scattering and deeply virtual meson production . . . . .	118
72	Scaling cross sections for the production of photons (DVCS), pseudoscalar mesons, and vector mesons . . . . .	119
73	Beam spin asymmetry measured with CLAS . . . . .	119
74	Comparison of data on the $Q^2$ dependence of the $\gamma\gamma^*\pi^0$ form factor with two calculations . . . . .	120
75	DVCS and Bethe-Heitler cross section for different beam energies . . . . .	121

76	Kinematics coverage for deeply virtual exclusive processes for experiments at various laboratories . . . . .	122
77	Kinematics for DVCS beam asymmetry measurements at 11 GeV . . . . .	123
78	Projected data for the $\sin \phi$ moment $A_{LU}^{\sin \phi}$ of the DVCS/BH asymmetry . . . . .	124
79	Projected Hall A data for the beam-helicity dependent cross section weighted by Bethe-Heitler denominator at $Q^2 = 7 \text{ GeV}^2$ . . . . .	125
80	Projected results for the separation of $\sin \phi$ and $\sin(2\phi)$ terms in Fig. 79. . . . .	126
81	Projected data for longitudinal target asymmetry measured in CLAS <sup>++</sup> . . . . .	127
82	The handbag diagrams for DVCS and DDVCS . . . . .	128
83	The handbag diagram for $\Delta$ DVCS . . . . .	129
84	Inelastic DVCS as measured at 4.3 GeV . . . . .	130
85	Asymmetry predicted for the $\Delta$ DVCS at 11 GeV. . . . .	130
86	World data for $R = \sigma_L/\sigma_T$ as a function of $Q^2$ . . . . .	132
87	Preliminary data from CLAS on the longitudinal cross section for $\rho$ production at 4.3 GeV beam energy . . . . .	133
88	Data from HERMES on longitudinal cross sections for $\rho^0$ production from protons at a beam energy of 27 GeV . . . . .	134
89	Projected data on $\rho^0$ production from protons using CLAS <sup>++</sup> . . . . .	135
90	Projected data for a Rosenbluth separation of $ep \rightarrow en\pi^+$ in Hall C at $t = t_{min}$ , $x_B = 0.55$ . . . . .	135
91	Projected CLAS <sup>++</sup> data for a Rosenbluth separation of $ep \rightarrow en\pi^+$ for $x_B = 0.45$ , $-t = 0.5 \text{ GeV}^2$ . . . . .	136
92	Projected CLAS <sup>++</sup> data on the transverse target asymmetry for $\rho^0$ production on protons . . . . .	137
93	Interaction of struck quark and the target spectators[Br02]. . . . .	139
94	Beam SSA: HERMES vs CLAS . . . . .	140

95	Projected transverse spin asymmetry ( $A_{UT}^{\sin\phi}$ ) in single $\pi^+$ production with CLAS at 12 GeV, and expected precision of the extracted $\delta u/u$ . . . . .	142
96	Kinematic coverage at JLab at 12 GeV. . . . .	142
97	Target SSA . . . . .	143
98	The $\Delta\epsilon$ range accessible at $x = 0.8$ in Hall C as a function of $Q^2$ . . . . .	146
99	The $(x, Q^2)$ ranges available with the SHMS and HMS spectrometers for $\Delta\epsilon$ ranges above 0.3. . . . .	146
100	Phase diagram for hadronic matter. . . . .	154
101	Distribution of super-fast quarks for deuteron assuming just two nucleons or including a 5% contribution from a 6-quark bag . . . . .	156
102	The scaling window for $\alpha = 1.4$ . . . . .	157
103	The $Q^2$ -dependence of nuclear transparency . . . . .	159
104	Data from the Hall A $^3He(e, e'p)d$ experiment . . . . .	161
105	Ratio $R = \sigma(p_m = 400 \text{ MeV}/c)/\sigma(p_m = 200 \text{ MeV}/c)$ for $D(e, e'p)$ reaction . . . . .	161
106	Projected uncertainties for a measurement of transparency in $\rho$ -electroproduction in Hall B . . . . .	162
107	Projected uncertainties for measurement of transparency in pion electroproduction in Hall C. . . . .	162
108	Projected uncertainties on the ratio of cross sections at transferred momenta $0.4 \text{ GeV}/c^2$ and $0.8 \text{ GeV}/c^2$ . . . . .	163
109	Variation of the cross sections of $J/\psi$ elastic photoproduction near threshold, for two or three gluon exchange mechanisms . . . . .	164
110	The simplest diagram to reveal hidden color state in deuterium . . . . .	165
111	Artist's concept of the hadronization process in the valence quark regime . . . . .	167
112	Schematic example of possible results for hadronization length scales . . . . .	169
113	Schematic example of possible results for transverse momentum broadening . . . . .	169

114	Statistical error per day of beam time as a function of beam energy for $Q^2=6$ (GeV/c) <sup>2</sup> at various recoil momenta . . . . .	173
115	Statistical error per day of beam time for a beam energy of 11 GeV as a function of missing momenta for a variety of values of $Q^2$ . . . . .	173
116	<sup>3</sup> He( $e, e'pp$ ) $n$ measured with CLAS in one day at $E_0 = 4.4$ GeV . . . . .	174
117	Prediction of the onset of scaling for the <sup>56</sup> Fe( $e, e'$ ) $X$ reaction. . . . .	177
118	The $\pi^+$ form factor . . . . .	180
119	The charged pion photoproduction differential cross-section ratio at a C.M. angle of 90°, as a function of $ t $ . . . . .	180
120	Projected data for the deuteron form factor $F_d(Q^2)$ with an 11 GeV beam. . . . .	182
121	Projected data for the <sup>3</sup> He elastic form factor $F(Q^2)$ with an 11 GeV beam. . . . .	182
122	High energy deuteron photodisintegration differential cross sections scaled by $s^{11}$ . . .	184
123	Projected results for deuteron photodisintegration polarizations with MAD. . . . .	184
124	The scaled differential cross-section for the $n(\gamma, \pi^-p)$ process at a C.M. angle of 90°, as a function of C.M. energy squared $s$ in GeV <sup>2</sup> . . . . .	185
125	The scaled differential cross-section for the $p(\gamma, \pi^+)n$ process at C.M. angle of 90°, as a function of cms energy squared, $s$ , in GeV <sup>2</sup> . . . . .	185
126	The scaled differential cross-section for the $p(\gamma, \pi^0)p$ process at C.M. angle of 90°, as a function of cms energy squared $s$ in GeV <sup>2</sup> . . . . .	187
127	Estimated uncertainties for the induced polarization in $\vec{\gamma}p \rightarrow \vec{p}\pi^0$ for $E_\gamma = 6.9$ GeV, as a function of $\pi^0$ angle. . . . .	187
128	The projected results for nuclear transparency for photo-pion production from a <sup>12</sup> C target . . . . .	188
129	The projected results for nuclear transparency for photo-pion production from a <sup>4</sup> He target . . . . .	188
130	Relative shifts in $Q_{\text{weak}}^e$ and $Q_{\text{weak}}^{\text{proton}}$ from SUSY effects . . . . .	192
131	There has been a steady progression with time in the difficulty of Standard Models tests which employ parity violating electron scattering . . . . .	194



132	Schematic of a 12 GeV Møller experiment . . . . .	195
133	The limits on $C_{2u}$ and $C_{2d}$ . . . . .	198
134	The running of $\sin^2 \theta_W$ in the $\overline{MS}$ scheme showing two measurements: e2ePV/Møller and DIS-Parity . . . . .	200
135	Symmetry breaking and quark mass effects for the light pseudoscalar mesons. . . .	201
136	The importance of $\Gamma_{\eta \rightarrow \gamma \gamma}$ in the measurement of $\mathcal{Q}$ . . . . .	204
137	Two-photon decay width for the $\eta$ meson . . . . .	205
138	The $\eta - \eta'$ mixing angle as determined by a previous Primakoff measurement, $\gamma - \gamma$ collisions, and the projected result with the Jefferson Laboratory 12 GeV upgrade. . . . .	206
139	Differential cross sections (electromagnetic and nuclear) for the $\gamma + {}^4He \rightarrow \eta + {}^4He$ reaction at small angles at 10 GeV. . . . .	207
140	The $\pi^0$ transition form factor . . . . .	211
141	The $\eta$ transition form factor . . . . .	211
142	Three-dimensional CAD drawing of Hall A showing the MAD Spectrometer with one of the present high resolution spectrometers . . . . .	216
143	The field vs. current for the MAD-1 and MAD-2 combined-function magnets . . . .	220
144	A TOSCA plot of the magnitude of the magnetic field in the warm bore of the combined-function MAD magnet . . . . .	221
145	Exterior view of one of MAD's combined function magnets. . . . .	221
146	Plot of the dipole component ( $B_y$ ) and of the field gradient of the MAD-1 magnet along the centerline from the magnet center to 300 cm along the axis. . . . .	222
147	The distribution of extreme trajectories in the MAD Spectrometer . . . . .	226
148	The MAD spectrometer's momentum, $y_0$ , $\theta$ , and $\phi$ resolution . . . . .	228
149	Configuration of the detector package for electrons and hadrons . . . . .	232
150	Number of photo-electrons expected for high-energy electrons in the gas Čerenkov counter . . . . .	235
151	The deviation of velocity from 1 vs. momentum for protons, pions and kaons . . . .	236

152	Layout of the MAD focal plane polarimeter. . . . .	239
153	The upgraded CLAS <sup>++</sup> detector. . . . .	245
154	CLAS <sup>++</sup> Central detector region . . . . .	248
155	Field distribution in the solenoid magnet and the flux return yoke . . . . .	250
156	Perspective view of the central electromagnetic calorimeter inside the solenoid magnet.	252
157	Central calorimeter . . . . .	252
158	Containment versus fraction of plastic. . . . .	254
159	Sampling errors versus fraction of plastic. . . . .	255
160	Perspective view of the central TOF system . . . . .	256
161	Time differences between protons and pions, and between kaons and pions over the 25 cm path length expected for the outer TOF system. . . . .	256
162	Rates summed over all six sectors as a function of threshold at a luminosity of $0.9 \times 10^{34} \text{cm}^{-2} \text{s}^{-1}$ . . . . .	257
163	Cathode chamber view of two superlayers. . . . .	258
164	Concept of a Silicon Strip Detector covering the angular range from $5^\circ$ to $135^\circ$ . . . .	259
165	Concept of the High Threshold Čerenkov Detector located inside the Torus coil arrangement. . . . .	263
166	Optics of the High Threshold Čerenkov Detector . . . . .	264
167	Distribution of the number of photoelectrons $N_{pe}$ for the HTCC in the $\phi - \theta$ plane and the average $N_{pe}$ versus the polar angle . . . . .	265
168	Time differences between protons and pions, and between kaons and pions over the 500 cm path length expected for the outer TOF system. . . . .	266
169	Previous measurements from two prototype tof detectors . . . . .	267
170	Expected resolution for the existing tof detectors . . . . .	267
171	Resolution for various scintillators showing the tradeoff between attenuation length and scintillator decay time. . . . .	269
172	Arrangement of the Inner Calorimeter covering the regions of the torus magnet coils	270

173	Distance between hit positions of the two photons from $\pi^0$ decay at the FEC plane as a function of the pion momentum . . . . .	271
174	$\pi^0$ reconstruction efficiency from the reaction $ep \rightarrow ep\pi^0$ with beam energy of 11.5 GeV . . . . .	272
175	3-d view of a corner of the pre-shower module . . . . .	273
176	CLAS <sup>++</sup> DAQ bloc diagram . . . . .	277
177	Sketch of the High-Momentum Spectrometer . . . . .	279
178	HMS Spectrometer Representative Data . . . . .	280
179	CAD Drawing of the Hall C Spectrometers . . . . .	282
180	SHMS Spectrometer Key Dimensions . . . . .	283
181	Comparison of the Q1 gradients along Z at 7.1 T/m and 8.6 T/m. . . . .	284
182	Magnetic Fields in Q1 at High Current. . . . .	285
183	Cut-Away View of QD30 Magnet . . . . .	285
184	Magnetic Field Magnitude in QD30 Midplane . . . . .	287
185	QD30 Yoke Saturation . . . . .	287
186	QD30 Dipole Field ( $B_y$ ) . . . . .	288
187	QD30 Quadrupole Field . . . . .	288
188	SHMS Pivot with Slider. . . . .	291
189	Hall C Pivot with SOS, SHMS, and HMS Attached . . . . .	291
190	The SHMS-HMS spectrometer pair in two extreme configurations. . . . .	292
191	Rays Tracked through the SHMS by COSY for the SSA Tune . . . . .	297
192	Polynomial Coefficients in the QD Magnetic Field Model . . . . .	298
193	Rays Tracked through the SHMS by COSY for the LSA Tune . . . . .	300
194	The Phase Space Acceptance for the LSA and SSA Tunes . . . . .	303
195	Particle Hit Density at $z = 0$ for Various Target Lengths . . . . .	304

196	Particle Hit Density at Detector Locations for the LSA Tune . . . . .	305
197	Resolutions at the Target vs. $\delta$ for the SSA Tune . . . . .	306
198	Block Diagram of SHMS Detector Arrangement. . . . .	307
199	Measured Residual Distributions in the SOS Wire Chambers . . . . .	309
200	Block diagram of the SHMS Wire Chamber Assembly . . . . .	310
201	Pion/Kaon Discrimination from $dE/dx$ . . . . .	310
202	Time-of-Flight Relative to Electrons vs. Momentum . . . . .	311
203	Placement of the Scintillator and Čerenkov Hodoscopes . . . . .	312
204	Summary of the SHMS Particle Identification Resolving Power . . . . .	315
205	Linearity and Resolution of a Lead Glass Calorimeter . . . . .	316
206	Electron – Pion Discrimination Power of a Lead Glass Calorimeter . . . . .	317
207	Pressure and Photoelectron Yield for the $C_4F_{10}$ Čerenkov . . . . .	319
208	Schematic Design for the SHMS Heavy Gas Čerenkov Detector. . . . .	320
209	Pion Efficiency of TRDs as a Function of the Detector Length . . . . .	322
210	TRD Module and Output Signals . . . . .	322
211	Hadron Velocity $1 - \beta$ as a Function of Momentum . . . . .	324
212	SHMS Detector Package using the Focal Plane Polarimeter . . . . .	325
213	A schematic view of the HALL D photon beam line. . . . .	329
214	The effect of collimation on the coherent bremsstrahlung spectrum . . . . .	330
215	Maximum polarization <i>vs</i> radiator-collimator distance for a coherent peak at 9 GeV	331
216	A 3D cutaway view of the GLUEX detector and schematic diagram of its major subsystems . . . . .	332
217	The GLUEX Start Counter and Central Tracker. . . . .	334
218	The Forward Calorimeter. . . . .	337
219	The GLUEX Barrel Calorimeter . . . . .	338

220	Sketch of a upstream photon veto segment . . . . .	340
221	Particle Identification in GLUEX . . . . .	341
222	The Čerenkov detector . . . . .	342
223	Block diagram of prototype FADC board. . . . .	344
224	Block diagram of prototype TDC board. . . . .	345
225	Simulated PWA Results in GLUEX . . . . .	350
226	The results of a double-blind Monte Carlo exercise showing the $J^{PC} = 1^{-+}$ exotic wave . . . . .	351
227	Polarization in PWA . . . . .	351
228	Side view of the experimental setup for $\eta$ and $\eta'$ two-gamma decay width measurements	353
229	Focal plane detectors for the proposed high energy tagging system . . . . .	355
230	Background events in the calorimeter projected to the horizontal (dispersive) plane for a photon tagging (photoproduction) run. . . . .	356
231	Energy distribution in calorimeter corresponding to the events in Fig. 230 (photon run). . . . .	356
232	Monte Carlo simulation of expected yield as a function of angle for $\eta\gamma\gamma$ events on ${}^4He$ .	358
233	Coulomb photoproduction of the $\eta'$ as a function of angle. . . . .	359

## List of Tables

1	Selected key parameters of the CEBAF 12 GeV Upgrade . . . . .	35
2	The design characteristics of the MAD spectrometer shown along with HRS performance. . . . .	37
3	CLAS <sup>++</sup> : acceptance and resolution . . . . .	41
4	CLAS <sup>++</sup> : operating luminosity . . . . .	41
5	HMS performance and SHMS specifications . . . . .	44
6	Summary of the GlueX detector's characteristics. . . . .	46
7	Photoproduction cross sections . . . . .	63
8	Comparison of the figure of merit for large $x$ measurements of the $A_1^n$ structure function at HERA, SLAC, and JLab. . . . .	102
9	Leading twist transverse momentum dependent distribution functions . . . . .	139
10	CLAS <sup>++</sup> Program Summary - Quark Transverse Momentum and Nucleon Orbital Angular Momentum in Semi-inclusive DIS . . . . .	144
11	The values of nuclear transparencies for $J/\psi$ propagation . . . . .	166
12	Parameters for the SLAC E158 experiment from the proposal compared to those for a potential Jefferson Lab experiment at 12 GeV. . . . .	193
13	Projected uncertainties for ongoing SLAC E158 (from the proposal) and for a potential Jefferson Lab measurement at 12 GeV. . . . .	194
14	Possible sources of systematic uncertainty in the measurement of $A_d$ . . . . .	198
15	The design characteristics of the MAD spectrometer shown along with the HRS performance. . . . .	214
16	The parameters necessary to evaluate the cryogenic stability by the Steckly criteria for the MAD Magnets . . . . .	222
17	Properties of the large-acceptance spectrometer magnets. . . . .	223
18	Performance estimates for the MAD spectrometer . . . . .	225

19	The first-order TRANSPORT matrices in natural units (m) for various configurations of the MAD spectrometer . . . . .	227
20	MAD detector parameters . . . . .	230
21	Single rates in MAD detector (kHz) with $E_{beam} = 11$ GeV , $I_{beam} = 70 \mu\text{A}$ , and a 15 cm long liquid hydrogen target. . . . .	231
22	Geometrical specifications for scintillator planes. . . . .	233
23	Collection efficiency of photons for each phototube. . . . .	235
24	The momentum threshold to produce Čerenkov radiation. . . . .	237
25	Equipment needed for the triggering system of the MAD detector package . . . . .	240
26	Comparison of Pb-Glass, $\text{PbF}_2$ , and $\text{PbWO}_4$ calorimeter properties. . . . .	241
27	Key parameters of Beam Quality - present and with upgrade . . . . .	243
28	Central Electromagnetic Calorimeter parameters . . . . .	251
29	Rise time for various PMTs. The existing CLAS detector uses XP2262 PMTs. . . . .	268
30	Properties of several scintillators. The existing CLAS detector utilizes BC-408 scintillator. . . . .	268
31	HMS Performance and SHMS Specifications . . . . .	281
32	Q1 comparison between HMS at 1010 A and SHMS at 1291 A. . . . .	284
33	SHMS QD30 Magnet Parameters. . . . .	289
34	SHMS Optics Parameters for SSA and LSA Tunes . . . . .	299
35	Sensitive Areas of the Detectors . . . . .	307
36	Nominal Dimensions of the Hodoscope Elements . . . . .	313
37	Operating parameters for an experiment using the coherent bremsstrahlung beam. . . . .	346
38	Rates and Processing Requirements . . . . .	347
39	Estimation of the experimental uncertainties for $\Gamma(\eta \rightarrow \gamma\gamma)$ measurement. . . . .	359

## Contributors to the pCDR

Name	Institution
Abbott, D.	Jefferson Lab
Ambrozewicz, P.	Temple University
Abu-raddad, L.J.	Florida State University
Adams, G.	Rensselaer Polytechnic Institute
Afanasev, A.	Jefferson Lab
Aghalaryan, A.	Yerevan Physics Institute
Ahmidouch, A.	North Carolina A&T State University
Akushevich, I.	North Carolina Central University
Amatuni, T.	Yerevan Physics Institute
Ananyan, S.	College of William and Mary
Angelescu, T.	Bucharest University
Anghinolfi, M.	Istituto Nazionale di Fisica Nucleare, Genova
Aniol, K.	California State at Los Angeles
Anklin, H.	Florida International University
Annand, J.	University of Glasgow
Anselmino, M.	Istituto Nazionale di Fisica Nucleare, Torino
Anthony, I.	University of Glasgow
Armstrong, C.	Jefferson Lab
Armstrong, D.	College of William and Mary
Arndt, R.	George Washington University
Arrington, J.	Argonne National Laboratory
Arvieux, J.	C.E.A. SACLAY
Asaturyan, R.	Yerevan Physics Institute
Assamagan, K.	Hampton University
Avakian, H.	Jefferson Lab
Averett, T.	College of William and Mary
Avery, S.	Hampton University
Aznauryan, I.	Yerevan Physics Institute
Bailey, K.	Argonne National Lab
Baker, O. K.	Hampton University
Ball, J.	C.E.A. SACLAY
Barbosa, F.	Jefferson Lab
Barden, H.	University of Heidelberg
Barnes, T.	Oak Ridge National Laboratory
Battaglieri, M.	Istituto Nazionale di Fisica Nucleare, Genova
Beard, K.	Jefferson Lab
Beck, D.	University of Illinois at Urbana-Champaign
Bedlinsky, I.	Institute of Theoretical and Experimental Physics, Moscow
Beedoe, S.	North Carolina A&T State University
Beise, E.	University of Maryland
Bektasoglu, M.	Ohio University
Belitsky, A.	University of Maryland
Benesch, J.	Jefferson Lab
Benhar, O.	Istituto Nazionale di Fisica Nucleare, Sanita
Benmerrouche, M.	University of Saskatchewan
Bennhold, C.	George Washington University
Berman, B.	George Washington University
Bernstein, A.	Massachusetts Institute of Technology
Bertin, P.	University of Clermont-Ferrand
Bertozi, W.	Massachusetts Institute of Technology
Beuville, E.	INDIGO Systems Corp
Bianchi, N.	Istituto Nazionale di Fisica Nucleare, Frascati
Bimbot, L.	Institute de Physique Nucleaire, Orsay



Bird, I.	CERN
Biselli, A.	Carnegie Mellon University
Black, T.	Massachusetts Institute of Technology
Blok, H.	Vrije Universiteit
Bodyagin, V.	Moscow State University
Boeglin, W.	Florida International University
Boglione, M.	Vrije Universiteit
Boiarinov, S.	Institute of Theoretical and Experimental Physics, Moscow
Boluchevskii, A.	Moscow State University
Bossingham, R.	Lawrence Berkeley Laboratory
Bosted, P.	University of Massachusetts
Boswell, M.	Randolph-Macon Woman's College
Bowman, D.	Los Alamos National Laboratory
Boyarinov, S.	Jefferson Lab
Boyce, J.	Jefferson Lab
Branford, D.	Edinburgh University
Brash, E.	University of Regina
Breuer, H.	University of Maryland
Brindza, P.	Jefferson Lab
Brisco, W.	George Washington University
Brodsky, S.	Stanford Linear Accelerator Facility
Brooks, W.	Jefferson Lab
Brower, R.	Boston University
Brown, D.	University of Maryland
Bruell, A.	Massachusetts Institute of Technology
Buck, W.	University of Washington
Burkert, V.	Jefferson Lab
Burks, M.	Lawrence Berkeley Laboratory
Burtin, E.	C.E.A. Saclay
Camsonne, A.	University de Clermont Ferrand
Capstick, S.	Florida State University
Cardarelli, F.	University of Rome
Cardman, L.	Jefferson Lab
Carlini, R.	Jefferson Lab
Carlson, C.	College of William and Mary
Carman, D.	Ohio University
Cates, G.	University of Virginia
Cha, J.	Mississippi State University
Chattopadhyay, S.	Jefferson Lab
Chang, C. C.	University of Maryland
Chang, T.	University of Illinois at Urbana-Champaign
Chant, N.	University of Maryland
Chen, J. -P.	Jefferson Lab
Choi, S.	Temple University
Christy, M.	Hampton University
Chudakov, E.	Jefferson Lab
Chung, S.	Brookhaven National Laboratory
Cisbani, E.	Istituto Nazionale di Fisica Nucleare Roma
Clark, R.	Carnegie-Mellon University
Close, F.	University of Oxford
Coffman, D.	Cornell University
Cole, P.	University of Texas at El Paso
Collins, G.	University of Maryland
Cords, D.	Jefferson Lab
Coriano, C.	Istituto Nazionale de Fisica Nucleare, Genova
Corvisiero, P.	Istituto Nazionale di Fisica Nucleare, Genova
Cowley, A.	University Stellenbosch
Crabb, D.	University of Virginia
Crannell, H.	Catholic University of America

Cummings, J.	Rensselaer Polytechnic Institute
Cummings, W.	Argonne National Laboratory
Cwetanski, P.	Lawrence Berkeley Laboratory
Dale, D.	University of Kentucky
Danagouliau, S.	North Carolina A&T State University
Davidson, R.	Princeton Plasma Physics Laboratory
Day, D.	University of Virginia
de Jager, K.	Jefferson Lab
De Leo, R.	Istituto Nazionale di Fisica Nucleare, Bari
de Witt Huberts, P.	NIKHEF
Degtiarenko, P.	Jefferson Lab
Demianov, A.	Moscow State University
Denisov, S.	Institute for Higher Energy Physics, Protvino
Dennis, L.	Florida State University
DeSanctis, E.	Istituto Nazionale di Fisica Nucleare, Frascati
De Vita, R.	Istituto Nazionale de Fisica Nucleare, Genova
Deur, A.	CEA, SACLAY
Didelez, J.-P.	IPN ORSAY
Diehl, M.	Stanford Linear Accelerator Center
Dieterich, S.	Rutgers University
Djalali, C.	University of South Carolina
Dodge, G.	Old Dominion University
Domingo, J.	Jefferson Lab
Dor, D.	C.E.A. Saclay
Doughty, D.	Christopher Newport University
Dragovitsch, P.	Florida State University
Dugger, M.	Arizona State University
Duncan, F.	Queens University
Dunne, J.	Mississippi State University
Dutta, D.	Massachusetts Institute of Technology
Dytman, S.	University of Pittsburgh
Dzierba, A.	Indiana University
Eckhardt, R.	Ruhr University-Bonn
Eden, T.	Norfolk State University
Edwards, R/	Jefferson Lab
Efremov, A.	Joint Institute for Nuclear Research, Moscow
Egiyan, H.	Jefferson Lab
Egiyan, K.	Yerevan Physics Institute
Elouadrhiri, L.	Jefferson Lab
Empl, A.	Rensselaer Polytechnic Institute
Ent, R.	Jefferson Lab
Epstein, M.	California State University
Ernst, D.	Vanderbilt University
Eugenio, P.	Florida State University
Ewell, L.	University of Maryland
Eyraud, L.	Institut des Sciences Nucleaires de Grenoble
Fang, G.	Harvard University
Fantoni, S.	University of Trieste
Fedotov, G.	Moscow State University
Fedyakin, N.	Institute for Higher Energy Physics, Moscow
Fenker, H.	Jefferson Lab
Feuerback, R.	
Jefferson Lab) Ficenec, J.	Virginia Polytechnic Institute
Filippone, B.	California Institute of Technology
Finn, M.	College of William and Mary
Fivozinsky, S.	U.S. Department of Energy
Forest, J.	Louisiana Tech University
Forest, T.	Louisiana Tech University
Fortune, T.	University of Pennsylvania

Fowler, M.	Jefferson Lab
Fox, G.	Indiana University
Frankfurt, L.	Tel Aviv University
Franklin, G.	Carnegie Mellon University
Freund, A.	Universität Regensburg
Freyberger, A.	Jefferson Lab
Frois, B.	C.E.A. Saclay
Frolov, V.	Rensselaer Polytechnic Institute
Frullani, S.	Istituto Nazionale di Fisica Nucleare, Roma
Funsten, H.	College of William and Mary
Furget, C.	Institut des Sciences Nucleaires de Grenoble
Furic, M.	University of Zagreb
Gai, M.	Yale University
Gan, L.	Hampton University
Gao, H.	Massachusetts Institute of Technology/Duke University
Garçon, M.	C.E.A. Saclay
Garibaldi, F.	Istituto Nazionale di Fisica Nucleare, Roma
Garrow, K.	TRIUMF
Gaskell, D.	Jefferson Lab
Gasparian, A.	North Carolina A & T/Jefferson lab
Gayou, O.	Massachusetts Institute of Technology
Gavalian, G.	University of New Hampshire
Geesaman, D.	Argonne National Laboratory
Gilad, S.	Massachusetts Institute of Technology
Gilfoyle, G.	University of Richmond
Gilman, R.	Rutgers University
Giovanni, S.	Istituto Nazionale di Fisica Nucleare
Glamazdin, A.	Kharkov State University
Glashausser, C.	Rutgers University
Godfrey, S.	Carleton University
Goity, J.	Hampton University/Jefferson Lab
Golovach, E.	Moscow State University
Gomez, J.	Jefferson Lab
Gothe, R.	University of South Carolina
Gorokhov, A.	Institute for Higher Energy Physics, Moscow
Grach, I.L.	Institute of Theoretical and Experimental Physics, Moscow
Gribushin, A.	Moscow State University
Griffioen, K.	College of William and Mary
Gross, F.	College of William and Mary/Jefferson Lab
Gueye, P.	Hampton University
Guidal, M.	I.P.N. Orsay
Guichon, P.	C.E.A. Saclay
Gustafsson, K.	University of Maryland
Guzey, V.	Universitat Bochum
Gyulassy, M.	Columbia University
Gyurjyan, V.	Jefferson Lab
Hadjidakis, C.	Institut de Physique Nucleaire, Orsay
Hafidi, K.	Argonne National Laboratory
Hansen, O.	Jefferson Lab
Hansper, J.	Ruhr University, Bochum
Harvey, M.	Hampton University
Hashimoto, O.	Tohoku University
Heddle, D.	Christopher Newport University
Heinz, D.	Indiana University
Hersman, B.	University of New Hampshire
Heyes, G.	Jefferson Lab
Hicks, K.	Ohio University
Hicks, R.	University of Massachusetts
Higinbotham, D. W.	Jefferson Lab

Hinton, W.	Hampton University
Holt, R.	Argonne National Lab
Holtrop, M.	University of New Hampshire
Hourany, E.	IPN-ORSAY
Hubbard, J.	Christopher Newport University
Huber, G.	University of Regina
Hungerford, E.	University of Houston
Huston, J.	Michigan State University
Hutton, A.	Jefferson Lab
Hyde-Wright C.	Old Dominion University
Iodice, M.	Istituto Nazionale di Fisica Nucleare, Roma
Ireland, D.	University of Glasgow
Isgur, N.	Jefferson Lab
Ishkhanov, B.	Moscow State University
Ito, M.	Jefferson Lab
Jackson, C.	Hampton University
Jackson, H.	Argonne National Laboratory
Jastrzemski, E.	Jefferson Lab
Jenning, B.	TRIUMF
Jeschonnek, S.	Ohio State University
Ji, C-R.	North Carolina State University
Ji, X.	University of Maryland
Jiang, X.	Rutgers University
Johnson, M.	Los Alamos National Laboratory
Jones, C.	California Institute of Technology
Jones, M.	Jefferson Lab
Jones, R.	University of Connecticut
Joo, K.	University of Connecticut
Jourdan, J.	University of Basel
Kaminski, R.	Henryk Niewodniczanski Institute of Nuclear Physics
Kashy, D.	Jefferson Lab
Katramatou, M.	Kent State University
Keister, B.	National Science Foundation
Keith, C.	Jefferson Lab
Kellie, J.	University of Glasgow
Keppel, C.	Hampton University
Khandaker, M.	Norfolk State University
Kharzeev, D.	RIKEN BNL
Kim, W.	Kyungpook National University, South Korea
Kinney, E.	University of Colorado
Kino, K.	Tohoku University
Klabucar, D.	Zagreb University
Klein, A.	Old Dominion University
Klein, F.	Catholic University of America
Klimenko, A.	Institute for High Energy Physics, Protvino
Kodolova, O.	Moscow State University
Koltenuk, D.	University of Pennsylvania
Kopeliovich, B.	Max Planck Institut für Kernphysik
Kornicer, M.	University of Connecticut
Korotkikh, V.	Moscow State University
Kossov, M.	Institute of Theoretical and Experimental Physics, Moscow
Kostin, M.	Moscow State University
Kotzinian, B.	CERN
Koubarovski, V.	Rensselaer Polytechnic Institute
Kovaltchouk, V.	University of Regina
Kovar, D.	U.S. Department of Energy
Kox, S.	Institut des Sciences Nucleaires de Grenoble
Kramer, L.	Florida International University
Kruglov, N.	Moscow State University

Kuhlmann, S.	Argonne National Laboratory
Kuhn, J.	Carnegie Mellon University
Kuhn, S.	Old Dominion University
Kuleshov, S.	Institute of Theoretical and Experimental Physics, Moscow
Kumar, K.	University of Massachusetts
Kumbartzki, G.	Rutgers University
Kurilov, A.	University of Connecticut
Kuss, M.	Jefferson Lab
Laget, J. M.	CEA Saclay
Landshoff, P.	University of Cambridge
Lassila, K.	Iowa State University
Lassiter, S.	Jefferson Lab
Lawrence, D.	University of Massachusetts
Leader, E.	Birkbeck College
Lebed, R.	Arizona State University
Leemann, C.	Jefferson Lab
Leinweber, D.	University of Adelaide
Leone, T.	Istituto Nazionale di Fisica Nucleare, Torino
LeRose, J.	Jefferson Lab
Lesniak, L.	Henryk Niewodniczanski Institute of Nuclear Physics
Levelt, J.	University of Erlangen-Nuernberg
Lewis, R.	University of Regina
Liang, M.	Jefferson Lab
Lieb, J.	George Mason University
Ligterink, N.	University of Pittsburgh
Lim, K.	Brown University
Lindgren, R.	University of Virginia
Liuti, S.	University of Virginia
Livingston, K.	University of Glasgow
Liyanage, N.	Jefferson Lab/University of Virginia
Lolos, G.	University of Regina
Lolos, J.	University of Pittsburgh
Loman, E.	Massachusetts Institute of Technology
Londergan, T.	Indiana University
Lorenzon, W.	University of Michigan
Lourie, R.	Renaissance Tech
Lu, D.	University of Adelaide
Lhuillier, D.	DAPNIA/SPhN, CEA Saclay
Liu, J.	University of Maryland
Lung, A.	Jefferson Lab
MacGregor, C.	University of Glasgow
MacGregor, D.	University of Glasgow
McCormick, K.	Rutgers University
McLerran, L.	Brookhaven National Laboratory
Mack, D.	Jefferson Lab
Macleod, R.	Jefferson Lab
Madey, R.	Jefferson Lab
Magahiz, R.	Carnegie-Mellon University
Majewski, S.	Jefferson Lab
Makins, N.	University of Illinois
Mammei, J.	University of Texas-El Paso
Manak, J.	Jefferson Lab
Marchand, C.	CEA Saclay
Margaryan, A.	Yerevan Physics Institute
Margaziotis, D.	California State University
Markov, N.	Moscow State University
Markowitz, P.	Florida International University
Martoff, C.	Temple University
McGeorge, C.	University of Glasgow

McIntyre, J.	College of William and Mary
McKee, P.	University of Virginia
McNabb, J.	Carnegie Mellon University
Meadows, B.	University of Cincinnati
Mecking, B.	Jefferson Lab
Meekins, D.	Jefferson Lab
Melnitchouk, W.	Jefferson Lab
Mestayer, M.	Jefferson Lab
Meyer, C.	Carnegie-Mellon University
Meziani, Z. E.	Temple University
Michaels, R.	Jefferson Lab
Mihul, A.	University of Bucharest
Mikhailov, K.	Institute of Theoretical and Experimental Physics, Moscow
Milana, J.	University of Maryland
Milbrath, B.	Eastern Kentucky University
Miller, G.	University of Washington
Miller, M.	University of Illinois
Milner, R.	Massachusetts Institute of Technology
Minehart, R.	University of Virginia
Mirazita, M.	Istituto Nazionale de Fisica Nucleare, Frascati
Mischke, R.	Los Alamos National Laboratory
Miskimen, R.	University of Massachusetts
Mitchell, J.	Jefferson Lab
Mkrtchyan, H.	Yerevan Physics Institute
Mohring, R.	University of Maryland
Moiseev, V.	Jefferson Lab
Monaghan, P.	Massachusetts Institute of Technology
Morfin, J.	Fermi National Accelerator Laboratory
Morninstar, C.	Carnegie Mellon University
Mtingwa, S.	North Carolina A&T State University
Mucifora, V.	Istituto Nazionale di Fisica Nucleare, Frascati
Mueller, A.	Columbia University
Mueller, J.	University of Pittsburgh
Mukhopadhyay, N.	Rensselaer Polytechnic Institute
Mulders, P.	NIKHEF
Murgia, F.	Istituto Nazionale di Fisica Nucleare, Cagliari
Mustapha, B.	Argonne National Laboratory
Mutchler, G.	Rice University
Nanda, S.	Jefferson Lab
Napolitano, J.	Rensselaer Polytechnic Institute
Nappi, E.	Istituto Nazionale di Fisica Nucleare, Bari
Narodetskii, I.	Institute of Theoretical and Experimental Physics, Moscow
Nathan, A.	University of Illinois at Urbana-Champaign
Nefkens, B.	University of California at Los Angeles
Nelyubin, V.	University of Virginia
Nemchik, J.	Institute of Experimental Physics SAV
Niculescu, G.	University of Virginia
Niculescu, I.	James Madison University
Niczyporuk, B.	Jefferson Lab
Nikolaev, N.	Forschungszentrum Julich
Norum, B.	University of Virginia
O'Brien, J.	The Catholic University of America
Olness, F.	Southern Methodist University
Osipenko, M.	Moscow State University
Ostrovidov, A.	Florida State University
Owens, B.	University of Glasgow
Owens, J.	Florida State University
Pace, E.	University of Rome
Page, P.	Los Alamos National Laboratory

Palounek, A.	Los Alamos National Laboratory
Pang, A.	North Carolina State University
Papandreou, Z.	University of Regina
Park, K.	Kyungpook National University, South Korea
Pasyuk, E.	Arizona State University
Peng, J.-C.	University of Illinois at Urbana-Champaign
Perdrisat, C.	College of William and Mary
Perrino, R.	Istituto Nazionale di Fisica Nucleare, Lecce
Petratos, G.	Kent State University
Piasetzky, E.	Tel Aviv University
Pichowsky, M.	Indiana University
Piekarewicz, J.	Florida State University
Piller, G.	University of Munich
Pitt, M.	Virginia Tech
Pivnyuk, N.	Institute of Theoretical and Experimental Physics, Moscow
Pogorelko, O.	Institute of Theoretical and Experimental Physics, Moscow
Polezhaeva, I.	Institute for High Energy Physics, Protvino
Polyakov, M.	Universitat Bochum
Popov, S.	Budker Institute of Nuclear Physics
Potterveld, D.	Argonne National Laboratory
Pozdnyakov, S.	Institute of Theoretical and Experimental Physics, Moscow
Freedom, B.	University of South Carolina
Price, J.E.	Louisiana Technical Institute
Price, J.W.	University of California at Los Angeles
Prout, D.	Kent State University
Puga, A.	University of Texas at El Paso
Pumplin, J.	Michigan State University
Punjabi, V.	Norfolk State University
Qiu, J.	Iowa State University
Quinn, B.	Carnegie-Mellon University
Radysushkin, A.	Old Dominion University/Jefferson Lab
Ramsey-Musolf, M.	Caltech/Univ. of Connecticut
Rangacharyulu, C.	University of Saskatchewan
Ransome, R.	Rutgers University
Raue, B.	Florida International University
Real, J.	Institute des Sciences Nucleaires de Grenoble
Reece, C.	Jefferson Lab
Reimer, P. E.	Argonne National Lab
Reinhold, J.	Florida International University
Reitz, B.	Jefferson Lab
Retiere, F.	Subatech Nantes Fr.
Ribeiro, E.	CENE, Portugal
Riccardi, G.	Florida State University
Ricco, G.	Istituto Nazionale di Fisica Nucleare, Genova
Richards, D.	Jefferson Lab
Ripani, M.	Istituto Nazionale di Fisica Nucleare, Genova
Ritchie, B.	Arizona State University
Roberts, W.	Old Dominion University/Jefferson Lab
Roblin, Y.	Clermont-Ferrand University
Roche, J.	Jefferson Lab
Roedelbronn, M.	University of Illinois at Urbana-Champaign
Ronchetti, F.	Istituto Nazionale de Fisica Nucleare, Frascati
Rondon, O.	University of Virginia
Roos, P.	University of Maryland
Rosner, G.	University of Glasgow
Rossi, P.	Istituto Nazionale de Fisica Nucleare, Frascati
Rubin, P.	University of Richmond
Rutt, P.	University of Georgia
Sabatini, F.	Old Dominion University

Saha, A.	Jefferson Lab
Saito, K.	Tohoku College
Saito, T.	Tohoku University
Salgado, C.	Norfolk State University
Salme, G.	Istituto Nazionale di Fisica Nucleare
Samoilenko, V.	Institute for Higher Energy Physics, Moscow
Sapunenko, V.	Jefferson Lab
Sargsian, M.	Florida International University
Sarty, A.	St. Mary's University
Sarycheva, L.	Moscow State University
Savkli, C.	University of Pittsburgh
Sawafta, R.	North Carolina A&T State University
Schaefer, A.	Regensburg University
Schiavilla, R.	Old Dominion University/Jefferson Lab
Schoch, B.	University of Bonn
Schukin, A.	Institute for Higher Energy Physics, Protvino
Schumacher, R.	Carnegie Mellon University
Scopetta, S.	Perugia University
Skopik, D.	Jefferson Lab
Scott, E.	Indiana University
Seely, M.	Jefferson Lab
Segal, J.	Jefferson Lab
Segel, R.	Northwestern University
Seth, K.	Northwestern University
Sharabian, Y.	Jefferson Lab
Sher, M.	College of William and Mary
Shin, B.	Kyungpook National University, South Korea
Shvedunov, N.	Moscow State University
Silvano, S.	Istituto Nazionale di Fisica Nucleare, Rome
Simula, S.	Istituto Nazionale di Fisica Nucleare, Rome
Sinclair, C.	Jefferson Lab
Širca, S.	University of Ljubljana
Skrinsky, A.	Budker Institute for Nuclear Physics
Slifer, K.	Temple University
Smirnov, N.	Yale University
Smith, C.	University of Virginia
Smith, E.	Jefferson Lab
Smith, G.	Jefferson Lab
Smith, P.	Indiana University
Smith, Y.	Jefferson Lab
Snellings, R.	Lawrence Berkeley Laboratory
Sober, D.	Catholic University of America
Soldatov, M.	Institute for High Energy Physics, Protvino
Solodov, E.	Budker Institute of Nuclear Physics
Solvignon, P.	Temple University
Souder, P.	Syracuse University
Stavinsky, A.	Institute of Theoretical and Experimental Physics, Moscow
Steffen, C.	Indiana University
Stepanyan, S.	Jefferson Lab
Stoler, P.	Rensselaer Polytechnic Institute
Strakovsky, I.	George Washington University
Strauch, S.	George Washington University
Strikman, M.	Pennsylvania State University
Sulanke, T.	Indiana University
Suleiman, R.	Massachusetts Institute of Technology
Sulkosky, V.	College of William and Mary
Swanson, E.	University of Pittsburgh
Swat, M.	Indiana University
Szczepaniak, A.	Indiana University



Tadevosyan, V.  
 Taiuti, M.  
 Takagi, F.  
 Tan, C. Tang, L.  
 Taylor, M.  
 Tedeschi, D.  
 Teige, S.  
 Templon, J.  
 Teodorescu, L.  
 Terasawa, T.  
 Teryaev, O.  
 Thomas, A.  
 Timmer, C.  
 Tippens, B.  
 Tipton, B.  
 Todor, L.  
 Trentalange, S.  
 Tsubota, H.  
 Tung, W.K.  
 Ulmer, P.  
 Ungaro, M.  
 Urciuoli, G.  
 Urner, D.  
 Uzzle, A.  
 Va'vra, J.  
 van den Brand, J.  
 Van Orden, W.  
 Vanderhaeghen, M.  
 Vineyard, M.  
 Vlahovic, B.  
 Vlassov, A.  
 Volmer, J.  
 Voutier, E.  
 Vulcan, W.  
 Walcher, T.  
 Wang, K.  
 Warren, G.  
 Watson, C.  
 Watts, D.  
 Weilhammer, P.  
 Weiman, H.  
 Weinstein, J.  
 Weinstein, L.  
 Weise, W.  
 Weisenberger, D.  
 Welch, P.  
 Welsh, R.  
 Weygand, D.  
 Whitmore, J.  
 Whitney, R.  
 Wieman, H.  
 Wijesooriya, K.  
 Williams, A.  
 Williams, R.  
 Wilson, J.  
 Winn, D.  
 Wise, J.  
 Wojtsekhowski, B.  
 Wolfe, C.

Yerevan Physics Institute  
 Istituto Nazionale di Fisica Nucleare Genova  
 Tohoku University  
 Hampton University  
 Jefferson Lab  
 University of South Carolina  
 Indiana University  
 University of Georgia  
 University of Bucharest  
 Tohoku University  
 Joint Institute for Nuclear Research, Moscow  
 University of Adelaide  
 Jefferson Lab  
 U.S. Department of Energy  
 California Institute of Technology  
 Carnegie Mellon University  
 University of California at Los Angeles  
 Tohoku University  
 Michigan State University  
 Old Dominion University  
 Istituto Nazionale de Fisica Nucleare, Genova  
 Istituto Nazionale di Fisica Nucleare, Rome  
 Cornell University  
 Hampton University  
 Stanford Linear Accelerator Center  
 Vrije Universiteit  
 Jefferson Lab  
 University Mainz  
 University of Richmond  
 North Carolina Central University  
 Institute of Theoretical and Experimental Physics, Moscow  
 Vrije Universiteit  
 Institut des Sciences Nucleaires de Grenoble  
 Jefferson Lab  
 University of Mainz  
 University of Virginia  
 Jefferson Lab  
 Jefferson Lab  
 University of Glasgow  
 CERN  
 Lawrence Berkeley Laboratory  
 University of Mississippi  
 Old Dominion University  
 University of Munich  
 Jefferson Lab  
 Oregon State University  
 Jefferson Lab  
 Jefferson Lab  
 Pennsylvania State University  
 Jefferson Lab  
 Lawrence Berkeley Laboratory  
 Duke University  
 University of Adelaide  
 Jefferson Lab  
 Jefferson Lab  
 Fairfield University  
 Jefferson Lab  
 Jefferson Lab  
 Indiana University

Wolin, E.	Jefferson Lab
Wood, S.	Jefferson Lab
Workman, R.	George Washington University
Wright, S.	University of Adelaide
Xiang, H.	Massachusetts Institute of Technology
Yan, C.	Jefferson Lab
Yang, J.	Chungnam University
Yarulin, R.	Kyungpook National University, South Korea
Yegneswaran, A.	Jefferson Lab
Yershov, A.	Moscow State University
Zakharov, B.	Institute of Experimental Physics
Zeidman, B.	Argonne National Laboratory
Zheng, X.	Argonne National Laboratory
Zhang, J.	Rensselaer Polytechnic Institute
Zhu, L. Y.	Massachusetts Institute of Technology
Zorn, C.	Jefferson Lab